HYDROCLIMATOLOGY OF THE GREAT LAKES REGION OF NORTH AMERICA

EDITED BY: Julie A. Winkler, Adam Burnett and Galina Guentchev
PUBLISHED IN: Frontiers in Water

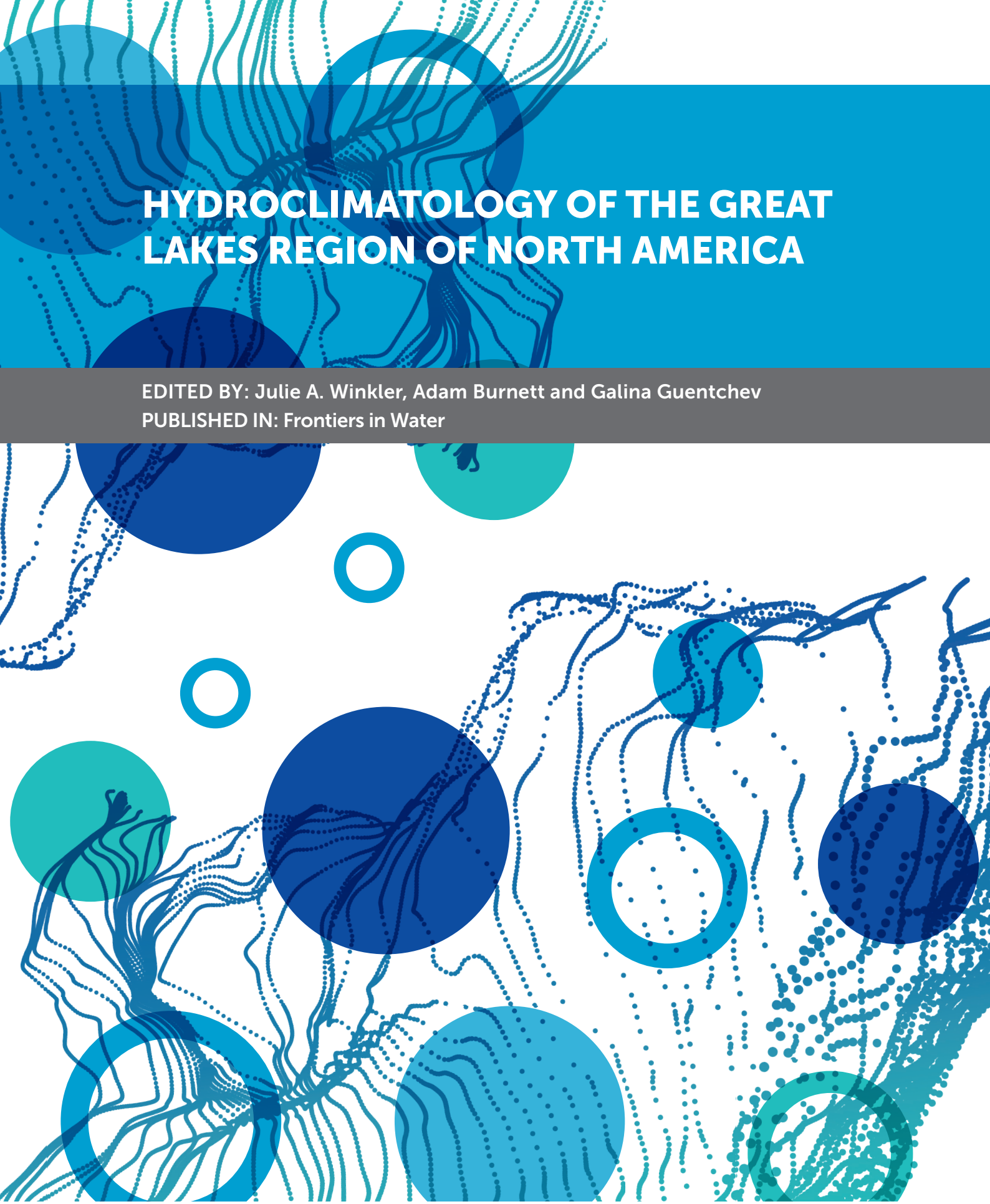

frontiers Research Topics

frontiers

ISSN 1664-8714
ISBN 978-2-83250-545-8
DOI 10.3389/978-2-83250-545-8

About Frontiers

Frontiers is more than just an open-access publisher of scholarly articles: it is a pioneering approach to the world of academia, radically improving the way scholarly research is managed. The grand vision of Frontiers is a world where all people have an equal opportunity to seek, share and generate knowledge. Frontiers provides immediate and permanent online open access to all its publications, but this alone is not enough to realize our grand goals.

Frontiers Journal Series

The Frontiers Journal Series is a multi-tier and interdisciplinary set of open-access, online journals, promising a paradigm shift from the current review, selection and dissemination processes in academic publishing. All Frontiers journals are driven by researchers for researchers; therefore, they constitute a service to the scholarly community. At the same time, the Frontiers Journal Series operates on a revolutionary invention, the tiered publishing system, initially addressing specific communities of scholars, and gradually climbing up to broader public understanding, thus serving the interests of the lay society, too.

Dedication to Quality

Each Frontiers article is a landmark of the highest quality, thanks to genuinely collaborative interactions between authors and review editors, who include some of the world's best academicians. Research must be certified by peers before entering a stream of knowledge that may eventually reach the public - and shape society; therefore, Frontiers only applies the most rigorous and unbiased reviews.
Frontiers revolutionizes research publishing by freely delivering the most outstanding research, evaluated with no bias from both the academic and social point of view. By applying the most advanced information technologies, Frontiers is catapulting scholarly publishing into a new generation.

What are Frontiers Research Topics?

Frontiers Research Topics are very popular trademarks of the Frontiers Journals Series: they are collections of at least ten articles, all centered on a particular subject. With their unique mix of varied contributions from Original Research to Review Articles, Frontiers Research Topics unify the most influential researchers, the latest key findings and historical advances in a hot research area! Find out more on how to host your own Frontiers Research Topic or contribute to one as an author by contacting the Frontiers Editorial Office: frontiersin.org/about/contact

HYDROCLIMATOLOGY OF THE GREAT LAKES REGION OF NORTH AMERICA

Topic Editors:
Julie A. Winkler, Michigan State University, United States
Adam Burnett, Colgate University, United States
Galina Guentchev, Met Office, United Kingdom

Citation: Winkler, J. A., Burnett, A., Guentchev, G., eds. (2022). Hydroclimatology of the Great Lakes Region of North America. Lausanne: Frontiers Media SA.
doi: 10.3389/978-2-83250-545-8

Table of Contents

frontiers | Frontiers in Water

TYPE Editorial
PUBLISHED 04 October 2022
DOI 10.3389/frwa.2022.1044734

OPEN ACCESS

EDITED AND REVIEWED BY
Richard Graham Taylor,
University College London,
United Kingdom

*CORRESPONDENCE
Julie A. Winkler
winkler@msu.edu

SPECIALTY SECTION
This article was submitted to Water and Climate, a section of the journal Frontiers in Water

RECEIVED 15 September 2022
ACCEPTED 21 September 2022
PUBLISHED 04 October 2022

CITATION
Winkler JA, Burnett A and Guentchev G (2022) Editorial: Hydroclimatology of the Great Lakes region of North America. *Front. Water* 4:1044734. doi: 10.3389/frwa.2022.1044734

Editorial: Hydroclimatology of the Great Lakes region of North America

Julie A. Winkler[1]*, Adam Burnett[2] and Galina Guentchev[3]

[1]Department of Geography, Environment and Spatial Sciences, Michigan State University, East Lansing, MI, United States, [2]Department of Geography, Colgate University, Hamilton, NY, United States, [3]Met Office, Exeter, United Kingdom

KEYWORDS

Great Lakes (North America), hydroclimatology, climate variability and change, decision making, uncertainty

Editorial on the Research Topic
Hydroclimatology of the Great Lakes region of North America

The Great Lakes region of North America encompasses the Laurentian Great Lakes and the surrounding provinces and states of Canada and the United States. Although the sensitivity of the Great Lakes region to climate variability and change has long been recognized, current understanding of the historical and potential future changes in the regional hydroclimatology, and the consequences for physical and human systems, remains incomplete.

For this Research Topic, we sought submissions that improve our understanding of the trends and projected changes in the various components of the hydrological cycle, with the overall goal of providing novel insights to facilitate climate-related decision making in the Great Lakes region. Below we first provide as context a brief overview of the Great Lakes region, after which we integrate the contributions comprising this Research Topic around four themes: (1) historical trends in precipitation, (2) future projections for fine-scale assessment of regional thermal and hydrological characteristics, (3) lake effect climatology, and (4) challenges and novel approaches to assessing lake level fluctuations.

An introduction to the Great Lakes region

The Laurentian Great Lakes of North America, a series of interconnected freshwater lakes (Lakes Superior, Michigan, Huron, Erie, and Ontario), constitute the largest supply of fresh water in the world with more than 20% of the global total (Quinn, 1988) and with a coastline exceeding 14,000 km in length (Gibb, 2013). The climate of the Great Lakes region is influenced by its continental location, seasonal shifts in the location and configuration of the polar jet stream, and the frequency and tracks of transient midlatitude cyclones (Andresen et al., 2014). The Great Lakes modify the thermal and moisture characteristics of air masses transported into the region,

with locations downwind of the lakes generally having a cloudier, wetter, and more moderate climate than those less influenced by the lakes (Andresen and Winkler, 2009).

Over 30% of the population of Canada, and ∼10% of the United States population, currently reside in the Great Lakes region (US EPA, 2021), and the region is home to over 40 Tribal Nations (Gibb, 2013). The availability of iron ore, the region's proximity to energy resources, and access to transportation contributed in the late 1800s and early 1900s to the development of manufacturing surrounding the Great Lakes, and the region remains the focus of the North American automobile industry (Sousounis and Albercook, 2000). Agriculture is the major regional land use (Niyogi and Mishra, 2013). The western portion of the Great Lakes region intersects the fertile North American Corn Belt (Hart, 1986) where corn (i.e., maize) and soybean production dominate (National Agricultural Statistics Service, 2022), whereas the eastern Great Lakes region is known for its diverse agriculture including fruit and vegetable production (Winkler et al., 2002). Tourism is an additional major revenue source and includes sport fishing, hiking and camping, and winter recreation (Shih et al., 2009; Nicholls, 2014). A multimodal transportation system, which includes marine ports and inland waterways, is central to the region's economy (Council of the Great Lakes Region, 2017).

Precipitation trends and mechanisms

Considerable uncertainty surrounds the sign and magnitude of historical trends in precipitation for the Great Lakes region, and several contributions to the Research Topic focus on the computation of robust estimates of regional precipitation trends. Motivated by previous studies that often found contradictory trends even for stations in close proximity, Baule et al. applied multiple quality control procedures to station-level precipitation observations to minimize the influence of station inhomogeneities on trend calculations. Temporal trends computed using the quality-controlled time series were, when significant, almost always positive, suggesting a general increase in recent decades in both high frequency, low magnitude and low frequency, high magnitude precipitation events. In contrast, Paxton et al. removed from trend calculations the autocorrelation in time series of extreme precipitation introduced by the persistence of large-scale modes of climate variability. They, too, found that all significant trends were positive in sign. Both studies, however, show that precipitation trends remain statistically insignificant for substantial portions of the Great Lakes region. Kunkel et al., who calculated temporal trends in extreme precipitation events for four overlapping periods spanning 1908–2020, note that significant trends were more likely for the more recent time periods. Together, these studies suggest a regional-scale trend toward a wetter climate that is emerging from interannual variability. Focusing on proxy measures of precipitation, Trumper et al. found that in the northern Great Lakes region the correlation between latewood tree-ring width from *Pinus resinosa* (red pine) with daily precipitation variability has weakened since the 1980s, limiting the utility of latewood for assessing ongoing trends in the regional hydroclimate.

These authors also consider atmospheric processes contributing to the precipitation trends. Both Kunkel et al. and Baule et al. explore the relationship between precipitable water and precipitation, with Kunkel et al. finding that precipitation amounts increase with precipitable water depths greater than 30 mm, whereas the insignificant temporal trends in precipitable water found by Baule et al. for large portions of the Great Lakes region point to cautious interpretation of the relationship between precipitable water trends and precipitation trends. On the other hand, Paxton et al.'s findings suggest that regional trends in extreme precipitation are associated with changes in the strength and frequency of jointly-considered 500 mb geopotential height and 850 mb relative humidity fields, as identified using bivariate self-organizing maps. Furthermore, Kunkel et al. found that over 78% of daily extreme precipitation events in the Great Lakes region occur along frontal boundaries of midlatitude cyclones.

Future projections of hydroclimatological variables

Future economic development of the Great Lakes region is greatly dependent on projected future changes in the temperature and precipitation climatology. Evaluating these changes on finer temporal and spatial scales by using local and regionally specific projections is imperative for successful planning for future resilience and adaptation. Several papers of this Research Topic (Grady et al., Kluver and Robertson, Xie et al., Shrestha et al.) address projected future changes in temperature and precipitation at a variety of spatial scales within and around the Great Lakes region. All of these papers base their investigation on dynamically downscaled projections using mostly the high emissions scenario RCP8.5.

Similar to existing research, the papers agree on the projected increases of temperatures in the future, e.g., rise in average daily maximum and minimum temperatures over the Saginaw Bay watershed (Kluver and Robertson) or in annual mean temperature over the Great Lakes region (Shrestha et al.). In parallel with these findings, Xie et al. show that extreme high temperature days are expected to increase exponentially with rising temperatures within the region, and this projected change is independent of physics parameterizations and global climate model (GCM) forcing.

Mean annual precipitation is projected to increase, mostly due to higher intensity as found, for example, over smaller areas such as the Saginaw Bay watershed

in Michigan by Kluver and Robertson. These changes in annual precipitation are also corroborated over the larger Great Lakes Basin by Shrestha et al. who indicate that the projected future changes in highest one-day precipitation and number of wet days may indicate increases in extreme precipitation in the region. Furthermore, Shrestha et al., considering additional land hydroclimatology characteristics, indicate that annual runoff is also expected to increase despite the fact that snowpack is projected to decrease and actual evapotranspiration, especially in summer, is projected to rise.

The seasonal and monthly projected changes in precipitation and runoff are dependent on the season and to an extent the location, as indicated by Grady et al. and Shrestha et al. For example, Grady et al. identify for the spring season good model agreement indicating an increase in precipitation amount and intensity, and a decrease in the length of dry spells and the number of dry days. For summer, however, projections of precipitation amount and intensity do not show such strong consensus in sign and strength and display smaller changes with higher spatial variability. Considering compound risk events such as dry summers following wet springs, a combination which can be highly detrimental to corn and soybean yields, Grady et al. find that the risk is projected to be small by mid and late-century.

Lake effect climatology

Lake effect snow (LES) plays an important role in the hydroclimatology of the Great Lakes region. A number of papers within the Research Topic explore LES climatology and revisit several questions that have been raised previously, yet remain unanswered. One such question involves the contribution of LES to the overall snow climatology of the region. Although LES is an important contributor to snowfall, significant snow is also associated with synoptic-scale systems. Separating the influence of each requires that snow events be linked to a storm type, such as lake effect, synoptic, or some combination. We see a number of different approaches represented in this special collection. Jones et al. used a dataset published by Laird et al. (2017) that was based on an examination of daily GOES imagery. Direct observation of lake effect precipitation structures was also used by Hartnett, who classified snow events using a combination of reanalysis data and radar observations. Ellis and Suriano used the Temporal Synoptic Index (TSI) developed by Suriano and Leathers (2017) and the Spatial Synoptic Classification (SSC) from Ellis et al. (2021) to build a record of lake effect days. Neither dataset represents direct observations of lake effect cloud bands or precipitation, but the TSI provides a record of days that possess the synoptic conditions most associated with LES and the SSC provides insight into the way air masses are modified as they cross the Great Lakes.

These differing approaches in determining LES, along with the varying influence of each lake, contribute to highly variable estimates of the climatological contribution of LES. Jones et al. compared the very active lake effect winter of 2012/13 to the relatively inactive 2009/10 winter and found that LES contributions in the vicinity of Lakes Michigan, Erie, and Ontario ranged from 10 to 70%. Hartnett found that 13–48% of snowfall in central and northern New York was lake effect in origin, although this result varied throughout the winter season. Finally, Ellis and Suriano, using a hybrid lake effect dataset that combined the TSI and SSC classifications for the eastern Great Lakes, estimated that 31% of snow was lake derived. Although these percentages are generally consistent with those of earlier research (see Jones et al. Table 2), the substantial differences in LES estimates highlight the continuing uncertainty in the climatological contribution of LES.

Temporal trends in LES also have received considerable prior attention (e.g., Hartnett et al., 2014) and are further evaluated in this Research Topic, although the findings are contradictory. Meng et al. examined eight quality controlled snow records from western and central Michigan and found that seven exhibited statistically significant increases from 1932–2015. In contrast, Ellis and Suriano's hybrid lake effect dataset showed a declining trend in lake effect synoptic patterns and air mass signatures from the late 1970s to the early 2000s. The persistence of this question reflects the difficulty in assessing snowfall records and the role that snow data quality, period of analysis, and methodology all play in the conclusions.

Clark et al. presented an analysis of snow band structure and snowfall along the southern end of Lake Michigan and linked these structures to wind and temperature characteristics. Chief among their findings is that bands parallel to the wind are most common and determine much of the spatial distribution of snowfall in this region. However, the less common shore parallel bands account for some of the largest snowfalls in the area. They also found that upstream inversion heights, which are an indicator of the depth through which lake effect convection operates, were not significantly correlated with snowfall, perhaps due to the erosion of the inversion with over-lake passage.

Lake level trends and projections

In spite of both record low and record high Great Lakes water levels observed during the early twenty-first century (Gronewold and Rood, 2019), long-term trends in lake levels remain poorly documented. Fry et al. argue that a constraining factor is the limited availability of appropriate hydroclimate data sources for large-scale hydrological modeling, in part due to discontinuities from the Canadian-U.S. international border and the sparse observations across the surface area of the Great Lakes. In addition, currently available datasets lack appropriate documentation for their shared use by water

managers and the earth system modeling community, arguing for greater engagement of these two communities. Moreover, the limitations of downscaling GCM simulations to the scale of the Great Lakes basin make assessing future lake level fluctuations challenging. VanDeweghe et al. illustrate an approach that links a lake-to-lake routing model to monthly values of the environmental components contributing to net basin supply that were estimated using a parametric regular vine copula. Application of these methods to two plausible water supply scenarios (one a continuation of current net basin supply trends and the other a blend of existing trends with downscaled projected trends from regional climate models) suggests only a modest increase, but continued large variability, in Great Lakes water levels.

Concluding remarks

This suite of papers point to the many complexities and uncertainties surrounding the historical and projected future changes in the hydroclimatology of the Great Lakes region of North America, as highlighted by the careful consideration of data issues (e.g., availability and inhomogeneities), the application of multiple methodologies, and the spatial variations that exist in many of the hydroclimate processes examined in this Research Topic. The submissions reflect the continuing efforts to improve our understanding of the fundamental components of the hydrological cycle in the Great Lakes region and to provide stakeholders with useful information for decision making.

Author contributions

JW, AB, and GG edited the Research Topic and wrote the editorial. All authors contributed to the editorial and approved the submitted version.

Conflict of interest

Author GG was employed by Met Office.

The remaining authors declare that the research was conducted in the absence of any commercial or financial relationships that could be construed as a potential conflict of interest.

Publisher's note

References

Andresen, J. A., Hilberg, S. D., and Kunkel, K. E. (2014). "Historical climate and climate trends in the Midwestern United States" in *Climate Change in the Midwest: A Synthesis Report for the National Climate Assessment*, eds J.A. Winkler, J.A. Andresen, J.L. Hatfield, D. Bidwell, and D. Brown (Washington, DC: Island Press), 8–36.

Andresen, J. A., and Winkler, J. A. (2009). "Weather and climate," in *Michigan Geography and Geology*, eds R. Schaetzl, J. Darden, and D. Brandt (New York, NY: Pearson Custom Publishing), 288–314.

Council of the Great Lakes Region (2017). *Great Lakes and St. Lawrence Region Transportation Trends, Issues and Opportunities.* Available online at: https://councilgreatlakesregion.org/wp-content/uploads/pdfs/GLSLR_Multimodal_Transportation_Strategy-Part2.pdf (accessed September 13, 2022).

Ellis, A. W., Marston, M. L., and Bahret, J. (2021). Changes in the frequency of cool season lake effects within the North American Great Lakes region. *Ann. Am. Assoc. Geogr.* 111, 385–401. doi: 10.1080/24694452.2020.1785270

Gibb, T. (2013). *HOMES Defines the Great Lakes Region*. Available online at: https://www.canr.msu.edu/news/h.o.m.e.s._defines_the_great_lakes_region (accessed September 13, 2022).

Gronewold, A. D., and Rood, R. B. (2019). Recent water level changes across Earth's largest lake system and implications for future variability. *J. Great Lakes Res.* 45, 1–3. doi: 10.1016/j.jglr.2018.10.012

Hart, J. F. (1986). Change in the Corn Belt. *Geogr. Rev.* 76, 51–72. doi: 10.2307/214784

Hartnett, J. J., Collins, J. M., Baxter, M. A., and Chambers, D. P. (2014). Spatiotemporal snowfall trends in central New York. *J. Appl. Meteorol. and Climatol.* 53, 2685–2697. doi: 10.1175/JAMC-D-14-0084.1

Laird, N. F., Metz, N., Gaudet, L., Grasmick, C., Higgins, L., Loeser, C., et al. (2017). Climatology of cold season lake-effect cloud bands for the North American Great Lakes. *Int. J. Climatol.* 37, 2111–2121. doi: 10.1002/joc.4838

National Agricultural Statistics Service (2022). United States Department of Agriculture. *Crop Production 2021 Summary.* Available online at: https://downloads.usda.library.cornell.edu/usda-esmis/files/k3569432s/sn00c1252/g158cj98r/cropan22.pdf (accessed September 13, 2022).

Nicholls, S. (2014). "Outdoor recreation and tourism" in *Climate Change in the Midwest: A Synthesis Report for the National Climate Assessment*, eds J.A. Winkler, J.A. Andresen, J.L. Hatfield, D. Bidwell, and D. Brown (Washington, DC: Island Press), 197–211.

Niyogi, D., and Mishra, V. (2013). "Climate-agriculture vulnerability assessment for the Midwestern United States" in *Climate Change in the Midwest*, ed S. C. Pryor (Bloomington, IN: Indiana University Press), 69–81.

Quinn, F. H. (1988). "Likely effects of climate changes on water levels in the Great Lakes" in *Proceedings, First North American Conference on Preparing for Climate Change* (Washington, DC: Climate Institute), 481–487.

Shih, C., Nicholls, S., and Holecek, D. F. (2009). Impact of weather on downhill ski lift ticket sales. *J. Travel Res.* 47, 359–372. doi: 10.1177/0047287508321207

Sousounis, P., and Albercook, G. (2000). "Historical overview and current situation" in *Preparing for a Changing Climate: The Potential Consequences of*

Climate Variability and Change in the Great Lakes Region, A Summary by the Great Lakes Region Assessment Group for the U.S. Global Change Research Program, eds P. Sousousnis and J. Bisanz (Washington, DC: U.S. Environmental Protection Agency), 13–17.

Suriano, Z. J., and Leathers, D. J. (2017). Synoptic climatology of lake-effect snowfall conditions in the eastern Great Lakes region. *Int. J. Clim.* 37, 4377–4389. doi: 10.1002/joc.5093

US EPA (2021). *Facts and Figures about the Great Lakes*. Available online at: https://www.epa.gov/greatlakes/facts-and-figures-about-great-lakes (accessed on September 13, 2022).

Winkler, J. A., Andresen, J. A., Guentchev, G., and Kriegal, R. D. (2002). Possible impacts of projected temperature change on commercial fruit production in the Great Lakes region. *J. Great Lakes Res.* 284, 608–625. doi: 10.1016/S0380-1330(02)70609-6

frontiers in Water

ORIGINAL RESEARCH
published: 03 November 2021
doi: 10.3389/frwa.2021.746354

Inter-annual Variability of Snowfall in the Lower Peninsula of Michigan

Lei Meng, Bandhan Dutta Ayon, Nirjala Koirala and Kathleen M. Baker*

Department of Geography, Environment, and Tourism, Western Michigan University, Kalamazoo, MI, United States

Winter snowfall, particularly lake-contributed snowfall, has a significant impact on the society and environment in the Great Lakes regions including transportation, tourism, agriculture, and ecosystem. Understanding the inter-annual variability of snowfall will provide sound basis for local community safety management and reduce its environmental impacts on agriculture and ecosystems. This study attempts to understand the trend and inter-annual variability in snowfall in the Lower Peninsula of Michigan (LPM) using statistical analysis based on snowfall measurements from eight weather stations. Our study demonstrates that snowfall has significantly increased from 1932 to 2015. Correlation analysis suggests that regional average air temperatures have a strong negative relationship with snowfall in the LPM. On average, approximately 27% of inter-annual variability in snowfall can be explained by regional average air temperatures. ENSO events are also negatively related to snowfall in the LPM and can explain ∼8% of inter-annual variability. The North Atlantic Oscillation (NAO) does not have strong influence on snowfall. Composite analysis demonstrates that on an annual basis, more snowfall occurs during the years with higher maximum ice cover (MIC) than during the years with lower MIC in Lake Michigan. Higher MIC is often associated with lower air temperatures which are negatively related to snowfall. This study could provide insight on future snow related climate model improvement and weather forecasting.

Keywords: snowfall, inter-annual variability, Lake Michigan, trend, maximum ice cover, ENSO

OPEN ACCESS

Edited by:
Adam Burnett,
Colgate University, United States

Reviewed by:
Satya Prakash,
India Meteorological Department, India
Amalava Bhattcharyya,
Birbal Sahni Institute of Palaeobotany, India
Jill Coleman,
Ball State University, United States

****Correspondence:***
Lei Meng
lei.meng@wmich.edu

Specialty section:
This article was submitted to Water and Climate, a section of the journal Frontiers in Water

Received: *23 July 2021*
Accepted: *11 October 2021*
Published: *03 November 2021*

Citation:
Meng L, Ayon BD, Koirala N and Baker KM (2021) Inter-annual Variability of Snowfall in the Lower Peninsula of Michigan. Front. Water 3:746354. doi: 10.3389/frwa.2021.746354

INTRODUCTION

Winter snowfall, particularly lake-contributed snowfall, has a significant impact on the society and environment in the Great Lakes regions including transportation, tourism, agriculture, and ecosystem (Norton and Bolsenga, 1993; Schmidlan, 1993). The Lower Peninsula of Michigan (LPM) experiences significant amounts of snowfall each year due to its geographic location east of Lake Michigan. In the winter season, the LPM is affected by both mid-latitude cyclones and lake-induced winter storms (Pettersen et al., 2020). Mid-latitude cyclones are often associated with low-pressure centers such as the Colorado Low or Gulf Low that follow the jet stream. The movement of mid-latitude cyclones over the LPM brings abundant moisture and snowfall to this region. In addition to these synoptic low-pressure systems, Lake Michigan drives meso-beta scale (20–200 km) convective lake-effect snowfall when cold-air moves over the relatively warm lake surface. Due to the localized convection, lake-effect snowfall distribution is spatially variable and is limited to the downwind shores of the Great Lakes. For instance, Scott and Huff (1996) defined an 80-km wide band around Lake Michigan as the area with significant lake effects while Braham and Dungey (1984) used a 40 km wide band for the lake effect region.

Contribution of lake-effect snowfall to seasonal snowfall totals could vary from region to region and from season to season. Scott and Huff (1996) suggested ∼35% increase in snowfall in southwestern lower Michigan due to lake effects. Changnon (1968) calculated a 30% increase for the same region and a much higher increase (∼50%) for northwestern Michigan. Hartnett (2020) classified snowstorms affecting central New York into non-direct cyclonic storms and direct cyclonic storms and found that lake effect storms contributed to ∼39.4% of total snowfall for the period of 1985–2015. Hartnett (2020) also suggested that heavy snow storms (>25.4 cm) contributed to more than 50% of total snowfall for every type of snowstorms. Suriano et al. (2019a) examined the contribution of snowfall from diverse synoptic conditions in south-central New York and found that lake effect snowfall accounted for 38% of season totals for the period of 1960–2009. Meng and Ma (2021) calculated the percentage of annual snowfall totals that can be classified as lake-effect snowfall in the LPM and found that it varied significantly from 63 to 7% with a long-term average of 39% for the period of 1933–2015.

Previous studies have suggested inconsistent trends in snowfall in the Laurentian Great Lakes depending on locations/time periods (Norton and Bolsenga, 1993; Kunkel et al., 2009; Clark et al., 2016, 2018). Kunkel et al. (2009) examined the trend in snowfall in the lake-effect snowbelts of the Laurentian Great Lakes using a quality-controlled dataset and found an upward trend for Lakes Superior and Michigan and no changes for Lakes Erie and Ontario. Hartnett et al. (2014) found an increase during the period 1931–1972 and a less decrease for 1972–2012 in total snowfall in central New York, similar to the trend found in Bard and Kristovich (2012). Suriano et al. (2019b) investigated the trend in snow depth using a 1-degree gridded snow depth dataset and found a significant decrease (25–30%) in average basin-wide snow depth for Lake Michigan. Clark et al. (2016) investigated the spatiotemporal trends in annual total snowfall in the Lake Michigan region and found no changes during the period of 1950–2013 based on station measurements. However, they found an increase in the fraction of snowfall that occurs from December to February. Their follow-up study in 2018 (Clark et al., 2018) suggested a decreasing trend in November and March snowfall in the same region. Baijnath-Rodino and Duguay (2018) found a significant decrease in total snowfall for the period of 1980 to 2015 along the Canadian leeward shores of Lakes Superior and Huron-Georgian Bay using the Daymet (version 3) gridded estimation. Our previous study (Meng and Ma, 2021) calculated the lake-effect snowfall (total snowfall minus non-lake effect snowfall) in the LPM from weather station measurements and found an overall increasing trend from 1933 to 2015. Within the overall increasing trend, there was a strong increase from 1933 to 1969 followed by a less change from 1970 to 2015.

Winkler et al. (2012) indicated that over 90% of the 21 General Circulation Models (GCMs) projected an increase in annual and wintertime precipitation by 2080–2099 for the LPM. Hayhoe et al. (2010) assessed the projected climate change in the U.S. Great Lake region under different greenhouse gas emissions scenarios and found that the projected change in precipitation ranges from decreases of a few percentages to increase of up to 7% from 2010 to 2039. By the end of twenty-first century, most models predict an increase in winter precipitation in the Great Lakes region and more precipitation falls as rain instead of snow due to the increase in winter temperatures.

Note that a large uncertainty remains in the future climate projection, particularly the precipitation projection (Winkler et al., 2011, 2012).

Two dominant factors that influence the intensity and frequency of U.S. winter storms are ENSO and the North Atlantic Oscillation (NAO) (Kunkel and Angel, 1999; Seager et al., 2010; Kunkel et al., 2013). Kunkel and Angel (1999) suggested a significant relationship between the frequency of cyclones and El Nino winters for the contiguous United States. Seager et al. (2010) found that snowfall anomalies during the winter season of 2009–2010 in the Northern Hemisphere can be attributed to the combination of a negative NAO and an El Nino event. Clark et al. (2016, 2018) also found that snowfall is very sensitive to the ENSO and NAO for the Lake Michigan region. Kluver and Leathers (2015) examined the factors that influence decadal-scale snowfall variations in the United States and found that both ENSO and NAO are useful predictors of snowfall for the period of 1930–2006. Smith and O'Brien (2001) found that snowfall decreased during both El Nino and La Nina years compared to ENSO neutral years in the Midwest and forecasting could be potentially improved with the inclusion of ENSO phases. Patten et al. (2003) investigated the impact of ENSO on snowfall frequencies in the United States and found that low and moderate snowfall frequencies increased during ENSO cold-phase winters relative to ENSO neutral winters. Coleman and Stefl (2016) examined the relationship between snowfall totals and three teleconnection patterns and found that NAO negative conditions are usually associated with higher snowfall totals in Eastern United States. Serreze et al. (1998) examined the relationships between snowfall and precipitation and the maximum temperature on precipitation days and found no consistent trends in snowfall and in the strength of the Pacific-North America (PNA), Tropical-Northern Hemisphere (TNH), and East Pacific (EP) teleconnection patterns.

In addition to the above teleconnection indices, local and regional environmental variables could also affect the intensity and distribution of snowfall. It has been suggested that winter maximum and minimum temperatures could influence snowfall trends over the Canadian Domain of the Great Lakes Basin (Baijnath-Rodino and Duguay, 2018). Suriano (2019) found that both lake-effect synoptic type circulation patterns and surface air temperatures contribute to the change in snowfall in the Great Lakes region. Model studies have suggested that both surface air temperature and lake ice cover influence the distribution and intensity of lake-effect snowfall (Notaro et al., 2013; Wright et al., 2013).

Given the complexity in factors that influence snowfall in the Great Lakes region, causes of inter-annual variability in snowfall are not satisfactorily understood. In this study, we will investigate the trends and inter-annual variability of seasonal snowfall in the LPM and their relationships with air temperature, ENSO, and NAO. Understanding of such statistical relationships will help future model development related to the mechanism of snowfall

and improve prediction of snowfall intensity and distribution. The major difference between this study and Meng and Ma (2021) is that Meng and Ma (2021) focused on the calculated lake-effect snow (total snowfall minus non-lake effect snowfall) with an emphasize on regional average and this study investigates seasonal snowfall totals, which have been used in most of the previous studies. As mentioned in Meng and Ma (2021), the calculated lake-effect snow was not validated again observations due to the lack of direct lake-effect snowfall measurements. Use of seasonal snowfall totals will make this study directly comparable with similar studies for different parts of the Great Lakes region.

DATA AND METHODS

Snowfall Data

Monthly snowfall data for the period of 1932–2015 is collected from the National Weather Service's Cooperative Observer Network (COOP) stations. Datasets obtained from the COOP stations have gone through a comprehensive set of fully automated quality assurance procedures to detect duplicate data, climatological outliers and various inconsistencies. Details on the quality control procedures can be found in Durre et al. (2010) and Lawrimore et al. (2020). Only eight COOP stations in the LPM are used (**Figure 1**). These eight stations were determined to be homogeneous through the expert quality assessment defined in Kunkel et al. (2009). Therefore, snowfall data from these eight stations is deemed appropriate for trend analysis and for studying the inter-annual variability of snowfall. Each snow year is defined as November-to-March. In this study, for instance, snow year 1950 refers to November and December in 1949 and January, February, and March in 1950. In the LPM, most of snowfall occurs between November and March (**Figure 2**). Due to the existence of missing data, the individual snow year will be excluded in our analysis if snowfall is missing from any month between November and March. The annual total snowfall in this analysis refers to the amount occurring between November and March and is represented as the sum of monthly snowfall between November and March. The statistics of annual total snowfall in the eight stations are listed in **Table 1**.

Surface Air Temperature Data

Monthly surface air temperature data is obtained from the Parameter-elevation Relationship on Independent Slope Model (PRISM) working group at Oregon Station University (accessible at http://www.prism.oregonstate.edu/) (Daly et al., 2008). The PRISM data were produced from the combination of weather station datasets and digital elevation model (DEM) through a climate-elevation regression method (Daly et al., 2008). The PRISM provides consistent and long-term records of climatic variables including precipitation and temperatures. Winter season temperatures are represented as the average of monthly temperatures between November and March over the entire LPM.

SSTs and NAO Dataset

The Nino 3.4 sea surface temperature (SST34) index (1932–2015) obtained from the Earth System Research Laboratory (ESRL) of National Oceanic and Atmospheric Administration (NOAA) (http://www.esrl.noaa.gov/psd/gcos_wgsp/Timeseries/Nino34/) is used in this study to represent the El Niño Southern Oscillation (ENSO) phenomena. Average monthly SST34 anomalies between November and March (NDJFM) are used to represent winter season ENSO conditions. In this study, El Niño (La Niña) years are defined when SST34 anomalies are greater (smaller) than $+0.5^{\circ}$C (-0.5°C).

The Hurrell NAO monthly index (station-based) (1932–2015) is used in this study (accessible at https://climatedataguide.ucar.edu/climate-data/hurrell-north-atlantic-oscillation-nao-index-station-based). November–March average NAO represents winter-season pressure conditions. The positive NAO index is often associated with stronger-than-average westerlies over the mid-latitudes (Hurrell, 1995). A winter with positive (negative) phase of the NAO is when the winter mean NAO value exceeds $+0.5$ (-0.5) standard deviation. The NAO-neutral phase is defined when the NAO index is between $+0.5$ standard deviation and -0.5 standard deviation. This method to define different NAO phases has been used in Bai et al. (2012).

Maximum Ice Cover in Lake Michigan

The maximum ice cover (MIC) dataset for Lake Michigan (1973–2015) is obtained from the NOAA Great Lakes Environmental Research Laboratory at http://www.glerl.noaa.gov/. An additional 10 years MIC data from 1963 to 1972 is digitized from Figure 2 in Bai et al. (2012). Therefore, the MIC dataset is available from 1963 to 2015. Our analysis related to the MIC dataset is restricted to the period of 1963–2015. This dataset has been used in Meng and Ma (2021).

Methods

The Mann-Kendall analysis will be used to identify the trend in snowfall at each station. In addition, sliding correlation analysis, linear regression, composite analysis, student *t*-test, and chi-square test will be used in this study to investigate the relationship between annual total snowfall and different climatic variables including surface air T, SST34, NAO, and MIC.

RESULTS

Long-Term Trend in Annual Total Snowfall in the LPM

The Mann-Kendall test is used to investigate the trend in annual total snowfall in the eight stations. Our analysis indicates that the amount of snowfall has generally increased from 1932 to 2015 (**Figure 3**). The rate of increase ranges from 0.095 cm/year in Kent City to 2.483 cm/year in East Jordan with an average rate of 0.91 cm/year. The increasing trend is statistically significant at the 95% confidence level in all stations except Kent City and Wellston. There are large variations in the annual total snowfall during the period of 1932–2015. The minimum annual snowfall in the eight stations ranges from 43.43 to 108.2 cm with an average of 63.47 cm. The maximum annual snowfall in the eight stations ranges from 210.8 to 465.84 cm with an average of 315.98 cm. At each station, the maximum annual snowfall is at least four times of the minimum annual snowfall

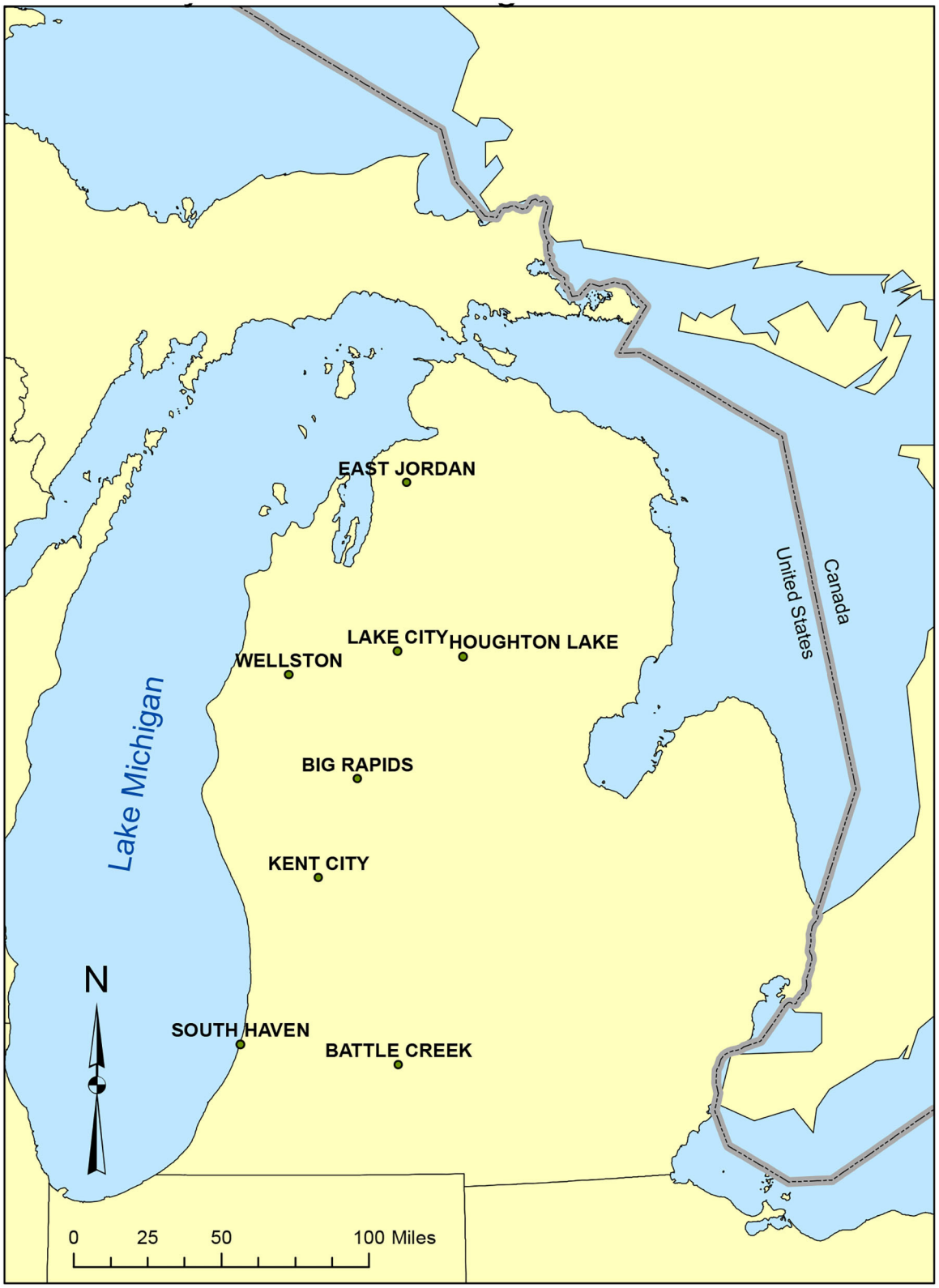

FIGURE 1 | The study area and the location of the eight Cooperative Observer Network (COOP) weather stations. These eight COOP stations are temporally homogeneous stations defined based on the criteria used in Kunkel et al. (2009).

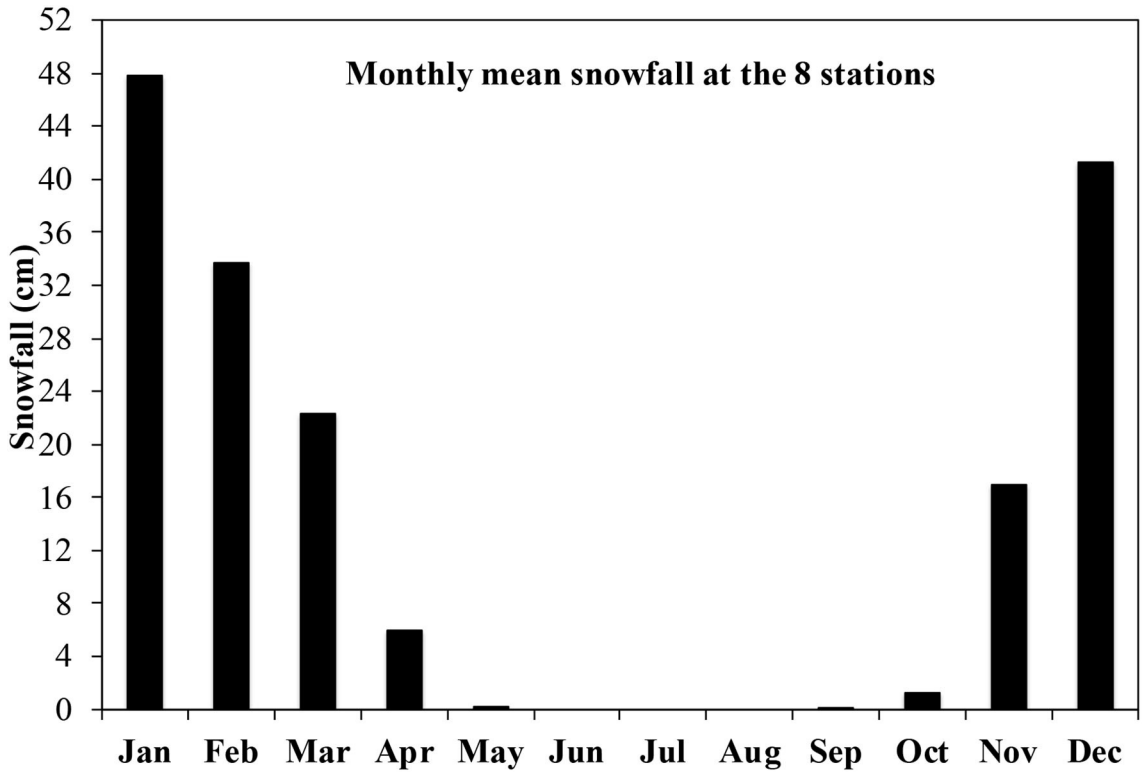

FIGURE 2 | Climatology of monthly snowfall averaged over the eight stations (refer to **Figure 1**) used in this study for the period of 1932–2015.

during the period of 1932 to 2015. **Figure 3** also suggests that the maximum annual snowfall at these eight stations did not occur in the same year. Four of the eight stations had the maximum annual snowfall in 2008/09 winter season (Battle Creek, East Jordan, Lake City, and Wellston). Seven of the eight stations had their maximum annual snowfall in the most recent years after 1997 except Big Rapids, which had maximum annual snowfall in 1951/52. Kent City did not show significant increasing trend, largely due to its minimum annual snowfall (only 43.43 cm) in 2014 when other stations had at least 231.14 cm of snowfall.

Snowfall and Air T

Strong negative correlations (significant at 95% confidence level) exist between regionally average air temperatures and annual total snowfall in all of these eight stations for the period of 1932–2015. The correlation at each individual station varies from −0.25 in Lake City to −0.54 in Wellston (**Table 2**) with an average of −0.40. It is also found that regionally average snowfall over the eight stations is highly correlated with regionally average air temperature with a correlation of −0.52 (**Figure 4**), suggesting that air temperatures in the LPM can explain approximately 27% variability in snowfall. Our analysis demonstrates that both snowfall at individual stations and regionally average snowfall are highly related to air temperatures in the LPM.

TABLE 1 | Basic statistics of annual total snowfall (cm) at the stations for the period of 1932–2015.

Station	Mean	Standard deviation	Min	Max
Battle Creek	131	48	46	278
South Haven	147	60	44	289
Kent City	129	37	43	211
Big Rapids	156	57	60	293
Wellston	228	63	108	397
Houghton Lake	141	44	61	273
Lake City	184	53	81	322
East Jordan	256	81	64	466

Stations are ordered from south to north based on latitudes. All numbers are rounded to the nearest cm.

Snowfall and ENSO

ENSO is considered to be one of the primary factors that influence stormy weather in eastern stations in the United States. In this study, SST anomalies in Nino 3.4 region (SST34) are used to indicate the ENSO events. Our study suggests negative correlations between SST34 and snowfall in the LPM (**Table 2**). The correlations vary from −0.07 to −0.37 and are significant at the 90% (95%) level in 6 (4) of the eight stations. We further divide the 84 years (from 1932 to 2015) into El Niño (SST34

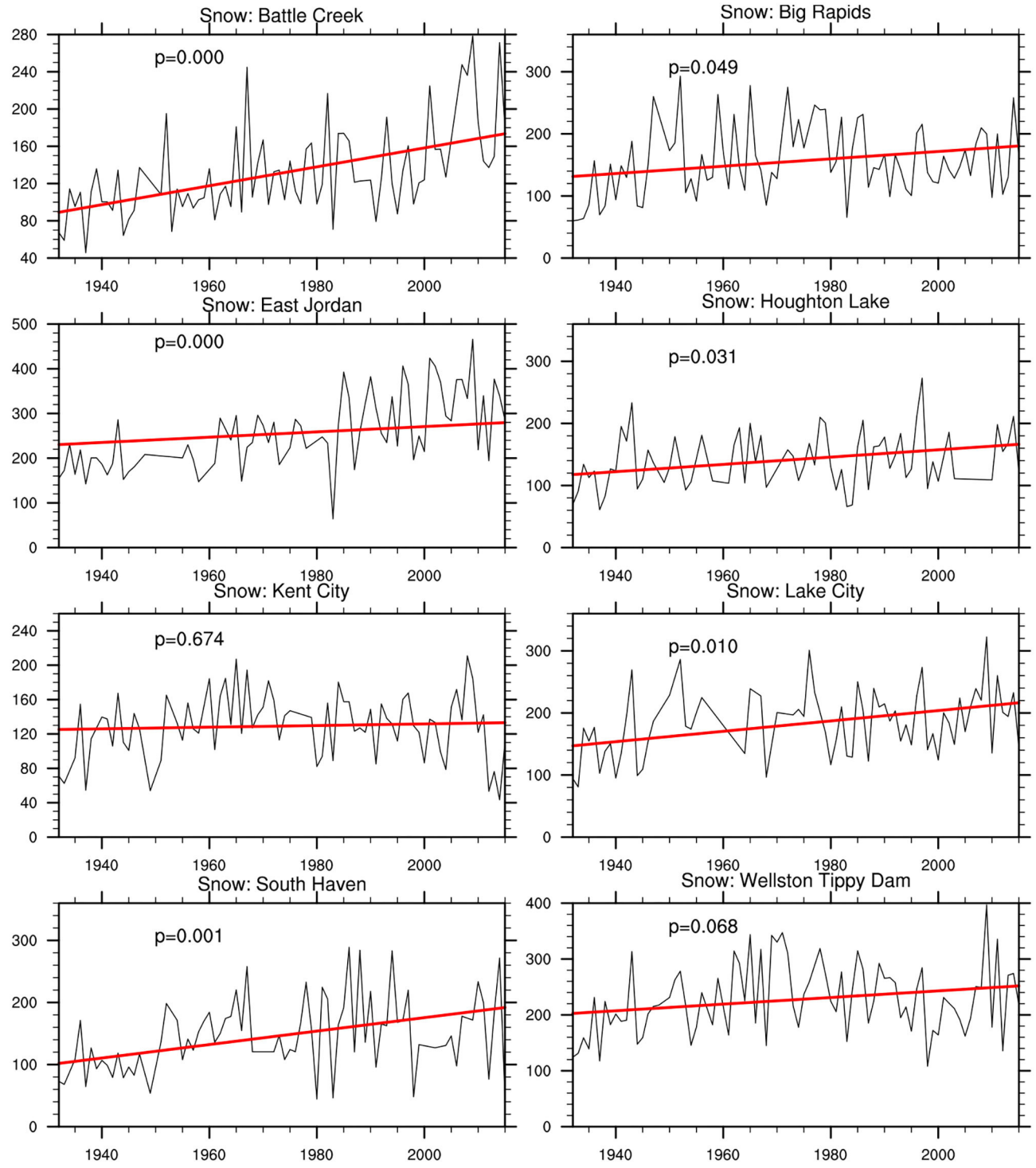

FIGURE 3 | Trends in annual total snowfall (cm) at the eight stations (refer to **Figure 1**) for the period of 1932–2015. The trend analysis was conducted using the Mann-Kendall test.

$\geq 0.5°C$), La Niña (SST $\leq -0.5°C$), and neutral (between -0.5 and $0.5°C$) years based on the SST anomalies. There are 18 and 26 La Niña years. The average mean snowfall over the eight stations is 157.99 and 190.75 cm during the El Niño and La Niña years, respectively (**Table 4**). This suggests that El Niño (La Niña) events tend to decrease (increase) snowfall in the LPM.

In addition, the regionally average air temperatures are −2.96 and −3.26°C during the El Niño and La Niña years, respectively. This suggests that during the El Niño years the LPM is warmer than during the La Niña years. Such results are consistent with the negative relationship between air temperatures and snowfall as demonstrated in section Snowfall and Air T. On the regional scale, approximately 8% of inter-annual variability in snowfall can be explained by SST34 anomalies (**Figure 5**).

A 21-year sliding correlation between SST34 and the annual snowfall averaged over the eight stations shows that a strong and significant (at the 95% confidence level) relationship only exists for the period of 1963–2015 (**Figure 6**). It is also found that the variation of SST34 is larger during the period of 1963–2015 than during the period of 1932–1962 (**Figure 6**). At each station, the correlation between SST34 and the annual snowfall is stronger for the period of 1963–2015 than the period of 1932–1962 (**Table 3**) for all the stations except East Jordan. This suggests that the increased variability of SST34 might contribute to the stronger correlations between SST34 and the annual snowfall. Further research is needed to validate this conclusion for other regions to determine whether it is unique to the LPM or it can be generally applied to other regions with similar climatological conditions.

TABLE 2 | Pearson correlation coefficients (*r*) between annual total snowfall and NAO/SST34/Air T for the whole study period (1932–2015) at the stations.

Station	Correlations with snowfall		
	NAO	SST34	Air T
Battle Creek	0.06	−0.17	−0.37**
South Haven	−0.08	−0.07	−0.48**
Kent City	−0.28*	−0.21*	−0.37**
Big Rapids	−0.13	−0.19*	−0.51**
Wellston	−0.20*	−0.25**	−0.54**
Houghton Lake	−0.16	−0.25**	−0.38**
Lake City	0.01	−0.35**	−0.25**
East Jordan	−0.04	−0.37**	−0.32**

The correlation analysis was conducted after the linear trend was removed for all the data involved.
**Significant at the 90% confidence level.*
***Significant at the 95% confidence level.*

Snowfall and NAO

Overall, the NAO does not have strong influence on snowfall in the LPM. The correlation between the NAO and snowfall in the eight stations is negative in six of the eight stations and is not significant at the 90% confidence level (**Table 2**) in all eight stations. Composite analysis suggests that average snowfall (183.14 cm) in the defined 22 negative (–) NAO years

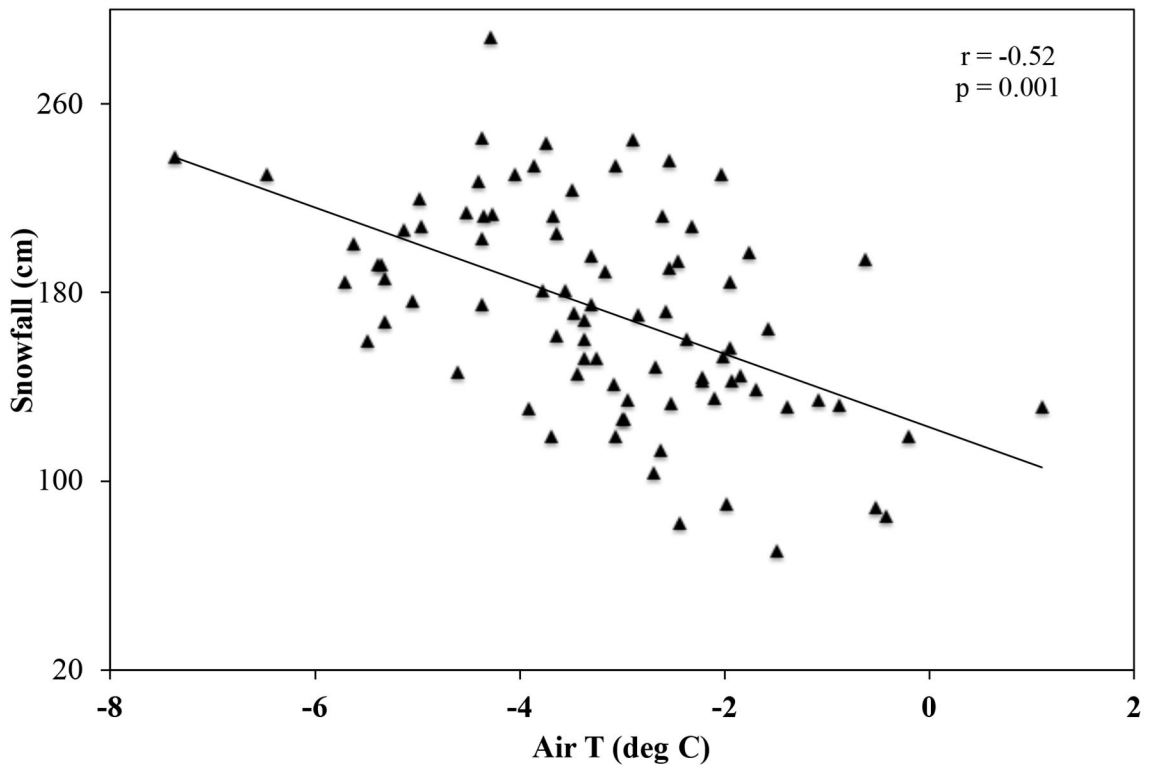

FIGURE 4 | Scatter plot of average annual total snowfall over the eight stations vs. regional average air temperatures. A Pearson correlation coefficient (*r*) and *p*-value are shown on the figure.

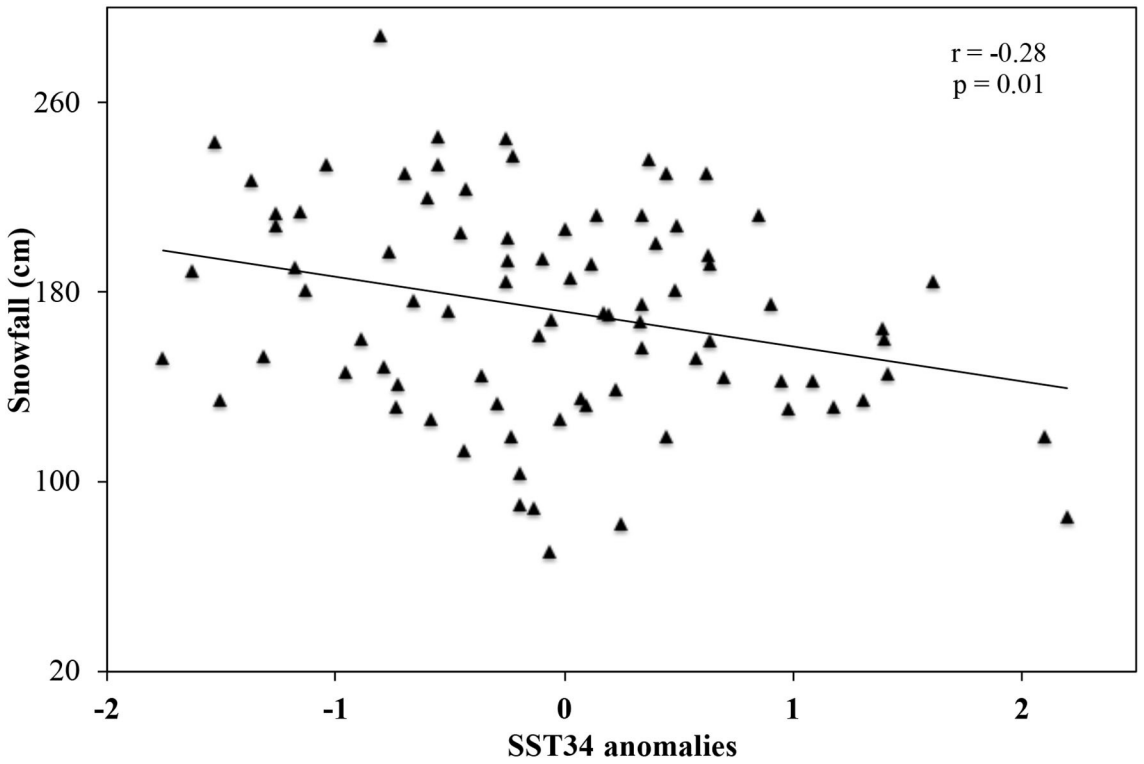

FIGURE 5 | Scatter plot of average annual total snowfall over the eight stations vs. SST34 anomalies. A Pearson correlation coefficient (*r*) and *p*-value are shown on the figure.

is slightly higher than that (169.93 cm) in the defined 28 positive (+) NAO years. The average regional temperature in these –NAO and +NAO years is −3.96 and −2.89°C, respectively (**Table 5**). Further, the average snowfall over these eight stations is negatively related to the NAO and only ∼2% of inter-annual variability can be explained by the NAO during the period of 1932–2015 (**Figure 7**).

A 21-year sliding correlation between NAO and the annual snowfall averaged over the eight stations suggests that the correlation is not significant at the 95% confidence level over most of the time period (not shown).

Snowfall and Maximum Ice Cover

The MIC dataset is only available starting from 1963. Our analysis related to MIC is restricted to the period of 1963–2015. Overall, there is a significant positive correlation (0.35, significant at the 95% confidence level) between annual total snowfall and MIC for the period of 1963–2015. The top five MIC (1963, 1977, 1979, 1994, and 2014) and bottom five MIC years (1964, 1969, 1998, 2002, and 2006) are selected to further investigate the relationship between the MIC and snowfall. Our results suggest that annual total snowfall is approximately 24% higher during the top five MIC years than that during the bottom five MIC years over the eight stations except Kent City (**Figure 8**). **Figure 9** indicates that the MIC has a strong negative correlation with air temperatures with a correlation coefficient of −0.76. Therefore, our relationship between the MIC and snowfall is in consistent with the negative air temperature-snowfall relationship. However, caution should be exercised here that the increase in snowfall during the top five MIC years compared to that during the bottom five MIC years is not statistically significant possibly due to the sample size.

DISCUSSIONS

Trend in Annual Total Snowfall in the LPM

This study indicates that annual total snowfall in the LPM has generally increased in all eight stations. This is consistent with the findings in Kunkel et al. (2009) who found an upward trend in snowfall in the Snowbelt area of Lake Michigan. The upward trend in snowfall in the LPM is accompanied by a decreasing trend (0.004°C/year, not significant at the 90% confidence level) in regional average winter T (not shown). The trend in regional average winter T in this study is different from those shown in Kunkel et al. (2009). Kunkel et al. (2009) found a slightly increasing trend in winter air temperatures averaged at the weather stations in the Michigan-Huron region used in their study. The differences between our study and Kunkel et al. (2009) are: (1) the period of study (1932–2015 in our study vs. 1900–1995 in Kunkel et al., 2009); (2) the domain size for average temperature (the whole LPM region in our study vs. several weather stations in Kunkel et al., 2009). These differences might

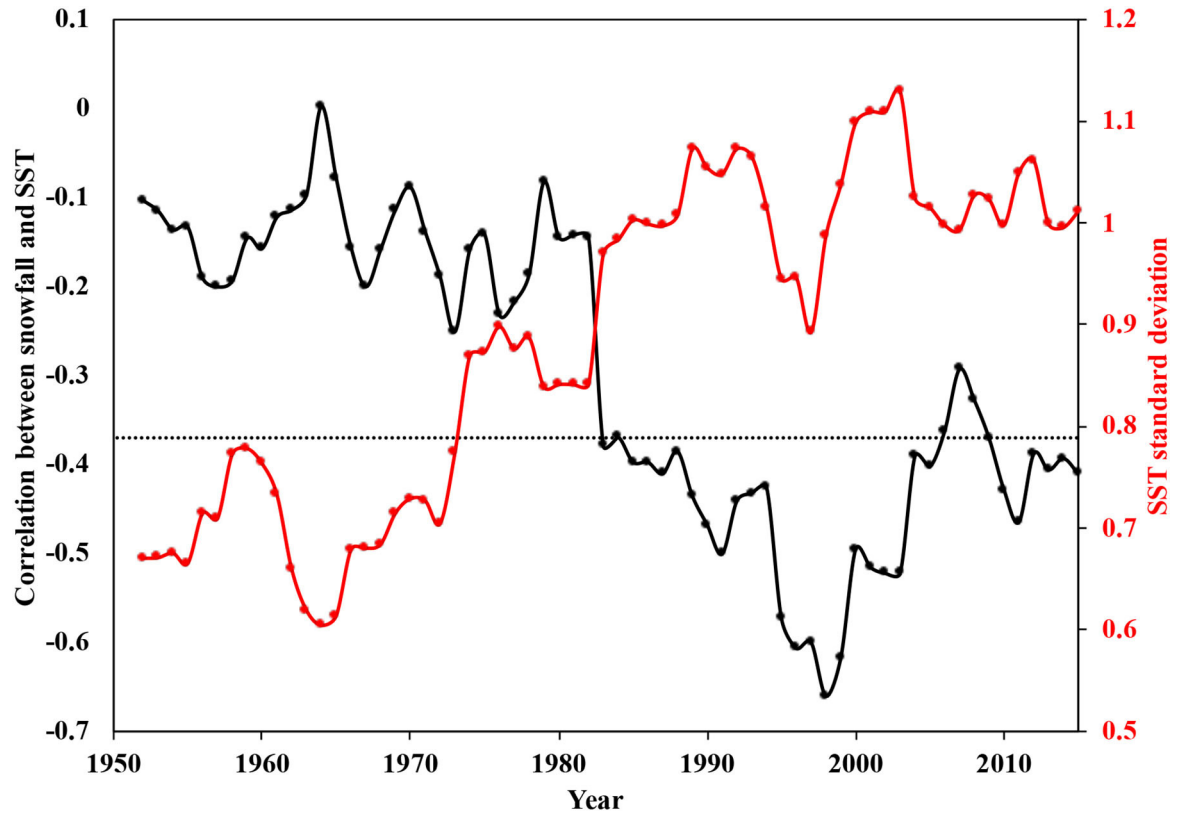

FIGURE 6 | Temporal variation in the 21-year sliding correlation between SST34 and the average annual snowfall over the eight stations (the solid black line). For example, the correlation at 1983 is calculated using SST34 and snowfall over the period of 1963–1983. The dashed straight line indicates correlation significance at the 95% confidence level. Also shown in this figure is the standard deviation of the corresponding 21 years of SST34 (the red solid line).

TABLE 3 | Pearson's correlations coefficients (*r*) between SST34 and snowfall for the periods of 1932–1962 and 1963–2015 at the stations.

Station	Correlation between SST34 and snowfall	
	1932–1962	1963–2015
Battle Creek	−0.04	−0.39*
South Haven	0.11	−0.12
Kent City	−0.01	−0.3*
Big Rapids	0.03	−0.33*
Wellston	−0.17	−0.31*
Houghton Lake	−0.24	−0.31*
Lake City	−0.32*	−0.39*
East Jordan	−0.5*	−0.45*

**Indicate correlation significance at the 95% confidence level.*

contribute to the different trend in winter air temperatures. Please note that temperatures at individual weather station might be affected by local topography, land-water distributions, and nearby urban areas.

Another factor that might influence the measurement of snowfall and temperatures is the land cover and land use change (LCLUC). It was shown in Wolter et al. (2006) that 2.5% of the U.S. portion of the Great Lakes had experienced changes from 1992 to 2001. The change in the land cover and land use influences surface wind conditions, temperatures, and surface convergence/divergence due to wind/temperature changes (Mahmood et al., 2010; Szczypta et al., 2015). Although efforts have been introduced to minimize any changes with the selected weather stations (Kunkel et al., 2009), it is still possible that LCLUCs around these weather stations influence the snowfall measurement and identified trends. These weather stations used in this study have gone through a rigorous expert selection process (Kunkel et al., 2009). Therefore, the LCLUC should have limited impacts on the snowfall measurement.

Negative Correlation Between Air Temperature and Snowfall

This study demonstrates that a statistically significant negative correlation exists between regional average winter air temperatures and annual total snowfall in the LPM, suggesting that annual total snowfall will increase when winter air temperatures decrease. The regional average air temperature in the LPM is largely affected by cold and continental air masses (i.e., cP or cA air masses) that move southeastward from the Arctic basin and the interior of Canada (Hayhoe et al., 2010). In the meantime, movement of the cP/cA cold air mass over

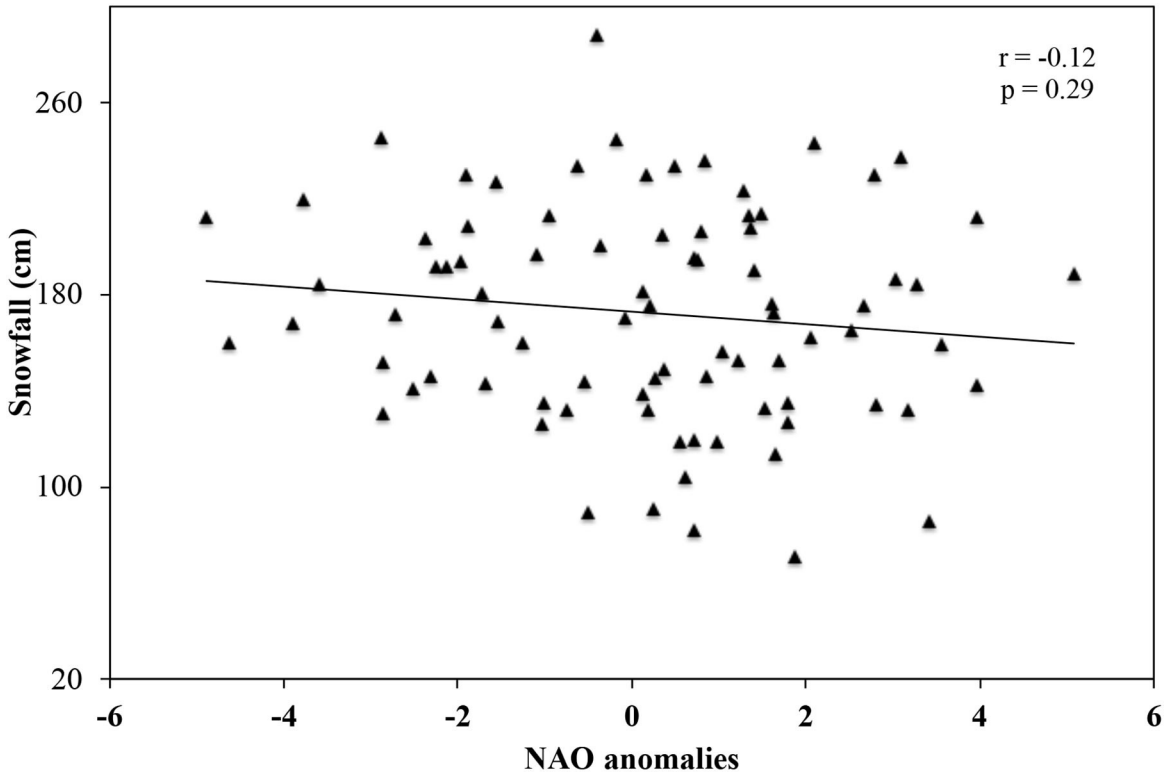

FIGURE 7 | Scatter plot of average annual total snowfall over the eight stations vs. the NAO index. A Pearson correlation coefficient (*r*) and *p*-value are shown on this figure.

the relatively warm water surface of the Great Lakes leads to enhanced production of the lake-effect snowfall on the lee of Lake Michigan due to the strong contrast of water-air temperatures (Dockus, 1985). Therefore, the cP/cA cold air mass will produce abundant lake-effect snowfall and bring cold air to the LPM, resulting in a negative correlation of air temperature and snowfall. Such negative correlations have also been found in other regions. For instance, Blechman (1996) found a strong negative correlation in winter mean monthly temperature and snowfall in western and central New York and the lee of Lakes and Ontario and Erie.

Relationship Between MIC and Snowfall

Previous research has suggested that higher ice cover in the Great Lakes region will decrease lake-effect snowfall on the downwind side of the Great Lakes through the reduction of evaporation and lake-climate interactions (Gerbush et al., 2008; Brown and Duguay, 2010). However, our study indicates an increase in annual total snowfall during the years with higher MIC. This is not in contrast with the idea that higher ice cover tends to reduce lake-effect snowfall. Notaro et al. (2013) conducted a model simulation of heavy lake-effect snowstorms in RegCM4 and found that lake-effect snowfall is most frequent and intensive in December–January. In Lake Michigan, MIC typically occurs in February–March based on the results in Assel (2005) (see the Figure 3 in Assel, 2005). **Figure 10** suggests that the amount of snowfall is comparable in November and December and almost doubled in January during the 5 years with highest MIC compared to those 5 years with lowest MIC in the LPM. As expected, snowfall has reduced in March after the ice cover has peaked in February in the years with higher MIC (Assel, 2005). The MIC and snowfall relationship is also consistent with the snowfall-air temperature relationship. Maximum ice cover and air temperatures have a strong negative relationship indicating that the winters with higher MIC are typically colder than those with lower MIC (**Figure 9**). This is consistent with our study on lake-effect snowfall (Meng and Ma, 2021).

Snowfall and ENSO/NAO

The SST34 has a stronger correlation with snowfall than the NAO (**Table 2**). The composite analysis suggests El Niño (or La Niña) events would likely decrease (or increase) snowfall in the LPM. The impact of different phases of ENSO on snowfall is significant at the 95% confidence level (**Table 4**). The different impact of El Niño and La Niña events on snowfall in the LPM might be due to different large-scale atmospheric circulations that affect the southeastward movement of cP and cA air masses. Smith and O'Brien (2001) found similar results and suggested that the decrease in snowfall during El Nino events might be associated with warmer surface temperatures and relative shift of jet stream locations to the south. Bai et al. (2012) found that El Niño events are associated with a unique atmospheric

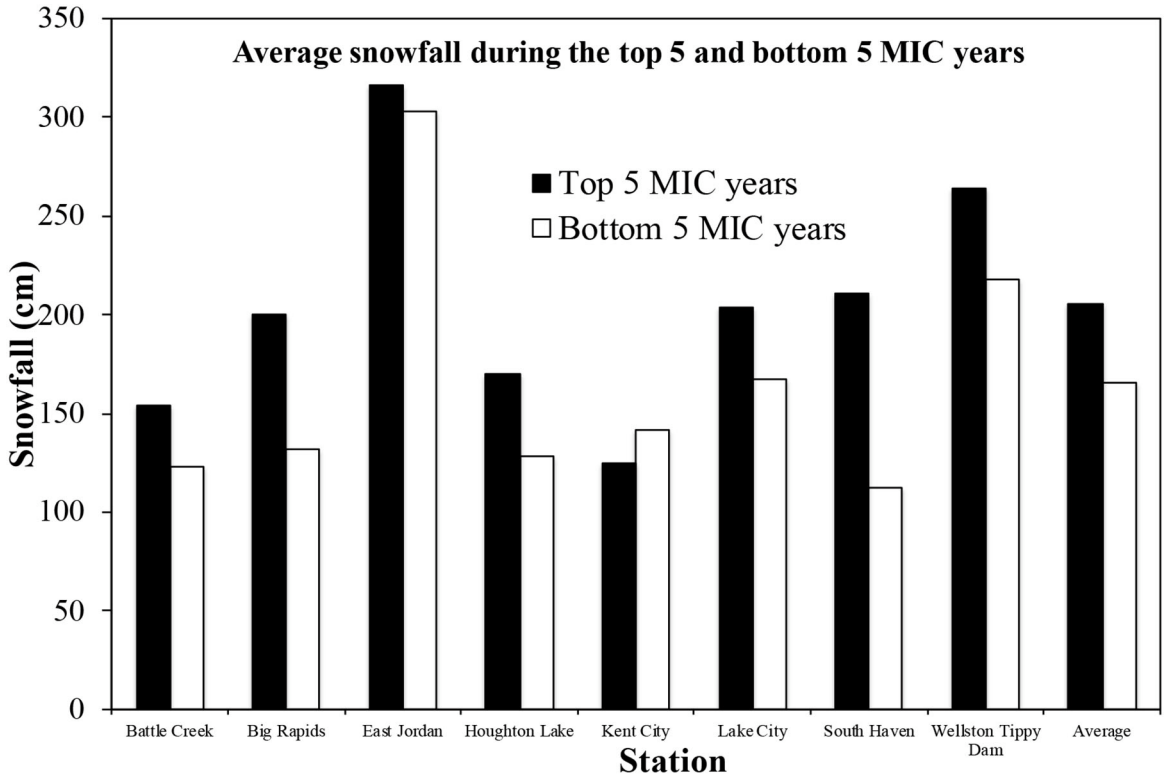

FIGURE 8 | Comparison of average annual total snowfall during the top five and bottom five maximum ice cover (MIC) years at each station and averaged over all stations.

circulation pattern (a deep-than-normal trough over the Gulf of Alaska, a weaker-than-normal ridge over the west coast, and a weaker-than-normal Hudson Bay trough over eastern Canada) that prevent a cold Arctic air mass from intruding the Great Lakes region resulting in a decrease in snowfall and warm temperatures in the LPM. For the LPM, the average air temperature is −2.96 and −3.26°C during the defined El Niño and La Niña years (**Table 4**), respectively. This further confirms the negative correlations between air temperatures and snowfall.

Our study also demonstrates that the negative (positive) phase of NAO tends to increase (decrease) snowfall in the LPM (**Table 5**). This might be related to the impact of the NAO on the strength of polar vortex and westerly winds. During the years with negative NAO phases, a stronger-than-normal trough and ridge are developed near the Great Lakes and the U.S. west coast, respectively. The locations of the trough and ridge in North America favor the southward movement of an Arctic air mass over the Great Lakes and promote lake-effect snowfall and deliver cold air to the LPM (Bai et al., 2012). However, the impact of the NAO on snowfall in the LPM is not statistically significant (at the 90% confidence level) between the positive and negative phases of NAO. A weak correlation between snowfall and the NAO was also demonstrated in Clark et al. (2016, 2018) and in Gong and Ge (2009). The weak linkage between snowfall and the NAO might be due to the NAO's complicated interactions with the snow cover and the ENSO. Gong et al. (2002) investigated the impact of snow cover variations on NAO patterns and suggested that NAO patterns can be modulated by inter-annual snow variations. Previous studies also suggest complicated relationships between NAO-ENSO (Zhang et al., 2018, 2019; Mezzina et al., 2020). Such complicated relationships between NAO-ENSO might explain why snowfall-ENSO relationship is significant while snowfall-NAO relationship is not significant. Modeling studies will be needed to find the physical mechanism for the weak snowfall-NAO relationship.

CONCLUSIONS

In this study, both the snowfall trend and the relationship between snowfall in the LPM and air temperature/ENSO/NAO/MIC are investigated using statistical analysis including Mann Kendall test, linear regression, and composite analysis. The eight stations with homogeneous time series dataset defined by Kunkel et al. (2009) are used. Our results indicate that snowfall has generally increased in the eight stations used in this study in the LPM during the period of 1932–2015 and the trend is statistically significant at the 95% confidence level in seven of the eight stations. The average rate of snowfall increase is 0.91 cm/year with a range of 0.094–2.48 cm/year.

Statistical analysis suggests that regional air temperatures in the LPM are the dominant factor influencing annual

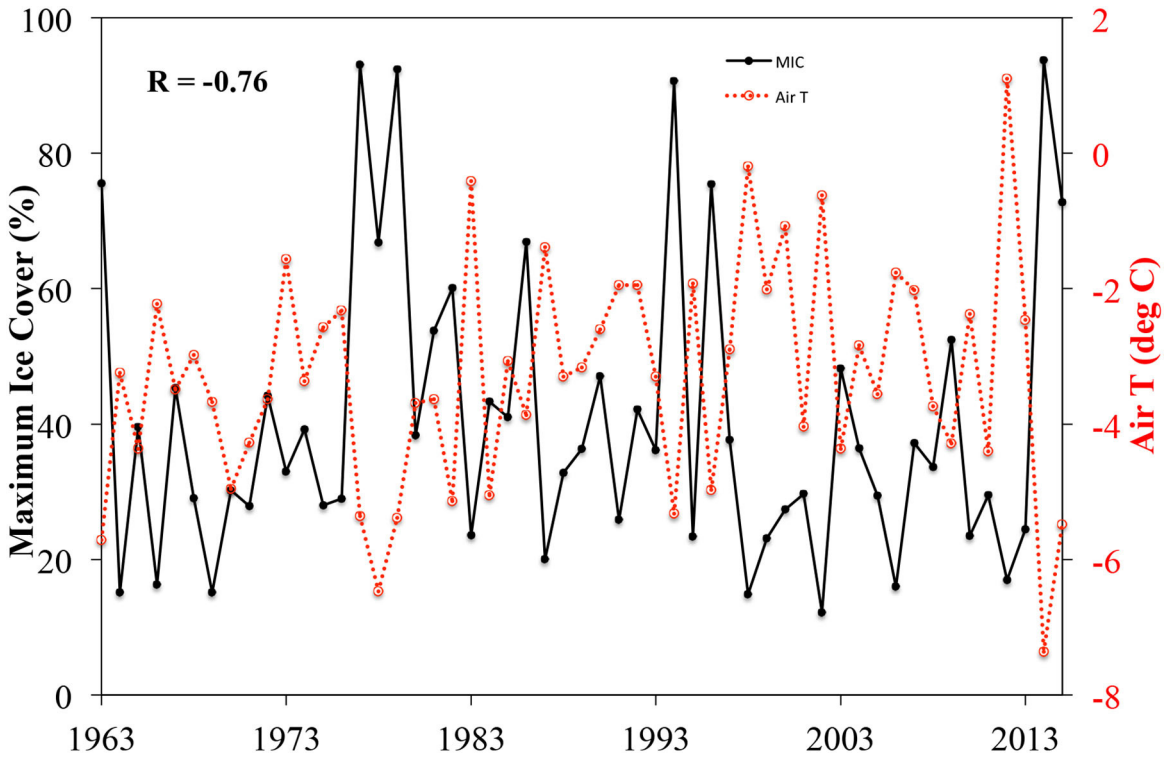

FIGURE 9 | The temporal variation in the maximum ice cover (MIC) (%) (solid black line) and surface air T (°C) (dashed red line) in the Lower Peninsula of Michigan.

TABLE 4 | Impact of the ENSO on annual total snowfall in the LPM.

	El Niño	La Niño
Number of years	18	26
Mean snowfall (cm)	157.99*	190.75*
Mean temperatures (°C)	−2.96#	−3.26#

*Indicate significance at the 95% confidence level.
#Not significant at the 95% confidence level.

TABLE 5 | Impact of the NAO on annual total snowfall in the LPM.

	NAO(+)	NAO(–)
Number of years	28	22
Mean snowfall (cm)	169.93#	183.14#
Mean temperatures (°C)	−2.89*	−3.96*

*Significant at the 95% confidence level.
#Not significant at the 95% confidence level.

total snowfall, followed by the ENSO and NAO. Regional air temperatures have statistically significant (at the 95% confidence level) negative correlations with annual total snowfall in all stations used. Sea surface temperature anomalies in the Niño region 3.4 are significantly correlated with snowfall in the LPM in six of the eight stations (**Table 2**) for the period of 1932–2015. Sliding correlation analysis suggests that the average snowfall over the eight stations is significantly (at the 95% confidence level) correlated with the ENSO during the period of 1963–2015. It is demonstrated that the NAO is not significantly related to snowfall in the LPM. Our study also suggests that increased annual total snowfall occur in the years with higher MIC in Lake Michigan. Most of the increased snowfall occurs before the ice cover peaks in February/March. Regionally average air temperature has a strong correlation with MIC during the period of 1963–2015.

In summary, our study suggests that air temperature is highly correlated with annual snowfall in the LPM. During the period of 1932–2015, the winter air temperature averaged over the entire LPM has slightly decreased (not shown), which corresponds well with the increased trend in snowfall. Currently global mean temperature has continuously increased during the past decades. If the winter air temperature of the LPM follows the global trend, the annual total snowfall in the LPM might decrease in the future if the relationship persists. Additional data collection and further analysis are necessary to confirm the relationship between air temperatures and snowfall. Further, this study only used the dataset from those weather stations in the LPM that are homogeneous and appropriate for the long-term trend analysis based on Kunkel et al. (2009). Inclusion of additional weather stations might slightly affect the trend. Lastly, it should be noted that one of the caveats in this study is that statistical analysis can only refer the possible linkage between snowfall and several

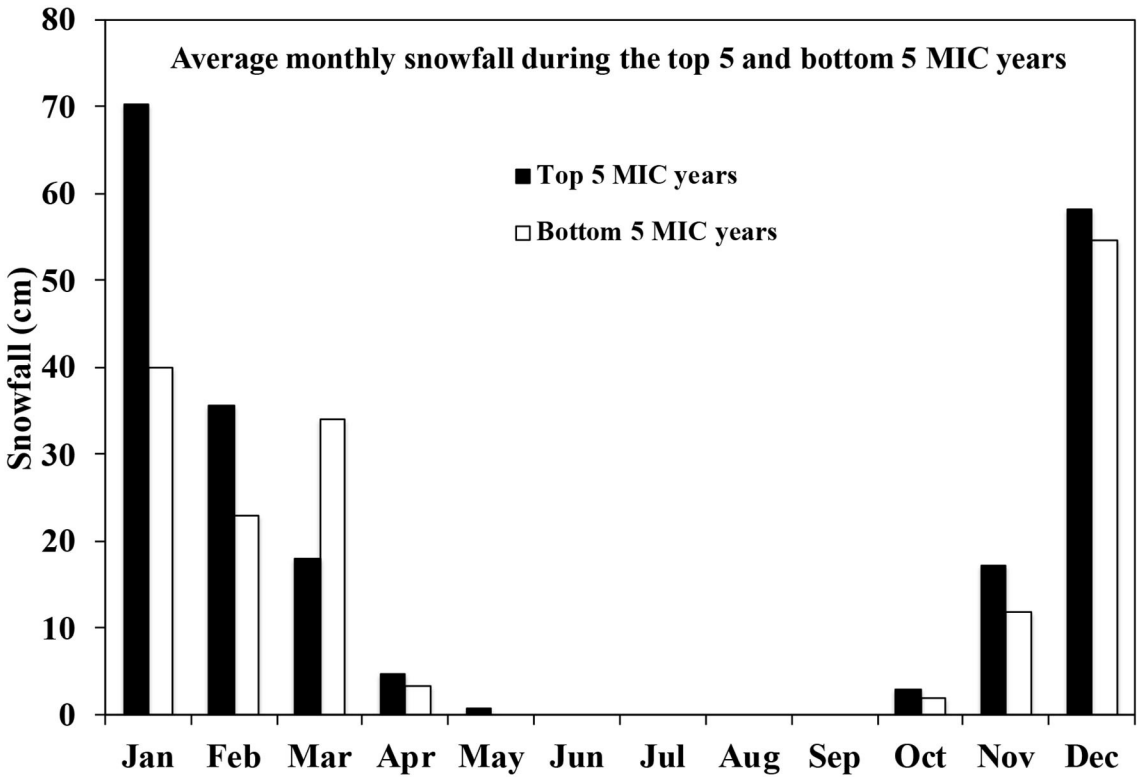

FIGURE 10 | Comparison of snowfall averaged over all eight stations during the top five and bottom five MIC years.

climatic variables. Modeling studies are required to provide the detailed mechanisms on how air temperatures/ENSO/NAO influence snowfall variability. This study on the trend of snowfall and its relationship with teleconnection patterns and regional temperatures/ice covers will provide scientific basis for policy makers on disaster clarification and severe winter storm policy and help local governments in preparation for winter seasons.

DATA AVAILABILITY STATEMENT

The original contributions presented in the study are included in the article/supplementary material, further inquiries can be directed to the corresponding author/s.

AUTHOR CONTRIBUTIONS

LM designed the study and performed the analysis with the assistance of BA and NK. LM wrote the manuscript in consultation with BA, NK, and KB. All authors discussed the results and commented on the manuscript.

FUNDING

The open access publication fees will be paid by Western Michigan University and W.E. Upjohn Center for the study of Geographical Change at WMU.

REFERENCES

Assel, R. A. (2005). Classification of annual Great Lakes ice cycles: winters of 1973–2002. *J. Clim.* 18, 4895–4905. doi: 10.1175/JCLI3571.1

Bai, X. Z., Wang, J., Sellinger, C., Clites, A., and Assel, R. (2012). Interannual variability of Great Lakes ice cover and its relationship to NAO and ENSO. *J. Geophys. Res. Oceans* 117, C03002. doi: 10.1029/2010JC006932

Baijnath-Rodino, J. A., and Duguay, C. R. (2018). Historical spatiotemporal trends in snowfall extremes over the Canadian domain of the Great Lakes Basin. *Adv. Meteorol.* 2018, 1–20. doi: 10.1155/2018/5404123

Bard, L., and Kristovich, D. A. R. (2012). Trend reversal in Lake Michigan contribution to snowfall. *J. Appl. Meteorol. Climatol.* 51, 2038–2046. doi: 10.1175/JAMC-D-12-064.1

Blechman, J. B. (1996). A comparison between mean monthly temperature and mean monthly snowfall in New York State. *Natl. Weather Dig.* 20, 41–53.

Braham, R. R., and Dungey, M. J. (1984). Quantitative estimates of the effect of Lake-Michigan on snowfall. *J. Clim. Appl. Meteorol.* 23, 940–949. doi: 10.1175/1520-0450(1984)023<0940:QEOTEO>2.0.CO;2

Brown, L. C., and Duguay, C. R. (2010). The response and role of ice cover in lake-climate interactions. *Prog. Phys. Geog.* 34, 671–704. doi: 10.1177/0309133310375653

Changnon, S. A. (1968). *Precipitation Climatology of Lake Michigan Basin*. Illinois Water Survey Bulletin, Illinois State Water Survey, Urbana. p. 46.

Clark, C., Ganesh-Babu, B., Elless, T., Lyza, A., Koning, D. M., Carne, A. R., et al. (2018). Spatio-temporal November and March snowfall trends in the Lake Michigan region. *Int. J. Climatol.* 38, 3250–3263. doi: 10.1002/joc.5498

Clark, C. A., Elless, T. J., Lyza, A. W., Ganesh-Babu, B., Koning, D. M., Carne, A. R., et al. (2016). Spatiotemporal snowfall variability in the Lake Michigan region: how is warming affecting wintertime snowfall? *J. Appl. Meteorol. Climatol.* 55, 1813–1830. doi: 10.1175/JAMC-D-15-0285.1

Coleman, J. S. M., and Stefl, D. J. (2016). Eastern united states snowfall variability with three atmospheric teleconnections patterns. *Int. J. Earth Atmos. Sci.* 3, 17–23.

Daly, C., Halbleib, M., Smith, J. I., Gibson, W. P., Doggett, M. K., Taylor, G. H., et al. (2008). Physiographically sensitive mapping of climatological temperature and precipitation across the conterminous United States. *Int. J. Climatol.* 28, 2031–2064. doi: 10.1002/joc.1688

Dockus, D. A. (1985). Lake-effect snow forecasting in the computer age. *Natl. Weather Dig.* 10, 5–19.

Durre, I., Menne, M. J., Gleason, B. E., Houston, T. G., and Vose, R. S. (2010). Comprehensive automated quality assurance of daily surface observations. *J. Appl. Meteorol. Climatol.* 49, 1615–1633. doi: 10.1175/2010JAMC2375.1

Gerbush, M. R., Kristovich, D. A. R., and Laird, N. F. (2008). Mesoscale boundary layer and heat flux variations over pack ice-covered Lake Erie. *J. Appl. Meteorol. Climatol.* 47, 668–682. doi: 10.1175/2007JAMC1479.1

Gong, G., Entekhabi, D., and Cohen, J. (2002). A large-ensemble model study of the wintertime AO–NAO and the role of interannual snow perturbations. *J. Clim.* 15, 3488–3499. doi: 10.1175/1520-0442(2002)015<3488:ALEMSO>2.0.CO;2

Gong, G., and Ge, Y. (2009). North American snow depth and climate teleconnection patterns. *J. Clim.* 22, 217–233. doi: 10.1175/2008JCLI2124.1

Hartnett, J. J. (2020). A classification scheme for identifying snowstorms affecting central New York State. *Int. J. Climatol.* 41, 1712–1730. doi: 10.1002/joc.6922

Hartnett, J. J., Collins, J. M., Baxter, M. A., and Chambers, D. P. (2014). Spatiotemporal snowfall trends in Central New York. *J. Appl. Meteorol. Climatol.* 53, 2685–2697. doi: 10.1175/JAMC-D-14-0084.1

Hayhoe, K., VanDorn, J., Croley, T., Schlegal, N., and Wuebbles, D. (2010). Regional climate change projections for Chicago and the US Great Lakes. *J. Great Lakes Res.* 36, 7–21. doi: 10.1016/j.jglr.2010.03.012

Hurrell, J. W. (1995). Decadal trends in the North-Atlantic oscillation - regional temperatures and precipitation. *Science* 269, 676–679. doi: 10.1126/science.269.5224.676

Kluver, D. B., Leathers, D. J. (2015). Winter snowfall prediction in the United States using multiple discriminant analysis. *Int. J. Climatol.* 35, 2003–2018. doi: 10.1002/joc.4103

Kunkel, K. E., and Angel, J. R. (1999). Relationship of ENSO to snowfall and related cyclone activity in the contiguous United States. *J. Geophys. Res. Atmos.* 104, 19425–19434. doi: 10.1029/1999JD900010

Kunkel, K. E., Ensor, L., Palecki, M., Easterling, D., Robinson, D., Hubbard, K. G., et al. (2009). A new look at lake-effect snowfall trends in the Laurentian Great Lakes using a temporally homogeneous data set. *J. Great Lakes Res.* 35, 23–29. doi: 10.1016/j.jglr.2008.11.003

Kunkel, K. E., Karl, T. R., Brooks, H., Kossin, J., Lawrimore, J. H., Arndt, D., et al. (2013). Monitoring and understanding trends in extreme storms state of knowledge. *Bull. Am. Meteorol. Soc.* 94, 499–514. doi: 10.1175/BAMS-D-11-00262.1

Lawrimore, J. H., Wuertz, D., Wilson, A., Stevens, S., Menne, M., Korzeniewski, B., et al. (2020). Quality control and processing of cooperative observer program hourly precipitation data. *J. Hydrometeorol.* 21, 1811–1825. doi: 10.1175/JHM-D-19-0300.1

Mahmood, R., Pielke, R. A. Sr., Hubbard, K. G., Niyogi, D., Bonan, G., Lawrence, P., et al. (2010). Impacts of land use/land cover change on climate and future research priorities. *Bull. Am. Meteorol. Soc.* 91, 37–46. doi: 10.1175/2009BAMS2769.1

Meng, L., and Ma, Y. (2021). On the relationship of lake-effect snowfall and teleconnections in the Lower Peninsula of Michigan, USA. *J. Great Lakes Res.* 47, 134–144. doi: 10.1016/j.jglr.2020.11.013

Mezzina, B., García-Serrano, J., Bladé, I., and Kucharski, F. (2020). Dynamics of the ENSO teleconnection and NAO variability in the North Atlantic–European late winter. *J. Clim.* 33, 907–923. doi: 10.1175/JCLI-D-19-0192.1

Norton, D. C., and Bolsenga, S. J. (1993). Spatiotemporal trends in lake effect and continental snowfall in the Laurentian Great-Lakes, 1951–1980. *J. Clim.* 6, 1943–1956. doi: 10.1175/1520-0442(1993)006<1943:STILEA>2.0.CO;2

Notaro, M., Zarrin, A., Vavrus, S., and Bennington, V. (2013). Simulation of heavy lake-effect snowstorms across the Great Lakes Basin by RegCM4: synoptic climatology and variability. *Month. Weather Rev.* 141, 1990–2014. doi: 10.1175/MWR-D-11-00369.1

Patten, J. M., Smith, S. R., and O'Brien, J. (2003). Impacts of ENSO on snowfall frequencies in the United States. *Weather Forecast* 18, 965–980. doi: 10.1175/1520-0434(2003)018<0965:IOEOSF>2.0.CO;2

Pettersen, C., Kulie, M. S., Bliven, L. F., Merrelli, A. J., Petersen, W. A., Wagner, T. J., et al. (2020). A composite analysis of snowfall modes from four winter seasons in Marquette, Michigan. *J. Appl. Meteorol. Climatol.* 59, 103–124. doi: 10.1175/JAMC-D-19-0099.1

Schmidlan, T. W. (1993). Impacts of severe winter weather during December 1989 in the Lake Erie snowbelt. *J. Climate* 6, 759–767. doi: 10.1175/1520-0442(1993)006<0759:IOSWWD>2.0.CO;2

Scott, R. W., and Huff, F. A. (1996). Impacts of the Great lakes on regional climate conditions. *J. Gt. Lakes Res.* 22, 845–863. doi: 10.1016/S0380-1330(96)71006-7

Seager, R., Kushnir, Y., Nakamura, J., Ting, M., and Naik, N. (2010). Northern Hemisphere winter snow anomalies: ENSO, NAO and the winter of 2009/10. *Geophys. Res. Lett.* 37, 14703. doi: 10.1029/2010GL043830

Serreze, M. C., Clark, M. P., and McGinnis, D. L. (1998). Characteristics of snowfall over the Eastern Half of the United States and relationships with principal modes of low-frequency atmospheric variability. *J. Clim.* 11, 234–250. doi: 10.1175/1520-0442(1998)011<0234:COSOTE>2.0.CO;2

Smith, S. R., and O'Brien, J. J. (2001). Regional snowfall distributions associated with ENSO: implications for seasonal forecasting. *B Am. Meteorol. Soc.* 82, 1179–1191. doi: 10.1175/1520-0477(2001)082<1179:RSDAWE>2.3.CO;2

Suriano, Z. J. (2019). Changing intra-synoptic type characteristics and interannual frequencies of circulation patterns conducive to lake-effect snowfall. *J. Appl. Meteorol. Climatol.* 58, 2313–2328. doi: 10.1175/JAMC-D-19-0069.1

Suriano, Z. J., Leathers, D. J., Hall, D. K., and Frei, A. (2019a). Contribution of snowfall from diverse synoptic conditions in the Catskill/Delaware watershed of New York state. *Int. J. Climatol.* 39, 3608–3618. doi: 10.1002/joc.6043

Suriano, Z. J., Robinson, D. A., and Leathers, D. J. (2019b). Changing snow depth in the Great Lakes basin (USA): implications and trends. *Anthropocene* 26, 100208. doi: 10.1016/j.ancene.2019.100208

Szczypta, C., Gascoin, S., Houet, T., Hagolle, O., Dejoux, J.-F., Vigneau, C., et al. (2015). Impact of climate and land cover changes on snow cover in a small Pyrenean catchment. *J. Hydrol.* 521, 84–99. doi: 10.1016/j.jhydrol.2014.11.060

Winkler, J. A., Arritt, R. W., and Pryor, S. C. (2012). "Climate projections for the midwest: availability, interpretation and synthesis," in *U.S. National Climate Assessment Midwest Technical Input Report*, eds J. Winkler, J. Andresen, J. Hatfield, D. Bidwell, and D. Brown, editors (Ann Arbor, MI: Great Lakes Integrated Sciences and Assessment (GLISA) Center). Available online at: https://glisa.umich.edu/media/files/NCA/MTIT_Future.pdf (accessed October 29, 2021).

Winkler, J. A., Guentchev, G. S., Liszewska, M., Perdinan and Tan, P. N. (2011). Climate scenario development and applications for local/regional climate change impact assessments: an overview for the non-climate scientist part II: considerations when using climate change scenarios. *Geography Compass* 5/6, 301–328. doi: 10.1111/j.1749-8198.2011.00426.x

Wolter, P. T., Johnston, C. A., and Niemi, G. J. (2006). Land use land cover change in the U.S. Great Lakes basin 1992–2001. *J. Great Lakes Res.* 32, 607–628. doi: 10.3394/0380-1330(2006)32[607:LULCCI]2.0.CO;2

Wright, D. M., Posselt, D. J., and Steiner, A. L. (2013). Sensitivity of lake-effect snowfall to lake ice cover and temperature in the Great Lakes

Region. *Month. Weather Rev.* 141, 670–689. doi: 10.1175/MWR-D-12-00038.1

Zhang, W., Mei, X., Geng, X., Turner, A. G., and Jin, F.-F. (2019). A nonstationary ENSO–NAO relationship due to AMO modulation. *J. Clim.* 32, 33–43. doi: 10.1175/JCLI-D-18-0365.1

Zhang, W., Wang, Z., Stuecker, M. F., Turner, A. G., Jin, F.-F., and annd Geng, X. (2018). Impact of ENSO longitudinal position on teleconnections to the NAO. *Clim. Dynam.* 52, 257–274. doi: 10.1007/s00382-018-4135-1

Conflict of Interest: The authors declare that the research was conducted in the absence of any commercial or financial relationships that could be construed as a potential conflict of interest.

Publisher's Note: All claims expressed in this article are solely those of the authors and do not necessarily represent those of their affiliated organizations, or those of the publisher, the editors and the reviewers. Any product that may be evaluated in this article, or claim that may be made by its manufacturer, is not guaranteed or endorsed by the publisher.

frontiers in Water

ORIGINAL RESEARCH
published: 07 December 2021
doi: 10.3389/frwa.2021.780869

The Seasonal Snowfall Contributions of Different Snowstorm Types in Central New York State

*Justin J. Hartnett**

Department of Geography and Environmental Sustainability, State University of New York College at Oneonta, Oneonta, NY, United States

Located at the eastern extent of the Great Lakes snowbelt, Central New York averages some of the highest annual snowfall totals east of the Rocky Mountains. This is in large part due to the variety of snowstorms that affect the region including lake-effect storms, coastal storms, and overrunning storms. Previous estimates suggest that lake-effect snowstorms account for approximately half of the seasonal snow in the Great Lakes basin, but ignore the spatial variability that exists within the region. Therefore, this study examines the seasonal snowfall contributions of the different snowstorm types to affect Central New York. Results suggest that although lake-effect snowstorms are the dominant snowstorm type in the region, their seasonal snowfall contributions vary between 13 and 48%. Although lake-effect snowstorms produce more snow during the peak and mid-seasons, their relative contribution is greatest during the early and mid-winter seasons. Generally, higher contributions occur near the Tug Hill Plateau, with lower contributions in southern Central New York. Instead, snowfall in southern Central New York is mostly dominated by Nor'easters (16–35%), with lesser contributions from Rocky lows (14–29%). Overrunning storms that originate in Canada (e.g., Alberta clippers) and non-cyclonic storms contribute the least to seasonal snowfall totals across Central New York; however, they are often the catalyst for lake-effect snowstorms in the region, as they advect continental polar air masses that destabilize across the lake. Understanding the actual snowfall contribution from different snowstorm types is needed for future climate predictions. Since the potential trajectory of future snowfall varies according to the type of storm, climate models must accurately predict the type of storm that is producing the snow.

Keywords: snowstorms, snowfall, lake-effect, Nor'easters, cokriging

OPEN ACCESS

Edited by:
Galina Guentchev,
Met Office, United Kingdom

Reviewed by:
Allan Frei,
Hunter College (CUNY), United States
Zachary Suriano,
University of Nebraska Omaha, United States

***Correspondence:**
Justin J. Hartnett
justin.hartnett@oneonta.edu

Specialty section:
This article was submitted to Water and Climate, a section of the journal Frontiers in Water

Received: *21 September 2021*
Accepted: *15 November 2021*
Published: *07 December 2021*

Citation:
Hartnett JJ (2021) The Seasonal Snowfall Contributions of Different Snowstorm Types in Central New York State. Front. Water 3:780869. doi: 10.3389/frwa.2021.780869

INTRODUCTION

Snow is an integral part of the environment and society of high latitudes and high elevations (Rooney, 1967; Sharratt et al., 1992; Kocin and Uccellini, 2004; Cortinas and Kitron, 2006; Rohr et al., 2011; Hagenstad et al., 2018). This is especially prevalent in areas surrounding the Laurentian Great Lakes, which experience some of the greatest seasonal snowfall totals in North America. The presence of the Great Lakes considerably affects the climate of this region, especially during cold-season months (October–May). As cold air advects across the relatively warmer lakes, there

is a destabilization of the air column and an influx of moisture (Peace and Sykes, 1966; Niziol, 1987; Pease et al., 1988). This leads to frequent, and sometimes intense lake-effect precipitation, downwind of the lakes (e.g., Niziol et al., 1995).

Lake-effect precipitation occurs approximately one out of every five days in the early winter season (September–November) of the Great Lakes basin (Miner and Fritsch, 1997). Precipitation is predominately rain from September through October, but often transitions to snow following the first week of November. Lake-effect storms become more frequent as the season progresses, peaking in early January (Niziol et al., 1995). Due to their relative frequency, it is estimated that lake-effect snowstorms contribute anywhere from 20 to 80% of the seasonal snowfall in the Great Lakes basin (Eichenlaub, 1970; Miner and Fritsch, 1997; Liu and Moore, 2004; Veals and Steenburgh, 2015). Eichenlaub (1970) suggests that lake-effect storms contribute at least 20% of the seasonal snowfall in areas lee of Lake Superior and Lake Michigan. This estimate is modest, compared to those from other studies that suggest contributions are closer to 50% in other subregions of the Great Lakes basin and during more recent years (Kelly, 1986; Braham and Dungey, 1995; Liu and Moore, 2004; Hartnett, 2020; Pettersen et al., 2020; Suriano and Wortman, 2021).

The influence of lake-effect snowstorms varies across the Great Lakes region. Multiple researchers have noted that seasonal snowfall is highly influenced by a location's elevation, and proximity and orientation to the lakes (e.g., Hjelmfelt, 1992; Scott and Huff, 1996; Perry and Konrad, 2006; Hartnett et al., 2014; Campbell et al., 2016). In general, areas downwind (east) of the lakes tend to be snowier than those upwind (west). For example, Changnon (1968) and Gatz and Changnon (1976) suggest that lake-effect snowstorms increase snowfall by up to 100% on the downwind shores of Lake Michigan compared to the upwind shores, especially in December. A more modest increase of 20–35% was found by subsequent studies conducted within the region (Kelly, 1986; Braham and Dungey, 1995; Scott and Huff, 1996, 1997). Some of the snowiest regions within the Great Lakes basin are found to the lee (downwind) of Lake Ontario, including the Tug Hill Plateau of New York State (further referred to as the Tug Hill). Using different approaches, the recent studies of Hartnett (2020) and Suriano and Wortman (2021) suggest that lake-effect snowstorms account for ∼35–42% of the snowstorm events to the lee of Lake Ontario, yet contribute between 42 and 48% of the seasonal snowfall. The percent contribution is even greater within the Tug Hill, as Veals and Steenburgh (2015) estimate that lake-effect snow accounts for ∼61–76% of the mean cool-season snowfall. The greater percentages in the Tug Hill are likely due to the more frequent and more intense lake-effect snowstorms that occur because of the land-breeze fronts that form along the southeastern shore of Lake Ontario, the localized ascent along the frontal boundary, and the intensified and broadened ascent regions induced by the Tug Hill (Campbell and James Steenburgh, 2017).

Although lake-effect snowstorms are found to dominate snowfall in this region, they are not the only snowstorm type to contribute to seasonal totals. Karmosky (2007) and Suriano et al. (2019) suggest that three distinctive weather patterns tend to produce snowfall in upstate New York including coastal mid-latitude cyclones, overrunning systems, and lake-effect or Great Lakes enhanced storms. Suriano et al. (2019) found that overrunning systems and coastal mid-latitude cyclones account for ∼55% of the seasonal snowfall in Catskill/Delaware Watershed. Hartnett (2020) found 11 different snowstorm types that contribute to seasonal snowfall totals in central New York State. These storms included clippers, Colorado lows, frontal storms, Great Lakes lows, Hudson lows, lake-effect snowstorms, Nor'easters, Oklahoma hooks, Texas hooks, tropical cyclones, and upper atmospheric disturbances. Similar to Kelly (1986), the author found that non-lake effect snowstorms occur more frequently than lake-effect snowstorms, with Nor'easters and clippers contributing ∼11.3 and 9.2%, respectively, of the seasonal snowfall between 1985 and 2015. However, distinguishing lake-effect snow from synoptically driven snow is complicated by mesoscale lake snow bands within large-scale cyclonic storms (e.g., Houze and Hobbs, 1982; Kristovich et al., 2000; Tardy, 2000; Owens et al., 2017; Kulie et al., 2021). This can result in additional snowfall, which is termed lake-enhanced snow (Eichenlaub and Hodler, 1979; Liu and Moore, 2004).

To date, most studies assessing snowfall contributions to the lee of Lake Ontario only focus on snowfall from lake-effect storms. Additionally, most studies use proxies to identify lake-effect snow versus non-lake-effect snow, such as synoptic patterns (Suriano et al., 2019; Suriano and Wortman, 2021) or cloud base heights (Pettersen et al., 2020), rather than a complete analysis of each individual snowstorm. There also is little attention given to the spatial variability that exists within the Lake Ontario basin, even though it is well document that lake-effect snow contributions decrease further from the Great Lakes (Dewey, 1970; Scott and Huff, 1996, 1997; Suriano et al., 2019). Snowstorms, especially lake-effect snowstorms, can produce extremely localized snow (e.g., Andersson and Nilsson, 1990; Steenburgh et al., 2000; Eito et al., 2005; Laird et al., 2009; Kindap, 2010). Relatively small topographic features such as hills and plateaus downwind of the lakes can dramatically increase snowfall totals (Hill, 1971; Hjelmfelt, 1992; Campbell and James Steenburgh, 2017). The objectives of this study are to provide the first comprehensive examination of snowstorms affecting the Lake Ontario basin and to determine how snowfall contributions from various storms varies spatially across the region. Since snowfall trends vary between lake-effect and non-lake-effect snowstorms (Norton and Bolsenga, 1993; Leathers and Ellis, 1996; Burnett et al., 2003; Kunkel et al., 2009a; Bard and Kristovich, 2012; Hartnett et al., 2014; Notaro et al., 2015; Suriano and Leathers, 2016), teasing out the snowfall contributions of different snowstorm types will help to better understand potential future changes.

METHODS

Snowstorm Categorization

Seasonal snowfall contributions were determined by identifying every snowstorm to influence central New York State (**Figure 1**) from the 1995/96 to 2014/15 cold seasons (October to May). Snowstorms were identified using data from the National

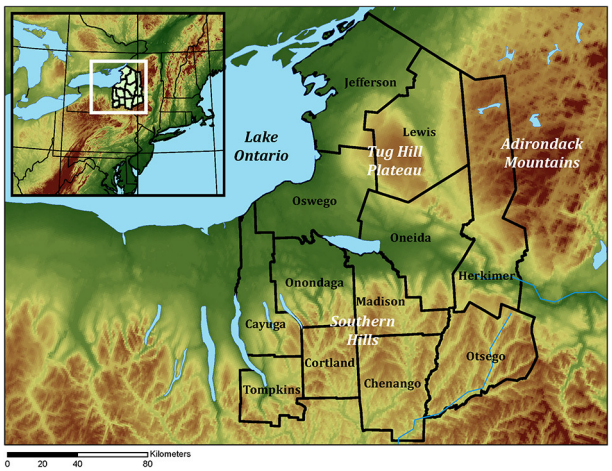

FIGURE 1 | Central New York study area. Included are the county names (black text) and prominent regions (white text).

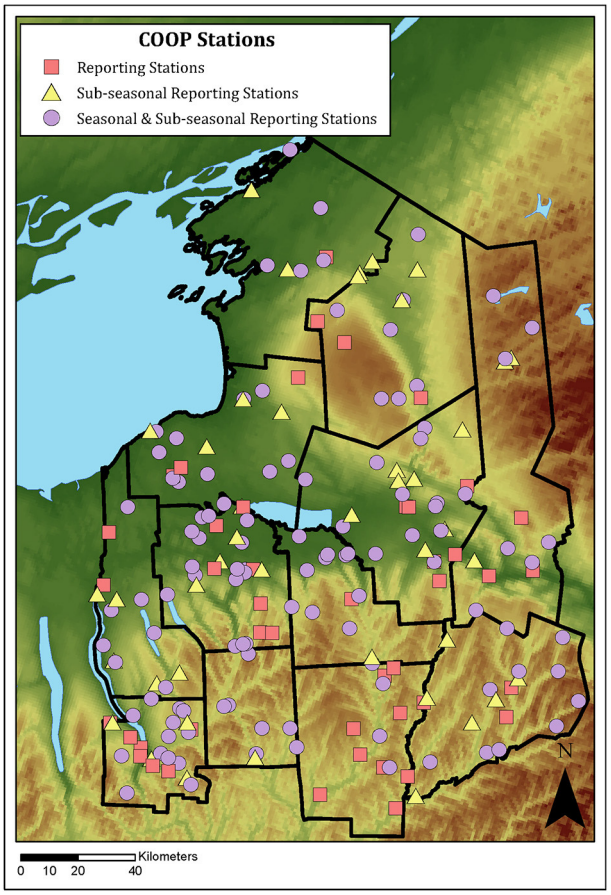

FIGURE 2 | COOP stations used for analysis in Central New York. Included are the 202 COOP stations reporting from 1995/96 to 2014/15 ("Reporting Stations"), 155 stations used for the sub-seasonal analysis ("Sub-seasonal Reporting Stations"), and the 111 stations used for seasonal analyses ("Seasonal and Sub-seasonal Reporting Stations").

Weather Service's Cooperative Observer Program (COOP) and are defined as any storm in which at least 0.1 cm of snow was observed for at least two of the two-hundred and two reporting stations within the study area (Perry et al., 2007; Hartnett, 2020; **Figure 2**). Using the methods outlined by Hartnett (2020), a storm was considered independent from other events if there was at least a 6-h gap in precipitation (e.g., 6-h gap in 15-min precipitation records and/or radar) anywhere within the study area. There were 1,285 snowstorms identified during the study period. Daily snowfall totals for the 202 reporting COOP stations were assigned to individual storms. In some instances, a single storm spanned multiple days, and therefore its snowfall total represents the summation of multiple daily snowfall observations. Due to snowfall measurement practices (Doesken and Judson, 1996; NWS, 2012), limitations exist on the temporal resolution of snowfall observations. Thus, it is assumed that a single storm produces the entire daily snowfall total observed on a day. Although there may be inaccuracies that emerge from this assumption (Wu et al., 2005; Daly et al., 2007; Kunkel et al., 2007; Leeper et al., 2015; Lundquist et al., 2015), it is an adequate method of interpretation and has been partly addressed later in this study with the inclusion of lake snow.

Following the methods and classification system outlined by Hartnett (2020), snowstorms were categorized into storm types using NCEP/NCAR reanalyzes and NEXRAD data. Due to a lack of NEXRAD data prior to the 1995/96 season, snowstorm observations are limited to the establishment of the Binghamton, NY (KBGM) and Montague/Ft. Drum (KTYX) radar sites. Lake-effect snowstorms were delineated as any storm lacking a central low pressure within 150 km of the study area and a quasi-stationary banded precipitation pattern connected to Lake Ontario that strengthened downwind of the lake and was independent from other mesoscale cloud structures. If these conditions were not met, yet there was no central low pressure within 150 km of Central New York, the storm was classified as a non-cyclonic snowstorm. Cyclonically driven snowstorms are those with a central low pressure within 150 km of the study area. These storms were further classified based on their zone of cyclogenesis and grouped into one of three categories: Nor'easters, Canadian lows (Clippers, Hudson lows, and Great Lakes lows), and Rocky lows (Colorado lows, Oklahoma hooks, and Texas hooks). Snowstorms originating as tropical storms were omitted from this study due to their infrequency (only one storm during the study period). Snowstorm counts for the five categories area found in **Table 1**.

Since there are instances where lake-enhanced snow bands occur during cyclonic storms (Eichenlaub and Hodler, 1979; Liu and Moore, 2004; Owens et al., 2017; Kulie et al., 2021), storms were also categorized as lake snowstorms and non-lake snowstorms (**Table 1**). Lake snowstorms attempt to account for lake-enhanced snowfall events and are categorized similar to lake-effect snowstorms; however, precipitation and cloud structure does not have to be independent from other mesoscale storms and there does not have to be a six-hour gap in

TABLE 1 | Number of snowstorms per storm type to affect Central New York from the 1995/96 season to the 2014/15 season.

Storm type	Count
Lake snow	495
Non-lake snow	790
Lake-effect	381
Non-cyclonic	255
Upper disturbance	172
Frontal	83
Nor'easters	144
Canadian lows	253
Clipper	136
Hudson low	23
Great Lakes low	94
Rocky lows	251
Colorado lows	100
Oklahoma hook	98
Texas hook	53
Tropical storm	1
Total	1,285

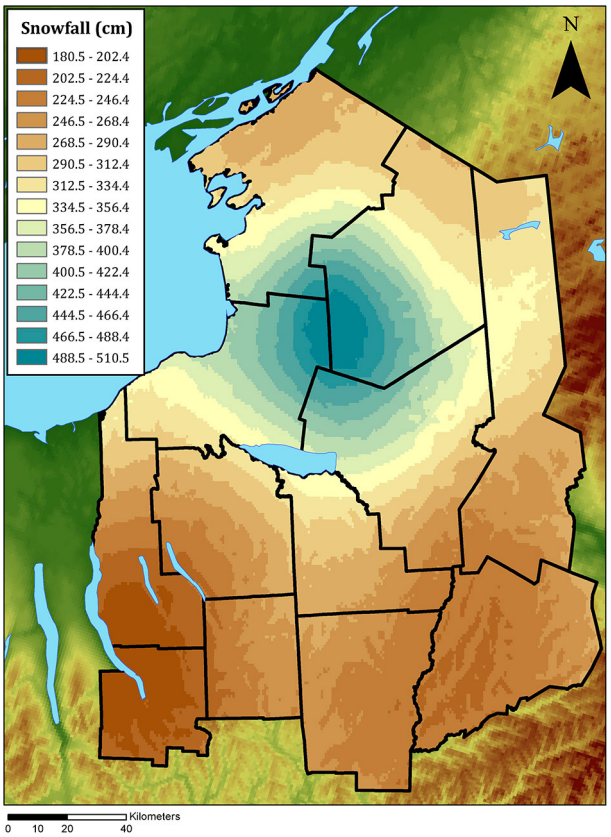

FIGURE 3 | Average seasonal snowfall totals (cm) for Central New York from 1995/96 to 2014/15.

precipitation between storm events (Hartnett, 2020). Non-lake snowstorms are all other storms. These categories are mutually exclusive from each other, but not from the other storm types. For example, a storm can be classified as both a Nor'easter and a lake snowstorm but cannot be classified as both a lake snowstorm and a non-lake snowstorm. The methods presented in this study are a more direct analysis of snowstorms, expanding upon the procedures outlined by Pettersen et al. (2020) and Suriano and Wortman (2021) who use proxies to distinguish lake-effect snow versus non-lake-effect snow.

Total Seasonal Snowfall Contributions

To determine the seasonal snowfall contributions of the different snowstorm types within Central New York, total monthly snowfall for each station was calculated for cold-season months from July 1995 to June 2015. A station's monthly snowfall total was calculated by summing the snowfall produced at that station by each snowstorm that occurred during that month. Since these are voluntary data, there are instances where snowfall measurements are missing for some snowstorms, most notably, during light snowfall events. Therefore, using the guidance of Kunkel et al. (2009b), a station's monthly snowfall total was only used if snowfall observations were reported for at least 90% of the monthly snowstorms during that month. Data were removed for all months that did not contain any snowstorms.

Prior to calculating snowfall contributions, seasonal snowfall totals for each station were calculated by summing the monthly snowfall totals for that station across the snowfall season, which was defined as July 1–June 30. A station's seasonal snowfall total was only reported if monthly observations existed for every cold season month (October–May). To increase the spatial coverage of observations, any station with at least one season that met the above criteria were used for analysis (111 stations; **Figure 2**). Using the 111 available stations, interpolated surfaces were created for every snowfall season from 1995/96 to 2014/15. Surfaces were created using simple cokriging interpolations in ArcGIS with elevation as an independent variable (Guan et al., 2005; Grieser, 2015). The twenty (one per season) interpolated surfaces were then averaged in ArcGIS (Norton and Bolsenga, 1993), to produce a single map representing the average seasonal snowfall across Central New York (**Figure 3**). This figure provides a reference to compare the percent contributions.

To address the percent contribution of the different snowstorm types to seasonal snowfall totals within Central New York, seasonal totals for each storm type were calculated for the 111 stations. To compare snowfall totals across the study area and reduce biases in the results, the ratio of snowfall produced by each storm type to the total snowfall produced at a station was calculated. These values are referred to as the percent contributions. The percent contributions were then used to create interpolated surfaces for each storm type for every cold season from 1995/96 to 2014/15. The average snowfall contribution across the study area was calculated for each storm type by averaging the 20 interpolated surfaces (**Figures 4**, **5**).

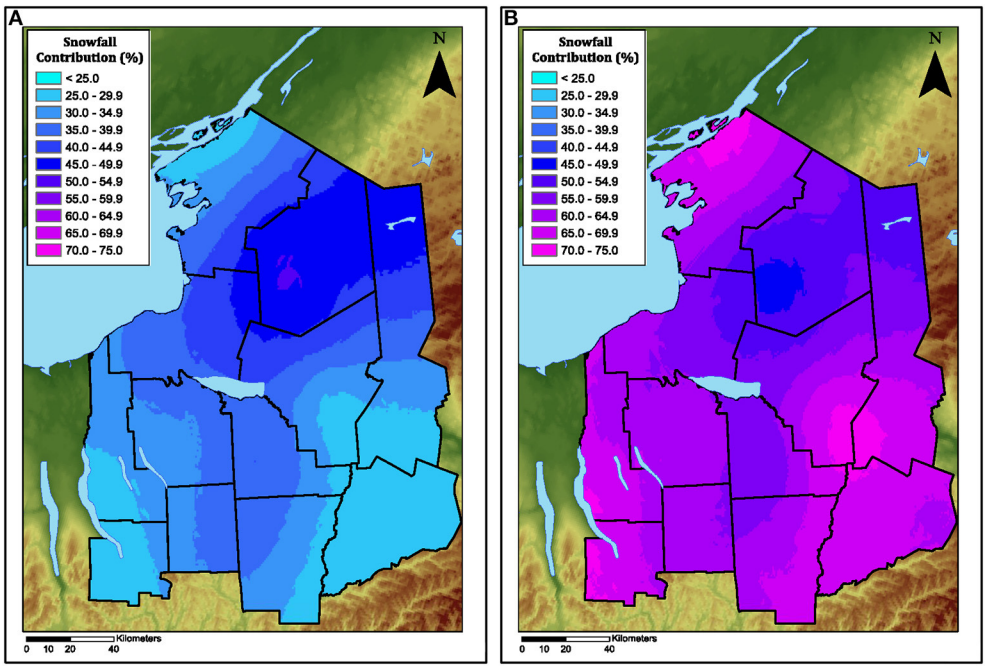

FIGURE 4 | Seasonal snowfall contributions of lake snowstorms **(A)** and non-lake snowstorms **(B)** from 1995/96 to 2014/15.

Sub-seasonal Lake-Effect Snow Contributions

To address the seasonal variability in snowfall contributions from lake-effect storms that exists within a cold season, monthly totals were grouped into four sub-seasonal categories: early season (October to November), peak season (December to January), mid-season (February to March), and late season (April to May) (Niziol et al., 1995; Veals and Steenburgh, 2015; Clark et al., 2016). Monthly snowfall totals for each cold season calculated in "Total Seasonal Snowfall Contributions" Section were summed across the sub-seasonal scale for each COOP station. Sub-seasonal totals were only reported if that station had reliable records (snowfall reports for 90% of the monthly snowstorms) for both months (e.g., reliable data for December 1995 and January 1996). To increase the spatial density of observations, COOP stations were retained for analysis if there was at least one reliable sub-seasonal snowfall total during the study period. Thus, 155 COOP stations were used for analysis in this section (**Figure 2**). Sub-seasonal lake-effect snowfall contributions for each station were calculated by comparing the sub-seasonal snowfall totals from these storms to the total sub-seasonal snowfall at that station. Like "Total Seasonal Snowfall Contributions" Section, interpolated surfaces were created in ArcGIS for each sub-season. The 20 surfaces were averaged to produce two figures for each sub-season, one representing the average snowfall contribution total and the other representing the percent contribution of lake-effect snow across Central New York.

RESULTS

Seasonal Snowfall Totals

The mean seasonal snowfall in Central New York from 1995/96 to 2014/15 is plotted in **Figure 3**. Seasonal snowfall totals are greatest (∼500 cm) over the Tug Hill, with lower totals generally further from the region. Seasonal snowfall contributions of lake-snowstorms and non-lake-snowstorms are presented in **Figure 4**. Throughout the majority of Central New York (98.4%), non-lake snowstorms contribute more to these seasonal snowfall totals than lake snowstorms. A small section of the Tug Hill is the only location that receives more snowfall from lake snow than non-lake snow. Instead, the majority (77.8%) of the area receives between 30 and 50% of its seasonal snowfall from lake snowstorms, including areas downwind of Lake Ontario, the western Adirondack Mountains, and the Southern Hills. Lake snow contributions were least in areas furthest from and sub-parallel to the horizontal axis of Lake Ontario.

Seasonal Snowfall Contributions

To examine the spatial variation of seasonal snowfall contributions from different storm types, snowfall contributions were mapped for the five snowstorm types (**Figure 5**). While it is widely believed that lake-effect snowstorms are the dominant snowfall producer in Central New York (e.g., Burnett et al., 2003; Hall et al., 2017; Suriano et al., 2019; Hartnett, 2020), the figures show that this is not the case throughout the entire study area (**Figure 5A**). Lake-effect snow accounts for 35–48% of the

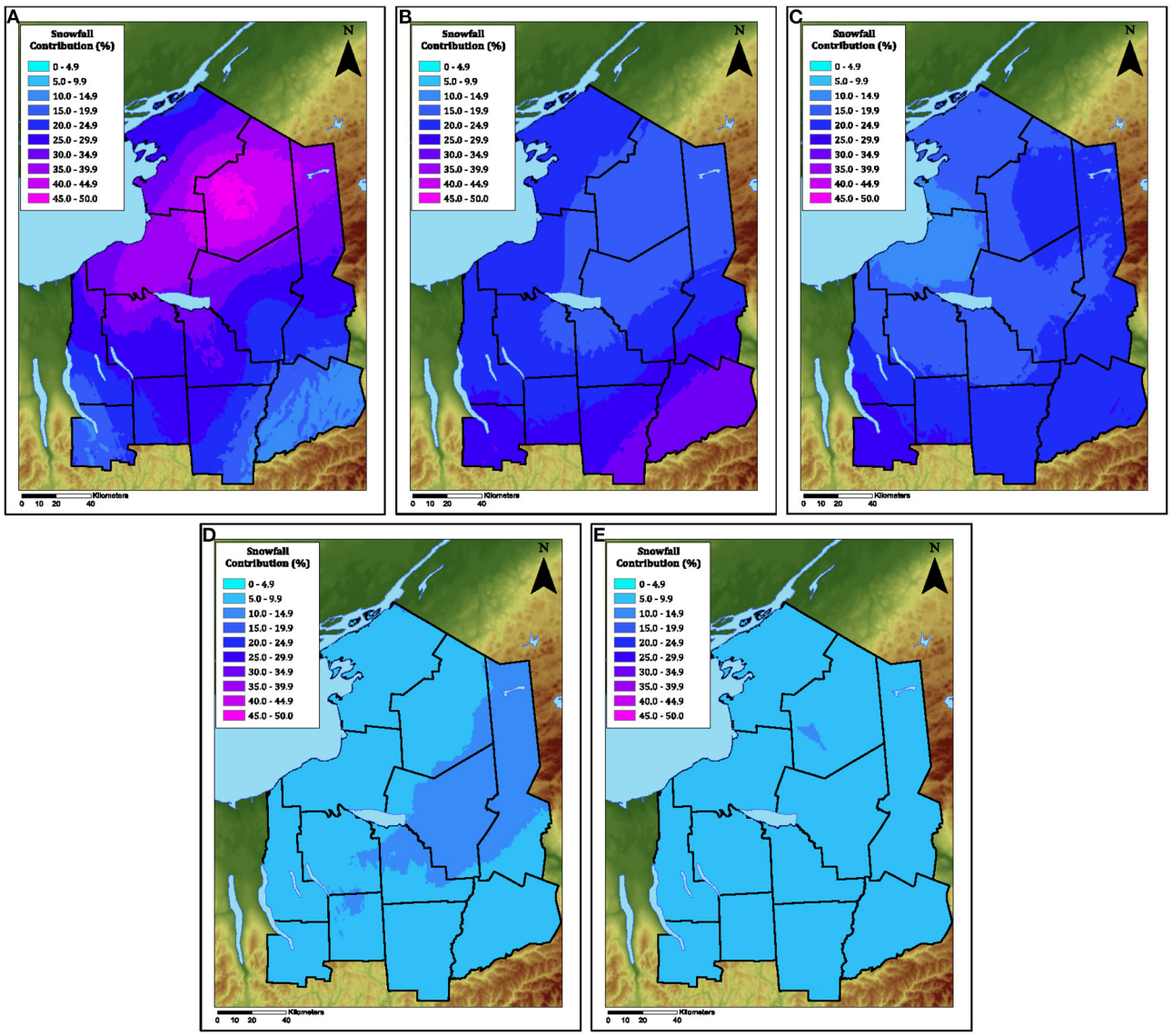

FIGURE 5 | Seasonal snowfall contributions for the five different snowstorms to affect Central New York from 1995/96 to 2014/15. Figures include contributions from lake-effect storms **(A)**, Nor'easters **(B)**, Rocky lows **(C)**, Canadian lows **(D)**, and non-cyclonic storms **(E)**.

seasonal snowfall over northern Central New York, whereas contributions are as low as 13–15% in southeastern Central New York. Lake-effect snowstorms for the majority (71.7%) of the region account for at least 20% of the seasonal snowfall.

Seasonal snowfall contributions of Nor'easters and Rocky lows are greatest for southern Central New York (**Figures 5B,C**). Although patterns are similar, there are noticeable differences in the spatial distribution of their contributions. Snowfall contributions from Nor'easters are greatest (30–35%) in southeastern Central New York, and generally decrease to the northwest (**Figure 5B**). Comparatively, there is a pronounced increase in the percent contribution (25–30%) from Rocky lows in southwestern Central New York and a noticeable decrease (10–15%) over Oswego County, just west of Lake Ontario (**Figure 5C**). It should be noted that these figures represent the percent contribution of a snowstorm to seasonal snowfall totals relative to the amount of snow a location receives. Therefore, even though Nor'easters only contribute between 15 and 20% of the annual snow in the Tug Hill, this region also averages ∼200 cm of more snowfall than other areas in Central New York (**Figure 3**). Conversely, the greater snowfall contributions in southern and southeastern Central New York are in large part due to the lower seasonal snowfall totals. However, the use of percentages allows for comparisons between different areas regardless of their seasonal snowfall totals.

Seasonal snowfall contributions from Canadian lows and noncyclonic storms are more homogeneous throughout the study area (**Figures 5D,E**). Although there is some spatial

variability that exists, it is not as prominent as the other three storm types. Snowfall contributions from Canadian lows are greatest (10–15%) over eastern Central New York, most notably around the western edge of the Adirondack Mountains (**Figure 5D**). Seasonal contributions from noncyclonic snowstorms exhibit a slightly higher contribution (10–15%) over a small area in Lewis County (**Figure 5E**).

Sub-seasonal Lake-Effect Snow Contributions

Multiple researchers have suggested that lake-effect snow exhibits sub-seasonal variability in its prevalence (Strommen and Harman, 1978; Niziol et al., 1995; Veals and Steenburgh, 2015; Clark et al., 2016, 2020; Fairman et al., 2016). Harrington and Dewey (1987) found that lake-effect snowstorms are most common from November to January, when the lake surface is the warmest, resulting in large surface to 850 hPa lapse rates and minimal ice cover. Therefore, cold seasons were divided into four time periods (early, peak, mid-, and late seasons) and contributions were averaged across the 20 seasons (**Figure 6**). The results suggest that lake-effect snowstorms contribute considerably more snowfall during the peak season and mid-season than during the early and late seasons (**Figures 6A,C,E,G**). Nontheless, lake-effect snow accounts for a greater percentage of the sub-seasonal snow during the early and peak-seasons (October–January) (**Figures 6B,D,F,H**). Spatial patterns were mostly consistent across the four sub-seasons, as lake-effect snowfall contributions were greatest directly east of Lake Ontario. However, there was a movement of the greatest snowfall totals closer to the lake as the season progressed (**Figures 6A,C,E,G**). Comparatively, the percent contribution of lake-effect snow exhibited greater variability throughout a season than snowfall totals. During the early and peak seasons, lake-effect contributed the most to seasonal snowfall totals in north-central Central New York, including the Tug Hill (**Figures 6B,D,F,H**). By the mid-season, the greatest contributions were near the southeastern shore of the lake, centered over western Oswego County. Come the late-winter, lake-effect was relatively sparse throughout Central New York.

Even though the general spatial patterns of lake-effect snowfall contributions remained relatively consistent across the four sub-seasons, the relative percentage of lake-effect snow compared to the other snowstorm types changed dramatically as winter progressed. In the early season (October–November), lake-effect snow dominates throughout Central New York, accounting for at least 40% of the snow throughout the majority (73.9%) of the study area (**Figure 6B**). The greatest contributions (> 65%) are centered over the Tug Hill, producing upwards of 30 cm per season (**Figure 6A**). Lake effect snow remains the dominant snowfall contributor in December and January for northern Central New York, but produces considerably more snowfall (225–300 cm) during this time (**Figures 6C,D**). The largest contributions from lake-effect snow shifted north, with parts of northern Lewis and northwest Jefferson Counties receiving 45–55% of their snowfall from lake-effect (**Figure 6D**). Lake effect is noticeably less prevalent in southern Central New York with contributions ranging from 9 to 15%. Later in the snowfall season, lake-effect contributions decrease further. Although these storms are still producing an average of 80–180 cm of snow over and around the Tug Hill from February–March, they only account for 25–35% of the snow, mostly near the lakeshore (**Figures 6E,F**). The maximum percentage that lake-effect contributed during this time (30–35%) was located on the southeastern shore of the lake over western Oswego County. By the late-snowfall season (April–May), lake-effect snow accounts for less than one centimeter of the snow, which equates to <5% of the snowfall that occurs throughout Central New York (**Figures 6G,H**).

DISCUSSION

Snowfall Contributions From Lake-Effect Snow

A persistent question in the climatological community has been how much of the Great Lakes' snowfall derives from lake-effect snow. Previous estimates suggest that lake-effect snowstorms contribute between 30–70% of the seasonal snowfall downwind of the Great Lakes (Eichenlaub, 1970; Miner and Fritsch, 1997; Liu and Moore, 2004; Veals and Steenburgh, 2015). However, these estimates ignore the spatial variability that exists within a lake's snow basin, and often assumes a single contribution at a coarse resolution. Findings from this research suggest that the greatest contributions (45–55%) from lake snowstorms are located directly east of Lake Ontario, including over the Tug Hill (**Figures 3**, **4**); findings that are consistent with those of Hartnett (2020) and Suriano and Wortman (2021). Although lake snowstorms account for over 50% of the seasonal snowfall in parts of Central New York, contributions are closer to 25% further from the lake. These findings align with those of Eichenlaub (1970), who found that lake-derived snowfall accounts for at least 20% of the seasonal snowfall in areas to the lee of the Great Lakes. However, this is notable variability within a relatively small area. It is well-documented that lake-effect snow can be highly localized, as it depends on factors such as wind speed and direction, fetch, and elevation (Peace and Sykes, 1966; Niziol, 1987; Reinking et al., 1993; Niziol et al., 1995; Lackmann, 2001). Slight changes in any of these factors can produce large magnitude differences in snowfall totals between locations only kilometers away. This research shows that seasonal snowfall contributions vary considerably across central New York State, and the importance of scale when working with lake-effect snow, something that has been largely ignored in previous studies.

Lake-effect storms contribute the most to seasonal snowfall totals to the lee of Lake Ontario, with enhanced contributions also over the Southern Hills and western Adirondack Mountains (**Figure 5A**). The higher elevations and orientations of these regions are prime for lake-effect snow, leading to greater contributions (Wilson, 1977; Hjelmfelt, 1992; Notaro et al., 2013b). Lake-effect snow is especially common from December to January with contributions between 100 and 300 cm of snow for over half of the study area (**Figure 6C**). Although still common in the early and mid-seasons, snowfall contributions are

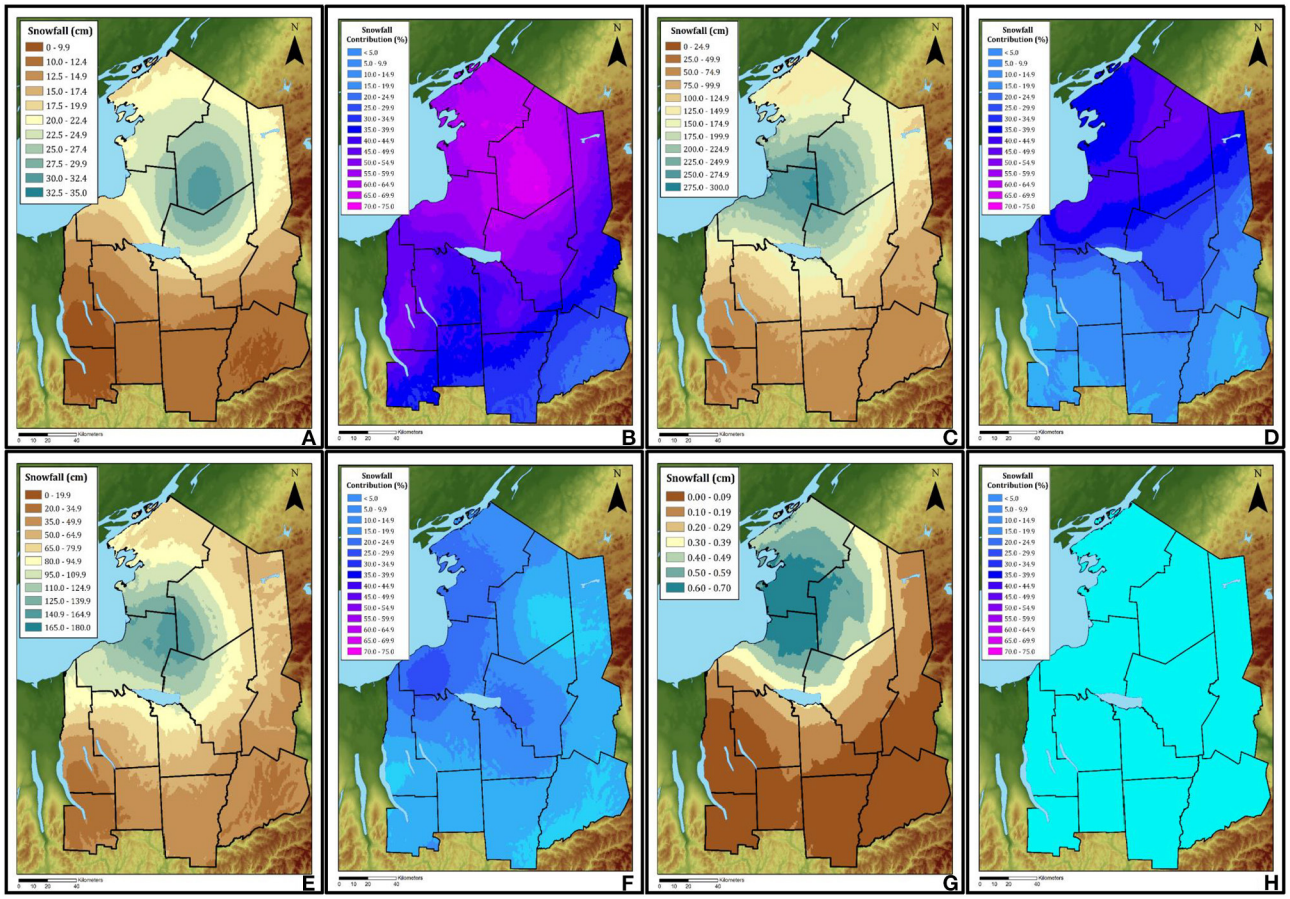

FIGURE 6 | Sub-seasonal snowfall contributions of lake-effect snow within Central New York from 1995/96 to 2014/15. Snowfall contributions (totals and percentage) are mapped for October to November **(A,B)**, December to January **(C,D)**, February to March **(E,F)**, and April to May **(G,H)**.

considerably lower than the peak season (**Figures 6A,E**). Relative to the total snowfall during each sub-season, the majority of the study area receives at least 25–35% of its snowfall from lake-effect snowstorms from October–January (**Figures 6A,B**). Lake-effect contributions decrease considerably from February–May across the study area. The decrease is likely due to changes in lake and atmospheric dynamics (e.g., colder surface lake temperature, greater ice cover extent, smaller surface to 850 hPa lapse rates and CAPE, lower boundary layer height, etc.) which inhibit the formation of lake-effect snow (Cordeira and Laird, 2008; Brown and Duguay, 2010; Notaro et al., 2013a; Vavrus et al., 2013). Additionally, by the late snowfall season, other snowstorms (e.g., Nor'easters and Rocky lows) become more frequent due to the southern displacement and meridional patterns of the polar jet stream (Hirsch et al., 2001; Hoskins and Hodges, 2019).

There is also a noticeable shift in the maximum contribution of lake-effect across a cold-season. Although lake-effect contributions are generally greatest directly east of Lake Ontario, there is a movement of the largest snowfall totals closer to the lake as the season progresses (**Figures 6A,C,E,G**). Additionally, the largest percent contributions of lake-effect snow are over the Tug Hill during the early season, shift north by the peak-season, and then southeast of and closer to the lake shore by the mid-season (**Figures 6B,D,F,H**). These intraseasonal shifts may be due to a weakening of the conditions necessary for the formation of lake-effect snow, most notably greater ice cover on Lake Ontario and a decreased surface to 850 hPa lapse rate (Wright et al., 2013). As Wright et al. (2013) suggest, frozen lakes and cooler lake surface temperatures will shrink the snow bands and confine them closer to the lake shore, which ultimately diminishes lake-effect contributions further from the lake. Furthermore, the location of snow bands is influenced by the presence of upper-tropospheric short-wave troughs (Metz et al., 2019). Metz et al. (2019) found that lake-effect bands concurrent with short-wave troughs were most common during the peak season (December–January), which may displace snow bands directly east or northeast of the long-axis of the lake.

Multiple researchers have noted a pronounced increase in snowfall in areas downwind of the Great Lakes compared to areas upwind of the lakes (Changnon, 1968; Gatz and Changnon, 1976; Kelly, 1986; Braham and Dungey, 1995; Scott and Huff, 1996, 1997); but few have examined the spatial variability that exists within a snow basin. From the results, lake-effect snow contributions are 150–250% greater in areas directly east of Lake

Ontario compared to southeastern, southwestern, and northern Central New York (**Figure 5A**). Although lake-effect snow is mostly confined to the nearshore of the lakes, snow bands can propagate inland (Eipper et al., 2019). The presence of lake-effect in this region requires strong, organized snow bands capable of retaining moisture over high terrain. To produce such snow bands there generally needs to be a multi-lake upwind connection. These connections produce lake-to-lake snow bands, snow bands that continuously extend across two or more lakes, that tend to be less organized and less frequent (Schultz et al., 2004), resulting in the lower lake-effect contributions. Nonetheless, this leads to challenges in defining a lake's snow basin. If defined by the influence of lake-effect snow, it may be argued that all of Central New York falls within the Lake Ontario snow basin. However, as per the results, there are clear spatial variations that exist throughout this relatively small region. The results highlight the importance of non-lake snowstorms in a region that is seemingly dominated by lake-effect snow. The pronounced occurrence of non-lake snowstorms is likely due to the additional moisture supply from the Atlantic Ocean, a source less available to other parts of the Great Lakes region (Sanders and Gyakum, 1980; Zishka and Smith, 1980; Jacobs et al., 2005; Changnon et al., 2008).

Snowfall Contributions From Non-lake-effect Snow

Of the non-lake-effect snowstorms that produce snowfall in Central New York, Nor'easters and Rocky lows contribute the most to seasonal snowfall totals. Most of the study area (67.6%) receives 16–25% of its seasonal snowfall from Nor'easters (**Figure 5B**), while 86.1% receives 16–25% of its seasonal snowfall from Rocky lows (**Figure 5C**). Nor'easters are especially influential in southeastern Central New York, while Rocky lows dominate in southwestern Central New York. The greater contributions in these areas are likely due to the source regions of the storms and their general tracks. Nor'easters, also known as east-coast storms, form along the baroclinic zone of the eastern United States or Gulf Coast (Sanders and Gyakum, 1980; Zishka and Smith, 1980; Cione et al., 1993; Hirsch et al., 2001; Kocin and Uccellini, 2004; Jacobs et al., 2005). As these storms propagate to the northeast, the central low moves to the southeast of Central New York, producing snowfall over the region (northwest quadrant of the storm) (Bosart, 1973; Hirsch et al., 2001; Kocin and Uccellini, 2004; Mercer and Richman, 2007). Central New York's position to the northwest of the storm's center often brings a period of significant snowfall sourced in Atlantic moisture brought in by the northeasterly winds. In the northwest sector of the storm, northwest winds often cause the formation of lake-effect and lake-enhanced snowfall to the southeast of Lake Ontario (Niziol, 1987; Liu and Moore, 2004; Suriano and Leathers, 2017). Rocky lows typically originate to the lee of the Rocky Mountains (Whittaker and Horn, 1981; Zielinski, 2002; Changnon and Changnon, 2006; Hartnett, 2020). As they move eastward, they tend to display a pronounced curvature in their track west of the Appalachian range (Changnon, 1969; Branick, 1997; Zielinski, 2002; Changnon et al., 2008). This displaces the low pressure west of the central low of Nor'easters, likely accounting for the greater snowfall contributions in southwestern Central New York.

A noticeable difference between snowfall contributions from Nor'easters and Rocky lows was the pronounced spatial variability across the study area. Although lake-effect snowstorms have the highest contribution of any snowstorm types to a single area, snowfall contributions from Nor'easters were more homogenous. This likely reflects the general size of these storms. Since Nor'easters are some of the largest snowstorms (Davis and Dolan, 1993), they tend to affect the entire study area. Additionally, there is a pronounced decrease in snowfall contributions from Rocky lows directly east of Lake Ontario over Oswego County. Since Rocky lows tend to occur more frequently in late winter (Whittaker and Horn, 1981), lake surface temperatures are cold and ice cover extent is at a maximum (Wang et al., 2012). Therefore, when these storms pass across the region, there is limited access to moisture from the lake inhibiting the formation of lake-effect and lake-enhanced snow which may be common with earlier season storms. Thus, areas that typically receive lake-effect snow do not receive any additional snow from the Rocky lows.

Snowfall contributions from Canadian lows and non-cyclonic storms are relatively low and homogenous throughout the study area (**Figures 5D,E**). The northern formation of Canadian lows is likely responsible for their low seasonal contribution (**Figure 5D**). Since these storms form at northern latitudes inland from major moisture sources, they are often associated with anomalously cold, yet dry conditions (Hutchinson, 1995; Thomas and Martin, 2007). Snowfall directly generated from the central is often light to moderate in magnitude with a high snow-to-liquid ratio (Rochette et al., 2017). Non-cyclonic storms are associated with an upper-level disturbance, cold air advection, or quasi-stationary fronts, but no central low pressure near the study area. Although they can be accompanied by significant lake-effect snow development, they tend to be varied in form and genesis (Lackmann, 2001; Scott and Sousounis, 2001; Chuang and Sousounis, 2003). Upper atmospheric disturbances tend to favor ascending air and an unstable atmosphere ahead of a westerly trough (NWS, 2014). Since the trough can extend to the Gulf of Mexico, the snowfall produced often occurs throughout Central New York, as shown by the relatively homogeneous percent contributions (**Figure 5E**). Behind the western trough, winds generally shift from the northwest, which are conducive for the formation of lake-effect snow, and the greater snowfall totals in northern Central New York. Stationary fronts can also produce a relatively homogenous percent snowfall contribution across Central New York when the warmer air mass contains a lot of water vapor (Neiman et al., 1998; Kusunoki et al., 2005). Since the front is stationary, this can lead to prolonged periods of intense precipitation. A storm's influence on snowfall is not just driven by the regional geography, but by the nature of the storm.

CONCLUSIONS

Lake-effect snow is a regional phenomenon that greatly influences the climate, hydrology, biology, and economy of the

Laurentian Great Lakes. Although it is considered the dominant snowstorm type in this region, it is not the only storm that produces snow. This research examines the seasonal snowfall contributions from the different snowstorm types in Central New York. The results suggest that although lake-effect storms are the dominant snowfall contributor (48%) in parts of the study area, notably the Tug Hill, seasonal contributions are as little as 13% in southeastern Central New York. Additionally, as the cold season progresses, there is a general decrease in the percent contribution from lake-effect throughout the study area and a movement of the maximum contributions. During the early and peak sub-season, the largest contributions are found tens of kilometers inland, directly east of Lake Ontario. By the mid to late cold season, greater snowfall totals from lake-effect snow are concentrated closer to the lakeshore with the largest percent contributions found southeast of the lake's longitudinal axis. Snowfall totals in southern Central New York are mostly dominated by Nor'easters (25–35%) and Rocky lows (15–20%). This is likely driven by moisture sourced from the Atlantic Ocean rather than the Great Lakes. To reduce the over homogenization of snowfall contributions, it is suggested that snowfall patterns within the Great Lakes basin are examined at the local level.

Understanding the actual snowfall contribution from different snowstorm types throughout a snowfall season is needed for future climate predictions. Since the early twentieth century, trends in lake-effect snowfall have fluctuated, while snowfall trends for areas less prone to lake-effect snow have remained unchanged or decreased (Norton and Bolsenga, 1993; Ellis and Leathers, 1996; Burnett et al., 2003; Kunkel et al., 2009a; Bard and Kristovich, 2012; Hartnett et al., 2014). Seasonal snowfall patterns within the Great Lakes region are closely tied to air temperatures, lake surface temperatures, and ice cover on the lakes (Tsuboki et al., 1989; Hanson et al., 1992; Segal and Kubesh, 1996; Wang et al., 2012; Notaro et al., 2015; Shi and Xue, 2019). Since the formation of lake-effect snowstorms and non-lake-effect snowstorms are fundamentally different, a warming climate may have contrasting influences on these storms. This is especially important for storms that occur near the beginning or end of the snowfall season, as recent studies have noted a transition from snow to rain in these storms (Schmidlin et al., 1987; Groisman and Easterling, 1994; Miner and Fritsch, 1997; Knowles et al., 2006; Pierce and Cayan, 2013; Kluver and Leathers, 2015; Clark et al., 2020). Since the potential trajectory of future snowfall varies according to the type of storm, for accurate snowfall predictions, models need to decipher the relative contributions of different snowstorm types to the seasonal snowfall total. Therefore, the analyses in this study help to better understand how snowfall may change in the future by directly teasing out the snowfall contributions from different snowstorm types. These analyses also emphasize the spatial variability of snowfall contributions, which suggest that future snowfall trends may vary across a region depending on the type of snowstorm that dominates seasonal totals. The results from this study provide an important baseline to track these future scenarios, and to help isolate the changes in frequency and contributions of all the storms that track across the region.

DATA AVAILABILITY STATEMENT

The original contributions presented in the study are included in the article/**Supplementary Materials**, further inquiries can be directed to the corresponding author/s.

AUTHOR CONTRIBUTIONS

This research was developed and completed by JH. All methodologies, analyses, and writing were conducted by JH.

ACKNOWLEDGMENTS

This research arose from authors' dissertation at Syracuse University. The author would like to acknowledge the input from Dr. Susan Millar, professor emeritus of Syracuse University, Dr. Jacob Bendix of Syracuse University, Dr. Peng Gao of Syracuse University, and Dr. Adam Burnett of Colgate University.

SUPPLEMENTARY MATERIAL

The Supplementary Material for this article can be found online at: https://www.frontiersin.org/articles/10.3389/frwa.2021.780869/full#supplementary-material

REFERENCES

Andersson, T., and Nilsson, S. (1990). Topographically induced convective snowbands over the Baltic Sea and their precipitation distribution. *Weather Forecast.* 5, 299–312.

Bard, L., and Kristovich, D. A. R. (2012). Trend reversal in Lake Michigan contribution to snowfall. *J. Appl. Meteorol. Climatol.* 51, 2038–2046. doi: 10.1175/JAMC-D-12-064.1

Bosart, L. F. (1973). Detailed analyses of precipitation patterns associated with mesoscale features accompanying United States East Coast Cyclogenesis. *Mon. Weather Rev.* 101, 1–12.

Braham, R. R., and Dungey, M. J. (1995). Lake-effect snowfall over Lake Michigan. *J. Appl. Meteorol.* 34, 1009–1019. doi: 10.1175/1520-0450(1995)034<1009:LESOLM>2.0.CO;2

Branick, M. L. (1997). A climatology of significant winter-type weather events in the contiguous United States, 1982–94. *Weather Forecast.* 12, 193–207. doi: 10.1175/1520-0434(1998)013<0884:COACOS>2.0.CO;2

Brown, L. C., and Duguay, C. R. (2010). The response and role of ice cover in lake-climate interactions. *Prog. Phys. Geogr.* 34, 671–704. doi: 10.1177/0309133310375653

Burnett, A. W., Kirby, M. E., Mullins, H. T., and Patterson, W. P. (2003). Increasing Great Lake-effect snowfall during the twentieth century: a regional response to global warming? *J. Clim.* 16, 3535–3542. doi: 10.1175/1520-0442(2003)016<3535:IGLSDT>2.0.CO;2

Campbell, L. S., and James Steenburgh, W. (2017). The OWLeS IOP2b lake-effect snowstorm: Mechanisms contributing to the Tug Hill precipitation maximum. *Mon. Weather Rev.* 145, 2461–2478. doi: 10.1175/MWR-D-16-0461.1

Campbell, L. S., W. J., Steenburgh, P. G., Veals, T. W., and Letcher, and, J. R., Minder (2016). Lake-effect mode and precipitation enhancement over the tug hill plateau during OWLeS IOP2b. *Mon. Weather Rev.*, 144, 1729–1748. doi: 10.1175/MWR-D-15-0412.1

Changnon, D., Merinsky, C., and Lawson, M. (2008). Climatology of surface cyclone tracks associated with large Central and Eastern U.S. Snowstorms, 1950–2000. *Mon. Weather Rev.*, 136, 3193–3202. doi: 10.1175/2008MWR 2324.1

Changnon, S. A. (1968). Precipitation climatology of Lake Michigan Basin. *Illinois State Water Surv. Bull.* 52:31.

Changnon, S. A. (1969). *Climatology of Severe Winter Storms in Illinois*. Champaign, IL, 1–42. Available online at: http://www.isws.uiuc.edu/pubdoc/B/ISWSB-53.pdf (accessed August, 2021).

Changnon, S. A., and Changnon, D. (2006). A spatial and temporal analysis of damaging snowstorms in the United States. *Nat. Hazards* 37, 373–389. doi: 10.1007/s11069-005-6581-4

Chuang, H.-Y., and Sousounis, P. J. (2003). The impact of the prevailing synoptic situation on the lake-aggregate effect. *Mon. Weather Rev.* 131, 990–1010. doi: 10.1175/1520-0493(2003)131<0990:tiotps>2.0.co;2

Cione, J. J., Raman, S., and Pietrafesa, L. J. (1993). The effect of gulf stream-induced baroclinicity on U.S. East Coast Winter Cyclones. *Mon. Weather Rev.* 121, 421–430. doi: 10.1175/1520-0493(1993)121<0421:TEOGSI>2.0.CO;2

Clark, C. A., Elless, T. J., Lyza, A. W., Ganesh-Babu, B., Koning, D. M., Carne, A. R., et al. (2016). Spatiotemporal snowfall variability in the Lake Michigan Region: How is warming affecting wintertime snowfall? *J. Appl. Meteorol. Climatol.* 55, 1813–1830. doi: 10.1175/JAMC-D-15-0285.1

Clark, C. A., Goebbert, K. H., Ganesh-Babu, B., Young, A. M., Heinlein, K. N., Casas, E. G., et al. (2020). Classification of Lake Michigan snow days for estimation of the lake-effect contribution to the downward trend in November snowfall. *Int. J. Climatol.* 40, 5656–5670. doi: 10.1002./joc.6542

Cordeira, J. M., and Laird, N. F. (2008). The influence of ice cover on two lake-effect snow events over Lake Erie. *Mon. Weather Rev.* 136, 2747–2763. doi: 10.1175/2007MWR2310.1

Cortinas, M. R., and Kitron, U. (2006). County-level surveillance of white-tailed deer infestation by *Ixodes scapularis* and *Dermacentor albipictus* (Acari: Ixodidae) along the Illinois River. *J. Med. Entomol.* 43, 810–819. doi: 10.1603/0022-2585(2006)43

Daly, C., Gibson, W. P., Taylor, G. H., Doggett, M. K., and Smith, J. I. (2007). Observer bias in daily precipitation measurements at United States Cooperative Network Stations. *Bull. Am. Meteorol. Soc.* 88, 899–912. doi: 10.1175/BAMS-88-6-899

Davis, R. E., and Dolan, R. (1993). Nor' easters. *Am. Sci.* 81, 428–439.

Dewey, K. F. (1970). *A Quantitative Analysis of Lake-Effect Snow*. Illinois: Northern Illinois State University.

Doesken, N. J., and Judson, A. (1996). The Snow Booklet: A Guide to the Science, Climatology and Measurement of Snow in the United States. Colorado: Colorado State University.

Eichenlaub, V. L. (1970). Lake effect snowfall to the lee of the Great Lakes: Its role in Michigan. *Bull. Am. Meteorol. Soc.* 51, 403–412. doi: 10.1175/1520-0477(1970)051<0403:LESTTL>2.0.CO;2

Eichenlaub, V. L., and Hodler, T. W. (1979). *Weather and Climate of the Great Lakes Region*. South Bend, IN: University of Notre Dame Press

Eipper, D. T., Greybush, S. J., Young, G. S., Saslo, S., Sikora, T. D., and Clark, R. D. (2019). Lake-effect snowbands in baroclinic environments. *Weather Forecast.*, 34, 1657–1674. doi: 10.1175/WAF-D-18-0191.1

Eito, H., Kato, T., Yoshizaki, M., and Adachi, A. (2005). Numerical simulation of the quasi-stationary snowband observed over the southern coastal area of the Sea of Japan on 16 January 2001. *J. Meteorol. Soc. Japan* 83, 551–576. doi: 10.2151/jmsj.83.551

Ellis, A. W., and Leathers, D. J. (1996). A synoptic climatological approach to the analysis of lake-effect snowfall: potential forecasting applications. *Weather Forecast.* 11, 216–229. doi: 10.1175/1520-0434(1996)011<0216:ASCATT>2.0.CO;2

Fairman, J. G., Schultz, D. M., Kirshbaum, D. J., Gray, S. L., and Barrett, A. I. (2016). Climatology of banded precipitation over the contiguous United States. *Mon. Weather Rev.* 144, 4553–4568. doi: 10.1175/MWR-D-16-0015.1

Gatz, D. F., and Changnon, S. A. (1976). *Atmospheric Environment of the Lake Michigan Drainage Basin*. Argonne, Illinois: ANLIES.

Grieser, J. (2015). Interpolation of global monthly rain gauge observations for climate change analysis. *J. Appl. Meteorol. Climatol.* 54, 1449–1464. doi: 10.1175/JAMC-D-14-0305.1

Groisman, P. Y., and Easterling, D. R. (1994). Variability and trends of total precipitation and snowfall over the United States and Canada. *J. Clim.* 7, 184–205. doi: 10.1175/1520-0442(1994)007<0184:VATOTP>2.0.CO;2

Guan, H., Wilson, J. L., and Makhnin, O. (2005). Geostatistical mapping of mountain precipitation incorporating autosearched effects of terrain and climatic characteristics. *J. Hydrometeorol.* 6, 1018–1031. doi: 10.1175/JHM448.1

Hagenstad, M., Burakowski, E., and Hill, R. (2018). "The economic contributions of winter sports in a changing climate," in *Prot. Our Winters*, 1–69.

Hall, D. K., Digirolamo, N. E., and Frei, A. (2017). "Contribution of lake-effect snow to the catskill mountains snowpack," in *74th East. SNOW Conference.*

Hanson, H. P., Hanson, C. S., and Yoo, B. H. (1992). Recent great lakes ice trends. *Bull. Am. Meteorol. Soc.*, 73, 577–584. doi: 10.1175/1520-0477(1992)073<0577:RGLIT>2.0.CO;2

Harrington, J. A. Jr, Cerveny, R. S., and Dewey, K. F. (1987). A climatology of mean monthly snowfall for the conterminous United States: temporal and spatial patterns. *J. Clim. Appl. Meteorol.* 26, 897–912.

Hartnett, J. J. (2020). A classification scheme for identifying snowstorms affecting central New York State. *Int. J. Climatol.* 41, 1712–1730. doi: 10.1002/joc.6922

Hartnett, J. J., Collins, J. M., Baxter, M. A., and Chambers, D. P. (2014). Spatiotemporal snowfall trends in Central New York. *J. Appl. Meteorol. Climatol.* 53, 2685–2697. doi: 10.1175/JAMC-D-14-0084.1

Hill, J. D. (1971). Snow Squalls in the Lee of Lake Erie and Lake Ontario: A Review of the Literature. Volume 43. Bohemia: NOAA - National Weather Service Eastern Region.

Hirsch, M. E., DeGaetano, A. T., and Colucci, S. J. (2001). An East Coast winter storm climatology. *J. Clim.* 14, 882–899. doi: 10.1175/1520-0442(2001)014<0882:AECWSC>2.0.CO;2

Hjelmfelt, M. R. (1992). Orographic effects in simulated lake-effect snowstorms over Lake Michigan. *Mon. Weather Rev.* 120, 373–377. doi: 10.1175/1520-0493(1992)120<0373:OEISLE>2.0.CO;2

Hoskins, B. J., and Hodges, K. I. (2019). The annual cycle of Northern Hemisphere storm tracks. Part II: Regional detail. *J. Clim.* 32, 1761–1775. doi: 10.1175/JCLI-D-17-0871.1

Houze, R. A., and Hobbs, P. V. (1982). "Organization and structure of precipitating cloud systems," in B.B.T.-A., ed G. Saltzman (New York: Elsevier), 225–315. Available online at: https://www.sciencedirect.com/science/article/pii/S006526870860521X

Hutchinson, T. A. (1995). An analysis of NCM's nested grid models of alberta clippers. *Weather Forecast.* 10, 632–641.

Jacobs, N. A., Lackmann, G. M., and Raman, S. (2005). The combined effects of Gulf Stream-induced baroclinicity and upper-level vorticity on US East Coast extratropical cyclogenesis. *Mon. Weather Rev.* 133, 2494–2501. doi: 10.1175/MWR2969.1

Karmosky, C. (2007). *Synoptic Climatology of Snowfall in the Northeastern United States: An Analysis of Snowfall Amounts From Diverse Synoptic Weather Types*. Delaware: University of Delaware.

Kelly, R. D. (1986). Mesoscale frequencies and seasonal snowfalls for different types of lake michigan snow storms. *J. Clim. Appl. Meteorol.* 25, 308–312.

Kindap, T. (2010). A severe sea-effect snow episode over the city of Istanbul. *Nat. Hazards* 54, 707–723. doi: 10.1007/s11069-009-9496-7

Kluver, D., and Leathers, D. (2015). Regionalization of snowfall frequency and trends over the contiguous United States. *Int. J. Climatol.* 35, 4348–4358. doi: 10.1002/joc.4292

Knowles, N., Dettinger, M. D., and Cayan, D. R. (2006). Trends in snowfall versus rainfall in the western United States. *J. Clim.* 19, 4545–4559. doi: 10.1175/JCLI3850.1

Kocin, P. J., and Uccellini, L. W. (2004). *Northeast Snowstorms*. Vol. 54. Massachusetts: American Meteorological Society.

Kristovich, D. A. R., Young, G. S., Verlinde, J., Sousounis, P. J., Mourad, P., Lenschow, D., et al. (2000). The lake-induced convection experiment and the snowband dynamics project. *Bull. Am. Meteorol. Soc.* 81, 519–542. doi: 10.1175/1520-0477(2000)081<0519:TLCEAT>2.3.CO;2

Kulie, M. S., Pettersen, C., Merrelli, A. J., Wagner, T. J., Wood, N. B., Dutter, M., et al. (2021). Snowfall in the Northern Great Lakes: lessons learned

from a multisensor observatory. *Bull. Am. Meteorol. Soc.* 102, E1317–E1339. doi: 10.1175/BAMS-D-19-0128.1

Kunkel, K. E., Ensor, L., Palecki, M., Easterling, D., Robinson, D., Hubbard, K. G., et al. (2009a). A new look at lake-effect snowfall trends in the Laurentian Great Lakes using a temporally homogeneous data set. *J. Great Lakes Res.* 35, 23–29. doi: 10.1016/j.jglr.11.2008.003

Kunkel, K. E., Palecki, M., Ensor, L., Hubbard, K. G., Robinson, D., Redmond, K., et al. (2009b). Trends in twentieth-century U.S. snowfall using a quality-controlled dataset. *J. Atmos. Ocean. Technol.* 26, 33–44. doi: 10.1175/2008JTECHA1138.1

Kunkel, K. E., Palecki, M. A., Hubbard, K. G., Robinson, D. A., Redmond, K. T., and Easterling, D. R. (2007). Trend identification in twentieth-century U.S. snowfall: the challenges. *J. Atmos. Ocean. Technol.* 24, 64–73. doi: 10.1175/JTECH2017.1

Kusunoki, K., Murakami M., Orikasa, N., Hoshimoto, M., Tanaka, Y., Yamada, Y., Mizuno, H., et al. (2005). Observations of quasi-stationary and shallow orographic snow clouds: spatial distributions of supercooled liquid water and snow particles. *Mon. Weather Rev.* 133, 743–751. doi: 10.1175/mwr2874.1

Lackmann, G. M. (2001). Analysis of a surprise western new york snowstorm. *Weather Forecast.* 16, 99–116. doi: 10.1175/1520-0434(2001)016<0099:AOASWN>2.0.CO;2

Laird, N., Sobash, R., and Hodas, N. (2009). The frequency and characteristics of lake-effect precipitation events associated with the New York State Finger lakes. *J. Appl. Meteorol. Climatol.* 48, 873–886. doi: 10.1175/2008JAMC2054.1

Leathers, D. J., and Ellis, A. W. (1996). Synoptic mechanisms associated with snowfall increases to the lee of Lakes Erie and Ontario. *Int. J. Climatol.* 16, 1117–1135. doi: 10.1002/(SICI)1097-0088(199610)16:10<1117::AID-JOC80>3.0.CO;2-4

Leeper, R. D., Rennie, J., and Palecki, M. A. (2015). Observational perspectives from U.S. Climate Reference Network (USCRN) and Cooperative Observer Program (COOP) Network: temperature and precipitation comparison. *J. Atmos. Ocean. Technol.* 32, 703–721. doi: 10.1175/JTECH-D-14-00172.1

Liu, A. Q., and Moore, G. W. K. (2004). Lake-effect snowstorms over Southern Ontario, Canada, and their associated synoptic-scale environment. *Mon. Weather Rev.* 132, 2595–2609. doi: 10.1175/MWR2796.1

Lundquist, J. D., Hughes, M., Henn, B., Gutmann, E. D., Livneh, B., Dozier, J., et al. (2015). High-elevation precipitation patterns: using snow measurements to assess daily gridded datasets across the Sierra Nevada, California*. *J. Hydrometeorol.* 16, 1773–1792. doi: 10.1175/jhm-d-15-0019.1

Mercer, A. E., and Richman, M. B. (2007). Statistical differences of quasigeostrophic variables, stability, and moisture profiles in north american storm tracks. *Mon. Weather Rev.* 135, 2312–2338. doi: 10.1175/MWR3395.1

Metz, N. D., Bruick, Z. S., Capute, P. K., Neureuter, M. M., Ott, E. W., and Sessa, M. F. (2019). An investigation of cold-season short-wave troughs in the Great Lakes Region and their concurrence with lake-effect clouds. *J. Appl. Meteorol. Climatol.* 58, 605–614. doi: 10.1175/JAMC-D-18-0177.1

Miner, T. J., and Fritsch, J. M. (1997). Lake-effect rain events. *Mon. Weather Rev.* 125, 3231–3248. doi: 10.1175/1520-0493(1997)125<3231:LERE>2.0.CO;2

Neiman, P. J., Ralph, F. M., Shapiro, M. A., Smull, B. F., and & Johnson, D. (1998). An observational study of fronts and frontal mergers over the continental United States. *Mon. Weather Rev.* 126, 2521–2554. doi: 10.1155/2014/816729

Niziol, T. A. (1987). Operational forecasting of lake effect snowfall in western and central New York. *Weather Forecast.* 2, 310–321. doi: 10.1175/1520-0434(1987)002<0310:OFOLES>2.0.CO;2

Niziol, T. A., Snyder, W. R., and Waldstreicher, J. S. (1995). Winter Weather Forecasting throughout the Eastern United States. Part IV: Lake Effect Snow. *Weather Forecast.* 10, 61–77. doi: 10.1175/1520-0434(1995)010<0061:WWFTTE>2.0.CO;2

Norton, D. C., and Bolsenga, S. J. (1993). Spatiotemporal trends in lake effect and continental snowfall in the Laurentian Great Lakes, 1951–1980. *J. Clim.* 6, 1943–1956. doi: 10.1175/1520-0442(1993)006<1943:STILEA>2.0.CO;2

Notaro, M., Bennington, V., Vavrus, S., and Zarrin, A. (2015). Dynamically downscaled projections of lake-effect snow in the Great Lakes Basin. *J. Clim.* 28, 1661–1684. doi: 10.1175/JCLI-D-14-00467.1

Notaro, M., Holman, K., Zarrin, A., Fluck, E., Vavrus, S., and Bennington, V. (2013a). Influence of the Laurentian Great Lakes on regional climate. *J. Clim.* 26, 789–804. doi: 10.1175/JCLI-D-12-00140.1

Notaro, M., Zarrin, A., Vavrus, S., and Bennington, V. (2013b). Simulation of heavy lake-effect snowstorms across the great lakes basin by RegCM4: synoptic climatology and variability. *Mon. Weather Rev.* 141, 1990–2014. doi: 10.1175/MWR-D-11-00369.1

NWS (2012). *Snow Measurement Guidelines for National Weather Service Snow Spotters*. Peachtree City, Georgia: NWS, 1–5.

NWS (2014). *Winter Weather Basics: Cold Air Outbreaks*. Gaylord, MI: Winter Talks Series, National Weather Service. Available online at: https://www.weather.gov/media/apx/spotter/Basics_Winter_Wx.pdf (accessed September, 2021).

Owens, N. D., Rauber, R. M., Jewett, B. F., and McFarquhar, G. M. (2017). The contribution of lake enhancement to extreme snowfall within the Chicago-Milwaukee urban corridor during the 2011 Groundhog Day Blizzard. *Mon. Weather Rev.* 145, 2405–2420. doi: 10.1175/MWR-D-17-0025.1

Peace, R. L., and Sykes, R. B. (1966). Mesoscale study of a lake effect snow storm. *Mon. Weather Rev.* 94, 495–507. doi: 10.1175/1520-0493(1966)094<0495:MSOALE>2.3.CO;2

Pease, S. R., Lyons, W. A., Keen, C. S., and Hjelmfelt, M. (1988). Mesoscale spiral vortex embedded within a Lake Michigan snow squall band—high resolution satellite observations and numerical model simulations. *Mon. Weather Rev.* 116, 1374–1380. doi: 10.1175/1520-0493(1988)116<1374:MSVEWA>2.0.CO;2

Perry, L. B., and Konrad, C. E. (2006). Relationships between NW flow snowfall and topography in the Southern Appalachians, USA. *Clim. Res.* 32, 35–47. doi: 10.3354/cr032035

Perry, L. B., Konrad, C. E., and Schmidlin, T. W. (2007). Antecedent upstream air trajectories associated with northwest flow snowfall in the Southern Appalachians. *Weather Forecast.* 22, 334–352. doi: 10.1175/WAF978.1

Pettersen, C., Kulie, M. S., Bliven, L. F., Merrelli, A. J., Petersen, W. A., Wagner, T. J., et al. (2020). A composite analysis of snowfall modes from four winter seasons in Marquette, Michigan. *J. Appl. Meteorol. Climatol.* 59, 103–124. doi: 10.1175/JAMC-D-19-0099.1

Pierce, D. W., and Cayan, D. R. (2013). The uneven response of different snow measures to human-induced climate warming. *J. Clim.* 26, 4148–4167. doi: 10.1175/JCLI-D-12-00534.1

Reinking, R. F., Caiazza, R., Kropfli, R. A., Orr, B. W., Martner, B. E., Niziol, T. A., et al. (1993). The Lake-Ontario winter storms (LOWS) project. *Bull. Am. Meteorol. Soc.* 74, 1828–1849. doi: 10.1175/1520-0477-74-10-1828

Rochette, S. M., Market, P. S., Gravelle, C. M., and Niziol, T. A. (2017). A case study of anomalous snowfall with an Alberta Clipper. *Adv. Meteorol.* 1–14. doi: 10.1155/2017/8406379

Rohr, J. R., Dobson, A. P., Johnson, P. T. J., Kilpatrick, A. M., Paull, S. H., Raffel, T. R., et al. (2011). Frontiers in climate change-disease research. *Trends Ecol. Evol.* 26, 270–277. doi: 10.1016/j.tree.03.2011.002

Rooney, J. F. (1967). The urban snow hazard in the United States: an appraisal of disruption. *Geogr. Rev.* 57, 538–559.

Sanders, F., and Gyakum, J. R. (1980). Synoptic-dynamic climatology of the "bomb." *Mon. Weather Rev.* 108, 1589–1606. doi: 10.1175/1520-0493(1980)108<1589:SDCOT>2.0.CO;2

Schmidlin, T. W., Dethier, B. E., and Eggleston, K. L. (1987). Freeze-thaw days in the northeastern United States. *J. Clim. Appl. Meteorol.* 26, 142–155.

Schultz, D. M., Arndt, D. S., Stensrud, D. J., and Hanna, J. W. (2004). Snowbands during the cold-air outbreak of 23 January 2003. *Mon. Weather* 132, 827–842. doi: 10.1175/1520-0493(2004)132<0827:SDTCOO>2.0.CO;2

Scott, C. P. J., and Sousounis, P. J. (2001). The utility of additional soundings for forecasting lake-effect snow in the Great Lakes Region. *Weather Forecast.* 16, 448–462. doi: 10.1175/1520-0434(2001)016<0448:TUOASF>2.0.CO;2

Scott, R. W., and Huff, F. A. (1996). Impacts of the Great Lakes on regional climate conditions. *J. Great Lakes Res.* 22, 845–863. doi: 10.1016/S0380-1330(96)71006-7

Scott, R. W., and Huff, F. A. (1997). *Lake Effects on Climatic Conditions in the Great Lakes Basin*. Report CR 617.

Segal, M., and Kubesh, R. (1996). Inferring snow-breeze characteristics from frozen-lake breezes. *J. Appl. Meteorol.* 35, 1033–1039. doi: 10.1175/1520-0450(1996)035<1033:ISBCFF>2.0.CO;2

Sharratt, B. S., Baker, D. G., Wall, D. B., Skaggs, R. H., and Ruschy, D. L. (1992). Snow depth required for near steady-state soil temperatures. *Agric. For. Meteorol.* 57, 243–251. doi: 10.1016/0168-1923(92)90121-J

Shi, Q., and Xue, P. (2019). Impact of lake surface temperature variations on lake effect snow over the Great Lakes region. *J. Geophys. Res. Atmos.* 124, 12553–12567. doi: 10.1029/2019JD031261

Steenburgh, W. J., Halvorson, S. F., and Onton, D. J. (2000). Climatology of lake-effect snowstorms of the Great Salt Lake. *Mon. Weather Rev.* 128, 709–727. doi: 10.1175/1520-0493(2000)128<0709:COLESO>2.0.CO;2

Strommen, N. D., and Harman, J. R. (1978). Seasonally changing patterns of lake-effect snowfall in western Lower Michigan. *Mon. Weather Rev.* 106, 503–509.

Suriano, Z. J., and Leathers, D. J. (2016). Twenty-first century snowfall projections within the eastern Great Lakes region: detecting the presence of a lake-induced snowfall signal in GCMs. *Int. J. Climatol.* 36, 2200–2209. doi: 10.1002/joc.4488

Suriano, Z. J., and Leathers, D. J. (2017). Synoptically classified lake-effect snowfall trends to the lee of Lakes Erie and Ontario. *Clim. Res.* 74, 1–13. doi: 10.3354/cr01480

Suriano, Z. J., Leathers, D. J., Hall, D. K., and Frei, A. (2019). Contribution of snowfall from diverse synoptic conditions in the Catskill/Delaware Watershed of New York State. *Int. J. Climatol.* 39, 3608–3618. doi: 10.1002/joc.6043

Suriano, Z. J., and Wortman, R. D. (2021). Temporal trends in snowfall contribution induced by lake-effect synoptic types. *Phys. Geogr.* 42, 416–433. doi: 10.1080/02723646.2020.1792048

Tardy, A. (2000). Lake-effect and lake-enhanced snow in the Champlain Valley of Vermont. *East. Reg. Tech. Attach.* 1–27. Available online at: http://www.erh.noaa.gov/er/btv/research/Tardy-ta2000-05.pdf (accessed August, 2021).

Thomas, B. C., and Martin, J. E. (2007). A synoptic climatology and composite analysis of the Alberta Clipper. *Weather Forecast.* 22, 315–333. doi: 10.1175/WAF982.1

Tsuboki, K., Fujiyoshi, Y., Wakahama, G., Tsuboki, K., and Wakahama, G. (1989). Structure of a Land Breeze and Snowfall Enhancement at the Leading Edge. *J. Meteorol. Soc. Japan*, 67, 757–770.

Vavrus, S., Notaro, M., and Zarrin, A. (2013). The role of ice cover in heavy lake-effect snowstorms over the great lakes basin as simulated by RegCM4. *Mon. Weather Rev.* 141, 148–165. doi: 10.1175/MWR-D-12-00107.1

Veals, P. G., and Steenburgh, W. J. (2015). Climatological characteristics and orographic enhancement of lake-effect precipitation East of Lake Ontario and over the Tug Hill Plateau. *Mon. Weather Rev.* 143, 3591–3609. doi: 10.1175/MWR-D-15-0009.1

Wang, J., Bai, X., Hu, H., Clites, A., Colton, M., and Lofgren, B. (2012). Temporal and spatial variability of Great Lakes ice cover, 1973–2010. *J. Clim.* 25, 1318–1329. doi: 10.1175/2011JCLI4066.1

Whittaker, L. M., and Horn, L. H. (1981). Geographical and seasonal distribution of North American Cyclogenesis, 1958–1977. *Mon. Weather Rev.* 109, 2312–2322. doi: 10.1175/1520-0493(1981)109<2312:GASDON>2.0.C;2

Wilson, J. W. (1977). Effect of Lake-Ontario on precipitation. *Mon. Weather Rev.* 105, 207–214. doi: 10.1175/1520-0493(1977)105<0207:EOLOOP>2.0.CO;2

Wright, D. M., Posselt, D. J., and Steiner, A. L. (2013). Sensitivity of lake-effect snowfall to lake ice cover and temperature in the great lakes region. *Mon. Weather Rev.* 141, 670–689. doi: 10.1175/MWR-D-12-00038.1

Wu, H., Hubbard, K. G., and You, J. (2005). Some concerns when using data from the cooperative weather station networks: a Nebraska case study. *J. Atmos. Ocean. Technol.* 22, 592–602. doi: 10.1175/JTECH1733.1

Zielinski, G. A. (2002). A classification scheme for winter storms in the Eastern and Central United States with an emphasis on Nor'easters. *Bull. Am. Meteorol. Soc.* 83, 37–51. doi: 10.1175/1520-0477(2002)083<0037:ACSFWS>2.3.CO;2

Zishka, K. M., and Smith, P. J. (1980). The climatology of cyclones and anticyclones over North America and surrounding ocean environs for January and July 1950–77. *Mon. Weather Rev.* 108, 387–401. doi: 10.1175/1520-0493(1981)109<1356:COCOCA>2.0.CO;2

Conflict of Interest: The author declares that the research was conducted in the absence of any commercial or financial relationships that could be construed as a potential conflict of interest.

frontiers in Water

ORIGINAL RESEARCH
published: 13 December 2021
doi: 10.3389/frwa.2021.782265

Great Lakes Basin Heat Waves: An Analysis of Their Increasing Probability of Occurrence Under Global Warming

Fengyi Xie[1]*, *Andre R. Erler*[2], *Deepak Chandan*[1] and *W. Richard Peltier*[1]*

[1] Department of Physics, University of Toronto, Toronto, ON, Canada, [2] Aquanty, Waterloo, ON, Canada

Extreme heat events in the Great Lakes Basin (GLB) region of eastern North America are expected to increase in concert with greenhouse gas (GHG) induced global warming. The extent of this regional increase is also influenced by the direct effects of the Great Lakes themselves. This paper describes results from an ensemble of dynamically downscaled global warming projection using the Weather Research and Forecast (WRF) regional climate model coupled to the Freshwater Lake (FLake) model over the Great Lakes region. In our downscaling pipeline, we explore two sets of WRF physics configurations, with the initial and boundary conditions provided by four different fully coupled Global Climate Models (GCMs). Three time periods are investigated, namely an instrumental period (1979–1989) that is employed for validation, and a mid-century (2050–2060) and an end-century (2085–2100) periods that are used to understand the future impacts of global warming. Results from the instrumental period are characterized by large variations in climate states between the ensemble members, which is attributed to differences in both GCM forcing and WRF physics configuration. Results for the future periods, however, are such that the regional model results have good agreement with GCM results insofar as the rise of average temperature with GHG is concerned. Analysis of extreme heat events suggests that the occurrence rate of such events increase steadily with rising temperature, and that the Great Lakes exert strong lake effect influence on extreme heat events in this region.

Keywords: FLake, CMIP5, WRF, climate change, extreme heat event, Great Lakes (North America)

OPEN ACCESS

Edited by:
Julie A. Winkler,
Michigan State University,
United States

Reviewed by:
Jimy Dudhia,
National Center for Atmospheric Research (UCAR), United States
Joni-Pekka Pietikäinen,
Climate Service Center Germany (GERICS), Germany

***Correspondence:**
Fengyi Xie
fengyi.xie@mail.utoronto.ca
W. Richard Peltier
peltier@atmosp.physics.utoronto.ca

Specialty section:
This article was submitted to Water and Climate, a section of the journal Frontiers in Water

Received: *24 September 2021*
Accepted: *01 November 2021*
Published: *13 December 2021*

Citation:
Xie F, Erler AR, Chandan D and Peltier WR (2021) Great Lakes Basin Heat Waves: An Analysis of Their Increasing Probability of Occurrence Under Global Warming. Front. Water 3:782265. doi: 10.3389/frwa.2021.782265

1. INTRODUCTION

Record breaking extreme heat events have been occurring more frequently around the world in recent years. Some, such as the extreme heat events over Europe in 2019 (Vautard et al., 2020) and over western North America in 2021 (Philip et al., 2021) were especially severe, causing significant loss of life and property. This trend of increasingly active heat events has attracted a great deal of attention from the public, businesses and policy makers. Interest is particularly great in attempting to understand the susceptibility of regions of interest, such as those at high risk of wildfires to changes in the frequency of these events.

The Great Lakes Basin (GLB) region of North America is the largest fresh-water system on Earth, by area, and supports a population in the tens of millions along with extensive agricultural

and industrial activity. Extreme heat events can be very debilitating to this region, and lead to impacts that would be felt far-and-away. It is therefore of great interest to understand climate change induced changes to extreme heat events and the extent to which the influence of such events may be affected by the presence of the Great Lakes. The purpose of the present paper is to begin a discussion on the expected frequency of occurrence of extreme heat events in the GLB in the future.

The climate of the GLB has traditionally been studied from either an observational perspective (Scott and Huff, 1996) or via the application of coupled Global Climate Models (GCMs; Lofgren, 1997). In recent years, however, there have been advances in the usage of high-resolution Regional Climate Models (RCMs), often in conjunction with a lake model, to study the impacts of global warming in this region at a resolution and fidelity higher than that which is afforded by GCMs.

The first attempt to examine the GLB region with an RCM together with a lake model was undertaken by Gula and Peltier (2012) who employed WRF in a dynamical downscaling pipeline wherein the NCAR CCSM3 global model (Collins et al., 2006) was used to force a nested WRF configuration with an outer domain covering the entire North American continent at 30 km resolution and an inner domain covering the GLB at 10 km resolution. The lake model in their study, FLake (Mironov, 2008), was run in offline mode, nevertheless, it was apparent from the study that FLake was able to accurately represent the area covered by lake ice in winter as well as the timing of onset and retreat of the lake ice. More importantly, the analysis demonstrated the capability of nested dynamical downscaling to fully resolve lake effect meteorological processes such the formation of snow belts in the lee of the lakes during winter, and to describe the impacts of the global warming in that region.

The nested downscaling pipeline of Gula and Peltier (2012) was enhanced further by fully coupling FLake to WRF and the improved configuration was used by d'Orgeville et al. (2014) to present the first study of the expected changes to extreme precipitation in the GLB under the influence of anthropogenic climate change. High resolution output from the inner WRF domain was employed to drive an analysis of precipitation extremes using a peak-over-threshold technique to quantitatively assess the extent to which the return times of extreme precipitation events of varying intensities are expected to decrease through the current century under the RCP8.5 "business as usual" radiative forcing scenario. It was found that the time separating extremes of any given precipitation intensity would decrease by at least a factor of two by mid-century. A follow up study by Peltier et al. (2018) made use of a larger ensemble of WRF physics configurations and investigated the "fattening of the tail" of the probability distribution under climate change by using the Generalized Extreme Values (GEV) distribution methodology. The results for end-century for both temperature and precipitation were in agreement with the earlier analyses of d'Orgeville et al. (2014).

Following Gula and Peltier (2012), results from the application of RCMs to the understanding of the climate of the GLB started to be reported by other researcher groups. Notaro et al. (2013) reported on an RCM configuration that employed the Abdus Salam International Center for Theoretical Physics Regional Climate Model, version 4 (ICTP RegCM4), forced by the National Centers for Environmental Prediction (NCEP)–NCAR reanalysis and the Global Sea Ice and Sea Surface Temperature (GISST) dataset from the UK Met Office, coupled to a one-dimensional energy-balance lake model. By comparing their results for the GLB with those obtained from another model run in which the lakes were replaced by a landscape similar to that of the surrounding region, they demonstrated that the presence of the Great Lakes reduces the amplitude of both diurnal and annual temperature change due to their large thermal inertia. Subsequently, Notaro et al. (2015b) forced their lake coupled RegCM4 model with the outputs of two Coupled Model Intercomparison Project Phase 5 (CMIP5) GCMs over the historical and future global warming periods. The results demonstrated, unsurprisingly, that winter temperature is expected to rise, and that reduced lake ice cover leads to an increase in lake effect precipitation which gradually shifts from snow to rain as the climate continues to warm. In an accompanying paper, Notaro et al. (2015a) discuss the effect of projected changes in precipitation and evaporation on future lake levels.

Mallard et al. (2014) also employed WRF coupled to the FLake model and showed that the configuration is able to simulate the regional climate with higher accuracy than reanalysis that has a lower spatial resolution. Xue et al. (2017) coupled RegCM4 with a different lake model based on the Finite Volume Community Ocean Model (FVCOM) 3D hydrodynamic model to obtain highly accurate lake fields. Recently, by coupling the NASA-Unified WRF model (NU-WRF) to both a 1D lake model and a 3D lake model, Notaro et al. (2021) showed that the 3D lake model performed better over the Great Lakes region.

A major shortcoming in this extensive literature on the application of RCMs to the GLB is that nearly all of these studies used global forcing data from only one GCM. Therefore, the effect of the choice of GCM data on the downscaled results for the GLB remains largely unconstrained. Zobel et al. (2018b) presented regional climate results over the Continent of US (CONUS) from the WRF model forced by 3 different GCMs and demonstrated that different GCM forcings lead to significant differences over their domain. Therefore, we could expect to see a similar variability in the downscaled climate over the GLB region depending on the GCM data. Here we make progress on filling this knowledge gap by using outputs from a selected set of GCMs that have participated in the Coupled Model Intercomparison Project Phase Five (CMIP5; Taylor et al., 2012) and whose data have been uploaded to the project archive. The CMIP5 models have been used to simulate both the twentieth century over which their results can be verified against high quality instrumental observations, and the twenty-first century over which we are interested in performing downscaled projections. The CMIP5 archive was key to the findings reported in the IPCC Fifth Assessment Report (IPCC, 2013a) and the data has been used for understanding climate change projections over North America (Sheffield et al., 2013a,b).

In addition to the mean climate state of the GLB region, the modeling of extreme events and projections of their change into

the future has also generated considerable interest. Modeling and projection of changes in extreme precipitation using a lake model coupled to a RCM has been previously reported (d'Orgeville et al., 2014; Peltier et al., 2018), but in contrast much less effort has been expended to studying extreme heat events using this configuration. While some studies have attended to the question of regional extreme heat events, those have been either based on observations (Peterson et al., 2008) and so cannot be used for future projections, or use low-resolution GCM data (Meehl and Tebaldi, 2004; Kharin et al., 2013; Sillmann et al., 2013a,b) or downscale GCM data without resolving lake dynamics (Jeong et al., 2016; Byun and Hamlet, 2018). The latter two approaches are unable to explicitly include lake effects in the Great Lakes region. Studies have shown that lakes are not immune to climate change (O'Reilly et al., 2015; Woolway et al., 2020), and therefore interaction between a warmed lake and its surroundings needs to be resolved by a lake model in order to obtain accurate climate change signal over the surrounding region.

This study will employ the dynamical downscaling pipeline that was recently used in Peltier et al. (2018) but apply it to CMIP5 data to construct a new ensemble of downscaled simulations. This new ensemble will be used to explore the variability in the downscaling process when forcing from different GCM models is employed, and thereby attempt to address the impact of GCM selection on regional climate results. Extreme heat event analysis is performed on this ensemble to explore the evolution of heat waves under the influence of different simulations for climate change.

2. EXPERIMENTAL DESIGN, CLIMATE MODELS, AND VALIDATION DATASETS

2.1. Experimental Design

The dynamical downscaling experiments presented in this paper follow the two-step nesting procedure established in Gula and Peltier (2012) and d'Orgeville et al. (2014) wherein the first of the nested domains, namely the outer domain, covers the continent of North America at a resolution of 30 km, and the nested inner domain covers the GLB at 10 km resolution. Technical details are described in Erler (2015). This pipeline has also been employed to perform downscaling experiments in other regions, such as Western Canada (Erler et al., 2015; Erler and Peltier, 2016, 2017),

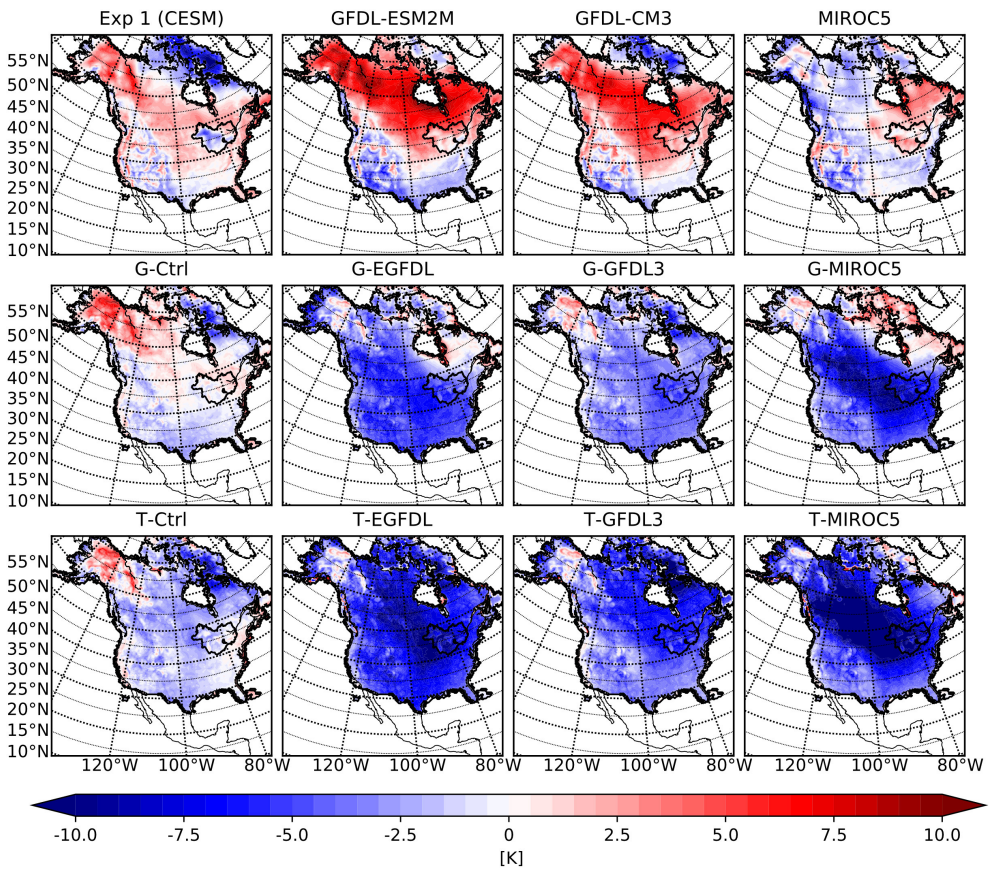

FIGURE 1 | Mean winter season 2 m air temperature biases with respect to the NRCan dataset over the outer WRF domain for the GCMs (top row), WRF ensemble members with G physics (middle row), and WRF ensemble members with T physics (bottom row). From left to right are experiments (GCM or GCM driven WRF) associated with CESM1, GFDL-ESM2M, GFDL-CM3 and MIROC5 respectively.

and India and South-east Asia (Huo and Peltier, 2019; Huo et al., 2021).

2.2. CMIP5 GCM Models

The CMIP5 archive contains data generated by over 50 climate models from 20 modeling groups from around the world. It is a comprehensive source of global climate data for both historical and future projection periods (Taylor et al., 2012). Several studies have used the CMIP5 archive to investigate future climate projections over various regions of the world (see for example Kug et al., 2015; Song and Yu, 2015; Cheng et al., 2017; Peings et al., 2017), and the relative performance of the models, over North America has been evaluated for the historical period (Kumar et al., 2013; Sheffield et al., 2013a,b) and the future (Maloney et al., 2014).

Our downscaling pipeline requires the availability of several atmospheric, sea ice and land surface variables from the GCM at 6-h resolution. At the time of this study, only data from MIROC5, GFDL-ESM2M and GFDL-CM3 stored on the CMIP5 archive satisfied these requirements. Accordingly, in this study we use data from these three GCMs, together with data from our own simulation using CESM1. Sheffield et al. (2013a) found that these models cover a broad range of performance and concluded that CESM1 is one of the better performing models, while GFDL-CM3 is among the models that perform worse over the historical period. Both GFDL-ESM2M and MIROC5 were ranked in between CESM1 and GFDL-CM3. We therefore expect this set of models to provide a good spread of climate states in the RCM ensemble.

The Model for Interdisciplinary Research on Climate (MIROC; Watanabe et al., 2010) is developed and operated by the Japanese research community. The atmospheric component of the model has a spectral dynamical core that operates at a horizontal resolution of T85 ($1.4^\circ \times 1.4^\circ$) and has 40 layers in the vertical. The ocean grid uses stereographic projection and conformal mapping to transfer the north pole to $80^\circ N, 40^\circ W$ and the south pole to $80^\circ S, 40^\circ W$ in order to prevent the geometric singularity due to the convergence of the meridians from existing in the oceanic domain. The grid resolution in the zonal direction is fixed at 1.4° but the meridional resolution decreases from 0.5° at 8° equivalent latitude to 1.4° at equivalent latitudes poleward of 65°. The vertical discretization includes 49 layers that are unevenly distributed with greater concentration near the surface. The atmospheric component uses parametrization

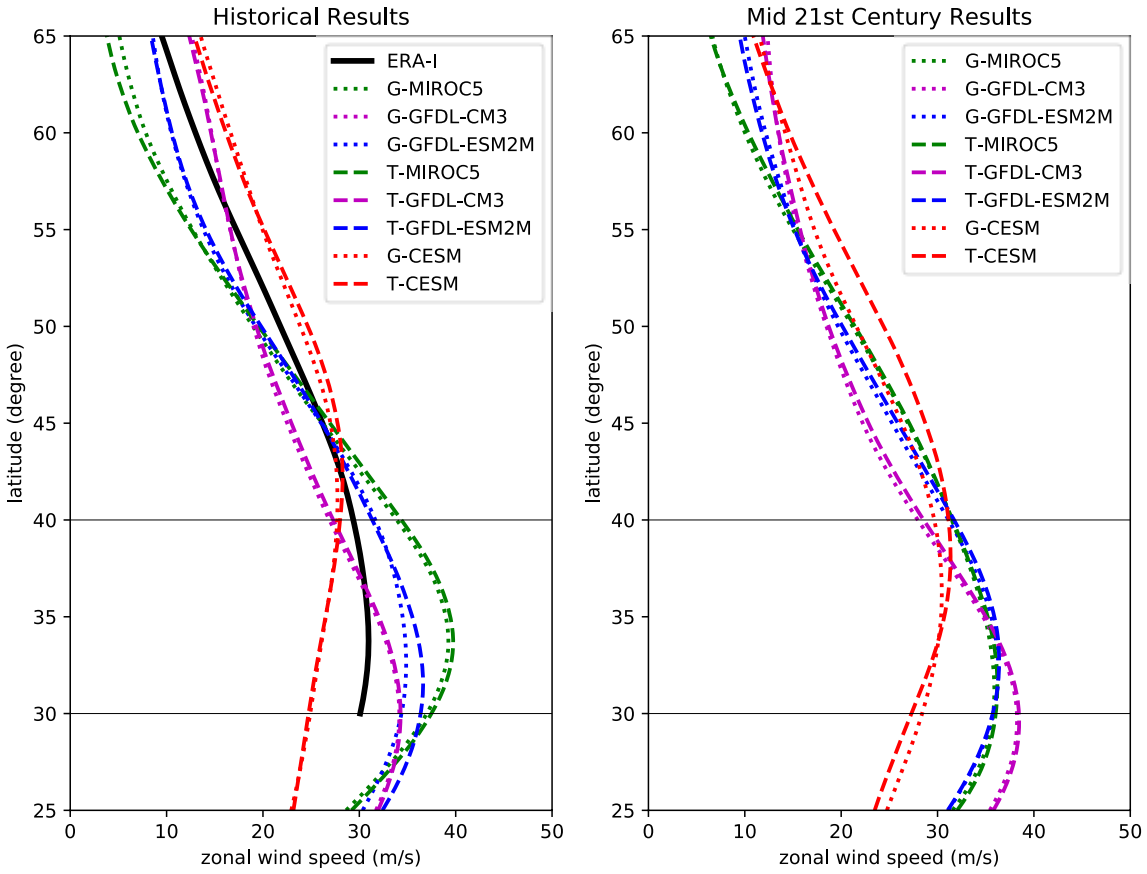

FIGURE 2 | Winter season zonally mean zonal wind speed at 250 hPa pressure level. Left panel shows results for the historical period where ERA-Interim reanalysis result is plotted in black as reference, and the right panel shows result for mid-century period. 30°and 40°latitude are marked to enable easier comparison between plotted curves.

schemes that includes a cumulus convection scheme, cloud and cloud microphysics schemes, turbulence diffusion scheme and an aerosol model. Sea ice is treated on ocean cells with dynamics and thermodynamics included. The land component operates with 6 soil layers and includes snow and ice albedo effects, and a lake submodel.

The Global Coupled Carbon–Climate Earth System Model (GFDL-ESM2M) is developed by the Geophysical Fluid Dynamics Laboratory (GFDL) of the National Oceanic and Atmospheric Administration (NOAA; Dunne et al., 2012, 2013). This model uses a finite volume dynamical coreon an atmospheric grid with 2.5° longitude and 2.0° latitude horizontal resolution and 24 vertical levels. The tripolar ocean grid has a horizontal grid spacing of 1° that gradually decreases to 1/3° meridionally at the equator and has 50 vertical levels. The land model parameterizes all physical and biological processes and the included carbon cycle simulates carbon transport between the model components. Components that treat sea ice and icebergs are also included in the model.

The GFDL Global Coupled Model (GFDL-CM3 Donner et al., 2011; Griffies et al., 2011) is also from GFDL. This model uses a finite-volume dynamical core with a cube-sphere grid that has 48 vertical levels and 48 cells along each edge of the cube, leading to grid cell sizes that range from 163 km to 231 km. The output data of this model are projected to an atmospheric grid with 2.5° longitude × 2.0° latitude resolution. This model includes the same ocean and land model components as GFDL-ESM2M. This model also employed various parametrization schemes including aerosol physics, cloud physics, and schemes for trace gas and ozone.

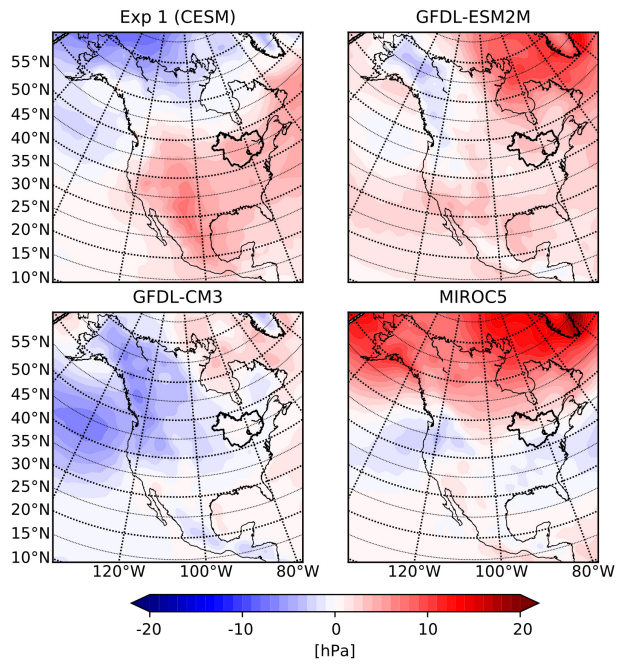

FIGURE 3 | Winter season sea level pressure biases with respect to the CFSR dataset for the GCMs over the WRF model outer domain.

Using multi-millennial runs performed with the two GFDL models, Paynter et al. (2018) show that GFDL-CM3 model has a higher equilibrium climate sensitivity than GFDL-ESM2M. Furthermore, Maloney et al. (2014) show that the GFDL-CM3 model experiences more warming compared to other models in the CMIP5 archive at the end of the twenty-first century. Therefore, we expect the GFDL-CM3 forced RCM experiments to be warmer than other members during the future projection periods.

The fourth member of our ensemble is driven by the Community Earth System Model version 1 (CESM1; Gent et al., 2011), which has been used in previous studies from the Toronto group. CESM1 is a fully coupled global climate model developed by the National Center for Atmospheric Research (NCAR) and contains submodels for all major components of the climate system. The atmospheric component, called CAM4, (Neale et al., 2013) operates on a latitude-longitude grid with resolution 1.26° × 0.9° and 26 vertical layers. The ocean component, called the Parallel Ocean Program (POP) version 2 (Danabasoglu et al., 2012), uses a displaced-dipole grid with 1° longitudinal resolution, varying latitudinal resolution from 0.27° near the equator to 0.54° near the pole and has 60 vertical level. The land component, Community Land Model version 4 (CLM4 Lawrence et al., 2012), runs on the same grid as the atmospheric component and has 15 soil layers. The sea ice component is the Community Ice Code version 4 (CICE Holland et al., 2012) that runs on the ocean grid and simulates both dynamics and thermodynamics.

The CESM1 data used in this study (and in other studies from this group) is from a local simulation performed with the model and therefore there will be subtle differences between this data and that on the CMIP5 archive. Peings et al. (2017) examined internal variability in a large ensemble of 40 CESM1 simulations and concluded that the model does not display significant internal variability. Therefore, using a local CESM1 simulation as forcing should not affect its reliability and the results can still remain comparable to those obtained using CESM1 data from the CMIP5 archive. Previous studies have thoroughly discussed the behavior of CESM1 forced dynamical downscaling experiments (d'Orgeville et al., 2014; Li et al., 2018; Peltier et al., 2018; Zobel et al., 2018b) with most of the studies concluding that CESM1 forced climate results match observations closely. Henceforth, to distinguish between the models whose data were directly obtained from the CMIP5 archive and CESM1 for which we use local data, we will use the phrase CMIP5 models to refer to the collection of GFDL-CM3, GFDL-ESM2M and MIROC5, and the term CMIP5 data as data for these three models. These terms will not refer to the CESM1 GCM or data from that model.

The representation of lakes in the GCMs and their performance deserve attention since we are interested in the GLB region. All GCMs that we employ in this study contain a lake submodel within the land component. However, given the resolution of the GCMs (1° for CESM, T85 for MIROC5, and 2° for the GFDL models), the representation of lakes is very coarse and they are often defined in terms of fractional units of land grid cells. This leads to a poor representation of lake extents and of land-lake contrast. As a result, those lake models cannot represent lake effects in a manner that is achievable when

using a high-resolution lake model within an RCM (Notaro et al., 2013). Briley et al. (2021) analyzed how CMIP5 models simulate the Great Lakes and concluded that representation to not be very credible.

Each GCM is forced by historical greenhouse gas concentrations for the historical period (pre-industrial to 2005) and by Representative Concentration Pathway 8.5 (RCP8.5) emissions scenario from year 2006 to year 2100.

2.3. RCM Model Configuration

The regional climate model employed for this study consists of the Weather Research and Forecasting (WRF) model, version V3.4.1, with the Advanced Research WRF (ARW) dynamical core (Skamarock and Klemp, 2008), fully coupled to the Freshwater Lake (FLake; Mironov, 2008) model. The FLake model is configured with a 70 m false bottom as in d'Orgeville et al. (2014) and Peltier et al. (2018). In these two studies, five different sets of physics configurations were employed and discussed, and here two of the sets, namely G and T (see Table 1 of Peltier et al., 2018, for details of the two sets), will be used so that variations in modeled result caused by differences in GCM forcing data could be cross compared with variations caused by different physics configuration sets. The T physics set use the WRF single-moment 6-class microphysics (Hong and Lim, 2006) and the Kain-Fritsch cumulus parameterization (Kain, 2004) schemes while the G physics set uses the Morrison microphysics scheme (Morrison et al., 2009) and the Grell-3 cumulus scheme (Grell and Dévényi, 2002). Other configurations, which are common to both sets, include the Noah land surface model (Chen and Dudhia, 2001), the Rapid Radiative Transfer Model for General Circulation Models (Iacono et al., 2008) radiation scheme and the Mellor-Yamada-Nakanishi-Niino level-2.5 (Nakanishi and Niino, 2009) planetary boundary layer parameterization scheme.

The dynamical downscaling process follows the procedure established in Gula and Peltier (2012), wherein forcing in the from of large-scale GCM data is used as initial condition and boundary condition for WRF. The boundary forcing data includes 6-h temperature, wind, humidity and pressure, whereas the initial conditions include land surface temperature, sea surface temperature, sea ice cover and assorted variables required for the initialization of the land component. A relaxation zone is used to apply boundary forcing smoothly into the WRF outer domain. Spectral nudging is also applied to the pressure, wind, potential temperature and humidity fields in

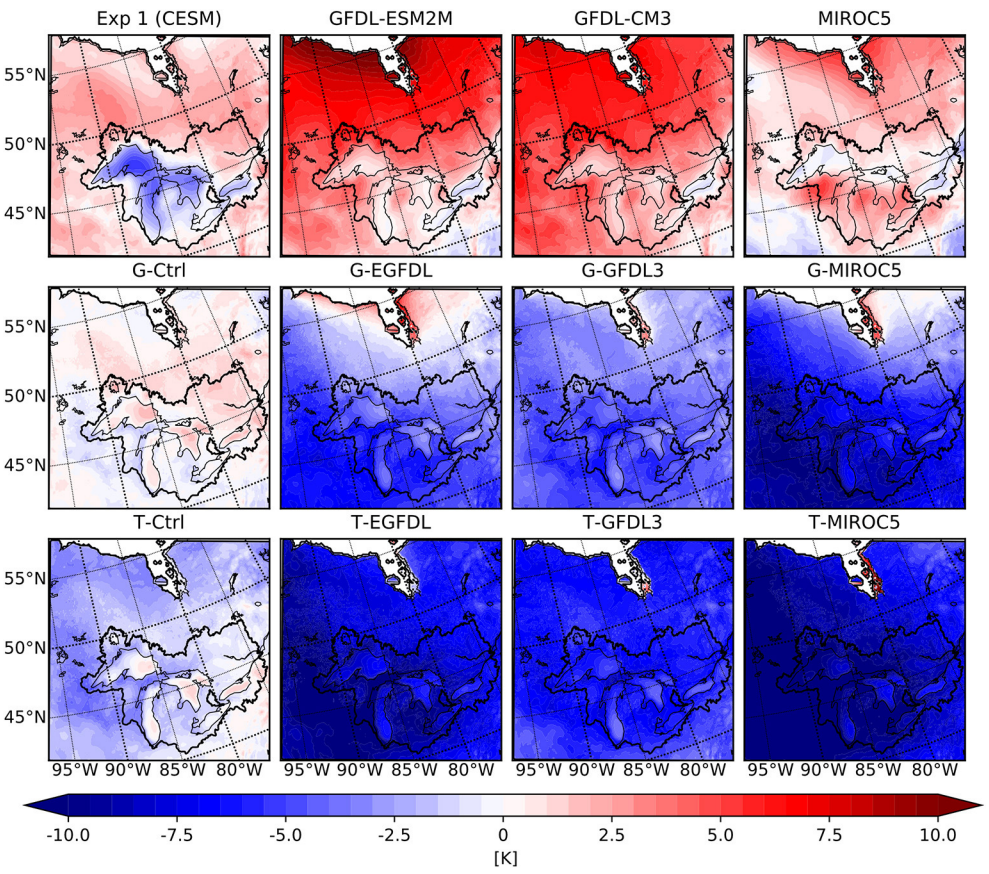

FIGURE 4 | Mean winter season 2 m air temperature biases with respect to the NRCan dataset over the inner WRF domain for the GCMs (top row), WRF ensemble members with G physics (middle row), and WRF ensemble members with T physics (bottom row). From left to right are experiments (GCM or GCM driven WRF) associated with CESM1, GFDL-ESM2M, GFDL-CM3 and MIROC5 respectively. The Great Lakes basin is outlined in black.

the outermost domain in all ensemble members in order to preserve the large-scale circulation features of the GCMs. For each ensemble member, we perform experiments for three different time periods: historical (1979–1989), mid-twenty-first century (2050–2060), and end-twenty-first century (2085–2100). The WRF simulations also employ the RCP8.5 emission scenario, so the strength of anthropogenic forcing is kept the same as in the GCMs. Lake data is not used to force WRF runs in this study, so the WRF results presented here are not affected by the lake representation in GCMs.

2.4. Validation Datasets

To validate simulations for the historical period, observational and reanalysis datasets are employed. The Natural Resource Canada (NRCan; McKenney et al., 2011) observational data is used to provide ground truth for surface temperature, precipitation, and incoming shortwave radiation. It should be noted explicitly that the NRCan dataset does not have direct measurements over the lakes, so surface temperatures over the lakes are interpolated from nearby land stations and therefore might deviate from true values. The Climate Forecast System Reanalysis dataset (CFSR; Saha et al., 2010) is used to compare surface pressure fields.

Throughout the paper, summer includes the months June, July, and August while winter includes December, January and February. Unless otherwise stated, model results presented are averaged over all years in the respective time periods.

2.5. Methods and Data Used for Extreme Heat Event Analysis

Before performing any analysis of extreme heat events, it is necessary to fix a working definition for such extremes. Several definitions have been proposed and used in the literature and studies have found that the detected heat events are sensitive to the choice of definition (Robinson, 2001; Perkins and Alexander, 2013). It has also been suggested that the definition of a heat event should be customized to suit the climate of the region of interest. For this study, this requires being cognizant of the lake effects that would be accurately simulated by our setup which includes a lake model. During summertime the lakes reduce the maximum atmospheric temperature achievable by absorbing heat, resulting in a cool zone around the lakes (Scott and Huff, 1996). This cooling effect will dampen the tail end of the distribution of extreme heat events extracted by percentile thresholds, so a static threshold method is preferred. For this reason, we choose the Environmental and Climate Change Canada's definition of a heat

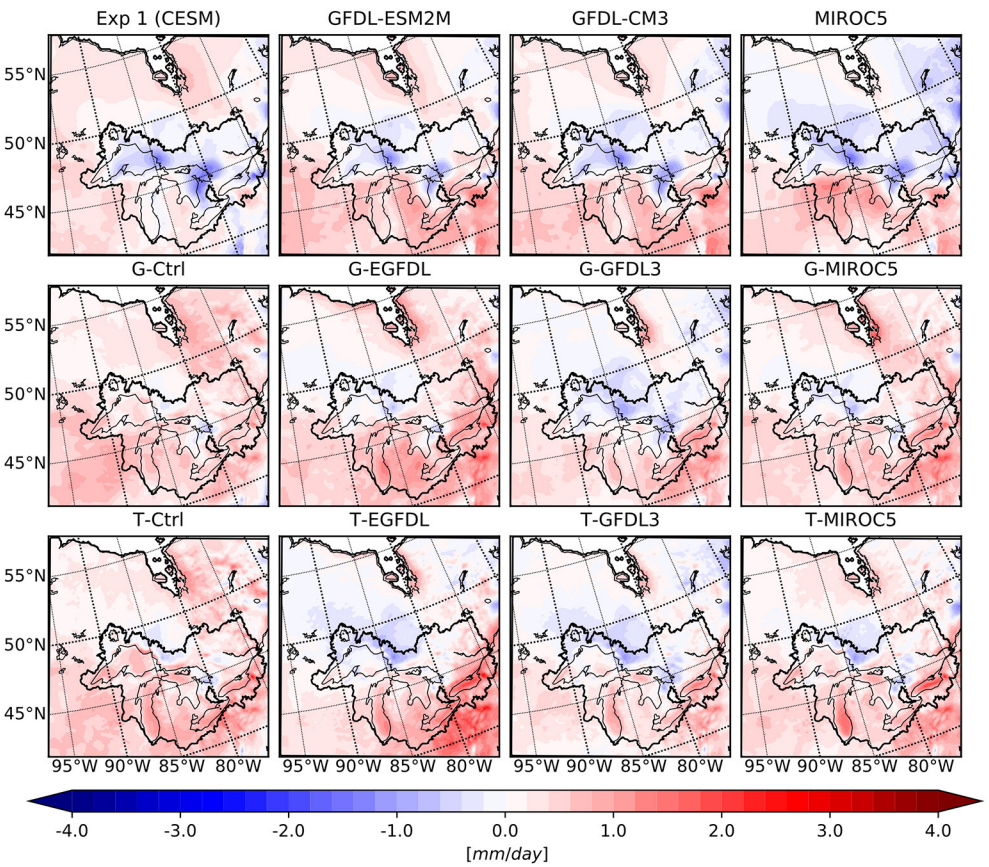

FIGURE 5 | Similar to **Figure 4** but for the mean winter precipitation differences.

wave as 'a period with more than three consecutive days of maximum temperatures at or above $32^{\circ}C/90^{\circ}F$' in this study.

At the same time, the lakes also serve as a source of moisture during the summer season. Although the evaporation process absorbs heat and moderates the temperature, the increase in relative humidity itself increases the risk to the health of the inhabitants of the region. Therefore, here we also use the Heat Index (HI) method from NOAA/National Weather Service (Anderson et al., 2013) which combines temperature and relative humidity into a single index (**Appendix A1**). There are several other widely used measures that also seek to combine temperature and humidity, including Environmental and Climate Change Canada's Humidex, (https://www.canada.ca/en/environment-climate-change/services/sky-watchers/glossary.html) and the wet bulb globe temperature (Li et al., 2017). Exploring their differences is beyond the scope of this study.

Calculating HI requires both temperature and relative humidity which are provided on daily interval by WRF. Days in each model year that experience extreme heat events are determined using the HI definition above (similarly extreme heat days are identified using temperature only when using the temperature metric). The threshold values for the definition of heat waves is kept the same in both the temperature and HI methods, and for all time periods without any bias correction. Original GCM output is not included in this analysis for two reasons: firstly, as discussed above none of the GCMs include a lake model that can suitably capture lake effect and secondly, extreme heat event analysis with GCMs has already been covered by other studies (e.g., Kharin et al., 2013; Sillmann et al., 2013a,b).

3. MEAN CLIMATE AND EXTREME HEAT EVENT ANALYSIS FROM DYNAMICAL DOWNSCALING

3.1. Simulation Results Over the Historical Period

The winter average near surface temperature (T2) biases with respect to the NRCan dataset (henceforth bias is defined as model minus observation) over the outermost WRF domain are presented for the selected GCM results and the GCM driven downscaled results in **Figure 1**. It is readily apparent that the downscaled experiments are producing results that are distinctly different from the GCM data that is used as their forcing. This

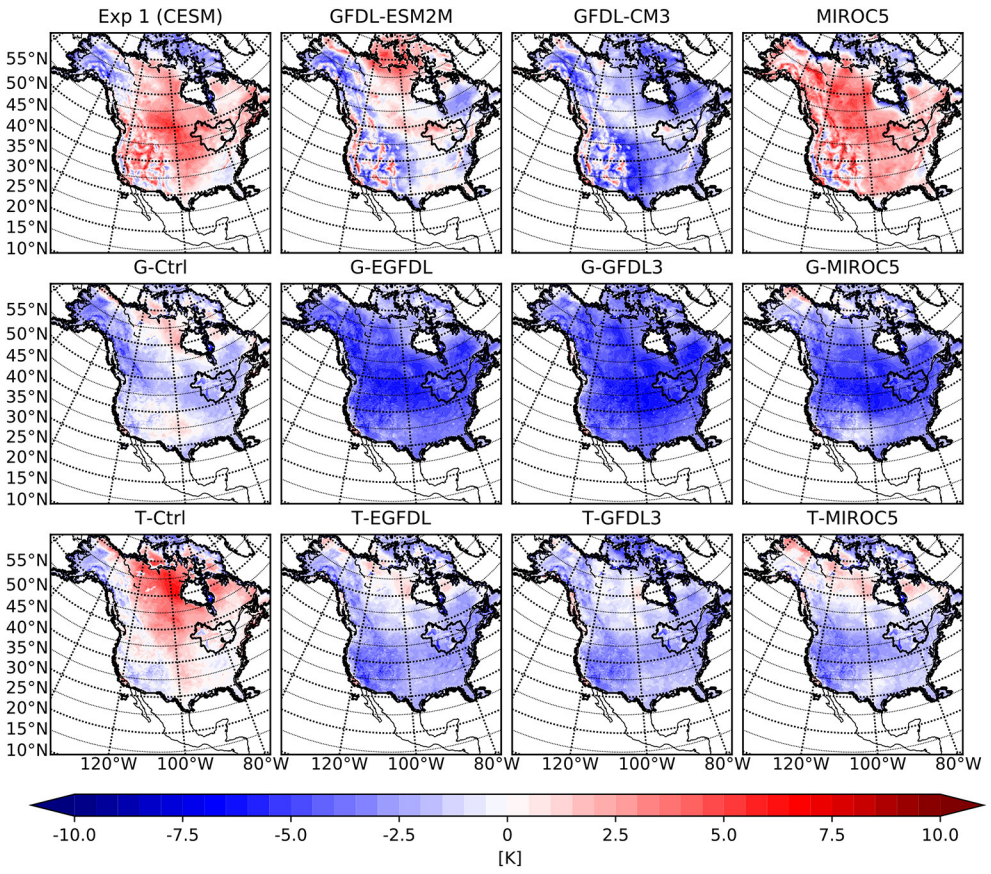

FIGURE 6 | Mean summer season 2 m air temperature biases with respect to the NRCan dataset over the outer WRF domain for the GCMs (top row), WRF ensemble members with G physics (middle row), and WRF ensemble members with T physics (bottom row). From left to right are experiments (GCM or GCM driven WRF) associated with CESM1, GFDL-ESM2M, GFDL-CM3, and MIROC5, respectively.

is particularly the case for WRF simulations forced with CMIP5 models, whereas WRF results forced with CESM1 show the smallest (but still sizeable) differences with the GCM data. The strongest biases in CESM1 are the warm bias over Alaska and northeastern Canada and the cold bias over northern Canada. These features are retained to varying degrees in the downscaled experiments, with the G physics version greatly attenuating the cold bias without effecting the warm bias and the T physics version being successful in reducing the magnitude of both biases. On the other hand, while the G physics version is able to improve the performance by attenuating the moderate warm bias throughout the interior of the continent, the T physics version replaces that with a moderate cold bias.

The MIROC5 model does not have a strong bias over North America, but the two GFDL models produce strong warm bias over Canada, Alaska and northwestern US. In contrast, the WRF results associated with these models all have a large cold bias over the continent, up to 5° C in most regions and up to 10° C in the coldest regions. The magnitude of this bias is larger than the natural variability in the models for this region as previous studies (d'Orgeville et al., 2014; Peltier et al., 2018) have shown that the typical range of bias with physics or initial condition ensemble is $\sim$ 4° C. This range is also applicable for other regions such as western Canada (Erler and Peltier, 2017), India (Huo and Peltier, 2019), and North America (Zobel et al., 2018b), and is in general also true for other models (for a discussion of variability in GCM results, see Deser et al., 2012, 2014; Peings et al., 2017).

The source of this large cold bias in WRF results with CMIP5 models can be traced to the large-scale wind and pressure fields, and the jet stream position. We begin with an examination of the jet stream position first. The left panel of **Figure 2** reveals that in WRF there is a 10° difference in the position of the jet stream between CESM1 forced and CMIP5 forced results. This bias in jet stream position is inherited from CMIP5 forcing data through the spectral nudging process. In order to give a reasonable ground state as reference, the zonal wind from ERA-Interim reanalysis data (Dee et al., 2011) is also plotted, and the ERA-Interim results lie right between the northward biased CESM1 and southward biased CMIP5 results. Since the position of the sub-tropical jet stream marks the northern extent of the Hadley Cell, a southward shift in the position of the jet stream means that heat transport from the tropics by the Hadley cell terminates further southward. This leaves the region north of the jet stream under the influence of colder polar air from the Arctic instead, which disrupts surface temperature fields in the WRF. Furthermore, the largest cold bias in each of the CMIP5 forced WRF results is centered in the range 40° N to 50° N, which overlaps with the region where a shift in the jet stream position would be most influential.

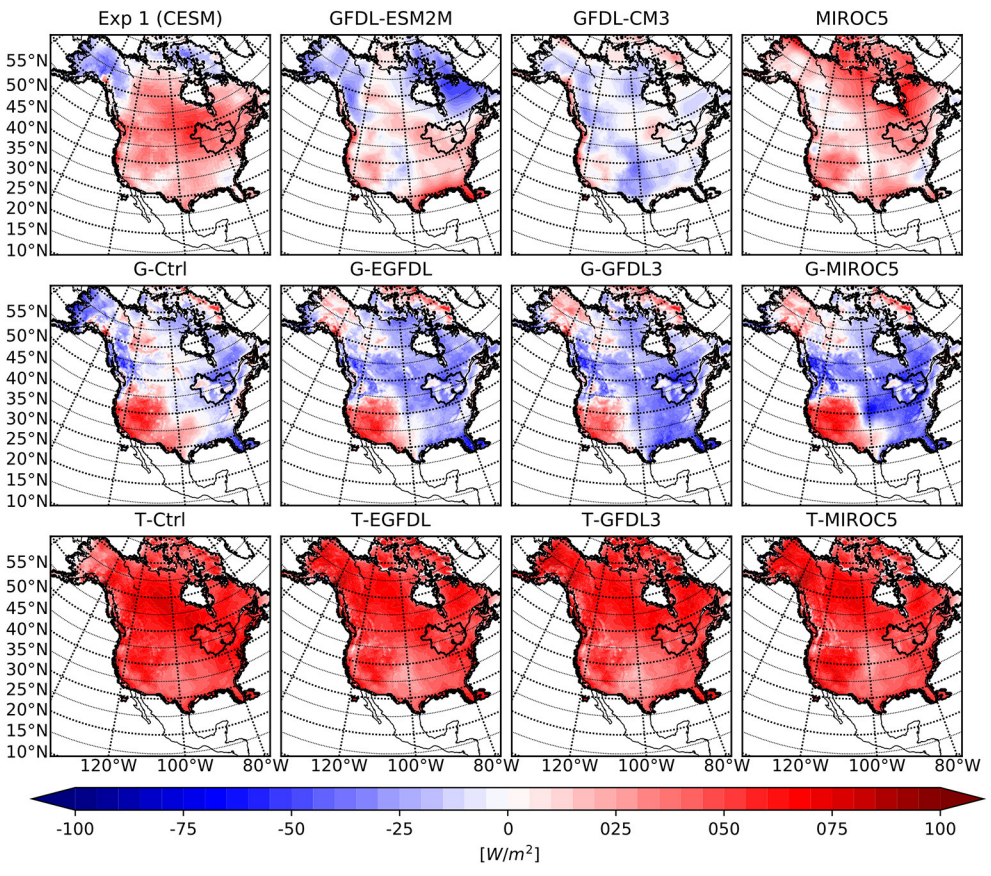

FIGURE 7 | Similar to **Figure 6** but for the incoming shortwave radiation differences.

The second cause for the bias in CMIP5 driven WRF results is the surface pressure field. **Figure 3** displays the bias of winter season average mean sea level pressure over the WRF outer domain. It is to be noted that the bias in the pressure fields for each GCM differ considerably as a function of increasing latitude: CESM1 varies from high to low, GFDL-CM3 is low over land and high over the Arctic Ocean, and both GFDL-ESM2M and MIROC5 vary from low to high. Since air flows outwards from high-pressure region, a high pressure bias over high latitude forces cold polar air southward thereby causing surface temperatures to drop. As a result, downscaled simulations forced by MIROC5 and GFDL-ESM2M have the largest surface cold bias while GFDL-CM3 forced results have a smaller cold bias and CESM forced results have almost no cold bias.

As discussed in Scott and Huff (1996), the Great Lakes moderate air temperature above them by absorbing heat from air during spring-summer season, and releasing it back during the fall-winter season. The release of heat continues until lake surfaces are completely frozen and thermal exchange between lake surface and the atmosphere is blocked. These lake characteristics are confirmed by previous work that employed RCMs coupled to lake models (Gula and Peltier, 2012; Notaro et al., 2013; Mallard et al., 2014). A closer look at winter average near surface temperature (T2) biases over the WRF inner domain (**Figure 4**) reveals that the cold biases over the lake surfaces and the surrounding regions is smaller by ∼2° C than biases over other regions in both CESM and CMIP5 members of the ensemble. This demonstrates that the lake model employed in this study is effective at resolving the temperature mitigating effects of the presence of the lakes even when the region is dominated by a large cold bias. In contrast, in GCM results regions over the lakes are colder than their surroundings, which is contrary to what is expected. This supports the findings of Briley et al. (2021) who found that GCMs do not simulate lake effects accurately because they do not contain a detailed lake model that explicitly resolves land-atmosphere-lake coupling and the exchange of fluxes between them. **Figure 5** shows the precipitation bias over the inner WRF domain for all ensemble members in winter, and again the WRF results are able to better capture the spatial distribution compared to their GCM counterparts. Although a smaller bias still exists in regions around the lakes where the lake effect matters, it is likely caused by the cold temperature bias that freezes the lakes early and suppresses evaporation, thereby reducing overall moisture source for those regions.

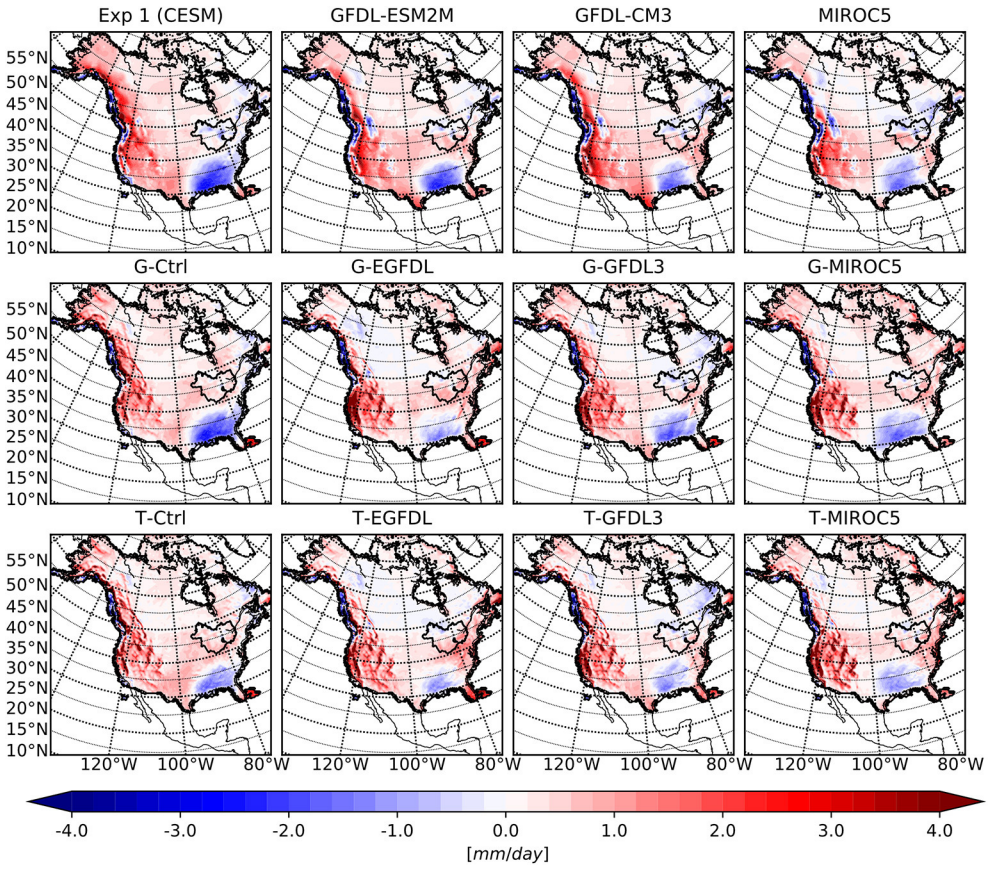

FIGURE 8 | Mean winter season precipitation biases with respect to the NRCan dataset over the outer WRF domain for the GCMs (top row), WRF ensemble members with G physics (middle row), and WRF ensemble members with T physics (bottom row). From left to right are experiments (GCM or GCM driven WRF) associated with CESM1, GFDL-ESM2M, GFDL-CM3, and MIROC5, respectively.

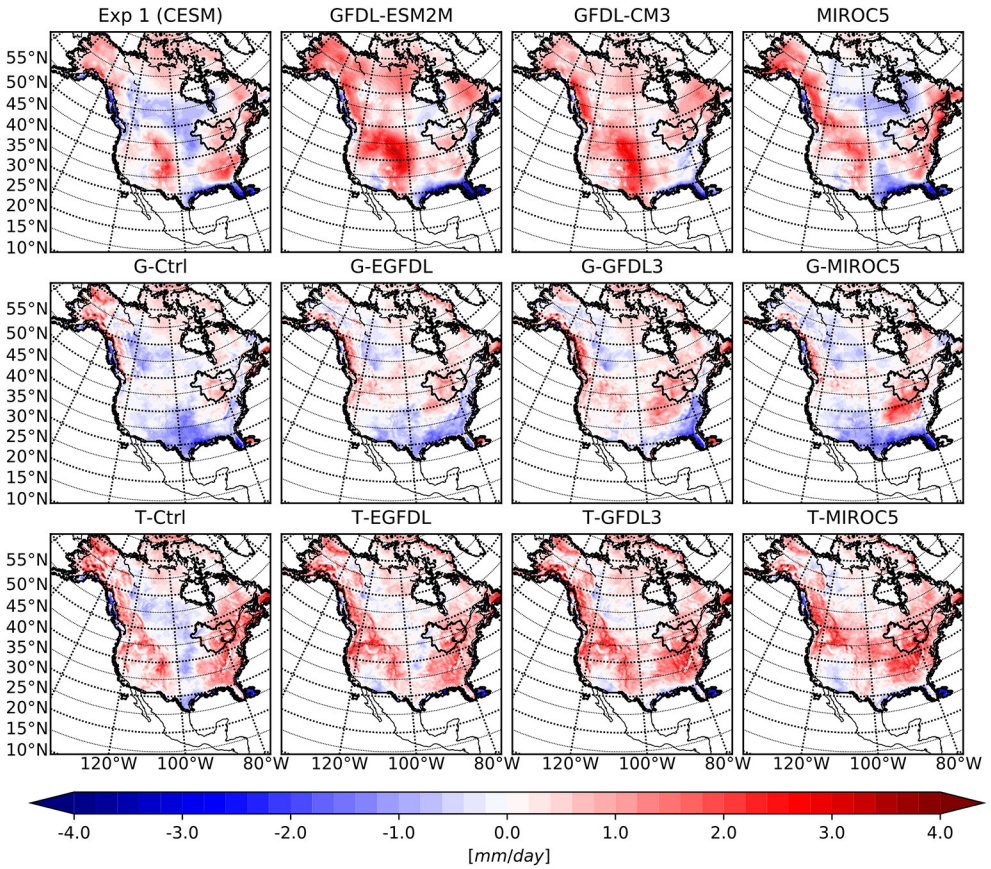

FIGURE 9 | Same as **Figure 8** but for summer precipitation biases.

The near surface temperature (T2) averaged over the summer season for all ensemble members and their respective GCMs are compared with the NRCan dataset over the outermost WRF domain in **Figure 6**. There is a noticeable difference between the G physics and T physics ensemble members; the latter are warmer than the former by ∼2 °C. In **Figure 7** the bias in the incoming shortwave radiation for all ensemble members during the summer season is displayed, and it is immediately clear that the primary discriminant in modeled results for this variable is the choice of parameterization set. This difference in surface incoming shortwave radiation is very likely caused by different cloud cover fractions in the atmosphere, which is determined by cumulus and microphysics schemes. These schemes affect cloud cover and cloud reflectance, thereby modifying the planetary albedo. The difference in incoming shortwave radiation also explains why simulations using G physics have a colder surface than those using T physics, which is consistent with earlier results reported in d'Orgeville et al. (2014), and Peltier et al. (2018) that different physics schemes lead to different bias in WRF results. For more information on the impact of physics schemes in atmospheric modelling, see Thompson et al. (2016) who examined the impact of cloud physics and radiation parametrization on WRF simulations, and also Fouquart et al. (1990) for general information on the influence of clouds on radiation in climate modelling.

In summer, the CESM1 driven WRF result is ∼2° C warmer than CMIP5 driven results, which is caused by differences in GCM forcing data. The jet streams are weaker and meridional pressure gradients are flatter in summer, thus the GCM caused cold bias is smaller in magnitude than in the winter season. Meanwhile in Gula and Peltier (2012) a 2–3° C temperature difference in the region around the lakes is also reported due to the inclusion of the lake model, which is of similar magnitude as biases from other causes discussed herein. Therefore, lake effect is a first order influence on the regional climate and we again confirm the findings in Bates et al. (1993), Lofgren (1997), Notaro et al. (2013) and Mallard et al. (2014) that including a proper lake model is absolutely necessary to properly resolve climate around the lakes.

Choice of physical parameterizations also has a strong influence on the modeled precipitation. The precipitation bias for the same collection of model results is presented in **Figure 8** for the winter season and in **Figure 9** for the summer season. For both season the primary difference in spatial pattern is between the group of WRF members using G physics and the group using T physics, stronger in summer season as there is little precipitation over winter, and little to no difference across members driven by different GCMs. Related works (d'Orgeville et al., 2014; Huo and Peltier, 2019) also revealed that different sets

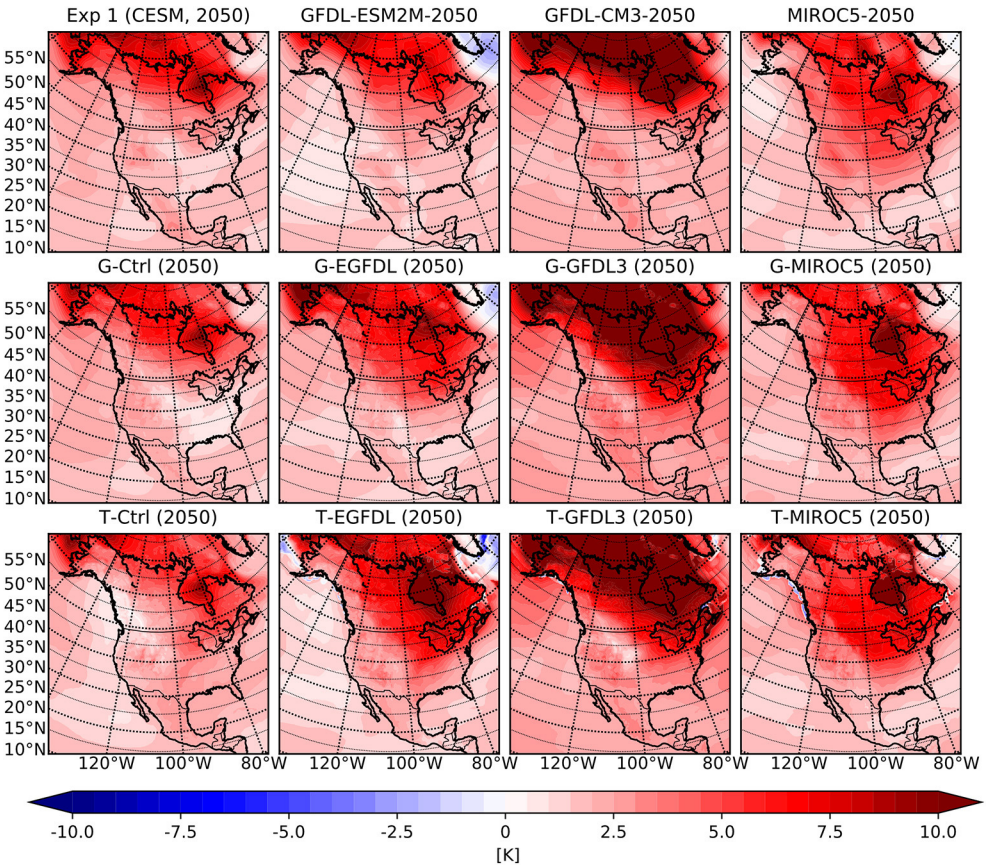

FIGURE 10 | Mean winter season 2 m air temperature anomaly for the 2050–2060 period with respect to the historical period over the outer WRF domain for the GCMs (top row), WRF ensemble members with G physics (middle row), and WRF ensemble members with T physics (bottom row). From left to right are experiments (GCM or GCM driven WRF) associated with CESM1, GFDL-ESM2M, GFDL-CM3, and MIROC5, respectively.

of physical parameterizations would create large differences in the precipitation result. Note that none of the WRF results have a spatial pattern that resembles the pattern of their respective GCM forcing data, so precipitation data from GCMs is rewritten by the RCM model over the regional domain. Results from (Zobel et al., 2018a) also show that precipitation from RCMs are completely different from GCMs that are used for forcing, indicating that model settings used in the RCM exert a strong influence over modeled precipitation.

3.2. Simulation Results Over Future Projection Periods

Before presenting climate results for the two climate projection periods discussed in section 2, several technical details need to be stated here. First, all comparisons of CMIP5 ensemble member for future projection period results have been performed with respect to the historical results of each individual ensemble member. Second, in order to preserve the model variability signal, no bias correction has been applied before comparing model results. Third, the two future projection periods (the mid-century (2050–2060) and the end-century (2085–2100) periods) have different time length, but results of the two periods will still be presented in the form of averages over all years over each time period.

According to conclusions in section 3.1, jet stream position has the potential to inflict large temperature bias in the RCM results. Therefore, changes in jet stream position during future projection periods should be examined to determine their contribution to projected climate changes. The right panel of **Figure 2** presents the zonally averaged zonal wind speed at 250 hPa vertical level for the CMIP5 ensemble members during mid-twenty-first century projection period, and similar to the left panel of **Figure 2** the WRF data forced by CMIP5 GCMs still have their jet stream centered around 30° N latitude, while CESM1 forced results position it at around 40° N latitude. This persistence in the bias of jet stream position indicates that the base state of climate for each CMIP5 member of the ensemble is likely unchanged during future projection periods, and the difference in model results (both WRF and GCMs) are more related to the change in GHG concentration toward the end of twenty-first Century.

Changes in the near surface temperature (T2) field between the mid-twenty-first century projection period and historical period are presented in **Figure 10** for the winter season and

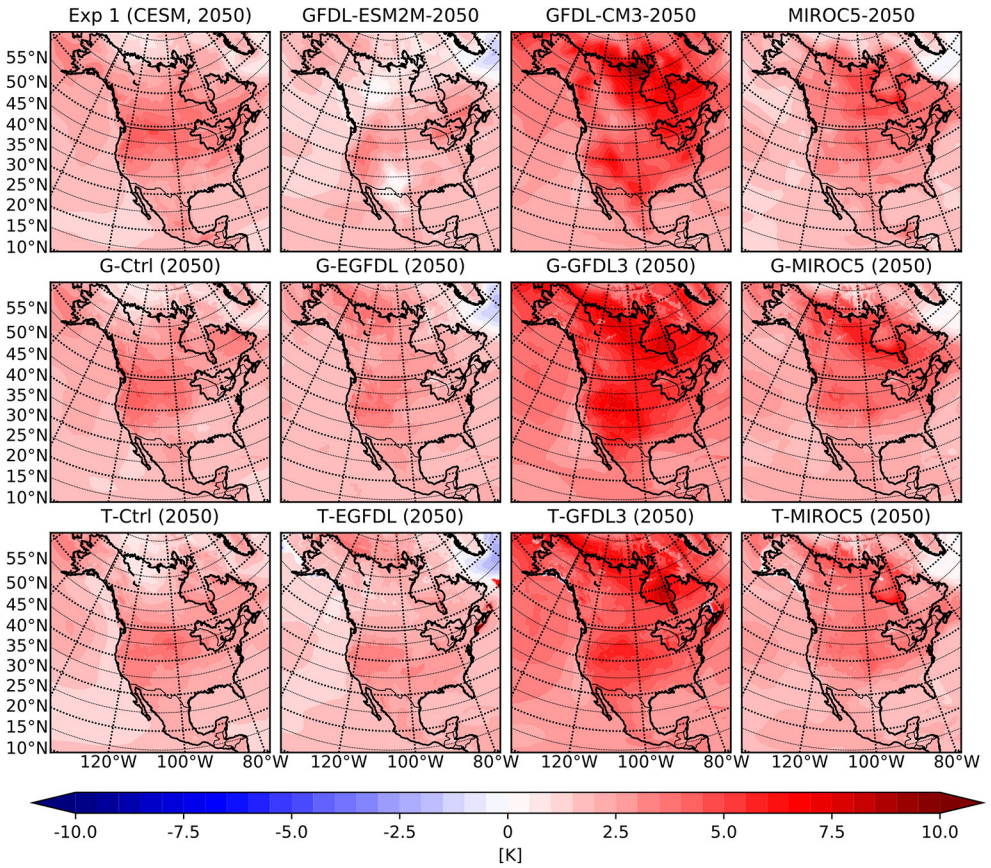

FIGURE 11 | Same as **Figure 10** but for the summer season temperature anomalies.

Figure 11 for summer season. The most important information that follows from these figures is that all of the WRF results, whether obtained using G or T physics, have a surface temperature change signal that closely mimics the strength of the signal in their respective GCM forcing data, regardless of season. Results for the end-twenty-first century period also have WRF regional T2 warming bias closely follow the T2 warming bias in their respective GCM forcing data and are mostly independent of the physics parametrization schemes employed. This closeness in the climate change temperature signal is very interesting given the large difference in the climate base state in both winter and summer season presented in section 3.1, indicating that given a forcing scenario including GHG forcing from emission pathway, general circulation patterns from GCM forcing data, WRF is able to recreate the same amount of surface warming in the GCM forcing data. The amount of climate sensitivity in the GCM is also preserved, as Paynter et al. (2018) has described the high climate sensitivity of the GFDL-CM3 model, and the WRF results forced by GFDL-CM3 data have the same high climate sensitivity in both winter and summer season. This closeness observed between WRF and GCM results shows that the climate change temperature signal is reasonably well captured by the GCMs with respect to their individual climate base state. Therefore, this study affirms that warming forecasts in the GCM model are reliable, and support works on future warming analysis using GCM results such as Kharin et al. (2013) and Maloney et al. (2014). On the other hand, the independence of this closeness from the physics parametrization used means that variability in the choice of cumulus and microphysics schemes within the 2 sets employed in this study will not dominate the temperature forecast results.

Another important potential implication of this closeness concerns the creation of climate projection forecasts for temperature using bias correction techniques: for the WRF settings used in this study, climate change signal for temperature is well captured at the GCM level, and the bias in the climate forecast result would be primarily in the base climate state. Therefore, bias correcting the GCM base climate state would be sufficient in providing reasonable climate predictions for future periods, at least for similar WRF settings. Other studies have employed bias correction as part of their scheme to forecast future climate (Byun and Hamlet, 2018; Zobel et al., 2018b) and it would be interesting to study future climate projection signals for the CMIP5 ensemble after bias correction. However, this is beyond the scope of this study and left for future works.

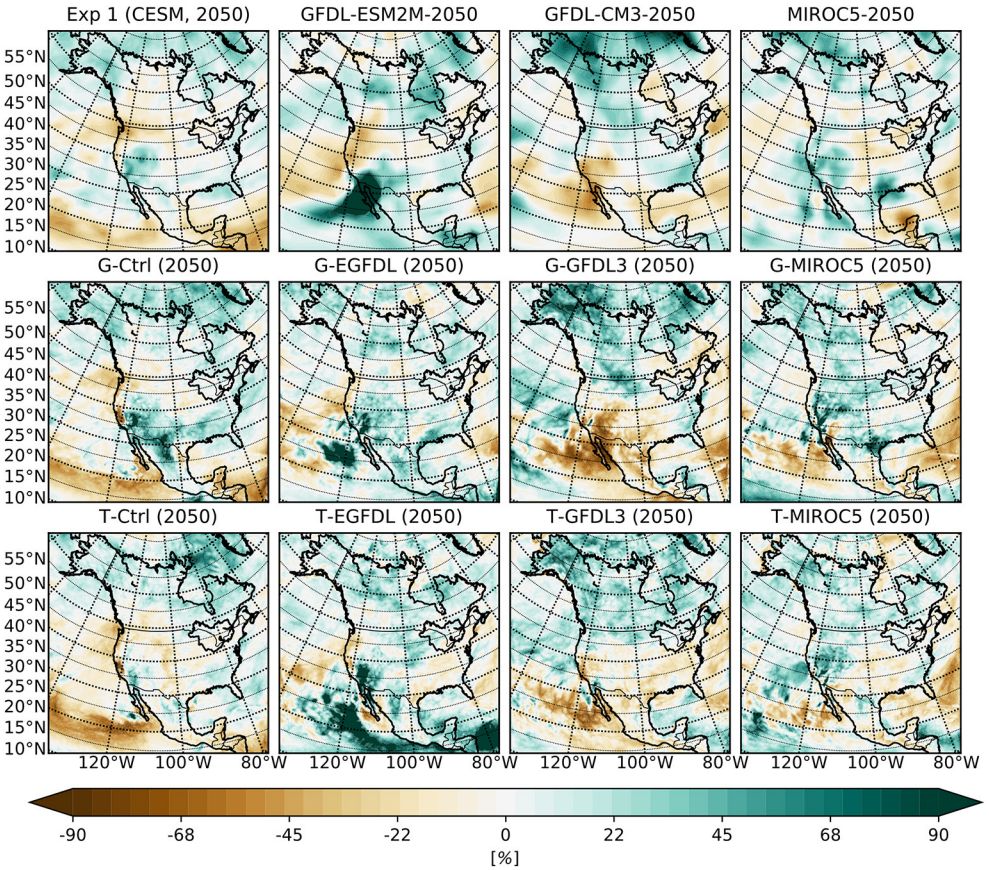

FIGURE 12 | Mean summer season relative change in precipitation for the 2050–2060 period with respect to the historical period over the outer WRF domain for the GCMs (top row), WRF ensemble members with G physics (middle row), and WRF ensemble members with T physics (bottom row). From left to right are experiments (GCM or GCM driven WRF) associated with CESM1, GFDL-ESM2M, GFDL-CM3 and MIROC5 respectively.

Justifying the reliability of GCM predictions in surface temperature warming does not undermine the scientific values of dynamical downscaling experiments, as dynamical downscaling remains capable of improving other variable fields. Precipitation, for example, is strongly dependent on resolution and local processes, and having increased resolution in the climate model will almost certainly improve the quality of precipitation results (Notaro et al., 2013; d'Orgeville et al., 2014; Zobel et al., 2018a). The mid-twenty-first century projection of precipitation changes for the CMIP5 ensemble is showed in **Figure 12**, where along with similarity between GCM and RCM results, a noticeable difference between results using G or T physics is observed. This means cumulus and microphysics scheme still have their role in refining local precipitation projections. The dependence on physics parametrizations is probably stronger if the outlier physics set 'g' described in Peltier et al. (2018) with Morricon microphysics scheme (Morrison et al., 2009), Grell-3 cumulus scheme (Grell and Dévényi, 2002) and Noah MP land surface scheme (Niu et al., 2011) is employed in this study. Details of the physics set dependence on precipitation distributions and precipitation extremes in WRF results over the regional domain of this study are discussed in details in d'Orgeville et al. (2014) and Peltier et al. (2018), so it will not be repeated in this study.

Overall, the results of CMIP5 ensemble over future projection periods may be summarized as follows: despite the large difference between WRF and GCM data in the historical period, the climate change signal in surface temperature for the WRF results is closely following the signal in their respective GCM forcing data when comparing to their counterparts in the historical period. Switching between G and T physics parameterizations does not change this closeness in temperature but does affect local change in precipitation projections. These future projection period climate data, along with historical data presented in 3.1, will serve as a reliable database for the extreme heat analysis below.

3.3. Extreme Heat Event Analysis Over the Great Lakes Region Based on the CMIP5 Ensemble Data

On the basis of results from section 3.1, summer season surface temperature between group members differs in magnitude of bias but not in spatial pattern. Therefore, most of our analysis on

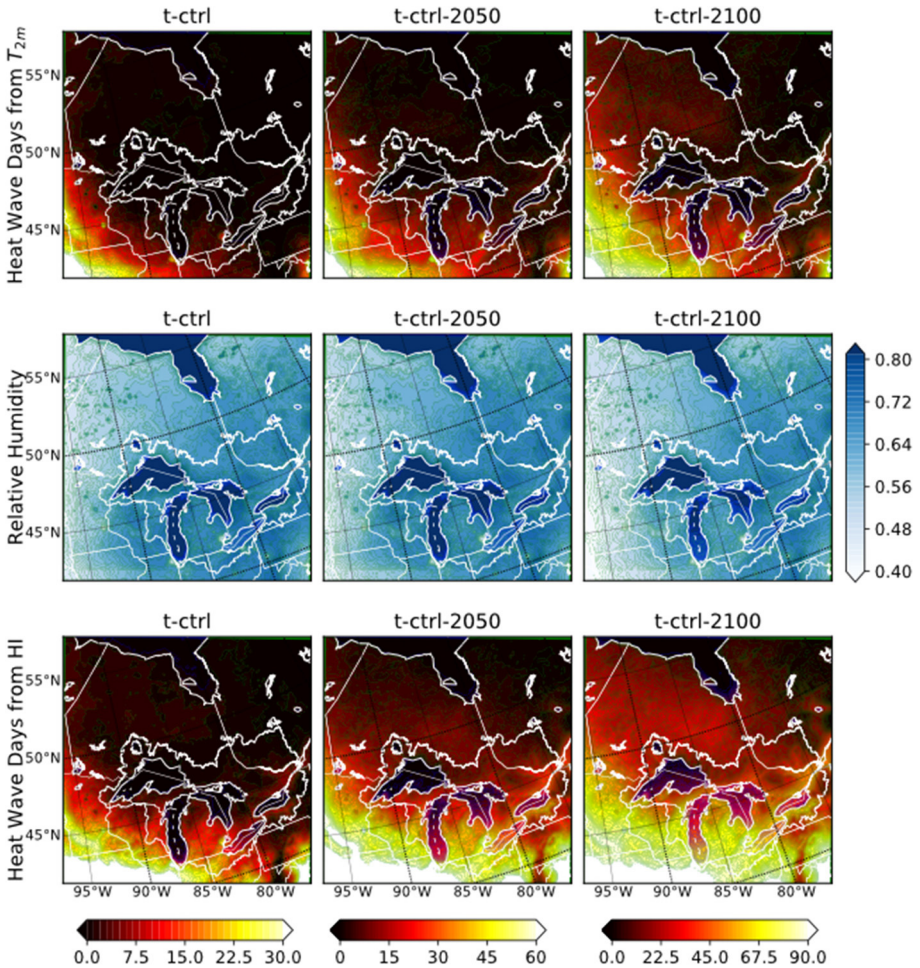

FIGURE 13 | Extreme heat event analysis for simulation with CESM forcing and T physics. The three rows display annually averaged number of extreme heat days per year computed using surface temperature, average summer surface relative humidity, and average number of extreme heat days per year computed using the HI. The three columns represent the historical, mid-twenty-first century and end-twenty-first century time periods. Color bar at the bottom represents the scale used for extreme heat days for each column respectively. Note that the scale of colorbars for heat event days differs between the time periods.

extreme heat will use a representative ensemble member and we will call upon the full ensemble for only selected analysis. We repeat here for the reader that the definition of a heat wave in this study is "a period with more than three consecutive days of maximum temperatures at or above $32^{\circ}C/90^{\circ}F$" (section 2.5). Daily data from WRF are used to compute days that have heat wave with temperature and HI metrics and with the same static threshold for all time periods. The wide range of climate covered by our ensemble enables us to explore the change of extreme events around a variety of climate states, and a range of biases. Therefore, no bias correction is applied to the model results before performing this analysis. A direct consequence of this is the preservation of cold biases in the historical results (**Figure 6**), and therefore we do not expect our extreme heat analysis to match observational records over the historical period.

For our representative ensemble member, we select the simulation with CESM1 forcing and T physics. The first row in **Figure 13** compares the number of extreme heat days (computed with surface temperature data and averaged over years within each time period) over the WRF inner domain, between the historical, mid-twenty-first century and end-twenty-first century periods from left to right. During the historical period, extreme heat events are largely confined to the southernmost part of the domain, but they progressively expand to influence most of the land area as the climate change signal strengthens by the end of the century. The number of extreme heat days per year averaged over the GLB (excluding lake surface) increases from 0.5 days during the historical period to 5.7 days during the mid-twenty-first century period to 13.6 days during the end-twenty-first century period. The entire Great Lakes region is largely free from extreme heat events in the historical period, but the number of extreme heat days increases to ∼30 days per year south of the lakes and ∼5 days per year north of the lakes by the end of the century. The middle row of the figure shows surface

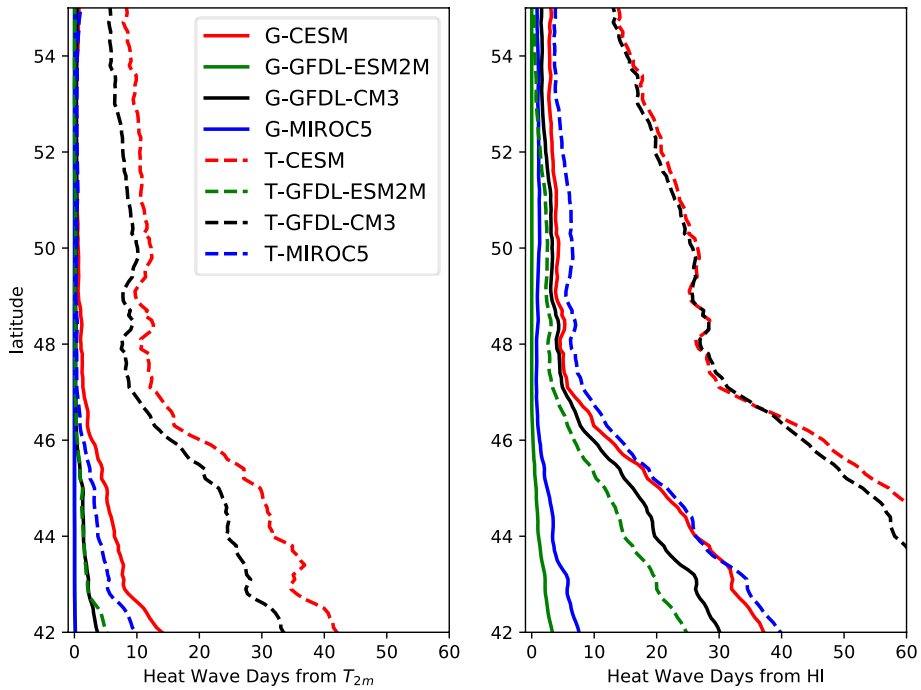

FIGURE 14 | Zonally averaged number of extreme heat days over the central part of the domain ($95 - 75W^{\circ}$,$41 - 56N^{\circ}$) for all end-century ensemble members. Water surfaces are excluded when taking average.

relative humidity averaged over the summer season, and which remains moderately high over the domain with little change between the different time periods. When the contribution of this humidity to extreme heat is included through the HI, the region that experiences extreme heat events increases considerably, as displayed in the bottom row of the figure. HI derived number of extreme heat days per year averaged over the GLB also increases to 4.5 days during historical period, 20.9 days during mid-twenty-first century period, and to 42.3 days in end-twenty-first century period. During the historical period, regions south of the Great Lakes experience ∼20 extreme heat days per year while such events remain extremely rare north of the Great Lakes. Toward the end of the century, the number of extreme heat days increases to 60–80 days south of the lakes and ∼30 days north of the lakes.

Spatially, it is very clear that the occurrence of extreme heat over the lake surfaces is lower than the surroundings. This is not surprising because the heat capacity of water is much higher than that of the surrounding landscape. Furthermore, when temperature is used as the metric, the number of extreme heat days is significantly lower in regions east of Lake Superior and northeast of Lake Huron compared to other regions at the same latitude. When HI is used the same spatial pattern is obtained, but with reduced magnitude. This is likely due to lake effect: when extremely hot air coming from the south passes over the lakes, both heat conduction and evaporation of lake water extracts sensible heat from that air mass, resulting in cooler air in the downwind region which reduces both temperature and HI. At the same time, the increase in the humidity of the air as it passes over the lakes leads to an increase in the HI. Thus employing the HI accounts for competing influences of lakes, through temperature and moisture, on the likelihood of heat events. The extent of the region with low extreme heat activity is larger than that described by Scott and Huff (1996), and the reasons for this difference will warrant a future study. In our results the differences between the analysis produced using temperature and using the HI is clear and similar for all ensemble members (not shown), and this difference reflects the importance of including moist effects in calculating extreme heat risks in a moist environment.

Influence of lake effects is also visible when the number of extreme heat days over land is zonally averaged, excluding lakes (**Figure 14**). Regardless of the metric used to determine the occurrence of extreme heat days, the zonally averaged number of heat days decreases as a function of latitude, and which is clearly due to the latitudinal decrease of temperature. However, at the latitudes of Lake Superior (47–49N°), there is a conspicuous drop in the number of days, punctuating the trend of a smooth decrease with latitude. This drop is clearly due to the temperature mitigating effect of the lakes that matches the region with low extreme heat activity described just above. Since part of the mitigation of extreme heat events is associated with the conversion of heat to humidity, the drop is smaller in the HI calculated results that capture moisture effect as part of extreme heat risk. Results over all time periods have this latitudinal drop, while end-twenty-first century result with the clearest signal is presented in **Figure 14**.

The dependence of extreme heat activity on the mean climate state is illustrated in **Figure 15** where results from all ensemble members is used. Each data point on this figure represents the

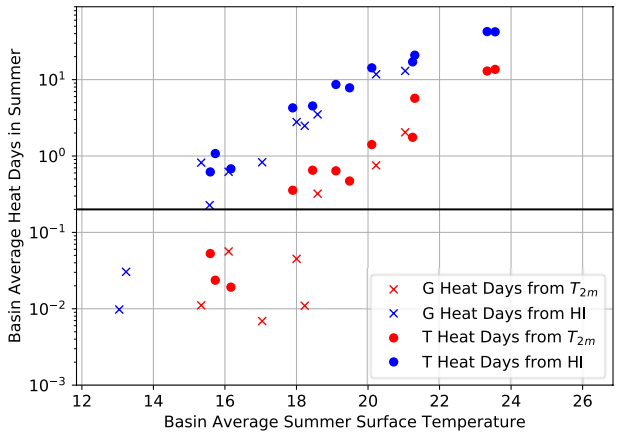

FIGURE 15 | Log plot of annually and spatially averaged number of extreme heat days vs. average summer surface temperature, for all members of the ensemble and all time periods. Dots and crosses represent ensemble members with different physical parameters, red color represent results calculated using temperature, with blue color represents results calculated using the HI. The black line marks reference value of 0.2.

GLB averaged surface temperature and number of extreme heat days (on a log scale), based upon either temperature or HI, for one ensemble member at one time period. From this figure it is noted first that the number of extreme heat days increase with increasing temperature, which is obvious since the method employed is static. With a rise in temperature, increasing extreme heat events is predicted by almost all studies that discuss extreme event frequency under climate change (see IPCC, 2013b, for a nice summary), regardless of the method of analysis employed. Secondly, when using the temperature metric for extreme, for average temperatures above 18° C (16° C when HI is used), the simulated number of extreme heat days scales roughly linear with respect to average temperature on the log plot, which implies an exponential growth in the number of heat days with temperature. This nonlinear increase of extreme heat days in the coming years deserves attention from policy makers to better understand the associated health risk.

Another point worth noting from **Figure 15** is that the exponential dependence of the number of extreme heat days on temperature starts a few degrees earlier using the HI method than temperature. This difference represents the effect of humidity in enhancing the severity of a heat wave event, which is important for a moisture rich region such as the GLB. This signal implies that for regions that have an abundant supply of moisture, increase in extreme heat events will commence earlier than predicted using only temperature as a metric. Future studies focusing on related fields should invest some attention on this moisture effect, to ensure the full risk of extreme heat event is captured.

4. SUMMARY AND DISCUSSION

An ensemble of WRF-based dynamically downscaled experiments for climate change projections over the Great Lakes Basin (GLB) has been completed using forcing data from four GCMs. Previous studies using the same dynamical downscaling process (d'Orgeville et al., 2014; Peltier et al., 2018) were focused on validating the experiment setup and model reliability and therefore their physics ensemble was driven only by simulations performed with the CESM1 global model. Here, we use multiple data from several GCMs available in the CMIP5 archive, along with data from our own simulations with CESM1 as forcing for the regional model in order to cover a wide range of possible climate states and to validate the quality of CMIP5 forced WRF results. We also perform analysis of extreme heat events with this ensemble to explore the evolution of such events around the GLB under increasing GHG toward the end of the twenty-first century.

The bias in our ensemble is governed by GCM forcing, WRF physics scheme selection, and inclusion of the lake model. Temperature bias is dominated by large scale effects in the winter season while in summer all sources of biases have first order impact. Precipitation bias in our ensemble is mostly influenced by the cumulus and microphysics schemes used in WRF, and the FLake lake model resolves lake effects effectively around the Great Lakes. However, sources of bias in WRF are not limited to just these factors, as Zobel et al. (2018b) have shown that spectral nudging is capable of generating large differences in WRF results, and Zagar et al. (2013) have shown that there can be uncertainty in WRF results associated with domain size and nesting. Despite large difference between GCM and RCM results in the historical period, the magnitude of climate warming signal is found to be the same between the downscaled simulations and their associated GCMs. This similarity is independent from the physics parametrization employed, indicating that this signal is primarily determined by the large scale circulation features resolved in GCMs, and well captured over the RCM domain by the dynamical downscaling process. Meanwhile, projected changes in local precipitation are still influenced by the physics parametrizations employed, which agrees with findings in previous studies (d'Orgeville et al., 2014; Peltier et al., 2018).

The wide spread of possible climate states in this expanded ensemble provides an excellent basis on which to perform extreme heat event analysis. This analysis reveals a steady increase of extreme heat days with respect to increasing GHG forcing toward the end of the twenty-first century. This increase of extreme heat days with temperature during the projection periods is not surprising, as it would emerge naturally from the definition of extreme heat events used in this study. Meanwhile, our analysis shows that the rate of growth of extreme heat days as a function of surface temperature is independent of physics parametrization and GCM forcing, suggesting that our conclusions for the increase in heat waves toward the end of the century is robust. The extreme heat analysis takes further advantage of the fact that WRF is coupled to a proper lake model (FLake) which helps us simulate the impact of lake effect on the frequency of heat waves in the surrounding regions. A key outcome is the reduction in the number of extreme heat days in the downwind region of the lakes as the lakes absorb heat from the atmosphere.

Along with high temperature, high moisture content in the atmosphere also increases the severity of extreme heat events. The Great Lakes region includes a significant source of moisture, the effect of which on the occurrence of extreme heat events is captured with the HI method for detecting the occurrence of such events. With this method it is shown that the presence of moisture will trigger the onset of extreme heat events in the GLB region at a lower temperature threshold, and that the effect of lake induced sensible cooling in regions downwind of the lakes is also reduced as a result of the conversion of sensible heat to humidity. Since humans are vulnerable to both high temperature and high humidity environments, decision makers should be fully aware of the consequence of high moisture in the Great Lakes region, especially when evaporation from lake surfaces converts high temperature to high relative humidity, leaving a change in the net heat effect that is smaller than that which would be expected from the reduction of air temperature.

DATA AVAILABILITY STATEMENT

The raw data supporting the conclusions of this article will be made available by the authors, without undue reservation.

AUTHOR CONTRIBUTIONS

FX, AE, and WP contributed to the conception and design of this study. FX, AE, and DC contributed to the software, data analysis and visualization of this study. All authors contributed to discussing the result and preparing the submitted version of the article.

FUNDING

Support for FX has been provided by NSERC Discovery Grant A9627 to WP.

ACKNOWLEDGMENTS

The simulations presented in this manuscript were performed on the SciNet High Performance Computing facility at the University of Toronto, which is a component of the Compute Canada HPC platform. The authors would like to thank Frédéric Laliberté for providing support with using the cdb_query software that processes CMIP5 data.

REFERENCES

Anderson, G. B., Bell, M. L., and Peng, R. D. (2013). Methods to calculate the heat index as an exposure metric in environmental health research. *Environ. Health Perspect*. 121, 1111–1119. doi: 10.1289/ehp.1206273

Bates, G. T., Giorgi, F., and Hostetler, S. W. (1993). Toward the simulation of the effects of the great lakes on regional climate. *Mon. Weather Rev*. 121, 1373–1387. doi: 10.1175/1520-0493(1993)121<1373:TTSOTE>2.0.CO;2

Briley, L. J., Rood, R. B., and Notaro, M. (2021). Large lakes in climate models: a great lakes case study on the usability of cmip5. *J. Great Lakes Res*. 47, 405–418. doi: 10.1016/j.jglr.2021.01.010

Byun, K., and Hamlet, A. F. (2018). Projected changes in future climate over the midwest and great lakes region using downscaled cmip5 ensembles. *Int. J. Climatol*. 38, e531–e553. doi: 10.1002/joc.5388

Chen, F., and Dudhia, J. (2001). Coupling an advanced land surface-hydrology model with the penn state-ncar mm5 modeling system. part i: Model implementation and sensitivity. *Mon. Weather Rev*. 129, 569–585. doi: 10.1175/1520-0493(2001)129<0569:CAALSH>2.0.CO;2

Cheng, G. H., Huang, G. H., Dong, C., Zhu, J. X., Zhou, X., and Yao, Y. (2017). An evaluation of cmip5 gcm simulations over the athabasca river basin, canada. *River Res. Appl*. 33, 823–843. doi: 10.1002/rra.3136

Collins, W. D., Bitz, C. M., Blackmon, M. L., Bonan, G. B., Bretherton, C. S., Carton, J. A., et al. (2006). The community climate system model version 3 (ccsm3). *J. Clim*. 19, 2122–2143. doi: 10.1175/JCLI3761.1

Danabasoglu, G., Bates, S. C., Briegleb, B. P., Jayne, S. R., Jochum, M., Large, W. G., et al. (2012). The ccsm4 ocean component. *J. Clim*. 25, 1361–1389. doi: 10.1175/JCLI-D-11-00091.1

Dee, D. P., Uppala, S. M., Simmons, A. J., Berrisford, P., Poli, P., Kobayashi, S., et al. (2011). The era-interim reanalysis: configuration and performance of the data assimilation system. *Q. J. R. Meteorol. Soc*. 137, 553–597. doi: 10.1002/qj.828

Deser, C., Phillips, A., Bourdette, V., and Teng, H. (2012). Uncertainty in climate change projections: the role of internal variability. *Climate Dyn*. 38, 527–546. doi: 10.1007/s00382-010-0977-x

Deser, C., Phillips, A. S., Alexander, M. A., and Smoliak, B. V. (2014). Projecting north american climate over the next 50 years: uncertainty due to internal variability. *J. Clim*. 27, 2271–2296. doi: 10.1175/JCLI-D-13-00451.1

Donner, L. J., Wyman, B. L., Hemler, R. S., Horowitz, L. W., Ming, Y., Zhao, M., et al. (2011). The dynamical core, physical parameterizations, and basic simulation characteristics of the atmospheric component am3 of the gfdl global coupled model cm3. *J. Clim*. 24, 3484–3519. doi: 10.1175/2011JCLI3955.1

d'Orgeville, M., Peltier, W. R., Erler, A. R., and Gula, J. (2014). Climate change impacts on great lakes basin precipitation extremes. *J. Geophys. Res. Atmos*. 119, 10799–10812 doi: 10.1002/2014JD021855

Dunne, J. P., John, J. G., Adcroft, A. J., Griffies, S. M., Hallberg, R. W., Shevliakova, E., et al. (2012). Gfdl's esm2 global coupled climate-carbon earth system models. part i: physical formulation and baseline simulation characteristics. *J. Clim*. 25, 6646–6665. doi: 10.1175/JCLI-D-11-00560.1

Dunne, J. P., John, J. G., Shevliakova, E., Stouffer, R. J., Krasting, J. P., Malyshev, S. L., et al. (2013). GFDL's ESM2 global coupled climate?carbon earth system models. part ii: carbon system formulation and baseline simulation characteristics. *J. Clim*. 26, 2247–2267. doi: 10.1175/JCLI-D-12-00150.1

Erler, A. R. (2015). *High Resolution Hydro-climatological Projections for Western Canada* (Ph.D. thesis). University of Toronto.

Erler, A. R., and Peltier, W. R. (2016). Projected changes in precipitation extremes for western canada based on high-resolution regional climate simulations. *J. Clim*. 29, 8841–8863. doi: 10.1175/JCLI-D-15-0530.1

Erler, A. R., and Peltier, W. R. (2017). Projected hydroclimatic changes in two major river basins at the canadian west coast based on high-resolution regional climate simulations. *J. Clim*. 30, 8081–8105. doi: 10.1175/JCLI-D-16-0870.1

Erler, A. R., Peltier, W. R., and D'Orgeville, M. (2015). Dynamically downscaled high-resolution hydroclimate projections for western canada. *J. Clim*. 28, 423–450. doi: 10.1175/JCLI-D-14-00174.1

Fouquart, Y., Buriez, J. C., Herman, M., and Kandel, R. S. (1990). The influence of clouds on radiation: A climate-modeling perspective. *Reviews of Geophysics*, 28, 145–166. doi: 10.1029/RG028i002p00145

Gent, P. R., Danabasoglu, G., Donner, L. J., Holland, M. M., Hunke, E. C., Jayne, S. R., et al. (2011). The community climate system model version 4. *J. Clim*. 24, 4973–4991. doi: 10.1175/2011JCLI4083.1

Grell, G. A., and Dévényi, D. (2002). A generalized approach to parameterizing convection combining ensemble and data assimilation techniques. *Geophys. Res. Lett*. 29, 38-1–38-4. doi: 10.1029/2002GL015311

Griffies, S. M., Winton, M., Donner, L. J., Horowitz, L. W., Downes, S. M., Farneti, R., et al. (2011). The gfdl cm3 coupled climate model: Characteristics of the ocean and sea ice simulations. *J. Clim*. 24, 3520–3544. doi: 10.1175/2011JCLI3964.1

Gula, J., and Peltier, W. R. (2012). Dynamical downscaling over the great lakes basin of north america using the wrf regional climate model: the impact of the great lakes system on regional greenhouse warming. *J. Clim.* 25, 7723–7742. doi: 10.1175/JCLI-D-11-00388.1

Holland, M. M., Bailey, D. A., Briegleb, B. P., Light, B., and Hunke, E. (2012). Improved sea ice shortwave radiation physics in ccsm4: The impact of melt ponds and aerosols on arctic sea ice. *J. Clim.* 25, 1413–1430. doi: 10.1175/JCLI-D-11-00078.1

Hong, S.-Y., and Lim, J.-O. J. (2006). The WRF single-moment 6-class microphysics scheme (WSM6). *J. Korean Meteor. Soc*, 42, 129–151.

Huo, Y., and Peltier, W. R. (2019). Dynamically downscaled climate simulations of the indian monsoon in the instrumental era: physics parameterization impacts and precipitation extremes. *J. Appl. Meteorol. Climatol.* 58, 831–852. doi: 10.1175/JAMC-D-18-0226.1

Huo, Y., Peltier, W. R., and Chandan, D. (2021). Mid-holocene monsoons in south and southeast asia: dynamically downscaled simulations and the influence of the green sahara. *Clim. Past* 17, 1645–1664. doi: 10.5194/cp-17-1645-2021

Iacono, M. J., Delamere, J. S., Mlawer, E. J., Shephard, M. W., Clough, S. A., and Collins, W. D. (2008). Radiative forcing by long-lived greenhouse gases: calculations with the aer radiative transfer models. *J. Geophys. Res. Atmos.* 113:D13103. doi: 10.1029/2008JD009944

IPCC (2013a). *The Fifth Assessment Report (AR5) of the United Nations Intergovernmental Panel on Climate Change (IPCC), Climate Change 2013: The Physical Science Basis, IPCC WGI AR5, Chapter 14*. Cambridge; New York, NY: Cambridge University Press; Climate Phenomena and their Relevance for Future Regional Climate Change.

IPCC (2013b). *The Fifth Assessment Report (AR5) of the United Nations Intergovernmental Panel on Climate Change (IPCC), Climate Change 2013: The Physical Science Basis, IPCC WGI AR5, Chapter 9*. Cambridge University Press; Evaluation of Climate Models.

Jeong, D. I., Sushama, L., Diro, G. T., Khaliq, M. N., Beltrami, H., and Caya, D. (2016). Projected changes to high temperature events for canada based on a regional climate model ensemble. *Clim. Dyn.* 46, 3163–3180. doi: 10.1007/s00382-015-2759-y

Kain, J. S. (2004). The kain?fritsch convective parameterization: An update. *J. Appl. Meteorol.* 43, 170–181. doi: 10.1175/1520-0450(2004)043<0170:TKCPAU>2.0.CO;2

Kharin, V. V., Zwiers, F. W., Zhang, X., and Wehner, M. (2013). Changes in temperature and precipitation extremes in the cmip5 ensemble. *Clim. Change* 119, 345–357. doi: 10.1007/s10584-013-0705-8

Kug, J.-S., Jeong, J.-H., Jang, Y.-S., Kim, B.-M., Folland, C. K., Min, S.-K., et al. (2015). Two distinct influences of arctic warming on cold winters over north america and east asia. *Nat. Geosci.* 8, 759–762. doi: 10.1038/ngeo2517

Kumar, S., Kinter, J., Dirmeyer, P. A., Pan, Z., and Adams, J. (2013). Multidecadal climate variability and the "warming hole" in north america: results from cmip5 twentieth- and twenty-first-century climate simulations. *J. Clim.* 26, 3511–3527. doi: 10.1175/JCLI-D-12-00535.1

Lawrence, D. M., Oleson, K. W., Flanner, M. G., Fletcher, C. G., Lawrence, P. J., Levis, S., et al. (2012). The ccsm4 land simulation, 1850–2005: assessment of surface climate and new capabilities. *J. Clim.* 25, 2240–2260. doi: 10.1175/JCLI-D-11-00103.1

Li, C., Zhang, X., Zwiers, F., Fang, Y., and Michalak, A. M. (2017). Recent very hot summers in northern hemispheric land areas measured by wet bulb globe temperature will be the norm within 20 years. *Earths Future* 5, 1203–1216. doi: 10.1002/2017EF000639

Li, K., Zhang, J., and Wu, L. (2018). Assessment of soil moisture-temperature feedbacks with the ccsm-wrf model system over east asia. *J. Geophys. Res. Atmos.* 123, 6822–6839. doi: 10.1029/2017JD028202

Lofgren, B. M. (1997). Simulated effects of idealized laurentian great lakes onregional and large-scale climate. *J. Clim.* 10, 2847–2858. doi: 10.1175/1520-0442(1997)010<2847:SEOILG>2.0.CO;2

Mallard, M. S., Nolte, C. G., Bullock, O. R., Spero, T. L., and Gula, J. (2014). Using a coupled lake model with wrf for dynamical downscaling. *J. Geophys. Res. Atmos.* 119, 7193–7208. doi: 10.1002/2014JD021785

Maloney, E. D., Camargo, S. J., Chang, E., Colle, B., Fu, R., Geil, K. L., et al. (2014). North american climate in cmip5 experiments: Part iii: assessment of twenty-first-century projections. *J. Clim.* 27, 2230–2270. doi: 10.1175/JCLI-D-13-00273.1

McKenney, D. W., Hutchinson, M. F., Papadopol, P., Lawrence, K., Pedlar, J., Campbell, K., et al. (2011). Customized spatial climate models for north america. *Bull. Am. Meteorol. Soc.* 92, 1611–1622. doi: 10.1175/2011BAMS3132.1

Meehl, G. A., and Tebaldi, C. (2004). More intense, more frequent, and longer lasting heat waves in the 21st century. *Science* 305, 994–997. doi: 10.1126/science.1098704

Mironov, D. V. (2008). *Parameterization of lakes in numerical weather prediction. description of a lake model*. Technical report, Deutscher Wetterdienst, Offenbach am Main, Germany.

Morrison, H., Thompson, G., and Tatarskii, V. (2009). Impact of cloud microphysics on the development of trailing stratiform precipitation in a simulated squall line: comparison of one- and two-moment schemes. *Mon. Weather Rev.* 137, 991–1007. doi: 10.1175/2008MWR2556.1

Nakanishi, M., and Niino, H. (2009). Development of an improved turbulence closure model for the atmospheric boundary layer. *J. Meteor. Soc. Jpn* 87, 895–912. doi: 10.2151/jmsj.87.895

Neale, R. B., Richter, J., Park, S., Lauritzen, P. H., Vavrus, S. J., Rasch, P. J., et al. (2013). The mean climate of the community atmosphere model (cam4) in forced sst and fully coupled experiments. *J. Clim.* 26, 5150–5168. doi: 10.1175/JCLI-D-12-00236.1

Niu, G.-Y., Yang, Z.-L., Mitchell, K. E., Chen, F., Ek, M. B., Barlage, M., et al. (2011). The community noah land surface model with multiparameterization options (noah-mp): 1. model description and evaluation with local-scale measurements. *J. Geophys. Res. Atmos.* 116:D12. doi: 10.1029/2010JD015139

Notaro, M., Bennington, V., and Lofgren, B. (2015a). Dynamical downscaling?based projections of great lakes water levels. *J. Clim.* 28, 9721–9745. doi: 10.1175/JCLI-D-14-00847.1

Notaro, M., Bennington, V., and Vavrus, S. (2015b). Dynamically downscaled projections of lake-effect snow in the great lakes basin. *J. Clim.* 28, 1661–1684. doi: 10.1175/JCLI-D-14-00467.1

Notaro, M., Holman, K., Zarrin, A., Fluck, E., Vavrus, S., and Bennington, V. (2013). Influence of the laurentian great lakes on regional climate. *J. Clim.* 26, 789–804. doi: 10.1175/JCLI-D-12-00140.1

Notaro, M., Zhong, Y., Xue, P., Peters-Lidard, C., Cruz, C., Kemp, E., et al. (2021). Cold season performance of the nu-wrf regional climate model in the great lakes region. *J. Hydrometeorol.* 22, 2423–2454. doi: 10.1175/JHM-D-21-0025.1

O'Reilly, C. M., Sharma, S., Gray, D. K., Hampton, S. E., Read, J. S., Rowley, R. J., et al. (2015). Rapid and highly variable warming of lake surface waters around the globe. *Geophys. Res. Lett.* 42, 10773–10781. doi: 10.1002/2015GL066235

Paynter, D., Frölicher, T. L., Horowitz, L. W., and Silvers, L. G. (2018). Equilibrium climate sensitivity obtained from multimillennial runs of two gfdl climate models. *J. Geophys. Res. Atmos.* 123, 1921–1941. doi: 10.1002/2017JD027885

Peings, Y., Cattiaux, J., Vavrus, S., and Magnusdottir, G. (2017). Late twenty-first-century changes in the midlatitude atmospheric circulation in the cesm large ensemble. *J. Clim.* 30, 5943–5960. doi: 10.1175/JCLI-D-16-0340.1

Peltier, W. R., d'Orgeville, M., Erler, A. R., and Xie, F. (2018). Uncertainty in future summer precipitation in the laurentian great lakes basin: dynamical downscaling and the influence of continental-scale processes on regional climate change. *J. Clim.* 31, 2651–2673. doi: 10.1175/JCLI-D-17-0416.1

Perkins, S. E., and Alexander, L. V. (2013). On the measurement of heat waves. *J. Clim.* 26, 4500–4517. doi: 10.1175/JCLI-D-12-00383.1

Peterson, T. C., Zhang, X., Brunet-India, M., and Vázquez-Aguirre, J. L. (2008). Changes in north american extremes derived from daily weather data. *J. Geophys. Res. Atmos.* 113:D7. doi: 10.1029/2007JD009453

Philip, S. Y., Kew, S. F., van Oldenborgh, G. J., Yang, W., Vecchi, G. A., Anslow, F. S., et al. (2021). *Rapid attribution analysis of the extraordinary heatwave on the pacific coast of the us and canada june 2021*. Technical report.

Robinson, P. J. (2001). On the definition of a heat wave. *J. Appl. Meteorol.* 40, 762–775. doi: 10.1175/1520-0450(2001)040<0762:OTDOAH>2.0.CO;2

Saha, S., Moorthi, S., Pan, H.-L., Wu, X., Wang, J., Nadiga, S., et al. (2010). The ncep climate forecast system reanalysis. *Bull. Am. Meteorol. Soc.* 91, 1015–1058. doi: 10.1175/2010BAMS3001.1

Scott, R. W., and Huff, F. A. (1996). Impacts of the great lakes on regional climate conditions. *J. Great Lakes Res.* 22, 845–863. doi: 10.1016/S0380-1330(96)71006-7

Sheffield, J., Barrett, A. P., Colle, B., Fernando, D. N., Fu, R., Geil, K. L., et al. (2013a). North american climate in cmip5 experiments. part i: evaluation of

historical simulations of continental and regional climatology*. *J. Clim*. 26, 9209–9245. doi: 10.1175/JCLI-D-12-00592.1

Sheffield, J., Camargo, S. J., Fu, R., Hu, Q., Jiang, X., Johnson, N., et al. (2013b). North american climate in cmip5 experiments. part ii: evaluation of historical simulations of intraseasonal to decadal variability. *J. Clim*. 26, 9247–9290. doi: 10.1175/JCLI-D-12-00593.1

Sillmann, J., Kharin, V. V., Zhang, X., Zwiers, F. W., and Bronaugh, D. (2013a). Climate extremes indices in the cmip5 multimodel ensemble: Part 1. model evaluation in the present climate. *J. Geophys. Res. Atmos*. 118, 1716–1733. doi: 10.1002/jgrd.50203

Sillmann, J., Kharin, V. V., Zwiers, F. W., Zhang, X., and Bronaugh, D. (2013b). Climate extremes indices in the cmip5 multimodel ensemble: Part 2. future climate projections. *J. Geophys. Res. Atmos*. 118, 2473–2493. doi: 10.1002/jgrd.50188

Skamarock, W. C., and Klemp, J. B. (2008). A time-split nonhydrostatic atmospheric model for weather research and forecasting applications. *J. Comput. Phys*. 227, 3465–3485. doi: 10.1016/j.jcp.2007.01.037

Song, Y., and Yu, Y. (2015). Impacts of external forcing on the decadal climate variability in cmip5 simulations. *J. Clim*. 28, 5389–5405. doi: 10.1175/JCLI-D-14-00492.1

Taylor, K. E., Stouffer, R. J., and Meehl, G. A. (2012). An overview of cmip5 and the experiment design. *Bull. Am. Meteorol. Soc*. 93, 485–498. doi: 10.1175/BAMS-D-11-00094.1

Thompson, G., Tewari, M., Ikeda, K., Tessendorf, S., Weeks, C., Otkin, J., et al. (2016). Explicitly-coupled cloud physics and radiation parameterizations and subsequent evaluation in wrf high-resolution convective forecasts. *Atmospheric Research*, 168, 92–104. doi: 10.1016/j.atmosres.2015.09.005

Vautard, R., van Aalst, M., Boucher, O., Drouin, A., Haustein, K., Kreienkamp, F., et al. (2020). Human contribution to the record-breaking june and july 2019 heatwaves in western europe. *Environ. Res. Lett*. 15:094077. doi: 10.1088/1748-9326/aba3d4

Watanabe, M., Suzuki, T., O'ishi, R., Komuro, Y., Watanabe, S., Emori, S., et al. (2010). Improved climate simulation by miroc5: mean states, variability, and climate sensitivity. *J. Clim*. 23, 6312–6335. doi: 10.1175/2010JCLI3679.1

Woolway, R. I., Kraemer, B. M., Lenters, J. D., Merchant, C. J., O'Reilly, C. M., and Sharma, S. (2020). Global lake responses to climate change. *Nat. Rev. Earth Environ*. 1, 388–403. doi: 10.1038/s43017-020-0067-5

Xue, P., Pal, J. S., Ye, X., Lenters, J. D., Huang, C., and Chu, P. Y. (2017). Improving the simulation of large lakes in regional climate modeling: two-way lake?atmosphere coupling with a 3d hydrodynamic model of the great lakes. *J. Clim*. 30, 1605–1627. doi: 10.1175/JCLI-D-16-0225.1

Zagar, N., Honzak, L., Zabkar, R., Skok, G., Rakovec, J., and Ceglar, A. (2013). Uncertainties in a regional climate model in the midlatitudes due to the nesting technique and the domain size. *J. Geophys. Res. Atmos*. 118, 6189–6199. doi: 10.1002/jgrd.50525

Zobel, Z., Wang, J., Wuebbles, D. J., and Kotamarthi, V. R. (2018a). Analyses for high-resolution projections through the end of the 21st century for precipitation extremes over the united states. *Earths Future* 6, 1471–1490. doi: 10.1029/2018EF000956

Zobel, Z., Wang, J., Wuebbles, D. J., and Kotamarthi, V. R. (2018b). Evaluations of high-resolution dynamically downscaled ensembles over the contiguous united states. *Clim. Dyn*. 50, 863–884. doi: 10.1007/s00382-017-3 0645-6

Conflict of Interest: AE is employed by Aquanty Inc.

The remaining authors declare that the research was conducted in the absence of any commercial or financial relationships that could be construed as a potential conflict of interest.

Publisher's Note: All claims expressed in this article are solely those of the authors and do not necessarily represent those of their affiliated organizations, or those of the publisher, the editors and the reviewers. Any product that may be evaluated in this article, or claim that may be made by its manufacturer, is not guaranteed or endorsed by the publisher.

A1. HEAT INDEX EQUATION

Heat Index (HI) equation we use following https://www.wpc.ncep.noaa.gov/html/heatindex_equation.shtml is given as:

$$\begin{aligned} HI = &-42.379 + 2.04901523 * T + 10.14333127 * RH \\ &- .22475541 * T * RH - .00683783 * T * T \\ &- .05481717 * RH * RH \\ &+ .00122874 * T * T * RH + .00085282 * T * RH * RH \\ &- .00000199 * T * T * RH * RH \end{aligned}$$

where T is temperature in degrees Fahrenheit and RH is relative humidity in percent. HI is the heat index expressed as an apparent temperature in degrees Fahrenheit. If the RH is less than 13% and the temperature is between 80°F and 112°F, then the following adjustment is subtracted from HI:

$$ADJUSTMENT = [(13 - RH)/4] * \sqrt{[17 - |T - 95|]/17}$$

On the other hand, if the RH is greater than 85% and the temperature is between 80°F and 87°F, then the following adjustment is added to HI:

$$ADJUSTMENT = [(RH - 85)/10] * [(87 - T)/5]$$

An alternative equation is used when heat index value is expected to fall below about 80°F where the regression analysis that leads to the main HI equation becomes inappropriate. The alternative simpler equation is the following:

$$HI = 0.5 * \{T + 61.0 + [(T - 68.0) * 1.2] + (RH * 0.094)\}$$

However, this alternative equation is less relevant for this study since HI threshold for extreme heat events is 32° C=89.6°F that is strictly above the 80°F limit.

frontiers in Water

ORIGINAL RESEARCH
published: 24 December 2021
doi: 10.3389/frwa.2021.779811

Validation and Projections of Climate Characteristics in the Saginaw Bay Watershed, MI, for Hydrologic Modeling Applications

Daria B. Kluver[1,2]* *and Wendy Robertson*[1,2]

[1] Department of Earth and Atmospheric Sciences, Central Michigan University, Mount Pleasant, MI, United States, [2] Institute for Great Lakes Research, Central Michigan University, Mount Pleasant, MI, United States

Fundamental differences in the nature of climate and hydrologic models make coupling of future climate projections to models of watershed hydrology challenging. This study uses the NCAR Weather Research and Forecast model (WRF) to dynamically downscale climate simulations over the Saginaw Bay Watershed, MI and prepare the results for input into semi-distributed hydrologic models. One realization of the bias-corrected NCAR CESM1 model's RCP 8.5 climate scenario is dynamically downscaled at a spatial resolution of 3 km by 3 km for the end of the twenty-first century and validated based on a downscaled run for the end of the twentieth century in comparison to ASOS and NWS COOP stations. Bias-correction is conducted using Quantile Mapping to correct daily maximum and minimum temperature, precipitation, and relative humidity for use in future hydrologic model experiments. In the Saginaw Bay Watershed the end of the twenty-first century is projected to see maximum and minimum average daily temperatures warming by 5.7 and 6.3°C respectively. Precipitation characteristics over the watershed show an increase in mean annual precipitation (average of +14.3 mm over the watershed), mainly due to increases in precipitation intensity (average of +0.3 mm per precipitation day) despite a decrease in frequency of −10.7 days per year. The projected changes have substantial implications for watershed processes including flood prediction, erosion, mobilization of non-point source and legacy contaminants, and evapotranspirative demand, among others. We present these results in the context of usefulness of the downscaled and bias corrected data for semi-distributed hydrologic modeling.

Keywords: dynamical downscaling from a global climate model, bias correction, precipitation, temperature, Saginaw Bay, hydrologic inputs

OPEN ACCESS

Edited by:
Julie A. Winkler, Michigan State University, United States

Reviewed by:
Sean Woznicki, Grand Valley State University, United States
Jared Bowden, North Carolina State University, United States

***Correspondence:**
Daria B. Kluver
kluve1db@cmich.edu.edu

Specialty section:
This article was submitted to Water and Climate, a section of the journal Frontiers in Water

Received: *19 September 2021*
Accepted: *07 December 2021*
Published: *24 December 2021*

Citation:
Kluver DB and Robertson W (2021) Validation and Projections of Climate Characteristics in the Saginaw Bay Watershed, MI, for Hydrologic Modeling Applications. Front. Water 3:779811. doi: 10.3389/frwa.2021.779811

INTRODUCTION

Climate change has the potential to substantially alter the abundance, availability, distribution, fluxes, and quality of water in the Great Lakes region (Hayhoe et al., 2010; D'Orgeville et al., 2014; Byun and Hamlet, 2018; Wang et al., 2018; Byun et al., 2019; Mahdiyan et al., 2021). Increases in extreme weather events, changes in the timing, type, and spatial distribution of precipitation, and alterations to evapotranspirative fluxes all have implications for streamflow and water quality. Effects of climate change on hydrologic extremes such as drought and flooding have the potential

to compound existing stressors in Great Lakes watersheds already impacted by decades of land use change, legacy and non-point source pollution, and loss of wetland habitat. Predictions from global scale climate modeling establish that rising temperatures will result in changes to the atmospheric characteristics in the Great Lakes region that will have direct effects on watershed health, such as increases in extreme precipitation and droughts (which impacts erosion, nutrient cycling, and flux of pollutants), increased temperatures (impacts to phenology, ecology, and agriculture), and changes to soil moisture (impacting nutrient cycling, hydrologic fluxes, phenology, and water quality; Angel et al., 2018). However, there remains significant uncertainty in how the projected climate changes modeled at the global scale translate to hydrologic impacts at the regional and watershed scales. One reason that uncertainty persists is the fundamentally different nature of global climate models (GCMs) and hydrologic models. While GCMs are applied at global scales for long periods of time, many of the processes that scientists and policy makers seek to model for watersheds, such as daily streamflows for ecological minimums and flood event timing and magnitude, are much smaller in extent and discrete in time. The contrast between spatial and temporal resolutions and modeling approaches poses challenges for model coupling. However, the gap between these two modeling paradigms is worth bridging, particularly for understanding the complex nature of changes in Great Lakes watersheds in response to future climate change. One notable effort toward reconciling the challenge of coupling atmospheric and terrestrial hydrologic models is WRF-Hydro, which provides high resolution (both spatially and temporally) streamflow predictions on short (sub-hourly) to seasonal time scales (Lin et al., 2018; Somos-Valenzuela and Palmer, 2018; Yin et al., 2020). A significant drawback to the WRF-Hydro modeling framework is that it is extremely computationally intensive to get streamflow in a fully or semi-distributed representation of a catchment which becomes prohibitive over the climate-scale simulations required to realize future hydrologic distributions.

Because GCMs use physical principles of the atmosphere to drive long-term simulations of climate variability and change (rather than observations, such as in Numerical Weather Prediction), they are computationally intensive, and must therefore be of a coarse spatial resolution, generally greater than 1° latitude by 1° longitude. Their purpose is to capture the physical processes that occur over the entire globe at timescales greater than weather forecasts and to indicate broad regional changes to climate parameters. Inputs and output are in the form of gridded fields at specific points in time. By contrast, hydrologic models are frequently applied to explore watershed and stream response to changes at the basin scale, which depending on the size of the catchment can range from as small as the contributing area to a local stream to as large as continental scales. Hydrologic models can be conceptual (based on physical concepts), empirical, or physically based and can range both in complexity of modeled processes and spatial distribution. To explore how streamflow responds to variations in watershed characteristics and perturbations such as land use and climate change, physically based distributed or semi-distributed hydrologic models (SDHMs) are necessary (Jajarmizdeh et al., 2012; Khakbaz et al., 2012). A benefit SDHMs can provide is prediction of streamflow in ungauged catchments, a capability that is critical where monitoring networks are sparse. SDHMs require input of spatially explicit datasets including watershed properties such as soil, topography, and land use, and climatological inputs such as precipitation, temperature, solar radiation, wind speed, and relative humidity. The type and detail of inputs varies between models; fully distributed models may use gridded data for all inputs, whereas semi-distributed models can incorporate both gridded and point data (which is then interpolated to provide the necessary input). For most SDHM applications, climatological inputs come from existing observation stations (e.g., NWS COOP network in the U.S.) or gridded products (e.g., CFSR; National Center for Atmospheric Research Staff, 2017). However, these inputs are not available for future conditions; this is where GCM or Regional Climate Model (RCM) output links to SDHMs (e.g., Das and Umamahesh, 2018; Singh and Saravanan, 2020; Martínez-Salvador et al., 2021); in these cases, resolving the difference in spatial resolution remains a challenge. To model hydrologic response to future climate conditions, climatological inputs based on those future conditions are needed. It is imperative that the climatological inputs are as representative of likely future atmospheric conditions (given a particular emissions scenario) as possible, as calibration of SDHMs relies on altering empirical fit parameters linked to physical characteristics and properties of the watershed rather than correction of climatological inputs (Arnold et al., 2012; Zhai et al., 2018; Gou et al., 2020). To take the low-resolution gridded outputs produced by GCMs and prepare them in such a way as to capture accurate sub-grid scale variability for hydrologic modeling is no simple task. It involves some form of downscaling to a resolution that is useful for quantifying watershed-scale variability, but also validation and bias correction from *in-situ* "ground truth" stations at such a resolution, which requires the transition from gridded spatial data to spatially explicit (point) data.

In order to address the challenge of coupling GCMs to hydrologic models, researchers have turned to two main approaches: statistical (empirical) and dynamic downscaling (Hewitson and Crane, 1996). Statistical downscaling involves development of empirical relationships between outputs from a course resolution GCM (a predictor) and a historic data set (a predictand). The type of statistical model used to define this relationship can vary, but is limited in that it does not represent the atmospheric processes that link the two scales together (large scale to local scale; Maraun and Widmann, 2018). Dynamical downscaling on the other hand is process-driven and is conducted *via* nested climate/weather models of progressively smaller domain and finer resolution [these can then be called Regional Climate Models (RCMs)]. While statistical downscaling is computationally much more efficient, dynamical downscaling has the ability to adapt to complex changes in future climate—assuming the relevant processes are represented in the model.

Dynamically downscaled climate model outputs have been used as inputs into several distributed and semi-distributed hydrologic models to address changes in physical characteristics and properties that impact streamflow (e.g., rainfall-runoff

ratio, snowmelt timing, and evapotranspirative demand) as well as extreme events (e.g., drought, flood risk, and extreme precipitation; Salathe et al., 2014; Mendoza et al., 2015; Vu et al., 2015 and others). Recent studies that have used downscaled climate model output in such a manner have taken a number of approaches. Most commonly the variables retained from the model output are limited to monthly mean temperature and precipitation [with the exception of Erler et al. (2019), which uitilized mean monthly precipitation, snow depth and PET in the HydroGeoSphere model]. Raghavan et al. (2014), Vu et al. (2015), and Tiwari et al. (2018) passed climate output fields to the SWAT hydrologic model un-corrected, and calibrated SWAT to make up for any discrepancies between modeled and observed stream gauge data. Shrestha et al. (2017) took another approach and found that applying simple corrections to only modeled temperature and precipitation improved hydrologic model performance (they also used SWAT).

The main limitations to the previous body of work revolve around incorporating the processes that are evolving in the atmosphere in future states of the climate with the impacts of those processes on hydrologic systems. Without a GCM that is based on coupled atmospheric, land, and ocean components, future climate estimates are likely to miss global- and hemispheric-scale drivers of climate, such as the El Niño Southern Oscillation, Arctic Oscillation, sea ice fluctuations, and others. However, the GCMs that are capable of simulating these global-scale processes are substantially mismatched in spatial resolution with the types of systems usually modeled in SDHMs. Such a mismatch will result in instances where GCMs and coarse-resolution RCMs are not capturing the sub-watershed spatial variability even if the atmospheric processes are accurately represented at the larger grid scale. This can leave out atmospheric drivers of hydrologic processes of interest, such as erosion, non-point source pollution, land use stressors, and point source pollutant mobilization.

This study presents a unique approach to addressing some of the challenges posed by the existing methodologies for preparation of future climate projections for coupling with hydrologic SDHMs. One realization of a GCM's projections of future climate are dynamically downscaled with a high-fidelity weather model, to retain the physical processes occurring within the atmosphere at subsequently smaller spatial and temporal resolutions. This is done at a very high resolution, with the inner-most domain having grid cells of 3 km by 3 km. After downscaling, bias correction is applied to atmospheric variables at locations within the watershed to leverage the *in-situ* observations available to provide improved atmospheric forcing for the hydrologic model, thereby reserving hydrologic model calibration for the streamflow parameters. Lastly, the steps for data preparation are applied to several variables (maximum temperature, minimum temperature, daily precipitation, and relative humidity) due to their potential to alter components on hydrologic systems such as flooding, ET demand, soil moisture storage, runoff, infiltration, nutrient cycling, and water levels.

In this paper, we focus on an example from the Saginaw Bay watershed in the lower peninsula of Michigan. We use the NCAR Weather Research and Forecast model (WRF) to dynamically downscale CMIP5 output to a nested domain of 3 km grids centered over the Great Lakes region, running this weather model as an RCM. We ran two 15-year periods; one at the end of the twentieth century and one at the end of the twenty-first century using RCP 8.5 to quantify climate change impacts on the region and explore the variability of such changes over a high spatial resolution within the watershed, which would not be captured in statistically downscaled climate output. Then, we applied quantile mapping to the precipitation, daily maximum and minimum temperatures, and relative humidity to bias correct the variables prior to using them as input for hydrologic modeling.

DATA AND METHODS

Study Area

The Saginaw Bay Watershed (SBW) is located in the eastern part of Michigan's lower Peninsula (**Figure 1**). It is the largest drainage basin in the state of Michigan, encompassing approximately 14,000 km^2, 22 counties, and a wide range of land uses from highly urbanized to agricultural and forested. Its outlet, Saginaw Bay, provides habitat for multiple federal and state recognized threatened and endangered species including resident and migratory birds, reptiles, insects, aquatic invertebrates, and plant species (U.S. Fish Wildlife Service., 2018; Michigan Natural Feathers Inventory) and is also a U.S. EPA designated Area of Concern with ongoing Beneficial Use Impairments (BUIs) related to nonpoint source pollution and legacy contamination in the sediments (Selzer et al., 2014). Eutrophication, nuisance algal blooms, beach closures, and ecosystem degradation are current challenges that also may be exacerbated by climate change impacts within the watershed. Many of the tributaries in the SBW are prone to rapid hydrologic response (Michigan Department of Natural Resources Surface Water Quality Division, 1988; Selzer et al., 2014) resulting from land use changes and low permeability soils; the "flashy" response may be compounded by climatic shifts, and, also have the potential to contribute to sediment and non-point source pollutant loading, negatively impacting water quality conditions and ecosystem services in Saginaw Bay.

The climate of this region is largely influenced by its position in the mid-latitude Westerlies, with sizable influence from the surrounding Great Lakes. The large bodies of water that surround the Michigan Lower Peninsula on 3 sides act to moderate the temperatures in this region, but also act as a moisture source for precipitation. Despite the maritime effect from the Great Lakes, in the last century Michigan has still experienced increasing annual temperatures of around 0.8°C and future warming is projected to be as much as 5.4°C (for RCP 8.5) by 2099 (Wuebbles et al., 2019). Precipitation is achieved in the SBW through transient synoptic weather patterns (such as fronts, or mid-latitude cyclones) or the moistening of cold air masses as they pass over the Great Lakes (Andresen, 2012). Over the twentieth century annual precipitation in the SBW region has increased by as much as 15% (Wuebbles et al., 2019), mostly due to the increases in extreme precipitation event sizes (Easterling et al., 2017). Future projections continue this trend of more annual precipitation, primarily due to extreme events (Wuebbles et al., 2019). When examining the CMIP5

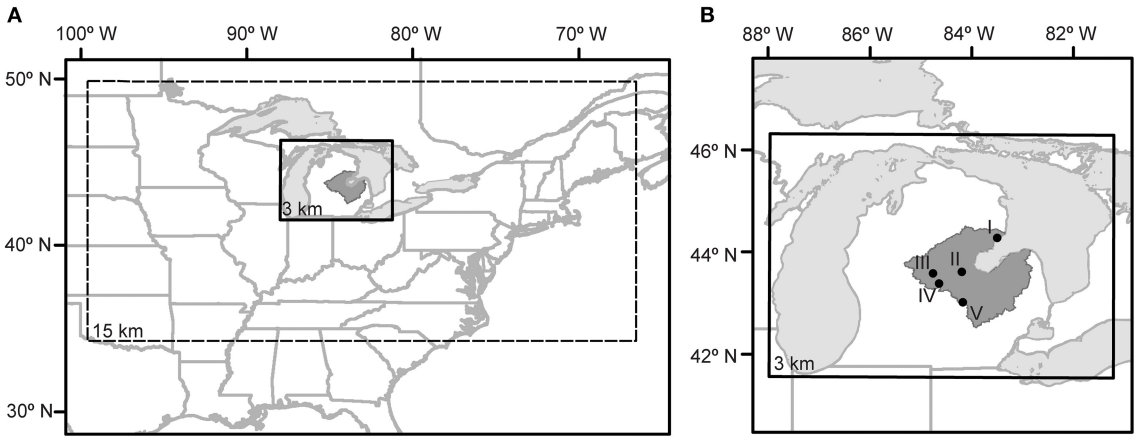

FIGURE 1 | Study area. **(A)** WRF downscaled domains, outer domain (dashed line) and inner domain (solid line). **(B)** Location of *in-situ* weather stations in relation to the Saginaw Bay Watershed: I. East Tawas/Oscoda, MI; II. Midland, MI; III. Mount Pleasant, MI; IV. Alma/Gratiot, MI; and V. Owosso, MI.

suite of GCMs' projections for the Great Lakes region, Notaro et al. (2015) found that the maximum precipitation increases by the end of the twenty-first century (RCP 8.5) occurred in March–April–May and were +0.61 mm day^{-1} compared to late twentieth century values. Increases in temperature were also documented, with a maximum warming of +7.0°C occurring in December–January–February.

Downscaling

The NCAR Weather Research and Forecast (WRF) model (version 3.7) with the Advanced Research WRF (ARW) core dynamical solver (Skamarock et al., 2008) is used to model the atmospheric parameters over the SBW. The WRF model is configured with the following physics schemes: the unified Noah Land Surface Model for surface physics (Tewari et al., 2004); the NCEP GFS boundary layer physics (Hong and Pan, 1996); the Kain-Fritsch convection scheme (applied to both domains; Kain, 2004); the Dudhia shortwave radiation scheme (Dudhia, 1989); the Rapid Radiation Transfer Model for longwave radiation (Mlawer et al., 1997); and the WRF Single-Moment 5-Class scheme for microphysics (Hong et al., 2004). Nudging is not applied in an effort to preserve precipitation variability within the inner domain (Alexandru et al., 2009), although it has been shown by multiple studies to improve WRF downscaling simulations of 1–3 year periods (Spero et al., 2018). The Climate simulations from the NCAR CESM Global Bias-Corrected CMIP5 Output to Support WRF/MPAS project (Monaghan et al., 2014) are used as initial boundary conditions for the WRF model. These data are bias-corrected using the ECMWF ERA-Interim from 1981 to 2005 (Bruyère et al., 2014, 2015) and are available for the IPCC AR5 RCP 4.5, 6.0, and 8.5 scenarios from 2006 to 2100. A simulation from 1950 to 2005 is also used to calibrate the GCM model and is available as a twentieth century run.[1] The bias-corrected CESM data set is useful, because systematic biases in the Great Lakes region can vary by season (too wet in winter and spring and too dry in fall) and be large (as much as −13% fall precipitation bias from CESM1; Briley et al., 2020). In all WRF model runs the 1° CESM1 6-hourly output files are used as the boundary conditions for an outer domain of 15 km horizontal grids and then are dynamically downscaled to a two-way nested inner domain of 3 km horizontal grids (shown in **Figure 1**). The WRF model was developed as a high-resolution weather forecasting tool (shorter time scales but higher spatial resolution) and has since started to be used as an RCM, sometimes simulating time periods as long as those used in this study. The advantage of using WRF in this application is its ability to simulate at a spatial resolution that is sufficient to represent atmospheric processes, such as precipitation, that are usually considered "sub-grid scale" for long-term global climate models (Wang and Kotamarthi, 2015). The trade-off to using this model is the cost of computation and data storage to produce such fine spatial-scale but long runs.

Due to the computationally demanding nature of numerical weather models, only one realization of the WRF model is run for two different 15-year periods. The first is a twentieth Century simulation from 1991 to 2005 for use in model validation, which we will refer to as the 'historical' run. The second 15-year WRF run is using the RCP 8.5 future scenario, simulated from 2085 to 2099, which assumes an increase in radiative forcing of +8.5 W/m2 over pre-industrial values (Van Vuuren et al., 2011; Stocker et al., 2013; Bruyère et al., 2014). We will refer to this run as the "future" run. Notaro et al. (2015) assessed the uncertainty in CMIP5 models over the Great Lakes region for this time period. They found that the deviation among the models in the end-of-twenty-first century RCP 8.5 scenario runs resulted in an average temperature and precipitation uncertainty of 1.29°C and 0.20 mm day^{-1}. For both WRF model runs the daily variables retained for future input into SDHMs are: maximum temperature (°C); minimum temperature (°C); total liquid precipitation (mm); average relative humidity (%); and average daily wind speed (m/s) computed for each grid cell in the SBW domain. Wind speeds are reduced to 2-m height

[1]https://rda.ucar.edu/datasets/ds316.1.

and adjusted to account for varying ground cover types using the Prandtl-von Karman Universal Velocity-Distribution for Turbulent Flows (Dingman, 2008). The friction velocity for the vegetation types are based on previous field experiments (Izumi and Caughey, 1976; Churchill and Csanady, 1983; Santoso and Stull, 2001; Jiao-jun et al., 2004). For the basin-wide figures and statistics, WRF output grids are clipped to only those within the Saginaw Bay Watershed, with a 1,000 m buffer for the centroids falling within the boundary of the watershed ($n = 2582$).

Validation and bias correction of the downscaled atmospheric variables is essential at the points for which data will be passed to the SDHM, because the coarse resolution GCMs lack some sub-grid scale features. One relevant shortcoming of the CMIP5 models (and this CESM1 contribution to CMIP5 in particular) is the lack of lake surface temperatures included in the output files for use in regional downscaling (Spero et al., 2016). Without lake water temperatures from the input GCM, the WRF model defaults to extrapolating water temperature from the nearest point designated as water. In this situation, different portions of the Laurentian Great Lakes are interpolated from grid cells over the Atlantic Ocean (southern lake areas), or from James and Hudson Bays (northern lake areas; Mallard et al., 2015; Spero et al., 2016). Mallard et al. (2015) found discontinuities in lake surface temperature of as much as 17 K in Lakes Michigan and Huron, and 3 K in Lake Superior during one simulated test date. Spero et al. (2016) examined the same CESM1 model used in the current study and found lake temperatures that were colder in the summer and warmer in the winter, compared to a WRF downscaling that included a lake model. The largest impacts were in the winter, where thermally induced low pressure and warmer air temperatures downwind of the lakes impacted the frequency of freeze days and number of days with precipitation (Spero et al., 2016). Since the default WRF treatment of "water" grids is used in the current study, careful validation and bias correction are of the utmost importance.

Bias Correction

WRF model validation is conducted by comparing the WRF downscaled model output against historical climate station data from the *in-situ* stations from the National Weather Service Cooperative Observer Program (NCEI., 2017), and wind data from the NOAA's Automated Surface Observation Stations (ASOS) locations (NCEI, 2019). The locations of the stations that have both COOP and ASOS data and lie inside the Saginaw Bay Watershed (SBW) are given in **Figure 1**. Errors are computed only at model grid cells that are co-located with historic *in-situ* stations, in order to avoid any potential bias that may be introduced by interpolation during error estimation or correction. However, it should be noted that since spatial autocorrelation decreases with distance, the representativeness of co-located *in-situ* stations and model grid cells can vary if station locations are offset by only a few tenths of a degree latitude or longitude. These historic *in-situ* locations are subsequently the only grid cells bias-corrected for ingest into a SDHM. The Kolmogorov-Smirnov test is conducted on each set of distribution comparisons to identify whether they could statistically be from the same distribution (Schuenemeyer and Drew, 2011).

After errors are identified in the historic run, by comparing the downscaled WRF output to the observational stations, bias correction is performed. We apply bias correction on temperature, precipitation, and humidity variables. Relative humidity is not often included or bias corrected for in GCM-hydrologic model coupling, however, Masaki et al. (2015) found that bias correction of humidity (even simplistic methods) reduce uncertainty in hydrologic models. Of the recent studies that have conducted bias correction on WRF data for use in hydrologic models, the majority used a gridded dataset or gridded historical observations as their ground truth. The interpolation of the historical station data to produce such a dataset can introduce additional biases, particularly for precipitation, which has increased interpolation error with increased station distances (Bussieres and Hogg, 1989). For this paper, the WRF grid cells that correspond to historical weather station locations are the ones at which bias correction is applied as these would be a standard input for climate variables into a SDHM.

Because the entire range of the statistical distributions of the variables that are input into the hydrologic model has implications for hydrologic processes within the watershed and therefore streamflow, quantile mapping is used for bias correction. Compared to the more commonly used change factor (add or subtract model anomalies from observations), the quantile mapping method allows for the amount of correction applied to the model data to vary along the distribution. The quantile mapping method of bias correction (Boé et al., 2007; Gudmundsson et al., 2012; Gudmundsson, 2014) estimates the empirical cumulative distribution function (ecdf) of both the modeled and observed variables. The model data is then corrected (or transformed) at the specific quantiles (we used every 10th percentile), and intermediate values must be interpolated (in this study, the non-linear monotonic tricubic spline interpolation is used; Gudmundsson et al., 2012; Mosier et al., 2014, 2018; Sippel et al., 2016; Alidoost et al., 2021). This produces a bias correction that is tailored to the correction needs at different levels in the distribution, rather than one correction applied unilaterally. This is particularly useful for distributions that require different corrections for the tails of the distributions compared to the means of the distributions, as the tails represent flood and drought conditions that can have important devastating impacts on hydrologic systems.

RESULTS

WRF Simulations of the SBW: 1991–2005 and 2085–2099

Annual average watershed values produced from the 1991 to 2005 historical WRF run are shown in **Figure 2A** through **Figure 7A** and future WRF model run in **Figure 2B** through **Figure 7B**. In order to examine the spatial changes projected to occur, annual average values from the entire modeled watershed are compared

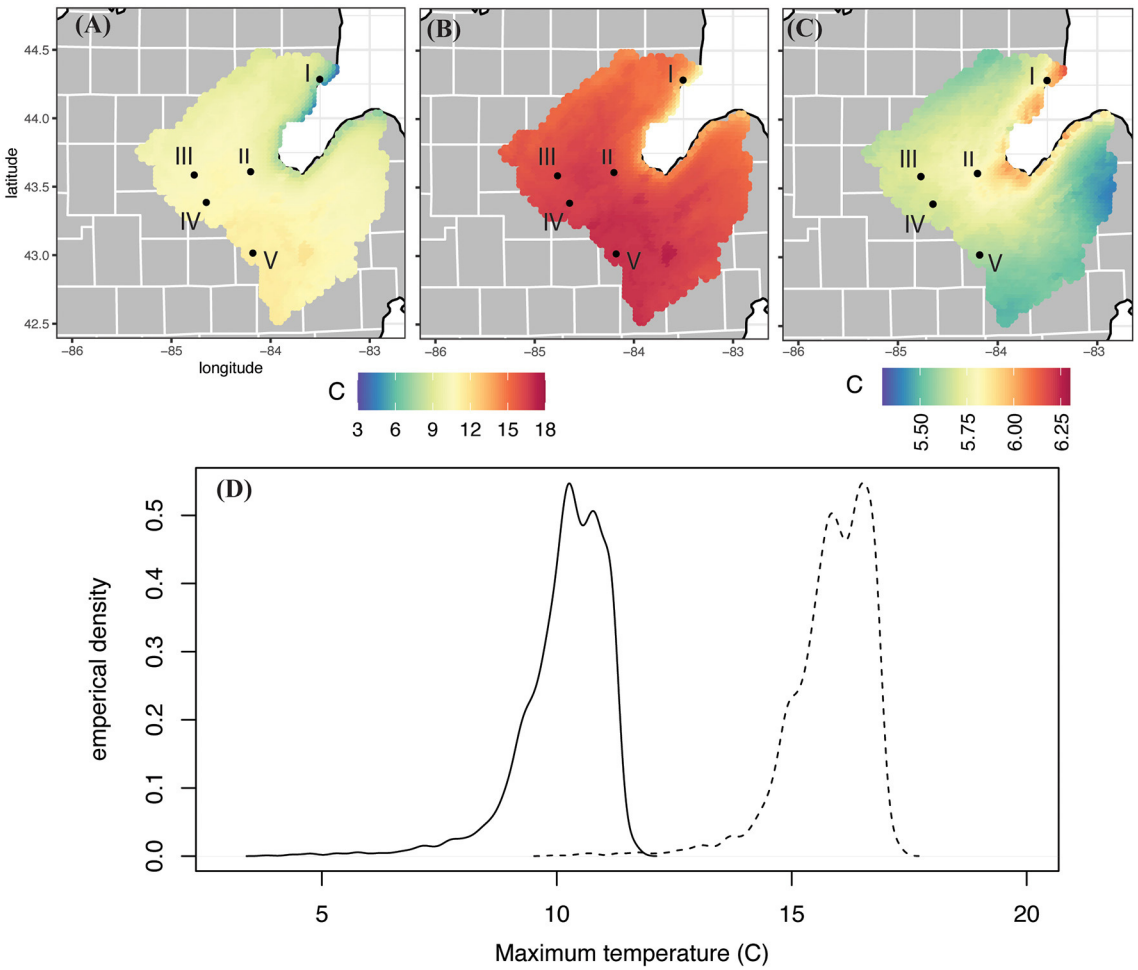

FIGURE 2 | Uncorrected WRF output of mean maximum daily temperature (°C) from **(A)** the 1991–2005 historical climate run; **(B)** the 2085–2099 future RCP 8.5 scenario; **(C)** the difference between the **(A)** and **(B)** future–past and **(D)** the empirical distribution from all of the grid cells in the watershed for mean maximum daily temperature for **(A)** (solid line) and **(B)** (dashed line).

for the twentieth century run to the end of the twenty-first century RCP 8.5 run and the change is displayed in **Figure 2C** through **Figure 7C**. Empirical distributions are generated from the grid cell values over the watershed to show the distribution of the data throughout the study area and how it changes between the two time periods (**Figure 2D** through **Figure 7D**).

For the historic WRF run the variables plotted show a spatially reasonable pattern, with cooler average maximum and minimum temperatures along the shores of the Saginaw Bay (3.8 and −5.3°C, respectively) and increased temperatures westward (11.7 and 1.5°C, respectively; **Figures 2A**, **3A**). Not only are the areas around the bay cooler, but they experience higher relative humidity (∼86% compared to 71.5% inland; **Figure 4A**). Precipitation characteristics around Saginaw Bay are also distinctly different than the inland part of the SBW. WRF grid cells near the bay experience precipitation more frequently (∼210 days/year compared to ∼176 days/year; **Figure 6A**), but at a lower intensity (3.69 mm/rain day compared to 5.14 mm/rain day; **Figure 7A**), resulting in lower total amounts of precipitation than inland (∼739 mm compared to 995.4 mm; **Figure 5A**).

In **Figure 2B**, future mean maximum temperatures across the SBW range from 17.3°C in the western portion of the watershed, to as low as 10.0°C along the Saginaw Bay. The mean value across the entire watershed is 15.8°C, with a standard deviation of 0.89 °C. Comparing this spatial distribution to the historic model run (**Figure 2A**), annual average maximum temperatures in the SBW shows a mean change of 5.7°C by the end of the twenty-first century for the RCP 8.5 scenario. The spatial difference map (**Figure 2C**) shows the warming is largest along the coast of the Saginaw Bay (highest warming in a single grid cell is 6.1°C) and lowest in "the Thumb" area of 5.4°C. The empirical distributions created from the grid cells in each watershed map show that the entire distribution of temperatures shifts to higher temperatures, putting the majority of grid cells at temperatures above even the warmest maximum temperatures in the historic time period (**Figure 2D**).

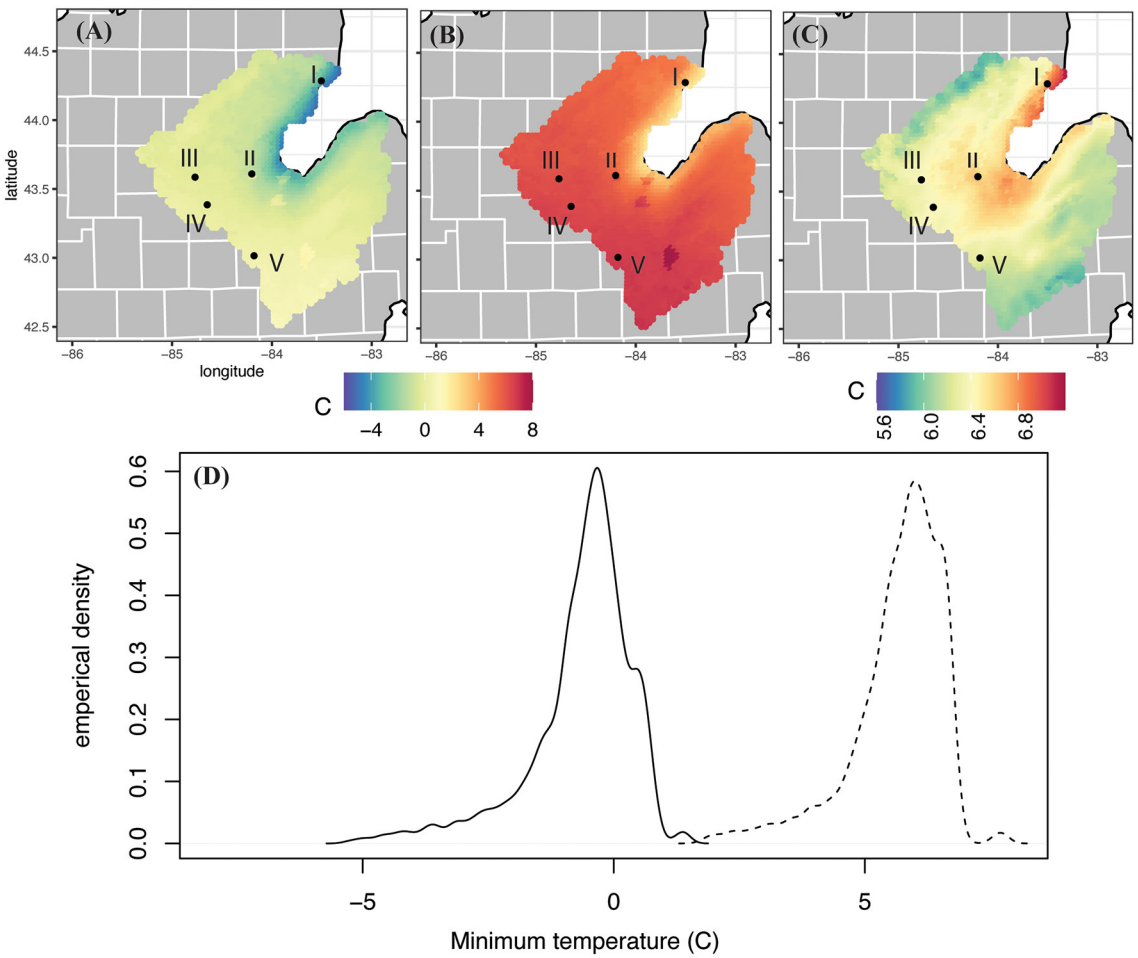

FIGURE 3 | Same as **Figure 2**, but for minimum daily temperature.

The change signal in minimum temperatures is similar to maximum temperatures (**Figure 3**). Future values of minimum temperature over the SBW range from a minimum value of 1.7°C to a maximum value of 7.8°C, with a watershed average 5.7°C. The average minimum temperature in the watershed is projected to increase by 6.3°C from the historic run. The map shows that these increases are the highest around the coast (7.1°C), and lowest in the southeast and northwest edged of the watershed (5.9°C). The empirical distribution shows that nearly all grid cells in this watershed experience minimum temperatures in the future time period above even the extreme minimum temperatures in the historic model run.

A slight reducing pattern is projected to occur in relative humidity across the SBW by the end of the century, as can be seen in **Figure 4B**. The maximum average relative humidity in the future WRF run is 83.9%, compared to 86.1% in the historic run, occurring along the Saginaw Bay. When compared to the historic run (**Figures 4A,C**), the drying signal appears the smallest (−1.9%) on the northern coast of the Saginaw Bay and is the largest (−3.1%) in the southwestern corner of the watershed, near Owosso, MI (station V). The empirical distribution shows a future shift of ∼2.7% drier in the future (watershed mean RH goes from 77.1 to 74.4%).

The northeastern side of the SBW is projected to receive more total annual precipitation by the end of the twenty-first century than it experienced in the historic model run (**Figure 5B**). When comparing the future projection map to the historic model run, the watershed's average increase of 14.3 mm (848.0 mm vs. the historic run's 833.7 mm) does not convey the spatial variability within the SBW. Particularly, drying occurs in the south and southwestern parts of the watershed, while moistening is isolated to the northeastern part of the SBW (**Figure 5C**). The maximum change over the twenty-first century at a single grid cell is an increase of 87.4 mm, and the largest drying is −63.0 mm. **Figure 5D** shows a flattening of the empirical distribution curve in the future model projections, with fewer grids having a precipitation value near the average, and more years with annual precipitation amounts occurring in the right tail of the curve. The reason for this can be more clearly seen by examining precipitation frequency and intensity.

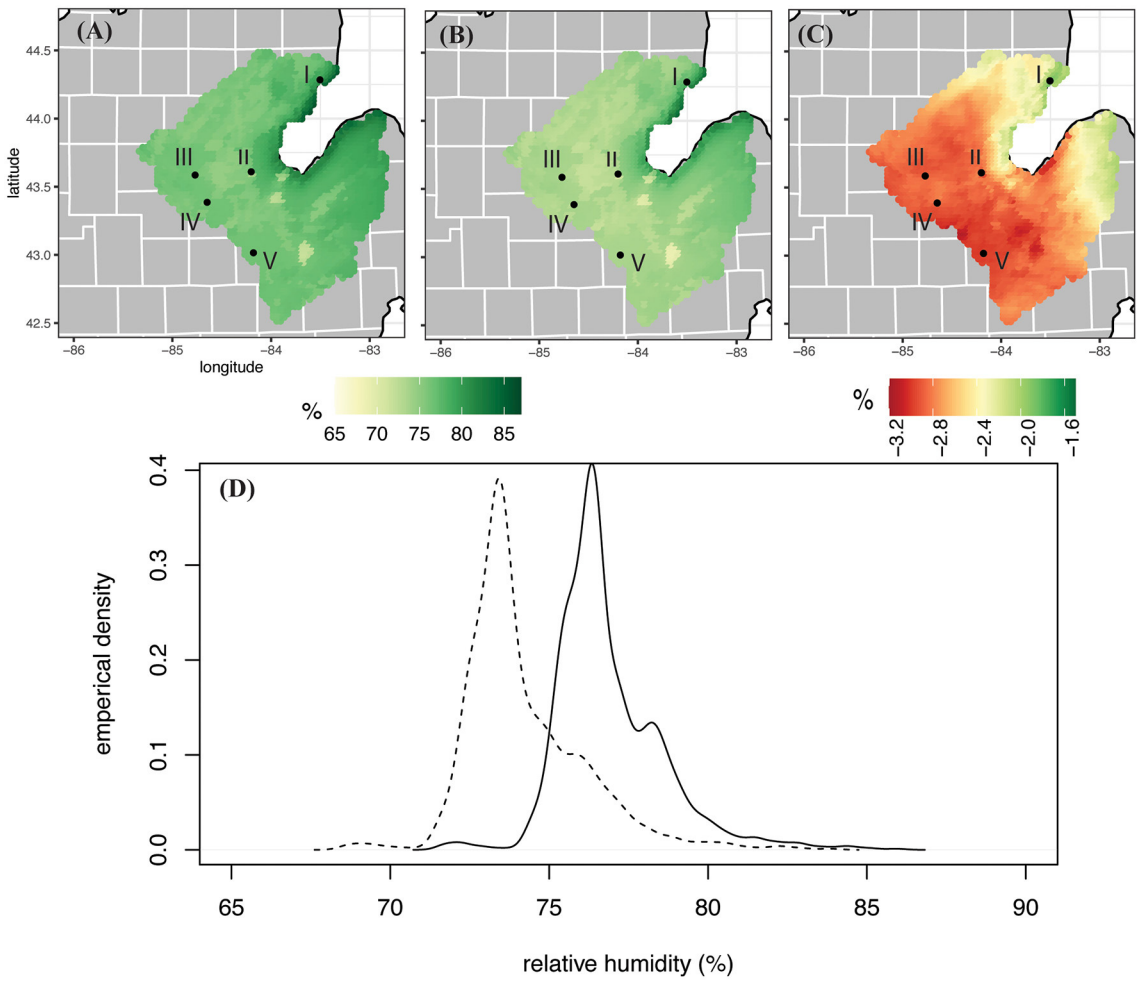

FIGURE 4 | Same as **Figure 2**, but for mean daily relative humidity.

Annual precipitation frequency (number of days with measurable precipitation per year) decreases in a future RCP 8.5 scenario at all grid cells in the Saginaw Bay Watershed (**Figure 6**) with a range of 4.7 to 24.4 fewer days per year. The average over the entire watershed is a decrease in precipitation frequency of 10.7 days per year. The empirical distributions show a similar shape to the two distributions, but the future distribution is shifted left (toward a lower frequency of days with precipitation) and the right tail of the distribution becomes shorter (fewer extremely high frequency years; **Figure 6D**).

Precipitation intensity is calculated as the mean annual precipitation value at a grid cell divided by the number of days in which precipitation occurs at that location. The average precipitation intensity over the SBW in the historic model run is 4.4 mm/precipitation day while the average intensity in the future model run is 4.8 mm/precipitation day. The model runs have a similar spatial pattern (**Figures 7A,B**), with the lowest intensities occurring around Saginaw Bay (3.7 mm/precipitation day in the historic model run and 4.2 mm per precipitation day in the future run) and increasing intensities in the northwestern and southeastern parts of the watershed (maximum of 5.1 mm/precipitation day in the historic run and 5.7 mm/precipitation day in the future run). When comparing the average precipitation intensity at each grid cell in the future model run to the historic model run, **Figure 7C** shows increases in intensity over the twenty-first century with the largest increases of 0.7 mm/precipitation day in the "thumb" region of the Lower Peninsula, the eastern portion of the watershed. This corresponds with the region that saw an increase in total annual precipitation in **Figure 6C**. The empirical distributions show that in the future time period the average intensity becomes larger and there is less variability within the watershed (as the size of the tails is reduced; **Figure 7D**). This indicates that by the end of the twenty-first century precipitation in the SBW will become more intense (larger amount per precipitation day) and there will be less variability in the range of intensities experienced.

The relative changes in the SBW variables indicate that on average this watershed will warm by 5.7°C in daily maximum temperatures and more (6.3°C) in daily minimum temperatures. Relative humidity shows a slight reducing trend

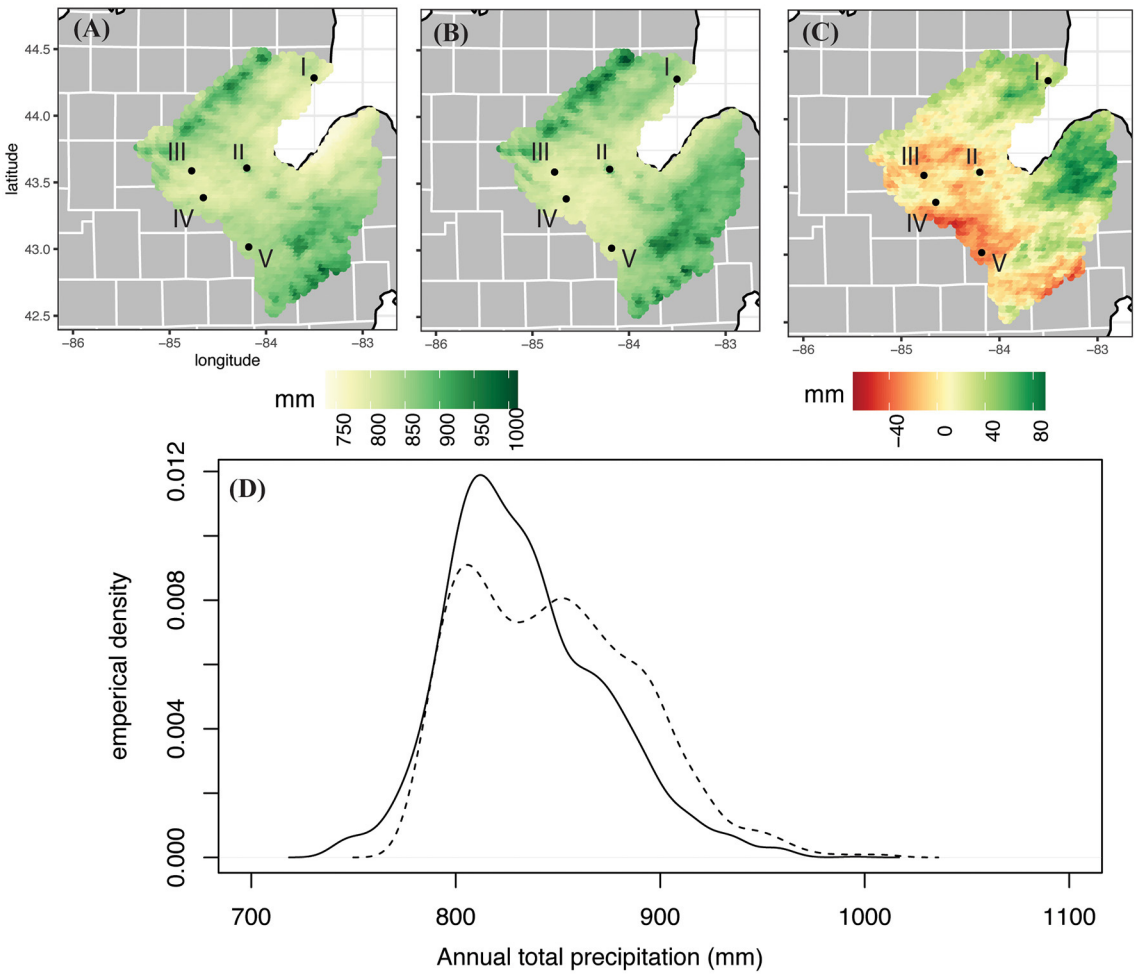

FIGURE 5 | Same as **Figure 2**, but for annual total precipitation amount.

when looking at annual averages. The projected change to total annual precipitation varies across the watershed, but the picture of the characteristics of SBW precipitation is consistent. Precipitation will occur less frequently across the watershed but will be more intense, as the amount that falls per precipitation day will increase. All of the SBW is not projected to have an increase in total annual precipitation because even though all locations are projected to experience increased precipitation intensity, decreases in precipitation frequency also occur across the watershed. In the west and southwestern parts of the watershed the increase in intensity is not enough to negate the decrease in frequency, and the annual total precipitation decreases. Grid cells near the Saginaw Bay coast are expected to experience more extreme changes than the rest of the watershed.

Validation and Bias Correction

WRF Model Validation

For the most accurate one-way coupling of the dynamically downscaled WRF data with a hydrologic model the data must be validated against "ground truth" observations to estimate errors, and bias corrected to compensate for those errors. Since the climate model inputs into SDHMs is spatially explicit both the validation and bias correction are performed at the locations in the SBW that also have *in-situ* meteorological data for the historic period (1991–2005; **Figure 1**). For the 5 *in-situ* weather stations in the study region the average differences between historic modeled data and the historic observations are given in **Table 1**.

For daily maximum temperature, the observed mean is warmer than the model output for all stations. The largest difference is 6.5°C, which is located at the north-eastern tip of the SBW. The temperature differences are much smaller near the central part of the lower peninsula [lowest is 2.6°C at Mount Pleasant, MI (station III)]. This indicates that for the SBW region the model keeps the daily maximum temperatures too cool by 3.9°C on average (more near the coast). Standard deviations of the daily maximum temperature show that all station locations have a larger modeled standard deviation than is observed (overall average of 2.0°C larger standard deviation).

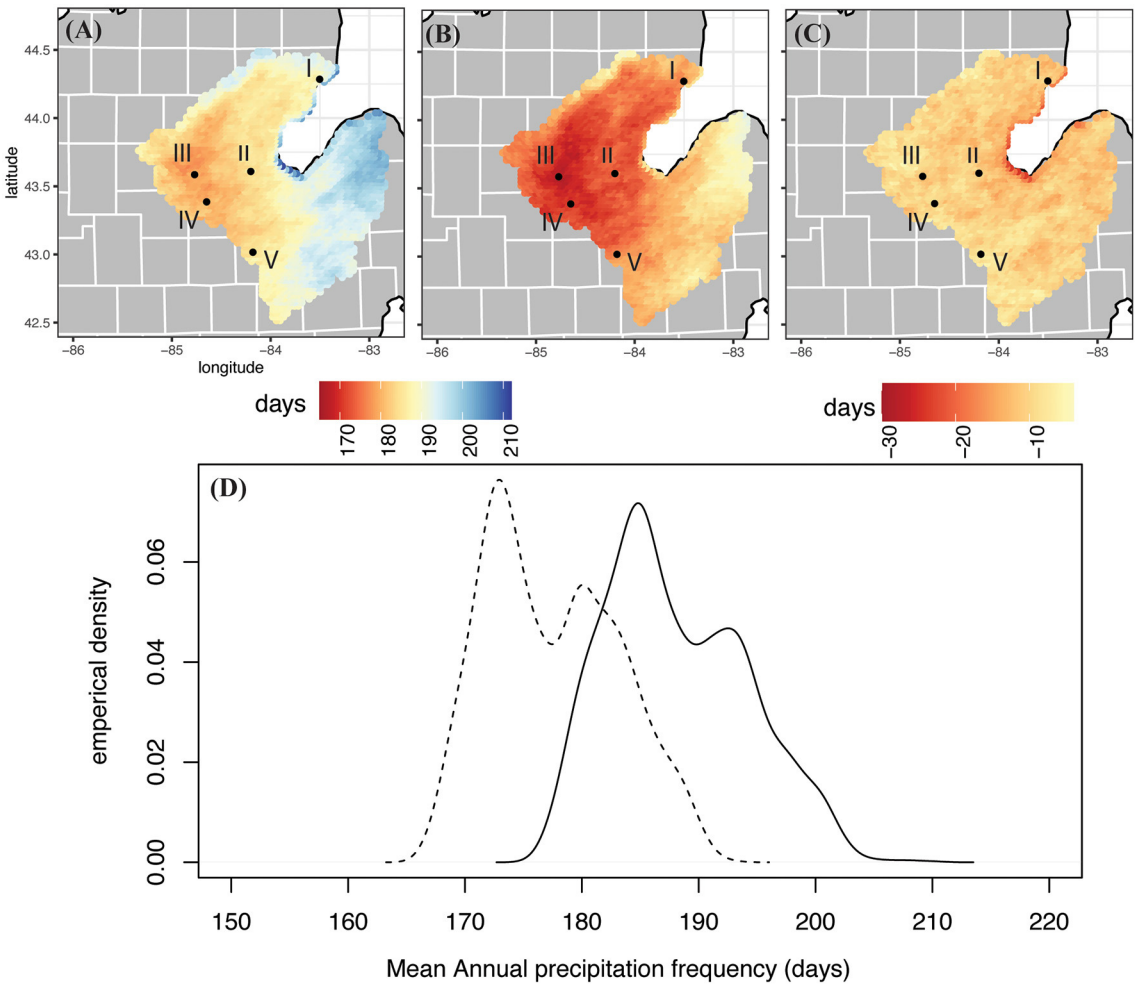

FIGURE 6 | Same as **Figure 2**, but for mean annual precipitation frequency.

The daily minimum temperature shows a similar relationship between modeled and observed values. The largest difference is where modeled temperatures are 6.5°C warmer and again occurs at the East Tawas station, in the north-eastern part of the watershed. Stations in the central part of the MI lower peninsula have smaller differences between the observed minimum temperatures and modeled temperatures, but overall the model generates minimum daily temperatures 4.0°C cooler on average. Differences in standard deviations of minimum temperatures are 2.6°C, indicating that the model produces a larger standard deviation than the observed data. For relative humidity, the WRF model is slightly more moist by 2.4%. It is also more variable, with a standard deviation 3.5% more than observed.

Annual total precipitation (mm) is slightly higher in the historic model run, by 25.5 mm on average. The discrepancy is the highest (765.1 mm observed vs. 861.6 mm modeled) at Midland, MI (station II) in the central part of the lower peninsula, near the western edge of the SBW. The source of this over-production of precipitation in WRF is due to the frequency of precipitation generated in the model. WRF causes precipitation to occur on average 64.4 days too often per year compared to the observed frequency. This is the worst at Mount Pleasant (station III), where the observed frequency is 88.5 days per year and the modeled frequency is 178.7 days per year. On the other hand, the WRF simulation under—produces with regard to precipitation intensity (mm/precipitation day), on average 2.4 mm less than observed [this is larger than the measurement accuracy for human recorded precipitation which is 0.5 mm (NOAA., 2018)]. This difference was also largest at Mount Pleasant, MI (station III) where the average intensity is observed at 9.1 mm/precipitation day and modeled to be 4.5 mm/precipitation day. The combination of too frequent precipitation events but less intense rain events result in close values at Mount Pleasant for total annual precipitation (795.5 mm observed vs. 793.1 mm modeled) although that is because the inaccuracies cancel each other out. This helps to illustrate why adjusting precipitation is still needed, even though errors of total annual precipitation might not seem that high. Accurate capture of precipitation frequency and

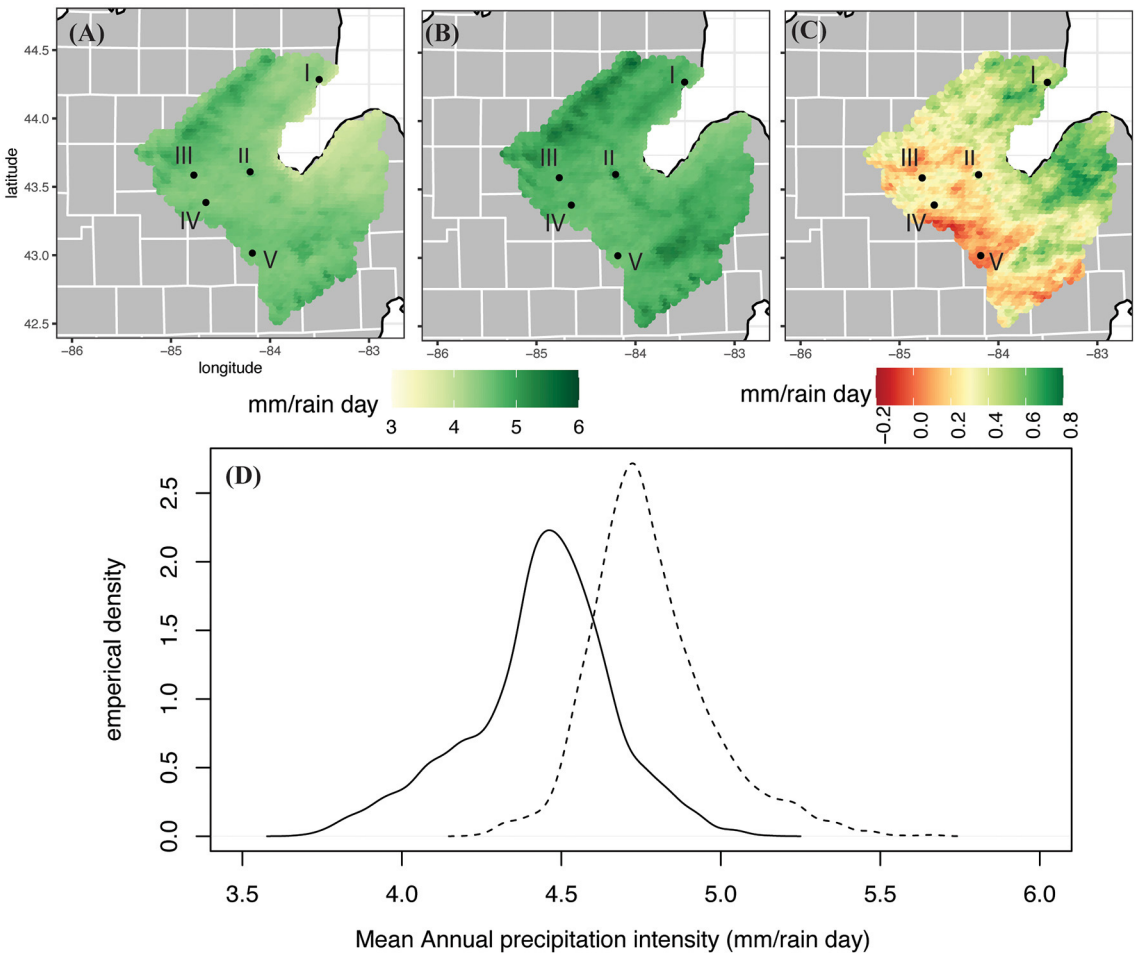

FIGURE 7 | Same as **Figure 2**, but for mean annual precipitation intensity.

TABLE 1 | Average (*standard deviation*) of station and WRF variables of interest for hydrologic inputs at the five observational stations within the watershed for 1991–2005.

Variable	Station (observed)	WRF (modeled)	Model error (modeled—observed)	Bias corrected WRF (modeled)	Model error after bias correction (modeled—observed)
Daily maximum temperature (°C)	13.8 (*11.8*)	9.9 (*13.8*)	−3.9 (*2.0*)	13.8 (*11.6*)	0.0 (*−0.2*)
Daily minimum temperature (°C)	3.0 (*10.0*)	−1.0 (*12.7*)	−4.0 (*2.6*)	3.1 (*10.2*)	0.1 (*0.2*)
Annual total precipitation (mm)	792.2 (*246.5*)	817.7 (*132.6*)	25.5 (*−113.9*)	798.7 (*140.5*)	6.5 (*−106.0*)
Annual precipitation frequency (days/year)	118.9 (*33.7*)	183.3 (*31.1*)	64.4 (*−2.6*)	122.8 (*12.3*)	3.9 (*−21.4*)
Annual average intensity (mm/day of precipitation)	6.9 (*1.1*)	4.5 (*0.9*)	−2.4 (*−0.2*)	6.6 (*1.0*)	−0.3 (*−0.1*)
Relative humidity (%, data from ASOS stations)	74.2 (*11.2*)	76.7 (*14.7*)	2.4 (*3.5*)	74.4 (*11.2*)	0.2 (*−0.1*)

Italicized values indicate the standard deviations.

intensity are particularly important for hydrologic modeling applications. The Kolmogorov-Smirnov test resulted in a p-value is near zero in all cases, indicating that the two distributions are likely not from the same population ($p < 0.05$) for all stations and all variables. Therefore, bias adjustments are required for the WRF data before ingesting the data into any hydrologic model.

Quantile Mapping Bias Correction

Quantile Mapping bias correction is applied to each of the 5 locations within the SBW that are co-located with *in-situ* weather stations. The data from the weather stations are used to generate the empirical cumulative distribution function used to transform the WRF historical run data. The transform functions are retained for use at those same locations in future model

runs. An example of the results of the bias correction is given in **Figure 8**, and comparison statistics for all of the variables are shown in **Table 1**. The Kolomorgov-Smirnov test is again used to determine whether the bias corrected model data is statistically similar to the observed values.

The differences between the bias corrected WRF output and the observational values have been reduced dramatically in **Table 1**, compared to the un-corrected differences (Model Error column in **Table 1**). Before, WRF was underpredicting temperatures by 3.9°C (maximum temperatures) and 4.0°C (minimum temperatures). After bias correction, the average difference between modeled maximum temperatures and observed maximum temperatures is 0.0°C, and the average difference for minimum temperatures is 0.1°C. The error associated with the relative humidity also became almost negligible, at a mere 0.2%. A graphical demonstration of the impact of this correction on maximum temperature at the Oscoda, MI location (station I) is shown in **Figure 8**.

Average annual total precipitation amount observed at the 5 stations is 792.2 mm/year and the un-corrected WRF historic model over-forecasted precipitation by 25.5 mm on average. However, after bias correcting the WRF output, the difference is reduced to 6.5 mm of precipitation per year (**Table 1**). The intensity of precipitation also shows substantial improvement. Without correction, the WRF model produces precipitation 64.4 more days than observed. After applying the Quantile Mapping bias correction, WRF only generates precipitation 3.8 days per year more than observed. The average intensity of precipitation events was under forecast by WRF by −2.4 mm/day. However, after bias correction this difference is −0.2 mm/day. All three of these variables show the improvements to WRF's ability to represent the nuances of the precipitation regimes after bias correction.

According to the K-S test for the likelihood of two sample distributions coming from the same population, all total precipitation samples (observed, modeled, and bias corrected modeled) are likely from the same population distribution ($p \leq 0.05$). This is mostly due to the low error for total annual precipitation values, which we have shown is an artifact of frequency and intensity errors canceling each other out. When considering precipitation frequency and intensity only, the observed and bias-corrected model distributions have statistically significant K-S D values, indicating they are likely from the same distribution (for all 5 stations in the watershed). This is also the case for the other variables, where only after bias-correction could observations and modeled output be assumed to come from the same distribution. The exceptions are with 2 stations failing to meet this assumption at the $p \leq 0.05$ significance level for minimum temperature, and one station for maximum temperature.

Bias Corrected Future run

The quantile mapping transforms developed between the station data and historical model data are applied to the 5 corresponding point locations for the RCP 8.5 WRF future run. The resulting values averaged over the 5 locations are given in **Table 2** for comparison with the historic model run values. Empirical density functions (edfs) are fit to the historic and future precipitation data in order to estimate the probability distribution functions of the data and to visualize the differences in the entire variable's distribution. The value for the 75th and 90th percentile are computed for precipitation, and the 10th and 90th percentiles for the other variables (**Figures 9–12**). Above/below average and extreme values can be used to develop relationships between climatological variables and streamflow; this is especially true for precipitation with regards to flood event prediction but also applies temperature and RH for their effects on watershed processes including evapotranspirative demand.

Average daily maximum temperature increases from 13.8 to 18.3°C during the twenty-first century (**Table 2**). The edfs of maximum temperature calculated for each of the station's historic and future bias corrected variables are displayed in **Figure 9**. All of the stations experience a shift in the future maximum temperature distributions toward the right, indicating higher temperatures. In addition, the 10th and 90th percentile temperature values increase at all locations with the maximum increase in the 10th percentile of 5.6°C (from −1.1 to 4.5°C) occurring at Oscoda, MI (station I), the northern most location in the SBW (**Figure 9B**). The largest increase in the size of the 90th percentile temperature is at Mount Pleasant, MI (station III) where the 90th percentile goes from 28.3°C in the historic edf to 35.1°C in the future edf (**Figure 9D**).

Likewise, the average daily minimum temperatures at the 5 stations within the SBW increase from 3.0 to 8.0°C (**Table 2**). The edfs of minimum temperatures (**Figure 10**) show that a shift of the entire distribution toward higher temperatures is consistent across the watershed. It is interesting to note from these comparative distributions that the 10th percentile values increase more than the 90th percentile values at almost all stations, indicating a substantial change in the frequency and value of extreme cold minimum temperatures. The largest of these 10th percentile warmings occurs at Oscoda, MI (station I) in the northern part of the SBW (**Figure 10B**). The largest warming of the 90th percentile minimum temperature is 8.9°C (from 17.2 to 26.1°C) and occurs at Midland, MI (station II), in the western part of the watershed (**Figure 10C**).

In the SBW, the future model run produces a signal of decreasing relative humidity from 74.2 to 71.6% (**Table 2**). Even though the average relative humidity decreases, the average standard deviation of relative humidity increases from 11.2 to 18.3%. This is more easily observed in **Figure 11**, which plots the historic and future bias corrected edfs of relative humidity at the 5 locations in the SBW. These figures show the flattening of the distribution and the corresponding increase in variability, particularly in the left tail. The 90th percentile values increase at all 5 stations [by as much as 5.3% at Gratiot, MI (station IV); **Figure 11A**], but the 10th percentiles show the largest amount of change. All of the stations experience a decrease of the 10th percentile values of at least 4.7%, and Gratiot, MI (in the southwestern part of the watershed) experiences a reduction of 15.6% over the twenty-first century. The increased intensity and decreased frequency of precipitation events may lead to longer periods of drier air between events.

Total annual precipitation does not appear to experience substantial change in the future model run once the WRF output is bias corrected (**Table 2**). There is a slight decrease

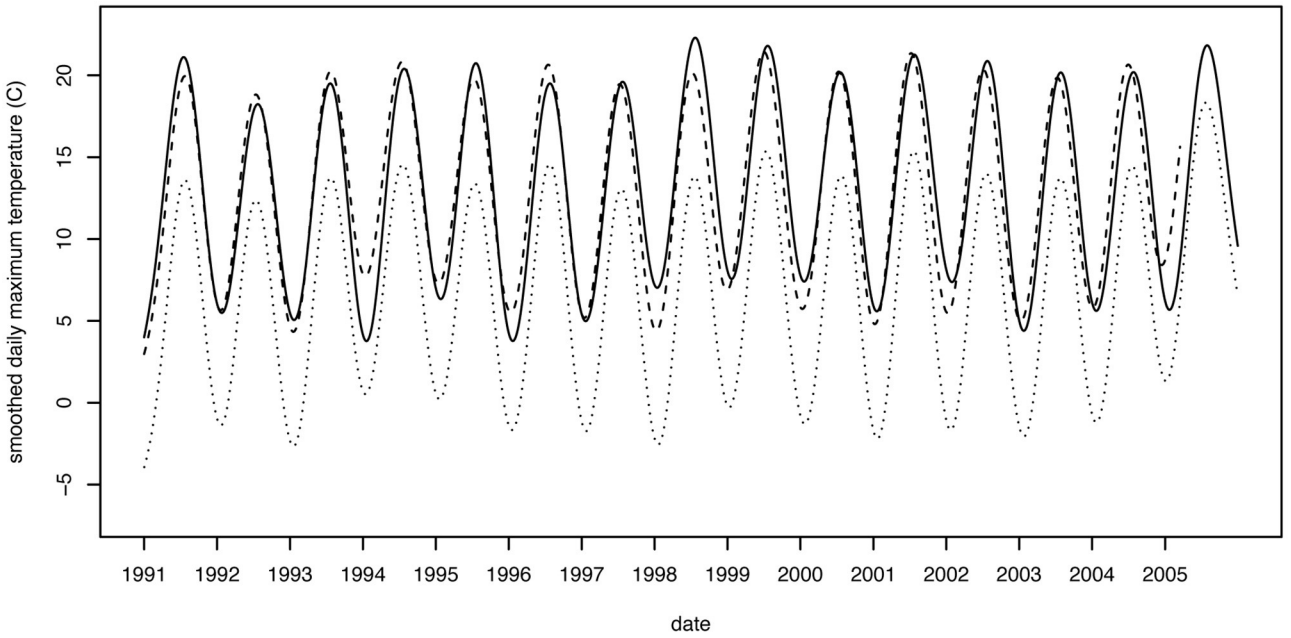

FIGURE 8 | Observed (solid), modeled (dotted), and bias corrected (dashed) modeled daily maximum temperatures for observational station 202423 (Oscoda, MI).

TABLE 2 | Average (*standard deviation*) of bias corrected WRF variables for the historic and future model runs.

Variable	Bias corrected modeled (1991–2005)	Modeled (2085–2099)	Bias corrected modeled (2085–2099)	Difference in bias corrected modeled (future-historic)
Daily maximum temperature (°C)	13.8 (*11.6*)	15.1 (*16.2*)	18.3 (*14.0*)	4.5 (*2.4*)
Daily minimum temperature (°C)	3.1 (*10.2*)	5.0 (*13.6*)	8.0 (*12.3*)	4.9 (*2.1*)
Annual total precipitation (mm)	798.7 (*140.5*)	819.3 (*143.1*)	793.4 (*132.9*)	−5.3 (−*7.6*)
Annual precipitation frequency (days/year)	122.8 (*12.3*)	173.3 (*24.4*)	116.2 (*12.4*)	−6.6 (*0.1*)
Annual average intensity (mm/day of precipitation)	6.6 (*1.0*)	4.8 (*0.9*)	7.0 (*0.9*)	0.4 (−*0.1*)
Relative humidity (%, data from ASOS stations)	74.4 (*11.2*)	73.1 (*21.4*)	71.6 (*18.3*)	−2.8 (*7.1*)

These are for the 5 observational stations within the watershed.
Italicized values indicate the standard deviations.

(−1.2 mm) in average annual precipitation totals at the 5 station locations, due to a decrease in frequency (−2.7 days/year) and increase in intensity (0.1 mm/precipitation day). However, from the spatial maps (**Figures 2**–**7**) it can be seen that the projected changes to precipitation vary in magnitude and sign across the watershed, and the bias-corrected future time series are only created at the 5 locations with station data. **Figure 12** shows the edfs for the historic and future bias corrected model values for daily precipitation events. For these distributions the 75th and 90th percentiles are indicated on the plots, since understanding above average and extreme precipitation events is paramount for modeling event-based flow. All of the locations experience a slight increase in the magnitude of 75th and 90th percentile events except for Owosso, MI (station V), in the southern part of the watershed (**Figure 12E**), which corresponds with the area of decreased precipitation intensity in **Figure 7C**. The largest magnitude increases in 90th percentile precipitation events occur at Gratiot, MI (station IV), Oscoda, MI (station I), and Mount Pleasant, MI (station III; **Figures 12A,B,D**). These locations experience extreme precipitation increases around 1.2 mm in magnitude and corresponds to areas of increased precipitation intensity in **Figure 7C**.

DISCUSSION

Inferences and Implications

End-of-century model runs indicate that the SBW will experience substantial and spatially variable effects from climate change. On the whole, the watershed will be slightly drier, with lower relative humidity and fewer precipitation days than at the end of the twentieth century. This change in relative humidity is consistent with what is expected from the Clausius-Clapeyron relation of increased atmospheric moisture capacity without

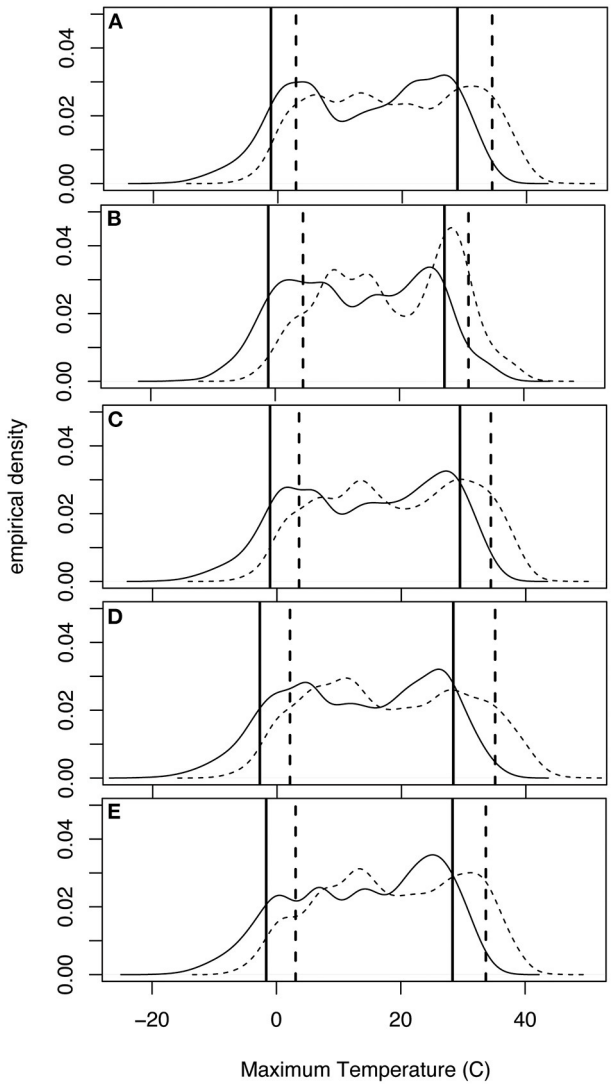

FIGURE 9 | Daily maximum temperature empirical density functions. The solid black line is the historic bias corrected data and the dashed line represents the future bias corrected data at each location. The solid vertical lines represent the 10 and 90% values at location **(A)** 200146 (Gratiot, IV), **(B)** 202423 (Oscoda, I), **(C)** 205434 (Midland, II), **(D)** 205662 (Mount Pleasant, III) and **(E)** 206300 (Owosso, V).

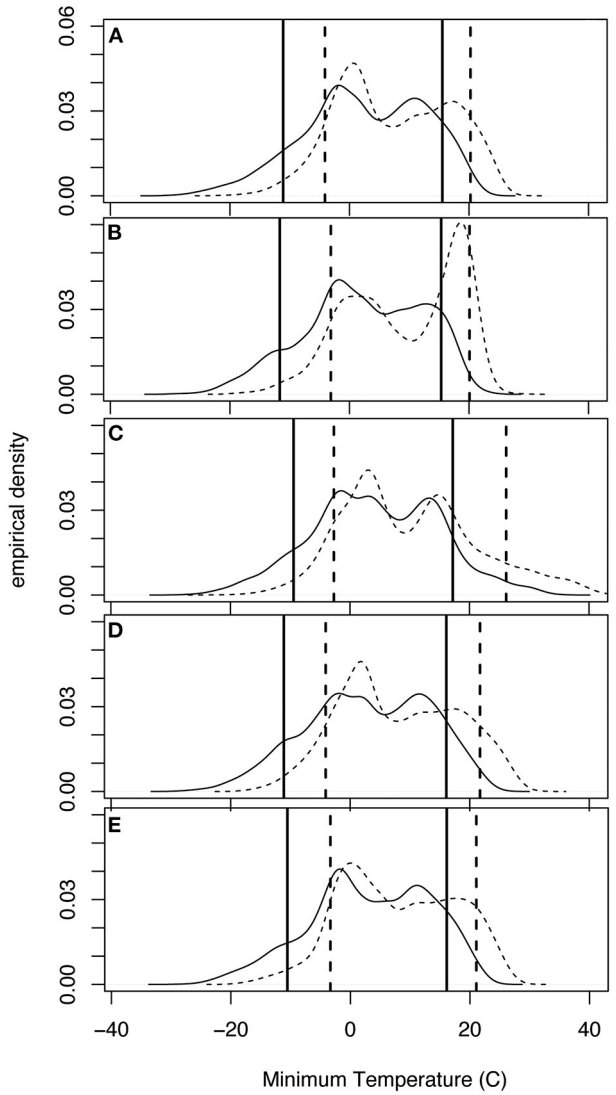

FIGURE 10 | Same as **Figure 9** but for daily minimum temperature.

large changes in moisture flux over land (Byrne and O'Gorman, 2016). Temperatures will increase substantially, with the largest changes occurring at the extremes (10th percentile maximum and 90th percentile minimum), meaning that it is likely that the SBW will see simultaneously more frost-free days in the winters and more exceptionally hot days in the summer months. This trend of decreasing diurnal temperature range due to a faster rate of warming by minimum temperatures is consistent with what has happened in the last century (Easterling et al., 1997; Thorne et al., 2016; Sun et al., 2019 among others) and what is expected to continue in a warming climate (Zhou et al., 2009). The small decline in total annual precipitation masks projected increases in precipitation intensity, with the increases in precipitation intensity modeled across nearly the entire watershed. The projected changes will not be uniform, with the coastal region experiencing some of the most extreme temperature changes and considerable spatial variability in precipitation frequency and intensity throughout the watershed. One of the benefits of dynamical downscaling with the WRF model is that finer resolution processes, such as convection, can identify spatial patterns within the study domain that would not be apparent in a coarse-resolution GCM (Qiu et al., 2021). The difference in projected characteristics between the coastal area and inland would have been sub-grid scale in the 1° spatial resolution of the parent climate simulations we used before downscaling, which could also be missed in statistical downscaling without observations to provide "predictand" distributions at those locations. It is important to

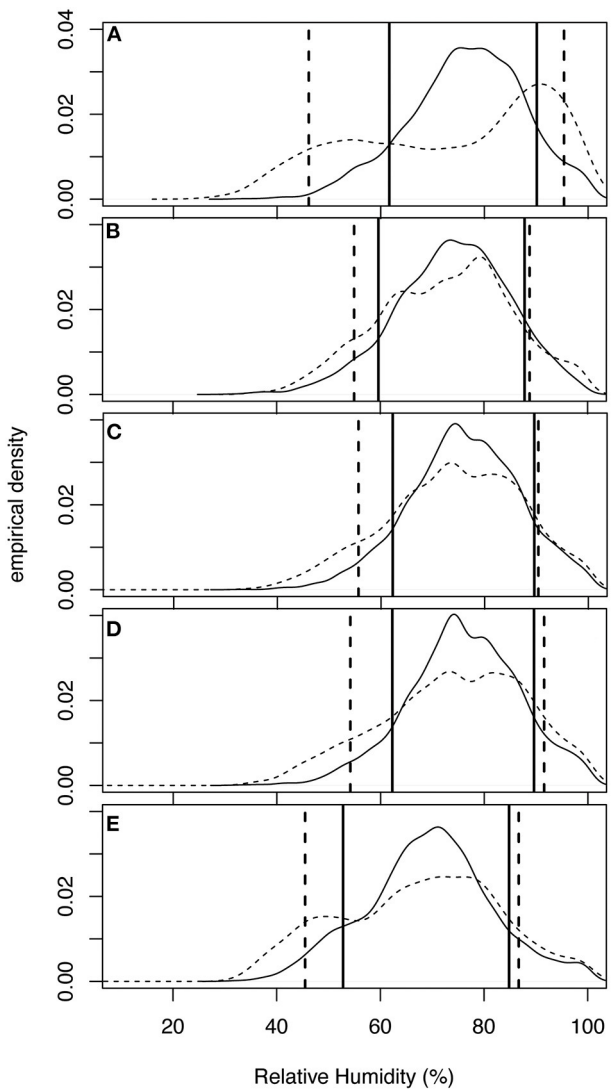

FIGURE 11 | Same as **Figure 9** but for daily relative humidity.

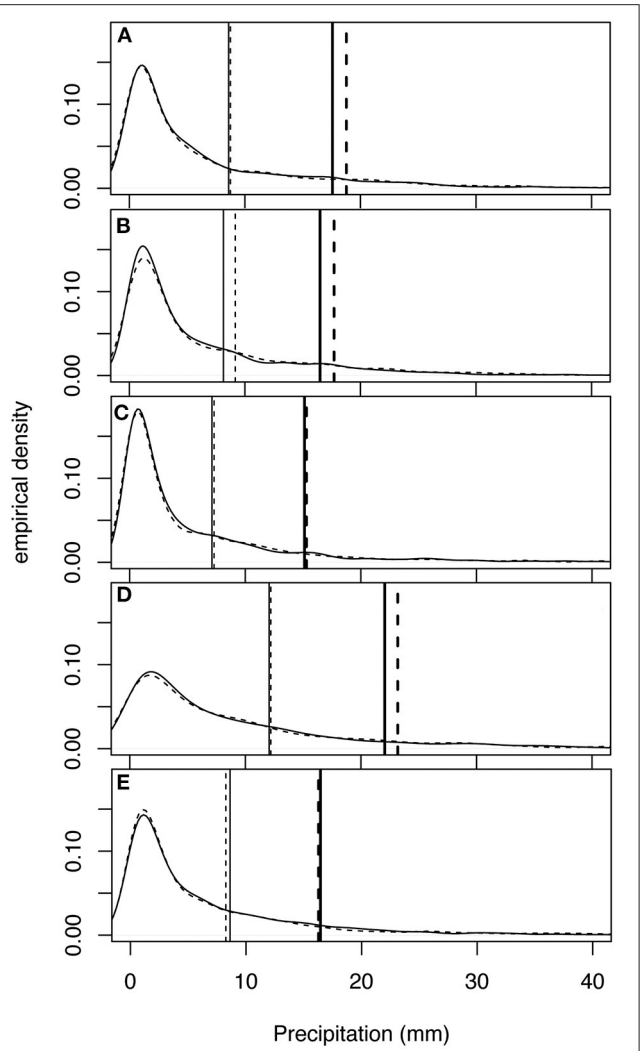

FIGURE 12 | Daily precipitation empirical density functions. The solid black line is the historic bias corrected data and the dashed line represents the future bias corrected data at each location. The dashed vertical lines represent the 75th and 90th (bold) percentile values for the future data and the solid vertical lines represent the 75th and 90th (bold) percentiles values for the historical data at location **(A)** 200146 (Gratiot, IV), **(B)** 202423 (Oscoda, I), **(C)** 205434 (Midland, II), **(D)** 205662 (Mount Pleasant, III) and **(E)** 206300 (Owosso, V).

note that this is on realization of just one GCM-RCM coupling. Other GCMs coupled to other RCMs or multiple realizations of the current GCM-RCM combination would produce different temperature, precipitation, and relative humidity projections. Therefore, the direction and general magnitude of the future projections are more important than the exact magnitude of the changes.

The large increases in mean minimum and maximum temperature along the coast of Saginaw Bay could be a substantial stressor on wetland vegetation; increased air and water temperatures and the associated declines in water level (for emergent wetlands) and water clarity (for submergent wetlands) all can negatively impact wetland plants and potentially decreasing associated ecosystem services including nutrient cycling, sediment trapping and deposition, and flood modulation (Erwin, 2009; Steinman et al., 2012; Junk et al., 2013; Short et al., 2016). Considering the substantial resources that have been committed to restoring coastal wetlands in Saginaw Bay (Hartig et al., 2020), a decline in function due to climate change impacts should be cause for concern. Capturing spatial variability in precipitation frequency and intensity is fundamental to effectively modeling rainfall-runoff ratios, flooding in ungauged catchments, erosion processes, and the potential for mobilization of non-point and point source pollutants. Recognizing that changes in precipitation intensity and frequency will not be uniform and may exacerbate existing watershed stressors like land use change is needed in order to quantify changes in hydrologic regime and prediction of extreme events.

Limitations and Future Work

The distinct difference between the Saginaw Bay coastal grids and the rest of the SBW's projected changes in climate merit future investigation. There are not *in-situ* stations from the NOAA COOP or ASOS networks within these cells to use for validation, so error cannot be ascertained in the same manner. The closest *in-situ* station is Oscoda, MI (station I), located along the northern coast of the Saginaw Bay, which had model errors (before bias correction) of less than 0.1 mm for precipitation, ∼6% for relative humidity, and ∼6.5°C for temperatures. Without further investigation it is unclear if the bias correction applied at Oscoda, MI is appropriate for the rest of the Saginaw Bay coast. Part of the uncertainty here is because the atmospheric model used in this study for dynamical downscaling does not contain a dynamic lake model, but rather designates a "water bodies" land cover type (WRF v3.7; Skamarock et al., 2008), which lacks realistic lake surface temperatures (Gula and Peltier, 2012; Xiao et al., 2016). The study uses a bias-corrected GCM with a nested RCM that was also validated and bias-corrected, which assists in removing some systematic errors that may be introduced because of this inaccurate lake grid treatment. However, research in the last several years has been actively seeking a better coupling between WRF and dynamic lake models for use in regional climate studies (Gu et al., 2015; Xiao et al., 2016; Peltier et al., 2018; Ma et al., 2019; and others). To better understand the reliability of the projections for the Saginaw Bay coastal area, and to what extent bias-correction can remediate a lack of some of the GCM's sub-grid-scale influences, future work may include comparison with some of these lake-coupled models. Additionally, it would be worthwhile to perform the historical downscaling simulation with nudging applied to the RCM, to examine the impact of this "relaxation" toward the GCM on the precipitation variability and extremes over such a fine spatial resolution as the inner domain and over such a long time scale. Another avenue of future work with these data will be to diagnose error and bias-correct all of the modeled grid points within the watershed, for sensitivity analyses with SDHMs. Alternative *in-situ* observations that are not as long-running as the stations used in this paper or gridded products may be used to supplement the stations within the watershed for these future analyses.

Such high spatial resolution climate data over a long time period processed for coupling with SDHMs is a valuable tool for examining climate change impacts on hydrologic systems. However, the full potential of this dataset is not realized in this study. Even though dynamic downscaling captures the variability in atmospheric processes throughout the watershed, without bias correction of that data before ingestion by hydrologic models errors are needlessly propagated into them and can obfuscate the empirical parameter calibration that must happen. Additionally, questions remain as to how many of the 3 km by 3 km grid cells within the SBW need to be provided as input to a SDHM to capture the necessary atmospheric variability within the watershed, and what is the best method for bias correcting those grid cells without *in-situ* validation data. Answering these questions will allow future research to more accurately bridge the spatial and temporal gap between GCMs run for future climate scenarios and SDHMs that are able to simulate multifaceted impacts of atmospheric variability on hydrologic processes.

DATA AVAILABILITY STATEMENT

The datasets presented in this study can be found in online repositories. The names of the repository/repositories and accession number(s) can be found below: the dynamically downscaled and bias corrected time series developed for 2085–2099 for the 5 locations can be found at CUASHI's HydroShare (http://www.hydroshare.org/resource/0754e9c2e5a84f90959b2aa9164a4b9e).

AUTHOR CONTRIBUTIONS

DK and WR contributed to the concept and design of the study. DK performed the dynamical downscaling and climate analysis. Both DK and WR wrote the paper and created the figures. All authors contributed to the article and approved the submitted version.

ACKNOWLEDGMENTS

The authors would like to thank Lucas Falsetta for technical assistance with the WRF setup at CMU and to the editors and reviewers for their suggestions to improve the manuscript.

REFERENCES

Alexandru, A., de Elia, R., Laprise, R., Separovic, L., and Biner, S. (2009). Sensitivity study of regional climate model simulations to large-scale nudging parameters. *Monthly Weather Rev.* 137, 1666–1686. doi: 10.1175/2008MWR2620.1

Alidoost, F., Stein, A., Su, Z., and Sharifi, A. (2021). Multivariate copula quantile mapping for bias correction of reanalysis air temperature data. *J. Spatial Sci.* 66, 299–315. doi: 10.1080/14498596.2019.1601138

Andresen, J. (2012). "Historical climate trends in Michigan and the Great Lakes Region," in *Climate Change in the Great Lakes Region: Navigating an Uncertain Future*, ed T. Dietz and D. Bidwell (East Lansing, MI: Michigan State University Press).

Angel, J., Swanston, C., Boustead, B. M., Conlon, K. C., Hall, K. R., Jorns, J. L., et al., (2018). "Midwest," in *Impacts, Risks, and Adaptation in the United States: Fourth National Climate Assessment, Volume II*, eds D. R. Reidmiller, C. W. Avery, D. R. Easterling, K. E. Kunkel, K. L. M. Lewis, T. K. Maycock, and B. C. Stewart (U.S. Global Change Research Program, Washington, DC), 872–940. doi: 10.7930/NCA4.2018.CH21

Arnold, J. G., Moriasi, D. N., Gassman, P. W., Abbaspour, K. C., White, M. J., Srinivasan, R. (2012). SWAT: model use, calibration, and validation. *Trans. ASABE.* 55, 1491–1508. doi: 10.13031/2013.42256

Boé, J., Terray, L., Habets, F., and Martin, E. (2007). Statistical and dynamical downscaling of the Seine basin climate for hydro-meteorological studies. *Int. J. Climatol.* 7183–7192. doi: 10.1002/joc.1602

Briley, L., Kelly, R., Blackmer, E. D., Troncoso, A. V., Rood, R. B., Andresen, J., et al. (2020). Increasing the usability of climate models throught he use of consumer-report-style resources for decision-making,

Bull. Am. Meteorol. Soc. 101, E1709–E1717. doi: 10.1175/BAMS-D-19-0099.1

Bruyère, C. L., Done, J. M., Holland, G. J., et al. (2014). Bias corrections of global models for regional climate simulations of high-impact weather. *Clim. Dyn*. 43, 1847–1856. doi: 10.1007/s00382-013-2011-6

Bruyère, C. L., Monaghan, A. J., and Steinhoff, D. F., and Yates, D. (2015). *Bias-Corrected CMIP5 Data in WRF/MPAS Intermediate File Format*. TN-515+STR, NCAR.

Bussieres, N., and Hogg, W. (1989). The objective analysis of daily rainfall by distance weighting schemes on a mesoscale grid. *Atmos. Ocean* 27, 521–541. doi: 10.1080/07055900.1989.9649350

Byrne, M. P., and O'Gorman, P. A. (2016). Understanding decreases in land relative humidity with global warming: conceptual model and GCM simulations. *J. Clim*. 29, 9045–9061. doi: 10.1175/JCLI-D-16-0351.1

Byun, K., Chiu, C. M., and Hamlet, A. F. (2019). Effects of twenty-first century climate change on seasonal flow regimes and hydrologic extremes over the Midwest and Great Lakes region of the US. *Sci. Total Environ.* 650, 1261–1277. doi: 10.1016/j.scitotenv.2018.09.063

Byun, K., and Hamlet, A. F. (2018). Projected changes in future climate over the Midwest and Great Lakes region using downscaled CMIP5 ensembles. *Int. J. Climatol.* 38, E531–E553. doi: 10.1002/joc.5388

Churchill, J. H., and Csanady, G. T. (1983). Near-surface measurements of quasi-lagrangian velocities in open water. *J. Phys. Oceanogr.* 13, 1669–1680. doi: 10.1175/1520-0485(1983)013<1669:NSMOQL>2.0.CO;2

Das, J., and Umamahesh, N. V. (2018). Spatio-temporal variation of water availability in a river basin under CORDEX simulated future projections. *Water Resour. Manag.* 32, 1399–1419. doi: 10.1007/s11269-017-1876-2

Dingman, S. L. (2008). *Physical Hydrology.* Illinois: Waveland Press, Inc.

D'Orgeville, M., Peltier, W. R., Erler, A. R., and Gula, J. (2014). Climate change impacts on Great Lakes basin precipitation extremes. *J. Geophys. Res. Atmos.* 119, 10799–10812. doi: 10.1002/2014JD021855

Dudhia, J. (1989). Numerical study of convection observed during the winter monsoon experiment using a mesoscale two-dimensional model. *J. Atmos. Sci.* 46, 3077–3107. doi: 10.1175/1520-0469(1989)046andlt;3077:NSOCODandgt;2.0.CO;2

Easterling, D. R., Horton, B., Jones, P. D., Peterson, T. C., Karl, T. R., Parker, D. E., et al. (1997) Maximum and minimum temperature trends for the globe. *Science* 277, 364–367 doi: 10.1126/science.277.5324.364

Easterling, D. R., Kunkel, K. E., Arnold, J. R., Knutson, T., LeGrande, A. N., Leung, L. R., et al. (2017). "Precipitation change in the United States," in *Climate Science Special Report: Fourth National Climate Assessment, Volume I*, eds D. J. Wuebbles, D. W. Fahey, K. A. Hibbard, D. J. Dokken, B. C. Stewart, and T. K. Maycock (Washington, DC: U.S. Global Change Research Program), 207–230. doi: 10.7930/J0H993CC

Erler, A. R., Frey, S. K., Khader, O., d'Orgeville, M., Park, Y.-J., et al. (2019). Simulating Climate Change Impacts on surface water resources within a lake-affected region using regional climate projections. *Water Resour. Res.* 55, 130–155. doi: 10.1029/2018WR024381

Erwin, K. L. (2009). Wetlands and global climate change: the role of wetland restoration in a changing world. *Wetlands Ecol. Manag.* 17, 71–84. doi: 10.1007/s11273-008-9119-1

Gou, J., Miao, C., Duan, Q., Tang, Q., Di, Z., Liao, W., et al., (2020). Sensitivity analysis-based automatic parameter calibration of the VIC model for streamflow simulations over China. *Water Resourc. Res.* 56:e2019WR025968. doi: 10.1029/2019WR025968

Gu, H., Jin, J., Wu, Y., Ek, M., and Subin, Z. (2015). Calibration and validation of lake surface temperature simulations with the coupled WRF-lake model. *Clim. Change* 129, 471–483. doi: 10.1007/s10584-013-0978-y

Gudmundsson, L., Bremnes, J. B., Haugen, J. E., and Engen-Skaugen, T. (2012). Technical Note: Downscaling RCM precipitation to the station scale using statistical transformations – a comparison of methods. *Hydrol. Earth Syst. Sci*., 16, 3383–3390. doi: 10.5194/hess-16-3383-2012

Gudmundsson, L. (2014). *qmap: Statistical transformations for post-processing climate model output*. R package version 1.0-3. Available online at: http://cran.r-project.org/web/packages/qmap/ (accessed May 1, 2019).

Gula, J., and Peltier, W. R. (2012). Dynamical downscaling over the Great Lakes basin of North America using the WRF regional climate model: the impact of the Great Lakes system on regional greenhouse warming, *J. Clim*. 25, 7723–7742. doi: 10.1175/JCLI-D-11-00388.1

Hartig, J. H., Krantzberg, G., and Alsip, P. (2020). Thirty-five years of restoring Great Lakes areas of concern: gradual progress, hopeful future. *J. Great Lakes Res.* 46, 429–442. doi: 10.1016/j.jglr.2020.04.004

Hayhoe, K., VanDorn, J., Croley, I. I., T., Schlegal, N., and Wuebbles, D. (2010). Regional climate change projections for Chicago and the US Great Lakes. *J. Great Lakes Res.* 36, 7–21. doi: 10.1016/j.jglr.2010.03.012

Hewitson, B., and Crane, R. (1996). Climate downscaling: techniques and application. *Clim. Res.* 7, 85–95. doi: 10.3354/cr007085

Hong, S.-Y., Dudhia, J., and Chen, S.-H. (2004). A revised approach to ice microphysical processes for the bulk parameterization of clouds and precipitation. *Mon. Weather Rev*. 132, 103–120. doi: 10.1175/1520-0493(2004)132<0103:ARATIM>2.0.CO;2

Hong, S.-Y., and Pan, H.-L. (1996). Nonlocal boundary later vertical diffusion in a medium-range forecast model. *Mon. Weather Rev.* 124, 2322–2339. doi: 10.1175/1520-0493(1996)124andlt;2322:NBLVDIandgt;2.0.CO;2

Izumi, Y., and Caughey, J. S. (1976). *Minnesota 1973 Atmospheric Boundary Layer Experiment Data Report*. AFCRL-TR-76-0038.

Jajarmizdeh, M., Harun, S., and Salarpour, M. (2012). A review on theoretical consideration and types of models in hydrology. *J. Environ. Sci. Technol*. 5, 249–261. doi: 10.3923/jest.2012.249.261

Jiao-jun, Z., Xiu-fen, L., Yutaka, C., and Takeshi, M. (2004). Wind profiles in and over trees. *J. For. Res.* 15, 305–312. doi: 10.1007/BF02844959

Junk, W. J., An, S., Finlayson, C. M., Gopal, B., Kvet, J., Mitchell, S. A., et al. (2013). Current state of knowledge regarding the world's wetlands and their future under global climate change: a synthesis. *Aquat. Sci*. 75, 151–167. doi: 10.1007/s00027-012-0278-z

Kain, J. S. (2004). The Kain-Fritsch convective parameterization: an update. *J. Appl. Meteorol.* 43, 170–181. doi: 10.1175/1520-0450(2004)043<0170:TKCPAU>2.0.CO;2

Khakbaz, B., Imam, B., Hsu, K., and Sorooshian, S. (2012). Calibration strategies for semi-distributed hydrologic models. *J. Hydrol*. 418–419, 61–77. doi: 10.1016/j.jhydrol.2009.02.021

Lin, P., Yang, Z.-L., Gochis, D. J., Yu, W., Maidment, D. R., Somos-Valenzuela, M. A., et al. (2018). Implementation of a vector-based river network routing scheme in the community WRF-Hydro modeling framework for flood discharge simulations. *Environ. Model. Softw.* 107, 1–11. doi: 10.1016/j.envsoft.2018.05.018

Ma, Y. Y., Yang, Y., Qiu, C., and Wang, C. (2019). Evaluation of the WRF-lake model over two major freshwater lakes in China. *J. Meteor. Res.* 33, 219–235. doi: 10.1007/s13351-019-8070-9

Mahdiyan, O., Filazzola, A., Molot, L., Gray, D., and Sharma, S. (2021). Drivers of water quality changes within the Laurentian Great Lakes region over the past 40 years. *Limnol. Oceanogr*. 66, 237–254. doi: 10.1002/lno.11600

Mallard, M. S., Nolte, C. G., Spero, T. L., Bullock, O. R., Alapaty, K., Herwehe, J. A., et al. (2015). Technical challenges and solutions in representing lakes when using WRF in downscaling applications. *Geosci. Model Dev*. 8, 1085–1096. doi: 10.5194/gmd-8-1085-2015

Maraun, D., and Widmann, M. (2018). *Statistical Downscaling and Bias Correction for Climate Research*. Cambridge: Cambridge University Press.

Martínez-Salvador, A., Millares, A., Eekhout, J. P. C., and Conesa-García, C. (2021). Assessment of streamflow from EURO-CORDEX regional climate simulations in semi-arid catchments using the SWAT model. *Sustainability* 13:7120. doi: 10.3390/su13137120

Masaki, Y., Hanasaki, N., Takahashi, K., and Hijioka, Y. (2015). Propagation of biases in humidity in the estimation of global irrigation water. *Earth System Dyn.* 6, 461–484. doi: 10.5194/esd-6-461-2015

Mendoza, P. D., Clark, M. P., Mizukami, N., Newman, A. J., Barlage, M., Gutmann, E. D., et al. (2015). Effects of hydrologic model choice and calibration on the portrayal of climate change impacts. *J. Hydrometeorol.* 16, 762–780. doi: 10.1175/JHM-D-14-0104.1

Michigan Department of Natural Resources and Surface Water Quality Division (1988). *Michigan Department of Natural Resources Remedial Action Plan for Saginaw River and Saginaw Bay Area of Concern*, Lansing, MI. Michigan Natural Features Inventory. (2021). Available online at: https://mnfi.anr.msu.edu/resources/county-element-data (accessed September 1, 2021).

Mlawer, E. J., Taubman, S. J., Brown, P. D., Iacono, M. J., and Clough, S. A. (1997). Radiative transfer for inhomogeneous atmospheres: RRTM, a validated correlated-k model for the long wave. *JGR Atmos.* 102, 16663–16682. doi: 10.1029/97JD00237

Monaghan, A. J., Steinhoff, D. F., Bruyére, C. L., and Yates, D. (2014). NCAR CESM Global Bias-Corrected CMIP5 Output to Support WRF/MPAS Research. *Research Data Archive at the National Center for Atmospheric Research, Computational and Information Systems Laboratory* (accessed May 01, 2015).

Mosier, T. M., Hill, D. F., and Sharp, K. V. (2014). 30-arcsecond monthly climate surfaces with global land coverage. *Int. J. Climatol.* 34, 2175–2188. doi: 10.1002/joc.3829

Mosier, T. M., Hill, D. F., and Sharp, K. V. (2018). Update to the Global Climate Data Package: analysis of empirical bias correction methods in the context of producing very high resolution climate projections. *Int. J. Climatol.* 38, 825–840. doi: 10.1002/joc.5213

National Center for Atmospheric Research Staff (eds). (2017). *The Climate Data Guide: Climate Forecast System Reanalysis (CFSR).* Available online at: https://climatedataguide.ucar.edu/climate-data/climate-forecast-system-reanalysis-cfsr (accessed September 1, 2021).

NCEI. (2017). *U.S. Historical Climatology Network.* Available online at: https://www.ncei.noaa.gov/products/land-based-station/us-historical-climatology-network (accessed July 5, 2017).

NCEI. (2019). *Automated Surface/Weather Observing Systems.* Available online at: https://www.ncei.noaa.gov/products/land-based-station/automated-surface-weather-observing-systems (accessed May 24, 2019).

NOAA. (2018). *National Weather Service Instruction 10-1302. Requirements and Standards for NWS Climate Observations*. Available online at: http://www.nws.noaa.gov/directives/ (accessed May 1, 2019).

Notaro, M., Bennington, V., and Vavrus, S. (2015). Dynamically downscaled projections of lake-effect snow in the Great Lakes Basin. *J. Clim.* 28, 1661–1684. doi: 10.1175/JCLI-D-14-00467.1

Peltier, W. R., d'Orgeville, M., Erler, A. R., and Xie, F. (2018). Uncertainty in future summer precipitation in the Laurentian Great Lakes basin: dynamical downscaling and the influence of continental-scale processes on regional climate change, *J. Clim.* 31, 2651–2673. doi: 10.1175/JCLI-D-17-0416.1

Qiu, Y., Feng, J., Yan, Z., Wang, J., and Li, Z. (2021). High-resolution dynamical downscaling for regional climate projection in Central Asia based on bias-corrected multiple GCMs. *Clim. Dyn.* 2021, 1–15. doi: 10.1007/s00382-021-05934-2

Raghavan, S. V., Tue, V. M., and Shie-Yui, L. (2014). Impact of climate change on future stream flow in the Dakbla river basin. *J. Hydroinform.* 16, 231–244. doi: 10.2166/hydro.2013.165

Salathe, J.r,., E. P., Hamlet, A. F., Mass, C. F., Lee, S., Stumbaugh, M., et al., (2014). Estimates of twenty-first-century flood risk in the Pacific Northwest based on regional climate model simulations. *J. Hydrometeorol.* 15, 1881–1899. doi: 10.1175/JHM-D-13-0137.1

Santoso, E., and Stull, R. (2001). Similarity Equations for wind and temperature profiles in the Radix Layer, at the bottom of the convective boundary layer. *J. Atmos. Sci.* 58, 1446–1464. doi: 10.1175/1520-0469(2001)058<1446:SEFWAT>2.0.CO;2

Schuenemeyer, J. H., and Drew, L. J. (2011). *Statistics for Earth and Environmental Scientists.* Hoboken, NJ: Wiley. doi: 10.1002/9780470650707

Selzer, M. D., Joldersma, B., and Beard, J. (2014). A reflection on restoration progress in the Saginaw Bay watershed. *J. Great Lakes Res.* 40, 192–200. doi: 10.1016/j.jglr.2013.11.008

Short, F. T., Kosten, S., Morgan, P. A., Malone, S., and Moore, G. E. (2016). Impacts of climate change on submerged and emergent wetland plants. *Aquat. Bot.* 135, 3–17. doi: 10.1016/j.aquabot.2016.06.006

Shrestha, M., Acharya, S. C., and Shrestha, P. K. (2017). Bias correction of climate models for hydrological modelling—are simple methods still useful? *Meteorol. Appl.* 24, 531–539. doi: 10.1002/met.1655

Singh, L., and Saravanan, S. (2020). Impact of climate change on hydrology components using CORDEX South Asia climate model in Wunna, Bharathpuzha, and Mahanadi, India. *Environ. Monit. Assess.* 192:678. doi: 10.1007/s10661-020-08637-z

Sippel, E., Otto, F. E. L., Forkel, M., Allen, M. R., Guillod, B. P., Heimann, M., et al. (2016). A novel bias correction methodology for climate impact simulations. *Earth Syst. Dyn.* 7, 71–88. doi: 10.5194/esd-7-71-2016

Skamarock, W. C., Klemp, J. B., Dudhia, J., Gill, D. O., Barker, D. M., Duda, M. G., et al., (2008). *A Description of the Advanced Research WRF Version 3. NCAR Tech. Note NCAR/TN-475+STR.*

Somos-Valenzuela, M. A., and Palmer, R. N. (2018). Use of WRF-hydro over the Northeast of the US to estimate water budget tendencies in small watersheds. *Water* 819:1709. doi: 10.3390/w10121709

Spero, T. L., Nolte, C. G., Bowden, J. H., Mallard, M. S., and Herwehe, J. A. (2016). The impact of incongruous lake temperatures on regional climate extremes downscaled from the CMIP5 archive using the WRF model. *Journal of Climate*, 29, 839–853. doi: 10.1175/JCLI-D-15-0233.1

Spero, T. L., Nolte, C. G., Mallard, M. S., and Bowden, J. H. (2018). A maieutic exploration of nudging strategies for regional climate applications using the WRF model. *J. Appl. Meteorol. Climatol.* 57, 1883–1906. doi: 10.1175/JAMC-D-17-0360.1

Steinman, A. D., Ogdahl, M. E., Weinert, M., Thompson, K., Cooper, M. J., and Uzarksi, D. G. (2012). Water level fluctuation and sediment-water nutrient exchange in Great Lakes coastal wetlands. *J. Great Lakes Res.* 38, 766–775. doi: 10.1016/j.jglr.2012.09.020

Stocker, T. F., D., Qin, G.-K., Plattner, L. V., Alexander, S. K., Allen, N. L., et al. (2013). "Technical Summary. In: Climate Change 2013: The Physical Science Basis," in *Contribution of Working Group I to the Fifth Assessment Report of the Intergovernmental Panel on Climate Change*, eds T. F. Stocker, D. Qin, G.-K. Plattner, M. Tignor, S.K. Allen, J. Boschung, et al. (Cambridge, New York: Cambridge University Press).

Sun, X., Ren, G., You, Q., Ren, Y., Xu, W., Xue, X., et al. (2019). Global diurnal temperature range (DTR) changes since 1901. *Clim. Dyn.* 52, 3343–3356. doi: 10.1007/s00382-018-4329-6

Tewari, M., Chen, F., Wang, W., Dudhia, J., LeMone, M. A., Mitchell, K., et al. (2004). "Implementation and verification of the Unified NOAH Land Surface Model in the WRF Model," in *Twentieth Conference on Weather Analysis and Forecasting/16th Conference on Numerical Weather Prediction*.

Thorne, P. W., Donat, M. G., Dunn, R. J. H., Dunn, H., Williams, C. N., Alexander, L. V., et al. (2016). Reassessing changes in diurnal temperature range: intercomparison and evaluation of existing global data set estimates. *J. Geophys. Res.* 121, 5115–5137. doi: 10.1002/2015JD024584

Tiwari, S., Kar, S. C., and Bhatla, R. (2018). Mid-21st century projections of hydroclimate in Western Himalayas and Satluj River basin. *Glob. Planet. Change* 161, 10–27. doi: 10.1016/j.gloplacha.2017.10.013

U.S. Fish and Wildlife Service. (2018). Available online at: https://www.fws.gov/midwest/endangered/lists/michigan-spp.html (accessed, September 1, 2021)

Van Vuuren, D. P., Edmonds, J., Kainuma, M., Riahi, K., Thompson, A., Hubbard, K., et al., (2011). The representative concentration pathways: an overview. *Clim. Change* 109, 5–31. doi: 10.1007/s10584-011-0148-z

Vu, M. T., Raghavan, V. S., and Liong, S.-Y. (2015). Ensemble climate projection for hydro-meteorological drought over a river basin in Central Highland, Vietnam. *KSCE J. Civil Eng.* 19, 427–433. doi: 10.1007/s12205-015-0506-x

Wang, J., and Kotamarthi, V. R. (2015). High-resolution dynamically downscaled projections of precipitation in the mid and late 21st century over North America. *Earth's Future* 3, 268–288. doi: 10.1002/2015EF000304

Wang, L., Flanagan, D. C., Wang, Z., and Cherkauer, K. A. (2018). Climate change impacts on nutrient losses of two watersheds in the Great Lakes Region. *Water* 10:442. doi: 10.3390/w10040442

Wuebbles, D., Cardinale, B., Cherkauer, K., Davidson-Arnott, R., Hellmann, J., Infante, D., et al. (2019). *An assessment of the impacts of climate change on the Great Lakes*. Environmental Policy Law Center Report.

Xiao, C., Lofgren, B. M., Wang, J., and Chu, P. Y. (2016). Improving the lake scheme within a coupled WRF-lake model in the Laurentian Great Lakes. *J. Adv. Model. Earth Syst.* 8:717. doi: 10.1002/2016MS000717

Yin, D., Xue, Z. G., Gochis, D. J., Yu, W., Morales, M., and Rafieeinasab, A. (2020). A process-based, fully distributed soil erosion and sediment transport model for WRF-Hydro. *Water* 12:1840. doi: 10.3390/w12061840

Zhai, R., Tao, F., and Xu, Z. (2018). Spatial-temporal changes in runoff and terrestrial ecosystem water retention under 1.5 and 2C warming scenarios across China. *Earth System Dyn.* 9, 717–738. doi: 10.5194/esd-9-717-2018

Zhou, L. M., Dickinson, R. E., Dirmeyer, P., Dai, A., and Min, S. K. (2009). Spatiotemporal patterns of changes in maximum and minimum temperatures in multi-model simulations. *Geophys. Res. Lett.* 36:L02702. doi: 10.1029/2008GL036141

Conflict of Interest: The authors declare that the research was conducted in the absence of any commercial or financial relationships that could be construed as a potential conflict of interest.

Publisher's Note: All claims expressed in this article are solely those of the authors and do not necessarily represent those of their affiliated organizations, or those of the publisher, the editors and the reviewers. Any product that may be evaluated in this article, or claim that may be made by its manufacturer, is not guaranteed or endorsed by the publisher.

frontiers in Water

ORIGINAL RESEARCH
published: 24 December 2021
doi: 10.3389/frwa.2021.782847

Extreme Precipitation in the Great Lakes Region: Trend Estimation and Relation With Large-Scale Circulation and Humidity

Andrew Paxton[1], *Justin T. Schoof*[1]*, *Trent W. Ford*[2] *and Jonathan W. F. Remo*[1]

[1] School of Earth Systems and Sustainability, Southern Illinois University, Carbondale, IL, United States, [2] Illinois State Water Survey, University of Illinois, Champaign, IL, United States

Extreme precipitation contributes to widespread impacts in the U.S. Great Lakes region, ranging from agricultural losses to urban floods and associated infrastructure costs. Previous studies have reported historical increases in the frequency of extreme precipitation in the region and downscaled model projections indicate further changes as the climate system continues to warm. Here, we conduct trend analysis on the 5 km NOAA NClimDiv data for the U.S. Great Lakes region using both parametric (Ordinary Least Squares) and non-parametric methods (Theil-Sen/Mann-Kendall) and accounting for temporal autocorrelation and field significance to produce robust estimates of extreme precipitation frequency trends in the region. The approaches provide similar overall results and reflect an increase in extreme precipitation frequency in parts of the U.S. Great Lakes region. To relate the identified trends to large scale drivers, a bivariate self-organizing map (SOM) is constructed using standardized values of 500 hPa geo-potential height and 850 hPa specific humidity obtained from the ECMWF ERA-5 reanalysis. Using a Monte Carlo approach, we identify six SOM nodes that account for only 25.4% of all days, but 50.5% of extreme precipitation days. Composites of days with and without extreme precipitation for each node indicate that extreme events are associated with stronger features (height gradient and background humidity) than their non-extreme counterparts. The analysis also identifies a significant increase in the frequency of one SOM node often associated with extreme precipitation (accounting for 8.5% of all extreme precipitation days) and a significant increase in the frequency of extreme precipitation days relative to all days across the six extreme precipitation nodes collectively. Our results suggest that changes in atmospheric circulation and related moisture transport and convergence are major contributors to changes in extreme precipitation in the U.S. Great Lakes region.

Keywords: Great Lakes region, climate extremes, extreme precipitation, self-organizing maps, global change

OPEN ACCESS

Edited by:
Julie A. Winkler, Michigan State University, United States

Reviewed by:
Art DeGaetano, Cornell University, United States
Thomas Mote, University of Georgia, United States

***Correspondence:**
Justin T. Schoof
jschoof@siu.edu

Specialty section:
This article was submitted to Water and Climate, a section of the journal Frontiers in Water

Received: *24 September 2021*
Accepted: *06 December 2021*
Published: *24 December 2021*

Citation:
Paxton A, Schoof JT, Ford TW and Remo JWF (2021) Extreme Precipitation in the Great Lakes Region: Trend Estimation and Relation With Large-Scale Circulation and Humidity. Front. Water 3:782847. doi: 10.3389/frwa.2021.782847

INTRODUCTION

Extreme precipitation is associated with wide-reaching impacts in the Great Lakes region of the United States, including direct effects on localized and large-scale flooding (Winters et al., 2015), transportation and infrastructure (Angel et al., 2018) and agriculture, and many indirect effects, such as heightened risk of gastrointestinal illness (Drayna et al., 2010), impacts on disease vector

habitats, and overall water quality. Improved understanding of the changing nature and drivers of extreme precipitation is therefore critical for reducing the impacts of current and future climate impacts in the region.

Extreme precipitation events occur in the absence of enhanced radiative forcing from greenhouse gases, but there is also a theoretical expectation, and growing observational evidence, of an increase in precipitation extremes associated with anthropogenically-driven global warming (Allan and Soden, 2008). The Clausius-Clapeyron (C-C) relation indicates an ∼7% increase in saturation specific humidity per degree of warming under constant relative humidity. Because regional changes in extreme precipitation are determined not only by background humidity, but also by transport of atmospheric moisture to regions of convergence, local, and regional changes in extreme precipitation can differ substantially from the expected C-C scaling (Lenderink and Van Meijgaard, 2010), especially for the most extreme precipitation values and at the shortest time scales (Pendergrass, 2018).

Multi-decadal climate projections from ensembles of climate models indicate further increases in extreme precipitation over most land areas (IPCC, 2021) as the atmospheric continues to warm. Regional studies conducted with multiple generations of climate models, statistical and dynamical downscaling approaches, and mid- and late-century time horizons have similarly pointed to more frequent and intense precipitation events in the region under additional global and regional warming (Pryor et al., 2013; D'orgeville et al., 2014; Byun and Hamlet, 2018; Zhang et al., 2019).

The nature of historical and potential future changes in extreme precipitation in the U.S. Great Lakes region, as well as their drivers, need to be well-understood so that appropriate mitigation and adaptation strategies can be identified and implemented. Precipitation extremes results from processes occurring across spatial scales, ranging from the micro-scale to the upper end of the mesoscale (sometimes referred to as synoptic scale) (Orlanski, 1975). There is growing interest in identifying the mesoscale and synoptic scale conditions associated with events (Barlow et al., 2019), including those occurring at the regional scale (e.g., the Northeast USA by Agel et al., 2018). As noted by Barlow et al. (2019), the synoptic scale is particularly critical for understanding extreme precipitation events as synoptic scale processes are (1) important for producing extreme precipitation events, (2) associated with some medium-range predictability, and (3) resolved in both weather and climate models.

To contribute to a better understanding of changes in extreme precipitation in the U.S. Great Lakes region, we first conduct a historical trend analysis of daily extreme precipitation events identified using a peaks-over-threshold framework [section Bivariate Synoptic Classification Using the Self-Organizing Map (SOM)]. The trend analysis includes both parametric and non-parametric trend estimation techniques that account for temporal autocorrelation in the time series and field significance. We then develop a bivariate synoptic classification by applying the self-organizing map (SOM) technique (section Linking SOM Nodes and Regional Precipitation Extremes) to synoptic scale atmospheric circulation and humidity fields. Finally, we investigate relationships between trends in precipitation extremes and their associated synoptic patterns.

STUDY REGION AND DATA

Study Region

The study region is defined as the states bordering the Laurentian Great Lakes, plus Iowa which is mostly contained within the convex hull of the lake-border states. The region therefore includes Illinois, Indiana, Iowa, Michigan, Minnesota, New York, Ohio, Pennsylvania, and Wisconsin (**Figure 1**) and includes parts of the drainage basin for the Great Lakes, but also for the Mississippi and Ohio Rivers. The general pattern of annual precipitation is characterized by a decreasing amounts from southeast to northwest (Pryor et al., 2013), driven primarily by variations in winter precipitation. Extreme precipitation has widespread impacts in the region, including those on agriculture, natural ecosystems, urban systems, and water quality, among others (Wuebbles et al., 2019).

Data

Precipitation Data

Our analysis of extreme precipitation is based on daily precipitation data from NOAAs NClimDiv data set (Vose et al., 2014), a 5 km resolution gridded temperature and precipitation product derived *via* climatologically aided interpolation (CAI; Willmott and Robeson, 1995) of station data from the daily Historical Climatological Network (HCN-D; Menne et al., 2012). Relative to previous divisional data sets, NClimDiv includes a larger number of stations, additional quality assurance tests, and bias adjustments for changes in observation technique as described in Vose et al. (2014). Daily precipitation grids are available from 1951 to present for the contiguous United States. The 5 km NClimDiv grid used in this study covers the labeled states shown in **Figure 1**.

Because NClimDiv is derived from interpolation of available station data, the product is spatially and serially complete. While NClimDiv does not provide information regarding sub-daily precipitation extremes, the consistent long-term perspective it provides regarding daily precipitation extremes is valuable for understanding regional changes in extreme precipitation over time. Additional details about the NClimDiv data set, including identification of extreme precipitation events is provided in section Precipitation Extremes.

Reanalysis Data

To characterize the synoptic environment as it relates to extreme precipitation events, we used the European Center for Medium-Range Weather Forecasts (ECMWF) ERA5 reanalysis (Hersbach et al., 2020). ERA5 represents an improvement over previous reanalysis products as a result of improved model accuracy and data assimilation techniques, resulting in more accurate estimates and at higher resolution. ERA5 currently provides global, hourly estimates of atmospheric and land surface variables at a resolution of 0.25° for pressure levels ranging for 1–1,000 hPa starting in 1979, with a plan to ultimately extend the analysis back

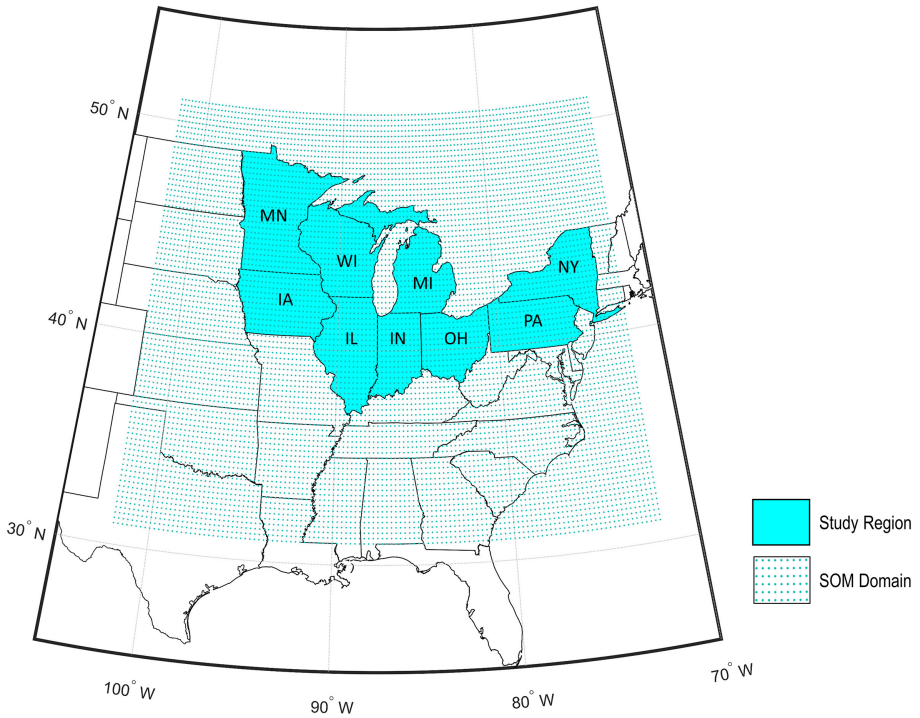

FIGURE 1 | Map showing Great Lakes region used for analysis of extreme precipitation and the ERA5 0.25° grid used for the synoptic classification using self-organizing map (SOM) algorithm.

to 1950. Our analysis of both precipitation extremes and their corresponding synoptic-scale patterns therefore starts in 1979 and ends in 2019.

Reanalysis data should be used cautiously in areas with sparse data. Because upper air conditions in the central and eastern United States are regularly observed using radiosondes, and these measurements are assimilated by ERA5, the reanalysis outputs should provide an excellent representation of the upper air conditions in the region. With high spatial resolution and spatial and serial completeness, ERA5 is ideal for investigating synoptic scale circulation variability and links with the surface extreme precipitation record. Previous studies (Junker et al., 1999; Schumacher and Johnson, 2005, 2006; Tryhorn and Degaetano, 2011; Kunkel et al., 2013; Nasri et al., 2016) have established that synoptic scale drivers of extreme precipitation include measures of circulation and atmospheric humidity. We therefore use 500-hPa geo-potential height to reflect circulation and 850-hPa specific humidity to characterize moisture availability. The ERA5 grid point used in this study are shown in **Figure 1**. For this application, the hourly ERA5 outputs were used to compute daily averages for use with the daily precipitation data described in section Precipitation Data.

METHODS

Our research design includes several types of analysis designed to meet the stated research objectives. First, we define our extreme precipitation metric and explore the climatology of extreme precipitation events in the U.S. Great Lakes region, including a detailed analysis of trends in extreme event frequency. Second, we classify regional circulation and humidity data in a bivariate synoptic classification to investigate large-scale drivers of extreme precipitation. Finally, we examine changes in extreme precipitation through the lens of the resulting synoptic classes.

Precipitation Extremes

Identification of Precipitation Extremes

Extreme values in climate science have been traditionally investigated using either a block maximum approach, in which the maximum value from each time block is identified and then the collection of block maxima are studied, or by the peaks-over-threshold approach, in which exceedances of a pre-specified threshold are counted and explored. We chose to use the peaks-over-threshold to ensure that no extreme events were discarded, following Acero et al. (2011). An additional subjective decision is the choice of an absolute or relative threshold. Because extreme precipitation magnitude varies across the region, a relative threshold is used. Specifically, for each grid point in NClimDiv, the threshold applied is the magnitude of precipitation associated with a 1-year recurrence interval based on a partial duration series (PDS, see Bonnin et al., 2005). Since the record of study is 1979–2019 (41 years), this value is determined by ranking the daily precipitation values across all years from largest to smallest and identifying the 41st ordered value. We then use this threshold value with the daily NClimDiv data to compute the number of exceedances per year from at each grid point in the region.

Extreme Precipitation Trend Analysis

Changes in extreme precipitation in the U.S. Great Lakes region are quantified by applying trend analysis to the extreme precipitation counts from the analysis of precipitation extremes. Because ordinary least squares (OLS) regression is sensitive to outliers and extreme values at the series endpoints, we follow previous studies that have considered both parametric and non-parametric approaches (Huth and Pokorna, 2004; Asadieh and Krakauer, 2015). The non-parametric technique adopted is Theil-Sen estimation (Sen, 1968), which is equivalent to median-of-pairwise slopes regression (see Lanzante, 1996). Both approaches have advantages and disadvantage. Despite sensitivity to outliers, OLS regression is powerful approach for estimating trends and assessing their differences from 0. In OLS, the trend magnitude and statistical significance are determined simultaneously. In the non-parametric technique, a Mann-Kendall test (Kendall, 1975) is used to assess the statistical significance of the monotonic trend estimated by the Theil-Sen approach. Both techniques are applied with a significance level of 0.1 ($\alpha = 0.1$) under the null hypothesis that there is no trend in the frequency of extreme precipitation events exceeding the magnitude associated with a 1-year recurrence interval. Rejection of the null hypothesis implies the existence of a monotonic trend.

The significance of a temporal trend in a time series can be inflated (deflated) in the presence of positive (negative) autocorrelation. Although our times series of frequencies of threshold exceedances are likely to be less persistent that the original daily series that they are derived from, they may still contain autocorrelation associated with persistence of large-scale modes of climate variability. Rather than assuming independence, modifications to the trend estimation technique can be implemented to better assess the trend significance (Santer et al., 2000; Yue and Wang, 2004). The modification is an adjustment on the sample variance. In both parametric and non-parametric techniques, this is a correction factor based on the effective sample size. That is,

$$S^* = S \cdot \frac{n}{n^*} \tag{1}$$

where S is the sample variance, n is the sample size, and n^* is the effective sample size, which is a function of the autocorrelation present in the time series. Because the trend can contaminate the estimate of sample autocorrelation, the estimate is based on the detrended time series. Here, the trend is removed by subtracting the product of the estimated trend (θ) and the position of that year within the time series from each year. In particular,

$$x_i{}^* = x_i - \theta \cdot (i-1)\,,\ i = 1, 2, \ldots, 41. \tag{2}$$

The lag-1 autocorrelation (ρ) is then determined from the detrended time series and the effective sample size is given by:

$$n^* = \frac{1-\rho}{1+\rho}. \tag{3}$$

With a positive autocorrelation, the effective sample size is smaller than n, which increases the variance of the test statistic, leading to a failure to reject the null hypothesis when a naïve test may have found the presence of a significant trend. On the other hand, the presence of negative autocorrelation in the time series increases the effective sample size, decreasing the test statistic variance, and can therefore either sustain already significant grid points or bring the non-significant points past the threshold needed to reject the null hypothesis.

We assess the significance of the parametrically- and non-parametrically-derived trends at the local level. However, with such a large number of tests conducted, there is an increased chance of identifying a significant result by chance when it does not truly exist. To avoid these issues, Wilks (2006, 2016) recommend the use of the false discovery rate criterion (FDR). In this meta-test, a maximum number of significant points are determined such that a global test of significance at all local points is met. In this case, the FDR procedure is used to evaluate the field significance of trends in precipitation days per year with $\alpha_{global} = 0.2$ (see Wilks, 2006 for details). First, the p-values of each local hypothesis test result are ordered from the lowest to the highest ($p_1, p_2, \ldots, p_n$) and compared to the corresponding value (i/N)*α_{global}. The maximum significant p-value is largest of the n p-values that satisfies the inequality:

$$p_i \ \leq (i/N)\alpha_{global} \tag{4}$$

Once this threshold is obtained, grid points with a lower p-value ($p_1, p_2, \ldots, p_i$) are designated as significant trends having satisfied the global meta-test.

Bivariate Synoptic Classification Using the Self-Organizing Map (SOM)

While several approaches exist for classification of atmospheric patterns, the self-organizing map, or SOM (Kohonen, 1998) has emerged as a leading approach in synoptic climatology. The SOM algorithm distributes a designated number of nodes across the multidimensional input space and sequentially moves each node toward the best matching input data based on a set learning rate and a predetermined number of iterations. The result is a two-dimensional map of nodes representative of the continuum of the input data (Hewitson and Crane, 2002; Sheridan and Lee, 2011). The SOM technique is also selected for its demonstrated skill in feature extraction and the interpretability of a map space (Liu et al., 2006; Agel et al., 2018).

Prior to classification with the SOM algorithm, several data preprocessing steps were necessary. First, the hourly ERA5 outputs of 500-hPa geo-potential height and 850-hPa specific humidity were aggregated to daily averages, producing 14,975 daily grids for the 1979–2019 study period. SOM results can be sensitive to the choice of spatial domain. We opted for a domain that closely corresponds to the Great Lakes region (**Figure 1**) to reduce the variability with the goal of better representation of rare patterns (Gibson et al., 2017), but with some additional grid points to the South and West, the predominant direction for approaching weather systems. Finally, to consider both geo-potential height and specific humidity, which differ by several orders of magnitude, each variable was standardized by subtracting the mean and dividing by the standard deviation.

This standardization is applied to each day in the sample on the basis of calendar year means and standard deviations. This allows for equal weighting in the classification process, as both geo-potential height and specific humidity input data will have a mean of 0 and a standard deviation of 1. The data presented to the SOM are therefore the daily standardized values of 500-hPa geo-potential height and 850-hPa specific humidity at each of the 9,801 ERA5 grid points in the region on each of the 14,975 days, producing a 19,602 × 14,975 input array.

There are a number of additional subjective decisions required for SOM-based classifications. Among these is the desired size (number of nodes) in the resulting SOM space. Given the relative rarity of the events of interest (precipitation extremes exceeding the value associated with a 1-year recurrence interval), the SOM dimensions must be sufficiently large to isolate the large-scale signal associated with extremes. We investigated SOM architectures ranging from 4 to 45 nodes in various configurations and used two approaches to assess the viability of the SOM and find a balance of within-type and between-type variability. Specifically, we used the root-mean-square error (between a sample grid and its representative node) and Sammon mapping of the resulting SOM nodes to justify our selection following (Jiang et al., 2015). The difference between the sample grid and its representative node decreases as map size increases, whereas smaller node numbers contribute to a more cohesive mapping pattern across space. Using these approaches, we converged on a 20 node (5 × 4) SOM solution. Given the SOM size, the learning rate and number of iterations are also parameters that influence the result of the mapping algorithm. Defaulting to recommendations of the software (Matlab's Deep Learning Toolbox), the initial learning rate in this instance was set to 4. The number of iterations was then set to 1,000 to ensure the success of the training while minimizing the computation time of the algorithm.

Linking SOM Nodes and Regional Precipitation Extremes

The output of the SOM algorithm includes the centroid for each node, a distance matrix relating the node centroids, and an index of the closest node for each of the 14,975 daily ERA5 grids. These outputs allow the construction of a synoptic catalog in which each day is assigned to one node of the SOM, which can then be considered in the context of the extreme precipitation climatology. To this end, we establish a framework for connecting the large-scale meteorological patterns with the established extreme precipitation climatology by identifying the nodes most associated with extreme precipitation. We classify a day as an extreme precipitation day if at least 1% of the 81972.5km NClimDiv grid points in the region exceeds its threshold.

Once we have identified the extreme precipitation days belonging to each node, we conduct a Monte Carlo experiment to determine which nodes are associated with a greater than expected number of extreme precipitation days, following Agel et al. (2018). For each node, a random sample of days equal to the number of days within the node are selected and the number of extreme precipitation days in the random sample are noted.

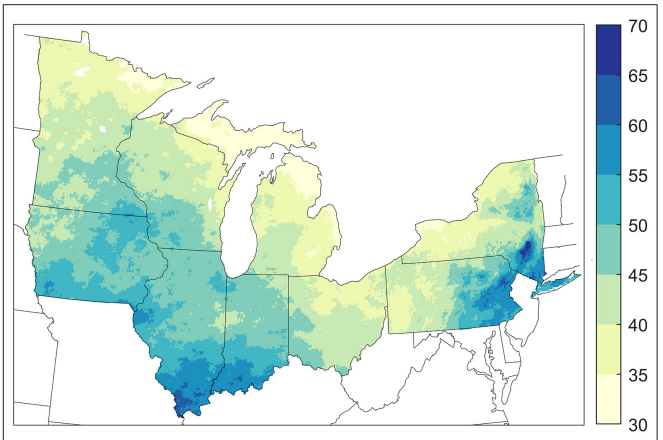

FIGURE 2 | Map of the study region showing the threshold used for identification of extreme precipitation days (the magnitude of the daily precipitation associated with a 1-year recurrence interval (mm).

Resampling 1,000 times establishes a distribution for the expected number of extreme precipitation days corresponding to a specific node size. A node is then established as a node associated with extreme precipitation, and thus classified as an "extreme node," if the number of extreme days associated with the node exceeds the 97.5th percentile of the resulting distribution.

Further analysis places these extreme nodes in the context of the entire SOM space and explores changes in node occurrence over time. First, the days belonging to each extreme node are separated into sets representing extreme and non-extreme days. Composites of these sets denote the differences in structure and magnitude due to internode variability and illustrate the characteristics of weather types favorable for extreme precipitation. After examining the structure of the extreme nodes, trend analysis is conducted to better understand the frequency of occurrence of extreme nodes over time, with the trend estimated by the Theil-Sen approach and the significance of the trend is assessed using a Mann-Kendall test.

RESULTS

Extreme Precipitation Climatology and Trends

The threshold used to identify extreme precipitation days (the value associated with a 1-year recurrence interval) exhibits considerable spatial variability across the U.S. Great Lakes region (**Figure 2**). There is a general south to north gradient with the largest values, ∼70 mm/day, occurring in southeastern NY and southern IL. The lowest values of the precipitation magnitude associated with a 1-year recurrence interval, around 35 mm/day, occur in the northern parts of MI and MN. The average value over all NClimDiv grid points in the region is 44.2 mm/day.

Our examination of precipitation extremes is based on a trend analysis designed to identify changes in Great Lakes extreme precipitation frequency over time. As described in section Extreme Precipitation Trend Analysis, our trend analysis

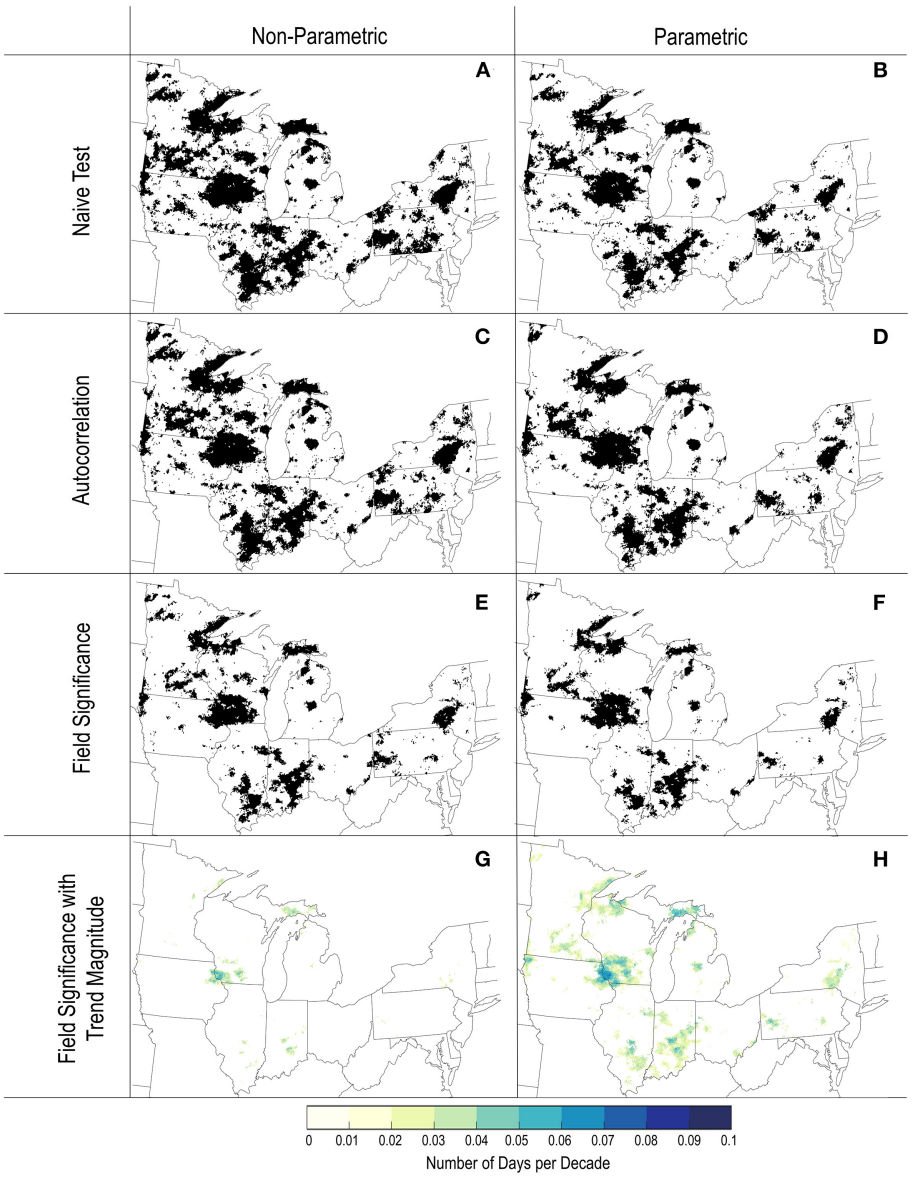

FIGURE 3 | Results of trend analysis for extreme precipitation frequency in the Great Lakes region. The points shown reflect grid points with significant trends for the Theil-Sen/Mann-Kendall non-parametric approach (left column) and OLS parametric approach (right column). The rows show the trends from the naïve approach (first row, **A,B**) and after accounting for temporal autocorrelation (second row, **C,D**), and field significance (third row, **E,F**). The trend magnitude at points identified as field significant are shown in the fourth row **(G,H)**.

includes both parametric (OLS) and non-parametric (Theil-Sen/Mann-Kendall) approaches for trend fitting and assessment of statistical significance. In both cases, additional considerations are made to account for autocorrelation in the time series and test multiplicity, and we draw additional comparisons between the parametric and non-parametric approaches at each step in the analysis. The non-parametric approach sometimes leads to a counterintuitive result when applied to time series containing many zeros (such as a time series of extreme event counts). Specifically, it is possible that the slope value will be 0, but the Mann-Kendall test will indicate significance. We therefore present our initial results only in terms of trend significance (binary) and discuss trend magnitude only for our final trend analysis results.

Significant trends in extreme precipitation frequency identified by the naïve Theil-Sen/Mann-Kendall and OLS approaches are shown in **Figures 3A,B**, respectively. Both approaches identify a large number of grid points in the U.S. Great Lakes region exhibiting significant trends (**Figure 3**, **Table 1**). The maps show strong qualitative similarity, with a slightly larger number of significant trends identified by the Theil-Sen/Mann-Kendall relative to OLS. Despite the greater

TABLE 1 | Summary of trend analysis.

	Theil-Sen/Mann-Kendall	Ordinary least squares (OLS)	Either	Both
Standard test	25,044 (31.4%)	18,363 (23.0%)	25,607 (32.1%)	17,800 (22.3%)
Accounting for temporal autocorrelation	23,328 (29.3%)	18,380 (23.1%)	25,145 (31.5%)	16,563 (20.8%)
Accounting for temporal autocorrelation and field significance	12,773 (16.0%)	10,799 (13.6%)	14,241 (17.9%)	9,331 (11.7%)

Table entries show the number of Great Lakes region NClimDiv grid cells (out of 79,679) for which computed trends were statistically significant ($\alpha = 0.1$). Results are shown for the standard test (top row), after accounting for temporal autocorrelation (middle row), and after also accounting for field significance (bottom row). The columns show the results from the non-parametric Theil-Sen/Mann-Kendall method and the parametric Ordinary Least Squares method. The final two columns reflect the level of agreement between the results, indicating how may grid points exhibit statistically significant trends using either method and both methods.

extent of significant trends from the Theil-Sen/Mann-Kendall approach, the region of significance overlaps well. A total of 25,607 out of 79,679, or 32.1% of points within the region, are identified as having significant trends by either approach with 69.5% of these 25,607 points identified as having significant trends by both approaches. Spatially, the locations with significant extreme precipitation frequency trends are scattered in clusters across the region but tend to be more widespread in the western portion.

To account for temporal autocorrelation in the time series, modified tests, which alter the sample variance based on the lag-1 autocorrelation, were conducted. As described in section Extreme Precipitation Trend Analysis, this correction is needed because an autocorrelated series violates the assumption that time series values are independent. The most common outcome is that significance is reduced by the presence of positive autocorrelation. However, in cases where the autocorrelation is negative, the effective sample size can be larger than the actual sample size. This can lead to points that were previously below the significance threshold becoming significant. Autocorrelation in our extreme precipitation time series (not shown) is highly variable over space and does not exhibit a clear spatial pattern. For the Theil-Sen/Mann-Kendall approach, accounting for autocorrelation reduced the number of points with significant trends in extreme precipitation frequency slightly (cf. **Figures 3A,C**, **Table 1**). The modified OLS approach, on the hand, led to virtually no change in the number of significant grid points (cf. **Figures 3B,D**, **Table 1**). In both cases, the maps before and after accounting for autocorrelation are qualitatively and quantitatively similar and agreement between the non-parametric and parametric approaches remains strong. A total of 25,145 grid points (31.5%) exhibit significant extreme precipitation frequency trends according to either approach and 65.9% of these points have significant trends under both approaches after accounting for autocorrelation.

When conducting a large number of hypothesis tests, there is potential for rejecting a substantial number of hypothesis incorrectly by chance or due to spatial autocorrelation. Consideration of field significance addresses these issues by using the false discovery rate (FDR) criterion. As described in section Extreme Precipitation Trend Analysis, for each approach, the number of field significant points is determined by ordering the p-values of the local tests and identifying their intersection with the false discovery rate threshold. Any grid point where the p-value is lower than the p-value at this intersection is said to have a regionally significant trend. For both the non-parametric and parametric approaches, accounting for field significance decreases the spatial extent of significant trends in extreme precipitation frequency (**Figures 3E,F**). For the Theil-Sen/Mann-Kendall approach, the ordered p-value curve intersects the FDR threshold at a p-value of 0.0328, so that 12,773 grid points in the region meet field significance criteria (i.e., those with $p < 0.0328$). In the OLS approach, the ordered p-value curve intersects the FDR threshold at a p-value of 0.0271, yielding 10,799 points meeting field significance criteria. Although accounting for field significance reduced the overall extent of significant trends in extreme precipitation frequency, there is still relatively strong agreement between the approaches with 65.5% of points with a significant result from either approach have a significant result from both approaches.

After accounting for both autocorrelation and field significance, we are left with considerable parts of the U.S. Great Lakes region exhibiting significant trends in extreme precipitation frequency regardless of the methodological approach used for trend analysis.

The magnitude of the estimated trends in extreme precipitation frequency is shown in **Figures 3G,H**. The greater spatial extent of the OLS-derived trends relative to those derived from the Theil-Sen/Mann-Kendall approach is related to the presence of significant trends with no magnitude, resulting from separately assessing the slope magnitude (Theil-Sen) and significance (Mann-Kendall) within this approach. As noted, this results from the time series being characterized by a relatively high proportion of zeros so that the median of pairwise slopes using in the Theil-Sen estimator is zero. Because of this, only a fraction (1,694 of 12,773, or 13.3%) of points with significant trends according to the Mann-Kendall test have a non-zero Theil-Sen slope estimate. These points are located primarily in a block along the Illinois-Iowa border, with some smaller regions of significance scattered in other parts of the domain. The average magnitude of significant non-zero trends is 0.328 days per decade, ranging from 0.125 to 0.556 days per decade. In the OLS approach, the trend magnitude and significance are more directly connected, so that any grid point found to be significant will have a non-zero slope. For the 10,799 points identified as having a significant trend in extreme precipitation frequency, the resulting trends varied from 0.085 to 0.706 days per decade, with an average of 0.324 days per decade.

Despite the differences resulting from the tendency of the Theil-Sen/Mann-Kendall approach to produce significant

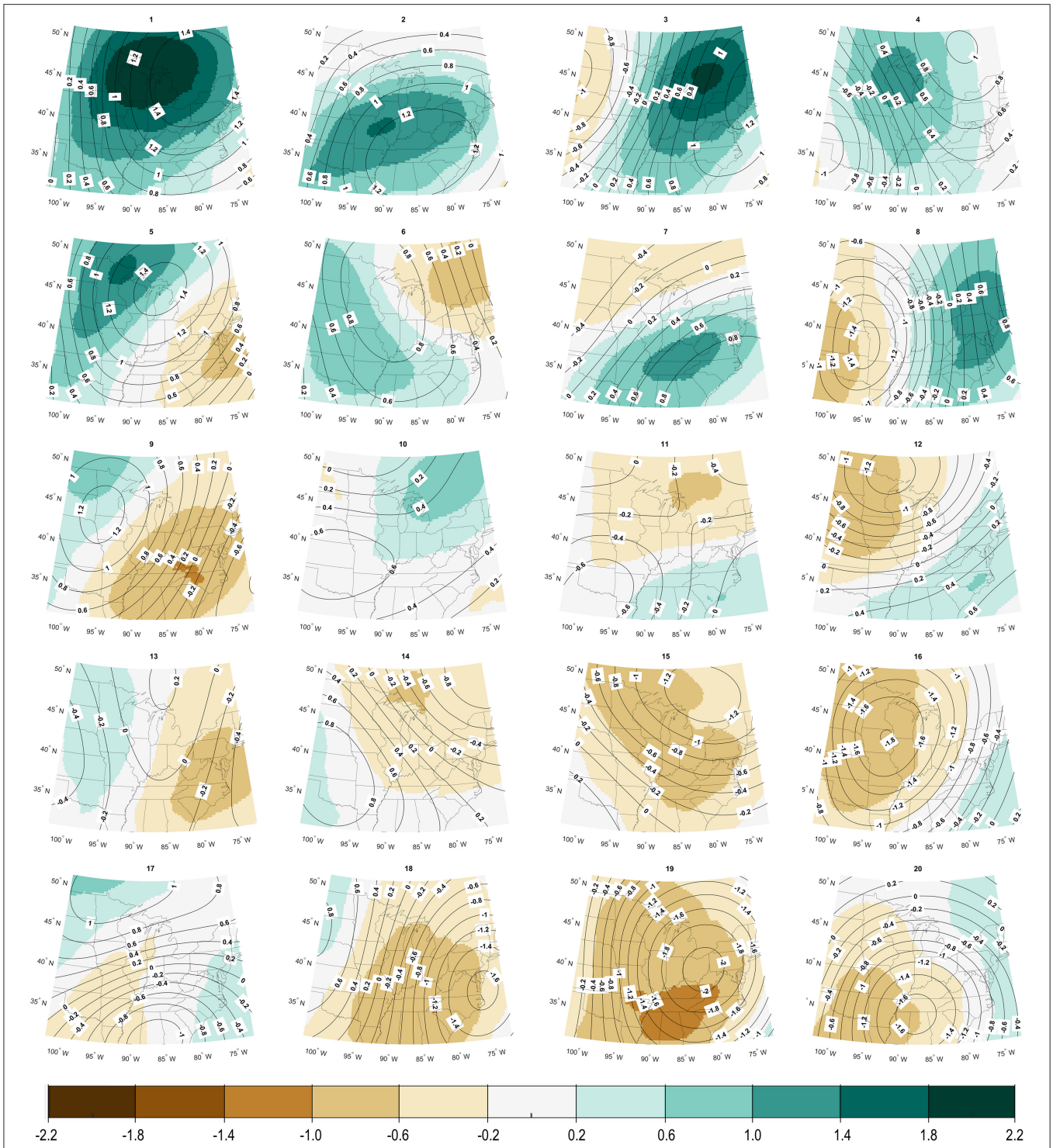

FIGURE 4 | The 20-node (5 × 4) SOM solution showing standardized anomalies of 500 hPa geo-potential height (black contours) and 850 hPa specific humidity (shaded in color). Nodes are numbered 1–20 for reference within text.

trends without magnitude, both parametric and non-parametric approaches indicate positive trends in the number of extreme precipitation days in the region, with strikingly similar location and magnitude. Overall, the clear indication from our trend analysis is that extreme precipitation frequency is increasing in the region, even when applying conservative approaches

to account for temporal and spatial autocorrelation and test multiplicity. These robust changes can now be explored in the context of the large-scale climate influencing the region.

Weather Type Classification

To better understand the large-scale circulation and humidity regimes associated with extreme precipitation in the U.S. Great Lakes region, we applied a bivariate self-organizing map (SOM) to 500 hPa geo-potential height and 850 hPa specific humidity as described in section Bivariate Synoptic Classification Using the Self-Organizing Map (SOM). Following experimentation with the SOM architecture, we developed a 20-node (5 × 4) solution, which is displayed in **Figure 4**. The right-hand side of the SOM is largely characterized by patterns with negative height anomalies over the western (top rows), central or eastern (bottom rows) parts of the region. Conversely, the left side of the SOM space is characterized by generally characterized by positive height anomalies over the central and western parts of the region. In terms of 850 hPa specific humidity, nodes with positive anomalies tend to be clustered along the top of the SOM space with drier patterns along the bottom of the SOM space. Considering both variables together, the SOM allows for identification of patterns that couple high values of humidity with strong height gradients, leading the moisture transport into the study region (e.g., Node 3).

To determine the association between the SOM nodes and the extreme precipitation days, we first computed the distribution of total days by node and extreme precipitation days by node (**Table 2**). The SOM classifies the original 14,975 days into 20 nodes ranging in size from 405 days (2.70%, Node 1) to 965 days (6.44%, Node 18). Using the criteria in section Linking SOM Nodes and Regional Precipitation Extremes, we identified a total of 1,024 extreme precipitation days. The share of these days belonging to each node is also shown in **Table 2** and ranges from just 15 days (1.46%, Nodes 9, 15, and 18) to 123 days (12.01%, Node 3). To identify nodes that are associated with a higher-than-expected share of extreme precipitation days, we apply a Monte Carlo approach (see section Linking SOM Nodes and Regional Precipitation Extremes), which identifies six nodes: 1, 2, 3, 4, 7, and 8, that account for 517 (50.5%) of the extreme precipitation days. More than half of the extreme precipitation days correspond to just 30% of the nodes that collectively represent 25.4% of all days.

Structurally, the nodes associated with extreme precipitation belong to the top portion of the SOM space and therefore have some common physical characteristics, including high standardized values of specific humidity across the domain. Aside from the nodes with the highest average specific humidity anomalies (1 and 2), the remaining nodes associated with extreme precipitation are characterized by high specific humidity anomalies and a geo-potential height gradient across the region with the lowest heights anomalies toward the west. This configuration leads to moisture transport into the region and may be reflective of mesoscale convective systems and/or frontal systems, which account for a large majority of the extreme precipitation events in the Central US (Schumacher and Johnson, 2005; Kunkel et al., 2012). While a majority of extreme precipitation days fall into the six extreme patterns, just 13.6% of the days within those patterns are classified as extreme, reflecting within-node variability. We therefore considered differences between non-extreme precipitation days and extreme precipitation days within each node using compositing. **Figure 5** displays each extreme node, along with composites of the non-extreme and extreme precipitation days for that pattern. In each case, we found that the overall structure of the pattern in the node (i.e., the location of height/humidity extrema) does not differ between extreme and non-extreme days. However, we often identified a stark difference in the magnitude of those extrema. For each extreme precipitation node, extreme precipitation days are characterized by stronger 500 hPa geo-potential height gradients and similar or larger 850 hPa specific humidity anomalies (**Figure 5**).

Examination of these specific nodes also reflects their association with extreme precipitation frequency across the U.S. Great Lakes region (**Figure 5**). As expected, for each node, the areas with the greatest extreme event frequency are located directly east of the negative geo-potential height center and near the area of positive specific humidity. Nodes 1 and 4 tend to produce extreme precipitation in the north-west part of the region, while Nodes 2, 3, and 7 produce extreme precipitation in the west-central part of the region, and Node 8 produces extreme precipitation in the east-central part of the region. Although (Schumacher and Johnson, 2005) use a much higher extreme precipitation threshold (the precipitation amount associated with the 50-year recurrence interval), our extreme nodes reflect some of the processes described in their work. For example, the circulation and humidity patterns characterized by Node 2 and Node 7 are consistent with the east-west orientation of the training line/adjoining stratiform (TL/AS) type of mesoscale convective system identified in their study. While a full analysis of node transitions is beyond our scope, we did assess the

TABLE 2 | (a) Frequency of occurrence for each SOM node (out of 14,975) and (b) frequency of occurrence of extreme precipitation days for each SOM node (out of 1,024).

(a)			
All days			
405 (2.70%)	631 (4.21%)	561 (3.75%)	706 (4.71%)
706 (4.71%)	812 (5.42%)	815 (5.44%)	683 (4.56%)
803 (5.36%)	874 (5.84%)	816 (5.45%)	807 (5.39%)
905 (6.04%)	926 (6.18%)	952 (6.36%)	680 (4.54%)
615 (4.11%)	965 (6.44%)	607 (4.05%)	706 (4.71%)
(b)			
Extreme precipitation days			
42 (4.10%)	87 (8.50%)	123 (12.01%)	71 (6.93%)
47 (4.59%)	57 (5.57%)	100 (9.77%)	94 (9.18%)
15 (1.46%)	56 (5.47%)	36 (3.52%)	61 (5.96%)
44 (4.30%)	18 (1.76%)	15 (1.46%)	39 (3.81%)
32 (3.13%)	15 (1.46%)	17 (1.66%)	55 (5.37%)

*Each table entry contains the number of occurrences and percentage [of all days in (a), of extreme precipitation days in (b)] corresponding to the same position in the 5 × 4 SOM (**Figure 3**).*

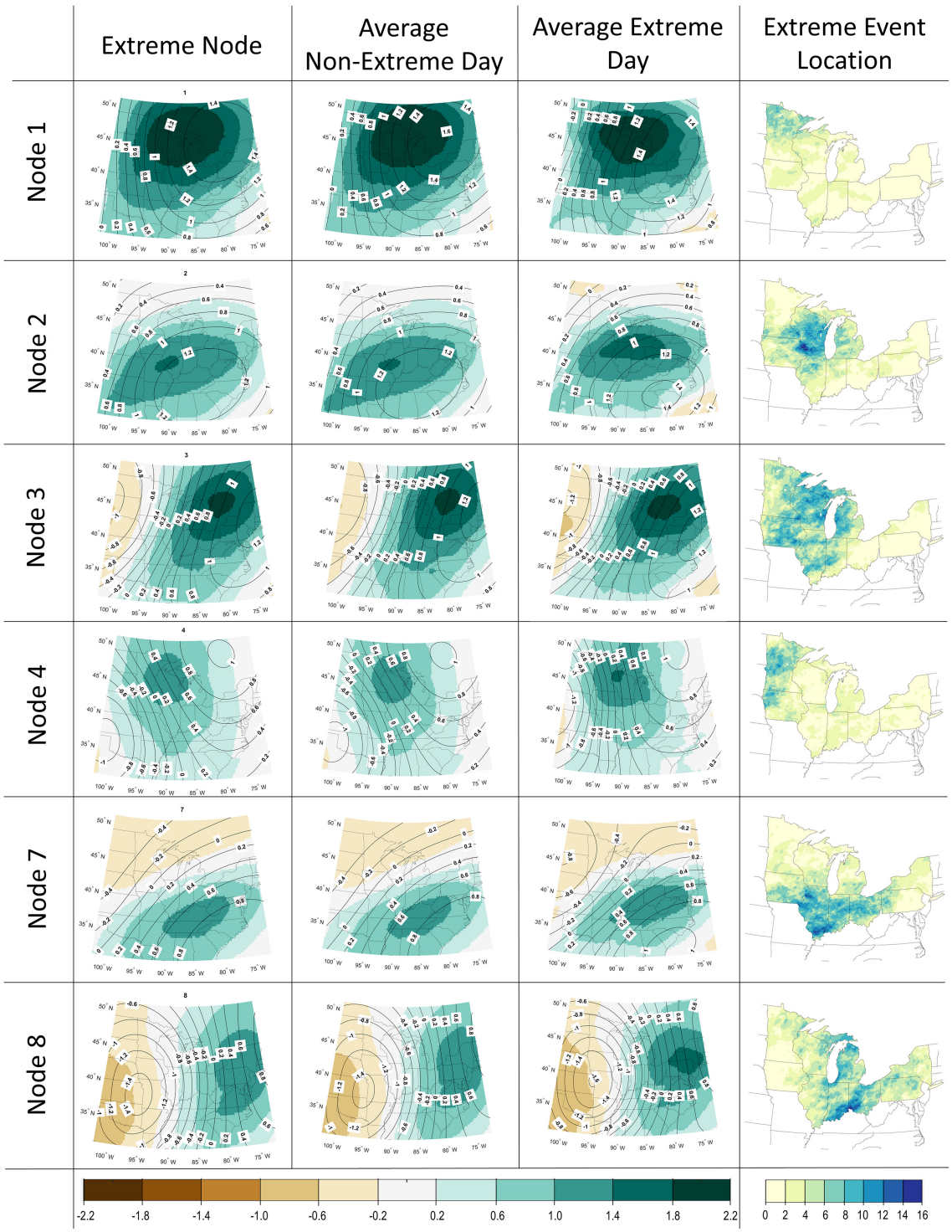

FIGURE 5 | SOM nodes associated with extreme precipitation in the Great Lakes region. For each of the six nodes, the figure shows the original SOM node from **Figure 4** (1st column), the composite pattern of days without extreme precipitation (2nd column), the composite pattern of days with extreme precipitation (3rd column), and the location of extreme precipitation associated with the SOM node events within the region, defined as the frequency of extreme precipitation at each NClimDiv grid cell on days belonging to the SOM node (4th column).

TABLE 3 | Seasonal characteristics of SOM nodes associated with extreme precipitation.

	DJF	MAM	JJA	SON	ANN
Node 1	7/129 (5.4%)	12/145 (8.3%)	15/56 (26.8%)	8/75 (10.7%)	42/405 (10.4%)
Node 2	2/145 (1.4%)	18/161 (11.2%)	38/161 (23.6%)	29/164 (17.7%)	87/631 (13.8%)
Node 3	6/123 (4.9%)	21/129 (16.3%)	52/151 (34.4%)	44/158 (27.9%)	123/561 (21.9%)
Node 4	0/168 (0.0%)	9/160 (5.6%)	34/183 (18.6%)	28/195 (14.4%)	71/706 (10.1%)
Node 7	10/205 (4.9%)	21/210 (10.0%)	51/229 (22.3%)	18/171 (10.5%)	100/815 (12.3%)
Node 8	14/178 (7.9%)	16/172 (9.3%)	17/115 (14.8%)	47/218 (21.6%)	94/683 (13.8%)
All extreme nodes	39/948 (4.1%)	97/977 (9.9%)	207/895 (23.1%)	174/981 (17.7%)	517/3,801 (13.6%)

For each node and season (and for the full year), each entry shows the number of extreme precipitation days relative to the total number of occurrences and the resulting season- and node-specific frequency of extreme precipitation days.

TABLE 4 | Summary of trend analysis on SOM nodes associated with extreme precipitation days.

	All days		Extreme precipitation days	
	Trend (days/decade)	*P*-value	Trend (days/decade)	*P*-value
Node 1	0.00	0.76	0.00	0.46
Node 2	**2.91**	**<0.01**	**0.48**	**0.02**
Node 3	0.91	0.09	0.00	0.29
Node 4	**−1.88**	**0.03**	0.00	0.36
Node 7	2.00	0.07	0.26	0.15
Node 8	–0.71	0.36	0.00	0.38
All Extreme Nodes	4.43	0.08	**1.27**	**0.03**

Trends (days/decade) and their associated p-values are shown for all days within the node and for days associated with extreme precipitation. Entries that are significant (with $\alpha = 0.05$) are in bold.

persistence of each node by examining the days preceding and following and extreme precipitation day. Nodes 2 and 7 were the most persistent nodes consistent with a stationary east-west moisture maximum across the region. Nodes 3 and 8, on the other hand, are the least persistent and are likely to be associated with faster moving synoptic systems and their associated fronts.

Extreme precipitation in the region exhibits notable seasonal variability which is evident in the seasonal frequencies of the associated SOM nodes. While the six specific nodes highlighted in **Figure 5** occur approximately evenly across the seasons, 40.0% of the extreme precipitation events (207 of 517 events) occur during the summer and 33.6% (174 of 517 events) occur during the autumn (**Table 3**). Most of the remaining events (97 of 517 or 18.6%) occur in the spring and only 7.5% (39/517) occur during the winter. Therefore, even across the nodes associated with extreme precipitation, winter extreme precipitation events are relatively uncommon. This may result partially from the SOM design, which uses daily standardized values of 500-hPa geo-potential height and 850-hPa specific humidity. Even anomalously high 850-hPa specific humidity in winter may be insufficient to support extreme precipitation. However, our results are consistent with previous studies (e.g., Schumacher and Johnson, 2006) that have identified a strong summer maximum in extreme precipitation. During the winter, within-type variability is also larger, and the percentages of each node associated with extreme precipitation are at a minimum. During summer, the six key nodes produce extreme precipitation on nearly 25% of days on which they occur, and for Node 3, extreme precipitation occurs on more 1/3 of summer days. Trend analysis of the frequency of SOM nodes associated with extreme precipitation provides an initial perspective on how synoptic-scale variability and change may be related to changes in extreme precipitation. The number of extreme precipitation days in the U.S. Great Lakes region is increasing at a rate of 1.27 days/decade, which may be at least partially explained by variations in the frequency of days belonging to those specific SOM nodes associated with elevated extreme precipitation frequency. We find that two extreme precipitation nodes exhibit significant trends over time (**Table 4**). Node 2 has a significant positive trend of 2.91 days/decade ($p < 0.01$), while Node 4 has a significant negative trend of −1.88 days/decade ($p \sim 0.03$). The other nodes associated with extreme precipitation have positive trends that do not meet the criteria for significance (with $\alpha = 0.05$). Finally, we assessed trends in the occurrence of extreme precipitation days within each extreme node and across all extreme nodes. Results indicate that across all extreme nodes, there is a significant trend of 1.27 extreme precipitation days per decade ($p \sim 0.03$). This is driven primarily by Node 2, which has a significant positive trend ($p \sim 0.02$) of 0.48 days/decade in days meeting the extreme precipitation criteria. The impact location associated with Node 2 (**Figure 5**) corresponds very well with the extreme precipitation trends presented in section Extreme Precipitation Climatology and Trends and **Figure 3**, suggesting a potentially substantive role for mesoscale and synoptic processes in the observed extreme precipitation increases.

SUMMARY AND DISCUSSION

The objectives of this study were to quantify changes in extreme precipitation frequency in the U.S. Great Lakes region and their links with large-scale circulation and humidity. We first conducted an analysis of trends in extreme event frequency, using both parametric and non-parametric trend estimation techniques and accounting for autocorrelation and field significance. While accounting for autocorrelation and field significance reduced the spatial extent of the identified trends, we identified the

existence of positive extreme frequency trends in the region using both techniques. No negative precipitation trends were identified in the region. To relate regional extreme precipitation events to atmospheric drivers, we applied a bivariate self-organizing map to assign each day in the record to one of 20 distinct nodes characterized by their standardized 500 hPa geo-potential height and 850 hPa specific humidity anomalies. A Monte Carlo approach was then used to identify six nodes associated with regional extreme precipitation occurrence. Each of these extreme nodes featured a unique structure, typically with a strong geo-potential height gradient and corresponding low-level humidity maximum. When considering only the extreme precipitation days within each node, we found these features to be exaggerated (i.e., a stronger gradient and higher humidity), indicating that structure and magnitude of these weather types are both essential for relating them to extreme precipitation. Finally, for each of the extreme nodes, and for all extreme nodes collectively, we quantified the trend in overall frequency and in the frequency of extreme precipitation days associated with the node. Collectively, the frequency of these extreme nodes is increasing over time (not significant) and the frequency of extreme days within the nodes is also increasing over time (significant with $\alpha = 0.05$). Node 2 specifically exhibits significant increases in overall frequency and in the frequency of extreme days within Node 2. The spatial structure of extreme precipitation frequency under Node 2 qualitatively matches the observed trend structure.

Our results are consistent with results of previous students, such as the significant increase in the frequency of heavy precipitation over the central United States reported by Mallakpour and Villarini (2015). Because they used alternative data sources with different spatial resolutions and time periods, a direct comparison is not possible. However, the greater spatial extent of extreme precipitation trends in the parts of their domain that overlap with ours, could result from our consideration of autocorrelation in the time series. We recommend that time series studies account for autocorrelation to avoid overconfidence in identified trends. The results of our synoptic classification (and the identified nodes associated with extreme precipitation) are also in agreement with previous studies. For example, each of the nodes that we associated with extreme precipitation are instantiations of the "Midwest water hose" pattern denoted by Zhang et al. (2019). In that study, the authors used a broader domain to identify a connection between extreme precipitation and circulation. In the current study, we've used a narrower domain leading to a wider array of identified circulation/humidity types. As discussed in section Results, Nodes 2 and 7 are consistent with the east-west "training" events described by Schumacher and Johnson (2005) that are responsible for a large number of extreme precipitation events identified in their study.

The vast majority of previous synoptic classifications with the SOM algorithm have relied on a single classification variable, usually geo-potential height or sea level pressure, to reflect the primary circulation features. Our results, based on a bivariate SOM, demonstrate that consideration of additional variables, 850 hPa specific humidity in our case, can improve the interpretation of the resulting weather types and their associations with extreme precipitation. Each of the nodes that we associated with extreme precipitation occurrence is characterized by a combination of geo-potential height and specific humidity anomalies in specific geographic regions. The SOM nodes that are not associated with extreme precipitation occurrence may exhibit similar structure in either geo-potential height or specific humidity, but not both. We also found that the magnitude of both of these parameters is vital. Our study suggests that extreme days are related to both steepened geo-potential height gradients and amplified specific humidity. Agel et al. (2019) similarly reported that extreme precipitation events were related to enhanced moisture transport.

Previous studies focused on the central United States have identified disparate drivers of extreme precipitation changes. Specifically, Kunkel et al. (2012), attributed increasing extreme events to be related to frontal systems, while Schumacher and Johnson (2005, 2006) and Barlow et al. (2019) identified mesoscale convective systems occurring during spring and summer as a major cause. These differences may result from different definitions and the extreme nodes identified in this study are consistent with both mesoscale convective systems and frontal systems. While direct comparison with previous studies is difficult, our results indicate that extreme precipitation frequency is increasing in many parts of our region, with substantial contributions from unique combinations of large-scale circulation and humidity patterns. Future studies may benefit from including additional information from reanalyses, such as the convective vs. large-scale rain rates to better differentiate between the large-scale mechanisms that produce extreme precipitation. The strength of the links between SOM nodes and extreme precipitation may be further improved by incorporating greater specificity regarding regional precipitation drivers, perhaps including aspects of the Great Plains low-level jet (Junker et al., 1999) or consideration of multi-day events and their associated large-scale drivers.

While our results contribute to greater understanding of changes in precipitation extremes in the U.S. Great Lakes region, there are some limitations worth noting. In synoptic classification problems, the goal is to minimize within-type variability and maximize between-type variability, but resulting nodes often suffer from a large degree of within-type variability (Brinkmann, 1999). Although we identified six patterns that account for more than half of all extreme precipitation days, each of the nodes identified as an extreme precipitation node also includes a large number of days without extreme precipitation. This limitation is also noted by Gibson et al. (2017) in the context of using SOMs to explore extreme event environments. Our analysis of the difference between large-scale patterns associated with extreme and non-extreme precipitation days within the nodes, determined by simple compositing, indicates that the pattern magnitudes are greater on extreme precipitation days, reflecting within-type variability. Another limitation is related to our use of standardized anomalies. While this was necessary to include both geo-potential height and specific humidity which differ by several orders of magnitude, it can also mask important seasonal variations in extreme precipitation drivers. For example, anomalously high specific humidity during winter may still be insufficient to produce

extreme precipitation. Specific analysis focused on each season may therefore provide greater insight into the physical processes involved. Despite these caveats, this study was successful in identifying trends in extreme precipitation in the U.S. Great Lakes region and relating them to specific circulation/humidity regimes. Key contributions of our work include insights gained from estimating trends using multiple techniques that account for autocorrelation and field significance and relating those trends to combinations of large-scale geo-potential height and humidity. The framework developed here could easily be expanded to other regions or to include more than two large-scale variables.

Projections from contemporary climate models indicate additional increases in the frequency of extreme precipitation under further large-scale warming (IPCC, 2021). However, regional changes in precipitation are still a challenge for climate models (Tabari et al., 2019), which often fail to produce the key precipitating systems, such as mesoscale convective systems (Gutowski et al., 2020). Analyses like those presented here can provide a basis for evaluation of climate models by specifically assessing the frequency with which they produce the large-scale conditions required for extreme precipitation. Studies in other regions (e.g., the NE by Agel et al., 2020) have begun to assess the ability of climate models to simulate extreme precipitation and its related circulation. Future work will expand upon these results to assess representation of the extreme precipitation nodes in contemporary climate models.

DATA AVAILABILITY STATEMENT

Publicly available datasets were analyzed in this study. Daily NOAA NClimDiv data is available via file transfer protocol (FTP) from ftp.ncdc.noaa.gov; ECMWF ERA5 data can be accessed at https://www.ecmwf.int/en/forecasts/datasets/reanalysis-datasets/era5.

AUTHOR CONTRIBUTIONS

Analysis was conducted by AP and JS with assistance from TF and JR. Writing was conducted by AP and JS. All authors contributed to the article and approved the submitted version.

FUNDING

The work was partially funded with support from NOAA (Grant #NA17OAR4310148).

ACKNOWLEDGMENTS

We acknowledge two reviewers whose constructive comments improved the manuscript substantially.

REFERENCES

Acero, F. J., Garcia, J. A., and Gallego, M. C. (2011). Peaks-over-threshold study of trends in extreme rainfall over the Iberian Peninsula. *J. Clim.* 24, 1089–1105. doi: 10.1175/2010JCLI3627.1

Agel, L., Barlow, M., Colby, F., Binder, H., Catto, J. L., Hoell, A., et al. (2019). Dynamical analysis of extreme precipitation in the US northeast based on large-scale meteorological patterns. *Clim. Dynamics* 52, 1739–1760. doi: 10.1007/s00382-018-4223-2

Agel, L., Barlow, M., Feldstein, S. B., and Gutowski, W. J. (2018). Identification of large-scale meteorological patterns associated with extreme precipitation in the US northeast. *Clim. Dynamics* 50, 1819–1839. doi: 10.1007/s00382-017-3724-8

Agel, L., Barlow, M., Polonia, J., and Coe, D. (2020). Simulation of northeast US extreme precipitation and its associated circulation by CMIP5 models. *J. Clim.* 33, 9817–9834. doi: 10.1175/JCLI-D-19-0757.1

Allan, R. P., and Soden, B. J. (2008). Atmospheric warming and the amplification of precipitation extremes. *Science* 321, 1481–1484. doi: 10.1126/science.1160787

Angel, J., Swanston, C., Bousted, B. M., Conlon, K. C., Hall, K. R., J.L. (2018). "Midwest," in *Impacts, Risks, and Adaptation in the United States: Fourth National Climate Change Assessment, Volume II,* eds. D. R. Reidmiller, C. W. Avery, D. R. Easterling, K. E. Kunkel, K. L. M. Lewis, T. K. Maycock, and B. C. Stewart (Washington, DC: U.S. Global Change Research Program). p. 872–940.

Asadieh, B., and Krakauer, N. Y. (2015). Global trends in extreme precipitation: climate models versus observations. *Hydrol. Earth Syst. Sci.* 19, 877–891. doi: 10.5194/hess-19-877-2015

Barlow, M., Gutowski, W. J., Gyakum, J. R., Katz, R. W., Lim, Y. K., Schumacher, R. S., et al. (2019). North American extreme precipitation events and related large-scale meteorological patterns: a review of statistical methods, dynamics, modeling, and trends. *Clim. Dynamics* 53, 6835–6875. doi: 10.1007/s00382-019-04958-z

Bonnin, G. M., Todd, D., Lin, B., Parzybok, T., Yekta, M., and Riley, D. (2005). "Precipitation-Frequency Atlas of the United States," in: *NOAA Atlas*. (Silver Spring, MD: National Weather Service). p. 1–301.

Brinkmann, W. A. R. (1999). Within-type variability of 700 hPa winter circulation patterns over the Lake Superior basin. *Int. J. Climatol.* 19, 41–58. doi: 10.1002/(SICI)1097-0088(199901)19:1<41::AID-JOC349>3.0.CO;2-U

Byun, K., and Hamlet, A. F. (2018). Projected changes in future climate over the Midwest and Great Lakes region using downscaled CMIP5 ensembles. *Int. J. Climatol.* 38, E531–E553. doi: 10.1002/joc.5388

D'orgeville, M., Peltier, W. R., Erler, A. R., and Gula, J. (2014). Climate change impacts on Great Lakes Basin precipitation extremes. *J. Geophys. Res.* 119, 10799–10812. doi: 10.1002/2014JD021855

Drayna, P., Mclellan, S. L., Simpson, P., Li, S. H., and Gorelick, M. H. (2010). Association between Rainfall and Pediatric Emergency Department visits for acute gastrointestinal illness. *Environ. Health Persp.* 118, 1439–1443. doi: 10.1289/ehp.0901671

Gibson, P. B., Perkins-Kirkpatrick, S. E., Uotila, P., Pepler, A. S., and Alexander, L. V. (2017). On the use of self-organizing maps for studying climate extremes. *J. Geophys. Res.* 122, 3891–3903. doi: 10.1002/2016JD026256

Gutowski, W. J., Ullrich, P. A., Hall, A., Leung, L. R., O'brien, T. A., Patricola, C. M., et al. (2020). The ongoing need for high-resolution regional climate models: process understanding and stakeholder information. *Bull. Am. Meteorol. Soc.* 101, E664–E683. doi: 10.1175/BAMS-D-19-0113.A

Hersbach, H., Bell, B., Berrisford, P., Hirahara, S., Horanyi, A., Munoz-Sabater, J., et al. (2020). The ERA5 global reanalysis. *Q. J. R. Meteorol. Soc.* 146, 1999–2049. doi: 10.1002/qj.3803

Hewitson, B. C., and Crane, R. G. (2002). Self-organizing maps: applications to synoptic climatology. *Clim. Res.* 22, 13–26. doi: 10.3354/cr022013

Huth, R., and Pokorna, L. (2004). Parametric versus non-parametric estimates of climatic trends. *Theor. Appl. Climatol.* 77, 107–112. doi: 10.1007/s00704-003-0026-3

IPCC (2021). "Summary for Policymakers," in *Climate Change 2001: The Physical Scientific Basis. Contribution of Working Group I to the Sixth Assessment Report of the Intergovernmental Panel on Climate Change*, eds. V. Masson-Delmotte, P. Zhai, A. Pirani, S. L. Connors, C. Pean, S. Berger, N. Caud, Y. Chen, L.

Goldfarb, M. I. Gomis, M. Huang, K. Leitzell, E. Lonnoy, J. B. R. Matthews, T. K. Maycock, T. Waterfield, O. Yelecki, R. Yu, and B. Zhou (Cambridge: Cambridge University Press). p. 1–30.

Jiang, N. B., Luo, K. H., Beggs, P. J., Cheung, K., and Scorgie, Y. (2015). Insights into the implementation of synoptic weather-type classification using self-organizing maps: an Australian case study. *Int. J. Climatol.* 35, 3471–3485. doi: 10.1002/joc.4221

Junker, N. W., Schneider, R. S., and Fauver, S. L. (1999). A study of heavy rainfall events during the great midwest flood of 1993. *Weather Forecasting* 14, 701–712. doi: 10.1175/1520-0434(1999)014<0701:ASOHRE>2.0.CO;2

Kendall, M. G. (1975). *Rank Correlation Methods*. London: Charles Griffin.

Kohonen, T. (1998). The self-organizing map. *Neurocomputing* 21, 1–6. doi: 10.1016/S0925-2312(98)00030-7

Kunkel, K. E., Easterling, D. R., Kristvich, D., A,.R., Gleason, B., Stoecker, L. Smith, R. (2012). Meteorological causes of the secular variations in observed extreme precipitation events for the conterminous United States. *J. Hydrometeorol.* 13, 1131–1141. doi: 10.1175/JHM-D-11-0108.1

Kunkel, K. E., Karl, T. R., Easterling, D. R., Redmond, K., Young, J., Yin, X. G., et al. (2013). Probable maximum precipitation and climate change. *Geophys. Res. Lett.* 40:50334. doi: 10.1002/grl.50334

Lanzante, J. R. (1996). Resistant, robust and non-parametric techniques for the analysis of climate data: theory and examples, including applications to historical radiosonde station data. *Int. J. Climatol.* 16, 1197–1226. doi: 10.1002/(SICI)1097-0088(199611)16:11<1197::AID-JOC89>3.0.CO;2-L

Lenderink, G., and Van Meijgaard, E. (2010). Linking increases in hourly precipitation extremes to atmospheric temperature and moisture changes. *Environ. Res. Lett.* 5:025208. doi: 10.1088/1748-9326/5/2/025208

Liu, Y. G., Weisberg, R. H., and Mooers, C. N. K. (2006). Performance evaluation of the self-organizing map for feature extraction. *J. Geophys. Res. Oceans* 111, 1–14. doi: 10.1029/2005JC003117

Mallakpour, I., and Villarini, G. (2015). The changing nature of flooding across the central United States. *Nat. Clim. Change* 5, 250–254. doi: 10.1038/nclimate2516

Menne, M. J., Durre, I., Vose, R. S., Gleason, B. E., and Houston, T. G. (2012). An overview of the global historical climatology network-daily database. *J. Atmos. Oceanic Technol.* 29, 897–910. doi: 10.1175/JTECH-D-11-00103.1

Nasri, B., Tramblay, Y., El Adlouni, S., Hertig, E., and Ouarda, T. B. M. J. (2016). Atmospheric predictors for annual maximum precipitation in North Africa. *J. Appl. Meteorol. Climatol.* 55, 1063–1076. doi: 10.1175/JAMC-D-14-0122.1

Orlanski, I. (1975). Rational subdivision of scales for atmospheric processes. *Bull. Am. Meteorol. Soc.* 56, 527–530. doi: 10.1175/1520-0477-56.5.527

Pendergrass, A. G. (2018). What precipitation is extreme? *Science* 360, 1072–1073. doi: 10.1126/science.aat1871

Pryor, S. C., Barthelmie, R. J., and Schoof, J. T. (2013). High-resolution projections of climate-related risks for the Midwestern USA. *Clim. Res.* 56, 61–79. doi: 10.3354/cr01143

Santer, B. D., Wigley, T. M. L., Boyle, J. S., Gaffen, D. J., Hnilo, J. J., Nychka, D., et al. (2000). Statistical significance of trends and trend differences in layer-average atmospheric temperature time series. *J. Geophys. Res.* 105, 7337–7356. doi: 10.1029/1999JD901105

Schumacher, R. S., and Johnson, R. H. (2005). Organization and environmental properties of extreme-rain-producing mesoscale convective systems. *Monthly Weather Rev.* 133, 961–976. doi: 10.1175/MWR2899.1

Schumacher, R. S., and Johnson, R. H. (2006). Characteristics of US extreme rain events during 1999-2003. *Weather Forecast.* 21, 69–85. doi: 10.1175/WAF900.1

Sen, P. K. (1968). Estimates of regression coefficient based on Kendalls Tau. *J. Am. Stat. Assoc.* 63:1379. doi: 10.1080/01621459.1968.10480934

Sheridan, S. C., and Lee, C. C. (2011). The self-organizing map in synoptic climatological research. *Progr. Phys. Geogr.* 35, 109–119. doi: 10.1177/0309133310397582

Tabari, H., Hosseinzadehtalaei, P., Aghakouchak, A., and Willems, P. (2019). Latitudinal heterogeneity and hotspots of uncertainty in projected extreme precipitation. *Environ. Res. Lett.* 14:ab55fd. doi: 10.1088/1748-9326/ab55fd

Tryhorn, L., and Degaetano, A. (2011). A comparison of techniques for downscaling extreme precipitation over the Northeastern United States. *Int. J. Climatol.* 31, 1975–1989. doi: 10.1002/joc.2208

Vose, R. S., Applequist, S., Squires, M., Durre, I., Menne, M. J., Williams, C. N., et al. (2014). Improved historical temperature and precipitation time series for U.S. climate divisions. *J. Appl. Meteorol. Climatol.* 53, 1232–1251. doi: 10.1175/JAMC-D-13-0248.1

Wilks, D. S. (2006). On "field significance" and the false discovery rate. *J. Appl. Meteorol. Climatol.* 45, 1181–1189. doi: 10.1175/JAM2404.1

Wilks, D. S. (2016). The stippling shows statistically signficant grid points: how research results are routinely overstated and overinterpreted, and what to do about it. *Bull. Am. Meteorol. Soc.* 97:2263. doi: 10.1175/BAMS-D-15-00267.1

Willmott, C. J., and Robeson, S. M. (1995). Climatologically aided interpolation (CAI) of terrestrial air-temperature. *Int. J. Climatol.* 15, 221–229. doi: 10.1002/joc.3370150207

Winters, B. A., Angel, J., Ballerine, C., Byard, J., Flegel, A., Gambill, D., et al. (2015). Report for the Urban Flooding Awareness Act. Office of Water Resources, Illinois Department of Natural Resources, p. 1–97. Available Online at: https://www2.illinois.gov/dnr/waterresources/documents/final_ufaa_report.pdf

Wuebbles, D. J., Cardinale, B., Cherkauer, K., Davidson-Arnott, R., Hellmann, J., Infante, D., et al. (2019). *An Assessment of the Impacts of Climate Change on the Great Lakes*. Chicago, IL: ELP Center.

Yue, S., and Wang, C. Y. (2004). The Mann-Kendall test modified by effective sample size to detect trend in serially correlated hydrological series. *Water Res. Manag.* 18, 201–218. doi: 10.1023/B:WARM.0000043140.61082.60

Zhang, L., Zhao, Y. M., Hein-Griggs, D., Barr, L., and Ciborowski, J. J. H. (2019). Projected extreme temperature and precipitation of the Laurentian Great Lakes Basin. *Glob. Planet. Change* 172, 325–335. doi: 10.1016/j.gloplacha.2018.10.019

Conflict of Interest: The authors declare that the research was conducted in the absence of any commercial or financial relationships that could be construed as a potential conflict of interest.

Publisher's Note: All claims expressed in this article are solely those of the authors and do not necessarily represent those of their affiliated organizations, or those of the publisher, the editors and the reviewers. Any product that may be evaluated in this article, or claim that may be made by its manufacturer, is not guaranteed or endorsed by the publisher.

frontiers in Water

ORIGINAL RESEARCH
published: 24 December 2021
doi: 10.3389/frwa.2021.780333

Projected Changes to Spring and Summer Precipitation in the Midwestern United States

*Kevin A. Grady, Liang Chen and Trent W. Ford**

Climate and Atmospheric Science Section, Illinois State Water Survey, Prairie Research Institute, University of Illinois at Urbana-Champaign, Champaign, IL, United States

Spring and summer precipitation are both important factors for agricultural productivity in the Midwest region of the United States. Adequate summer precipitation, particularly in the reproductive and grain fill stages in July and August, is critical to corn and soybean success. Meanwhile, excessive spring precipitation can cause significant planting delays and introduces challenges with weed and pest management, and soil erosion and compaction. However, uncertainty especially in future summer precipitation changes, translates to uncertainties in how the joint distributions of spring and summer precipitation are expected to change by mid- and late-century across the Midwest. This study examines historical and projected changes in the characteristics of spring and summer precipitation in the Midwest using 12 dynamically downscaled simulations under the high-emission representative concentration pathway (RCP 8.5) from the NA-CORDEX project. Historical increases in spring precipitation and precipitation intensity are projected to continue into the mid- and late-century across the region, with strong model agreement. By comparison, projected changes in Midwest summer precipitation are more modest than for spring and have much less model agreement. Despite a projected three- to four-fold increase in the frequency of wet springs by late-century, relative to the model ensemble historical average, the lack of substantial and robust projected change in summer precipitation results in only a small increase in the risk of dry summers following wet springs in the Midwest by mid- and late-century.

Keywords: drought, climate projections, climate change, Midwest, agriculture, NA-CORDEX

OPEN ACCESS

Edited by:
Julie A. Winkler, Michigan State University, United States

Reviewed by:
Scott Robeson, Indiana University, United States
Jonathan Winter, Dartmouth College, United States

****Correspondence:***
Trent W. Ford
twford@illinois.edu

Specialty section:
This article was submitted to Water and Climate, a section of the journal Frontiers in Water

Received: *20 September 2021*
Accepted: *24 November 2021*
Published: *24 December 2021*

Citation:
Grady KA, Chen L and Ford TW (2021) Projected Changes to Spring and Summer Precipitation in the Midwestern United States. Front. Water 3:780333. doi: 10.3389/frwa.2021.780333

INTRODUCTION

The Midwest region of the United States is an area crucial to the nation's production of corn and soybeans. Seven Midwest states—Iowa, Illinois, Minnesota, Indiana, Ohio, Missouri, and Wisconsin—rank among the top 10 for corn harvested for grain (National Agricultural Statistics Service, 2021), and six Midwest states—Illinois, Iowa, Minnesota, Indiana, Missouri, and Ohio—are also in the top 10 for soybean production (National Agricultural Statistics Service, 2021). Altogether, the Midwest produced over 9 billion bushels of corn and over 2.6 billion bushels of soybeans in 2020, accounting for about 64% of the yearly total produced for each crop in the United States. Corn production in the Midwest United States alone falls between the total corn production of China and Brazil, the second and third highest corn-producing countries (Foreign Agricultural Service, 2021).

The distribution of precipitation throughout the growing season can have a significant impact on corn and soybean production in the Midwest. Both corn and soybean yields tend to be positively correlated with summer precipitation (Goldblum, 2009; Liu and Basso, 2020), especially in July and August, during critical reproductive stages of corn and soybeans, respectively (El Mourid et al., 1986; Hatfield et al., 2018). Therefore, precipitation in July and August tends to be a strong predictor of end-of-season yield in both corn and soybeans across the Midwest (Hu and Buyanovsky, 2003; Westcott et al., 2005), such that drought in mid- to late-summer typically results in below-trend corn and soybean yields (Mishra and Cherkauer, 2010). Concurrently, excessive precipitation in the spring can have a negative impact on Midwest corn and soybeans. This is particularly the case with excessively wet conditions in April and May, which can delay fieldwork and planting, reduce flexibility for pre- and post-emergence herbicide application, discourage deep root growth, increase pressure from disease, weeds, and insect pests, and increase the risk of soil compaction (Hatfield et al., 2018; Daigh et al., 2020; Winsor, 2020). Urban et al. (2015) found that an extremely wet spring can reduce yields by 10% in Iowa, Illinois, and Indiana.

Given the negative impacts of both excessively wet springs and excessively dry summers on Midwest crop production, years with consecutive wet springs and dry summers are of great concern for Midwest producers. Climate model projections indicate Midwest spring precipitation will increase throughout the twenty-first century (Swain and Hayhoe, 2015; Byun and Hamlet, 2018; Bukovsky and Mearns, 2020), which is in line with historical spring precipitation trends across the Midwest. In northern Illinois, for example, April–May precipitation has increased by 4.6 mm per decade since 1895 and has increased 6.9 mm per decade since 1950 (NOAA NCEI, 2011). However, the picture is less clear for future changes in summer precipitation by mid- and late-century. While July–August precipitation has increased over the past 125 years across much of the Midwest, recent studies project decreased summer precipitation across all or part of the Midwest (Winkler et al., 2012; Byun and Hamlet, 2018; Gautum et al., 2021). Summer precipitation projections often come with more uncertainty than their corresponding springs due to poorer summertime ensemble agreement (Byun et al., 2019). Bukovsky and Mearns (2020) found in their models for North American summer precipitation "consistent inconsistency within regions and across the ensemble in the sign of the precipitation projections." The ensemble changes in summer precipitation tend to be smaller than the ensemble changes in spring precipitation as well.

Uncertainty in future summer precipitation changes in the Midwest translates to uncertainties in how the joint distributions of spring and summer precipitation are expected to change. For example, Ford et al. (2021) found transitions from extremely wet to extremely dry conditions on subseasonal to seasonal timescales were occurring both more quickly and more frequently in recent decades in parts of the central and southern Midwest. Christian et al. (2015) found increasing interannual variability in recent decades, resulting in a higher likelihood of a significant wet year following a significant drought year in the central United States.

Given the importance of spring and summer precipitation for agriculture in the Midwest, it is crucial to gain a better understanding of how spring and summer precipitation patterns are projected to simultaneously change across the Midwest, and how these changes are expected to affect Midwest agriculture. By employing a suite of climate models, we estimate the projected changes in spring and summer precipitation, and examine how the frequency of wet springs, dry summers, and combinations of the two are expected to change in coming decades.

DATA

To examine the projected changes in these precipitation patterns, we employ 12 model combinations from the North America Coordinated Regional Downscaling Experiment (NA-CORDEX) (Mearns et al., 2017). North America Coordinated Regional Downscaling Experiment provides dynamically downscaled climate simulations at spatial resolutions of 50 and 25 km over a domain covering most of North America from multiple regional climate models (RCMs), which are driven by the output of different global climate models (GCMs) from the Coupled Model Intercomparison Project-Phase 5 (CMIP5). In this study, we use the NA-CORDEX simulations at a spatial resolution of 25 km. **Table 1** shows the details of the available 12 GCM-RCM combinations used in our analysis. There are seven GCMs (CanESM2, GEMatm-Can, GEMatm-MPI, GFDL-ESM2M, HadGEM2-ES, MPI-ESM-LR, and MPI-ESM-MR) used as lateral boundary conditions for four RCMs (CanRCM4, CRCM5-UQAM, RegCM4, and WRF). Among the seven GCMs, GEMatm-Can and GEMatm-MPI have bias-corrected sea ice and sea-surface temperatures (SSTs) from a separate GCM simulation (Hernández-Díaz et al., 2019). Therefore, the boundary conditions GEMatm-Can (or GEMatm-MPI) include the atmospheric fields from CanESM2 (or MPI-ESM-MR) and the bias-corrected SSTs. Among the four regional models, both CanRCM4 and CRCM5-UQAM are Canadian Regional Climate Model. The former is version 4 developed in Canadian Center for Climate Modeling and Analysis, and the latter is version 5 developed in Université du Québec à Montréal. Daily precipitation is obtained from the 12 GCM-RCM downscaling simulations for the historical period (1950–2005) and the Representative Concentration Pathway 8.5 (RCP 8.5) future period (2006–2100). The RCP8.5 represents a high-emission scenario. It allows us to examine the precipitation changes under the worst-case scenario of climate change. The RCP4.5 scenario, which represents mid-range emissions, is only available for very limited simulations at a spatial resolution of 25 km, and therefore not included in our analysis. It also should be noted that we use the raw downscaling output in this study because of the recently reported errors in its bias-corrected data (McGinnis, 2021).

We investigate changes in both spring (April–May) and summer (July–August) precipitation characteristics. We focus on April and May for spring and July and August for summer because excessive (deficient) rainfall in April–May (July–August) is associated with negative impacts to both corn and soybean

TABLE 1 | The 12 NA-CORDEX GCM-RCM combinations used in this study.

No.	Global climate model (GCM)	Regional climate model (RCM)
1	CanESM2	CanRCM4
2	CanESM2	CRCM5-UQAM
3	GEMatm-Can	CRCM5-UQAM
4	GEMatm-MPI	CRCM5-UQAM
5	GFDL-ESM2M	RegCM4
6	GFDL-ESM2M	WRF
7	HadGEM2-ES	RegCM4
8	HadGEM2-ES	WRF
9	MPI-ESM-LR	CRCM5-UQAM
10	MPI-ESM-LR	RegCM4
11	MPI-ESM-LR	WRF
12	MPI-ESM-MR	CRCM5-UQAM

yields in the Midwest (Westcott et al., 2005; Hatfield et al., 2018). Specifically, spring and summer precipitation is characterized by four metrics: (1) total seasonal precipitation, (2) the simple daily intensity index (SDII), (3) the number of heavy precipitation days in a season, (4) and the number of dry days in a season. Total precipitation is calculated from all days, including those with non-zero totals that are <2.5 mm. A heavy precipitation day is one in which at least 25 mm of precipitation is observed, and a dry day is one in which <2.5 mm is observed. Conversely, we define a wet day as one in which 2.5 mm or more of precipitation is observed, and the SDII is the average precipitation that falls on wet days during a season. We also employ three different versions of the dry day metric. While the seasonal total number of dry days is the one primarily used, we also consider both the average and maximum dry spell length in a season in later sections, where a dry spell is a period of consecutive dry days.

Verification of the NA-CORDEX simulation ensemble is done using gridded precipitation observations from the National Oceanic and Atmospheric Administration Monthly United States Climate Divisional Database (NClimDiv, Vose et al., 2014). The NClimDiv historical record covers the period 1951 through the present and contains precipitation data interpolated to 5-km grids spanning the contiguous United States. For comparison, the NClimDiv data is upscaled to the NA-CORDEX spatial resolution. The study area, defined as the Midwest United States, spans 35.5° and 48°N latitude and 83° and 95°W longitude.

RESULTS

Precipitation Climatology and NA-CORDEX Validation

Figure 1 shows the upscaled spring and summer NClimDiv observed precipitation climatology across the Midwest during the period 1951–2005. Total spring precipitation follows a strong south-to-north gradient across the region, ranging from nearly 300 mm in western Kentucky to <120 mm in northern Minnesota. Spring precipitation intensity—represented by both SDII and the frequency of heavy precipitation days—are also highest in the southern Midwest and lowest in the northern Midwest. Specifically, parts of southern Missouri and western Kentucky experience, on average, 3–4 heavy precipitation days (>25 mm) per spring season, while much of Minnesota, Wisconsin, and Michigan experience fewer than one heavy precipitation day on average in spring. Conversely, the northern Midwest experiences more dry days in spring, 45–50 in Minnesota, Wisconsin, and Michigan, compared with 40–45 dry days in Indiana, Ohio, and Kentucky.

Summer precipitation characteristics are less spatially coherent than in spring. Summer tends to be wetter in the western and southeastern Midwest, with totals ranging from nearly 250 mm in parts of Iowa and Kentucky to <150 mm in Michigan (**Figure 1**). The patterns of precipitation intensity and dry day frequencies in the summer distinguish multiple, diverse summer precipitation regimes in the Midwest. Specifically, the southwest quadrant of the Midwest experiences both highest summer SDII (i.e., highest precipitation intensity) and highest dry day frequency. For example, parts of northwest Missouri experience, on average, among the highest rates of both heavy precipitation days (2–3) and dry days (48–50) in the summer. This implies the southwest Midwest experiences highly variable summer precipitation climatology, with prolonged dry periods broken up by intense precipitation. In contrast, the areas adjacent to Lake Superior, including parts of Minnesota, Wisconsin, and Michigan, experience relatively low frequencies of both heavy precipitation days (0.5–1.5) and dry days (43–45) per summer. This pattern suggests a more consistent, less intense summer precipitation climatology in the northern part of the Midwest.

We compare the NClimDiv observed data with the NA-CORDEX multi-model ensemble median during the 55-year period 1951–2005. **Figure 2** shows the median of differences from this comparison. The NA-CORDEX simulations exhibit a wet bias across most of the region in spring of about 25–50 mm, or approximately 10–20% of the regionally averaged observed spring precipitation climatology (**Figure 2A**). The largest biases can be seen in the southwest and northeast parts of the Midwest, where the multi-model ensemble median shows spring precipitation totals that are 50–75 mm greater than the observed climatology (15–25% of historical climatology). The simulations exhibit slightly higher spring precipitation intensity than the observed climatology across the Midwest, especially in the Great Lakes region, with SDII biases mostly <2 mm (**Figure 2B**) and 1 or fewer additional heavy precipitation days (**Figure 2C**). The models produce 1–4 fewer dry days than observed across virtually the entire Midwest (**Figure 2D**).

The simulations show a dry bias in summer in the western Midwest of 10–50 mm, 10–25% of the regionally averaged observed summer precipitation climatology, and a wet summer bias of similar magnitude in the northeast and southeast Midwest (**Figure 2E**). The simulations also show lesser summer precipitation intensity outside of Michigan and parts of Ohio and Kentucky, with SDII biases between 1 and 2.5 (**Figure 2F**). Simulations produce 1–1.5 fewer (additional) heavy precipitation days in the western Midwest (Michigan) (**Figure 2G**), and

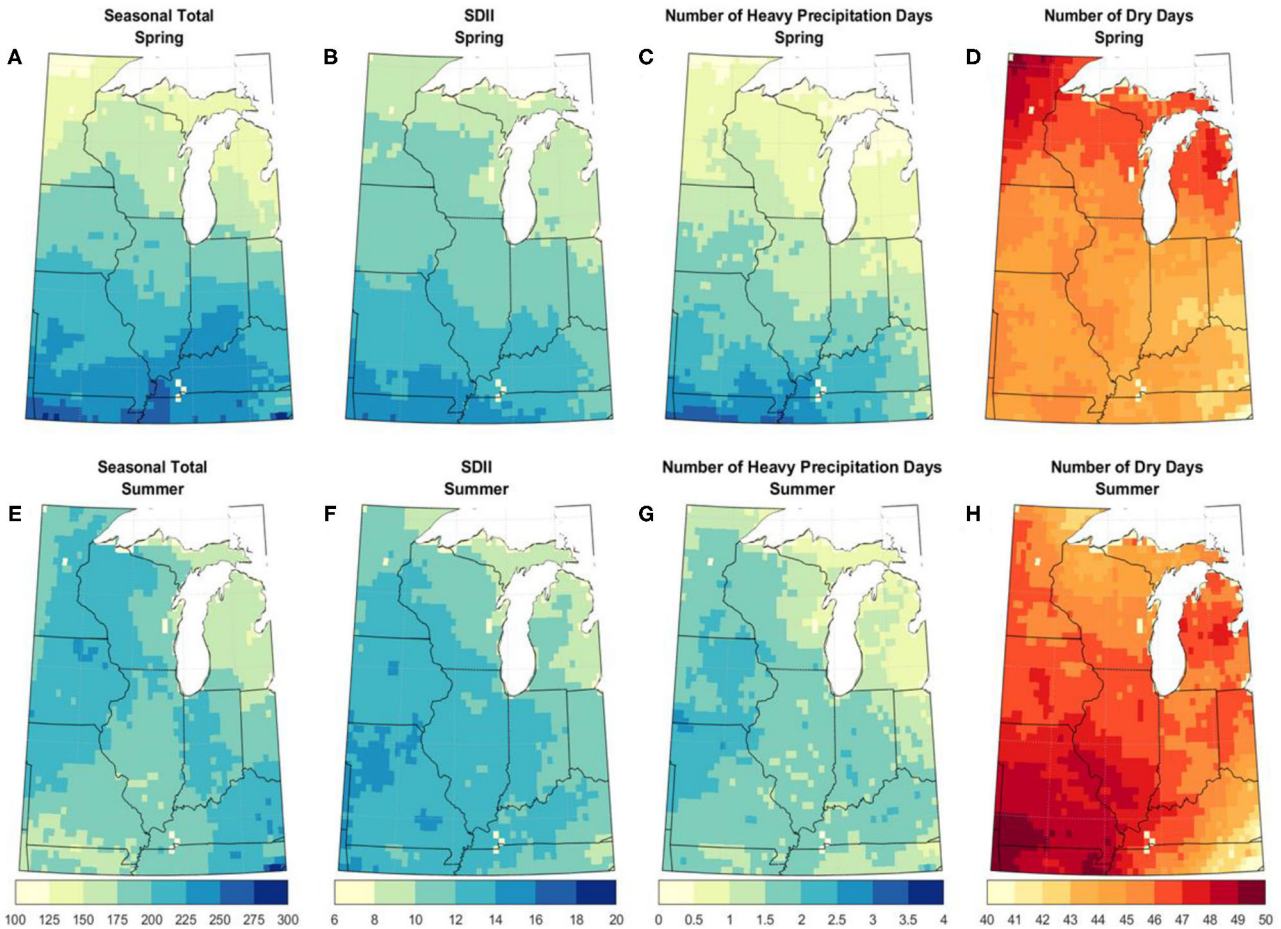

FIGURE 1 | The upscaled NClimDiv spring and summer climatology for the seasonal precipitation totals [**(A,E)**, mm], SDII [**(B,F)**, mm day^{-1}], seasonal number of heavy precipitation days [**(C,G)**, days], and seasonal number of dry days [**(D,H)**, days] for the historical period 1951–2005.

generally have 1–2 additional summer dry days across the region (**Figure 2H**).

The performance of NA-CORDEX model combinations in simulating spring and summer Midwest precipitation are summarized in **Table 2**. The region-average mean absolute error (MAE) of spring season total precipitation is 45.1 mm, representing approximately 20% of the observed climatological spring totals. Region-average summer total precipitation MAE was 22.2 mm, between 11 and 12% of the observed climatological summer total. Despite the relatively high differences in spring, the simulations do a good job representing the spatial gradient of spring precipitation (spatial correlation of 0.97). Comparatively, simulation underestimation (overestimation) of summer precipitation in the western (eastern) Midwest (e.g., **Figure 2**) results in a low summer precipitation spatial correlation of 0.13. The NA-CORDEX simulations do a better job representing spring and summer precipitation intensity (SDII) and dry day frequency, with MAE representing <7% of the observed climatology and spatial correlations ranging from 0.70 to 0.95. The MAE values of both spring and summer heavy precipitation day frequency are <0.5 day. However, while the simulations capture the spatial gradient of heavy precipitation days in the spring (spatial correlation of 0.95), their performance in the summer is lacking (spatial correlation of 0.21).

Projected Changes in Spring Precipitation

Our investigation of projected changes in spring and summer Midwest precipitation focuses on three 30-year periods: historical 1976–2005, mid-century 2030–2059, and late century 2070–2099. We compare projections from RCP 8.5 to the model historical period to characterize projected changes in both spring and summer precipitation. Comparison of the NA-CORDEX multi-model ensemble median projections for mid- and late-century spring precipitation with the historical period reveals several noteworthy patterns. Overall, total precipitation, precipitation intensity (SDII), and the frequency of heavy precipitation days in April and May are all projected to increase across the Midwest.

The largest increases in both total spring precipitation and spring precipitation intensity by the late-century are in the western parts of the Midwest, ranging from 50 to 80 mm of additional spring precipitation west of the Mississippi River, representing a 25–50% increase relative to the model

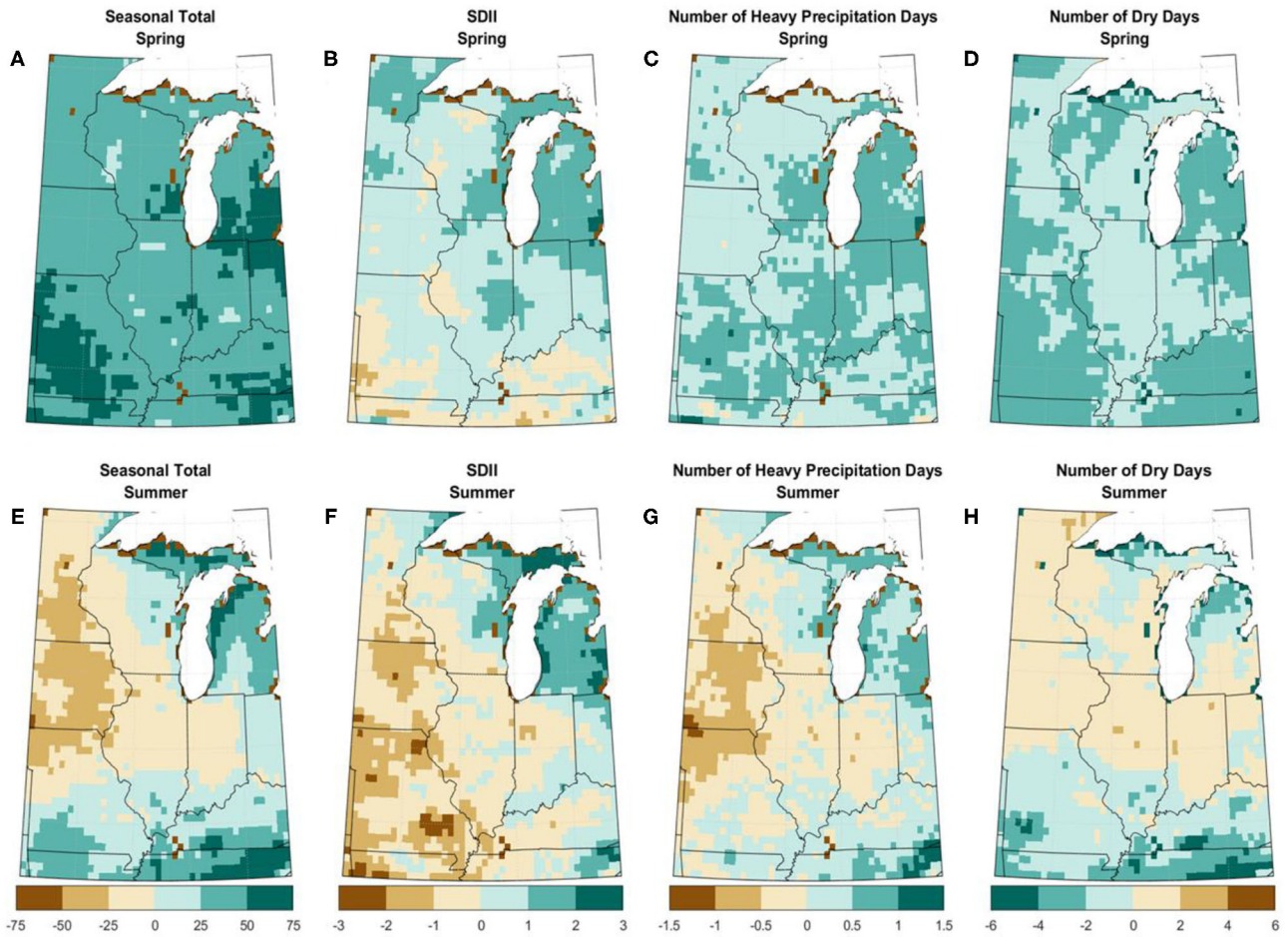

FIGURE 2 | The NA-CORDEX multi-model ensemble median error when compared with the upscaled NClimDiv observed climatology for the spring and summer over the historical period 1951–2005. Shown are the results for the seasonal precipitation totals [**(A,E)**, mm], SDII [**(B,F)**, mm day^{-1}], seasonal number of days with heavy precipitation [**(C,G)**, days], and seasonal number of dry days [**(D,H)**, days].

TABLE 2 | Model validation summary statistics.

Metric	Mean absolute error		Spatial correlation	
Season	**Spring**	**Summer**	**Spring**	**Summer**
Seasonal total (mm)	41.5 (20.0%)	22.2 (11.3%)	0.97 (<0.01)	0.13 (0.23)
SDII (mm day^{-1})	0.69 (5.6%)	0.82 (6.7%)	0.95 (<0.01)	0.72 (0.01)
Number of heavy days (days)	0.47 (25.5%)	0.31 (19.3%)	0.95 (<0.01)	0.21 (0.12)
Number of dry days (days)	2.05 (4.5%)	1.15 (2.5%)	0.89 (<0.01)	0.70 (0.02)

Left columns show region-average mean absolute error and—in parentheses—percent mean absolute error for each of the four metrics. The right columns show the spatial correlation between models and observations for each of the four metrics. The p-values from correlation statistical significance tests are shown in parentheses in the right columns.

historical baseline. The simulations show good agreement in increasing spring precipitation by mid-century for most of the Midwest outside of southeast Wisconsin and northern Michigan (**Figures 3A–C**), while agreement is strong across the entire region for increases by late-century (**Figures 3D–F**). Projected increases in precipitation intensity, both SDII and heavy precipitation day frequency, by mid-century are robust across most of the Midwest region (**Figures 3B,C**). Meanwhile, there is widespread agreement across the entire Midwest for late-century projected increases in both precipitation intensity metrics (**Figures 3E,F**). Late-century projections indicate increased SDII by 1–4 mm region-wide and an additional 1–2 spring heavy precipitation days, with the largest projected increases in the southern and western halves of the region.

Coinciding with projected increases in April–May precipitation and precipitation intensity across the Midwest,

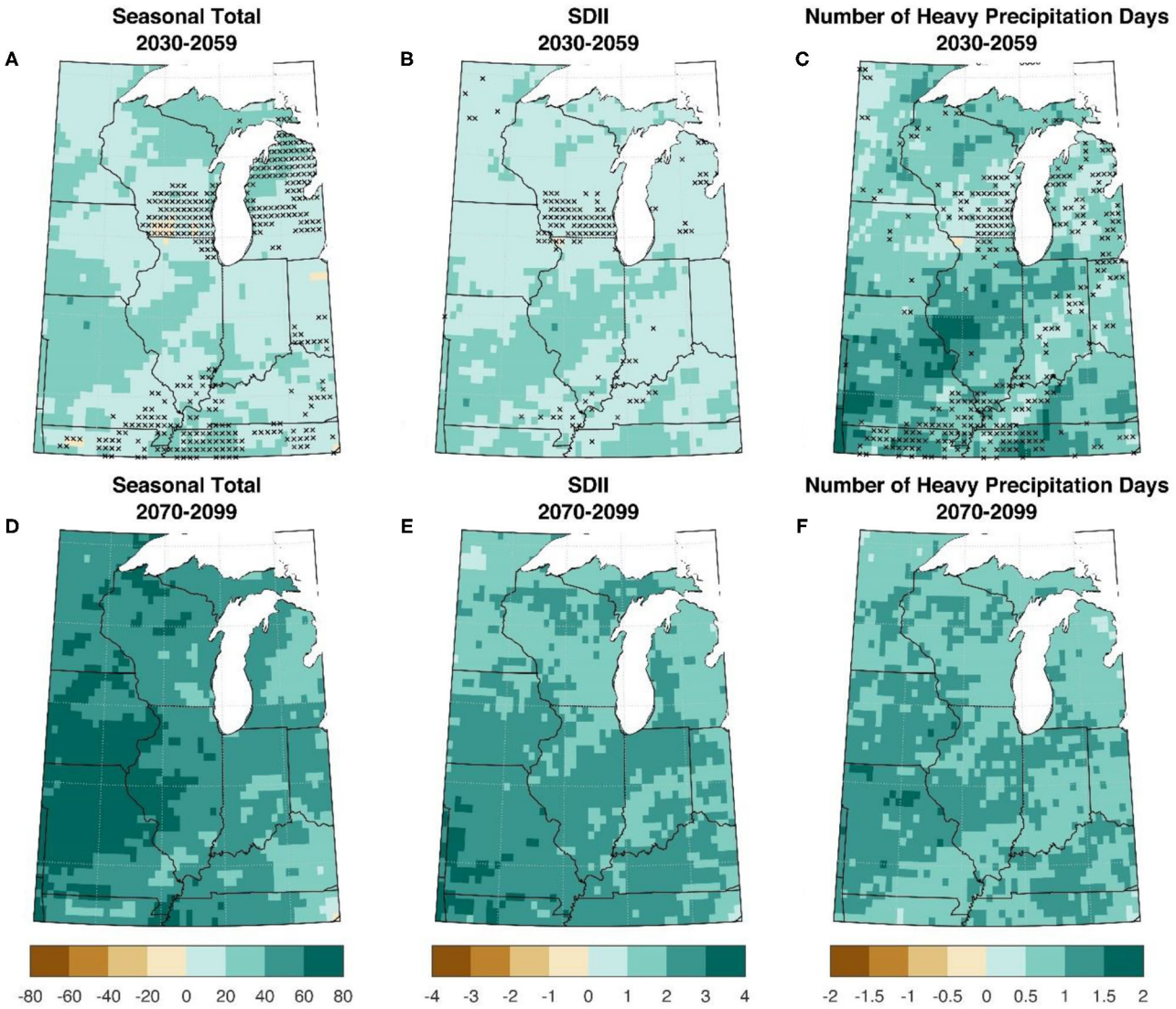

FIGURE 3 | Projected changes in the 30-year spring climatology of the NA-CORDEX multi-model ensemble median in mid- (2030–2059) and late-century (2070–2099), relative to the model historical period (1976–2005). Maps show the seasonal precipitation totals [**(A,D)**, inches], SDII [**(B,E)**, mm day^{-1}], and heavy precipitation day frequency [**(C,F)**, days]. Stippling represents areas where fewer than 9 of the 12 simulations agreed on the sign of the change.

projections indicate overall decreases in the frequency of dry days and length of dry spells in spring (**Figure 4**). There is a distinct spatial gradient, however, in both the average and maximum dry spell lengths in projections for both mid- and late-century. Namely, the multi-model mean shows slight (0.3–1 day per year) increases in the average and maximum dry spell lengths across the southeast Midwest, while most of the northwest quadrant of the Midwest exhibits decreased average and maximum dry spell lengths of 0.5–2 days per year by mid-century. The simulations do not show good agreement in mid-century projections of changes in dry days or dry spell length (**Figures 4A–C**). Meanwhile, late-century projections of decreases in spring dry days and dry spell length are more widespread, more robust, and of larger magnitude (**Figures 4D–F**). Namely, the average dry spell length is projected to decrease by 0.5 to over 2 days by late century, with the largest changes in northern Wisconsin and Minnesota. Overall, we find good agreement in both mid- and late-century projections of increased spring precipitation and precipitation intensity across the Midwest.

Projected Changes in Summer Precipitation

We compare projected summer precipitation metrics in the mid- and late-century to the model historical period (**Figure 5**). Projected changes in summer precipitation and precipitation intensity are more variable in both sign and strength and exhibit more spatial variability than spring projections. Ensemble

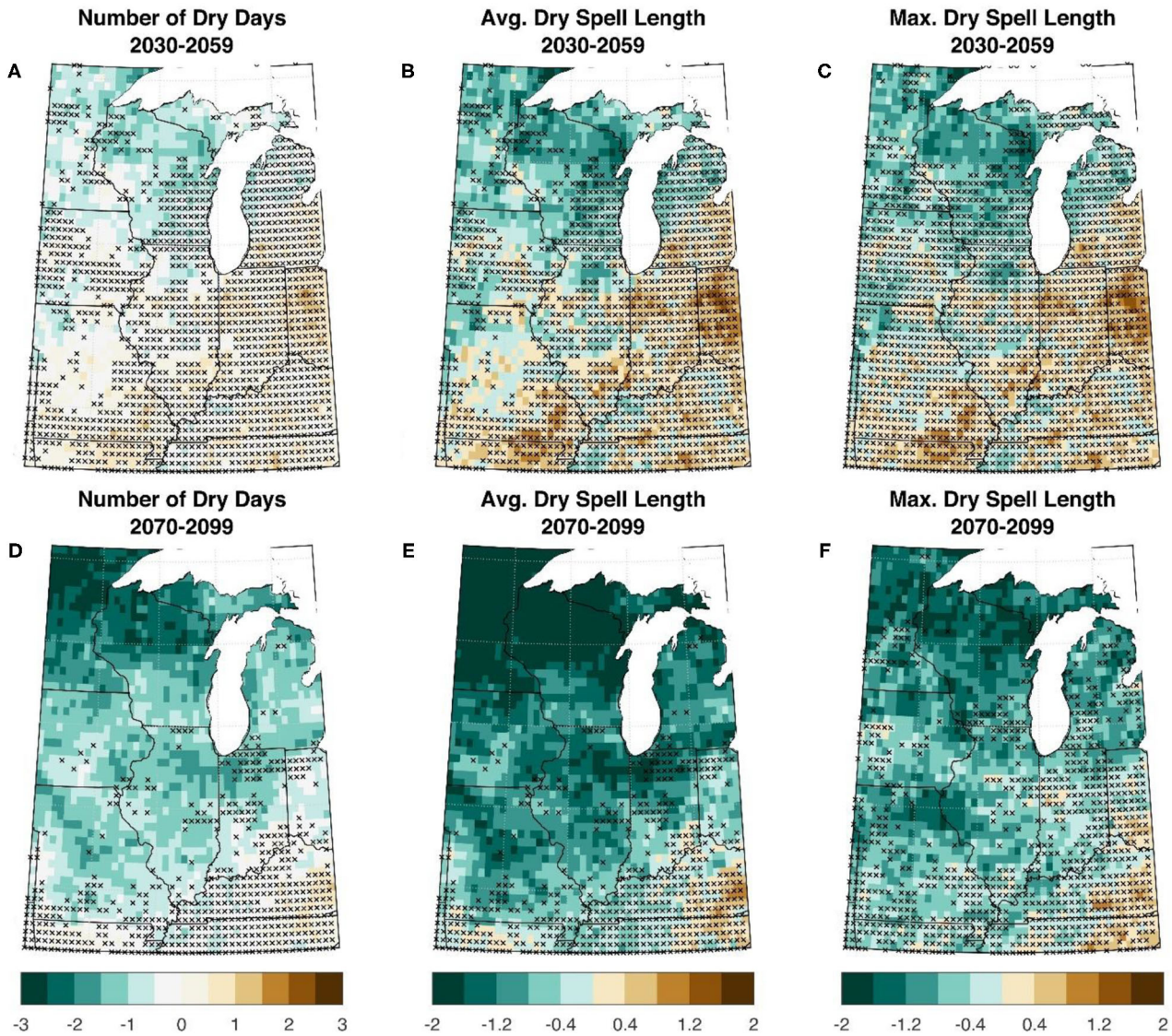

FIGURE 4 | The projected change in the 30-year spring climatology of the NA-CORDEX multi-model ensemble median in mid- (2030–2059) and late-century (2070–2099), relative to the model historical period (1976–2005). Shown are the number of dry days **(A,D)**, the average dry spell length **(B,E)**, and the maximum dry spell length **(C,F)**. Stippling represents areas where fewer than 9 of the 12 simulations agree on the sign of the change.

median projections indicate 10–30 mm decreases in summer precipitation across most or parts of Missouri, Illinois, Indiana, Michigan, and Ohio, and increased precipitation of the same magnitude in the northwest and southeast Midwest (**Figure 5A**). Meanwhile, late-century projections show more widespread 10–40 mm increases in summer precipitation across the Midwest (**Figure 5D**). However, projections of modest increases or decreases in total summer precipitation and precipitation intensity by mid- and late-century are overwhelmed by the lack of simulation agreement. As indicated by widespread stippling in **Figure 5** maps, agreement in the projected sign of summer precipitation and precipitation intensity change was low across most of the Midwest. The lone exception is for late-century projected increases in summer SDII on the order of 1–2.5 mm, which are robust for much of the northwest Midwest (**Figure 5E**).

Simulations indicate an increase of 1–3 additional summer dry days by mid- and late-century in the northern and western Midwest, with more modest projections of <1 fewer summer dry day in the southern Midwest (**Figure 6**). Mid- and late-century projections also show increased dry spell length, particularly in the northern and western Midwest. However, like summer precipitation and intensity projections, agreement for summer dry day frequency and dry spell length is low across the region.

We compare individual model projected changes in region-wide summer precipitation characteristics to better understand the lack of consistency between models. Each simulation's mid- and late-century projections of region-wide summer total

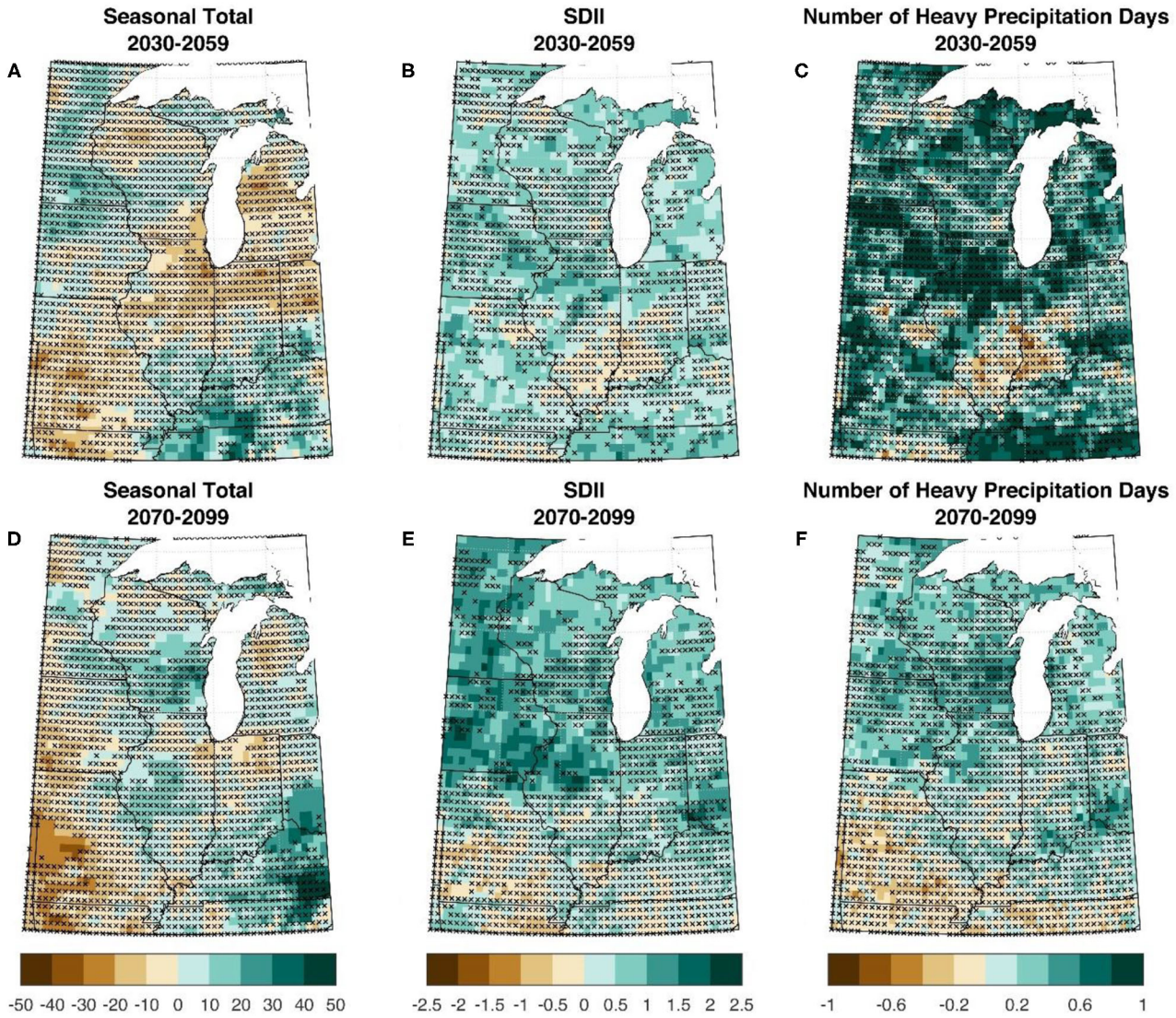

FIGURE 5 | The projected change in the 30-year summer climatology of the NA-CORDEX multi-model ensemble median in mid- (2030–2059) and late-century (2070–2099), relative to the model historical period (1976–2005). Shown are the seasonal precipitation totals [**(A,D)**, mm], SDII [**(B,E)**, mm day^{-1}], and the number of heavy precipitation days [**(C,F)**, days]. Stippling represents areas where fewer than 9 of the 12 simulations agree on the sign of the change.

precipitation, SDII, and heavy precipitation days (**Figure 7**) along with total dry day frequency and average and maximum dry spell lengths (**Figure 8**) are compared to that simulation's historical values using a two-sample *t*-test. Projected changes are considered statistically significant at the 95% confidence level. Only 7 of the 12 simulations project increases in region-wide summer precipitation by mid- and late-century, although 5 of the 7 late-century projections are significantly different from the model historical climatology (**Figures 7A,B**). In general, the simulations are a bit more consistent in projected increases in summer SDII, with at least 9 of 12 projecting increased SDII by mid- and late-century. Five simulations project significant increases in SDII by mid- and late-century (**Figures 7C,D**). Projected changes in region-wide spring precipitation have considerably stronger agreement between simulations compared to those for summer (**Supplementary Figure 1**). All 12 simulations show significant increases in total spring precipitation, spring SDII, and the frequency of spring heavy precipitation days by late-century (**Supplementary Figure 1**).

Late-century projections of summer dry days and dry spell length have a bit more agreement between models than mid-century for the Midwest region (**Figure 8**). Disregarding whether the projected change is statistically significant or not, only 3 of the 12 simulations project decreased dry day frequency and 2 out of 12 project decreased average or maximum dry spell length by late-century (**Figures 8D,F**). This compares to five simulations that project decreased dry day frequency and four simulations

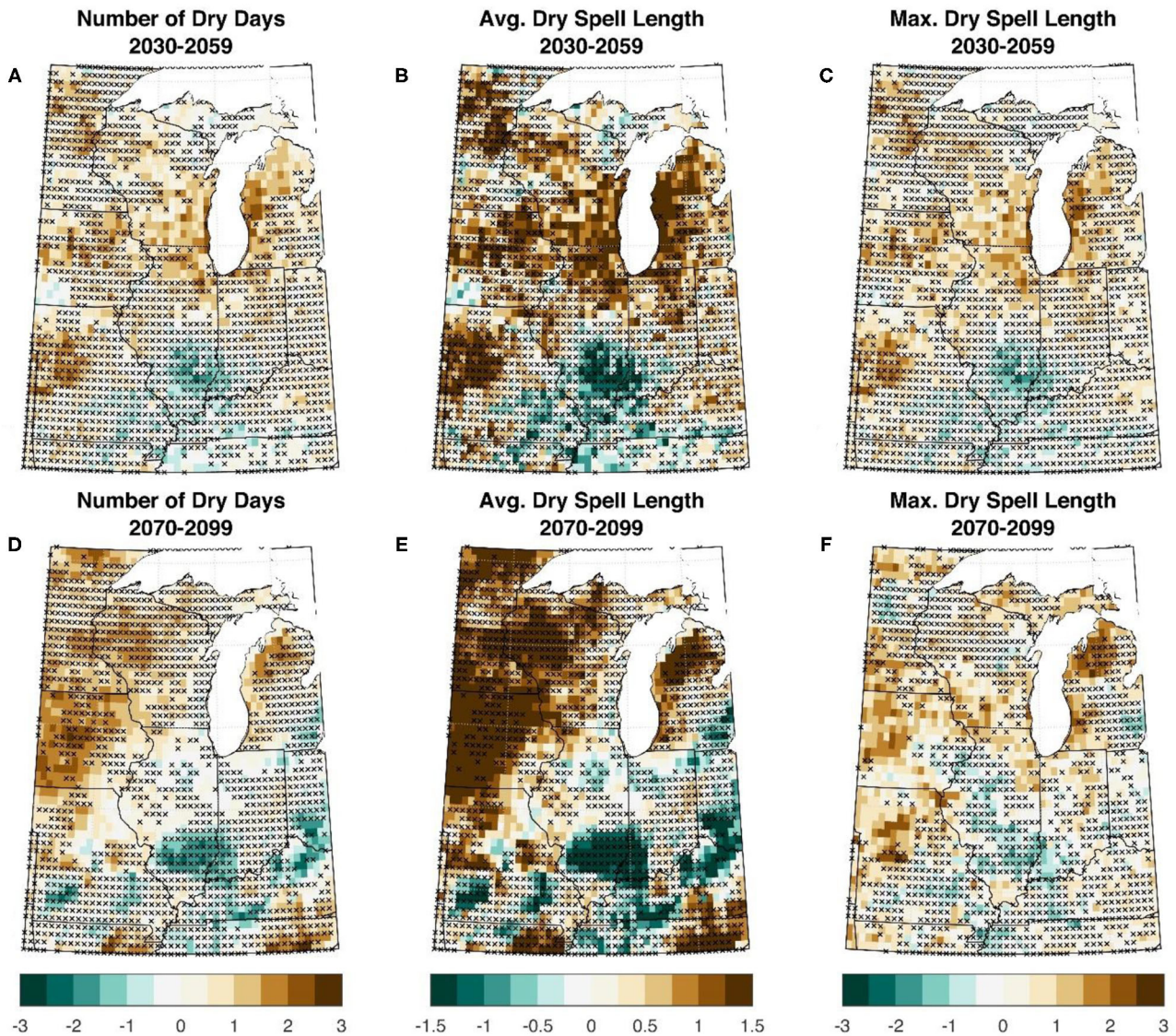

FIGURE 6 | The projected change in the 30-year summer climatology of the NA-CORDEX multi-model ensemble median in mid- (2030–2059) and late-century (2070–2099), relative to the model historical period (1976–2005). Shown are the number of dry days **(A,D)**, the average dry spell length **(B,E)**, and the maximum dry spell length **(C,F)**. Stippling represents areas where fewer than 9 of the 12 simulations agreed on the sign of the projected change.

that project decreased dry spell length by mid-century. Late-century projections of spring dry days and dry spell length show better agreement between simulations than those for summer (**Supplementary Figure 2**). Only 1 out of 12 simulations show increased spring dry days, average dry spell length, and maximum dry spell length (**Supplementary Figure 3**).

Region-wide projected changes in summer precipitation characteristics, including totals, frequency, and intensity, are more consistent between the 12 NA-CORDEX model combinations than when comparing projections locally; and agreement on the sign of summer precipitation change tends to increase from mid- to late-century projections. Overall, most simulations project increased summer precipitation in the Midwest region by mid- and late-century, but with a higher frequency of dry days and longer average and maximum dry spell lengths. Taken together, the projections indicate a wetter, but more variable Midwest summer precipitation climatology throughout the remainder of the twenty-first century.

Changing Risk of Wet Spring-Dry Summer Seasons

Projections of continued increases in April and May precipitation and concurrent (albeit less consistent) increased July and August precipitation variability imply the potential risk of more frequent excessively wet springs followed by dry summers. We investigate the joint changes to spring and summer Midwest precipitation

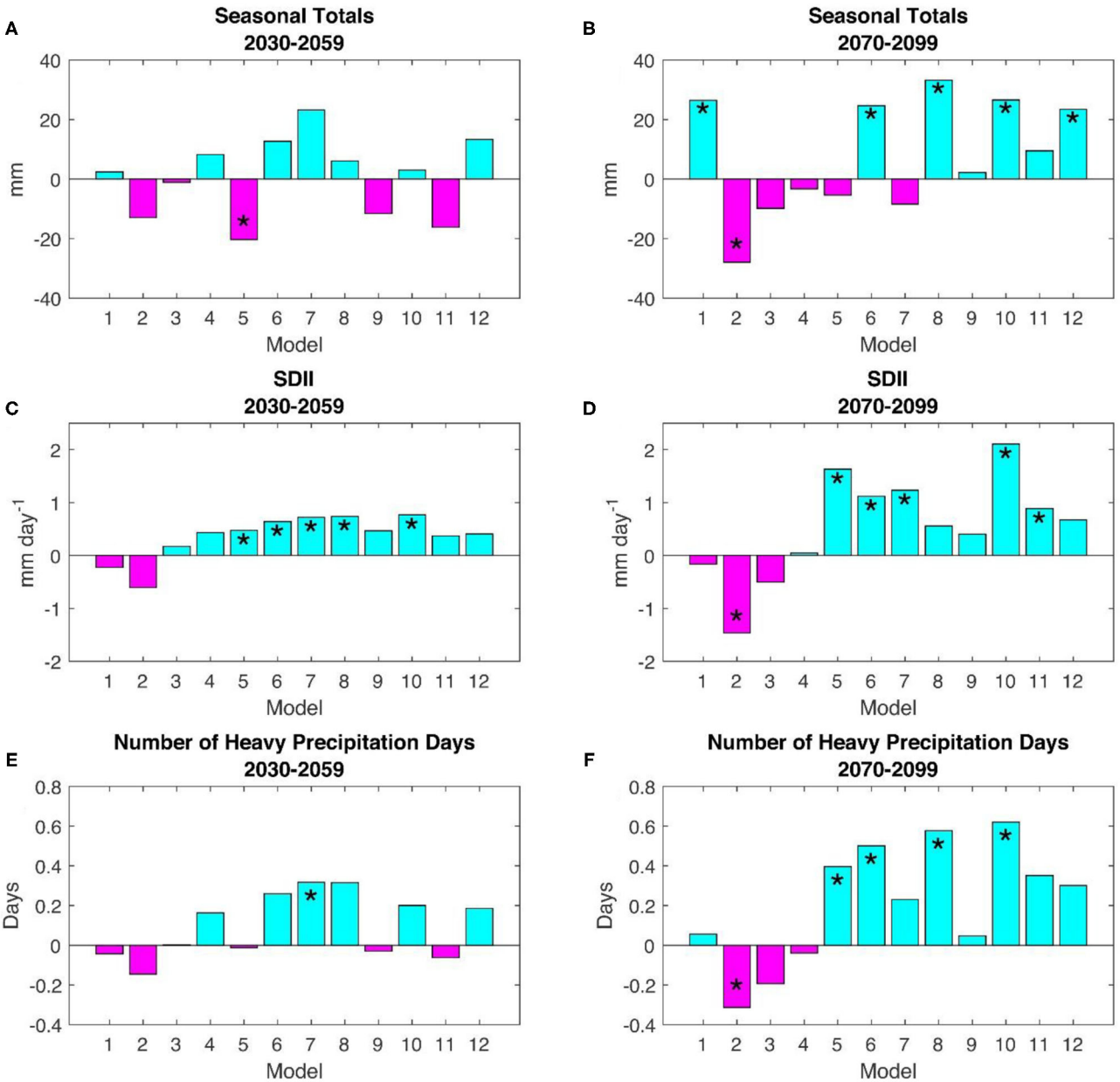

FIGURE 7 | The projected changes in the 30-year, regionally averaged summer climatologies for each NA-CORDEX model in mid- (2030–2059) and late-century (2070–2099), relative to the model historical period (1976–2005). Shown are the seasonal precipitation totals [**(A,B)**, mm], SDII [**(C,D)**, mm day^{-1}], and the number of heavy precipitation days [**(E,F)**, days]. Model numbers are the same as in **Table 1**. Asterisks indicate models where the regional change was statistically significant at the 5% level.

in the Midwest in more detail. Specifically, we examine how the frequency of years with both wet springs and dry summers is projected to change through the end of the century. We examine the difference between each season's precipitation total and the corresponding historical average at each grid point. Spring seasonal precipitation totals at a particular grid point that are at least 1.3 standard deviations above the historical average at that point will be considered wet. Likewise, summer totals that are at least 1.3 standard deviations below the historical average at a point will be considered dry. The 1.3 standard deviation threshold is commonly used to denote severe drought, as in the U.S. Drought Monitor (Svoboda et al., 2002), and has been used in past studies to represent both severe dryness and wetness (e.g., Ford et al., 2021).

Figure 9 shows the occurrences of wet springs, dry summers, and years with both in the observed NClimDiv data during the 30-year period 1976–2005. Although there is quite a bit of spatial variability, in general the frequency of wet springs outweighs that

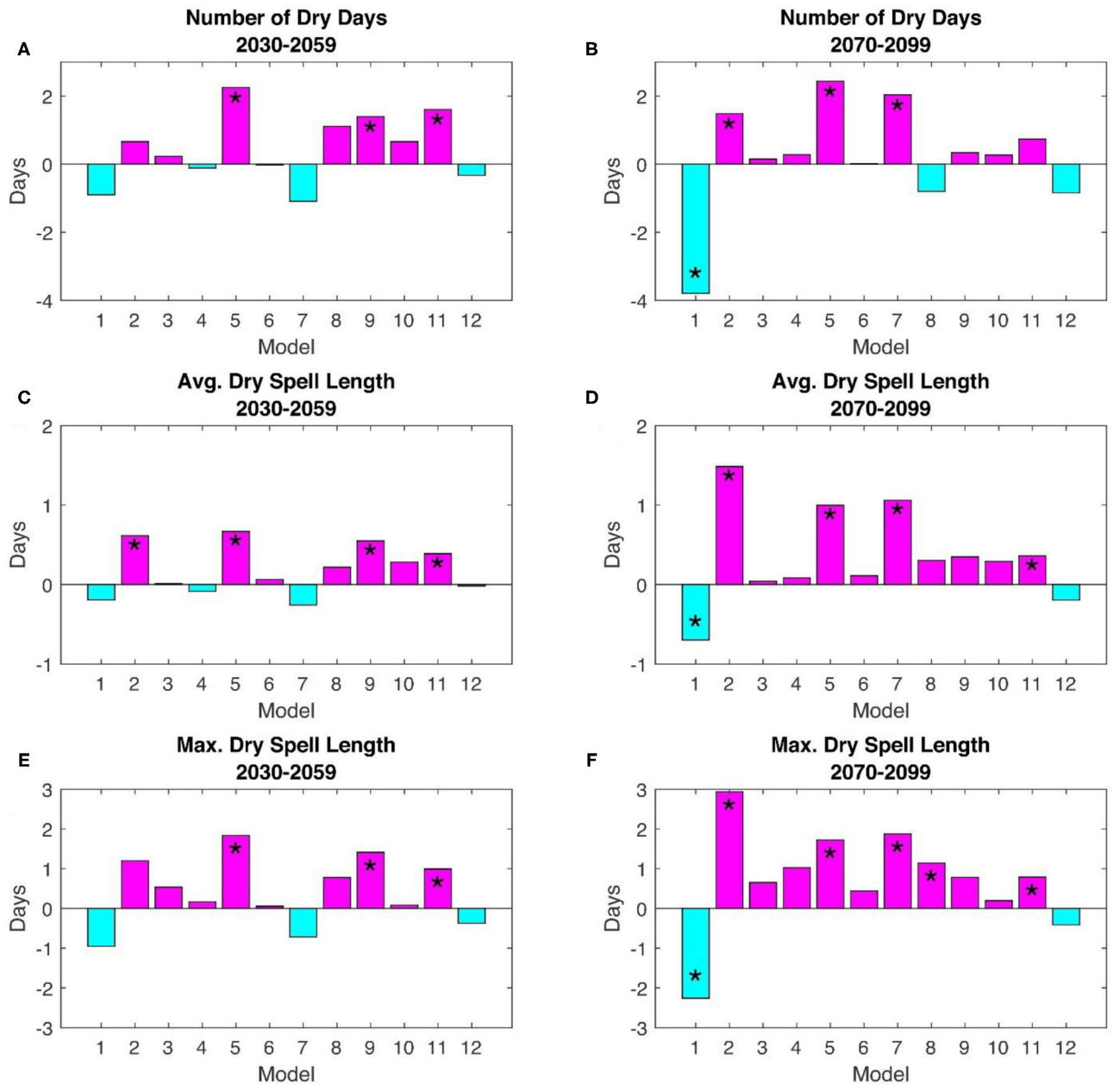

FIGURE 8 | The projected changes in the 30-year, regionally averaged summer climatologies for each NA-CORDEX model in mid- (2030–2059) and late-century (2070–2099), relative to the model historical period (1976–2005). Shown are the number of dry days **(A,B)**, average dry spell length **(C,D)**, and the maximum dry spell length **(E,F)**. Model numbers are the same as in **Table 1**. Asterisks indicate models where the regional change was statistically significant at the 5% level.

of dry summers in the Midwest. The region-wide average number of wet springs was 5.6, or 1 in every 5–6 years over the 30-year historical period, while the average number of dry summers was 3.2, or 1 in every 9–10 years. However, dry summers rarely follow wet springs in the Midwest, and most areas did not experience a wet spring to dry summer transition between 1976 and 2005. With that said, a small region in southern Illinois and Indiana has experienced between 2 and 4 of these events in the 30-year historical period. This is also a region shown by Ford et al. (2021) to have an increasing propensity for wet-to-dry transitions on subseasonal timescales over the past several decades.

Compared with the historical observations, NA-CORDEX model combinations produce far fewer historical wet springs (**Figure 10A**) and slightly fewer historical dry summers (**Figure 10D**). For the simulations, the region-wide average number of historical wet springs is around 3.2, and the average number of historical dry summers is around 2.5, compared with 5.6 and 3.2 for the NClimDiv data, respectively. Analysis

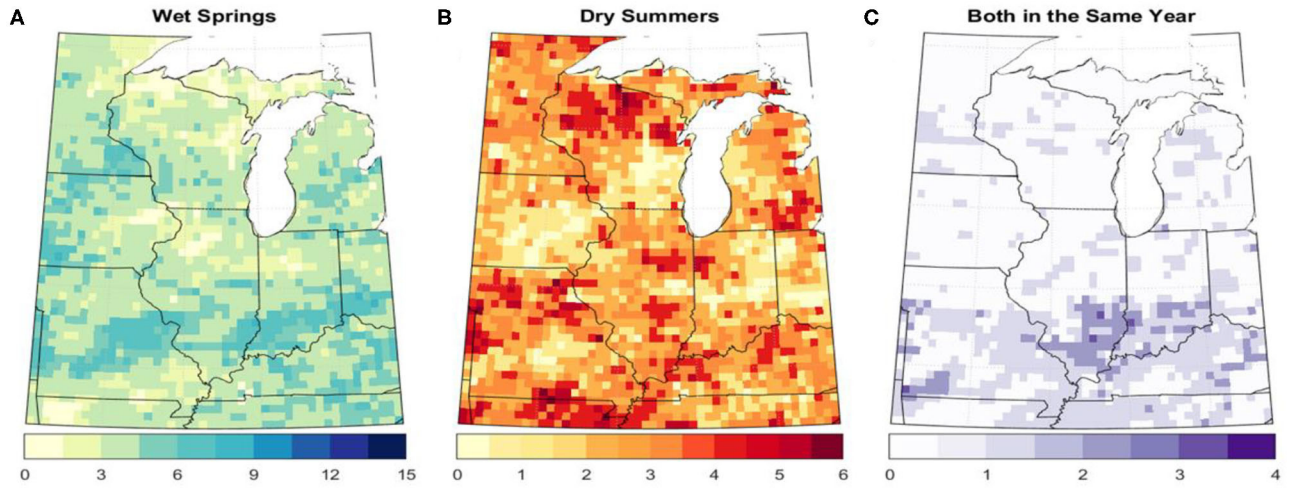

FIGURE 9 | Observed historical (1976–2005) frequency of wet springs **(A)**, dry summers **(B)**, and years with adjacent wet springs and dry summers **(C)**. The thresholds used to identify wet springs and dry summers were calculated using the data from 1951 to 2005.

of the individual model ensemble members revealed none of the members produced wet spring frequency equal to or exceeding that in the observations. These discrepancies could be partly attributed to the lower interannual variability in spring precipitation in the simulations relative to the observations. When averaged across all simulations and the entire study region, the simulated standard deviation of spring precipitation during the historical (1951–2005) period represents 27% of the simulated mean total spring precipitation. Meanwhile, the observed standard deviation of spring precipitation represents 36% of the mean total, implying overall more interannual variability in the observations than the simulations. Due to the relative dearth of wet springs in the simulations, there are virtually no years with both wet springs and dry summers anywhere in the Midwest during the model historical period (**Figure 10G**).

The projected frequency of wet springs increases to a regional average of 7 springs for the 30-year mid-century period and 12 springs for the 30-year late-century period (**Figures 10B,C**). Meanwhile, the frequency of dry summers is projected to increase only in the far western and northern Midwest, by 2–3 summers for the 30-year mid-century and late-century periods (**Figures 10E,F**). Despite the sizeable projected increase in wet spring frequency, the modest projected change in summer precipitation limits projected wet-spring to dry-summer years to 1 additional for the 30-year late-century period (**Figures 10H,I**).

Excessively wet springs can cause significant impacts to agriculture, irrespective of conditions in the following summer. The Midwest experienced one such year in 2011, when persistent rains across the Midwest caused damaging floods, saturated soils, and significant planting delays, all of which placed enormous physical, emotional, and financial strain on Midwest farmers (Olson and Wright Morton, 2012; NOAA NCEI, 2021). Region-wide April–May 2011 was the wettest in the historical observed period of record. To put this record season in the context of projected increased spring precipitation across the region, we compared the wettest spring in the 55-year historical period for each simulation and found its corresponding rank in spring total precipitation in the last 55-years of each simulations' projection (2045–2099). The rank of the historically wettest spring in each simulations' 2045–2099 projections ranged from 5th wettest to 18th wettest, with a 12-simulation median rank of 10th wettest. These results suggest a substantial increase in the likelihood of excessive and damaging spring precipitation, akin to 2011, by mid- to late-century in the Midwest.

SUMMARY AND CONCLUSIONS

In this study, we have examined changes to spring and summer precipitation characteristics in the Midwest by the mid- and late-century as projected by an ensemble of NA-CORDEX model combinations. The simulations strongly agree that springs will become increasingly wetter through the end of the century. Heavy and persistent spring precipitation can be detrimental to Midwest agriculture through delays in planting, pre- and post-emergence disease and pest control, and increasing soil erosion (Landau et al., 2021; Thaler et al., 2021). Increased river nitrogen loads in the Midwest are directly attributable to heavy precipitation in the region, particularly in the spring (Baeumler and Gupta, 2020). Issues caused by excessively high spring precipitation can significantly affect crop yield, but also increase stress on farmers, farm workers, and rural economies (Cianconi et al., 2020; Henning-Smith et al., 2021).

We find projections of changes in summer precipitation are variable in both sign and strength across the Midwest. Simulation agreement on summer precipitation changes by mid- and late-century is low relative to spring projections. This agrees with Bukovsky and Mearns (2020), who find a robust increase in spring total precipitation and consistent inconsistency in the sign of the summer total precipitation projections in NA-CORDEX.

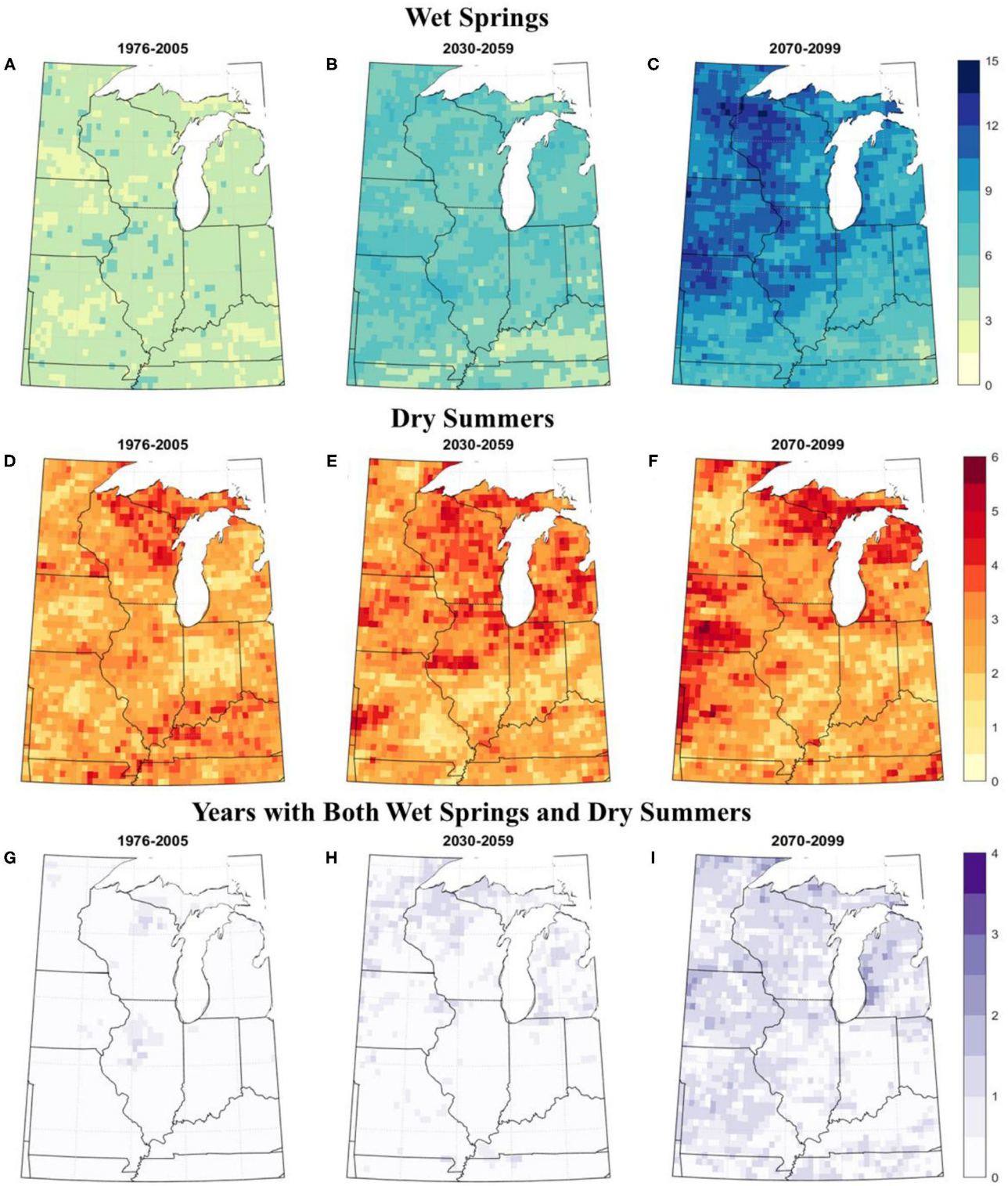

FIGURE 10 | The number of wet springs **(A–C)**, dry summers **(D–F)**, and years with both **(G–I)** during each period based off the multi-model ensemble median seasonal totals for the NA-CORDEX historical period 1950–2005.

Although, when examining projections on a region-wide scale we find more consistent indications of increases in Midwest summer precipitation by late-century, albeit with more frequent summer dry days and longer summer dry spells. These findings indicate a potential transition to a wetter but more variable summer precipitation climatology for the Midwest as a whole, while agreement on future changes in local summer precipitation characteristics is much more uncertain.

Projected changes to precipitation in the NA-CORDEX simulations can be influenced by the forcing GCM output. Consistent with the downscaling results, each of the five CMIP5 models, which are used as the lateral boundary conditions for the NA-CORDEX downscaling, showed increased precipitation in the Midwest during spring in the mid-century, with even higher totals evident by the end of the century (**Supplementary Figure 3**). However, changes to summer precipitation are more mixed. Two models (HadGEM2-ES and MPI-ES-LR) show an overall drying trend, and the changes in the other models are less evident, suggesting less robustness in the projections of summer precipitation. CanRCM4 downscaling. Meanwhile, we noted many NA-CORDEX simulations show opposite changes in summer precipitation between the mid-century and late-century (**Figures 7A,B**), which are not found in the CMIP5 models (**Supplementary Figure 3**). This discrepancy can possibly be associated with the physics and configurations of the downscaling models. Previous comparison studies have documented the difference in summertime precipitation projections between GCMs and RCMs (e.g., Mariotti et al., 2011; Liu et al., 2017; Coppola et al., 2021), which can possibly be attributed to the different treatments of aerosol forcings and local land-atmosphere feedbacks.

This may also explain why our summertime results differ from those in other recent studies (e.g., Winkler et al., 2012; Swain and Hayhoe, 2015; Byun and Hamlet, 2018; Byun et al., 2019; Hamlet et al., 2020). While most of these studies agree with our results that spring precipitation will continue to increase in the Midwest through the end of the century, some disagree about late-century summers, projecting that the mid-century dryness will continue through the late-century. This could be attributable to the specific data sets and models used and how they are downscaled in each study. While our models are dynamically downscaled, those in Byun and Hamlet (2018), Byun et al. (2019), and Hamlet et al. (2020) for example are statistically downscaled, and Swain and Hayhoe (2015) directly use the GCMs instead. Although downscaling relies on projections from the driving GCMs, RCMs have the potential to capture some of the synoptic and mesoscale convective processes that dominate mid- to late-summer precipitation in the Midwest, which could explain the different results. In other words, the regional assessment based on the downscaled results can be affected by the choice of RCMs due to their different parameterizations of physical processes. For instance, with the same driving GCM as their boundary conditions, RCMs show different changes in summer precipitation (**Figures 7**, **8**). The different treatments of climate forcings (e.g., aerosols) in GCMs and RCMs can also lead to different behaviors of climate variables (Chen, 2021; Coppola et al., 2021). However, the inconsistency in summer projections implies further model refinement and inter-comparison are needed to better understand and communicate the potential risks of summer precipitation changes in the Midwest.

It should be noted, in both discussion of the observed precipitation climatology and the comparison with the model historical climatology that our use of the gridded NClimDiv dataset to represent observations comes with its own limitations. Spatial interpolation that is necessary to move from individual gauge-based to gridded precipitation datasets has been shown to reduce the frequency of heavy precipitation events in the Midwest (Ensor and Robeson, 2008). We demonstrate this issue by comparing high-quality gauge observations from the National Weather Service Cooperative Observer station in Champaign, Illinois with the NClimDiv grid cell in which the station resides over the period 1951–2020. The gridded NClimDiv dataset consistently underestimates the frequency of heavy precipitation days (>25 mm) and overestimates the frequency of wet days (>2.5 mm) in both spring and summer, relative to the gauge-based observations (**Supplementary Figure 4**). The differences between gridded and gauge-based heavy precipitation days in Champaign are 0.56 days in spring and 0.61 days in summer, representing 29 and 26% of the 1951–2020 gauge-based average in spring and summer, respectively. Differences in wet days in Champaign are 1.9 days in spring and 3.2 days in summer, representing 13 and 27% of the gauge-based average for each season. Although gridded observation-based datasets provide many advantages over gauge-based observations, particularly in comparison to or validation of gridded model simulations, the biases reported in prior literature and demonstrated in **Supplementary Figure 3** are important to acknowledge.

This study does not consider projected changes to temperature, which are widely expected to increase through mid- and late-century in the Midwest (Hamlet et al., 2020; Wuebbles et al., 2021). Increased growing season temperatures are associated with increases in evaporation and evaporative demand, which can induce additional stress to crops. Elevated evaporative demand, when combined with preexisting dryness, can create damaging flash drought in the Midwest, as was the case in 2012 (Otkin et al., 2018). Vapor pressure deficit has been shown to be an important precursor to agricultural drought impacts in the Midwest (Kimm et al., 2020). However, studies of historical changes in vapor pressure deficit in the Midwest have yielded varying results. Ficklin and Novick (2017) find significant increases in vapor pressure deficit in the Midwest between 1979 and 2013. However, Seager et al. (2015) found vapor pressure deficit in the Midwest has decreased over the longer period between 1961 and 2013, driven by observed increases in actual vapor pressure in the region. Similarly, Basso et al. (2021) find growing season potential evapotranspiration in the Midwest has decreased between 1960 and 2019, but more importantly find that the sign and strength of apparent Midwest evapotranspiration and vapor pressure deficit trends are highly sensitive to the historical record length. These inconsistencies are partly due to the complex change in Midwest temperatures both over the past century and in the past 30 years. Over both long-term (e.g., 50–100 year) and short-term (20–30 year) periods, growing season minimum temperatures have risen at

a faster rate than maximum temperatures (Pathak et al., 2016; Angel et al., 2018; Basso and Ritchie, 2018), which has caused actual vapor pressure to increase at a similar rate to saturation vapor pressure (Basso et al., 2021). Importantly, summertime maximum temperatures in the Midwest have increased at a faster rate over the past 30 years relative to their rate of change since the turn of the twentieth century (Wuebbles et al., 2021). If changes in summertime maximum temperatures begin to outpace those of minimum temperatures in the Midwest, vapor pressure deficit will increase. However, if minimum temperature increases continue to exceed maximum temperature changes through the twenty-first century, increased vapor pressure deficit in the Midwest is not inevitable. Differences in the magnitude of daily minimum and maximum temperatures, as well as humidity, will continue to be important considerations for drought research in the Midwest.

Our study also only considered the high emissions RCP8.5 scenario, and it is possible that different pathways, such as RCP4.5 for example, may show different results. However, Midwest precipitation response to emissions reductions, particularly spring and summer precipitation, have been shown to be less dramatic than temperature (Wuebbles et al., 2021). It also should be noted that the climate projections in this study are based on downscaled CMIP5 simulations. Although CMIP5's successor, CMIP6, provides climate simulations from state-of-the-art climate models with improved model physics (Eyring et al., 2016), most of their spatial resolutions (e.g., 50 km or more coarse) are still not adequate for regional climate assessments.

DATA AVAILABILITY STATEMENT

The raw data supporting the conclusions of this article will be made available by the authors, without undue reservation.

AUTHOR CONTRIBUTIONS

KG led data analysis, manuscript writing, and figure creation. LC contributed to data analysis, project scoping, manuscript writing, and figure creation. TF lead project scoping, contributed to data analysis, manuscript writing, and figure creation. All authors contributed to the article and approved the submitted version.

FUNDING

This work was supported by NOAA Contract NA18OAR4310253B.

ACKNOWLEDGMENTS

The authors thank the Illinois Farm Bureau for supporting this work.

SUPPLEMENTARY MATERIAL

The Supplementary Material for this article can be found online at: https://www.frontiersin.org/articles/10.3389/frwa.2021.780333/full#supplementary-material

REFERENCES

Angel, J., Swanston, C., Boustead, B. M., Conlon, K. C., Hall, K. R., Jorns, J. L., et al. (2018). "Midwest," in Impacts, Risks, and Adaptation in the United States: Fourth National Climate Assessment, Vol. II, eds D. R. Reidmiller, C. W. Avery, D. R. Easterling, K. E. Kunkel, K. L. M. Lewis, T. K. Maycock, and B. C. Stewart (Washington, DC: U.S. Global Change Research Program), 872–940. doi: 10.7930/NCA4.2018.CH21

Baeumler, N. W., and Gupta, S. C. (2020). Precipitation as the primary driver of variability in river nitrogen loads in the Midwestern United States. *J. Am. Water Resour. Assoc.* 56, 113–133. doi: 10.1111/1752-1688.12809

Basso, B., Martinez-Feria, R. A., Rill, L., and Ritchie, J. T. (2021). Contrasting long-term precipitation trends reveal minor changes in projected potential evapotranspiration in the US Midwest. *Nat. Commun.* 12, 1–10, doi: 10.1038/s41467-021-21763-7

Basso, B., and Ritchie, J. T. (2018). Evapotranspiration in high-yielding maize and under increased vapor pressure deficit in the US Midwest. *Agr. Env. Lett.* 3:170039. doi: 10.2134/ael2017.11.0039

Bukovsky, M. S., and Mearns, L. O. (2020). Regional climate change projections from NA-CORDEX and their relation to climate sensitivity. *Clim. Change* 162, 645–665. doi: 10.1007/s10584-020-02835-x

Byun, K., Chiu, C. M., and Hamlet, A. F. (2019). Effects of 21st century climate change on seasonal flow regimes and hydrologic extremes over the Midwest and Great Lakes region of the US. *Sci. Total Environ.* 650, 1261–1277. doi: 10.1016/j.scitotenv.2018.09.063

Byun, K., and Hamlet, A. F. (2018). Projected changes in future climate over the Midwest and Great Lakes region using downscaled CMIP5 ensembles. *Int. J. Climatol.* 38, e531–e553. doi: 10.1002/joc.5388

Chen, L. (2021). Uncertainties in solar radiation assessment in the United States using climate models. *Clim. Dyn.* 56, 665–678. doi: 10.1007/s00382-020-05498-7

Christian, J., Christian, K., and Basara, J. B. (2015). Drought and pluvial dipole events within the Great Plains of the United States. *J. Appl. Meteorol. Climatol.* 54, 1886–1898. doi: 10.1175/JAMC-D-15-0002.1

Cianconi, P., Betrò, S., and Janiri, L. (2020). The impact of climate change on mental health: a systematic descriptive review. *Front. Psychiatry*. 11:74. doi: 10.3389/fpsyt.2020.00074

Coppola, E., Nogherotto, R., Ciarlo', J. M., Giorgi, F., van Meijgaard, E., Kadygrov, N., et al. (2021). Assessment of the European climate projections as simulated by the large EURO-CORDEX regional and global climate model ensemble. *J. Geophys. Res. Atmos.* 126, e2019JD032356. doi: 10.1029/2019JD032356

Daigh, A. L. M., DeJong-Hughes, J., and Acharya, U. (2020). Projections of yield losses and economic costs following deep wheel-traffic compaction during the 2019 harvest. *Agric. Environ. Lett.* 5, e20013. doi: 10.1002/ael2.20013

El Mourid, M., He, G. Q., Andrade, F. H., and Anderson, I. C. (1986). Relationship of corn and soybean yields to weekly moving averages for precipitation and temperature at four climatic locations in Iowa. *Iowa State J. Res.* 61, 49–64.

Ensor, L. A., and Robeson, S. M. (2008). Statistical characteristics of daily precipitation: comparisons of gridded and point datasets. *J. Appl. Meteorol. Climatol.*, 47, 2468–2476, doi: 10.1175/2008JAMC1757.1

Eyring, V., Bony, S., Meehl, G. A., Senior, C. A., Stevens, B., Stouffer, R. J., et al. (2016). Overview of the couple model intercomparison project phase 6 (CMIP6) experimental design and organization. *Geosci. Model Dev.* 9, 1937–1958. doi: 10.5194/gmd-9-1937-2016

Ficklin, D. L., and Novick, K. A. (2017). Historic and projected changes in vapor pressure deficit suggest a continental-scale drying of the United States atmosphere. *J. Geophys. Res.* 122, 2061–2079, doi: 10.1002/2016JD025855

Ford, T. W., Chen, L., and Schoof, J. T. (2021). Variability and transitions in precipitation extremes in the Midwest United States. *J. Hydrometeor.* 22, 533–545. doi: 10.1175/JHM-D-20-0216.1

Foreign Agricultural Service (2021). United States Department of Agriculture. *World Agricultural Production*.

Gautum, S., Costello, C., Baffaut, C., Thompson, A., and Sadler, E. J. (2021). Projection of future drought and extreme events occurrence in Goodwater Creek Experimental Watershed Midwestern US. *Hydrol. Sci. J.* 66, 1045–1058. doi: 10.1080/02626667.2021.1906878

Goldblum, D. (2009). Sensitivity of corn and soybean yield in Illinois to air temperature and precipitation: the potential impact of future climate change. *Phys. Geogr.* 30, 27–42, doi: 10.2747/0272-3646.30.1.27

Hamlet, A. F., Byun, K., Robeson, S. M., Widhalm, M., and Baldwin, M. (2020). Impacts of climate change on the state of Indiana: ensemble future projections based on statistical downscaling. *Clim. Change* 163, 1881–1895. doi: 10.1007/s10584-018-2309-9

Hatfield, J. L., Wright-Morton, L., and Hall, B. (2018). Vulnerability of grain crops and croplands in the Midwest to climatic variability and adaptation strategies. *Clim. Change* 146, 263–275. doi: 10.1007/s10584-017-1997-x

Henning-Smith, C., Alberth, A., Bjornestad, A., Becot, F., and Inwood, S. (2021). Farmer mental health in the US Midwest: key Informant perspectives. *J. Agromed.* 2021, 1–10. doi: 10.1080/10599924X.2021.1893881

Hernández-Díaz, L., Nikiéma, O., Laprise, R., Winger, K., and Dandoy, S. (2019). Effect of empirical correction of sea-surface temperature biases on the CRCM5-simulated climate and projected climate changes over North America. *Clim. Dyn.* 53, 453–476. doi: 10.1007/s00382-018-4596-2

Hu, Q., and Buyanovsky, G. (2003). Climate effects on corn yield in Missouri. *J. Appl. Meteorol.* 42, 1626–1635. doi: 10.1775/1520-0450(2003)042<1626:CEOCYI>2.0.CO;2

Kimm, H., Guan, K., Gentine, P., Wu, J., Bernacchi, C. J., Sulman, B. N., et al. (2020). Redfining droughts for the US Corn Belt: the dominant role of atmospheric vapor pressure deficit over soil moisture in regulating stomatal behaviro in Maize and Soybean. *Agr. For. Meteorol.* 287, 107930. doi: 10.1016/j.agrformet.2020.107930

Landau, C. A., Hager, A. G., and Williams, I. I., M. M. (2021). Diminishing weed control exacerbates maize yield loss to adverse weather. *Glob. Chang. Biol.* 27, 6156–6165. doi: 10.1111/gcb.15857

Liu, C., Ikeda, K., Rasmussen, R., Barlage, M., Newman, A. J., Prein, A. F., et al. (2017). Continental-scale convection-permitting modeling of the current and future climate of North America. *Clim. Dyn.* 49, 71–95. doi: 10.1007/s00382-016-3327-9

Liu, L., and Basso, B. (2020). Impacts of climate variability and adaptation strategies on crop yields and soil organic carbon in the US Midwest. *PLoS ONE.* 15:e0225433. doi: 10.1371/journal.pone.0225433

Mariotti, L., Coppola, E., Sylla, M. B., Giorgi, F., and Piani, C. (2011). Regional climate model simulation of projected 21st century climate change over an all-Africa domain: comparison analysis of nested and driving model results. *J. Geophys. Res. Atmos.* 116:D15111. doi: 10.1029/2010JD 015068

McGinnis, S. (2021). *NA-CORDEX Bias Correction Error*. Available online at: https://na-cordex.org/bias-correction-error.html (accessed October 10, 2021).

Mearns, L. O., McGinnis, S., Korytina, D., Scinocca, J., Kharin, S., Jiao, Y., et al. (2017). "The NA-CORDEX Dataset, Version 1.0," in *NCAR Climate Data Gateway* (Boulder, CO: The National Center of Atmospheric Research.

Mishra, V., and Cherkauer, K. A. (2010). Retrospective droughts in the crop growing season: implications to corn and soybean yield in the Midwestern United States. *Agric. For. Meteorol.* 150, 1030–1045. doi: 10.1016/j.agrformet.2010.04.002

National Agricultural Statistics Service (2021). United States Department of Agriculture. *Crop Production 2020 Summary.*

NOAA NCEI (2011). *NOAA National Centers for Environmental Information, State of the Climate, National Climate Report for May 2011, published online June 2011.* Available online at: https://www.ncdc.noaa.gov/sotc/national/201105/supplemental/page-3 (accessed September 20, 2021).

NOAA NCEI (2021). *NOAA National Centers for Environmental Information, Climate at a Glance: Regional Time Series. published August 2021.* Available online at: https://www.ncdc.noaa.gov/cag/ (accessed September 2, 2021).

Olson, K. R., and Wright Morton, L. (2012). The impacts of 2011 induced levee breaches on agricultural lands of Mississippi River Valley. *J. Soil Water Conserv.* 67, 5A—10A. doi: 10.2486/jswc.67.1.5A

Otkin, J. A., Svoboda, M., Hunt, E. D., Ford, T. W., Anderson, M. C., Hain, C., et al. (2018). Flash droughts: a review and assessment of the challenges imposed by rapid-onset droughts in the United States. *Bull. Am. Meteorol. Soc.* 99, 911–919. doi: 10.1175/BAMS-D-17-0149.1

Pathak, P., Kalra, A., and Ahmad, S. (2016). Temperature and precipitation changes in the Midwestern United States: implications for water management. *Int. J. Water Res. Develop.* 6, 1003–1019. doi: 10.1080/07900627.2016.1238343

Seager, R., Hooks, A., Williams, A. P., Cook, B., Nakamura, J., and Henderson, N. (2015). Climatology, variability, and trends in the US vapor pressure deficit, an important fire-related meteorological quantity. *J. Appl. Meteorol. Climatol.* 54, 1121–1141. doi: 10.1175/JAMC-D-14-0321.1

Svoboda, M., LeComte, D., Hayes, M., Heim, R., Gleason, K., Angel, J., et al. (2002). The drought monitor. *Bull. Am. Meteorol. Soc.* 83, 1181–1190. doi: 10.1175/1520-0477-83.8.1181

Swain, S., and Hayhoe, K. (2015). CMIP5 projected changes in spring and summer drought and wet conditions over North America. *Clim. Dyn.* 44, 2737–2750. doi: 10.1007/s00382-014-2255-9

Thaler, E. A., Larsen, I. J., and Yu, Q. (2021). The extent of soil loss across the US Corn Belt. *Proc. Nat. Acad. Sci. U.S.A.* 118:e1922375118. doi: 10.1073/pnas.1922375118

Urban, D. W., Roberts, M. J., Schlenker, W., and Lobell, D. B. (2015). The effects of extremely wet planting conditions on maize and soybean yields. *Clim. Change* 130, 247–260. doi: 10.1007/s10584-015-1362-x

Vose, R. S., Applequist, S., Squires, M., Durre, I., Menne, M. J., Williams, C. N., et al. (2014). *Data from: NOAA Monthly U.S. Climate Divisional Database (NClimDiv)*. NOAA National Climatic Data Center. (2014). doi: 10.7289/V5M32STR

Westcott, N. E., Hollinger, S. E., and Kunkel, K. E. (2005). Use of real-time multisensor data to assess the relationship of normalized corn yield with monthly rainfall and heat stress across the central United States. *J. Appl. Meteorol.* 44, 1667–1676. doi: 10.1175/JAM2303.1

Winkler, J. A., Arritt, R. W., and Pryor, S. C. (2012). "Climate projections for the Midwest: Availability, interpretation and synthesis," in U. S. National Climate Assessment Midwest Technical Input Report, eds J. Winkler, J. Andresen, J. Hatfield, D. Bidwell, and D. Brown (Ann Arbor, MI: Great Lakes Integrated Sciences and Assessment (GLISA) Center), 1–24.

Winsor, S. (2020). Keep your eyes open for these wet-season soybean diseases. *Crops Soils*. 53, 16–23. doi: 10.1002/crso.20033

Wuebbles, D., Angel, J., Petersen, K., and Lemke, A. M. (2021). *An Assessment of the Impacts of Climate Change in Illinois*. Chicago, IL: The Nature Conservancy. doi: 10.13012/B2IDB-126094

Conflict of Interest: The authors declare that the research was conducted in the absence of any commercial or financial relationships that could be construed as a potential conflict of interest.

Publisher's Note: All claims expressed in this article are solely those of the authors and do not necessarily represent those of their affiliated organizations, or those of the publisher, the editors and the reviewers. Any product that may be evaluated in this article, or claim that may be made by its manufacturer, is not guaranteed or endorsed by the publisher.

frontiers in Water

BRIEF RESEARCH REPORT
published: 25 January 2022
doi: 10.3389/frwa.2021.801265

Pinus resinosa Tree-Ring Latewood Response to Daily-Scale Precipitation Variability at Lake Itasca, Minnesota

Matthew L. Trumper, Daniel Griffin, Evan E. Montpellier and Kurt F. Kipfmueller*

Department of Geography, Environment, and Society, University of Minnesota, Minneapolis, MN, United States

Analysis of daily scale climate observations alongside sub-annual tree-ring data offers new potential for contextualizing climate change in the Great Lakes region. This pilot study combined daily observations from a high-quality station record with a co-located chronology of *Pinus resinosa* latewood width at Lake Itasca, Minnesota. We evaluate trends in observational data and use multiple methods to compare day-wise aggregated climate observations with tree rings over the eleven-decade common period. The Itasca record exhibited strong increases in warm-season precipitation, minimum temperature in all seasons, and lengthening of the freeze-free season. Correlation analyses verified a strong, multi-month warm-season precipitation response in *Pinus resinosa* latewood width. Distinct from previous work, daily data analyses were used to fingerprint an ∼2-week period starting in late July when rainfall variability was historically a major control on interannual tree growth. Climatologically, the timing of this subseasonal critical climate period corresponds with a relative minimum in mean midsummer precipitation. Since the 1980s, the latewood correlation with midsummer rainfall has vanished, and the seasonal-scale rainfall response diminished considerably. This result, new for *Pinus resinosa* in Minnesota, is consistent with studies showing a declining relationship between tree growth and drought in the Midwest United States. Further attribution analyses emphasizing daily-scale phenomena are needed to elucidate mechanisms responsible for the tree-growth response to variability, change, and extremes in climate throughout the Great Lakes region, where the biophysical and socioeconomic impacts of climate change are multifaceted issues of increasing urgency.

Keywords: daily observations, dendroclimatology, warm season hydroclimate, red pine, bimodal precipitation, latewood width, Itasca State Park

OPEN ACCESS

Edited by:
Adam Burnett,
Colgate University, United States

Reviewed by:
Scott Robeson,
Indiana University, United States
Trent Ford,
University of Illinois at Urbana-Champaign, United States

****Correspondence:***
Matthew L. Trumper
trump022@umn.edu

Specialty section:
This article was submitted to Water and Climate, a section of the journal Frontiers in Water

Received: *25 October 2021*
Accepted: *20 December 2021*
Published: *25 January 2022*

Citation:
Trumper ML, Griffin D, Montpellier EE and Kipfmueller KF (2022) Pinus resinosa Tree-Ring Latewood Response to Daily-Scale Precipitation Variability at Lake Itasca, Minnesota. Front. Water 3:801265. doi: 10.3389/frwa.2021.801265

INTRODUCTION

Climate change in the Great Lakes region is clearly identifiable in observational data and model projections (Hayhoe et al., 2010; Andresen et al., 2012; Cook et al., 2020). These general trends toward warmer and wetter conditions give urgency to refining understanding about how climatic change in the coming decades will alter agricultural systems, ecological communities, culture, and society in the Great Lakes region (Kling et al., 2003; Frelich et al., 2021). Tree rings can offer critical long-term context for climate changes in the Great Lakes region. Moisture-sensitive tree-ring chronologies have been used to investigate growth sensitivity to climate conditions

(Graumlich, 1993; Kipfmueller et al., 2010), and to evaluate century- to millennial-scale variability in warm season drought and precipitation (Blasing and Duvick, 1984; Meko et al., 1993; St. George et al., 2009; Cook et al., 2010; Maxwell J.T. et al., 2020; Stahle et al., 2020; Larson et al., 2021a).

A possible weakening of the statistical relationship between tree rings and warm-season drought has been detected in recent decades in the Great Lakes region (Maxwell et al., 2016; Maxwell J.T. et al., 2020; Heilman et al., 2021). This "Fading Drought Signal" has been attributed to a lack of recent droughts in the region that could reduce radial growth (Maxwell et al., 2016), as well as higher CO_2 and plant intrinsic Water Use Efficiency (Heilman et al., 2021). If further replicated across space and tree species, a fading drought signal result would underscore the need to better understand the coupled systems linking climate, environment, and tree growth to ensure robust interpretation of tree rings as a proxy record of Great Lakes hydroclimate. Diagnosing temporal changes in tree growth-climate relationships would be particularly important if the ongoing period of wetness, identified in both observational and paleoclimatic records, persists (Andresen et al., 2012; Ford, 2014; Stahle et al., 2020). Most studies investigating tree growth-climate relationships in the Great Lakes region have used monthly-aggregated climate data and total ring-width. It is unknown if the mechanisms underlying the fading drought signal may be better understood by evaluating climate and growth relationships at multiple timescales, including those that operate at the daily to biweekly timescales which can be obfuscated by time and space aggregation to monthly, seasonal, and regional scales.

A subtle but intriguing feature of precipitation seasonality in the Upper Midwest that could influence tree growth is the presence of two wet peaks during the warm season (Trewartha, 1981; Harrington and Brown, 1985; Keables, 1989). Trewartha (1981) identified two peaks of rainfall (commonly June and September) and described spatiotemporal variability in this bimodal behavior, which fluctuated by decade and between stations. The bimodal precipitation profile can be viewed as a decrease in midsummer precipitation that climatologically follows the primary peak in June and precedes a secondary peak later in the warm season. This precipitation minima has been linked to an increased frequency of circulation patterns in midsummer that favor northerly flow and the advection of cooler, continental air to the Upper Midwest (Keables, 1989). It is reasonable to expect that this subseasonal precipitation variability could influence soil moisture availability and forest stress during the summer growing season. However, to our knowledge, the regional bimodal profile has not been systematically studied in relation to tree growth or tree-ring data. This is despite evidence elsewhere in North America that tree rings can respond to subseasonal precipitation climatologies and anomalies (Edmondson, 2010). A classic example of tree-growth response to a secondary peak in precipitation is the North American summer monsoon in the southwestern United States, which has been reconstructed using networks of latewood tree-ring chronologies (Griffin et al., 2013 and references therein), and more recently investigated used daily climate data and adjusted latewood chronologies (Howard et al., 2021).

Advancing methods in dendroclimatology provide new opportunities to investigate tree growth response to subseasonal climate variability and change. For example, day-wise aggregated climate data is increasingly used to compare with tree-ring proxies instead of the traditional month-wise approach (Vaganov et al., 1999; Ackerman et al., 2017; Jevšenak and Levanič, 2018; Howard and Stahle, 2020; Maxwell R.S. et al., 2020). A principal advantage of this method is that the day-wise approach can highlight tree-growth response to hydroclimate regimes with variability and dynamics that do not conform to Julian calendar months (Howard et al., 2021). Additionally, daily data can be used to characterize changes in the optimal window of tree growth response during the growing season (Jevšenak, 2019). Ideally, the daily data observations would be located in close proximity to the site from which tree-ring data were developed.

The use of sub-annual growth chronologies is another increasingly common method in dendroclimatology. Annual growth rings can be partitioned into sub-annual growth increments (i.e., earlywood and latewood) that can contain stronger and season-specific climate signals (Watson and Luckman, 2016; Stahle et al., 2020). Sub-annual chronologies have been developed across North America (Torbenson et al., 2016), but a gap in publicly-available data exists both in the Great Lakes region, and for red pine (*Pinus resinosa*), a long-lived and climatically sensitive tree species (Kipfmueller et al., 2010). Across North America, species from the *Pinus* subgenus have been somewhat unique in terms of their response to late growing season precipitation (Stahle et al., 2020), and the prospects for using red pine in the Great Lakes region are substantial.

Kipfmueller et al. (in press) developed new sub-annual red pine chronologies near Lake Itasca, the headwaters of the Mississippi River, in Itasca State Park (ISP), Minnesota. In comparison to earlywood-width and total ring-width, the latewood-width timeseries from ISP exhibited stronger internal crossdating in ring-width patterns and statistical covariance within and between trees. Kipfmueller et al. (in press) found the strongest relationships between warm-season precipitation and summer forming latewood-width. However, analyses of daily-scale observations and temporal stability of the climate-tree growth relationships were not conducted in that study. Subsequently, exploratory analysis of the correlation between their latewood data and divisional PDSI data (Vose et al., 2014) indicated: (1) a notable decline in PDSI-latewood covariance during recent decades (not shown), and (2) the dominant role of precipitation as a historical driver of PDSI variability, consistent with the results of St. George et al. (2010). Exploratory analysis also indicated a decrease in midsummer rainfall in the daily precipitation climatology, raising the question as to whether red pine growth at ISP is sensitive to this subseasonal precipitation variability over time.

This pilot study offers a close examination of changes and trends in the daily observational climate record at ISP, and a diagnosis of the strength and temporal stability of the tree-growth response to climate across daily to multidecadal timescales. Specific objectives of this study are to (1) assess trends in the observational climate record at ISP, (2) investigate the climatic drivers of sub-annual growth chronologies at ISP using daily

climate data, and (3) examine the temporal stability of the daily precipitation response of latewood width at ISP using multiple methods.

DATA

We collected increment cores from living red pine trees in Itasca State Park, located in north central Minnesota. Each series was surfaced using a core microtome, visually cross-dated (Stokes and Smiley, 1996), and earlywood-, latewood-, and total ring widths were measured to the nearest 0.001 mm. Ring-width measurements were detrended using a 150-year cubic spline and the 131 individual series were combined into a single chronology using Tukey's bi-weight robust mean (Kipfmueller et al., in press). Daily precipitation and temperature data were acquired from the University of Minnesota Itasca Biological Station and Laboratories weather station located in ISP (**Figures 1D,E**; GHCND ID: USC00214106). We focused our analyses on unadjusted latewood and precipitation and minimum temperature, which were found to be the strongest tree-ring climate covariates by Kipfmueller et al. (in press). The ISP station, located <10 kilometers from the trees we sampled, has a daily record that extends from 1911 to present with <2% missing values.

METHODS

We used a multiple linear regression approach to estimate missing daily data from the ISP station. Daily precipitation and minimum temperature data were acquired from three Historical Climatology Network stations surrounding ISP (Menne et al., 2012). Multiple linear regression was used with the ISP record as the predictand and the other three stations as predictors to estimate missing precipitation and minimum temperature values for the full 1912–2020 period. We used quantile mapping to adjust the distribution of the filled-in precipitation values toward the distribution of the observed ISP precipitation data, in an attempt to mitigate errors common to regression-based imputation methods, i.e., the overestimation of the number of wet days and underestimation of the number of heavy precipitation events (Simolo et al., 2010; Gudmundsson et al., 2012). Trends in precipitation and temperature from 1912 to 2020 were assessed using linear regression. We calculated the length of the freeze-free season using the traditional definition based on the number of days between the last spring freeze and first autumn freeze ($T_{min} < 0°C$). Differences in mean daily precipitation were identified using the non-parametric Kruskal-Wallis test and a *post-hoc* Dunn's test with *p*-values adjusted using the Holm method.

We assessed tree growth response to daily climate data using the *daily_response()* function in the R package *dendroTools* which compares tree-ring parameters and a daily climate variable using a moving window of variable widths (Jevšenak and Levanič, 2018). Earlywood-, latewood-, and total-ring width were correlated with daily total precipitation and mean minimum temperature aggregated into all windows between 10 and 365 days. Windows of daily-aggregated climate data advance in 1-day increments starting with day of year (DOY) 1 and finishing with DOY 365. Pearson correlation coefficients were calculated using a window of 24 months from January in the previous year to December in the current year for the years 1913–2018. The large number of correlation tests carried out by the *daily_response()* function inflates the number of theoretical type I errors (Jevšenak, 2019). To correct for test multiplicity and reduce the risk of identifying spurious correlations as significant, we applied the False Discovery Rate procedure (Benjamini and Hochberg, 1995) with a *q*-value of 0.05 to match our *p*-value threshold.

We used multiple approaches to assess the time stability of growth-climate relationships. First, we used the *daily_response()* function to calculate correlations between latewood width and daily climate data for the full common period (1913–2018). Second, we repeated use of this approach for three non-overlapping subperiods of approximately equal length (early, 1913–1947; middle, 1948–1983; late, 1984–2018). As described fully below, the strongest latewood correlations in the full period analysis were for a 12-day critical climate period in late July and early August (July 27–August 7; hereafter "12-day CCP") and a 109-day critical climate period from late May through early September (May 25–September 10; hereafter "seasonal CCP"). Third, to investigate the time stability of latewood response to the 12-day and seasonal CCPs, we extracted daily-aggregated precipitation each year corresponding to the July 27–August 7 and the May 25–September 10 periods, resulting in two precipitation time series for the full period from 1913–2018. Fourth, we used a 31-year running correlation to compare each precipitation time series with the latewood chronology from 1913 to 2018. The power of running correlation analysis is hampered by the reduced degrees of freedom, particularly when using climatic timeseries that exhibit routinely characteristic autocorrelation (Hu et al., 2017). Consequently, we also investigated possible time-dependence in growth-climate relationships using a Bayesian generalized linear model as a dynamic regression modeling procedure (Helske, 2021). Like the application of the Kalman filter method in dendroclimatology (Visser and Molenaar, 1988; Cook et al., 2002), this method allows regression coefficients to vary as a random walk and uses the Kalman filter to objectively identify time-dependence in the relationship between predictor and predictand variables. However, this Bayesian method uses Markov chain Monte Carlo sampling of the posterior distribution to estimate the unknown regression coefficients rather than maximum likelihood estimation. All analysis presented here was conducted in the statistical software R [version 4.0.3; R Core Team, 2020].

RESULTS

May–October is the season that may be most relevant to red pine radial growth (Kipfmueller et al., in press), and the ISP station showed an increasing linear trend in warm season (May–October) precipitation (11.6 mm decade^{-1}; **Figure 1B**).

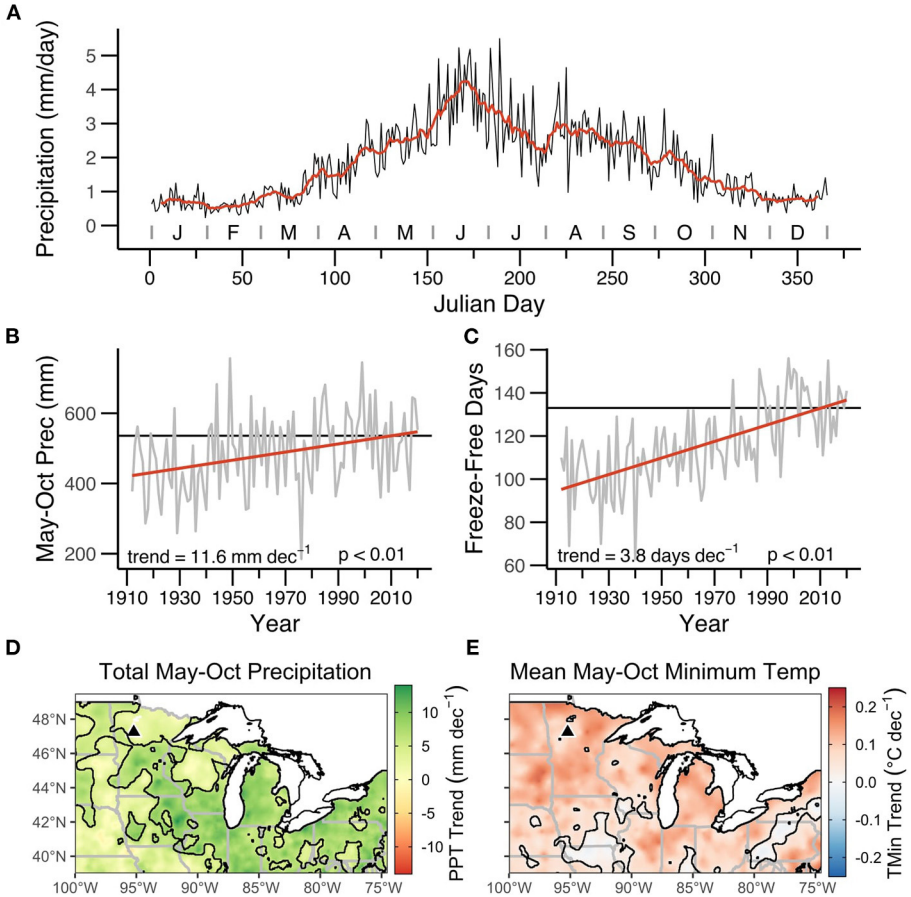

FIGURE 1 | Characteristics of climatology and change at Itasca State Park. Mean daily precipitation (black line) and 11-day moving average precipitation (red line) for the period 1912–2020 **(A)**. Timeseries (gray) and linear trend (red), and 1991–2020 mean (black) for warm-season (May–October) precipitation and freeze-free season length (days; 0°C minimum temperature threshold) for 1912–2020 **(B,C)**. Regional-scale linear trends in CLIMGRID warm season (May–October) precipitation **(D)** and minimum temperature **(E)** for 1895–2020, with the black contour encompassing areas where trend test *p*-values were <0.05.

Although increasing trends in precipitation were found in every season and in every month except for January at ISP, the strongest increases were found in September, October, and the SON season (**Supplementary Figure 1**). Warming trends at ISP were reflected in a substantially longer freeze-free season (3.8 days decade^{-1}; **Figure 1C**). Additionally, large increases in minimum temperature were found in every season and month except February, April, October, and November (**Supplementary Figure 2**). These increases in precipitation and minimum temperature from the ISP station are consistent with the broad scale spatial pattern of trends toward warmer and wetter warm-season conditions in the Great Lakes region (**Figures 1D,E**).

Sub-annual tree-ring chronologies from ISP exhibited correlation coefficients with daily precipitation and minimum temperature with magnitudes that can be considered strong for red pine in this region (i.e., $r > 0.45$) over intervals ranging from 10 to 365 days, but in general the strongest relationships were between warm-season precipitation and latewood (**Figures 2A–C**; **Supplementary Figure 3**). Over the full period from 1913 to 2018, the daily precipitation window that had the highest correlation with latewood width was from Julian Day 145–253, or May 25 to September 10 ($r = 0.508$; **Supplementary Figure 3**; seasonal CCP). In addition to long seasonal windows of response, strong to moderate correlations between warm-season precipitation and latewood were also observed for shorter time windows (e.g., 10–20 days; **Figures 2A,B**). Over the full period, the short daily precipitation window that had the highest correlation with latewood width was from Julian Days 208–219, or July 27 to August 7 ($r = 0.383$; **Supplementary Figure 3**; 12-day CCP). Growth-climate results were similar using daily climate data containing imputed or missing values.

Daily analysis for non-overlapping periods revealed a strong to moderate summer precipitation signal in red pine latewood with a growth response that was similar in magnitude and timing in the early and middle periods (**Figures 2A,B**). However, the magnitude and frequency of positive correlations diminished in the most recent late period (**Figure 2C**). The optimal windows of warm-season precipitation response in latewood, as calculated

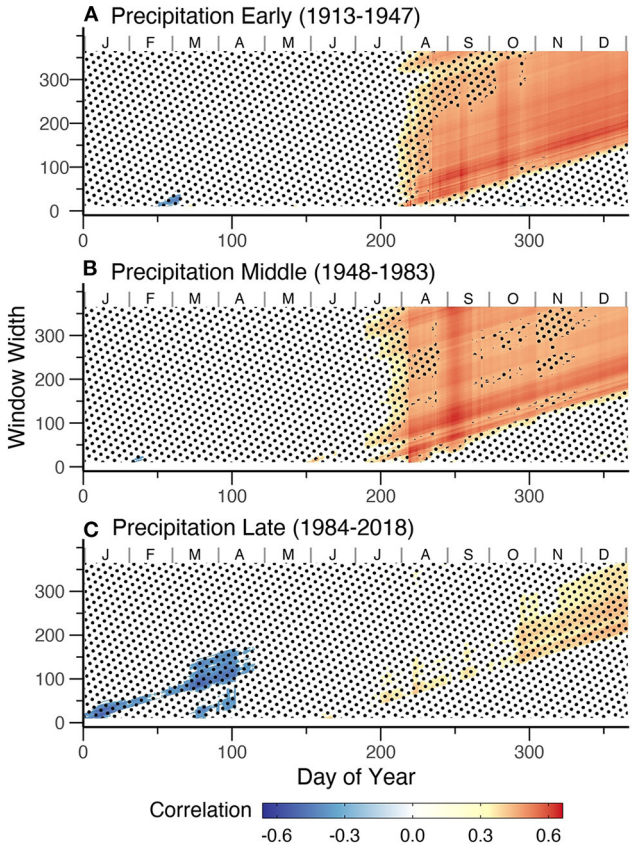

FIGURE 2 | Heat maps from the *daily_response()* function (Jevšenak and Levanič, 2018) illustrate correlations between the ISP latewood chronology and weekly to annual scale precipitation sums for three non-overlapping subperiods **(A–C)**. Correlations are calculated in relation to the ending day of the window (e.g., the correlation coefficient between latewood and total precipitation from DOY 10 to DOY 50 is plotted on DOY 50). Only correlations with *p*-values <0.05 are shown. Black dots indicate that the correlation does not pass the significance threshold after correcting *p*-values for test multiplicity.

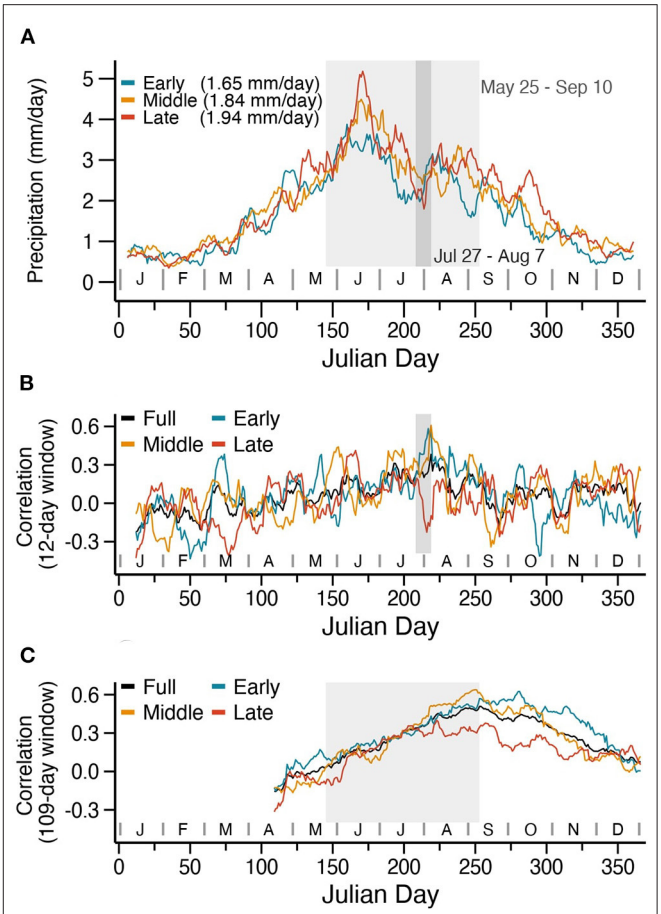

FIGURE 3 | Daily precipitation climatology and tree ring latewood correlations for early (1913–1947, blue), middle (1948–1983, orange), late, (1984–2018, red), and full (1913–2018, black) periods. Eleven-day moving averages of mean daily precipitation **(A)**. Tree ring correlations with overlapping 12-day precipitation intervals, advancing 1 day at a time **(B)**. Tree ring correlations with overlapping 109-day precipitation intervals, advancing 1 day at a time **(C)**. Dark and light gray boxes correspond to the 12-day and 109-day critical climate periods diagnosed in the full period analyses.

using the *daily_response()* function, differed between the early ($r = 0.651$; June 21 to September 10), middle ($r = 0.658$; July 27 to August 6), and late ($r = 0.458$; June 6 to June 15) periods.

The daily precipitation climatology in split periods showed increasing annual precipitation over time at ISP (**Figure 3A**). Running correlations using a fixed 12-day window revealed correlations between latewood and precipitation that peaked on the 12-day CCP straddling July and August (**Figure 3B**). This 12-day response over late July to early August was moderate for the full period ($r = 0.383$; July 27 to August 7), although split-period analysis revealed that this response was temporally unstable (**Figures 3B**, **4A**). Twelve-day correlations in midsummer were considerably stronger in the early ($r = 0.583$; July 25 to August 5) and middle ($r = 0.608$; July 27 to August 7) periods, and close to zero in the late period. Notably, this 2-week interval in midsummer coincides with a local minima in the daily precipitation climatology at ISP that is evident in the full period (**Figure 1A**). While this minima in the precipitation climatology also appears relatively stable in the split periods (**Figure 3A**), mean precipitation for the 2-week period immediately preceding the minima (July 12–27) has increased from the early to late period (Kruskal-Wallis test statistic = 2.84; $p = 0.014$). The deteriorating tree-ring response to midsummer conditions is further illustrated with a time series comparison of latewood and total precipitation for the 12-day CCP (**Figure 4B**). Dynamic regression analysis between latewood and the 12-day CCP shows a relationship that was positive and strong throughout the early- to mid-20th century before weakening markedly to zero after the 1970s (**Figure 4C**).

Running correlations using a fixed 109-day window revealed correlations between latewood and total precipitation that were strong to moderate in all three periods (**Figures 3C**, **4D**). The seasonal scale response was strongest in the early ($r = 0.626$; June 22 to October 8) and middle ($r = 0.639$; May 22 to September 7)

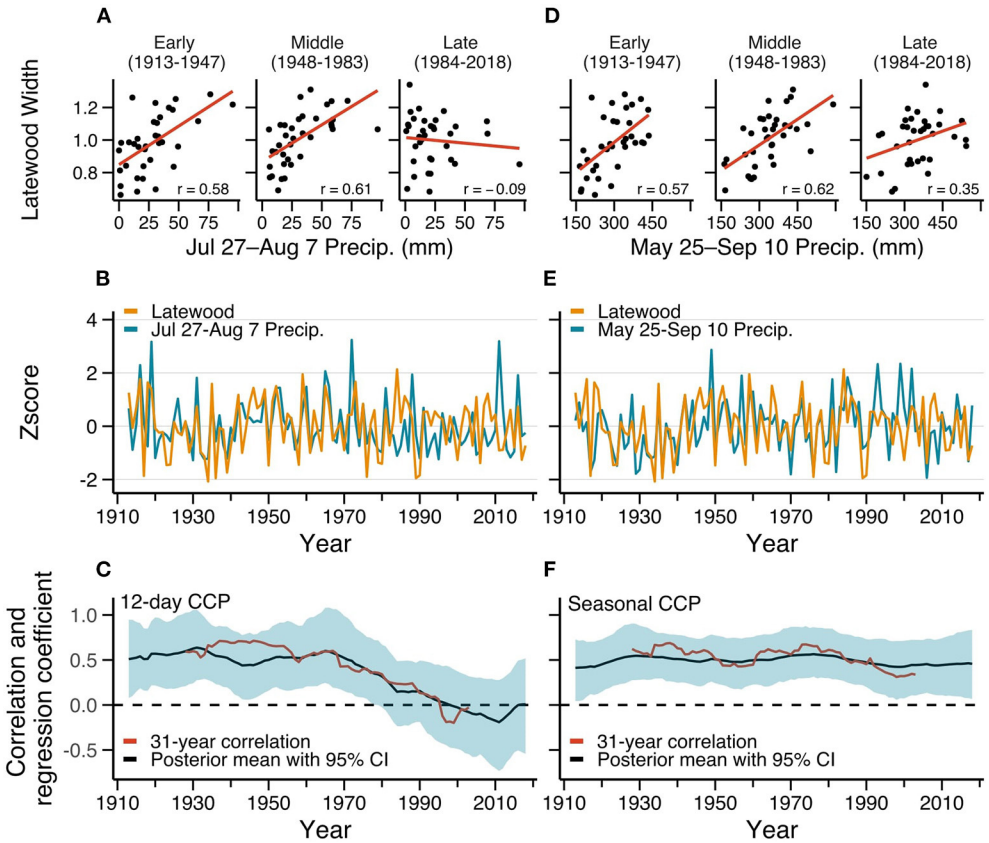

FIGURE 4 | Tree ring latewood vs. daily precipitation for the July 27–August 7 subseasonal **(A–C)** and the May 25–September 10 seasonal **(D–F)** windows determined to exhibit maximum covariance. Scatter plots illustrate the linearity of relationships for three non-overlapping periods spanning the full common period **(A,D)**. Timeseries plots illustrate z-scores for the data standardized over the 1912–2018 common period **(B,E)**. The bottom row **(C,F)** illustrates running 31-year correlations (red lines) and Bayesian generalized linear models of time varying coefficients (solid black lines). Blue shaded areas represent uncertainty estimated with 95% credible intervals for the regression coefficients.

periods before weakening in the late ($r = 0.4$; April 25 to August 11) period. The differences between latewood-precipitation correlations in the three non-overlapping periods were not statistically clear (all $p > 0.05$). A time series comparison shows additional evidence for time-dependence in the relationship between latewood width and total precipitation for the seasonal CCP (**Figure 4E**). Dynamic regression analysis showed a positive relationship between latewood and the seasonal CCP that varied throughout the early- to mid-20th century before weakening after about 1980 (**Figure 4F**). The 95% credible intervals of the time-varying regression coefficients do not contain zero throughout the full period of 1913–2018 (**Figure 4C**), suggesting a response that has diminished in the past several decades but remains moderate.

DISCUSSION

A short term, midsummer window of precipitation variability seems to have been a major control on red pine tree growth and latewood width at ISP from the 1910s through the early 1980s. This 12-day CCP was found to be embedded within the broader, multi-month seasonal response to warm-season precipitation at ISP. Results from several statistical approaches robustly indicate that the strength of these subseasonal and seasonal precipitation signals has diminished in recent decades. Precipitation in the 12-day CCP has not been strongly correlated with latewood width since the 1980s. The seasonal CCP correlation also weakened appreciably in recent decades, though hydroclimatic variability during this multi-month period must still be important for tree growth. The late May through early September season does correspond to the historical timing of cambial activity for red pine, as detected through observations in north-eastern Minnesota (Ahlgren, 1957). Nevertheless, it is abundantly clear that the strength of the precipitation signal in red pine at ISP has faded over recent decades.

As scientists increasingly recognize the prevalence of non-stationary relationships between tree growth and climate (e.g., D'Arrigo et al., 2008), there has been a growing effort to critically examine the stability of climate-growth relationships over the full instrumental climate record (Wilmking et al., 2020). Some studies in the Great Lakes region demonstrate a decrease in sensitivity of radial tree growth to precipitation and drought (Maxwell et al., 2016; Heilman et al., 2021). Our results, although limited to a single site, are consistent with these studies and show what is,

to our knowledge, the first evidence for declining precipitation sensitivity in red pine.

Daily climate data analysis facilitated improved understanding of short-term (days to weeks) changes in the hydroclimatology at ISP that could not be easily detected at coarser temporal scales but may contribute to the weakening latewood-precipitation relationship. Specifically, the response of latewood to warm-season precipitation at ISP remains moderate for the seasonal CCP but the 12-day CCP response is absent in recent decades (**Figures 2**, **4C**). The declining precipitation sensitivity in red pine latewood co-occurs with climatic changes at ISP that could hypothetically alter the conditions limiting to radial tree growth, including increases in precipitation (**Supplementary Figure 1**) and minimum temperature (**Supplementary Figure 2**), and a lengthening freeze-free season (**Figure 1C**). In addition, increases in atmospheric CO_2 (Heilman et al., 2021), and the local disturbance history at ISP could contribute to the fading strength of the rainfall signal in red pine at this site. Known disturbances at ISP include reduced fire activity and possible changes in understory composition and density since the park's establishment in 1891 (Frissell, 1973), wind events (Webb et al., 2001), and changes in nutrient status (Howard and McLauchlan, 2015).

The once important 12-day CCP from late July to early August has coincided with a relative minima in the climatological mean of midsummer rainfall at ISP. While this midsummer break in mean-state precipitation has remained relatively stable over time at ISP, the magnitude and timing of climatological rainfall bursts in the weeks before and after this dry period have been variable at ISP (**Figure 3A**), and elsewhere in the Midwest (Trewartha, 1981). It could be relevant that the 2 weeks leading up to the 12-day CCP were wetter in the late (1984–2018) period (**Figure 3A**). This is a key multi-week season in midsummer when temperature and evaporative demand remain near their annual maximum. Might wetter conditions leading into the start of the 12-day CCP impart enough moisture to buffer trees against enhanced moisture stress during the relatively dry 12-day CCP? Though beyond the brief scope of this pilot study, systematic attribution research is needed to diagnose the interplay of the coupled and non-stationary systems linking climate, environment, and tree growth at ISP. This might be accomplished with analysis of additional datasets from elsewhere in the region, and with careful modeling of water balance across multiple timescales and time periods. Forward models that simulate tree-ring formation using daily climate data constitute another powerful tool to understand temporal shifts in growth-limiting factors (Anchukaitis et al., 2006, 2020; Bunn et al., 2018; Jevšenak et al., 2021) and this approach could provide a complementary perspective of relevance to the use of red pine for making paleoclimate inference.

Using daily precipitation data, we observed many growth-climate correlations with higher magnitudes than those observed in other red pine studies using monthly data (e.g., Kipfmueller et al., 2010; D'Amato et al., 2013). However, there are limitations to this approach. While the day-wise method is flexible in that it ignores calendar month boundaries, the substantial number of correlations calculated greatly inflates the number of theoretical type I errors (Jevšenak, 2019). For precipitation data in particular, short-term (days to weeks) totals are frequently noisy and heavily skewed, which could lead to spurious correlations with tree-ring data. It is thus important to ensure that daily windows with correlation magnitudes deemed meaningful fit with site-specific understanding of the environmental processes leading to ring width formation. In this study, we focused covariance analysis on the precipitation and minimum temperature variables, which Kipfmueller et al. (in press) detected to be potentially relevant controls on tree growth. Although our results show relatively weak correlations between latewood and minimum temperature data, the increases in minimum temperature and lengthening freeze-free season evident at ISP, and indeed across much of the Great Lakes region (e.g., Skaggs and Baker, 1985; Robeson, 2002), have significant practical implications for plant communities including red pine. For example, a lengthened growing season could have a strong influence on red pine phenology and the timing of growth responses to temperature in the transition spring and fall seasons. The application of multiple tree-ring proxies, ranging from quantitative wood anatomy (Arnič et al., 2021) to stable isotopes (Maxwell R.S. et al., 2020), as well as cambial phenology (Moser et al., 2010), constitute a promising way forward to improve process-level understanding of the daily-scale drivers of wood formation at this site.

Many forest systems are experiencing alarming signs of decline (Allen et al., 2010, 2015). Climate change in the Great Lakes region holds unknown consequences for the future health of red pine. Here we identify a diminishing moisture signal that may continue to decay with projected changes in the amount and timing of precipitation. Moreover, frequent fire in red pine ecosystems results in a xerification of the landscape that benefits red pine regeneration and persistence (Larson et al., 2021b). Projected increases in precipitation, coupled with the ongoing removal of fire from Great Lake forests, may jeopardize the overall health of red pine. Nearly a century of fire suppression in remnant red pine forests of the Great Lakes region may have also led to dramatic changes in forest composition, structure, and competitive effects. These factors have been shown to alter red pine radial growth and climate sensitivity (Aakala et al., 2013; D'Amato et al., 2013; Magruder et al., 2013), highlighting the uncertainty of red pine growth response to climate change.

CONCLUSION

This pilot study provides a new perspective on the timescales of climatic response of red pine, an important tree species for reconstructions of drought and seasonal precipitation in the upper Great Lakes region. In addition to long seasonal windows, the daily data covariance approach identified a critical climate period for tree growth that coincided with a distinct but perhaps understudied feature of the regional precipitation climatology. If replicated across additional locations and tree species, the short-term response shown here could indicate an important coupling between tree growth in the late growing season and the bimodal warm-season precipitation profile previously identified in the Upper Midwest. We believe there is potential to diagnose critical climate periods for tree growth using daily data elsewhere in the Great Lakes region. Further, close

evaluation of the daily climate record over time at sites with co-located tree-ring and observational data may highlight possible mechanisms driving the fading drought signal in regional tree-ring chronologies. The statistical growth-climate relationships presented here do not imply causal links and developing better process-based understanding of the multivariate climate response of red pine remains a priority. Nonetheless, the results presented here suggest that the daily-scale approach can be a valuable complement to typical dendroclimatic studies that use monthly data.

DATA AVAILABILITY STATEMENT

The tree-ring data for this study will be found in the International Tree-Ring Data Bank (ITRDB) upon publication: https://www.ncei.noaa.gov/products/paleoclimatology/tree-ring.
The University of Minnesota Itasca Biological Station and Laboratories weather station data is available from the National Oceanic and Atmospheric Administration: https://www.ncdc.noaa.gov/cdo-web/datasets/GHCND/stations/GHCND:USC00214106/detail.

AUTHOR CONTRIBUTIONS

KK secured funding and sampling permission for field collection of tree ring data. MT and DG designed the methods. MT performed analyses and prepared figures with oversight and feedback from DG, EM, and KK. MT wrote the first draft of the paper and managed writing contributions from DG, EM, and KK. All authors participated in fieldwork and tree-ring chronology development and contributed to the interpretation of the data.

FUNDING

This work was not funded by a grant or other funding sources. We declare no specific funding for this work.

ACKNOWLEDGMENTS

The lands currently defined as Itasca State Park were frequently used by the Dakota and more recently the Ojibwe, besides its use by earlier cultural groups, prior to European colonization. We acknowledge and are grateful for the opportunity to gather and deploy tree-ring resources from this land to inform our research and findings. We thank the personnel from the Minnesota Department of Natural Resources for granting us sampling permission in Itasca State Park. We also thank the personnel at the University of Minnesota Itasca Biological Station and Laboratories, especially Jonathan Schilling, Lesley Knoll, and Laura Domine, for logistical support and helpful discussions about research in the park. Daniel Brumm, Daniel Crawford, Jared Stachiw, Evan Larson, Lane Johnson, Elizabeth Schneider, and undergraduate students from the University of Wisconsin-Platteville provided critical assistance in the field and laboratory work. We thank the personnel from the Chippewa National Forest and students and staff from the Leech Lake Tribal College STEM Club for their fieldwork assistance and insightful comments and perspectives.

SUPPLEMENTARY MATERIAL

The Supplementary Material for this article can be found online at: https://www.frontiersin.org/articles/10.3389/frwa.2021.801265/full#supplementary-material

REFERENCES

Aakala, T., Fraver, S., D'Amato, A. W., and Palik, B. J. (2013). Influence of competition and age on tree growth in structurally complex old-growth forests in northern Minnesota, USA. *For. Ecol. Manage.* 308, 128–135. doi: 10.1016/j.foreco.2013.07.057

Ackerman, D., Griffin, D., Hobbie, S. E., and Finlay, J. C. (2017). Arctic shrub growth trajectories differ across soil moisture levels. *Glob. Chang. Biol.* 23, 4294–4302. doi: 10.1111/gcb.13677

Ahlgren, C. E. (1957). Phenological observations of nineteen native tree species in Northeastern Minnesota. *Ecology* 38, 622–628. doi: 10.2307/1943128

Allen, C. D., Breshears, D. D., and McDowell, N. G. (2015). On underestimation of global vulnerability to tree mortality and forest die-off from hotter drought in the Anthropocene. *Ecosphere* 6, 1–55. doi: 10.1890/ES15-00203.1

Allen, C. D., Macalady, A. K., Chenchouni, H., Bachelet, D., McDowell, N., Vennetier, M., et al. (2010). A global overview of drought and heat-induced tree mortality reveals emerging climate change risks for forests. *For. Ecol. Manage.* 259, 660–684. doi: 10.1016/j.foreco.2009.09.001

Anchukaitis, K. J., Evans, M. N., Hughes, M. K., and Vaganov, E. A. (2020). An interpreted language implementation of the Vaganov–Shashkin tree-ring proxy system model. *Dendrochronologia* 60:125677. doi: 10.1016/j.dendro.2020.125677

Anchukaitis, K. J., Evans, M. N., Kaplan, A., Vaganov, E. A., Hughes, M. K., Grissino-Mayer, H. D., et al. (2006). Forward modeling of regional scale tree-ring patterns in the southeastern United States and the recent influence of summer drought. *Geophys. Res. Lett.* 33:L04705. doi: 10.1029/2005GL025050

Andresen, J., Hilberg, S., Kunkel, K., and Center, M. R. C. (2012). "Historical climate and climate trends in the midwestern USA," in *U.S. National Climate Assessment Midwest Technical Input Report*, eds J. Winkler, J. Andresen, J. Hatfield, D. Bidwell, D. Brown, et al. [The Great Lakes Integrated Sciences and Assessments (GLISA) Center]. Available from: http://glisa.msu.edu/docs/NCA/MTIT_Historical.pdf (accessed September 20, 2021).

Arnič, D., Gričar, J., Jevšenak, J., BoŽič, G., von Arx, G., and Prislan, P. (2021). Different wood anatomical and growth responses in European Beech (*Fagus sylvatica* L.) at three forest sites in Slovenia. *Front. Plant Sci.* 1551. 12. doi: 10.3389/fpls.2021.669229

Benjamini, Y., and Hochberg, Y. (1995). Controlling the false discovery rate: a practical and powerful approach to multiple testing. *J. R. Stat. Soc. Ser. B* 57, 289–300. doi: 10.1111/j.2517-6161.1995.tb02031.x

Blasing, T. J., and Duvick, D. (1984). Reconstruction of precipitation history in North American corn belt using tree rings. *Nature* 307, 143–145. doi: 10.1038/307143a0

Bunn, A. G., Salzer, M. W., Anchukaitis, K. J., Bruening, J. M., and Hughes, M. K. (2018). Spatiotemporal variability in the climate growth response of high elevation Bristlecone Pine in the White Mountains of California. *Geophys. Res. Lett.* 45, 13312–13321. doi: 10.1029/2018GL080981

Cook, B. I., Mankin, J. S., Marvel, K., Williams, A. P., Smerdon, J. E., and Anchukaitis, K. J. (2020). Twenty-first century drought projections in the CMIP6 forcing scenarios. *Earths Fut.* 8:e2019EF001461. doi: 10.1029/2019EF001461

Cook, E. R., D'Arrigo, R. D., and Mann, M. E. (2002). A well-verified, multiproxy reconstruction of the winter North Atlantic

Oscillation index since A.D. 1400. *J. Clim.* 15, 1754–1764. doi: 10.1175/1520-0442(2002)015<1754:AWVMRO>2.0.CO;2

Cook, E. R., Seager, R., Heim, R. R., Vose, R. S., Herweijer, C., and Woodhouse, C. (2010). Megadroughts in North America: placing IPCC projections of hydroclimatic change in a long-term palaeoclimate context. *J. Quat. Sci.* 25, 48–61. doi: 10.1002/jqs.1303

D'Amato, A. W., Bradford, J. B., Fraver, S., and Palik, B. J. (2013). Effects of thinning on drought vulnerability and climate response in north temperate forest ecosystems. *Ecol. Appl.* 23, 1735–1742. doi: 10.1890/13-0677.1

D'Arrigo, R., Wilson, R., Liepert, B., and Cherubini, P. (2008). On the 'Divergence Problem' in Northern Forests: a review of the tree-ring evidence and possible causes. *Global Planet. Change* 60, 289–305. doi: 10.1016/j.gloplacha.2007.03.004

Edmondson, J. R. (2010). The meteorological significance of false rings in eastern redcedar (*Juniperus virginiana* L.) from the Southern Great Plains, U.S.A. *Tree Ring Res.* 66, 19–33. doi: 10.3959/2008-13.1

Ford, T. W. (2014). Precipitation anomalies in Eastern-Central Iowa from 1640 – Present. *J. Hydrol.* 519, 918–924. doi: 10.1016/j.jhydrol.2014.08.021

Frelich, L. E., Montgomery, R. A., and Reich, P. B. (2021). Seven ways a warming climate can kill the Southern Boreal Forest. *Forests.* 12:560. doi: 10.3390/f12050560

Frissell, S. S. (1973). The importance of fire as a natural ecological factor in Itasca State Park, Minnesota. *Quat. Res.* 3, 397–407. doi: 10.1016/0033-5894(73)90005-7

Graumlich, L. J. (1993). Response of tree growth to climatic variation in the mixed conifer and deciduous forests of the upper Great Lakes region. *Can. J. For. Res.* 23, 133–143. doi: 10.1139/x93-020

Griffin, D., Woodhouse, C. A., Meko, D. M., Stahle, D. W., Faulstich, H. L., Carrillo, C., et al. (2013). North American monsoon precipitation reconstructed from tree-ring latewood. *Geophys. Res. Lett.* 40, 954–958. doi: 10.1002/grl.50184

Gudmundsson, L., Bremnes, J. B., Haugen, J. E., and Engen-Skaugen, T. (2012). Technical Note: Downscaling RCM precipitation to the station scale using statistical transformations - A comparison of methods. Hydrology and Earth System Sciences, 16:3383–3390. doi: 10.5194/hess-16-3383-2012

Harrington, J. A., and Brown, B. J. (1985). A synoptic climatology of depressions in warm season precipitation profiles from the upper middle west. *Phys. Geogr.* 6, 186–197. doi: 10.1080/02723646.1985.10642270

Hayhoe, K., VanDorn, J., Croley, T., Schlegal, N., and Wuebbles, D. (2010). Regional climate change projections for Chicago and the US Great Lakes. *J. Great Lakes Res.* 36, 7–21. doi: 10.1016/j.jglr.2010.03.012

Heilman, K. A., Trouet, V. M., Belmecheri, S., Pederson, N., Berke, M. A., and McLachlan, J. S. (2021). Increased water use efficiency leads to decreased precipitation sensitivity of tree growth, but is offset by high temperatures. *Oecologia* 1, 1–16. doi: 10.1007/s00442-021-04892-0

Helske, J. (2021). *walker: Bayesian Generalized Linear Models With Time-Varying Coefficients*. R package version 1.0.2. Available online at: https://github.com/helske/walker (accessed December 3, 2021).

Howard, I., and McLauchlan, K. K. (2015). Spatiotemporal analysis of nitrogen cycling in a mixed coniferous forest of the northern United States. *Biogeosciences* 12, 3941–3952. doi: 10.5194/bg-12-3941-2015

Howard, I. M., and Stahle, D. W. (2020). Tree-ring reconstruction of single-day precipitation totals over Eastern Colorado. *Monthly Weather Rev.* 148, 597–612. doi: 10.1175/MWR-D-19-0114.1

Howard, I. M., Stahle, D. W., Torbenson, M. C. A., and Griffin, D. (2021). The summer precipitation response of latewood tree-ring chronologies in the southwestern United States. *Int. J. Climatol.* 41, 2913–2933. doi: 10.1002/joc.6997

Hu, J., Emile-Geay, J., and Partin, J. (2017). Correlation-based interpretations of paleoclimate data – where statistics meet past climates. *Earth Planet. Sci. Lett.* 459, 362–371. doi: 10.1016/j.epsl.2016.11.048

Jevšenak, J. (2019). Daily climate data reveal stronger climate-growth relationships for an extended European tree-ring network. *Quat. Sci. Rev.* 221:105868. doi: 10.1016/j.quascirev.2019.105868

Jevšenak, J., and Levanič, T. (2018). dendroTools: R package for studying linear and nonlinear responses between tree-rings and daily environmental data. *Dendrochronologia* 48, 32–39. doi: 10.1016/j.dendro.2018.01.005

Jevšenak, J., Tychkov, I., Gričar, J., Levani,č, T., Tumajer, J., Prislan, P., et al. (2021). Growth-limiting factors and climate response variability in Norway spruce (*Picea abies* L.) along an elevation and precipitation gradients in Slovenia. *Int. J. Biometeorol.* 65, 311–324. doi: 10.1007/s00484-020-02033-5

Keables, M. J. (1989). A synoptic climatology of the bimodal precipitation distribution in the upper midwest. *J. Clim.* 2, 1289–1294. doi: 10.1175/1520-0442(1989)002<1289:ASCOTB>2.0.CO;2

Kipfmueller, K. F., Elliott, G. P., Larson, E. R., and Salzer, M. W. (2010). An assessment of the dendroclimatic potential of three conifer species in Northern Minnesota. *Tree Ring Res.* 66, 113–126. doi: 10.3959/2009-12.1

Kipfmueller, K. F., Montpellier, E.E., Trumper, M.L., and Griffin, D. (in press). Intra-annual ring width and climate response of red pine in Itasca State Park in north-central Minnesota. *Can. J. For. Res.*

Kling, G. W., Hayhoe, K., Johnson, L. B., Magnuson, J. J., Polasky, S., Robinson, S. K., et al. (2003). *Confronting Climate Change in the Great Lakes Region: Impacts on Our Communities and Ecosystems*. Cambridge, MA: Union of Concerned Scientists; Washington, DC: Ecological Society of America.

Larson, E. R., Allen, S. A., and Underwood, C. A. (2021a). The driftless oaks: a new network of tree-ring chronologies to improve regional perspectives of drought in the Upper Midwest, USA. *Progr. Phys. Geogr.* 45:375–406. doi: 10.1177/0309133320960670

Larson, E. R., Kipfmueller, K. F., and Johnson, L. B. (2021b). People, fire, and pine: linking human agency and landscape in the boundary waters canoe area wilderness and beyond. *Ann. Am. Assoc. Geogr.* 111, 1–25. doi: 10.1080/24694452.2020.1768042

Magruder, M., Chhin, S., Palik, B., and Bradford, J. B. (2013). Thinning increases climatic resilience of red pine. *Can. J. For. Res.* 43, 878–889. doi: 10.1139/cjfr-2013-0088

Maxwell, J. T., Harley, G. L., Matheus, T. J., Strange, B. M., Van Aken, K., Fung Au, T., et al. (2020). Sampling density and date along with species selection influence spatial representation of tree-ring reconstructions. *Climate Past* 16, 1901–1916. doi: 10.5194/cp-16-1901-2020

Maxwell, J. T., Harley, G. L., and Robeson, S. M. (2016). On the declining relationship between tree growth and climate in the Midwest United States: the fading drought signal. *Climat. Change* 138, 127–142. doi: 10.1007/s10584-016-1720-3

Maxwell, R. S., Belmecheri, S., Taylor, A. H., Davis, K. J., and Ocheltree, T. W. (2020). Carbon isotope ratios in tree rings respond differently to climatic variations than tree-ring width in a mesic temperate forest. *Agric. For. Meteorol.* 288–289:108014. doi: 10.1016/j.agrformet.2020.108014

Meko, D., Cook, E. R., Stahle, D. W., Stockton, C. W., and Hughes, M. K. (1993). Spatial patterns of tree-growth anomalies in the United States and Southeastern Canada. *J. Clim.* 6, 1773–1786. doi: 10.1175/1520-0442(1993)006<1773:SPOTGA>2.0.CO;2

Menne, M. J., Durre, I., Vose, R. S., Gleason, B. E., and Houston, T. G. (2012). An overview of the global historical climatology network-daily database. *J. Atmos. Ocean. Technol.* 29, 897–910. doi: 10.1175/JTECH-D-11-00103.1

Moser, L., Fonti, P., Büntgen, U., Esper, J., Luterbacher, J., Franzen, J., et al. (2010). Timing and duration of European larch growing season along altitudinal gradients in the Swiss Alps. *Tree Physiol.* 30, 225–233. doi: 10.1093/treephys/tpp108

R Core Team (2020). *R: A Language and Environment for Statistical Computing*. Vienna: R Foundation for Statistical Computing. Available online at: https://www.R-project.org/ (accessed September 20, 2021).

Robeson, S. M. (2002). Increasing Growing-Season Length in Illinois during the 20th Century. *Climat Change* 52, 219–238. doi: 10.1023/A.:1013088011223

Simolo, C., Brunetti, M., Maugeri, M., and Nanni, T. (2010). Improving estimation of missing values in daily precipitation series by a probability density function-preserving approach. *Int. J. Climatol.* 30, 1564–1576. doi: 10.1002/joc.1992

Skaggs, R. H., and Baker, D. G. (1985). Fluctuations in the length of the growing season in Minnesota. *Clim. Change* 7, 403–414. doi: 10.1007/BF00139055

Stahle, D. W., Cook, E. R., Burnette, D. J., Torbenson, M. C. A., Howard, I. M., Griffin, D., et al. (2020). Dynamics, variability, and change in seasonal precipitation reconstructions for North America. *J. Clim.* 33, 3173–3195. doi: 10.1175/JCLI-D-19-0270.1

St. George, S., Meko, D. M., and Cook, E. R. (2010). The seasonality of precipitation signals embedded within the North American Drought Atlas. *Holocene* 20, 983–988. doi: 10.1177/0959683610365937

St. George, S., Meko, D. M., Girardin, M. P., MacDonald, G. M., Nielsen, E., Pederson, G. T., et al. (2009). The tree-ring record of drought on the Canadian Prairies. *J. Clim.* 22, 689–710. doi: 10.1175/2008JCLI2441.1

Stokes, M. A., and Smiley, T. L. (1996). *An Introduction to Tree-Ring Dating*. Chicago, IL: Univ. of Chicago Press.

Torbenson, M. C. A., Stahle, D. W., Villanueva Díaz, J., Cook, E. R., and Griffin, D. (2016). The relationship between earlywood and latewood ring-growth across North America. *Tree Ring Res.* 72, 53–66. doi: 10.3959/1536-1098-72.02.53

Trewartha, G. T. (1981). The bimodal warm season precipitation profile of the upper Middle West. *Ann. Assoc. Am. Geogr.* 71, 566–571. doi: 10.1111/j.1467-8306.1981.tb01375.x

Vaganov, E. A., Hughes, M. K., Kirdyanov, A. V., Schweingruber, F. H., and Silkin, P. P. (1999). Influence of snowfall and melt timing on tree growth in subarctic Eurasia. *Nature* 400, 149–151. doi: 10.1038/22087

Visser, H., and Molenaar, J. (1988). Kalman filter analysis in dendroclimatology. *Biometrics* 44:929. doi: 10.2307/2531724

Vose, R. S., Applequist, S., Squires, M., Durre, I., Menne, C. J., Williams, C. N., et al. (2014). Improved historical temperature and precipitation time series for U.S. climate divisions. *J. Appl. Meteorol. Climatol.* 53, 1232–1251. doi: 10.1175/JAMC-D-13-0248.1

Watson, E., and Luckman, B. H. (2016). An investigation of the snowpack signal in moisture-sensitive trees from the Southern Canadian Cordillera. *Dendrochronologia* 38, 118–130. doi: 10.1016/j.dendro.2016.03.008

Webb, S. L., Marty, B. S., and Conklin, P. S. (2001). *Forest Changes Due to Prescribed Burns and Windstorms in Itasca State Park, Minnesota: A Preliminary Report*. Saint Paul, MN: Minnesota Department of Natural Resources, Division of Ecological Sciences.

Wilmking, M., Maaten-Theunissen, M., van der, Maaten, E., van der, Scharnweber, T., Buras, A., Biermann, C., et al. (2020). Global assessment of relationships between climate and tree growth. *Glob. Chang. Biol.* 26, 3212–3220. doi: 10.1111/gcb.15057

Conflict of Interest: The authors declare that the research was conducted in the absence of any commercial or financial relationships that could be construed as a potential conflict of interest.

Publisher's Note: All claims expressed in this article are solely those of the authors and do not necessarily represent those of their affiliated organizations, or those of the publisher, the editors and the reviewers. Any product that may be evaluated in this article, or claim that may be made by its manufacturer, is not guaranteed or endorsed by the publisher.

frontiers in Water

REVIEW
published: 08 February 2022
doi: 10.3389/frwa.2022.803869

Navigating Great Lakes Hydroclimate Data

Lauren M. Fry[1], Andrew D. Gronewold[2], Frank Seglenieks[3], Samar Minallah[4], Deanna Apps[5] and Jamie Ferguson[6]*

[1] Great Lakes Environmental Research Laboratory, Office of Oceanic and Atmospheric Research, National Oceanic and Atmospheric Administration, Ann Arbor, MI, United States, [2] School for Environment and Sustainability, University of Michigan, Ann Arbor, MI, United States, [3] Environment and Climate Change Canada, Canadian Centre for Inland Waters, Burlington, ON, Canada, [4] Department of Climate and Space Sciences and Engineering, University of Michigan, Ann Arbor, MI, United States, [5] Hydraulics and Hydrology Branch, United States Army Corps of Engineers, Detroit, MI, United States, [6] Environment and Climate Change Canada, Great Lakes and St. Lawrence River Regulation Office, Cornwall, ON, Canada

Despite the fact that the Great Lakes contain roughly 20% of the world's surface freshwater, there is a relatively limited body of recent work in peer reviewed literature that addresses recent trends in lake levels. This work is largely coming from a handful of authors who are most well-versed in the complexities of monitoring and modeling in a basin that spans an international border and contains vast areas of surface water connected by both natural and managed connecting channel flows. At the same time, the recent dramatic changes from record low water levels in the early 2010's to record high water levels across the Great Lakes in 2019 and 2020 have brought significant attention to the hydroclimatic conditions in the basin, underscoring the need to bring new approaches and diverse perspectives (including from outside the basin) to address hydroclimate research challenges in the Great Lakes. Significant effort has led to advancements in data and model coordination among U.S. and Canadian federal agencies throughout the decades, and at the same time research from the broader community has led to higher resolution gridded data products. In this paper, we aim to present the current state of data and models for use in hydrological simulation with the objective of providing a guide to navigating the waters of Great Lakes hydroclimate data. We focus on data for use in modeling water levels, but we expect the information to be more broadly applicable to other hydroclimate research. We approach this by including perspectives from both the Great Lakes water management community and the broader earth science community.

Keywords: Great Lakes (North America), hydroclimate, data products, coordination, binational

OPEN ACCESS

Edited by:
Galina Guentchev, Met Office, United Kingdom

Reviewed by:
Paul Roebber, University of Wisconsin–Milwaukee, United States
Val Bennington, Lamont Doherty Earth Observatory (LDEO), United States

****Correspondence:***
Lauren M. Fry
lauren.fry@noaa.gov

Specialty section:
This article was submitted to Water and Climate, a section of the journal Frontiers in Water

Received: *28 October 2021*
Accepted: *12 January 2022*
Published: *08 February 2022*

Citation:
Fry LM, Gronewold AD, Seglenieks F, Minallah S, Apps D and Ferguson J (2022) Navigating Great Lakes Hydroclimate Data. Front. Water 4:803869. doi: 10.3389/frwa.2022.803869

INTRODUCTION

Anthropogenic climate change, population growth and the accompanying urbanization and agricultural demand, and economic development have been increasingly placing pressure on the world's freshwater (Wada et al., 2017). In addition, there is general agreement that intensification of the hydrologic cycle as a result of anthropogenic change means that assumptions of stationarity are not sufficient to inform water management. In the Great Lakes region, changes in the hydrologic cycle have been observed in the form of increasingly variable water levels (Gronewold and Rood, 2019). From the late 1990's to 2020, the Great Lakes have experienced both record low water levels,

during an extended period of low water on Lake Superior and Lake Michigan-Huron, and record high water levels, following a dramatic multi-year rise culminating in record high water levels on all lakes in 2017, 2019, and/or 2020, depending on the lake. Adaptive management of Great Lakes water resources requires understanding and predicting changes in Great Lakes water balance components under a changing hydroclimate. The intensification of the hydrologic cycle, along with increasing pressure on Great Lakes water resources, motivates the need for advancing hydroclimate modeling in the Great Lakes basin.

Early development of Great Lakes basin runoff and evaporation models (Croley II, 1983, 1989) was arguably at the forefront of large scale hydrological modeling, and was driven largely by the need to understand and predict changes in Great Lakes water levels. Since then, significant advancements have been made in the arena of large basin, continental, and earth systems modeling and data due to water scarcity and flooding concerns (e.g., Salas et al., 2017; Xue et al., 2017; Lakshmi et al., 2018, among others).

Despite the growing body of research (and researchers) aimed at advancing large basin hydrological models, improvements to Great Lakes regional modeling have been limited. This is, in part, due to challenges related to identifying appropriate hydroclimate data sources for use in model development and simulation. Data discontinuities that result from both the international border and the vast surface area of the lakes themselves, where surface observations are scarce, pose unique challenges in hydroclimate data development and use (Gronewold et al., 2018). The authors of this article have observed that although there is significant effort put toward developing, compiling, and coordinating hydroclimate data across the border (Gronewold et al., 2018), there is a need to communicate these data to the broader hydroclimate and hydrological modeling communities. The objectives of this article are to (1) document the unique hydroclimate data requirements for Great Lakes hydrological modeling, and (2) direct the reader to readily available datasets coming from both the water management and numerical modeling communities that have been developed with these requirements in mind. Focus is geared toward datasets used for model development and historical simulation of water supply and water levels.

Resolving Earth Systems and Water Science Perspectives

Monitoring, forecasting, and managing Great Lakes water supplies and water levels requires complex, internationally-coordinated hydroclimate models and data sets. Nowhere else on Earth is there such a large chain of interconnected lakes (only Lake Baikal has a larger volume than the collective volume of the Great Lakes, and Lake Superior alone is the largest lake on Earth by surface area) and such a diverse range of thermodynamic behavior (including, for example, seasonal ice cover formation and the propagation of lake effect snow events). The challenges of developing and applying hydroclimate models and data to this massive freshwater system are further exacerbated by differences in federal agency monitoring protocols and modeling frameworks on either side of the U.S.-Canada international border. These differences can propagate into severe biases and anomalies in widely-distributed data products. For example, the National Oceanic and Atmospheric Administration (NOAA) National Center for Environmental Prediction North American Regional Reanalysis (NCEP-NARR) spatial patterns of precipitation and evaporation reveal dry conditions directly over the U.S.-Canada border. This is likely a result of the differences in observation datasets assimilated by NARR where a sharp contrast exists between the two countries, with considerable sparsity of surface observations incorporated by NARR over the Canadian side of the Great Lakes basin (**Figure 1**; Minallah and Steiner, 2021a).

In light of these challenges, it is the authors' belief that two distinct approaches to developing and applying Great Lakes hydroclimate data and models have evolved. A primary goal of this paper is to address and begin to reconcile those two approaches. The first approach directly embraces and responds to the needs of Great Lakes regional water resources management authorities. The second perspective is rooted in the historical and ongoing development of complex numerical models covering broad spatial domains that rely on explicit modeling of critical physical processes.

The regional water resources management perspective is largely driven by the mandate facing the three Great Lakes International Boards of Control, all of which operate under the auspices of the 1909 Boundary Waters Treaty and subsequent formation of the International Joint Commission, or IJC (Lemarquand, 1993). The three Boards work collectively to ensure that outflows from Lake Superior and Lake Ontario, as well as ice and flow control structures above Niagara Falls, are all operated in accordance with IJC regulation plans. The decisions made by these boards are guided by regulation plans and treaties that have been developed using historical records of incoming water supplies, connecting channel flows, and lake water levels. In addition, current conditions can act as triggers for decisions within the regulation plans. For example, the relative difference between the water levels of Lake Superior and Lake Michigan-Huron is one of the factors for how much water is released from Lake Superior.

Of course, having coordinated values of water levels, connecting channel flows, and historical water supply is crucial, as even differences of 1 cm in water level could result in different decisions being made. It is also imperative to coordinate values communicated to the public. This is especially critical during times of extreme conditions, when differing values could result in public confusion if mixed messages are received from the regulation agencies. Finally, coordinated historical datasets are an integral part of the process of developing and evaluating regulation plans, which includes examining the trends in water levels and their drivers.

The need for such tight coordination has led some of the management boards to form subcommittees that specifically look at these issues. For instance, the International Lake Ontario St. Lawrence River Board has granted authority to the St. Lawrence Committee on River Gauging to oversee and ensure the accuracy of flow estimates and water level measurements

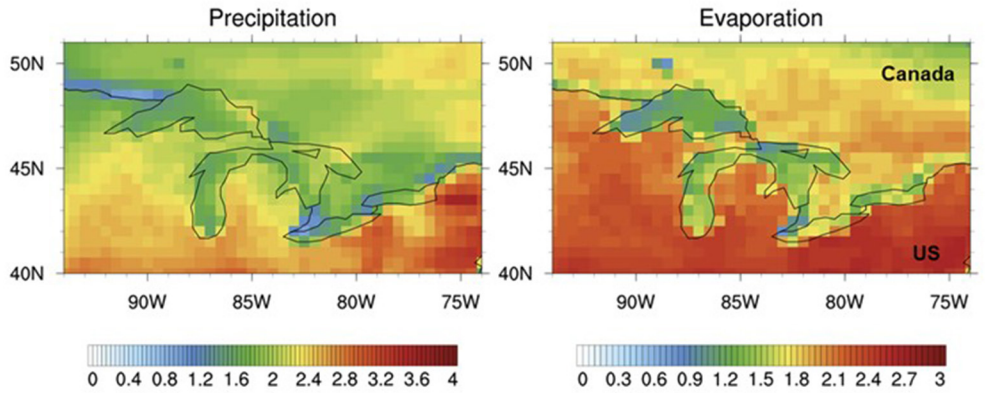

FIGURE 1 | Visible discontinuities in (left) precipitation and (right) evaporation (evapotranspiration over the land surface) along the US-Canada border in the NCEP North American Regional Reanalysis.

TABLE 1 | Water level data products.

Dataset (bold = officially coordinated)	Begin	End	Spatial resolution	Annual	Monthly	1/4 Monthly	Daily	Subdaily	Distribution
Coordinated lake-wide average water levels	1918	Last month	Average over lake surface	x	x				www.greatlakescc.org
Daily lake-wide average water levels	2005	Yesterday	Average over lake surface				x		Available from USACE or ECCC upon request
Beginning of period levels	1900	Current month	Average over lake surface		x	x			www.greatlakescc.org
Water level gage observations (Canada)	Varying record length		Point					x	https://www.waterlevels.gc.ca/eng
Water level gage observations (U.S.)	Varying record length		Point		x	x	x	x	https://tidesandcurrents.noaa.gov/
Change in storage	1950	2019	Average over lake		x				https://deepblue.lib.umich.edu/data/concern/data_sets/sb3978457

in the international section of the St. Lawrence River. This Committee inspects the computational methods and conducts an annual field inspection of the water level gages used by the Board to monitor river conditions and performs monthly audits of the water level and outflow data collected and archived by the power entities. In addition, the need to coordinate data to inform water management decisions on the Great Lakes led to the establishment of the Coordinating Committee for Great Lakes Basic Hydraulic and Hydrologic Data (subsequently referred to as "Coordinating Committee") in 1953. This group, which consists of members from U.S. and Canadian federal agencies responsible for water balance monitoring, forecasting, and management, works to coordinate data required by the Boards of Control. Datasets that have been officially coordinated are in bold text in **Tables 1**–**5**. In addition to coordinating official datasets, the Coordinating Committee also serves as a forum for federal scientists and engineers to compile, understand, and evaluate recent advancements in available data products for all variables of the water balance.

While the models and data sets used by the Boards of Control (and other regional management authorities) were developed by scientists and practitioners with this "first" perspective and explicitly include local-scale hydroclimate phenomena and anthropogenic impacts on the hydrology cycle, they typically do not adequately reflect climatological dynamics at regional to continental scales, nor do they typically reflect broad advancements in the state-of-the-art in hydroclimate modeling.

The second perspective on the development of Great Lakes hydroclimate models and data is, in fact, directly aligned with the earth systems modeling community. Numerical earth systems models require spatially consistent data spanning regional to global areas. Although this perspective does not conflict with the water management perspective, we find that there is significant

TABLE 2 | Connecting channel and diversion flow products.

Dataset (bold = officially coordinated)	Begin	End	Spatial resolution	Annual	Monthly	1/4 monthly	Daily	Subdaily	Distribution
Longlac diversion flows	1939	2 months ago	Average for diversion		x				www.greatlakescc.org
Ogoki diverson flows	1943	2 months ago	Average for diversion		x				www.greatlakescc.org
Longlac and Ogoki (LLO) combined flows	1939	2 months ago	Average for diversion		x				www.greatlakescc.org
Welland Canal flows	1900	2 months ago	Average for diversion		x				www.greatlakescc.org
NYSBC flows	1900	last year	Average for diversion		x				www.greatlakescc.org
Chicago diversion flows	1900	Several years ago	Average for diversion		x				www.greatlakescc.org
St. Marys, St. Clair, Detroit River gages	2008	Present	Point					x	https://waterdata.usgs.gov/nwis/rt
L2SWBM (LLO, Welland, and Chicago)	1950	2019	Average for diversion		x				https://deepblue.lib.umich.edu/data/concern/data_sets/sb3978457
St. Marys River discharge	1900	Last month	Average for river		x				www.greatlakescc.org
St. Clair River discharge	1900	Last month	Average for river		x				www.greatlakescc.org
Detroit River discharge	1900	Last month	Average for river		x				www.greatlakescc.org
Niagara River discharge	1900	Last month	Average for river		x				www.greatlakescc.org
St. Lawrence River discharge	1900	Last month	Average for river		x				www.greatlakescc.org
L2SWBM (connecting channel flows)	1950	2019	Average for river		x				https://deepblue.lib.umich.edu/data/concern/data_sets/sb3978457

room for improving the integration of research advances by the earth systems modeling community, and likewise improving the application of advancements in Great Lakes region specific data resulting from collaborations in the Water Management arena. This paper represents a step toward reconciling these two approaches.

SUMMARY OF AVAILABLE DATASETS AND CONVENTIONAL APPLICATIONS

The following subsections describe datasets for each variable of the Great Lakes water balance, shown in Equation (1). Datasets are summarized in **Tables 1**–**5**.

$$dS = Q_{in} - Q_{out} + P + R - E + \varepsilon \quad (1)$$

where dS is the change in storage (i.e., the change in volume due to changes in lake level), Q_{in} is the inflow from the upstream lake and through diversions as described in Section Diversion Flows, Q_{out} is the outflow to the downstream lake (or, in the case of Lake Ontario, to the St. Lawrence River) and through diversions as described in Diversion Flows, P is the precipitation falling directly over the lake surface, R is the lateral tributary runoff into the lake, E is the evaporation from the lake surface, and ε is the uncertainty term. Conventional practice is to lump direct groundwater inflow and thermal expansion into this uncertainty term.

Water Levels

Water level data products are shown in **Table 1**. For the purpose of monitoring and predicting the water budget of the Great Lakes, officially coordinated water levels are computed as lake-wide averages. Also, since Lake Michigan and Lake Huron are connected *via* the Straits of Mackinac, hydrologically they are considered one lake, referenced as "Lake Michigan-Huron." Lake-wide average water levels are calculated using a network of gages that has been agreed upon by the Coordinating Committee to give a complete depiction of the water level across the entire lake surface. Lake-wide average levels have been computed using a different set of gages over time on each lake due to data

TABLE 3 | Net basin supply (NBS) and NBS component data products.

Dataset (bold = officially coordinated)	Begin	End	Spatial resolution	Annual	Monthly	1/4 monthly	Daily	Subdaily	Distribution
Residual net basin supply	1900	Last month	Averaged over lake surface		x	x			www.greatlakescc.org
L2SWBM Component NBS	1950	2019	Averaged over lake surface		x				https://deepblue.lib.umich.edu/data/concern/data_sets/sb3978457
Runoff									
GLERL Hydromet Database Runoff	1940	Recent	Total runoff into lake		x				https://www.glerl.noaa.gov/ahps/mnth-hydro.html
L2SWBM	1950	2019	Total runoff into lake		x				https://deepblue.lib.umich.edu/data/concern/data_sets/sb3978457
Precipitation (overlake)									
GLERL Hydromet Database Overlake	1940	Recent	Averaged over lake area		x				https://www.glerl.noaa.gov/ahps/mnth-hydro.html
Binational Precipitation Grids	2002	Yesterday	10-km resolution				x		https://mrcc.purdue.edu/gismaps/naprecip.htm
CaPA-10km							x		https://mrcc.purdue.edu/gismaps/naprecip.htm
RDRS_v2	2000	2018	10-km resolution					x	https://caspar-data.ca/
CaPA-2.5km	2018	Days ago	2.5-km resolution					x	https://caspar-data.ca/
MPE	2002	Yesterday	4-km resolution				x		https://mrcc.purdue.edu/gismaps/naprecip.htm
L2SWBM	1950	2019	Averaged over lake surface		x				https://deepblue.lib.umich.edu/data/concern/data_sets/sb3978457
Evaporation (overlake)									
GLERL Hydromet Database Evaporation	1940	Recent	Averaged over lake surface		x				https://www.glerl.noaa.gov/ahps/mnth-hydro.html
Next Gen GLCFS Nowcast		YTD	Averaged over lake surface		x		x		https://www.glerl.noaa.gov/res/glcfs/glcfs.html
Water cycle prediction system	2016	Yesterday	Averaged over lake surface					x	www.greatlakescc.org
L2SWBM	1950	2019	Averaged over lake surface		x				https://deepblue.lib.umich.edu/data/concern/data_sets/sb3978457
GLEN stations	Varying record length		Point data				x		https://superiorwatersheds.org/GLEN/

availability dating back to the 1860's. The gages listed below are the locations included in lake-wide average water level calculations currently:

Lake Superior: Point Iroquois, Michipicoten, Thunder Bay, Marquette, and Duluth
Lake Michigan-Huron: Harbor Beach, Thessalon, Mackinaw City, Milwaukee, Ludington, Tobermory
Lake St. Clair: Belle River and St. Clair Shores
Lake Erie: Port Colborne, Port Stanley, Toledo, Cleveland
Lake Ontario: Oswego, Toronto, Kingston, Rochester, Port Weller, Cobourg.

The U.S. locations are gages operated by the National Oceanic and Atmospheric Administration (NOAA) and the gages in Canada are operated by the Canadian Hydrographic Service (CHS).

Officially coordinated monthly mean (MM) lakewide average water levels are computed using the same procedure by both the U.S. Army Corps of Engineers (USACE) and Environment and Climate Change Canada (ECCC): (1) compute daily means for each gage and round to the nearest 0.01 m, (2) compute the lakewide average (using gage pairing logic described in **Supplementary Tables 1–5** when a gage is missing daily data) and round to the nearest 0.01 m, (3) compute monthly mean

TABLE 4 | Lake surface water temperature (LSWT) and ice cover data products.

Dataset (bold = officially coordinated)	Begin	End	Spatial resolution	Annual	Monthly	1/4 monthly	Daily	Subdaily	Distribution
GLSEA LSWT and Ice cover data	1992	2020	1024 × 1024 pixel or lakewide	.			x		https://coastwatch.glerl.noaa.gov/glsea/
ARC-Lake and Globo Lake	1995	2016	0.025°				x		http://www.laketemp.net/home/
Buoy data	Varying record length		Point					x	https://www.ndbc.noaa.gov/
Great Lakes Ice Cover Database	1973	Present	1024 × 1024 pixel map				x		https://www.glerl.noaa.gov/data/ice/

lakewide average water levels by taking the mean daily values for each day in the month and round to the nearest 0.01 m. The same procedure is used to compute beginning of month water levels, except that in the third step, the beginning of month (BOM) level is computed by taking the average of the daily lakewide average water level on the last day of the month just ending and the 1st day of the month just starting for each lake. Coordinated BOM and MM water levels are significant data for use in outflow management, as described in Section Resolving Earth Systems and Water Science Perspectives. Accordingly, considerable attention is given to ensuring that both agencies use the same procedure, including the rounding. For each rounding application, the practice is to round to the nearest *even* centimeter when the thousandth of a meter is 5 (National Aeronautics Space Administration, 1994). For example, if the water level is 183.565 m, the rounded water level would be rounded to 183.56 m.

MM water levels and BOM levels are coordinated between federal agencies in both the U.S. and Canada. Those agencies are the USACE and ECCC. At the end of every month, MM and BOM levels are preliminarily coordinated as part of operational forecasting procedures. In the spring, when daily water level data has been verified by NOAA and CHS through December of the previous year, final coordination is done for all months of the year that just ended. MM water levels as of September 2021 are shown in **Figure 2**, with 2021 data still provisional. Data for the full coordinated period of record back to 1918 can be obtained from the Coordinating Committee.

Water levels are measured as a surface elevation with reference to the International Great Lakes Datum (IGLD) 1985. The IGLD 1985 reference zero point is located at Rimouski, Quebec. The datum is updated every 25–35 years to account for isostatic rebound or crustal movement from the weight of the glaciers that once covered the Great Lakes—St. Lawrence River system during the last ice age (Coordinating Committee on Great Lakes Basic Hydraulic Hydrologic Data, 1992). At the time of writing this manuscript, the Coordinating Committee is working on updating the IGLD (Coordinating Committee on Great Lakes Basic Hydraulic Hydrologic Data, 2017).

Diversion Flows

Diversion flows are shown in **Table 2**. There are anthropogenic diversions of water both into and out of the Great Lakes basin that are other avenues where water enters or leaves the system. Beginning furthest upstream, the Long Lac and Ogoki Diversions flow into Lake Superior. The Chicago Diversion flows out of Lake Michigan and is the only diversion that diverts water out of the system. The Welland Canal is another way water flows from Lake Erie to Lake Ontario and was built to aid with navigation due to Niagara Falls. The New York State Barge Canal also diverts water from the Lake Erie basin to the Lake Ontario basin. A map of the Great Lakes basin including the locations of the Great Lakes Diversions is shown in **Figure 3**.

Long Lac and Ogoki

The Long Lac Diversion was completed in 1941 and flows into Lake Superior *via* the Aguasabon River with headwaters at the Kenogami River (International Joint Commission, 1985). The Ogoki Diversion was completed in 1943 and connects the Ogoki River to Lake Nipigon, which then flows into Lake Superior (International Joint Commission, 1985). Since they both flow into Lake Superior, they are usually referenced together as the Long Lac and Ogoki Diversions. Both diversions are located on the Canadian side of the border and are operated by Ontario Power Generation (OPG), which provides hydropower generation to northern Ontario. The combined diversion flow averages about 150 m^3/s (5,300 ft^3/s) into Lake Superior. Measured flows are made available by OPG and provided to ECCC for Great Lakes water budget monitoring efforts. Information on monthly flow rates derived from OPG reports can be obtained from the Coordinating Committee.

Chicago

The Chicago Diversion diverts water out of Lake Michigan. In 1900, the construction of the Chicago Sanitary and Ship Canal was completed and in 1922 the Calumet-Sag Channel was completed, which allowed the water to be diverted out of Lake Michigan into the Illinois River system (**Figure 4**; International Joint Commission, 1985). There are multiple components of the diversion, such as lockages, leakages, navigation make-up flow, and discretionary flow, which contribute to the total flow (Lake Michigan Diversion Committee, 2019). The total diversion flow is set by a Supreme Court Decree, which was last modified in 1980, that allows a total diversion of 91 m^3/s or 3,200 ft^3/s. The USACE Chicago District has the responsibility to monitor and audit the diversion. An annual report is published once a year that will

TABLE 5 | Meteorological forcing data products.

Dataset (bold = officially coordinated)	Begin	End	Spatial resolution	Annual	Monthly	1/4 monthly	Daily	Subdaily	Distribution
NAM	2012	Present	12 km					x	https://www.ncei.noaa.gov/products/weather-climate-models/north-american-mesoscale
GFS	15 Jan 2015	Present	0.25°					x	https://www.ncei.noaa.gov/products/weather-climate-models/global-forecast
RAP/HRRR	Varies	Realtime	3 km					x	https://rapidrefresh.noaa.gov/hrrr/
ERA-Interim	Jan 1979	Aug 2019	~ 80 km (0.75°)		x		x	x	https://www.ecmwf.int/en/forecasts/datasets/reanalysis-datasets/era-interim
ERA5	1950	Present	~ 31 km (0.25°)		x			x	https://www.ecmwf.int/en/forecasts/datasets/reanalysis-datasets/era5
NASA MERRA-2	1980	Present	~ 50 km (0.5 × 0.625°)		x		x	x	https://gmao.gsfc.nasa.gov/reanalysis/MERRA-2/
NCEP-CFSR	Jan 1979	Mar 2011	~ 38 km		x			x	https://www.ncei.noaa.gov/products/weather-climate-models/climate-forecast-system
NCEP-CFSv2	Apr 2011	Present	~ 100 km (~0.93°		x			x	https://www.ncei.noaa.gov/products/weather-climate-models/climate-forecast-system
NCEP-NARR	1979	Present	~ 36 km		x		x	x	https://psl.noaa.gov/data/gridded/data.narr.html
RDRS_v2	2000	2018	10-km resolution					x	https://caspar-data.ca/
CMIP5	1850	2005	Variabe resolutions		x		x	x	https://esgf-index1.ceda.ac.uk/projects/cmip5-ceda/
CMIP6	1850	2014	Variabe resolutions		x		x	x	https://esgf-index1.ceda.ac.uk/projects/cmip6-ceda/
NARCCAP	1971	2000 (?)	Variabe resolutions					x	https://www.narccap.ucar.edu/data/index.html
CRU	1901	2020	0.5°		x				https://crudata.uea.ac.uk/cru/data/hrg/
GPCC	1891	2018	0.5°		x		x		https://www.dwd.de/EN/ourservices/gpcc/gpcc.html
UoD	1900	2017	0.5°		x				https://psl.noaa.gov/data/gridded/data.UDel_AirT_Precip.html
CPC-Unified over CONUS	1948	Present	0.25°		x		x		https://psl.noaa.gov/data/gridded/data.unified.daily.conus.html
Coordinated overbasin precipitation	1900	2 years ago	Averaged over lake + land area	x	x				www.greatlakescc.org
GLERL Hydromet Database Overbasin	1940	Recent	Averaged over lake + land area		x				https://www.glerl.noaa.gov/ahps/mnth-hydro.html
GLERL Hydromet Database Overland	1940	Recent	Averaged over land surface		x				https://www.glerl.noaa.gov/ahps/mnth-hydro.html

contain the diversion accounting for one or more of the previous years. Data, reports, and further information can be found on the USACE Chicago District website at: https://www.lrc.usace.army.mil/Missions/Lake-Michigan-Diversion-Accounting/. Monthly flow rates derived from the USACE Chicago District reports can be obtained from the Coordinating Committee.

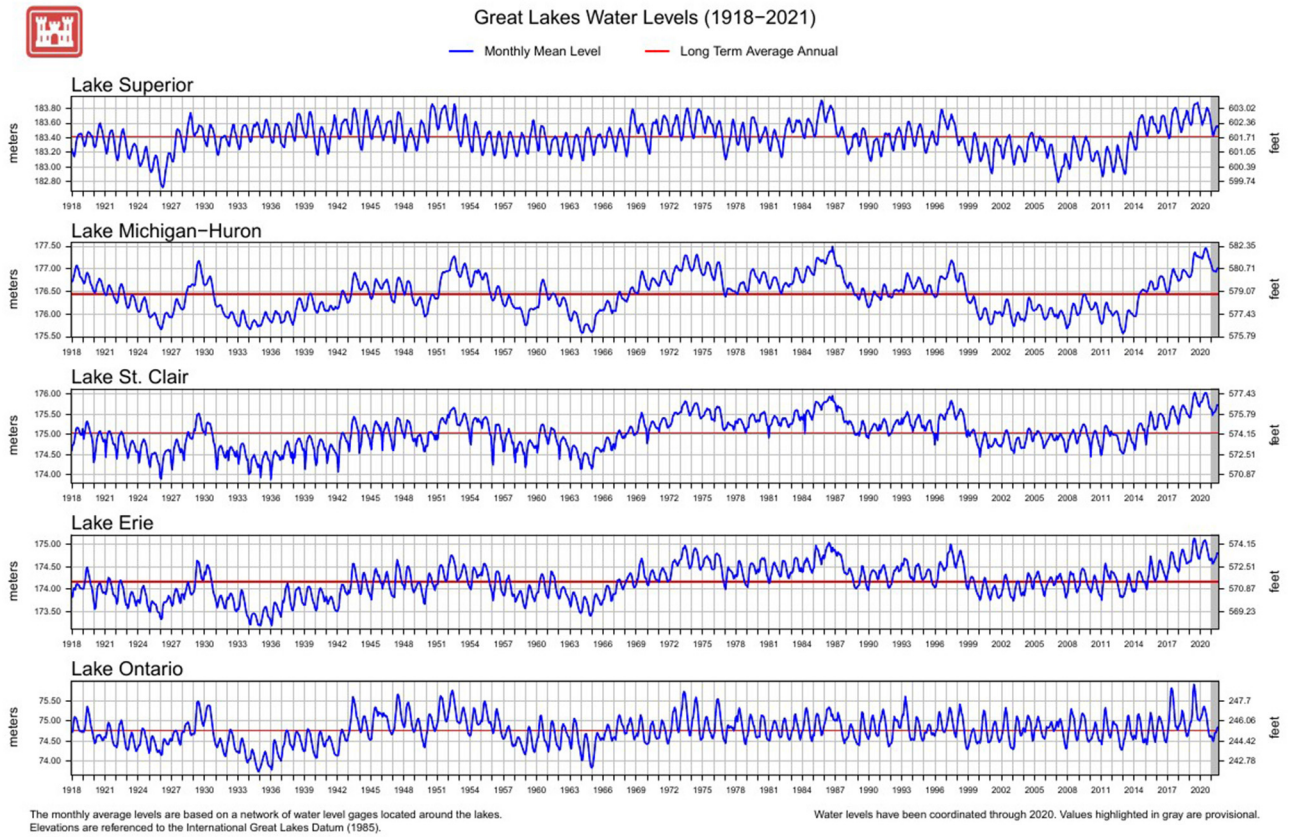

FIGURE 2 | Monthly mean water levels for each of the Great Lakes and Lake St. Clair shown as a blue line (as of September 2021). 2021 data highlighted in gray is still provisional (source: www.lre.usace.army.mil).

Welland Canal

The Welland Canal was originally constructed in 1829, but has been modified and reconstructed and the current structure of the canal was completed in 1932 (International Joint Commission, 1985; St. Lawrence Seaway Management Corporation, 2003). The primary use for the canal was to provide a navigational route for ships that bypassed the Niagara Falls, however, the canal also provides water for hydropower, industrial and municipal uses. The present structure consists of eight locks that span between Port Colborne, Ontario and Port Weller, Ontario (St. Lawrence Seaway Management Corporation, 2003). The flow through the Welland Canal varies but is typically about 200 m^3/s (7,100 ft^3/s). The data is provided *via* the St. Lawrence Seaway Corporation. Monthly flow rates can be obtained from the Coordinating Committee.

New York State Barge Canal

The New York State Barge Canal takes water from the Niagara River at Tonawanda, NY and returns it back to Lake Ontario *via* tributaries and the Oswego Canal (International Joint Commission, 1985). The amount of water diverted varies by the time of year, but ultimately has no hydraulic effect on the Great Lakes. During the navigation season, the flow is estimated to be 31 m^3/s (1,100 ft^3/s) (International Joint Commission, 1985). Since 1956, the winter flow estimate is typically 0 m^3/s due to the gates installed on the Erie Canal at Pendleton, which will close the canal for maintenance and repair. The New York State Barge Canal data is provided by the New York State Canal Corporation. Flows prior to 1951 are documented in reports (International Niagara Falls Engineering Board, 1953). Monthly flow rates can be obtained from the Coordinating Committee.

Connecting Channel Flows

Connecting channel flows are shown in **Table 2**. In the Great Lakes basin, the Great Lakes and Lake St. Clair are connected by the connecting channels, which are the St. Marys River, St. Clair River, Detroit River, Niagara River, and the St. Lawrence River.

St. Marys River

The amount of water that flows through the St. Marys River is prescribed monthly by the International Lake Superior Board of Control (ILSBC), although actual flow can differ from the prescribed flow due to potential unintentional deviations and differences between expected minor components (e.g., lockages and domestic use) and actual flows of these smaller components. The ILSBC was established by the International Joint Commission (IJC) through a 1914 Order of Approval

FIGURE 3 | A view of the Great Lakes basin, highlighting the diversions in the system. Source: USACE, Detroit.

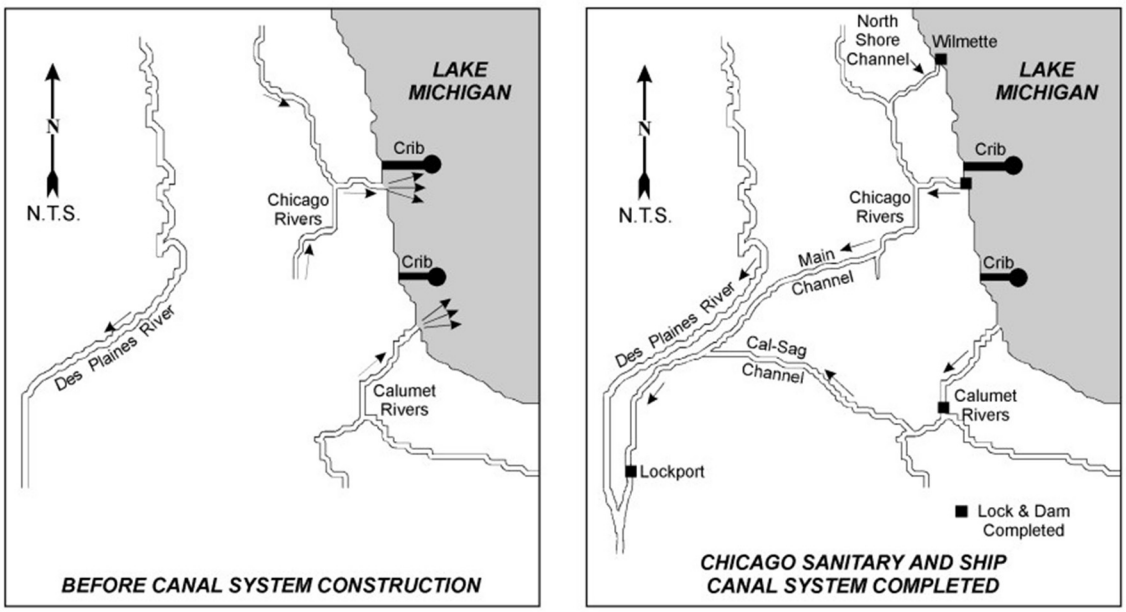

FIGURE 4 | Before and after diagram of the Chicago diversion based on the completion of the canal system [source: United States Army Corps of Engineers (2019)].

(International Joint Commission, 1914), which gives the Board the objective to regulate the outflow from Lake Superior. There have been Supplementary Orders of Approval (https://ijc.org/en/lsbc/who/orders) over the years that have included updates to procedures and regulation plans that have been used to determine the flow. The current regulation plan is Plan 2012, which was implemented in January 2015 because of the 2014 Supplementary Order of Approval (International Joint Commission, 2014).

Plan 2012 provides operational guidelines and procedures to be followed when determining outflow each month. The main objective of Plan 2012 is to regulate outflow with consideration of conditions that are occurring both upstream and downstream,

while maintaining much of the natural variability in lake levels. This is achieved by using a pre-project flow relationship, which is the flow that would have occurred prior to the canals and dams being built in the St. Marys River. This preproject relationship is based on the year 1887, which is generally thought of as the last year of the natural system (Clites and Quinn, 2003). Also, further adjustments are made by a balancing factor that adjusts flows depending on the level of Lake Superior and Lake Michigan-Huron relative to seasonal targets based on average conditions. Lastly, operational and physical limits are applied. Some examples of when limits would need to be considered include stable ice formation in the St. Marys River, conditions in regard to navigation or hydropower, flood risk, and safe operations of the control structures (International Lake Superior Board of Control., 2016). Once the total outflow for the month is determined, the flow is allocated through various control structures on the St. Marys River (**Figure 5**). This accounts for flow that is used for fish passage and other environmental considerations in the St. Marys Rapids, navigation and domestic users, and flow that goes to U.S. and Canadian hydropower plants (International Lake Superior Board of Control., 2016). For more information on the ILSBC, the current regulation plan, and flow data, visit the Board's website at https://www.ijc.org/en/lsbc.

As noted above, the actual flow through the St. Marys River can differ from the prescribed flow for unforeseen reasons. Therefore, the ILSBC determines the actual flow after-the-fact by summing the various components of flow through the structures in **Figure 5** (referred to as "flow accounting"). These component flows are determined using reports from the various contributing agencies shown in **Figure 5**. These monthly flows can be obtained from the Coordinating Committee. In addition to the historical flows determined using flow accounting, real-time point estimates of discharge on the St. Marys River are available at U.S. Geological Survey (USGS) station 04127885. This station is operated through collaboration among USGS, ECCC, and USACE.

St. Clair River and Detroit River

Water flows out of Lake Huron and enters Lake St. Clair *via* the St. Clair River and then water leaves Lake St. Clair *via* the Detroit River into Lake Erie. The flows through the St. Clair River and Detroit River are unregulated and are coordinated periodically between federal agencies in the U.S. and Canada through the auspices of the Coordinating Committee. In the past, the flows have been calculated monthly using stage fall discharge (SFD) relationships and unsteady flow models. Reports produced by the committee have tracked these changes over time (Coordinating Committee on Great Lakes Basic Hydraulic Hydrologic Data, 1982, 1988; International Upper Great Lakes Study Board, 2009; Thompson et al., 2020). Most recently, index-velocity ratings have been used to calculate discharge measurements for the St. Clair River and Detroit River since 2009 (Thompson et al., 2020). The development of acoustic Doppler velocity meters (ADVMs) and index-velocity ratings has allowed for high temporal resolution computation and reporting of discharges. The method was developed by Levesque and Oberg (2012). ADVMs were installed in the St. Clair River at Port Huron and in the Detroit River at Fort Wayne in 2008 (Thompson et al., 2020) and since 2009 the daily data have been used to estimate the monthly average flow in the St. Clair and Detroit Rivers (McClerren, 2021). The data at these gages on the St. Clair at Port Huron and Detroit River at Fort Wayne are provided by USGS (stations 04159130 and 04165710). In the absence of data at these ADVM gages for more than a 24-h period, the SFD equations would be used to compute the flow by the Coordinating Committee (Thompson et al., 2020).

Niagara River

The outflow from Lake Erie into Lake Ontario is computed in two parts, first, the discharge in the Niagara River, and second, the discharge through the Welland Canal, although the discharge through the Welland Canal is typically <5% of the Niagara River discharge. The Niagara River section has many flow components shown in **Figure 6**.

The Niagara River flow is determined by accounting for flows at different parts of the river, including the outflow from the Maid-of-the-Mist (MoM) Pool, diversion through the New York State Barge Canal, the flow over the Niagara Falls, Welland River flow, flow diverted to hydropower entities in U.S. and Canada, and locally estimated flows. The MoM outflow (Q_{MoM}) is determined using the rating equation shown in Equation (2).

$$Q_{MoM} = 0.6429\,(AA - 82.814)^3 \tag{2}$$

In Equation (2), AA represents the water level at the Ashland Avenue gage (shown **Figure 6**) in meters.

Over time, this rating equation has been adjusted, due to changes in the river and gauging stations (Noorbakhsh, 2009). Each month, flows are estimated for the Niagara River at Buffalo ($Q_{Buffalo}$) by summing the outflow at the MoM Pool, flow diverted for hydropower, and the New York State Barge Canal Diversion, and subtracting local inflows and the portion of the Welland Canal Diversion (Welland River) that is returned to the river upstream of the Falls using Equation (3) (Noorbakhsh, 2009).

$$Q_{Buffalo} = Q_{MoM} + BD + MD + NYSBCD - WR - LI \tag{3}$$

In Equation (3), BD is the water diverted to the Sir Adam Beck Power Plants, MD is the water diverted to the Robert Moses Niagara Power Plant, $NYSBCD$ is the New York State Barge Canal Diversion flow, WR is the Welland River flow, and the LI is local inflows. This is also represented in **Figure 7**.

The MoM flow, Beck, and Moses discharges and diversions are provided by the International Niagara Committee, which includes the New York Power Authority and Ontario Power Generation. The Welland Canal River flow and Diversion flow are provided by the St. Lawrence Seaway Management Corporation (SLSMC). The New York State Barge Canal data is provided by the New York State Canal Corporation. Monthly Niagara River flows can be obtained from the Coordinating Committee.

St. Lawrence River

Water leaving Lake Ontario flows through the St. Lawrence River, which eventually leads to the Atlantic Ocean. Flow through the

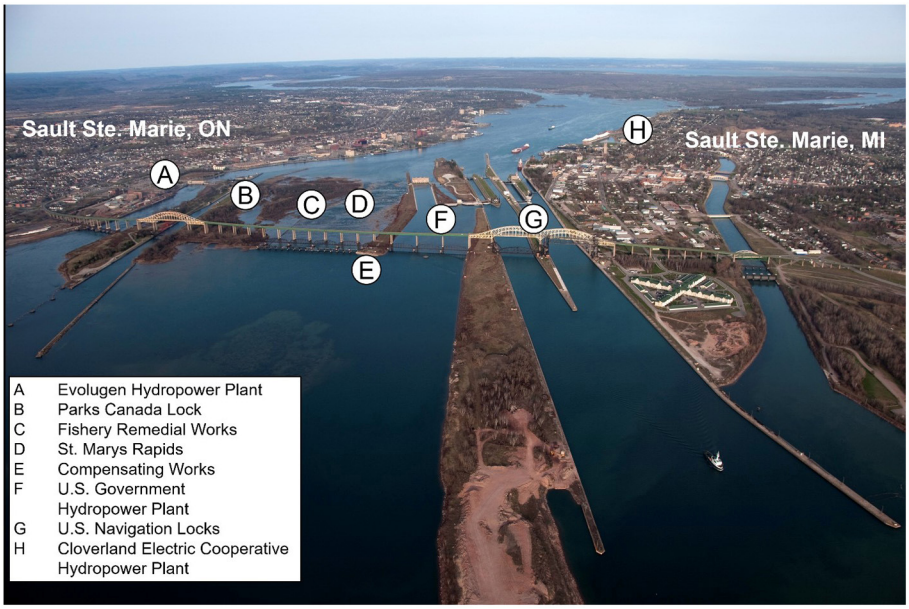

FIGURE 5 | View of the various structures at the head of the St. Marys River that are considered in determining monthly outflow from Lake Superior (source: ILSBC).

St. Lawrence River is primarily determined by the flow through the hydropower plants, which include the Moses-Saunders and Long Sault Dams. These computations are performed by the hydropower operators and the ratings are regularly verified by ECCC field staff using a vessel mounted acoustic Doppler current profiler. Discharges are reported to the International Lake Ontario-St. Lawrence River Board (ILOSLRB). However, other smaller components of the total flow also must be accounted for and this includes flow through the navigation canals and water diverted for domestic use. This Board of Control was established in 1952 under its first Order of Approval through the IJC (International Joint Commission, 1952). Outflows have been regulated since 1960, however, through Supplemental Orders of Approval modifications have been made to the regulation plan over time (International Joint Commission, 2016). The most recent Supplemental Order of 2016 commenced the Plan 2014 as the regulation plan to aide in determining outflows. The flow is primarily regulated through the Moses-Saunders Dam, which is located near Cornwall, ON and Massena, NY and jointly owned and operated by OPG and NYPA (International Lake Ontario St. Lawrence River Board, 2020).

Plan 2014 determines its weekly outflow based on the inflow of water to the lake from Lake Erie, water supplies to the lake *via* components (precipitation, runoff, and evaporation), the water level of Lake Ontario, and conditions upstream and downstream of the lake. Also, physical and operational limits are considered in regard to navigation and municipal uses, hydropower, flood risk, and stable ice formation in the St. Lawrence River in the winter.

For more information on the regulation, history, and flow data, visit https://ijc.org/en/loslrb and https://ijc.org/en/loslrb/watershed/outflow-changes. Monthly flows can also be obtained from the Coordinating Committee.

Net Basin Supply

From a lake water balance modeling perspective, it is convenient to combine over-lake precipitation, over-lake evaporation, and lateral tributary runoff into a single term representing the portion of a lake's water originating within a lake's basin (exclusive of connecting channel inflows and outflows). This single term is commonly referred to as a lake's net basin supply (or NBS).

There are two methods for estimating the NBS: the residual NBS (NBS_R, computed from change in storage (dS), inflows (Q_{in}), and outflows (Q_{out}) using a water balance approach) and the component NBS (NBS_C, computed as the sum of overlake precipitation (P), overlake evaporation (E), and lateral tributary runoff (R) into the lakes). The component and residual NBS are derived by rearranging the lake water balance (Equation 1), shown in Equations (4, 5).

$$Q_{out} - Q_{in} + dS = P + R - E + \varepsilon \tag{4}$$

$$NBS_R = NBS_C + \varepsilon \tag{5}$$

In practice, the residual NBS is considered to be more easily observed, due to the challenges of estimating the overlake precipitation, evaporation, and lateral tributary runoff into the lakes resulting from vast ungaged areas over the lakes themselves and data discontinuities across the U.S.-Canada border. Net basin supply and its components are shown in **Table 3**.

Residual Net Basin Supply

The Coordinating Committee computes the residual NBS (in m^3/s) using Equation (6):

$$NBS_R = kdS + Q_{out} - Q_{in} \tag{6}$$

where k is a conversion factor based on lake surface area.

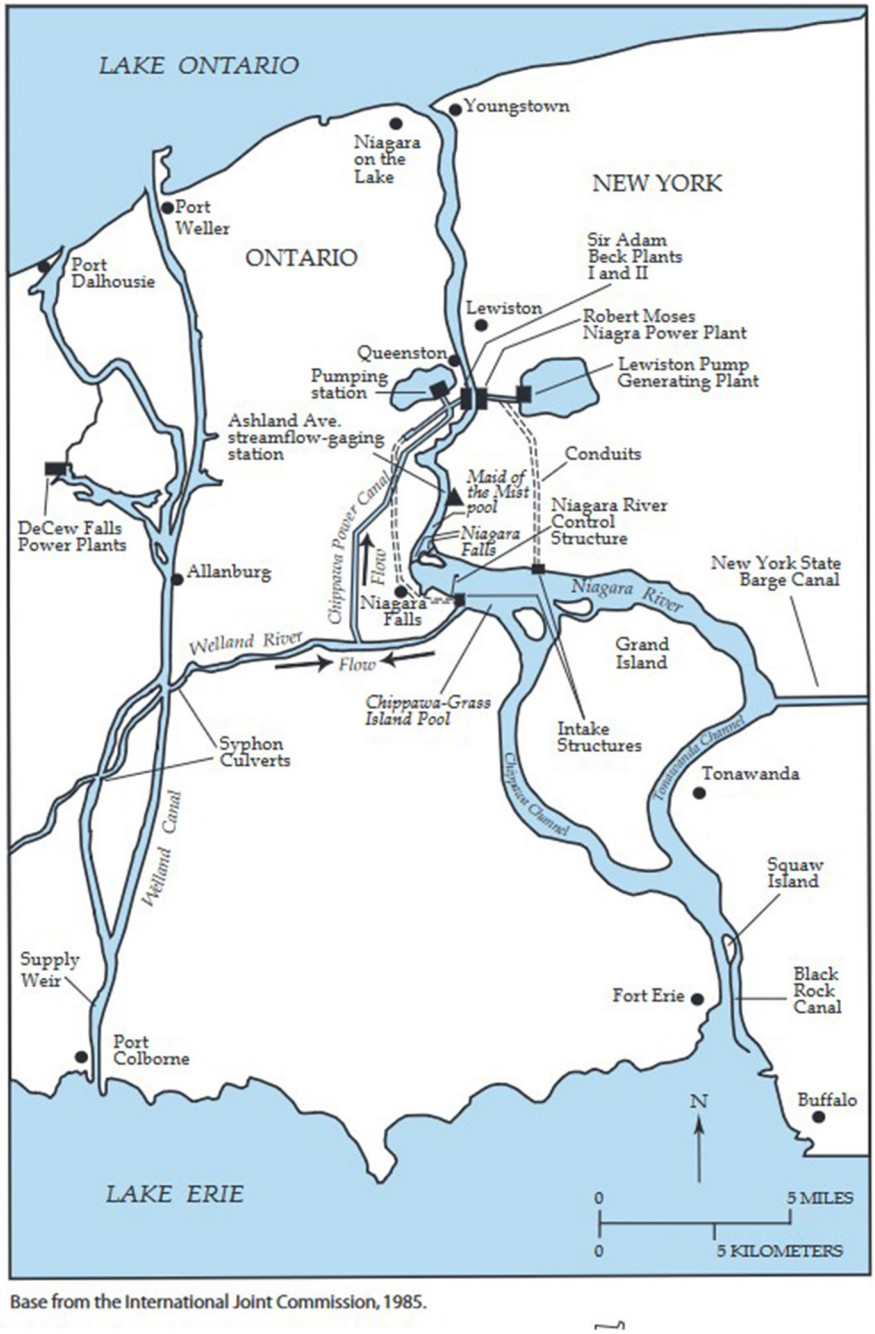

FIGURE 6 | Map of the Niagara River and Welland Canal [source: Neff and Nicholas (2005)].

Change in storage is calculated by taking the difference in water levels from the beginning to the end of a time period, typically monthly, that describes the total sum of water entering and leaving the lake *via* the components described above. Beginning of Month levels are determined using the approach described in Section Water Levels. Inflows and outflows are determined using diversion flows and connecting channel flows described in Sections Diversion Flows and Connecting Channel Flows. Note that the NYSBC diversion does not factor into any NBS_R calculations, as water is diverted from the Niagara River and returned to Lake Ontario.

Residual NBS is another dataset that is coordinated by the Coordinating Committee, and coordinated data go back to 1900. The long historical record of this dataset makes it acceptable to be used in operational and regulation efforts that are conducted on both sides of the border (International Upper Great Lakes Study,

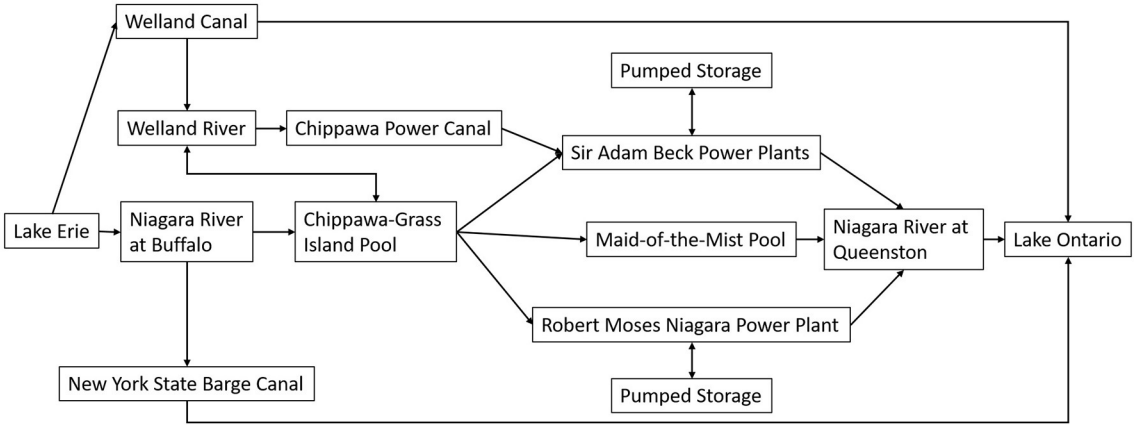

FIGURE 7 | Diagram of how water flows from Lake Erie to Lake Ontario. Note that the size of the arrows does not reflect the relative size of the flows. For example, the arrow pointing from the Welland Canal to the Welland River represents a siphon system discharging only about 6 m^3/s, compared to flows of around 8,000 m^3/s for the Niagara River at Buffalo [adapted from: Coordinating Committee on Great Lakes Basic Hydraulic Hydrologic Data (1976)].

2012). However, there can be uncertainties when calculating NBS due to the magnitude of connecting channel flows and change in storage (Neff and Nicholas, 2005) in addition to other uncertainty in minor diversions, consumptive use, and thermal volumetric changes (Bruxer, 2010; International Upper Great Lakes Study, 2012). Despite uncertainties, this dataset helps water management agencies express water supply in the Great Lakes over an extended historical period and can provide insight moving forward in our changing climate.

Component Net Basin Supply and Lumped P, E, R Estimates

Component NBS

For decades, Great Lakes scientists had followed a practice of combining individual estimates of *P, E, and R* (sometimes from different data sources) to estimate NBS. However, even when these estimates come from a common model, we find that none of these models explicitly constrain them to be faithful to the water balance. Relatively recently, regional scientists developed a statistical model, commonly called the Large Lake Statistical Water Balance Model (L2SWBM) that assimilates output from multiple models and data sets to infer constrained estimates of each water balance component, for each lake, that is consistent with all other water balance components across the Great Lakes system (including observed changes in lake storage). As such, simulations from L2SWBM are generally considered to be the only source of component NBS that is faithful to the holistic water balance. For a recent data product produced by L2SWBM, see Do et al. (2020).

Precipitation

Although precipitation is also included in forcing datasets described in Section Meteorological Data, it is included here in order to specify datasets that can be used for representing the *overlake* component of net basin supply. As noted in the introduction, the challenge of representing this important NBS component is complicated by both the vast surface area of the lakes themselves, resulting in the need to interpolate surface observations over broad areas, as well as the international border, resulting in discontinuities in some datasets. As a result, a handful of Great Lakes specific datasets have been developed for the purpose of water supply monitoring and simulation (**Table 3**).

The GLERL Hydrometeorological Database overlake precipitation uses a Thiessen weighting approach to compute overlake precipitation [described by Hunter et al. (2015)]. This dataset is not an operational dataset, and is updated on a roughly annual basis for the purpose of providing data for research to monitor the Great Lakes water balance.

More recently, to support Coordinating Committee needs, the Midwest Regional Climate Center has operationalized a binational gridded precipitation product that combines the state-of-the-art operational precipitation products from the U.S. and Canada. The current version of this gridded bi-national product (referred to as "Binational Precipitation Grids" in **Table 3**) blends the 10-km Canadian Precipitation Analysis (CaPA, described by Fortin et al., 2015 and Lespinas et al., 2015) with the U.S. Multi-sensor Precipitation Estimate [MPE, described by Kitzmiller et al. (2013)] resampled to the same 10-km grid. These two products combine gage and radar data, and CaPA also includes a numerical weather prediction model. An archive of this binational gridded data and anomalies can be accessed through the Midwest Regional Climate Center. This product represents a promising pathway for developing future coordinated datasets produced by the Coordinating Committee. It is worth noting that as a result of the collaborative process of blending the two data sets, special attention has been given to improving the representation of precipitation by the two products over the lakes and across the border.

In addition to contributing to the binational gridded precipitation product, various versions of the CaPA product are available at multiple resolutions through the Canadian Surface Prediction Archive (CaSPAr). Among these CaPA products is

the 10-km precipitation included in the Regional Deterministic Reanalysis System (v2), described in Section Reanalysis (referred to as RDRS_v2 in **Table 3**). The reanalysis includes hourly data from 1980–2018. It is anticipated that, due to the use of modeled data in addition to surface observations, estimates of historical overlake precipitation derived from this reanalysis product will be a more appropriate representation of actual overlake precipitation than the Thiessen-weighting product provided with the GLERL Hydrometeorological Database.

The other Great Lakes specific dataset comes from the L2SWBM *via* Do et al. (2020), described in Section Component NBS.

Runoff

The precipitation that falls on the land surface can take various paths to get to the lakes, this can be by overland flow across the land surface, sub-surface flow through the top soil layers, or baseflow through the groundwater system. The combination of these flows can be summed for each grid square or hydrological unit and is the more traditional definition of runoff for the scientific community; for example, when obtaining data from a reanalysis product such as the North American Land Data Assimilation System (NLDAS) or the European Centre for Medium-range Weather Forecasts (ECMWF) reanalyses.

The runoff from the land surface travels down the streamflow channels to eventually be deposited into the lakes. For the purposes of the calculation of NBS, the runoff for each lake is the amount of water that enters the lakes through the incoming river systems, with the exception of the flow from the upstream lake if there is one. Ideally, all of these rivers would have their flow measured at the point that they enter the lakes, however this is only true on a small number of the rivers in the Great Lakes. The percentage of the drainage area that is gaged varies depending on the lake and often the most downstream station may not be close to the outlet into the lake [for a representation of the portion of the basin that is gaged over time, see Fry et al. (2013)]. The location of gauging stations is often determined by local considerations and thus may not be the ideal location for the purpose of calculating flow into the lakes. Thus, there is a requirement to model the ungaged portion of the basin in some manner.

This modelling can range from simple area-ratio methods that transfer the amount of measured flow proportionally to the ungaged areas to sophisticated hydrological models that simulate the flow of water throughout the water cycle. The choice of model that is used can be based on many factors such as the final use of the results, the time required to run the model, or the availability of the input data. At the time of writing of this manuscript, there are two publicly available datasets for total runoff into the lakes. The GLERL Hydrometeorological Database (Hunter et al., 2015) includes runoff estimates computed using an area ratio estimate using a set of "most downstream" gages (Croley II and Hartman, 1986; Croley II and He, 2002). This approach has been shown to provide reliable estimates of total discharge to the lakes for gage combinations with similar catchment characteristics to the outlet's catchment (Fry et al., 2013). The second publicly available historical runoff dataset comes from the L2SWBM (described in Section Component NBS), and includes uncertainty estimates determined by resolving the Great Lakes water balance (Do et al., 2020).

There are many different agencies and research groups that run hydrological models around the Great Lakes, however there are only a few agencies that have an interest in obtaining data from both sides of the international border. Of course, flows from both sides of the international border are required in order to calculate the runoff into the lakes.

Initiated in 2014, the Great Lakes Runoff Intercomparison Projects (GRIP) are a series of studies that have focused on comparing the runoff generated by models from various academic institutions and federal agencies. The first study concentrated on Lake Michigan (Fry et al., 2014), second on Lake Ontario (Gaborit et al., 2017), and a third on Lake Erie (Mai et al., 2021a). The latest of the GRIP projects involves a wide range of lumped and distributed models that are being run over the entire Great Lakes watershed (Mai et al., 2021b), and represents an example of productive coordination between the research community and the Great Lakes water management community. In addition to including a broader variety of models, the later phases of GRIP have evolved to harmonize both the input datasets as well as the land surface database used by all models for both calibration and verification. It is hoped that once this latest GRIP project is completed, at least some of the different models would be adopted for operational monitoring of runoff by the Great Lakes water management community.

Evaporation

Like most runoff estimates, evaporation estimates for the Great Lakes are primarily determined using models driven by atmospheric forcing. There are a number of models that have been developed and applied specifically to the Great Lakes for simulating total evaporation from the lakes' surfaces. The GLERL Hydrometeorological Database, for example, provides time series of monthly evaporation from each of the lakes, computed by the Large Lake Thermodynamics Model [LLTM, described by Croley II (1989)]. The LLTM is a 1-dimensional thermodynamics model that computes evaporation by simulating the energy balance in the atmosphere above the lake, heat storage throughout the lake's vertical column, and aerodynamic evaporation. The estimates provided in the GLERL Hydrometeorological Database are driven by meteorological forcing computed by interpolation of surface observations using a Thiessen weighting approach. More recently, GLERL has begun providing estimates of lake-wide average evaporation aggregated from output from Next Generation Great Lakes Coastal Forecast System nowcast (Anderson et al., 2018). Fluxes in the Next Generation GLCFS are computed by experimental runs of the Finite Volume Coastal Ocean Model (Chen et al., 2003).

Atmospheric reanalyses and General Circulation Models (GCMs) also provide estimates of over-lake evaporation, however, the representation of lakes within the modeling system can considerably alter the simulation of lake-effect processes and lake-atmosphere interactions. In such modeling systems, lakes are either represented by prescribing the lake surface water temperatures through various observational and

operational sources or parameterized through shallow 1-dimensional lake models, while inclusion of more involved 3-dimensional lake models is generally absent in Earth System Models due to computational costs and other challenges (Mironov et al., 2010; Fiedler et al., 2014; Minallah and Steiner, 2021b,c). It is important to note that differences in lake representation in models can considerably alter the lake surface water temperatures, evaporation, and lake-effect precipitation magnitudes. For example, Minallah and Steiner (2021c) assess the effects of lake representation differences between two generations of the ECMWF reanalyses, ERA-Interim and the newer ERA5, where the former prescribes surface temperatures through external data sources while the later introduces the 1-dimensional Freshwater Lake (FLake) model. This difference in lake simulation resulted in ERA5 showing much warmer Great Lakes surface temperatures (by up to 5K) in the summer and producing twice the magnitude of evaporation as compared to ERA-Interim. This significantly alters the simulation of the regional hydroclimate and the water cycle both on climatological and short-term meteorological timescales between these two datasets, emphasizing the importance of careful examination of how lakes are simulated in the models before conducting more involved regional hydroclimatic assessments.

Validation of simulated evaporation by models can be a challenge due to spatial sparsity of buoy data and general absence of spatiotemporally consistent observational datasets. The Great Lakes Evaporation Network (GLEN) currently provides flux tower observations of evaporation for six sites over the Great Lakes, with four platforms located on offshore lighthouse sites (Stannard Rock, White Shoal, Spectacle Reef, shown in **Figure 8**, as well as Granite Island located on Lake Superior) and the remaining two located on nearby land. Half hourly data for each station are available, which have undergone only basic flux corrections, so careful pre-processing is required before it can be used to validate model outputs. The GLEN station data has been used to assess and improve Great Lakes hydrodynamics models (e.g., Durnford et al., 2018; Fujisaki-Manome et al., 2020). However, similar analyses have not been conducted between the lake surface fluxes from earth systems models and these stations. A visual comparison is included here in **Figure 8**, and indicates that both the global products and station data likely have significant biases that would need to be corrected before application to Great Lakes regional climate studies and water resources management.

Lake Surface Water Temperature (LSWT) and Ice Cover

Lake surface water temperature (LSWT, shown in **Table 4**) is one of the primary drivers of the lake-atmosphere interaction and related processes; e.g., lake-effect precipitation, lake breeze circulation patterns, cloud formation, etc. (Wright et al., 2013; Laird et al., 2017; Minallah and Steiner, 2021c). These LSWT are highly sensitive to climate warming and show an amplified response as compared to the surrounding land (Zhong et al., 2016; Kravtsov et al., 2018). Recent research has shown that LSWT have increased worldwide along with air temperatures, which has implications for ecosystems and water supply (Woolway et al., 2020). Further, the Coupled Model Intercomparison Project (CMIP) 6 projections reveal that earth systems models with some lake representation simulate a higher increase in the lake surface evaporation as compared to the surrounding land by the mid-century, especially in the winter months (Minallah and Steiner, 2021b) which has implications for NBS assessments. Interestingly, there is far less monitoring of subsurface temperatures, although the subsurface observations can provide indication of changes in thermal regimes in the lakes (Anderson et al., 2021).

LSWT can be measured both directly over the water body (buoy data) and through satellite retrievals of the water surface temperature. For the Great Lakes, two main satellite-derived LSWT datasets are available. The first is the Great Lakes Surface Environmental Analysis (GLSEA) Surface Water Temperature, produced by NOAA Great Lakes Environmental Research Laboratory using AVHRR (Advanced Very High Resolution Radiometer) imagery from the NOAA satellite series. This data is available for the 1992–2020 period as 1024 × 1024 pixel maps or as lake-averaged temperatures. The second dataset is produced at the University of Reading using the Earth Observing missions of the European Space Agency for all lakes globally (including lakes in the Great Lakes basin). This includes the ARCLake (Along-Track Scanning Radiometer (ATSR) Reprocessing for Climate: Lake Surface Water Temperature and Ice Cover) dataset and the newer generation GloboLakes (Global Observatory of Lake Responses to Environmental Change) dataset. Both datasets provide daily LSWT averages, with the GloboLakes having a finer resolution of 0.025 × 0.025 (1995–2016 period), while ARCLake has a resolution of 0.05 × 0.05 (1995–2013 period; Merchant and MacCallum, 2018; Carrea and Merchant, 2019).

While these datasets provide high resolution estimates of LSWT, caution must be exercised in their use as satellite retrievals can have errors due to sensor limitations, especially under cloudy conditions. Past assessment of these datasets for the Great Lakes region (Minallah and Steiner, 2021c) has shown spatiotemporal inconsistencies in data availability that introduce biases in lake-averaged measurements. This issue is especially pronounced in the winter months when data availability is almost non-existent and lake averages produce relatively warmer LWSTs. For example, **Figure 9B** shows the long-term lake-average LSWT for the three satellite-based datasets and different reanalyses over Lake Superior, where the months from Jan to Mar are consistently warm (∼275 K) for the three satellite-based datasets, whereas the reanalysis datasets show varying magnitudes below 273 K, depending on how lakes are simulated in these models. For GLSEA, we again note that while there is a clear distinction in the LSWT for the five Great Lakes in the summer months (with Lake Erie being the warmest and Lake Superior coldest), the winter months show near same magnitude of ∼275 K for all the lakes (**Figure 9A**).

For the summer months (ice-free season), buoy observations for the lake surface and air temperatures are also available; however, buoys are removed at the end of the autumn season and therefore they cannot supplement the satellite-derived LSWT

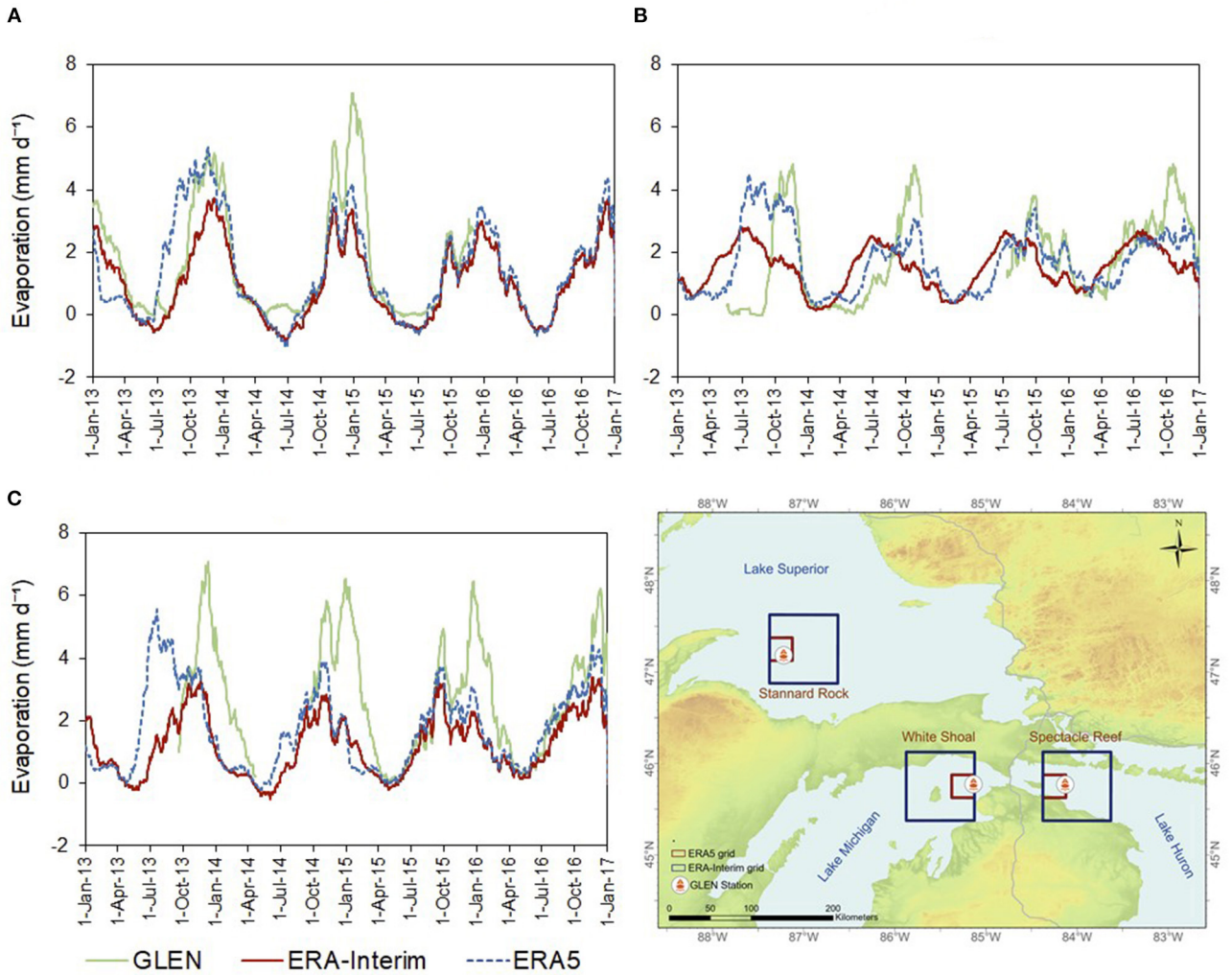

FIGURE 8 | 30-day running mean evaporation rate (mm/day) for three GLEN stations (location shown on map) and corresponding magnitudes for ERA-Interim (0.75°) and ERA5 (0.25°) grid cells. The running mean is computed after pre-processing and removal of erroneous and extreme values in the GLEN station data. **(A)** Stannard rock. **(B)** White Shoal. **(C)** Spectacle Reef.

for winter months to establish the ground truth (Gronewold and Stow, 2014).

In addition to LSWT, surface ice cover data (also shown in **Table 4**) is informative for verification of lake thermodynamics models. NOAA Great Lakes Environmental Research Laboratory maintains a Great Lakes Ice Cover Database, which compiles data from the Great Lakes Ice Atlas [1973–2002, described by Assel et al. (2002)], with addendums in separate reports for 2003–2005 described by Assel (2005) and updates for 2006-present using the same methods as the Great Lakes Ice Atlas (Wang et al., 2012, 2017). Daily gridded data are available for the ice season, which varies somewhat by year.

Meteorological Data

Global and regional meteorological data products, including precipitation, are included in **Table 5**.

Precipitation

Various global-scale observation-based gridded precipitation products are available for assessment of precipitation time series and spatial patterns; however, due to lack of observations over the lake surfaces and employment of land-based gage measurements, these products are better suited for over-land analyses. Commonly used global datasets include CRU time series (University of East Anglia Climate Research Unit; Harris et al., 2014), UoD time series (University of Delaware Global Land Data; Willmott, 2000), GPCC dataset (Global Precipitation Climatology Center; Schneider et al., 2014), and NOAA CPC Unified Gauge-Based Analysis over CONUS. These datasets can provide an adequate benchmark for assessment of model outputs (**Figure 10**); however, the quality of the time series is affected by the varying gage density both spatially and temporally. In general, their time series are similar in magnitudes, however, we note some differences from 1997 onward, likely due to

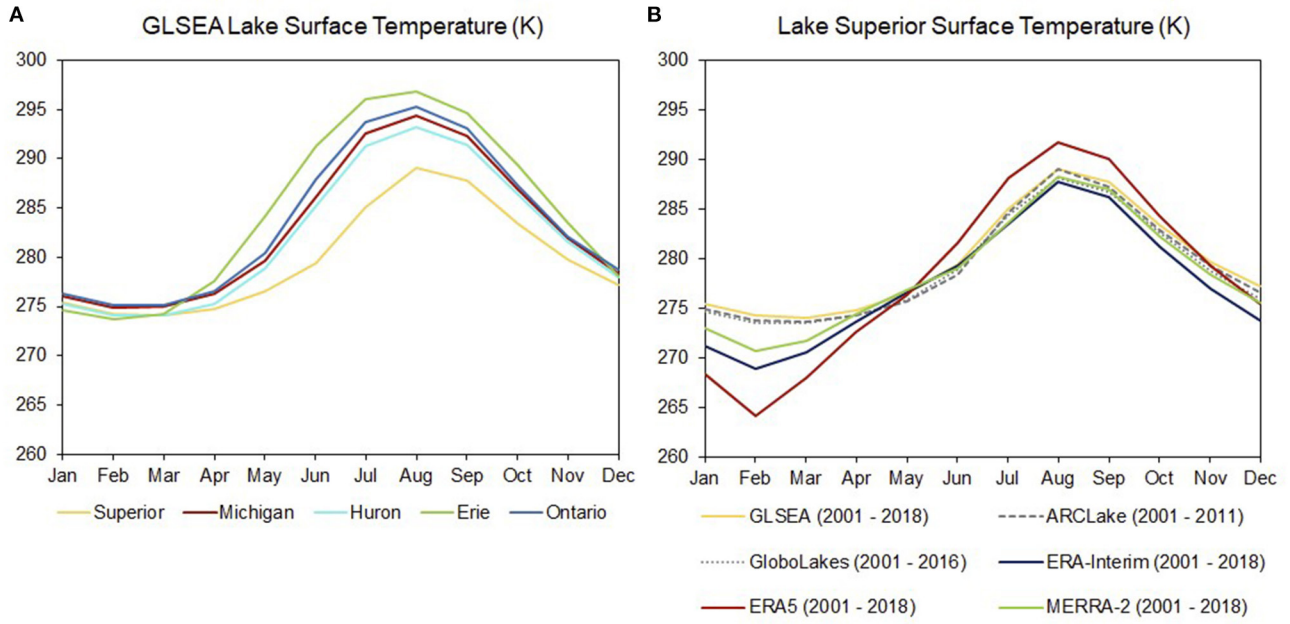

FIGURE 9 | 2001–2018 climatology of lake-average GLSEA LSWT for the five Laurentian Great Lakes **(A)** and Lake Superior LSWT for the different satellite-based and reanalysis datasets [**(B)**; averaging period included in the legend]. **(B)** Is adapted from Minallah and Steiner (2021c).

differences in the number of gages assimilated to produce the gridded products.

In addition to the gridded products described above, several precipitation products have been developed specifically for the Great Lakes region. For example, the Coordinating Committee produces monthly overbasin (including lake and land area) precipitation estimates on an annual basis. A primary goal of the coordinated dataset is to provide a long term record of precipitation that can be used to compute anomalies and statistics in order to monitor the water budget of the Great Lakes. Accordingly, the coordinated precipitation product is compiled from a number of interpolated station-based datasets with records dating back to 1900. At the time of writing of this manuscript, the coordinated dataset includes data from three interpolated products: the U.S. Army Corps of Engineers' Areally-Weighted District product (1900–1930), the NOAA GLERL Monthly Thiessen Polygon estimates (1931–1947), and daily Thiessen polygon estimates produced by the Great Lakes Seasonal Hydrologic Forecasting System (referred to as GLSHyFS, 1948-recent). These three products are described by Hunter et al. (2015), however it should be noted that the GLSHyFS software has replaced the Great Lakes Advanced Hydrologic Prediction System which was previously used to compute the daily estimates, and recent quality control efforts have resulted in using a smaller set of station observations. The GLERL Hydrometeorological Database also includes GLSHyFS-derived estimates of precipitation, which also include overbasin and overland precipitation in addition to the overlake precipitation described in Precipitation. These lumped estimates are conventionally used to (a) develop climatologies and (b) drive lumped rainfall-runoff models, notably the Large Basin Runoff Model, which is used to inform the U.S. contribution to the internationally coordinated 6-month Great Lakes water level forecast (Fry et al., 2020). In addition, the binational precipitation grids and CaPA products described in Section Precipitation are consistent across the border.

Reanalysis

Reanalysis products are helpful to provide a consistent process-based assessment of the various hydroclimatic variables and can be used as both forcing or validation datasets for hydrological modeling. Due to limitations of the interpolated gage-based estimates, reanalysis datasets are often more suitable and accurate (Essou et al., 2017). The commonly used global reanalyses are listed in **Table 5**. Past assessments on inter-comparison of these datasets reveal that the regional reanalysis NCEP-NARR has lowest overall magnitudes of precipitation but one of the highest magnitudes for evaporation (**Figure 10**), especially in the summer months. The other NCEP product, Climate Forecast System Reanalysis (CFSR), has considerable biases in the seasonal cycle of precipitation and evaporation, despite getting relatively reasonable estimates of the annual magnitudes. These reanalyses are somewhat inadequate in capturing the various water budget quantities. NASA MERRA-2 reanalysis is also relatively wetter as compared to gage-based datasets and other reanalyses (**Figure 10**) and is especially wet in the spring and early summer months (Minallah and Steiner, 2021a). The two ECMWF reanalyses (ERA-Interim and ERA5) generally capture better annual and seasonal magnitudes; however, as explained in Section Evaporation, the differences in how lakes are simulated in the two versions result in significant differences in the over-lake conditions which subsequently alters

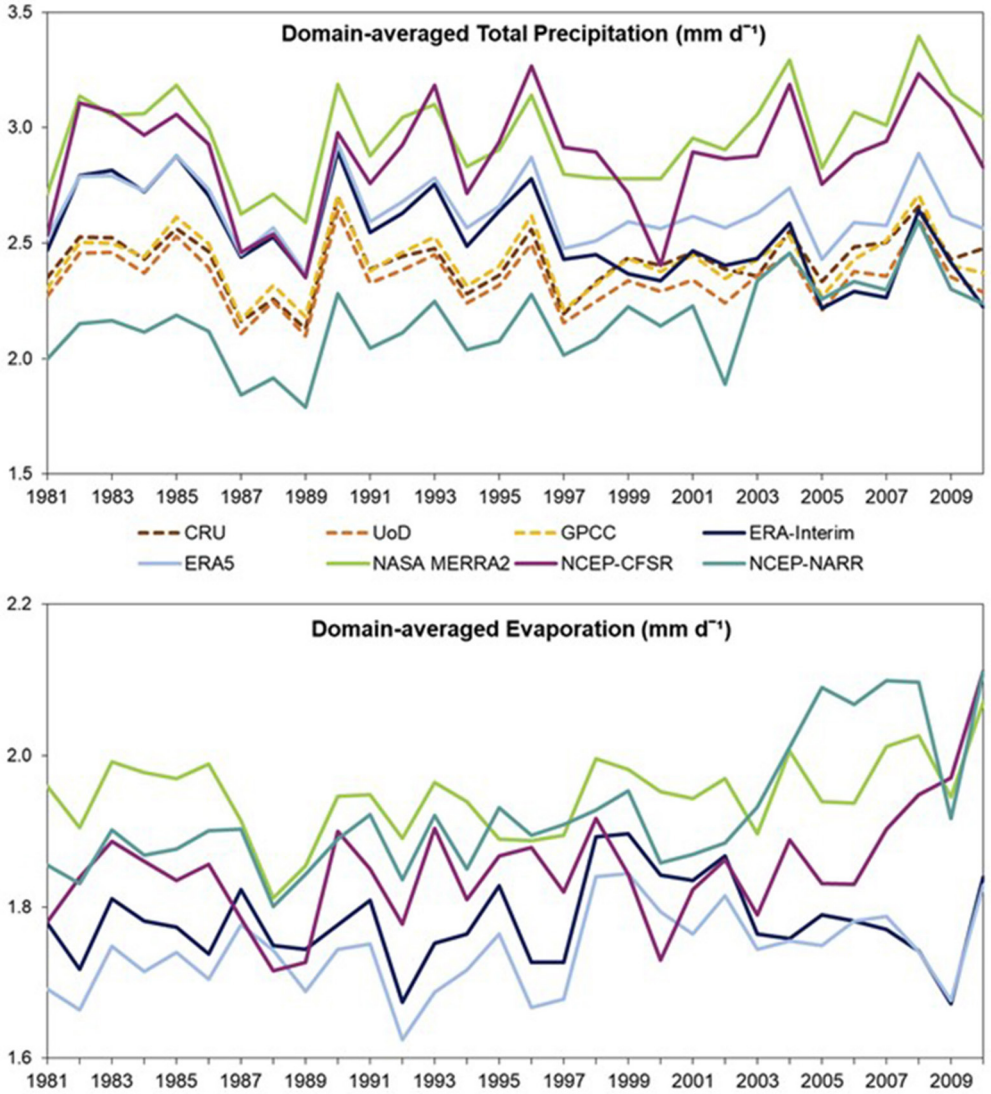

FIGURE 10 | Great Lakes domain-averaged (40–51 N, 74–94 W) precipitation and evaporation timeseries as simulated by various reanalysis datasets. Dashed lines in the top panel show gridded gage-based precipitation products.

the simulation of lake-effect processes. Therefore, users must exercise caution in employing these datasets as their quality will depend on the spatiotemporal scales and objectives of the study.

In addition to the global products described above, one newer surface reanalysis product that is noted to be of particular interest for transboundary and northern watersheds in North America is the Canadian 10 km North American precipitation and land-surface reanalysis (Gasset et al., 2021). This reanalysis (listed as RDRS_v2 in **Table 5**) is the result of initializing the Global Deterministic Reforecast System with ERA-Interim and dynamically downscaling the output using the Regional Deterministic Reforecast System (RDRS), coupled with the Canadian Land Data Assimilation System (CaLDAS) and the Canadian Precipitation Analysis (CaPA). The reanalysis includes hourly data from 1980 to 2018. Data are available for download from the Canadian Surface Prediction Archive (CaSPAr, at https://caspar-data.ca/). This product was used to construct the forcing for the later phases of the Great Lakes Runoff Intercomparison Project, described in Section Runoff.

High-Resolution Meteorological Forcing

Various numerical weather prediction model outputs are available as atmospheric forcing datasets for hydrological modeling. These include HRRR (High-Resolution Rapid Refresh), RAP (Rapid Refresh), GFS (Global Forecast System), and NAM (North American Mesoscale Forecast System). These operational datasets provide high resolution weather forecasts that are available on 3–6 hourly time steps for historical periods (2010's - present), but they do not go farther back in time. Furthermore, frequent changes in the model physics and assimilation schemes of the operational systems can

introduce some irregularities if assessments over multiple years are conducted.

General Circulation Models (GCMs)

GCM outputs are often used as direct input to hydrological models as they can provide both historical simulations and future projections under various climate scenarios. Before conducting assessments of future changes in the hydrological cycle, assessment of historical simulation must be conducted as GCMs contain multiple biases, especially for precipitation (Sperna Weiland et al., 2010). For the Great Lakes region, such assessments have been conducted for GCMs participating in the CMIP5 and CMIP6 programs. Briley et al. (2021) conducted a usability study for CMIP5 climate models in the Great Lakes region and found that many GCMs do not simulate these lakes in a way that can capture their impact on the regional climate, therefore use of these models for future assessments is impractical. They propose a framework to categorize various CMIP5 GCMs under three categories; simulation of lake dynamics, crude representation of lakes, and absence of lake simulation. They concluded that only 4 CMIP5 GCMs have adequate representation of the lakes that provide credible information for practitioners.

For the most recent CMIP6, Minallah and Steiner (2021c) conducted an assessment of the water cycle as simulated by 15 available GCMs. They find that most GCMs (10/15) either do not simulate large inland water bodies at all (represented as land cells) or have major inconsistencies in how the lakes are simulated. They find that these lakes have prominent effects on moisture generation and distribution processes at both meteorological and climatic time scales. Therefore, representation of detailed lake processes in GCMs is important for accurate assessments of the regional hydroclimate. Dynamical downscaling of GCMs using regional climate models (RCMs) has emerged as an approach for improving the representation of lakes [see Delaney and Milner (2019) for a summary of recent developments in regional climate modeling for the Great Lakes]. Further, the GCMs that can provide credible information for hydrological modelers require bias-correction of the atmospheric variables (specifically precipitation) using the various station-based or reanalysis datasets before they can be input as forcing for hydrological models to ensure consistencies in surface runoff and streamflows.

CONCLUDING REMARKS

In conducting this exercise of aggregating and describing data sources for use in Great Lakes hydroclimate monitoring and simulation, we identified two key gaps that create barriers to appropriate data selection and application.

First, there are important successes in coordinating data for water management across the lakes and across the border; however, we find a general lack of shared documentation, communication, and data use across perspectives (i.e., water management and earth systems modeling communities). For many of the Great Lakes region specific datasets, there is a lack of formal documentation, or, where documentation does exist, it is in the form of reports (and sometimes internal operating procedures) that are not discovered under traditional academic research. On the other hand, important advancements achieved by the earth systems modeling community are not always evaluated, documented, or communicated with region-specific water management activities in mind.

Second, we find that this lack of formal documentation and communication results in earth system and forecast models being developed in the absence of consistent data across the U.S.-Canada border. If regional datasets are not consistent or readily available (in terms of format, accessibility, and discoverability), they will not be assimilated into earth systems models. Discontinuities across the border in region- or country-specific datasets often render them impractical for transboundary basin-wide assessments resulting in use of coarser and less precise, but spatiotemporally consistent, global datasets by the earth sciences community.

We make two recommendations to address the gaps identified above. First, we believe it is incumbent on the earth systems modeling community to engage regional practitioners to understand unique data gaps, limitations, and challenges, particularly those associated with monitoring and modeling large freshwater surfaces and domains that interact across an international border. Second it is imperative that the individuals and organizations that make up the water management community improve documentation and communication of region-specific hydroclimate data. This action will enable the global earth science community (and other research groups outside of the Great Lakes basin) to use the data that have been evaluated and coordinated across both sides of the international border. This advancement has the potential to broadly diversify the range of models and datasets available for improved understanding and management of water resources of the Great Lakes.

AUTHOR CONTRIBUTIONS

LF led the development of the manuscript. LF, AG, FS, SM, and DA contributed sections of the manuscript. JF provided details on water level, connecting channel, diversion data products, and reviewed the manuscript. All authors contributed to manuscript revision, read, and approved the submitted version.

ACKNOWLEDGMENTS

The authors gratefully acknowledge input and feedback during the development of the manuscript from Tim Calappi, Chuck Sidick, Matt McClerren, and Allison Steiner. In addition, we thank members and associates of the Coordinating Committee for their thoughtful review. This is NOAA GLERL contribution number 1998.

SUPPLEMENTARY MATERIAL

The Supplementary Material for this article can be found online at: https://www.frontiersin.org/articles/10.3389/frwa.2022.803869/full#supplementary-material

REFERENCES

Anderson, E. J., Fujisaki-Manome, A., Kessler, J., Lang, G. A., Chu, P. Y., Kelley, J. G., et al. (2018). Ice forecasting in the next-generation great lakes operational forecast system (GLOFS). *J. Mar. Sci. Eng.* 6:123. doi: 10.3390/jmse6040123

Anderson, E. J., Stow, C. A., Gronewold, A. D., Mason, L. A., McCormick, M. J., Qian, S. S., et al. (2021). Seasonal overturn and stratification changes drive deep-water warming in one of Earth's largest lakes. *Nat. Commun.* 12, 1–9. doi: 10.1038/s41467-021-21971-1

Assel, R. A. (2005). *Great Lakes Ice Cover Climatology Update, Winters 2003, 2004, and 2005. NOAA Technical Memorandum GLERL-135*. Ann Arbor, MI: National Oceanic and Atmospheric Administration Great Lakes Environmental Research Laboratory.

Assel, R. A., Norton, D. C., and Cronk, K. C. (2002). *A Great Lakes Ice Cover Digital Data Set for Winters 1973–2000. NOAA Technical Memorandum GLERL-121*. Ann Arbor, MI: National Oceanic and Atmospheric Administration Great Lakes Environmental Research Laboratory.

Briley, L. J., Rood, R. B., and Notaro, M. (2021). Large lakes in climate models: a Great Lakes case study on the usability of CMIP5. *J. Great Lakes Res.* 47, 405–418. doi: 10.1016/j.jglr.2021.01.010

Bruxer, J. (2010). *Uncertainty Analysis of Lake Erie Net Basin Supplies as Computed Using the Residual Method*. (Master's thesis), McMaster University, Hamilton, ON, Canada.

Carrea, L., and Merchant, C. J. (2019). *GloboLakes: Lake Surface Water Temperature (LSWT) v4.0 (1995–2016)*. Centre for Environmental Data Analysis, 29 March 2019. doi: 10.5285/76a29c5b55204b66a40308fc2ba9cdb3

Chen, C., Liu, H., and Beardsley, R. C. (2003). An unstructured grid, finite-volume, three-dimensional, primitive equations ocean model: application to coastal ocean and estuaries. *J. Atmos. Oceanic Technol.* 20, 159–186. doi: 10.1175/1520-0426(2003)020<0159:AUGFVT>2.0.CO;2

Clites, A. H., and Quinn, F. H. (2003). The history of Lake Superior regulation: implications for the future. *J. Great Lakes Res.* 29, 157–171. doi: 10.1016/S0380-1330(03)70424-9

Coordinating Committee on Great Lakes Basic Hydraulic and Hydrologic Data (1976). *Lake Erie Outflow 1860-1964 (with Addendum 1965-1975)*. Available online at: http://www.GreatLakesCC.org (accessed January 20, 2022).

Coordinating Committee on Great Lakes Basic Hydraulic and Hydrologic Data (1982). *Lakes Michigan–Huron Outflows, St. Clair and Detroit Rivers 1900–1978*. Available online at: http://www.GreatLakesCC.org (accessed January 20, 2022).

Coordinating Committee on Great Lakes Basic Hydraulic and Hydrologic Data (1988). *Lakes Michigan–Huron Outflows, St. Clair and Detroit Rivers 1900–1986*. Available online at: http://www.GreatLakesCC.org (accessed January 20, 2022).

Coordinating Committee on Great Lakes Basic Hydraulic and Hydrologic Data (1992). *IGLD 1985*. Available online at: https://www.lre.usace.army.mil/Portals/69/docs/GreatLakesInfo/docs/IGLD/BrochureOnTheInternationalGreatLakesDatum1985.pdf (accessed January 21, 2022).

Coordinating Committee on Great Lakes Basic Hydraulic and Hydrologic Data (2017). *Updating the International Great Lakes Datum*. Available online at: http://www.GreatLakesCC.org (accessed January 20, 2022).

Croley II, T. E. (1983). Great Lake basins (USA-Canada) runoff modeling. *J. Hydrol.* 64, 135–158. doi: 10.1016/0022-1694(83)90065-3

Croley II, T. E. (1989). Verifiable evaporation modeling on the laurentian Great Lakes. *Water Resour. Res.* 25, 781–792. doi: 10.1029/WR025i005p00781

Croley II, T. E., and Hartman, H. C. (1986). *Near-Real-Time Forecasting of Large-Lake Water Supplies: A User's Manual*. Ann Arbor, MI: NOAA Technical Memorandum ERL GLERL-61, Great Lakes Environmental Reesearch Laboratory. Available online at: https://www.glerl.noaa.gov/ftp/publications/tech_reports/glerl-061/tm-061.pdf

Croley II, T. E., and He, C. (2002). "Great Lakes large basin runoff model," in *Proceedings, Second Federal Interagency Hydrologic Conference*. Las Vegas, NV.

Delaney, F., and Milner, G. (2019). "The state of climate modeling," in *The Great Lakes Basin – A Synthesis in Support of a Workshop Held on June 27, 2019 in Ann Arbor, MI* (Toronto, CA: Ontario Climate Consortium), 1–80. Available online at: https://climateconnections.ca/app/uploads/2020/05/The-State-of-Climate-Modeling-in-the-Great-Lakes-Basin_Sept132019.pdf (assessed September 13, 2019).

Do, H. X., Smith, J. P., Fry, L. M, and Gronewold, A. D. (2020). Seventy-year long record of monthly water balance estimates for Earth's largest lake system. *Sci. Data* 7:276. doi: 10.1038/s41597-020-00613-z

Durnford, D., Fortin, V., Smith, G., Archambault, B., Deacu, D., Dupont, F., et al. (2018). Toward an operational water cycle prediction system for the Great Lakes and St. Lawrence River. *Bull. Am. Meteorol. Soc.* 99, 521–546. doi: 10.1175/BAMS-D-16-0155.1

Essou, G. R., Brissette, F., and Lucas-Picher, P. (2017). The use of reanalyses and gridded observations as weather input data for a hydrological model: comparison of performances of simulated river flows based on the density of weather stations. *J. Hydrometeorol.* 18, 497–513. doi: 10.1175/JHM-D-16-0088.1

Fiedler, E. K., Martin, M. J., and Roberts-Jones, J. (2014). An operational analysis of lake surface water temperature. *Tellus A Dyn. Meteorol. Oceanogr.* 66, 21247. doi: 10.3402/tellusa.v66.21247

Fortin, V., Roy, G., Donaldson, N., and Mahidjiba, A. (2015). Assimilation of radar quantitative precipitation estimations in the Canadian Precipitation Analysis (CaPA). *J. Hydrol.* 531, 296–307. doi: 10.1016/j.jhydrol.2015.08.003

Fry, L., Hunter, T., Phanikumar, M., Fortin, V., and Gronewold, A. (2013). Identifying streamgage networks for maximizing the effectiveness of regional water balance modeling. *Water Resour. Res.* 49, 2689–2700. doi: 10.1002/wrcr.20233

Fry, L. M., Apps, D., and Gronewold, A. D. (2020). Operational seasonal water supply and water level forecasting for the laurentian great lakes. *J. Water Resour. Plan. Manag.* 146:04020072. doi: 10.1061/(ASCE)WR.1943-5452.0001214

Fry, L. M., Gronewold, A. D., Fortin, V., Buan, S., Clites, A. H., Luukkonen, C., et al. (2014). The great lakes runoff intercomparison project phase 1: lake Michigan (GRIP-M). *J. Hydrol.* 519, 3448–3465. doi: 10.1016/j.jhydrol.2014.07.021

Fujisaki-Manome, A., Mann, G. E., Anderson, E. J., Chu, P. Y., Fitzpatrick, L. E., Benjamin, S. G., et al. (2020). Improvements to lake-effect snow forecasts using a one-way air–lake model coupling approach. *J. Hydrometeorol.* 21, 2813–2828. doi: 10.1175/JHM-D-20-0079.1

Gaborit, É., Fortin, V., Tolson, B., Fry, L., Hunter, T., and Gronewold, A. D. (2017). Great Lakes Runoff Inter-comparison Project, phase 2: lake Ontario (GRIP-O). *J. Great Lakes Res.* 43, 217–227. doi: 10.1016/j.jglr.2016.10.004

Gasset, N., Fortin, F., Dimitrijevic, M., Carrera, M., Bilodeau, B., Muncaster, R., et al. (2021). A 10 km North American precipitation and land-surface reanalysis based on the GEM atmospheric model. *Hydrol. Earth Syst. Sci.* 25, 4917–4945. doi: 10.5194/hess-25-4917-2021

Gronewold, A. D., Fortin, V., Caldwell, R., and Noel, J. (2018). Resolving hydrometeorological data discontinuities along an international border. *Bull. Am. Meteorol. Soc.* 99, 899–910. doi: 10.1175/BAMS-D-16-0060.1

Gronewold, A. D., and Rood, R. B. (2019). Recent water level changes across Earth's largest lake system and implications for future variability. *J. Great Lakes Res.* 45, 1–3. doi: 10.1016/j.jglr.2018.10.012

Gronewold, A. D., and Stow, C. A. (2014). Water loss from the Great Lakes. *Science* 343, 1084–1085. doi: 10.1126/science.1249978

Harris, I., Jones, P. D., Osborn, T. J., and Lister, D. H. (2014). Updated high-resolution grids of monthly climatic observations–the CRU TS3. 10 dataset. *Int. J. Climatol.* 34, 623–642. doi: 10.1002/joc.3711

Hunter, T. S., Clites, A. H., Campbell, K. B., and Gronewold, A. D. (2015). Development and application of a North American Great Lakes hydrometeorological database—part I: precipitation, evaporation, runoff, and air temperature. *J. Great Lakes Res.* 41, 65–77. doi: 10.1016/j.jglr.2014.12.006

International Joint Commission (1914). *Orders of Approval*. Available online at: https://ijc.org/sites/default/files/1914%20Order%20of%20Approval.pdf (accessed September 30, 2021).

International Joint Commission (1952). *Hydro-Power – St. Lawrence River*. Available online at: https://ijc.org/en/68a (accessed September 30, 2021).

International Joint Commission (1985). *Great Lakes Diversions and Consumptive Uses: A Report to the Governments of the United States and Canada under the 1977 Reference*. International Joint Commission. Available online at: https://www.ijc.org/sites/default/files/ID279.pdf (accessed October 26, 2021).

International Joint Commission (2014). *Supplementary Orders of Approval*. Available online at: https://ijc.org/sites/default/files/2014%20Supplementary%20Order%20of%20Approval.pdf (accessed September 30, 2021).

International Joint Commission (2016). *Supplementary Orders of Approval*. Available online at: https://ijc.org/sites/default/files/Docket_68_Order_SupRegulationOfLakeOntarioOutlfows-2016-12-08.pdf (accessed September 30, 2021).

International Lake Ontario St. Lawrence River Board (2020). *Lake Ontario St. Lawrence River Regulation*. Available online at: https://ijc.org/en/loslrb/who/regulation (accessed September 1, 2021).

International Lake Superior Board of Control. (2016). *Operational Guide for Plan 2012. A Report to the International Joint Commission by the International Lake Superior Board of Control*.

International Niagara Falls Engineering Board (1953). *Preservation and enhancement of Niagara Falls, report to the International Joint Commission. Also included as part of report of the International Joint Commission of the same title*. Washington, DC; Ottawa ON: International Niagara Falls Engineering Board.

International Upper Great Lakes Study (2012). *Lake Superior Regulation: Addressing Uncertainty in Upper Great Lakes Water Levels*. Available online at: https://legacyfiles.ijc.org/publications/Lake_Superior_Regulation_Full_Report.pdf (accessed October 15, 2021).

International Upper Great Lakes Study Board (2009). *Impacts on Upper Great Lakes Water Levels, St. Clair River Final Report to the International Joint Commission*. Available online at: http://www.iugls.org/Final_Reports (Accessed September 1, 2021).

Kitzmiller, D., Miller, D., Fulton, R., and Ding, F. (2013). Radar and multisensor precipitation estimation techniques in National Weather Service hydrologic operations. *J. Hydrol. Eng.* 18, 133–142. doi: 10.1061/(ASCE)HE.1943-5584.0000523

Kravtsov, S., Sugiyama, N., and Roebber, P. (2018). "Role of nonlinear dynamics in accelerated warming of great lakes," in *Advances in Nonlinear Geosciences*, ed A. A. Tsonis (Berlin: Springer), 279–295. doi: 10.1007/978-3-319-58895-7_15

Laird, N. F., Metz, N. D., Gaudet, L., Grasmick, C., Higgins, L., Loeser, C., et al. (2017). Climatology of cold season lake-effect cloud bands for the North American Great Lakes. *Int. J. Climatol.* 37, 2111–2121. doi: 10.1002/joc.4838

Lake Michigan Diversion Committee (2019). *Findings of the Eighth Technical Committee for Review of Diversion Flow Measurements and Accounting Procedures*. Chicago, IL: United States Army Corps of Engineers.

Lakshmi, V., Fayne, J., and Bolten, J. (2018). A comparative study of available water in the major river basins of the world. *J. Hydrol.* 567, 510–532. doi: 10.1016/j.jhydrol.2018.10.038

Lemarquand, D. (1993). The International Joint Commission and changing Canada–United States boundary relations. *Nat. Resour. J.* 33, 59–91.

Lespinas, F., Fortin, V., Roy, G., Rasumussen, P., and Stadnyk, T. (2015). Performance evaluation of the canadian precipitation analysis (CaPA). *J. Hydrometeorol.* 16, 2045–2064. doi: 10.1175/JHM-D-14-0191.1

Levesque, V. A., and Oberg, K. A. (2012). *Computing Discharge Using the Index Velocity Method*. Reston, VA: US Department of the Interior, US Geological Survey. doi: 10.3133/tm3A23

Mai, J., Tolson, B., Shen, H., Craig, J. R., Fortin, V., and Fry, L. M. (2021b). "The runoff model-intercomparison project over lake erie and the great lakes," in *American Geophysical Union Fall Meeting*. New Orleans. doi: 10.5194/egusphere-egu2020-10319

Mai, J., Tolson, B. A., Shen, H., Gaborit, É., Fortin, V., Gasset, N., et al. (2021a). Great lakes runoff intercomparison project phase 3: lake Erie (GRIP-E). *J. Hydrol. Eng.* 26:05021020. doi: 10.1061/(ASCE)HE.1943-5584.0002097

McClerren, M. (2021). *Personal Communications*.

Merchant, C., and MacCallum, S. (2018). *Lake Surface Water Temperature ARC-Lake v3 (1995-2012)*. Reading: University of Reading.

Minallah, S., and Steiner, A. L. (2021a). Role of the atmospheric moisture budget in defining the precipitation seasonality of the Great Lakes region. *J. Climate* 34, 643–657. doi: 10.1175/JCLI-D-19-0952.1

Minallah, S., and Steiner, A. L. (2021b). Analysis of the atmospheric water cycle for the laurentian great lakes region using CMIP6 models. *J. Climate* 34, 4693–4710. doi: 10.1175/JCLI-D-20-0751.1

Minallah, S., and Steiner, A. L. (2021c). The effects of lake representation on the regional hydroclimate in the ECMWF reanalyses. *Monthly Weather Rev.* 149, 1747–1766. doi: 10.1175/MWR-D-20-0421.1

Mironov, D., Heise, E., Kourzeneva, E., Ritter, B., Schneider, N., and Terzhevik, A. (2010). Implementation of the lake parameterisation scheme flake into the numerical weather prediction model COSMO. *Boreal Environ. Res.* 15, 218–230. Available online at: https://helda.helsinki.fi/bitstream/handle/10138/233087/ber15-2-218.pdf?sequence=1

National Aeronautics and Space Administration (1994). *Engineering Drawing Standards Manual X-673-64-1F*. Greenbelt, MD: National Aeronautics and Space Administration.

Neff, B. P., and Nicholas, J. (2005). *Uncertainty in the Great Lakes Water Balance*. Reston, VA: US Geological Survey. doi: 10.3133/sir20045100

Noorbakhsh, N. (2009). *Revising the Historical Monthly Mean Niagara River Flow at Buffalo to Reflect Better Estimates of Maid-of-the-Mist Pool Outflows 1961-2007*. Detroit, MI: United States Army Corps of Engineers.

Salas, F. R., Somos-Valenzuela, M. A., Dugger, A., Maidment, D. R., Gochis, D. J., David, C. H., et al. (2017). Towards real-time continental scale streamflow simulation in continuous and discrete space. *J. Am. Water Resour. Assoc.* 54, 7–27. doi: 10.1111/1752-1688.12586

Schneider, U., Becker, A., Finger, P., Meyer-Christoffer, A., Ziese, M., and Rudolf, B. (2014). GPCC's new land surface precipitation climatology based on quality-controlled in situ data and its role in quantifying the global water cycle. *Theoret. Appl. Climatol.* 115, 15–40. doi: 10.1007/s00704-013-0860-x

Sperna Weiland, F., Van Beek, L., Kwadijk, J., and Bierkens, M. (2010). The ability of a GCM-forced hydrological model to reproduce global discharge variability. *Hydrol. Earth Syst. Sci.* 14, 1595–1621. doi: 10.5194/hess-14-1595-2010

St. Lawrence Seaway Management Corporation (2003). *The Welland Canal Section of the St. Lawrence Seaway*. Available online at: https://greatlakes-seaway.com/wp-content/uploads/2019/10/welland.pdf (accessed October 15, 2021).

Thompson, A. F., Rodrigues, S. N., Fooks, J. C., Oberg, K. A., and Calappi, T. J. (2020). Comparing discharge computation methods in great lakes connecting channels. *J. Hydrol. Eng.* 25:05020007. doi: 10.1061/(ASCE)HE.1943-5584.0001904

United States Army Corps of Engineers (2019). *Water Management and Diversion Accounting Activities 2019 Annual Report (October 2018 – September 2019)*. Chicago, IL: United States Army Corps of Engineers.

Wada, Y., Bierkens, M. F., Roo, A.,d., Dirmeyer, P. A., Famiglietti, J. S., Hanasaki, N., et al. (2017). Human–water interface in hydrological modelling: current status and future directions. *Hydrol. Earth Syst. Sci.* 21, 4169–4193. doi: 10.5194/hess-21-4169-2017

Wang, J., Assel, R. A., Walterscheid, S., Clites, A. H., and Bai, X. (2012). *Great Lakes Ice Climatology Update, Winters 2006–2011, Description of the Digital Ice Cover Dataset*. Ann Arbor, MI: NOAA Technical Memorandum GLERL-155, Great Lakes Environmental Research Laboratory. Available Online at: https://www.glerl.noaa.gov/pubs/tech_reports/glerl-155/tm-155.pdf

Wang, J., Kessler, J., Hang, F., Hu, H., Clites, A., and Chu, P. (2017). *Great Lakes Ice Climatology Update of Winters 2012-2017: Seasonal Cycle, Interannual Variability, Decadal Variability, and Trend for the Period 1973–2017*. Ann Arbor, MI: NOAA Technical Memorandum GLERL-170, Great Lakes Environmental Research Laboratory. Available online at: https://www.glerl.noaa.gov/pubs/tech_reports/glerl-170/tm-170.pdf

Willmott, C. J. (2000). *Terrestrial Air Temperature and Precipitation: Monthly and Annual Time Series (1950–1996)*. Available online at: http://climate.geog.udel.edu/\simclimate/html_pages/README.ghcn_ts.html (accessed January 20, 2022).

Woolway, R. I., Kraemer, B. M., Lenters, J. D., Merchant, C. J., O'Reilly, C. M., and Sharma, S. (2020). Global lake responses to climate change. *Nat. Rev. Earth Environ.* 1, 388–403. doi: 10.1038/s43017-020-0067-5

Wright, D. M., Posselt, D. J., and Steiner, A. L. (2013). Sensitivity of lake-effect snowfall to lake ice cover and temperature in the Great Lakes region. *Monthly Weather Rev.* 141, 670–689. doi: 10.1175/MWR-D-12-00038.1

Xue, P., Pal, J. S., Ye, X., Lenters, J. D., Huang, C., and Chu, P. Y. (2017). Improving the simulation of large lakes in regional climate modeling: two-way lake-atmosphere coupling with a 3D hydrodynamic model of the Great Lakes. *J. Climate* 30, 1605–1627. doi: 10.1175/JCLI-D-16-0225.1

Zhong, Y., Notaro, M., Vavrus, S. J., and Foster, M. J. (2016). Recent accelerated warming of the Laurentian Great Lakes: physical drivers. *Limnol. Oceanogr.* 61, 1762–1786. doi: 10.1002/lno.10331

Conflict of Interest: The authors declare that the research was conducted in the absence of any commercial or financial relationships that could be construed as a potential conflict of interest.

Publisher's Note: All claims expressed in this article are solely those of the authors and do not necessarily represent those of their affiliated organizations, or those of the publisher, the editors and the reviewers. Any product that may be evaluated in this article, or claim that may be made by its manufacturer, is not guaranteed or endorsed by the publisher.

frontiers in Water

ORIGINAL RESEARCH
published: 11 February 2022
doi: 10.3389/frwa.2022.817342

Trends in Quality Controlled Precipitation Indicators in the United States Midwest and Great Lakes Region

William J. Baule[1,2]*, *Jeffrey A. Andresen*[1,2] *and Julie A. Winkler*[1]

[1] *Department of Geography, Environment, and Spatial Sciences, Michigan State University, East Lansing, MI, United States,* [2] *Great Lakes Integrated Sciences + Assessments, School for Environment and Sustainability, University of Michigan, Ann Arbor, MI, United States*

Changes in precipitation can have broad and significant societal impacts. A number of previous studies that analyzed changes in precipitation across the Great Lakes and Midwest for a variety of time periods and using a range of quality-control standards and methods observed increased precipitation rates and totals, although there was considerable site-to-site variability, even for sites in close physical proximity. Biases and discontinuities in precipitation observations may contribute to this variability. This study identifies and examines changes in precipitation utilizing a unique approach to observation series screening over a region encompassing the Great Lakes and broader Midwestern region of the United States for the period 1951–2019. A multiple tier procedure was utilized to identify high quality input data series from the Global Historical Climatology Network-Daily dataset. Annual and seasonal time series of precipitation indicators were calculated and subjected to breakpoint analysis as further quality control. Trends were analyzed across a broad range of related indicators, from totals and frequencies of threshold events to event duration and potential linkages with total precipitable water. Results indicate that annual precipitation has generally increased across the region in terms of totals, although there is substantial variation across the study domain in the significance and magnitude of annual trends by indicator. Annual trends were spatially most consistent across eastern areas of the study domain while relatively greater station-to-station variability in trend significance and magnitude was observed across northern and western portions. Significant trends were generally fewer in number for seasonal precipitation indicators and less spatially coherent. The greatest number of significant trends occurred in fall with the fewest in spring. Correlation of indicator trends with trends of mean total precipitable water suggests weak correlations annually and moderate correlations at the seasonal scale. The trends of the precipitation indicators in our study exhibited more coherent spatial patterns when compared with studies with different quality control criteria, illustrating the importance of quality control of observations in climatic studies and highlighting the complexity of the changing character of precipitation.

Keywords: hyrdoclimatology, precipitation, climate change, temporal trend, quality control procedures, regional climatology

OPEN ACCESS

Edited by:
Congsheng Fu, Nanjing Institute of Geography and Limnology, Chinese Academy of Sciences (CAS), China

Reviewed by:
Semih Kale, Çanakkale Onsekiz Mart University, Turkey
Charles Onyutha, Kyambogo University, Uganda

***Correspondence:**
William J. Baule
baulewil@msu.edu

Specialty section:
This article was submitted to Water and Climate, a section of the journal Frontiers in Water

Received: *18 November 2021*
Accepted: *17 January 2022*
Published: *11 February 2022*

Citation:
Baule WJ, Andresen JA and Winkler JA (2022) Trends in Quality Controlled Precipitation Indicators in the United States Midwest and Great Lakes Region. Front. Water 4:817342. doi: 10.3389/frwa.2022.817342

INTRODUCTION

Precipitation is the longest observed and most widely reported meteorological variable and is an essential component of the Earth's hydrologic cycle (Legates and Willmott, 1990). Precipitation is commonly defined as "the amount, usually expressed in millimeters or inches of liquid water depth, of the water substance that has fallen at a given point over a specified period of time" (Huschke, 1959, p. 438). Although precipitation accumulation at daily, monthly, seasonal and annual scales has received the most attention in the climatological literature (e.g., Contractor et al., 2021), other precipitation characteristics such as frequency, intensity, and duration are as much, if not more, of a concern for many natural and human systems (Trenberth et al., 2003; Bartels et al., 2020). Moreover, changes in one or more precipitation characteristics can have substantial societal implications impacting many sectors, including, among others, agriculture (e.g., Pielke and Downton, 2000; Rosenzweig et al., 2002; Hunt et al., 2020; Kiefer et al., 2021), transportation (e.g., Attavanich et al., 2013; Talukder and Hipel, 2020), and tourism (e.g., Chin et al., 2018).

Changes in precipitation characteristics are a particular concern for the Midwest and Great Lakes region of the United States given the region's unique hydrology (Gronewold et al., 2021) and its agricultural importance and contribution to regional, national and global food security (Angel et al., 2018; Takle and Gutowski, 2020). Not surprisingly, a number of studies have investigated temporal trends in precipitation characteristics either specifically for the region (e.g., Zhang and Villarini, 2019) or as part of larger analyses of precipitation trends in the United States (e.g., Kunkel et al., 2020a). For the most part, these analyses have focused on trends in annual and seasonal precipitation totals (e.g., Schoof et al., 2010), extreme precipitation (e.g., Pryor et al., 2009; Walsh et al., 2014), and/or the frequency of wet days (e.g., Roque-Malo and Kumar, 2017; Bartels et al., 2020). In general, precipitation frequency and total accumulation appear to have increased across the region over the last several decades (Higgins et al., 2007; Dai et al., 2016; Contractor et al., 2021). In addition, the amount of precipitation falling during the heaviest events has increased at a greater rate in the Midwest and Great Lakes region compared to the national average (Angel et al., 2018). Extended dry periods have become less frequent, but their intensity (i.e., length) has increased slightly in recent decades (Groisman and Knight, 2008).

One constraint to comprehensive and accurate analysis of temporal trends in precipitation characteristics at the regional scale is the availability and quality of precipitation observations (Costa and Soares, 2009). Although numerous authors have examined the homogeneity of time series for various climatic variables including daily precipitation (Winkler, 2004; Daly et al., 2007; Wang et al., 2010), many studies employing *in-situ* climate observations fail to take data quality, other than data completeness, into account, even though the magnitude and sign of temporal trends can be biased by changes in technology, station siting, observing practices and other inhomogeneities that are not necessarily captured by station record completeness or recorded in standard metadata archives (Wang et al., 2010; Williams et al., 2012; Baule and Shulski, 2014). Recent progress in the development of spatial and temporal interpolation schemes and gridded datasets, the integration of radar and satellite derived precipitation estimates with *in-situ* observations, the development of atmospheric reanalysis products, and the availability of simulations from regional and global climate models have only partially alleviated concerns about data quality (Zhang et al., 2011). The limited periods of record for radar and satellite precipitation estimates constrain their use for estimating temporal trends, and gridded datasets can inherit the inhomogeneities of the underlying station observations, with developers of these datasets often advising against their use for time series analysis (e.g., Daly et al., 2010). Consequently, station-based climatologies, in spite of their limitations, remain the benchmark for the assessment of long-term trends (Kiefer et al., 2021), although caution in their application is critical to guard against misinterpreting temporal trends. Earlier studies of precipitation trends for the Midwest and Great Lakes region frequently used station-level daily precipitation observations from the Global Historical Climatology Network-Daily (GHCN-D) database (Menne et al., 2012) for trend estimation (e.g., Villarini et al., 2011; Janssen et al., 2014; Guilbert et al., 2015; Wu, 2015; Hoerling et al., 2016; Huang et al., 2017, 2018; Roque-Malo and Kumar, 2017; Kunkel et al., 2020a,b). For the most part, quality-control procedures have been limited to those applied by the GHCN-D dataset developers to identify and/or correct for errors and inhomogeneities in the precipitation data (Durre et al., 2008, 2010), supplemented by an evaluation of data completeness (e.g., Kunkel et al., 2020b).

Other studies have investigated the synoptic-scale drivers of precipitation, particularly those associated with extreme precipitation, finding that extreme precipitation events across the Midwest and Great Lakes region are often associated with a westward expansion and strengthening of subtropical high pressure across the western Atlantic Basin (Gutowski et al., 2008) as well as the advection of low-level moisture from the Gulf of Mexico ahead of slow moving tropospheric waves (Winkler, 1988; Zhang and Villarini, 2019), with the latter being more prevalent in the western portions of the region and the former in the eastern areas (Bell and Janowiak, 1995; Konrad, 2001; Weaver and Nigam, 2008). Consistent with these findings, Kunkel et al. (2020a) showed that extreme daily precipitation events across the contiguous United States, including the Midwest and Great Lakes region, are directly related to total precipitable water. Specifically, Kunkel et al. (2020b) examined the relationship between regional trends in total precipitable water and regional trends in extreme precipitation as calculated from GHCN-D station-level time series. These large-scale drivers of precipitation are often amplified or suppressed by regional and local climate drivers such as topography, water bodies, and land use/land cover (Myhre et al., 2016; Kunkel et al., 2020a), which can introduce considerable spatial variability in the temporal trends of precipitation characteristics, especially in the Midwest and Great Lakes region with its large water bodies and varied land use/land cover. For the most part, quality control of the precipitation observations employed in these studies of the synoptic, regional and local drivers of precipitation and their

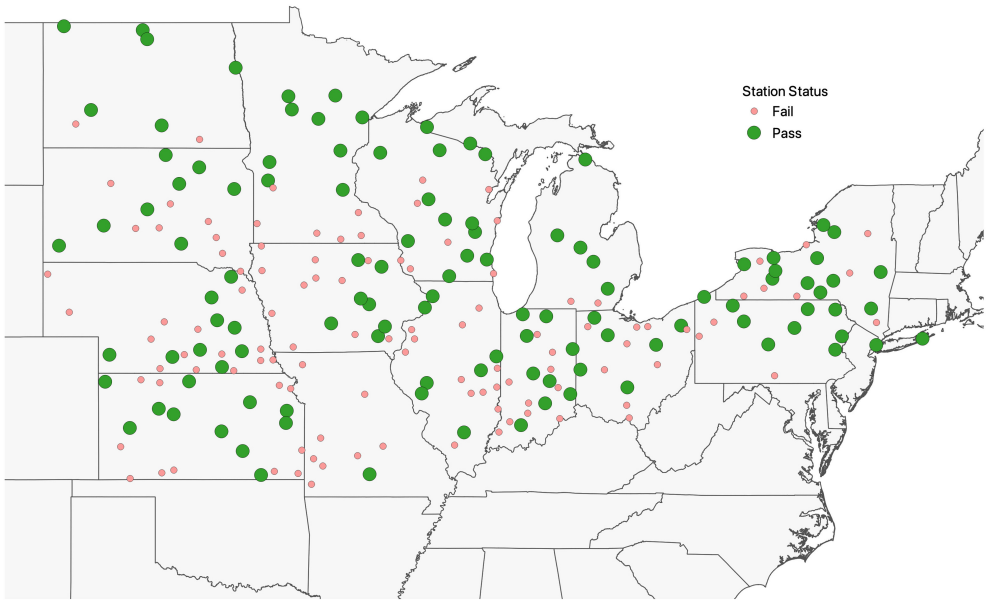

FIGURE 1 | Study region and the United States Historical Climate Network (USHCN) stations (green circles) within the study region that passed the quality control checks for data completeness and lack of observer bias as outlined in the methods. Stations that passed the data completeness check but failed at least one of the tests for lack of observer bias are shown as pink circles. The number of stations that passed the third quality control test (no breakpoints) is given in **Table 2**.

contribution to temporal trends in precipitation was confined to an assessment of data completeness of the precipitation time series.

This study provides a comprehensive assessment of the temporal trends in precipitation characteristics for the Midwest and Great Lakes region that focuses on the quality of available precipitation time series. We employ a three-step quality-control procedure that evaluates the GHCN-D precipitation time series for data completeness, possible observer bias, and potential breakpoints (i.e., discontinuities) with the goal of identifying those GHCN-D stations in which we have the greatest confidence for precipitation trend analysis, thereby increasing confidence in the sign, magnitude, significance, and spatial coherence of precipitation trends. We include a range of precipitation indicators that capture the frequency and persistence of high frequency, low magnitude and low frequency, high magnitude events. Furthermore, we examine the associations between temporal trends in the quality-controlled suite of precipitation indicators and trends in atmospheric moisture. The study findings provide the region's many stakeholders with needed information on long-term trends in precipitation characteristics of concern to them, greater certainty in incorporating these data in planning processes and a high-quality baseline for assessing future trends.

METHODS

Study Region and Precipitation Data

For this study, the Midwest and Great Lakes region was defined as the states of Pennsylvania, Ohio, Indiana, Michigan, Illinois, Wisconsin, Minnesota, Iowa, Missouri, Kansas, Nebraska, South Dakota, New York, and North Dakota (**Figure 1**).

We analyzed a subset of individual site climate series from the National Centers for Environmental Information's (NCEI) GHCN-D collection (Menne et al., 2012). As a first step in selecting stations for the analysis, we examined the GHCN-D database for station series included in the United State Historical Climatology Network (USHCN; Easterling, 2002) which had at least 90% data completeness for daily precipitation during 1951-2019. Only USHCN sites were considered, as these stations were preselected by NCEI based on record length, data completeness, and historical stability (Menne et al., 2012). Data flagged by the GHCN-D quality control procedures as suspicious were marked as missing (Menne et al., 2012). The length of the study period allowed for trends in the second half of the 20th century and the early 21st century to be assessed while maintaining a relatively large pool of potential stations and reasonable spatial coverage. This first data quality control step led to an initial subset of 317 stations over the study region.

The next quality control step involved using tests proposed by Daly et al. (2007) to check for observer bias in precipitation time series, specifically the underreporting of light (1.26 mm) precipitation amounts and the over-reporting of precipitation amounts evenly divisible by 5 and/or 10 when expressed as inches. As these tests were designed for data originally measured in inches, they are described here using inches (in.) in place of millimeters. The under-reporting check consisted of calculating the ratio of counts between 0.06–0.10 in. (C_{6-10}) and 0.01–0.05 in. (C_{1-5}) as follows:

$$R_L = \frac{C_{6-10}}{C_{1-5}},$$

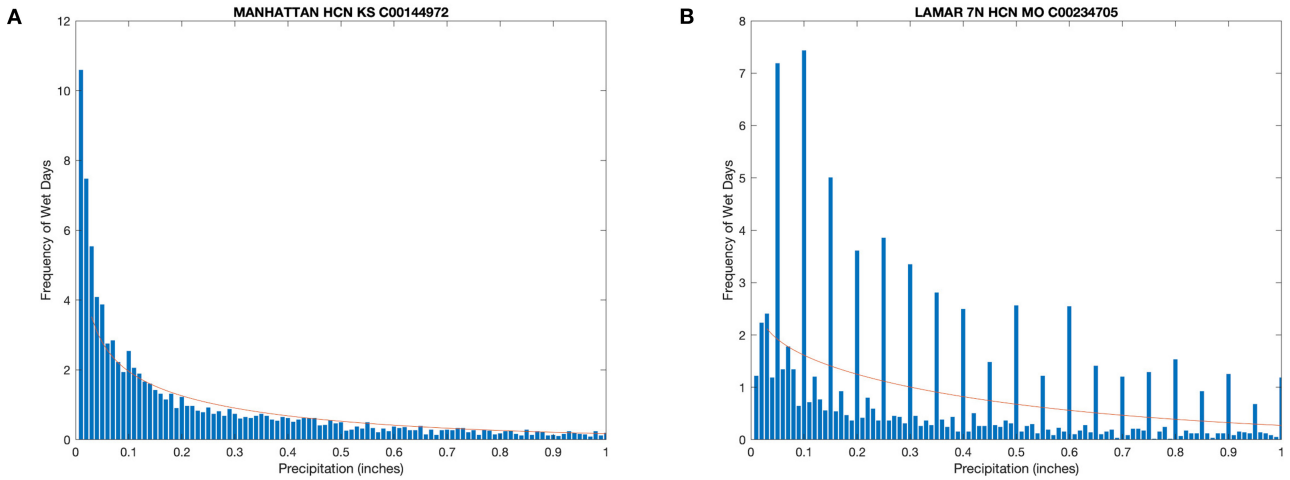

FIGURE 2 | Histograms from two example stations in the study region showing precipitation frequency (blue bars) over the period from 1951 to 2019 binned in 0.01 increments and a gamma distribution (red line) fit to the data following Daly et al. (2007). **(A)** Manhattan, KS HCN passes ($p \leq 0.01$) the tests for underreporting of daily precipitation amounts <0.05 in. (1.26 mm) and for over-reporting of daily precipitation amounts (in inches) evenly divisible by 5 or 10 despite showing a small divisible by 10 bias. (B) Lamar 7N, MO HCN fails all three tests ($p \leq 0.01$), showing a strong under reporting bias, a strong divisible by 5 bias, and a strong divisible by 10 bias.

where C_{6-10} is the total observation count in the 0.06–0.10-in. range, and C_{1-5} is the total observation count in the 0.01–0.05-in. range. If the ratio, $R_{L,}$ between C_{6-10} and C_{1-5} exceeded 0.60, the station failed the check (Daly et al., 2007).

The tests for errant reporting of values divisible by 5 or 10 were conducted by binning precipitation into 0.01 in. bins, fitting a gamma distribution to the data between 0.03 and 1.00 in., and comparing the predicted (P) and observed (O) frequency of the binned observations with the residual (R) calculated as:

$$R = 100*(P - O)$$

The test for biases in amounts divisible by 5 and amounts only divisible by 10 were carried out separately. For the divisible by 5 test, the first residual mean was calculated by averaging the residuals over all amounts except those divisible by 5 (R_1) and the second residual (R_5) consisted of the mean of residuals for only amounts divisible by 5 as follows:

$$\overline{R}_1 = \frac{\sum_{i=1}^{n_1} R_{1_i}}{n_1};\ \overline{R}_5 = \frac{\sum_{i=1}^{n_5} R_5}{n_5}$$

where n_1 and n_5 are the number of ones and fives bins and R_1 and R_5 are residuals calculated from equation 2. The means for the divisible by 10 bias were calculated similarly, instead using values only divisible by 10. The means were compared using a two-tailed *t*-test with an alpha level of 0.01.

Examples of output from the second quality control procedures are shown in **Figure 2** for two locations, Manhattan, KS HCN which passed all the bias tests at $p \leq 0.01$ or $R_L \leq 0.6$ despite showing a small divisible by 10 bias, and Lamar 7N, MO HCN which failed the bias tests showing a strong under reporting bias, a strong divisible by 5 bias, and a strong divisible by 10 bias. Stations that failed any of the tests were removed from the analysis, leaving a subset of 114 long-term climate series across the Midwest and Great Lakes region for the period from 1951 to 2019 for precipitation indicators.

The third quality control step involved checking the time series of the precipitation indicators for breakpoints. Possible sources of discontinuities in the time series include, among others, instrument changes, station moves, and changes in observation protocols including time of observation (Winkler, 2004). Following Mallakpour and Villarini (2016), the Pettitt test (Pettitt, 1979) was applied to identify years when a breakpoint is likely, indicating a non-homogenous time series. A breakpoint was considered significant at $p \leq 0.01$, and the time series for that station was excluded from further analysis. This resulted in a variable number of stations per indicator, with the number of excluded stations ranging from none to a maximum of 17. The description of the Pettitt test, following Jaiswal et al. (2015) is: a method that detects a significant change in the mean of a time series, where the exact time of the change (i.e., breakpoint) is unknown, According to the Pettit test, if $x_1,x_2,x_3,\ldots x_n$ is a series of observed data which has a break point at t so that $x_1,x_2,x_3,\ldots x_t$ has a distribution $[F_1(x)]$ which is different from the distribution $[F_2(x)]$ of the second part of the series $x_{t+1},x_{t+2},x_{t+3},\ldots x_n$. The non-parametric test statistic is described as follows:

$$U_t = \sum_{i=1}^{t} \sum_{j=t+1}^{n} sgn(x_i - x_j)$$

$$sgn\left(x_i - x_j\right) = \begin{cases} 1, \ if\ \left(x_i - x_j\right) > 0 \\ 0, \ if\ \left(x_i - x_j\right) = 0 \\ -1, \ if\ \left(x_i - x_j\right) < 0 \end{cases}$$

TABLE 1 | Precipitation indicators included in the analysis.

Index name	ID	Definition	Units
Accumulation/simple intensity			
Annual total wet day precipitation	PRCPTOT	Total precipitation on wet days (PRCP ≥ 1.26 mm)	mm
Simple daily intensity index	SDII	Total precipitation divided by the number of wet days	mm day^{-1}
Duration			
Consecutive wet days	CWD	Maximum number of consecutive days with PRCP ≥1.26 mm	days
Consecutive dry days	CDD	Maximum number of consecutive days with PRCP < 1.26 mm	days
Percentile (Percentile values were calculated for the period 1951–1980)			
Precipitation on very wet days	R95pTOT	Total precipitation on days when PRCP ≥ 95th percentile	mm
Precipitation on extremely wet days	R99pTOT	Total precipitation on days when PRCP ≥ 99th percentile	mm
Threshold			
Number of days with measurable precipitation	R1.26mm	Number of days with PRCP ≥ 1.26 mm	days
Number of heavy precipitation days	R10mm	Number of days with precipitation ≥ 10 mm	days
Number of very heavy precipitation days	R20mm	Number of days with precipitation ≥ 20 mm	days
Number of days with consecutive days with measurable precipitation	WW	Annual count of days when PRCP ≥ 1.26 mm on consecutive days	days
Number of days with consecutive days without measurable precipitation	DD	Annual count of days when PRCP < 1.26 mm on consecutive days	days
Absolute			
Maximum 1-day precipitation*	Rx1day	Maximum 1-day precipitation	mm
Maximum 5-day precipitation*	Rx5day	Maximum consecutive 5-day precipitation	mm

All indicators were calculated annually and seasonally except those marked with an asterisk(*). These were only calculated annually.

The test statistic K and the associated confidence level (ρ) for the sample length (n) is described as:

$$K = Max\,|U_t|$$
$$\rho = e^{\left(\frac{-K}{n^2+n^3}\right)}$$

When ρ is smaller than the specified confidence level (p), a breakpoint is considered significant.

Precipitation Indicators

This study included a range of precipitation indicators. Several indicators were used to characterize the frequency of non-extreme precipitation, including the number of days with measurable precipitation (e.g., Pryor et al., 2009) and the probabilities of wet-wet day and dry-dry day sequences (e.g., Ines et al., 2011). A wet day was defined as a precipitation total ≥ 1.26 mm (0.05 in) (Groisman et al., 1999). Extreme precipitation was represented in the analysis by indices developed by the Expert Team on Climate Change Detection and Indices (ETCCDI) (Donat et al., 2013) and annual values were calculated using the software packages provided by the ETCCDI Working Group (available at http://www.climdex.org). The extreme precipitation indicators include 10 wet indices and 1 dry index that can be further grouped into percentile-based indices (2), threshold indices (3), absolute value indices (2), duration indices (2), annual accumulation, and "simple" intensity (annual total precipitation divided by the number of wet days). For the percentile-based indices, the base period for defining the percentile value was the 30-year climate normal period of 1981–2010. Descriptions of each of the non-extreme and extreme precipitation indicators are provided in **Table 1**.

All precipitation indicators were also defined for the climatological seasons of spring (MAM), summer (JJA), fall (SON), and winter (DJF). This is in contrast to most previous studies where precipitation indicators were calculated for annual time steps, with less attention paid to the seasonal variations in the precipitation indicators beyond the frequency of high intensity daily precipitation events (e.g., Mallakpour and Villarini, 2017). Given the importance of precipitation timing and sequencing for numerous regional applications, such as soil moisture and nitrogen movement in agricultural systems (Riha et al., 1996; Bowles et al., 2018) and plant disease risk (Komoto et al., 2021), this study extended the precipitation indicators to the seasonal time step. Additionally, the seasonal analyses provides greater context to more clearly interpret annual trends.

Following the lead of numerous recent studies (e.g., Alexander et al., 2006; Pryor et al., 2009; Shulski et al., 2015; Dai et al., 2016; Roque-Malo and Kumar, 2017), non-parametric statistical methods were employed to estimate the significance and magnitude of temporal trends in the precipitation indicators at the study locations. While a number of potential non-parametric methods were available (e.g., Sneyers, 1990; Sen, 2015; Onyutha, 2021), we chose the two-tailed Mann-Kendall trend test (Mann, 1945; Kendall, 1955, 1975) to test for the significance of potential temporal trends due to its prevalence in previously mentioned studies across the region to allow for intercomparison of results. A strength of the Mann-Kendall method is its ability to assess the significance of trends that are monotonic but not necessarily linear in character. For those locations with

significant trends as identified by the Mann-Kendall test, the non-parametric Kendall's tau-based slope estimator (Sen, 1968) was used to obtain a numerical estimate of the temporal trend. All analyses were conducted using three significance levels ($p \leq 0.05$, $p \leq 0.10$, and $p \leq 0.20$) to examine how significance level affects the number of significant trends and their spatial representation. The equations describing the Mann-Kendall test are as follows:

$$S = \sum_{i=1}^{n} \sum_{j=1}^{i-1} sgn(x_i - x_j)$$

where n is the total length of data, x_i and $x_j$are two generic sequential data values, and the following function assumes the values:

$$sgn\left(x_i - x_j\right) = \begin{cases} 1, \ if \ \left(x_i - x_j\right) > 0 \\ 0, \ if \ \left(x_i - x_j\right) = 0 \\ -1, \ if \ \left(x_i - x_j\right) < 0 \end{cases}$$

The mean of S is E[S] = 0 and the variance σ^2 is

$$\sigma^2 = \frac{1}{n}\left[n\left(n-1\right)\left(2n+5\right) - \sum_t t(t-1)(2t+5)\right)\right]$$

where n is the length of the time series and t is the extent of any given ties and Σt denotes the summation over all tied values. The statistic S is approximately normally distributed provided that the following Z-transformation is employed:

$$Z = \begin{cases} \frac{S-1}{\sigma} & if \ S < 0 \\ 0 & if \ S = 0 \\ \frac{S+1}{\sigma} & of \ S > 0 \end{cases}$$

The Sen's (1968) slope was calculated as follows: first, a set of linear slopes is calculated

$$d_k = \frac{X_j - X_i}{j - i}$$

for ($1 \leq i < j \leq n$), where d is the slope, X denotes the variable, n is the sample length, and i, j, and k are indices. Sen's slope is then calculated as the median from all slopes (d_k).

Total Precipitable Water

Daily values of total precipitable water (TOTPRCPWAT) were obtained from the NCEP/NCAR I Reanalysis (Kalnay et al., 1996) at a 2.5 x 2.5° spatial resolution. The daily values were used to calculate mean daily annual and seasonal total precipitable water for each year during the 1951–2019 study period for a bounding box ranging from 106 to 69°W longitude and 34–54°N latitude. Only grid cells that contained observing sites used in our analyses were subjected to analysis. Pearson correlation coefficients (r) and non-parametric Kendall rank correlation coefficients (τ) were calculated between the trend value of four representative precipitation indicators (WW, PRCPTOT, R1.26 mm, R95pTOT) at each station considered previously and the trend of total precipitable water of the nearest reanalysis grid cell. Pettitt tests were conducted on the NCEP NCAR time series of precipitable water for each grid cell to examine for potential heterogeneities prior to the satellite era (e.g., Kunkel et al., 2020b). Significant breakpoints ($p < 0.01$) were evident at some grid cells, however they were not clustered in time. Given the noted strength of the NCEP-NCAR reanalysis in areas where radiosonde observations are available (Trenberth et al., 2005), as in our study region, we deemed the data appropriate for our analyses.

RESULTS

Trends in Precipitation Indicators

Annual Indicators

For the annually-derived precipitation indictors, the number of stations with statistically-significant ($p \leq 0.10$) trends varied substantially among the different indicators, ranging from 67% of the station sites for annual total precipitation (PRCPTOT) to only 20% of the stations for the maximum number of consecutive wet days per year (CWD) (**Table 2**). With the exception of the maximum number of consecutive dry days (CDD) and the number of dry-dry day sequences (DD), more than 90% of the statistically significant trends over time when summed across the indicator variables are positive, indicating a generally wetter climate. The negative trends observed for CDD and DD are also indicative of a wetter climate. In addition to PRCPTOT, the majority of the locations display significant upward trends for the simple intensity index (PRCPTOT divided by the number of days with precipitation $\geq$ 1 mm; SDII), the number of days per year with precipitation $\geq$ 10 mm (R10 mm), the number of days per year with precipitation $\geq$ 20 mm (R20 mm), and the total precipitation on days with daily precipitation $\geq$ 95th percentile (R95pTOT). A majority (54%) of stations also have statistically significant negative trends for DD, whereas only 39% of the locations have statistically significant positive trends in the annual number of wet-wet day sequences (WW). A considerably smaller number of stations displayed significant trends for several of the other indicators, with the fraction of stations with significant trends falling below 30% for CDD, CWD, total precipitation on days with daily precipitation $\geq$ 99th percentile (R99pTOT), maximum one-day precipitation amount (Rx1day) and maximum consecutive 5-day precipitation (Rx5day). With the exception of CDD and DD, statistically significant negative trends were infrequent for the various indicators, ranging from no significant negative trends for CWD, SDII, R95pTOT, R99pTOT, SDII, Rx1day, and Rx5day to 6% of the locations for WW. The number of stations exhibiting significant breakpoints was greatest for PRCPTOT (14) and R.126MM (17). Rx1day, Rx5day, CDD, and CWD showed no significant breakpoints.

A subset of indicators that encompass the range of precipitation characteristics included in the analysis, namely PRCPTOT, WW, the number of wet days with precipitation $\geq$ 1.26 mm (R1.26 mm), and R95pTOT, is used to illustrate the spatial variability across the study region in the temporal trends for the annual indicators (**Figure 3**). For all four indicators, statistically significant positive trends are distributed across the study region, although the magnitude of these trends is generally

TABLE 2 | Number of stations exhibiting statistically significant trends (Mann Kendall, $p \leq 0.05$ two-tailed, $p \leq 0.10$ two-tailed, $p \leq 0.20$, two-tailed) from 1951 to 2019 in the annual precipitation indicators.

Precipitation indicator	Total number of stations after breakpoint analysis	Number of stations with significant positive trends ($p \leq 0.05$)	Number of stations with significant positive trends ($p \leq 0.10$)	Number of stations with significant positive trends ($p \leq 0.20$)	Number of stations with significant negative trends ($p \leq 0.05$)	Number of stations with significant negative trends ($p \leq 0.10$)	Number of stations with significant negative trends ($p \leq 0.20$)
PRCPTOT	100	47	**75**	**79**	1	1	1
R1.26mm	97	42	**53**	**61**	1	3	5
SDII	112	42	52	**62**	0	0	3
CWD	114	17	23	36	0	0	0
CDD	113	0	2	2	16	28	44
WW	105	27	44	51	5	7	9
DD	107	2	3	3	41	**61**	**65**
R10mm	104	42	**60**	**72**	0	1	1
R20mm	101	35	**58**	**59**	1	1	1
R95pTOT	104	38	**62**	**63**	0	0	0
R99pTOT	108	11	33	39	0	0	0
Rx1day	114	13	29	43	0	0	0
Rx5day	114	23	33	47	0	0	2

*Indicators where more than 50% of stations analyzed showed a significant trend are shown in bold. See **Table 1** for definition of the abbreviations for the precipitation indicators.*

larger in the eastern two-thirds of the study area, including in the vicinity of the Great Lakes. In the western third of the study region, although the trends in the selected indicators are generally positive, the magnitude of the trends is smaller with relatively fewer stations meeting the threshold for statistical significance. Regardless of precipitation indicator, negative trends are evident for only a few stations and are insignificant. Significance of the same indicators but with a weaker significance threshold ($p \leq 0.20$) is shown in **Supplementary Figure 1**. When the significance level is lowered, the number of significant positive trends increases substantially with no or very little increase in the number of significant negative trends and the stations with significant positive trends are more spatially coherent. When a stricter ($p \leq 0.05$) threshold is used, the number of stations exhibiting significant trends decreases when compared to the moderate ($p \leq 0.10$) and weak ($p \leq 0.20$) thresholds. Spatially, when the strict threshold is used, the largest groupings of sites with significant trends are in the central and eastern portions of the study region (**Supplementary Figure 2**). The number and spatial coherence of significant positive trends in the western areas of the study region are reduced under the strict criterion.

We also evaluated the ratio of the trend estimates for the annual indicators of R95pTOT and PRCPTOT for stations with a significant positive trend in PRCPTOT, as an indicator of the relative contribution of precipitation on very wet days to trends in total precipitation (**Supplementary Figure 3**). In general, precipitation on very wet days has contributed the most (ratios >0.60 and at some locations >1.0) to annual total precipitation in eastern New York/Pennsylvania, Indiana, southern Wisconsin/eastern Iowa, and eastern Nebraska/Kansas, compared to elsewhere in the study region. The modest (<0.60) ratios at many locations elsewhere suggest that the overall increase in total precipitation is not exclusively, or even primarily, tied to increases in the frequency of higher intensity events. Rather, changes in the frequency of lighter accumulations are also contributing to the trends in total precipitation.

To better understand the consistency at individual locations of the trends across precipitation indicators, a four-sided Venn diagram was used to plot the number of significant positive trends and the percentage of significant positive trends for all possible combinations of the four representative precipitation indicators, PRCPTOT, WW, R1.26 mm, and R95pTOT, recognizing that the number of available stations varies among indicators due to differing frequency of breakpoints identified in the time series (**Figure 4**). The number of locations with significant positive trends for multiple indicators is substantial, with 16.3% of the stations with positive trends for all the indicators considered and 19.8% stations with positive trends for the two accumulation indicators PRCPTOT and R95pTOT. The number of stations with significant trends for the three variable combinations and the other two variable combinations is relatively small.

Seasonal Indicators

For brevity, seasonal results are shown only for PRCPTOT, R95pTOT, WW, and R1.26 mm, which capture the breadth of the different precipitation indicators. As for the annual precipitation characteristics, we observe that in all seasons the number of significant positive trends at all significance thresholds considered substantially exceeds the number of significant negative trends for the selected indicators (**Table 3**). However, the proportion of stations with significant trends varies by season. The seasonal trends for PRCPTOT indicate that no single season is solely responsible for the annual increase in precipitation observed at the majority of the stations. Significant ($p \leq 0.10$) positive trends are observed at over 35% of the stations in fall and winter, 30% of the stations in summer, and 20% of stations

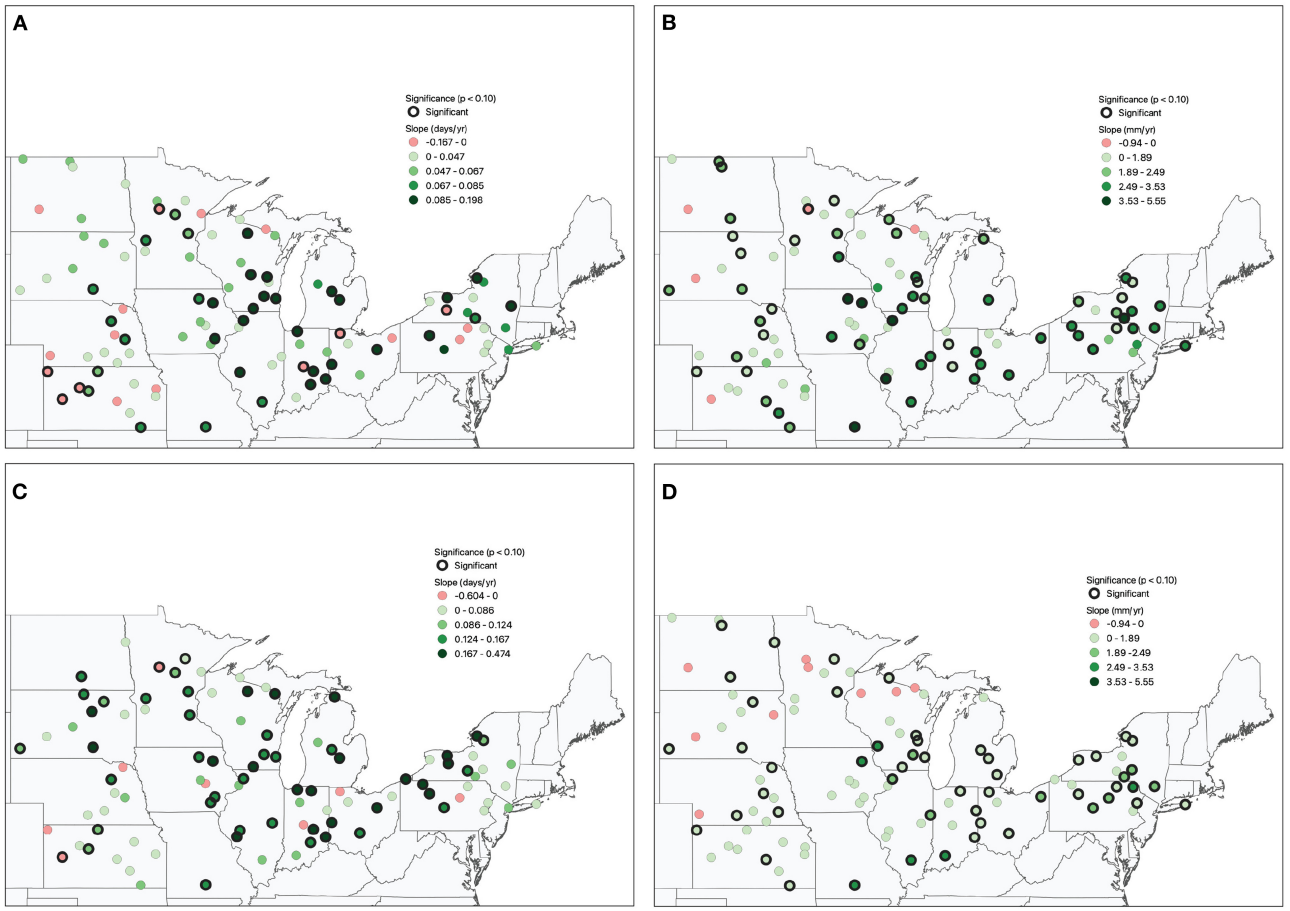

FIGURE 3 | Trends for 1951–2019 in representative annual indicators of precipitation characteristics at locations in the Midwest and Great Lakes region that passed the quality control checks described in the methods section: **(A)** annual counts of wet-wet day sequences (ANN WW; days; count year^{-1}; upper left), **(B)** annual total precipitation on wet days (PRCPTOT; mm year^{-1}; upper right), **(C)** number of days with precipitation $\geq$ 1.26 mm (R1.26mm; days year^{-1}; lower left), and **(D)** total precipitation on days when precipitation is $\geq$ 95th percentile (R95pTOT; mm year^{-1}; lower right).

in spring. With the exception of one location in winter, no significant negative trends in seasonal PRCPTOT are evident. For R95pTOT, significant positive trends are evident at 33% of the stations in fall but at only approximately 20% of stations in the other seasons. For WW, over 24% percent of the station locations have significant positive trends in summer, fall, and winter, whereas only 15% of all stations observed in spring have positive trends. When the threshold for significance is weaker ($p < 0.20$), the number of significant trends increases substantially for most indicators in most seasons. Almost all of the additional significant trends that emerge by lowering the threshold are positive in sign. The number of significant trends in any one season is typically less than the number of significant trends for the corresponding annual indicator. Under the weak ($p \leq 0.20$) threshold, no individual seasonal indicator presents significantly positive trends at more than 50% of stations, with the exception of R1.26 mm in fall Similar to the annual indicators, when the threshold for significance is stricter ($p \leq 0.05$), fewer stations exhibit statistically positive trends, while the number of statistically significant negative trends remains largely unchanged.

Seasonal variations in the spatial patterns in trends over time are shown for PRCPTOT, R95pTOT, and WW. The spatial distributions for R1.26 mm are not shown as they are similar to those for WW. Large between season differences in the spatial variability of the temporal trends are evident. For instance, locations with significant ($p \leq 0.10$) positive trends in seasonal PRCPTOT are distributed across the study area in fall but are largely confined to the vicinity of the Great Lakes (Wisconsin, the Lower Peninsula of Michigan, northeastern Ohio, western Pennsylvania, western New York) in winter (**Figure 5**). In spring, most of the significant positive trends are found in the western two thirds of the study region with few significant trends in New York, Pennsylvania, and Ohio, whereas in summer the greatest density of significant trends along with the largest trend magnitudes are found in the eastern and central portions of the study region. For most stations, significant positive trends are observed in only one or two seasons. A

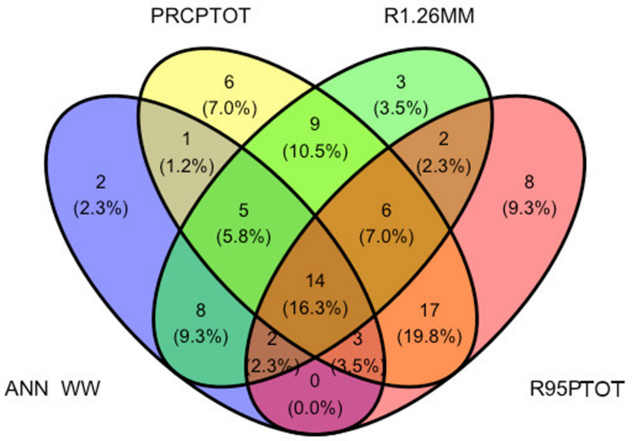

FIGURE 4 | Venn Diagram of the number of stations with significant positive trends for all possible combinations of four representative annual precipitation indicators: the probability of wet-wet days (WW), total annual precipitation (PRCPTOT), the number of wet days (R1.26mm), total precipitation on days with precipitation $\geq$ 95th percentile (R95pTOT). Percentages are relative to largest number of significant positive trends which was 86. Percentage of significant ($p \leq 0.10$) positive trends falling in each category is shown in parentheses.

significant negative trend across all seasons is observed at only one location.

The seasonal trends of R95pTOT display less spatial coherence when compared to seasonal PRCPTOT and to annual R95pTOT, with locations with significant positive trends often surrounded by locations with insignificant positive, and sometimes insignificant negative, trends (**Figure 6**). The number of locations in winter with significant positive trends is relatively small and these locations are mostly found in the vicinity of the western Great Lakes. The spatial extent of significant positive trends expands in spring to include most of the southern and eastern portions of the study area, with few significant trends evident in the northwestern portion of the study area. In summer, locations with significant positive trends are clustered in New York/Pennsylvania, Ohio/Indiana, and southern Wisconsin. The largest magnitude trends in R95pTOT are generally observed during the summer months. Significant positive trends are evident in fall across much of the area except for the extreme western portion of the study region and in the Lower Peninsula of Michigan. Although negative trends are evident for a number of locations in all seasons for R95pTOT, these trends are significant at only one location in spring and two locations in winter.

Significant trends in seasonal WW are less spatially coherent than the annual WW indicator (**Figure 7**). As with seasonal R95pTOT, significant positive trends are often surrounded by insignificant trends or in a few cases significant negative trends. In general, stations with significant positive trends are more clustered for WW than for seasonal R95pTOT but less so than for seasonal PRCPTOT. The number of stations with significant positive trends is small in spring, and there are several (5) significant negative trends. The stations with significant positive trends are relatively dispersed, although some clustering is evident near the center of the study region. A more distinct spatial pattern is present in summer. Stations with significant positive trends are concentrated in Iowa, Indiana, Wisconsin, Ohio, Pennsylvania, and New York. In contrast, mostly insignificant trends are evident throughout the Plains states and east across Minnesota and northern Wisconsin, and the few significant trends in this area are negative. In fall, significant positive trends in WW are found across the northern half of the study region, whereas mostly insignificant trends of mixed sign are observed for the southern half of the region with the exception of Illinois. Little spatial coherence is evident in the wintertime trends of WW, other than some clustering of significant positive trends in the central and extreme northeast sections of the study region.

When compared to annual indicators, the Venn diagrams of seasonal indicators show that the groupings of indicators are more dispersed among the possible combinations of the four representative indicators (**Supplementary Figure 4**). In fall and winter the three-indicator combination of PRCPTOT, WW, and R1.26MM and the two-indicator combination of PRCPTOT and R95pTOT are more frequent, while in summer the most common combination is PRCPTOT and R1.26MM. In spring, locations are less likely compared to the other seasons to experience significant positive trends for two or more of the representative precipitation indicators, in part a reflection the smaller number of significant trends. For all seasons except spring a substantial number of stations display a significant trend only for R95pTOT. Venn diagrams can also be used to assess whether individual locations are likely to experience significant trends in a particular indicator during more than one season. Our results indicate that, regardless of the indicator type, significant positive trends are most likely to be observed during only one season (**Supplementary Figure 5**).

Total Precipitable Water

Trends in annual daily mean TOTPRCPWAT during the 1951–2019 study period are positive in sign and significant over the southern two-thirds of the study region (**Figure 8**). The largest trends are in the south-central portion of the study region with the smallest trends located over the central and western Great Lakes. A significant increase in TOTPRCPWAT is also evident over the Great Plains, with the magnitude of the trend decreasing from south to north. Correlations between the trends in annual TOTPRCPWAT and the trends in the annual values of the four representative precipitation indicators are weak to moderate (**Table 4** and **Supplementary Figure 6**), as indicated by the parametric Pearson's r and non-parametric Kendall's τ correlation coefficients. Correlations for the annual trends are insignificant ($p \leq 0.05$) and negative for WW and R1.26 mm, and insignificant but positive for PRCPTOT. Only the correlation between the annual trends in TOTPRCPWAT and those in R95pTOT is significant, with the sign of the correlation indicating a positive association between the annual trends of these two variables.

Assessment of the possible contribution of seasonal trends in TOTPRCPWAT to seasonal trends in the representative

TABLE 3 | Number of stations exhibiting statistically significant trends (Mann Kendall, $p \leq 0.05$ two-tailed, $p \leq 0.10$ two-tailed, $p \leq 0.20$, two-tailed) from 1951 to 2019 in four representative seasonal indicators: total seasonal precipitation (PRCPTOT), the number of wet days (R1.26mm), the count of wet-wet days (WW), and the total precipitation on days with precipitation ≥ 95th percentile (R95pTOT).

Precipitation indicator	Season	Total number of stations after breakpoint analysis	Number of stations with significant positive trends ($p \leq 0.05$)	Number of stations with significant positive trends ($p \leq 0.10$)	Number of stations with significant positive trends ($p \leq 0.20$)	Number of stations with significant negative trends ($p \leq 0.05$)	Number of stations with significant negative trends ($p \leq 0.10$)	Number of stations with significant negative trends ($p \leq 0.20$)
PRCPTOT								
	Annual	100	47	**75**	**79**	1	1	1
	Spring	112	12	21	31	0	0	5
	Summer	111	20	31	49	0	0	2
	Fall	114	34	42	50	0	0	0
	Winter	104	22	32	44	0	0	1
R1.26mm								
	Annual	97	42	**53**	**61**	1	3	5
	Spring	114	10	15	21	4	6	12
	Summer	113	21	31	37	0	1	3
	Fall	111	25	33	**66**	0	0	1
	Winter	110	23	27	35	1	2	5
WW								
	Annual	105	27	44	51	5	7	9
	Spring	113	8	17	26	4	5	9
	Summer	111	16	24	35	4	6	9
	Fall	111	18	27	41	0	1	1
	Winter	106	18	25	39	0	0	1
R95pTOT								
	Annual	104	47	**62**	**63**	0	0	0
	Spring	111	12	22	37	0	0	0
	Summer	114	15	22	37	0	0	3
	Fall	114	28	38	56	0	0	0
	Winter	111	15	22	37	0	0	0

Indicators where more than 50% of stations analyzed showed a significant trend are shown in bold.

precipitation indicators is complicated by seasonal variations in the significance of the TOTPRCPWAT trends, although in general correlation coefficients at the seasonal time scale are larger than those at the annual scale. Significant ($p \leq 0.05$) positive trends in TOTPRCPWAT (**Supplementary Figure 7**) are evident during spring, summer, and fall for portions of the study area, although insignificant trends are observed for a substantial number of the reanalysis grid cells, with the location of the insignificant trends varying by season. In contrast, trends in TOTPRCPWAT are insignificant for all grid cells in winter. Most of the significant ($p = 0.05$) correlations between the seasonal trends in TOTPRCPWAT and the season trends in the precipitation indicators are positive, although the significance of the trends varies by season and indicator. Correlations between the seasonal trends are significant in spring (PRCPTOT, R1.26mm, R95pTOT), summer (WW, PRCPTOT, R1.26mm, R95pTOT), and winter (PRCPTOT and R95pTOT), although the significant winter trends should be treated cautiously given the weak trends in TOTPRCPWAT at this time of year. No significant correlations were observed in the fall under Pearson's r. When Kendall's τ is used, correlations for fall are significant and negative for PRCPTOT and R95pTOT.

DISCUSSION/CONCLUSION

The impact of the additional quality control measures on the number of stations available for precipitation trend analysis is striking. Of the 317 stations in the Midwest and Great Lakes region that met the initial criterion of 90% completeness, 203 stations were removed at the second step because they failed the tests for observer bias (underreporting of precipitation ≤ 1.26 mm and over-reporting of precipitation amounts divisible by 5 or 10 when precipitation is recorded in inches). In contrast, the breakpoint analyses, which were conducted separately for each precipitation indicator in recognition that discontinuities can impact the indicators differently, removed only a small portion of the remaining stations (17 or fewer, depending on the indicator). This is a somewhat surprising result given the well-documented discontinuities in observations from the United States Cooperative Observer Network (Karl et al., 1987; Winkler, 2004; Menne et al., 2010), which is the largest source

FIGURE 5 | Trends (mm year^{-1}) in seasonal total precipitation (PRCPTOT) for: **(A)** spring, **(B)** summer, **(C)** fall, and **(D)** winter.

of precipitation data for the United States in the GHCN-D database (Menne et al., 2012). One interpretation is that many of the precipitation time series were affected by both observer bias and discontinuities and were removed following the tests for observation bias. The number of stations with breakpoints was largest for the "accumulation" and "threshold" precipitation indicators, suggesting the tests for observation bias did not remove all afflicted time series for these indicators. The final suite of quality-controlled time series has a much coarser station density than the datasets used in previous studies, and, while not suitable for investigating local-scale variations in precipitation trends, provides high confidence in the estimation of regional-scale variations. The quality-control routines implemented here also allow for more confidence in trends across the range of indicators from high frequency light events to low frequency extreme events, as observer bias affects various indicators differently and may not be captured in studies relying solely on data completeness and documented changes for data screening.

One finding from the use of the carefully quality-controlled time series is that the estimated trends for 1951–2019 in the Midwest and Great Lakes region are predominantly positive for all the "wet" precipitation indicators and negative for the "dry" precipitation indicators. In fact, there is a near absence of significant negative trends across the region for all indicators, with the exception of DD and CDD, and for all seasons and at all three significance levels included in the analysis. On the other hand, the proportion of stations with significant positive trends varies by precipitation indicator, season, and significance level. In general, significant trends at the moderate ($p \leq 0.10$) significance level are most likely for the indicators involving precipitation accumulation and counts of days with precipitation above specified thresholds, and less likely for indicators of maximum reported precipitation and the indictors defined in terms of the sequencing of precipitation. Thus, users need to be cautious of inferring from significant trends in common precipitation characteristics, such as total precipitation, that significant trends are also occurring in other precipitation characteristics at a particular location. The larger number of significant positive trends for the "wet" indicators under the weak ($p \leq 0.20$) significant level obviously need to be interpreted cautiously because of the greater probability of a Type I error (rejecting the null hypothesis of no trend when it is true). However, the greater spatial coherence of the locations with significant trends for the weak significance level compared to the moderate and stringent

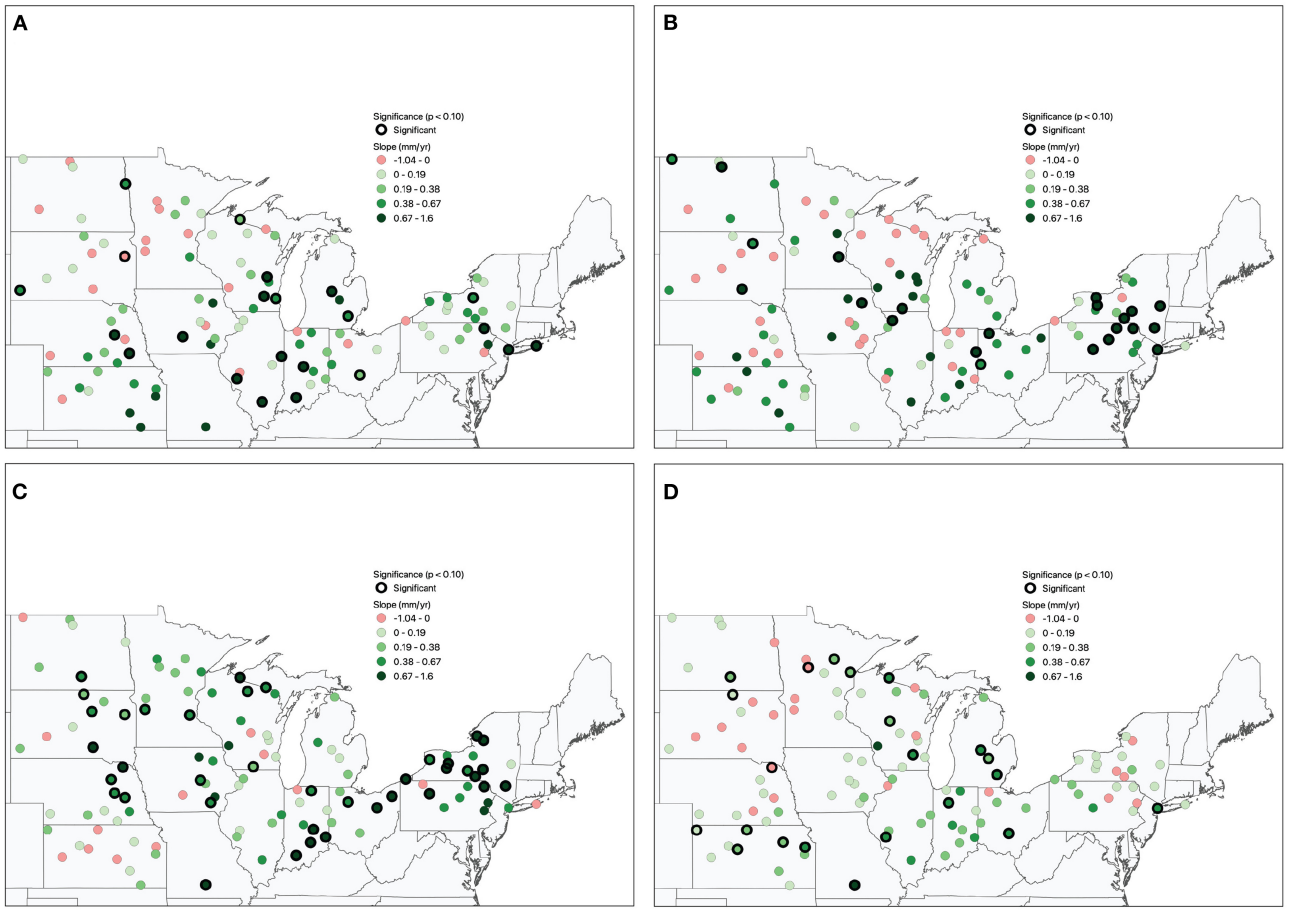

FIGURE 6 | Trends (mm year^{-1}) in the seasonal amount of total precipitation falling on days with precipitation $\geq$ 95th percentile (R95pTOT) for **(A)** spring, **(B)** summer, **(C)** fall, and **(D)** winter.

levels is consistent with a regional-scale trend toward a wetter climate that is emerging from interannual variability.

Our results also confirm that precipitation indicators that are defined annually often mask strong seasonal variations in the temporal trends of both high frequency, low magnitude events and low frequency, high magnitude events. For almost all locations, one cannot assume based on the trends in an annual precipitation indicator that a location is experiencing similar trends seasonally. Instead, a significant trend in a particular precipitation indicator typically is observed during only one season.

While the low spatial density of the stations that met all three of the quality control criteria somewhat constrains inferences regarding subregional variations in precipitation trends, our results, especially those using the weaker and moderate significance levels, suggest that the character of precipitation is not changing uniformly across the Midwest and Great Lakes region. In terms of the annual values of four representative precipitation indicators (PRCPTOT, R1.26mm, WW, R95pTOT), significant positive trends are observed across the central and eastern portions of the study region for all four indicators, whereas in the west there is a notable absence of significant positive trends for R1.26mm events. Seasonal differences in the spatial distribution of significant trends are also evident, particularly for winter when significant trends for the four representative indicators are largely confined to western Great Lakes portion of the study region. The smaller number of significant trends present under the strict criteria, highlights the strength and relative cohesiveness of trends in precipitation in the central and eastern portions of the region, where most of the significant ($p \leq 0.05$) trends are located.

The quality-controlled time series are also useful for evaluating relationships between trends in the precipitation characteristics and physical processes potentially contributing to these trends. Expanding on the intriguing findings of Kunkel et al. (2020b) who found a significant positive correlation between regionally-averaged trends in extreme precipitation and trends in precipitable water for the contiguous United States, we correlated, at annual and seasonal temporal scales, the trends in PRCPTOT, R1.26mm, WW, and R95pTOT for the quality-controlled station time series with trends in average daily precipitable water at a 2.5° latitude x 2.5° longitude

FIGURE 7 | Trends (days year^{-1}) in the seasonal count of wet-wet-day sequences (WW) for **(A)** spring, **(B)** summer, **(C)** fall, and **(D)** winter.

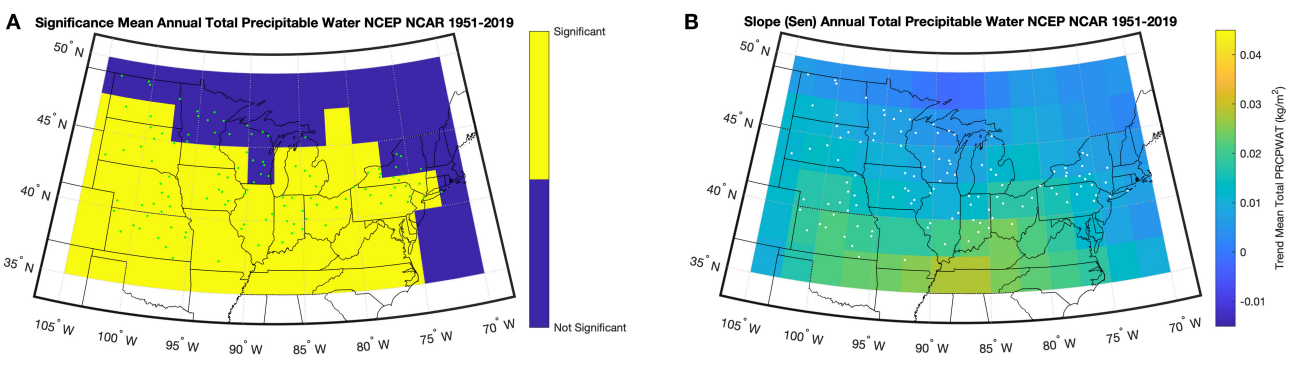

FIGURE 8 | (A) Significance ($p \leq 0.05$) and **(B)** Sen's slope (kg m^{-2} yr-^{1}) of the trend in annual mean daily total precipitable water for the study region from 1951 to 2019. The stations with quality-controlled precipitation time series are shown on both maps as dots.

resolution from the NCEP/NCAR reanalysis (Kalnay et al., 1996). The correlations for R95pTOT support for the Midwest and Great Lakes region the coarser-scale findings from Kunkel et al. (2020a) that the trend in extreme precipitation increases with an increasing trend in precipitable water, but also point to a more complex interpretation of the relationship between in trends in precipitation characteristics and trends in precipitable water for the study region. In particular, significant ($p \leq 0.05$) correlations are evident during spring and summer for PRCPTOT and R1.26mm and in summer for WW, suggesting that increases in precipitable water may also contribute to positive trends in high frequency precipitation events and even

TABLE 4 | Pearson correlation coefficients (r) and Kendall rank correlation coefficients (τ) between annual and seasonal trends from 1951 to 2019 in precipitation indicators and total precipitable water.

Indicator	Season	*r*	p_r	τ	$p\tau$
WW	Spring	0.11	0.26	0.062	0.33
	Summer	**0.37**	**<0.01**	**0.23**	**<0.01**
	Fall	−0.18	0.06	−0.10	0.13
	Winter	0.036	0.71	0.03	0.68
	Annual	−0.089	0.37	−0.023	0.73
PRCPTOT	Spring	**0.33**	**<0.01**	**0.21**	**<0.01**
	Summer	**0.4**	**<0.01**	**0.26**	**<0.01**
	Fall	−0.14	0.15	**−0.13**	**0.05**
	Winter	**0.25**	**0.01**	**0.18**	**0.01**
	Annual	0.13	0.20	0.097	0.15
R1.26MM	Spring	**0.2**	**0.04**	**0.15**	**0.02**
	Summer	**0.42**	**<0.01**	**0.27**	**<0.01**
	Fall	−0.086	0.36	−0.04	0.55
	Winter	0.058	0.55	0.01	0.85
	Annual	−0.076	0.45	−0.015	0.82
R95pTOT	Spring	**0.19**	**0.05**	0.06	0.33
	Summer	**0.26**	**0.01**	**0.17**	**0.01**
	Fall	−0.13	0.16	**−0.16**	**0.014**
	Winter	**0.32**	**<0.01**	**0.22**	**<0.01**
	Annual	**0.21**	**0.03**	**0.15**	**0.03**

Significant correlations ($p \leq 0.05$) are noted in bold. P-values for Pearson's r are noted in p_r and Kendall's τ are noted under $p\tau$.

to the sequencing of wet days. Also, the correlation between the trend in R95pTOT and that for precipitable water is insignificant in fall for the parametric correlation coefficient and significant but negative for the non-parametric correlation coefficient, suggesting that changes in atmospheric lifting mechanisms (e.g., fronts, extratropical cyclones) rather than increased atmospheric humidity may be more important for explaining the positive trend in R95pTOT in the Midwest and Great Lakes region in fall. Our findings of insignificant trends in precipitable water for large portions of the study area, especially in winter when the precipitable water trends are insignificant for the entire NCEP/NCAR grid over the study area, point to the need for cautious interpretation of the relationship between trends in precipitable water and trends in precipitation characteristics.

We have demonstrated the usefulness of quality-controlled precipitation time series for evaluating trends in precipitation characteristics and for investigating their relationship with processes. However, the limitations of the quality-controlled dataset should also be considered in interpreting the findings presented here and when applying the time series in future work. A key limitation is the coarse spatial resolution of the quality-controlled time series, limiting their usefulness in investigating potential contributions of local-scale features such as lake surfaces or topography on trends in precipitation characteristics. Another concern is that identified breakpoints in the time series that are attributed to changes in instrumentation, station moves or observation protocols may instead be caused by changes in circulation regimes. Also, some types of precipitation indicators may be less sensitive to observer bias than others, and a less stringent protocol for removing time series for consideration would be appropriate. Moreover, for any quality control routine that is not manual, there are almost always time series with data issues relevant to a particular analysis that pass through filters and checks and those without data issues that are incorrectly removed.

In sum, our analysis focused on quality control of station time series to improve the quality of data prior to analysis. As a result of this effort, the trends in our study tended to exhibit a more cohesive spatial and temporal similarities when compared with studies with different quality control criteria, illustrating the importance of quality control of observations in climatic studies. Also, our results indicate, at least for the Midwest and Great Lakes region, that not only is extreme precipitation increasing but the entire distribution of precipitation has been shifting upward over time.

DATA AVAILABILITY STATEMENT

The original contributions presented in the study are included in the article/**Supplementary Material**, further inquiries can be directed to the corresponding author/s.

AUTHOR CONTRIBUTIONS

WB, JA, and JW conceived the research questions, reviewed/edited manuscript drafts, approved of submission, and designed the methodology. WB wrote original manuscript draft, acquired data, conducted analyses, and prepared figures. JA supervised and secured funding for the research. All authors contributed to the article and approved the submitted version.

FUNDING

Funding for this project was provided by the Great Lakes Integrated Sciences and Assessments Program (GLISA), a collaboration of the University of Michigan and Michigan State University (MSU) funded by the National Oceanic and Atmospheric Administration (NOAA) Oceanic and Atmospheric Research (OAR) office [NOAA-OAR-CPO Grant no. NA15OAR4310148].

SUPPLEMENTARY MATERIAL

The Supplementary Material for this article can be found online at: https://www.frontiersin.org/articles/10.3389/frwa.2022.817342/full#supplementary-material

REFERENCES

Alexander, L. V., Zhang, X., Peterson, T. C., Caesar, J., Gleason, B., Klein Tank, A. M. G., et al. (2006). Global observed changes in daily climate extremes of temperature and precipitation. *J. Geophys. Res.* 111:D05109. doi: 10.1029/2005JD006290

Angel, J., Swanston, C., Boustead, B. M., Conlon, K. C., Hall, K. R., Jorns, J. L., et al. (2018). "Midwest," *in Impacts, Risks, and Adaptation in the United States: Fourth National Climate Assessment, Volume II, eds D. R. Reidmiller, C. W. Avery, D. R. Easterling, K. E. Kunkel, K. L. M. Lewis, T. K. Maycock, and B. C. Stewart (Washington, DC: U.S. Global Change Research Program)*. doi: 10.7930/NCA4.2018.CH21

Attavanich, W., McCarl, B. A., Ahmedov, Z., Fuller, S. W., and Vedenov, D. V. (2013). Effects of climate change on US grain transport. *Nat. Clim. Chang. 37*, 638–643. doi: 10.1038/nclimate1892

Bartels, R. J., Black, A. W., and Keim, B. D. (2020). Trends in precipitation days in the United States. *Int. J. Climatol.* 40, 1038–1048. doi: 10.1002/joc.6254

Baule, W. J., and Shulski, M. D. (2014). Climatology and trends of wind speed in the Beaufort/Chukchi Sea coastal region from 1979 to 2009. *Int. J. Climatol.* 34:3881. doi: 10.1002/joc.3881

Bell, G. D., and Janowiak, J. E. (1995). Atmospheric circulation associated with the midwest floods of 1993. *Bull. Am. Meteorol. Soc.* 76, 681–695. doi: 10.1175/1520-0477(1995)076<0681:ACAWTM>2.0.CO;2

Bowles, T. M., Atallah, S. S., Campbell, E. E., Gaudin, A. C. M., Wieder, W. R., and Grandy, A. S. (2018). Addressing agricultural nitrogen losses in a changing climate. *Nat. Sustain.* 1, 399–408. doi: 10.1038/s41893-018-0106-0

Chin, N., Byun, K., Hamlet, A. F., and Cherkauer, K. A. (2018). Assessing potential winter weather response to climate change and implications for tourism in the U.S. *Great Lakes and Midwest. J. Hydrol. Reg. Stud.* 19, 42–56. doi: 10.1016/J.EJRH.2018.06.005

Contractor, S., Donat, M. G., and Alexander, L. V. (2021). Changes in observed daily precipitation over global land areas since 1950. *J. Clim.* 34, 3–19. doi: 10.1175/JCLI-D-19-0965.1

Costa, A. C., and Soares, A. (2009). Homogenization of climate data: review and new perspectives using geostatistics. *Math. Geosci.* 41, 291–305. doi: 10.1007/s11004-008-9203-3

Dai, S., Shulski, M. D., Hubbard, K. G., and Takle, E. S. (2016). A spatiotemporal analysis of Midwest US temperature and precipitation trends during the growing season from 1980 to 2013. *Int. J. Climatol.* 36, 517–525. doi: 10.1002/joc.4354

Daly, C., Conklin, D. R., and Unsworth, M. H. (2010). Local atmospheric decoupling in complex topography alters climate change impacts. *Int. J. Climatol.* 30, 1857–1864. doi: 10.1002/JOC.2007

Daly, C., Gibson, W. P., Taylor, G. H., Doggett, M. K., and Smith, J. I. (2007). Observer bias in daily precipitation measurements at United States Cooperative Network Stations. *Bull. Am. Meteorol. Soc.* 88, 899–912. doi: 10.1175/BAMS-88-6-899

Donat, M. G., Alexander, L. V., Yang, H., Durre, I., Vose, R., Caesar, J., et al. (2013). Global land-based datasets for monitoring climatic extremes. *Bull. Am. Meteorol. Soc.* 94, 997–1006. doi: 10.1175/BAMS-D-12-00109.1

Durre, I., Menne, M. J., Gleason, B. E., Houston, T. G., and Vose, R. S. (2010). Comprehensive automated quality assurance of daily surface observations. *J. Appl. Meteorol. Climatol.* 49, 1615–1633. doi: 10.1175/2010JAMC2375.1

Durre, I., Menne, M. J., and Vose, R. S. (2008). Strategies for evaluating quality assurance procedures. *J. Appl. Meteorol. Climatol.* 47, 1785–1791. doi: 10.1175/2007JAMC1706.1

Easterling, D. R. (2002). *United States Historical Climatology Network Daily Temperature and Precipitation Data (1871-1997). Oak Ridge, TN: Oak Ridge National Laboratory.*

Groisman, P. Y., Karl, T. R., Easterling, D. R., Knight, R. W., Jamason, P. F., Hennessy, K. J., et al. (1999). Changes in the probability of heavy precipitation: important indicators of climatic change. *Clim. Change* 42, 243–283. doi: 10.1023/A:1005432803188

Groisman, P. Y., and Knight, R. W. (2008). Prolonged dry episodes over the conterminous United States: New tendencies emerging during the last 40 years. *J. Clim.* 21, 1850–1862. doi: 10.1175/2007JCLI2013.1

Gronewold, A. D., Do, H. X., Mei, Y., and Stow, C. A. (2021). A tug-of-war within the hydrologic cycle of a continental freshwater basin. *Geophys. Res. Lett.* 48:e2020GL090374. doi: 10.1029/2020GL090374

Guilbert, J., Betts, A. K., Rizzo, D. M., Beckage, B., and Bomblies, A. (2015). Characterization of increased persistence and intensity of precipitation in the northeastern United States. *Geophys. Res. Lett.* 42, 1888–1893. doi: 10.1002/2015GL063124

Gutowski, W. J., Willis, S. S., Patton, J. C., Schwedler, B. R. J., Arritt, R. W., and Takle, E. S. (2008). Changes in extreme, cold-season synoptic precipitation events under global warming. *Geophys. Res. Lett.* 35:L20710. doi: 10.1029/2008GL035516

Higgins, R. W., Silva, V. B. S., Shi, W., and Larson, J. (2007). Relationships between climate variability and fluctuations in daily precipitation over the United States. *J. Clim.* 20, 3561–3579. doi: 10.1175/JCLI4196.1

Hoerling, M., Eischeid, J., Perlwitz, J., Quan, X. W., Wolter, K., and Cheng, L. (2016). Characterizing recent trends in U.S. *heavy precipitation. J. Clim.* 29, 2313–2332. doi: 10.1175/JCLI-D-15-0441.1

Huang, H., Winter, J. M., and Osterberg, E. C. (2018). Mechanisms of abrupt extreme precipitation change over the Northeastern United States. *J. Geophys. Res. Atmos.* 123, 7179–7192. doi: 10.1029/2017JD028136

Huang, H., Winter, J. M., Osterberg, E. C., Horton, R. M., and Beckage, B. (2017). Total and extreme precipitation changes over the Northeastern United States. *J. Hydrometeorol.* 18, 1783–1798. doi: 10.1175/JHM-D-16-0195.1

Hunt, E. D., Birge, H. E., Laingen, C., Licht, M. A., McMechan, J., Baule, W., et al. (2020). A perspective on changes across the U.S. *Corn Belt. Environ. Res. Lett.* 15:071001. doi: 10.1088/1748-9326/ab9333

Huschke, R. E. (1959). *Glossary of Meteorology*. Boston, MA: American Meteorological Society.

Ines, A. V. M., Hansen, J. W., and Robertson, A. W. (2011). Enhancing the utility of daily GCM rainfall for crop yield prediction. *Int. J. Climatol.* 31, 2168–2182. doi: 10.1002/joc.2223

Jaiswal, R. L., Lohaniu, A. K., and Tiwari, H. L. (2015). Statistical analysis for change detection and trend assessment in climatological parameters. *Environ. Processes*. 2, 729–749. doi: 10.1007/s40710-015-0105-3

Janssen, E., Wuebbles, D. J., Kunkel, K. E., Olsen, S. C., and Goodman, A. (2014). Observational- and model-based trends and projections of extreme precipitation over the contiguous United States. *Earth's Futur.* 2, 99–113. doi: 10.1002/2013EF000185

Kalnay, E., Kanamitsu, M., Kistler, R., Collins, W., Deaven, D., Gandin, L., et al. (1996). The NCEP/NCAR 40-year reanalysis project. *Bull. Am. Meteorol. Soc.* 77, 437–471. doi: 10.1175/1520-0477(1996)077<0437:TNYRP>2.0.CO;2

Karl, T. R., Williams, C. N., and Karl, T. R. (1987). An approach to adjusting climatological time series for discontinuous inhomogeneities. *J. Clim. Appl. Meteorol.* 26, 1744–1763. doi: 10.1175/1520-0450(1987)026<1744:AATACT>2.0.CO;2

Kendall, M. G. (1955). *Rank Correlation Methods*. 2nd ed. Oxford: Hafner Publishing Co.

Kendall, M. G. (1975). *Rank Correlation Methods*. London: Griffin Publishers.

Kiefer, M. T., Andresen, J. A., McCullough, D. G., Baule, W. J., and Notaro, M. (2021). Extreme minimum temperatures in the Great Lakes region of the United States: A climatology with implications for insect mortality. *Int. J. Climatol.* 33, 1585–1600. doi: 10.1002/JOC.7434

Komoto, K., Soldo, L., Tang, Y., Chilvers, M. I., Dahlin, K., Guentchev, G., et al. (2021). Climatology of persistent high relative humidity: An example for the Lower Peninsula of Michigan, USA. *Int. J. Climatol.* 41, E2517–E2536. doi: 10.1002/JOC.6861

Konrad, C. E. (2001). The most extreme precipitation events over the Eastern United States from 1950 to 1996: considerations of scale. *J. Hydrometeorol.* 2, 309–325. doi: 10.1175/1525-7541(2001)002<0309:TMEPEO>2.0.CO;2

Kunkel, K. E., Karl, T. R., Squires, M. F., Yin, X., Stegall, S. T., and Easterling, D. R. (2020b). Precipitation extremes: trends and relationships with average precipitation and precipitable water in the contiguous United States. *J. Appl. Meteorol. Climatol.* 59, 125–142. doi: 10.1175/JAMC-D-19-0185.1

Kunkel, K. E., Stevens, S. E., Stevens, L. E., and Karl, T. R. (2020a). Observed climatological relationships of extreme daily precipitation events with precipitable water and vertical velocity in the contiguous United States. *Geophys. Res. Lett.* 47:e2019GL086721. doi: 10.1029/2019GL086721

Legates, D. R., and Willmott, C. J. (1990). Mean seasonal and spatial variability in gauge-corrected, global precipitation. *Int. J. Climatol.* 10, 111–127. doi: 10.1002/joc.3370100202

Mallakpour, I., and Villarini, G. (2016). A simulation study to examine the sensitivity of the Pettitt test to detect abrupt changes in mean. *Hydrol. Sci. J.* 61, 245–254. doi: 10.1080/02626667.2015.1008482/SUPPL_FILE/THSJ_A_1008482_SM3561.DOC

Mallakpour, I., and Villarini, G. (2017). Analysis of changes in the magnitude, frequency, and seasonality of heavy precipitation over the contiguous USA. *Theor. Appl. Climatol.* 130, 345–363. doi: 10.1007/s00704-016-1881-z

Mann, H. B. (1945). Nonparametric tests against trend. *Econometrica* 13:245. doi: 10.2307/1907187

Menne, M. J., Durre, I., Vose, R. S., Gleason, B. E., and Houston, T. G. (2012). An overview of the global historical climatology network-daily database. *J. Atmos. Ocean. Technol.* 29, 897–910. doi: 10.1175/JTECH-D-11-00103.1

Menne, M. J., Williams, C. N., and Palecki, M. A. (2010). On the reliability of the U.S. *surface temperature record. J. Geophys. Res. Atmos.* 115:11108. doi: 10.1029/2009JD013094

Myhre, G., Forster, P. M., Samset, B. H., Hodnebrog, Ø., Sillmann, J., Aalbergsjø, S. G., et al. (2016). PDRMIP: A precipitation driver and response model intercomparison project, protocol and preliminary results. *Bull. Am. Meteorol. Soc.* 98, 1185–1198. doi: 10.1175/BAMS-D-16-0019.1

Onyutha, C. (2021). Graphical-statistical method to explore variability of hydrological time series. *Hydrol. Res.* 52, 266–283. doi: 10.2166/NH.2020.111

Pettitt, A. N. (1979). A non-parametric approach to the change-point problem. *Appl. Stat. 28,* 126–135.

Pielke, R. A., and Downton, M. W. (2000). Precipitation and damaging floods: Trends in the United States, 1932–1997. *J. Clim.* 2000, 3625–3637. doi: 10.1175/1520-0442(2000)013<3625:PADFTI>2.0.CO;2

Pryor, S. C., Howe, J. A., and Kunkel, K. E. (2009). How spatially coherent and statistically robust are temporal changes in extreme precipitation in the contiguous USA? *Int. J. Climatol.* 29, 31–45. doi: 10.1002/joc.1696

Riha, S. J., Wilks, D. S., and Simoens, P. (1996). Impact of temperature and precipitation variability on crop model predictions. *Clim. Change* 32, 293–311. doi: 10.1007/BF00142466

Roque-Malo, S., and Kumar, P. (2017). Patterns of change in high frequency precipitation variability over North America. *Sci. Rep.* 7:10853. doi: 10.1038/s41598-017-10827-8

Rosenzweig, C., Tubiello, F. N., Goldberg, R., Mills, E., and Bloomfield, J. (2002). Increased crop damage in the US from excess precipitation under climate change. *Glob. Environ. Chang.* 12, 197–202. doi: 10.1016/S0959-3780(02)00008-0

Schoof, J. T., Pryor, S. C., and Surprenant, J. (2010). Development of daily precipitation projections for the United States based on probabilistic downscaling. *J. Geophys. Res. Atmos.* 115:D13106. doi: 10.1029/2009JD013030

Sen, P. K. (1968). Estimates of the regression coefficient based on Kendall's Tau. *J. Am. Stat. Assoc.* 63:1379. doi: 10.2307/2285891

Sen, Z. (2015). Innovative trend significance test and applications. *Theor. Appl. Climatol.* 127, 939–947. doi: 10.1007/S00704-015-1681-X

Shulski, M. D., Baule, W., Stiles, C., and Umphlett, N. (2015). A historical perspective on Nebraska's variable and changing climate. *Gt. Plains Res.* 25:23. doi: 10.1353/gpr.2015.0023

Sneyers, R. (1990). *On the Statistical Analysis of Series of Observations*. Geneva: Secretariat of the World Meteorological Organization.

Takle, E. S., and Gutowski, W. J. (2020). Iowa's agriculture is losing its Goldilocks climate. *Phys. Today* 73:26. doi: 10.1063/PT.3.4407

Talukder, B., and Hipel, K. W. (2020). Diagnosis of sustainability of trans-boundary water governance in the Great Lakes basin. *World Dev.* 129:104855. doi: 10.1016/J.WORLDDEV.2019.104855

Trenberth, K. E., Dai, A., Rasmussen, R. M., and Parsons, D. B. (2003). The changing character of precipitation. *Bull. Am. Meteorol. Soc.* 84, 1205–1217. doi: 10.1175/BAMS-84-9-1205

Trenberth, K. E., Fasullo, J., and Smith, L. (2005). Trends and variability in column-integrated atmospheric water vapor. *Clim. Dyn.* 24, 741–758. doi: 10.1007/S00382-005-0017-4/FIGURES/15

Villarini, G., Smith, J. A., Baeck, M. L., Vitolo, R., Stephenson, D. B., and Krajewski, W. F. (2011). On the frequency of heavy rainfall for the midwest of the United States. *J. Hydrol.* 400, 103–120. doi: 10.1016/j.jhydrol.2011.01.027

Walsh, J., Wuebbles, D., Hayhoe, K., Kossin, J., Kunkel, K., Stephens, G., et al. (2014). *Ch. 2: Our Changing Climate*. Climate Change Impacts in the United States: The Third National Climate Assessment.

Wang, X. L., Chen, H., Wu, Y., Feng, Y., Pu, Q., Wang, X. L., et al. (2010). New techniques for the detection and adjustment of shifts in daily precipitation data series. *J. Appl. Meteorol. Climatol.* 49, 2416–2436. doi: 10.1175/2010JAMC2376.1

Weaver, S. J., and Nigam, S. (2008). Variability of the great plains low-level jet: large-scale circulation context and hydroclimate impacts. *J. Clim.* 21, 1532–1551. doi: 10.1175/2007JCLI1586.1

Williams, C. N., Menne, M. J., and Thorne, P. W. (2012). Benchmarking the performance of pairwise homogenization of surface temperatures in the United States. *J. Geophys. Res. Atmos.* 117:16. doi: 10.1029/2011JD016761

Winkler, J. A. (1988). Climatological characteristics of summertime extreme rainstorms in Minnesota. *Ann. Assoc. Am. Geogr.* 78, 57–73.

Winkler, J. A. (2004). "The impact of technology upon in situ atmospheric observations and climate science," in *Geography and Technology* (Dordrecht: Springer). doi: 10.1007/978-1-4020-2353-8_20

Wu, S. Y. (2015). Changing characteristics of precipitation for the contiguous United States. *Clim. Change* 132, 677–692. doi: 10.1007/S10584-015-1453-8/TABLES/2

Zhang, W., and Villarini, G. (2019). On the weather types that shape the precipitation patterns across the U.S. Midwest. *Clim. Dyn.* 2019, 1–16. doi: 10.1007/s00382-019-04783-4

Zhang, X., Alexander, L., Hegerl, G. C., Jones, P., Tank, A. K., Peterson, T. C., et al. (2011). Indices for monitoring changes in extremes based on daily temperature and precipitation data. *Wiley Interdiscip. Rev. Clim. Chang.* 2, 851–870. doi: 10.1002/wcc.147

Conflict of Interest: The authors declare that the research was conducted in the absence of any commercial or financial relationships that could be construed as a potential conflict of interest.

Publisher's Note: All claims expressed in this article are solely those of the authors and do not necessarily represent those of their affiliated organizations, or those of the publisher, the editors and the reviewers. Any product that may be evaluated in this article, or claim that may be made by its manufacturer, is not guaranteed or endorsed by the publisher.

frontiers in Water

ORIGINAL RESEARCH
published: 21 February 2022
doi: 10.3389/frwa.2022.788493

A Hybrid Dataset of Historical Cool-Season Lake Effects From the Eastern Great Lakes of North America

Andrew W. Ellis[1]* *and Zachary J. Suriano*[2]

[1] Department of Geography, Virginia Tech, Blacksburg, VA, United States, [2] Department of Geography and Geology, University of Nebraska Omaha, Omaha, NE, United States

The moistening of cold air passing over the Great Lakes of North America has a profound impact on the cool season climate of regions downwind, from relatively benign air mass modification to highly-impactful snowfall events. The importance of lake effects has led to the development of varying techniques for systematically identifying lake-effect days. The results of two such methods are merged here to yield a more thorough record of lake-effect days for the eastern Great Lakes. Comparative analysis of the data sets illustrates the different objectives of the two methodologies, where one identifies days with a synoptic setup conducive to lake-effect snowfall, and the other identifies days with lake-effect modification of the overlying air mass. A smaller population of "absolute" lake-effect days are those identified by both methods, while a larger population of "hybrid" lake-effect days are absolute days plus those identified by one method but not the other. For a 51-year study period ending with the 2014–15 cool season, the absolute data set yields a mean of about 15 lake-effect days per year, or 8% of the November through April season, while the hybrid data set yields a mean of 56 lake-effect days per year, or 31% of the season. The frequencies of absolute, air mass modification-defined, and hybrid lake-effect days decreased through the study period, with days within the hybrid data set declining at a statistically significant rate of 2.8 days per decade, although most obviously from the late 1970s through the early 2000s. The result is a general drying of the cool-season lake-effect hydroclimate. The merged data set offers a more thorough historical record of days available for atmospheric and hydroclimatic study of the lake-effect phenomenon within the eastern Great Lakes region.

Keywords: Great Lakes, lake-effect, cool season, Synoptic Classification, hydroclimate

OPEN ACCESS

Edited by:
Adam Burnett,
Colgate University, United States

Reviewed by:
Munir Ahmad Nayak,
Indian Institute of Technology Indore, India
Arthur Samel,
Bowling Green State University, United States
Art DeGaetano,
Cornell University, United States

***Correspondence:**
Andrew W. Ellis
awellis@vt.edu

Specialty section:
This article was submitted to Water and Climate, a section of the journal Frontiers in Water

Received: *02 October 2021*
Accepted: *25 January 2022*
Published: *21 February 2022*

Citation:
Ellis AW and Suriano ZJ (2022) A Hybrid Dataset of Historical Cool-Season Lake Effects From the Eastern Great Lakes of North America. Front. Water 4:788493. doi: 10.3389/frwa.2022.788493

INTRODUCTION

Like a number of water bodies globally, the Great Lakes of North America (**Figure 1**) are capable of modifying the thermal and moisture characteristics of the lower atmosphere, altering the weather and climate of areas downwind (Andresen, 2012; Notaro et al., 2013). Great Lakes "lake effects" are most distinct early within the cool season, when energy that has accumulated within the lakes during the warmth of the year interacts with southward moving cold air. The vertical stability of the deeply cold atmosphere is reduced with low-level warming and moistening, initiating upward

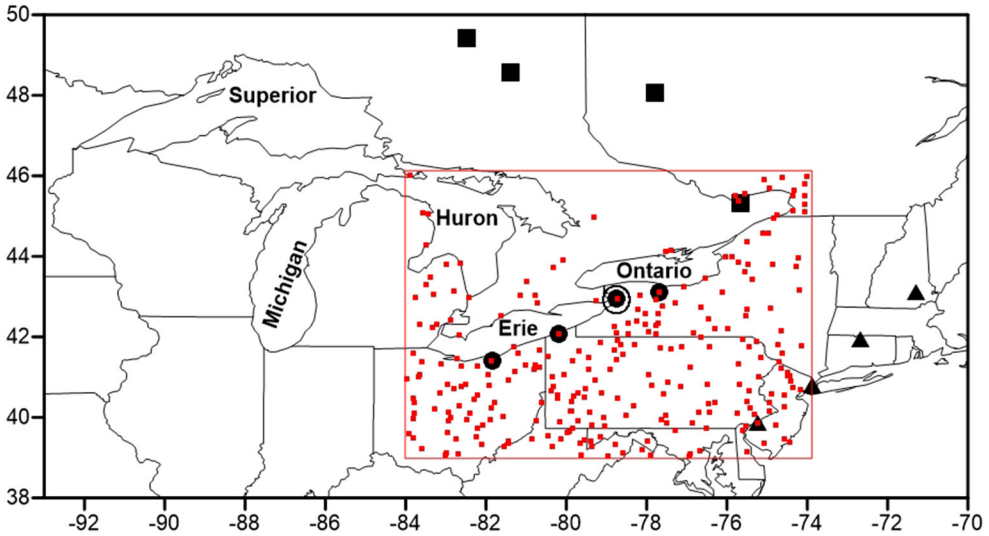

FIGURE 1 | The North American Great Lakes and the locations of GHCN-Daily precipitation stations (red squares within red boundary), the location of Buffalo, New York (large open circle) for which Suriano and Leathers (2017a) constructed a Temporal Synoptic Index, and the three sets of four locations for which Spatial Synoptic Classification data were applied by Ellis et al. (2021), with black-filled circles representing lake-effect stations, and black-filled squares and triangles representing northern and eastern non-lake-effect stations.

motion that is often enhanced by friction above the land surface downwind to yield clouds and lake-effect precipitation (Scott and Huff, 1996). The result is an acute impact on the weather and hydroclimate of areas generally east and southeast of each lake. The advection of cold air across the lakes is typically associated with a rather distinct weather pattern, most often involving some variation of a surface low-pressure center to the east and surface high-pressure to the west (Ellis and Leathers, 1996; Suriano and Leathers, 2017a). The integrated portrayal of atmospheric pressure centers and the air masses arranged around them is referenced as the synoptic atmosphere; thus, the cool season effect of the Great Lakes, with distinct cold air advection between opposing pressure centers, is a phenomenon that lends itself to synoptic atmospheric classification techniques.

The Temporal Synoptic Index (TSI) has been used effectively to identify cool season synoptic atmospheric patterns conducive to lake-effect precipitation within the historical record (Ellis and Leathers, 1996; Suriano and Leathers, 2017a). The TSI method (Kalkstein and Corrigan, 1986) involves using principal components analysis (PCA) on 24 daily weather observations (six variables, four times per day) to determine primary modes of variability seasonally. Average linkage clustering is then used to cluster PCA component scores with large eigenvalues to yield clusters of days, or synoptic types, with a similar surface meteorological profile. Most recently, Suriano and Leathers (2017a) applied the TSI methodology to daily data for Buffalo, New York (**Figure 1**) to identify synoptic patterns conducive to lake-effect snowfall downwind of the eastern Great Lakes Erie and Ontario. The TSI was constructed using data for the autumn (September–November), winter (December–February), and spring (March–May) seasons separately. Suriano and Leathers (2017a) identified seven TSI types conducive to lake-effect snowfall based on composites of their sea-level pressure pattern, lower-atmospheric wind direction and speed, vertical wind direction shear through the lower atmosphere, and temperature difference between the lake surface and lower atmosphere. The latter is predicated on the lake-850 hPa temperature difference threshold of about 13°C necessary to initiate convection (Holroyd, 1971). As with any classification, variability exists within the population of days that comprise each TSI type. Undoubtedly, there are individual days for which the sea-level pressure pattern, winds, or the lake and air temperatures may not have met the criteria that Suriano and Leathers (2017a) applied to the mean values calculated for each TSI type.

Recently, Ellis et al. (2021) used historical daily weather type data to detect cool season modification of cold, dry air upwind of the Great Lakes to cool, moist air downwind of the lakes. The work was predicated on the Spatial Synoptic Classification (SSC) database (Sheridan, 2002). In contrast to the fully-automated TSI, the classification of daily weather within the SSC methodology is guided by sets of manually-selected days from the historical record that best represent six weather types for that location. An automated discriminant analysis then assigns each day in the historical record to the weather type it most resembles based on twelve daily meteorological variables. Weather types are defined by their humidity and air temperature characteristics: dry-polar (DP), dry-moderate (DM), dry-tropical (DT), moist-polar (MP), moist-moderate (MM), moist-tropical (MT). The SSC methodology includes a seventh classification for days exhibiting changes in the weather variables symbolic of a transition from one weather type to another—the transition (TR) classification. Ellis et al. (2021) used a spatial arrangement of weather types across the Great Lakes and surrounding regions to identify days within the historical record for which modification

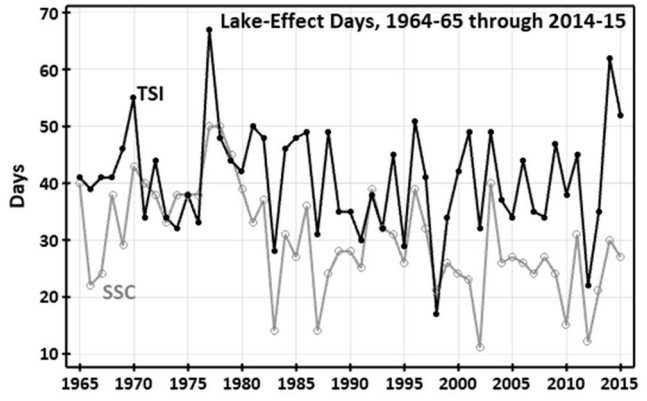

FIGURE 2 | Seasonal number of lake-effect days for the eastern Great Lakes as determined by the TSI (black) and SSC (gray) methodologies.

by the lakes seems apparent. Using an array of SSC stations (**Figure 1**), their method identified days for which the dry-polar (DP) weather type predominantly surrounds the lakes (northern and eastern station locations in **Figure 1**), but the moist-polar (MP) weather type is evident within the traditional lake-effect regions (lake-effect locations in **Figure 1**). The method of Ellis et al. (2021) is obviously dependent on classification accuracy within the SSC database, but also on a limited SSC station density, both of which are important in the nuanced identification of the sometimes-subtle lake effect phenomenon. For example, while an SSC station east of the long axis of Lake Ontario is desirable, Ellis et al. (2021) noted that the daily records of the two candidate stations within the SSC database (Watertown and Fort Drum, New York) are marred by 10- and 35-year gaps and otherwise poor data completeness through the record. Clear evidence of air mass modification within the regional array of weather type data is possibly restricted to the purest or most recognizable cases of lake effects, possibly eliminating less clearly-defined days that are no-less impactful.

Each of the TSI and SSC methodologies yields a daily calendar of lake-effect days. As the SSC calendar begins in November 1964, and the TSI calendar, available only for the eastern Great Lakes, ends in 2015, a 51-year period of cool seasons for which the databases overlap extends from November 1964 through April 2015. The SSC methodology identifies fewer lake-effect days for the eastern lakes than does the TSI method (**Figure 2**), which is logical, as the SSC-based approach is necessarily more particular in its daily discernment of a sometimes-subtle lake effect (air mass modification) using an array of stations across the region. In contrast, the TSI approach uses daily synoptic types at one location as a generalization for the region, and then generalizes all days within certain synoptic types as conducive to lake-effect snowfall. This likely passes a wider net through the historical record than does the SSC methodology. Neither method is viewed as superior; rather, the two methods simply meet slightly different objectives. Merging the two data sets may yield a more thorough history of lake-effects for the eastern Great Lakes region to support atmospheric and hydroclimatic research.

Aside from TSI-based classifications (Ellis and Leathers, 1996; Karmosky, 2007; Suriano and Leathers, 2017a; Suriano et al., 2019), automated identification of regional lake-effect days to yield a usable historical data set is rare. Most recently, Hartnett (2021) identified snowstorms within the daily snowfall record of stations east of Lake Ontario, and used a manual scheme to classify each storm as directly associated with a mid-latitude cyclone or not. Storms not directly related to a cyclone, including lake-effect storms, were identified for the period 1985–2015. Given the manual nature of the classification methodology, the results are necessarily for a relatively small region of central New York state, and the storm classification data are not publicly accessible. Classification data from the two TSI-based studies that focus on lake-effect snowfall (Ellis and Leathers, 1996; Suriano and Leathers, 2017a) are not publicly accessible, nor are the data from the two studies that include lake-effect snowfall as an element of their classification results—study of the Catskill Mountains region of south-central New York state (Suriano et al., 2019) and study of the broader northeastern United States (Karmosky, 2007). At the opposite end of the temporal spectrum, case-study analyses of individual lake-effect storms or seasons abound (e.g., Kristovich et al., 2017).

The primary objective of this study is to present justified blends of the results of the TSI and SSC methodologies for identifying lake-effect days within the eastern Great Lakes region. Complementary analysis of the two lake-effect products aims to illustrate their differences, but rationalize their integration. The secondary purposes of the study are to characterize the lake-effect hydroclimate of the region through the study period using the blended datasets, and to render the full hybrid data set of historical lake-effect days accessible.

MATERIALS AND METHODS

Comparative Analysis

The daily lake-effect calendars generated using the TSI and SSC methodologies were provided by the authors of the prior studies (Suriano and Leathers, 2017a; Ellis et al., 2021) and were aligned for comparison. Three groups of days are analyzed—the 742 lake-effect days identified as such by both methods, the 1,330 TSI lake-effect days unsupported by the SSC method, and the 794 SSC lake-effect days unsupported by the TSI method. TSI-only days are those for which the synoptic atmospheric flow suggests lake-effect, but air mass modification does not, while the opposite is the case for SSC-only days. From the TSI methodology, we chose not to include days from what Suriano and Leathers (2017a) deemed the "lake-enhanced" synoptic pattern, when moisture input from the lakes may have enhanced a mid-latitude weather system that produced precipitation on a broader scale.

We examined the 51-year time series of the annual fraction of lake-effect days for which the two methods agree and disagree for changes in the relationship between the two data sets through time, using Sen's slope estimator to calculate trend magnitude and the Mann-Kendall test to establish significance. We also segregated lake-effect days by month to identify dataset differences intra-seasonally. As the TSI yields multiple synoptic pattern types conducive to lake-effect precipitation, we

determined the distribution of conflicting lake-effect days by TSI synoptic pattern to identify any obvious outlier in the level of agreement with the SSC methodology.

To assess disagreement between the two lake-effect data sets in terms of the synoptic atmosphere, we generated composites of sea-level pressure and 850 hPa air temperature from lake-effect days identified by both methods, and from lake-effect days identified by each method that were uncorroborated by the other method. North American Regional Reanalysis (NARR) data (Mesinger et al., 2006) were used to create gridded regional composites (∼0.3° latitude × 0.3° longitude). The data were accessed through the United States Earth System Research Laboratory Physical Sciences Division's compositing platform (https://psl.noaa.gov/cgi-bin/data/narr/plotday.pl). We used the gridded composite data to create contour maps, focusing on the sea-level pressure pattern as the most distinct synoptic-scale variable associated with cool season lake effects (Ellis et al., 2021), but supplemented by 850 hPa air temperature when prudent, given its importance in the TSI-based methodology of Suriano and Leathers (2017a). A caveat is that NARR data extend back only to 1979, but we believe that the ∼37-year record (January 1979 through April 2015) is of sufficient length for depicting mean atmospheric conditions, particularly given the advantage of a finer spatial resolution compared to other similar products of longer record.

We further evaluated the three sets of lake-effect days (TSI+SSC, TSI-only, and SSC-only) by portraying the magnitude and spatial pattern of precipitation frequency derived from the station-level Global Historical Climate Network (GHCN)-Daily database of the National Centers for Environmental Information (NCEI) (https://www.ncei.noaa.gov/products/land-based-station/global-historical-climatology-network-daily). All data within the GHCN-Daily database are subject to a suite of NCEI reviews before inclusion, forming one of the most complete repositories of *in-situ* precipitation data available (Menne et al., 2012). To focus on the area around the eastern Great Lakes, we identified 403 United States and Canadian stations within a region from 74° to 84° west longitude and from 39° to 46° north latitude (**Figure 1**). Requiring 90% data completeness for each of the three sets of lake-effect days reduced the number of stations to 298 (**Figure 1**). For each set of lake-effect days, the percentage of days with precipitation was calculated for each station, and the resulting station-level data were gridded to a resolution of ∼0.5° latitude × 0.5° longitude grid to create mapped contours. The spatial pattern of precipitation frequency is most relevant for synoptic setup-defined lake-effect days (i.e., TSI-defined days), as the synoptic patterns are characterized as conducive to precipitation (Suriano and Leathers, 2017a). Still, a lake-effect spatial pattern depicted by the frequency of precipitation occurrence, even if weak, is anticipated to be evident for air mass modification-defined lake-effect days (i.e., SSC-defined days), despite their representation of air mass modification by the lakes rather than precipitation generation. The spatial pattern of precipitation frequency for each set of lake-effect days allows for an objective verification of lake effects across the different sets of days.

Hybrid Data Set Analysis

Results of the comparative analysis of the TSI- and SSC-based data sets supported their blending to create two hybrid data sets for analysis and dissemination. The "absolute" data set consists of days for which the methods agree are lake-effect days. The "hybrid" data set includes the days of agreement plus all days identified by one method but not the other, or what we term synoptic-defined (TSI, not SSC) and air mass modification-defined (SSC, not TSI). Replicating the approach of Ellis et al. (2021), we analyzed time series of lake-effect day occurrence graphically and with computation of the Sen's Slope estimator and Mann-Kendall significance test, while also testing the difference in the populations of lake-effect day frequency for the early and late halves of the record using a two-sample *t*-test. To portray the cool-season lake-effect hydroclimate across the region, we characterized station-level precipitation on lake-effect days using the array of GHCN-Daily stations. For each station, we computed mean seasonal lake-effect values of precipitation amount, precipitation frequency, and the percentage of seasonal precipitation and precipitation frequency attributed to lake-effect days. As outlined earlier, we gridded the derived data and generated mapped contours. Replicating the method of Ellis et al. (2021), we created mean regional values for each of the hydroclimate variables using 45 of the GHCN-Daily stations. The stations are within 160 km (100 mi) downwind of each of the lakes, and represent the 47 years 1968–69 through 2014–15 so to maximize station density per Ellis et al. (2021). To analyze hydroclimate change, we created time series of the mean regional values (annual seasonal means from the 45 stations) of each of the hydroclimatic variables and applied the aforementioned statistical tests for trend through the record and for difference between the temporal halves of the record.

RESULTS

General Dataset Comparatives

When combined, the two methods yield 2,866 lake-effect days across the 51-year study period, for an average of about 56 per year, or about 31% of the 6-month season. The TSI method identified 2,072 lake-effect days, or an average of about 41 per year with a standard deviation of 9 days. The SSC method identified 1,536 days, or an average of about 30 days per year with a standard deviation of 9 days. The two methods agree on 742 days, or 35.8% of TSI lake-effect days and 48.5% of those identified by the SSC method. The annual frequencies of lake-effect days from the two methods covary, with a Pearson pairwise correlation value of 0.51 ($p < 0.01$). The percentage of annual lake-effect days ($n = 2{,}866$) for which the methods agree ($n = 742$) does not exhibit a statistically significant trend. The same is true when segregating the data into the sub-seasonal periods November (early-season), December through February (mid-season), and March/April (late-season), which align with the TSI seasons of Suriano and Leathers (2017a). Likewise, the percentage of TSI-defined lake-effect days ($n = 2{,}072$) supported by the SSC methodology ($n = 742$) is not characterized by a statistically significant trend, either seasonally or sub-seasonally. However, the percentage of SSC-defined lake-effect days ($n =$

TABLE 1 | For lake-effect days identified by the TSI method, SSC method, and the methods combined (TSI/SSC), the monthly distribution, the percentage of seasonal days occurring within each month, and the percentage of days each month that are supported by the other method (TSI, SSC), or by both methods (TSI/SSC), 1964–65 through 2014–15.

Month	TSI			SSC			TSI/SSC		
	nDays	Percent of total	Percent agree	nDays	Percent of total	Percent agree	nDays	Percent of total	Percent agree
November	466	22.5	19.1	145	9.4	61.4	522	18.2	17.0
December	381	18.4	41.5	317	20.6	49.8	540	18.8	29.3
January	614	29.6	42.7	427	27.8	61.4	779	27.2	33.6
February	517	24.9	38.7	331	21.6	60.4	648	22.6	30.9
March	80	3.9	35.0	196	12.8	14.3	248	8.7	11.3
April	14	0.7	35.7	120	7.8	4.2	129	4.5	3.9
Total	**2,072**	**100.0**	**35.8**	**1,536**	**100.0**	**48.3**	**2,866**	**100.0**	**25.9**

1,536) supported by the TSI methodology ($n = 742$) exhibits a statistically significant positive trend, indicating increasing validation of SSC days by the TSI methodology. The magnitude of the trend is not large at +0.27 percent year^{-1} ($p = 0.02$), amounting to approximately a 13% change over the course of the 51-year period. While a positive trend in early-season is somewhat evident ($p = 0.10$), the seasonal trend is largely a product of a positive trend of 0.24 percent year^{-1} ($p = 0.04$) in mid-season. There is not a statistically significant trend for the late-season period.

Lake-effect days within one dataset uncorroborated by the other are temporally isolated within the lake-effect calendar. For the 1,330 TSI-defined lake-effect days that do not appear within the SSC data, 68.1% are not preceded or followed by another lake-effect day from either data set, and for only 8.2% of days is there an SSC-only day before or after. For the SSC data set, 77.8% of the 794 SSC-only lake-effect days do not have a lake-effect day from either data set preceding or following, and for only 6.3% of days is there a TSI-only day before or after. Thus, it does not appear that uncorroborated lake-effect days within either data set are commonly associated with a timing difference between data sets. Generally, the days of disagreement appear to be rather uniquely defined by each method.

Intra-seasonal differences between the TSI and SSC data sets are evident within the monthly climatology of lake-effect day frequency. While the percentage of seasonal lake-effect days occurring in mid-season are comparable between the two methods, the TSI method yields a much greater percentage of seasonal lake-effect days in the early-season period than does the SSC method (**Table 1**). The opposite is the case for the late-season period (March–April), when the percentage of seasonal lake-effect days generated by the SSC method is much greater than that for the TSI method (**Table 1**). So, while the TSI method yields more lake-effect days across all months than does the SSC, the two methods fundamentally differ in the shoulder periods of early- and late-season. This is made clear by the fraction of monthly lake-effect days within each data set that are corroborated by the other data set. For the TSI data, ∼40% of lake-effect days in mid-season appear within the SSC data set, and about 35% for the late-season period, but only 19% during the early-season (**Table 1**). For the SSC data, about 60% of lake-effect days in November, January, and February appear in the TSI data set, 50% in December, but only 14% in March and 4% in April (**Table 1**). When the data sets are combined into one record, the percentage of days for which the methods corroborate one another ranges from about 30 to 34% in mid-season, but declines to 17% in early-season, and 11% and 4% in the late-season months of March and April (**Table 1**). Of the 742 lake-effect days upon which the two methods agree, 620 (84%) are within mid-season.

Uncorroborated TSI Data

The greatest number of uncorroborated TSI-defined lake-effect days is in mid-season (December–February), when the rate of corroboration is actually greatest, but the frequency of lake-effect days is also greatest. Conversely, the early-season (November) has the lowest rate of corroboration, yielding a relatively large number of days not supported by the SSC data. There are few TSI-defined lake-effect days in late-season (March–April), with a corroboration rate rivaling that of mid-season, possibly owing simply to a high frequency of SSC-defined lake-effect days in spring relative to the low frequency within the TSI dataset.

There is very little difference in the mean sea-level pressure pattern for TSI-defined lake-effect days corroborated by SSC data (**Figures 3A–C**) and those uncorroborated (**Figures 3D–F**). The classic lake-effect pattern, with a high-pressure center over the central United States and a low-pressure center along the northeastern coastline of North America, is evident for the early- and mid-seasons. In late-season, the high-pressure center is located farther north, while the low-pressure center is farther south, imparting a more north-to-south flow across the eastern Great Lakes than the northwest-to-southeast orientation earlier in the season. However, this pattern is specific to the single TSI synoptic atmospheric setup judged by Suriano and Leathers (2017a) as conducive to lake-effect snowfall in spring. Across the 6-month season it does not appear that uncorroborated TSI-defined lake-effect days are associated with a mean sea-level pressure pattern that is noticeably different from that associated with corroborated days. A feature more subtle than synoptic-scale sea-level pressure, such as lower-atmospheric temperature,

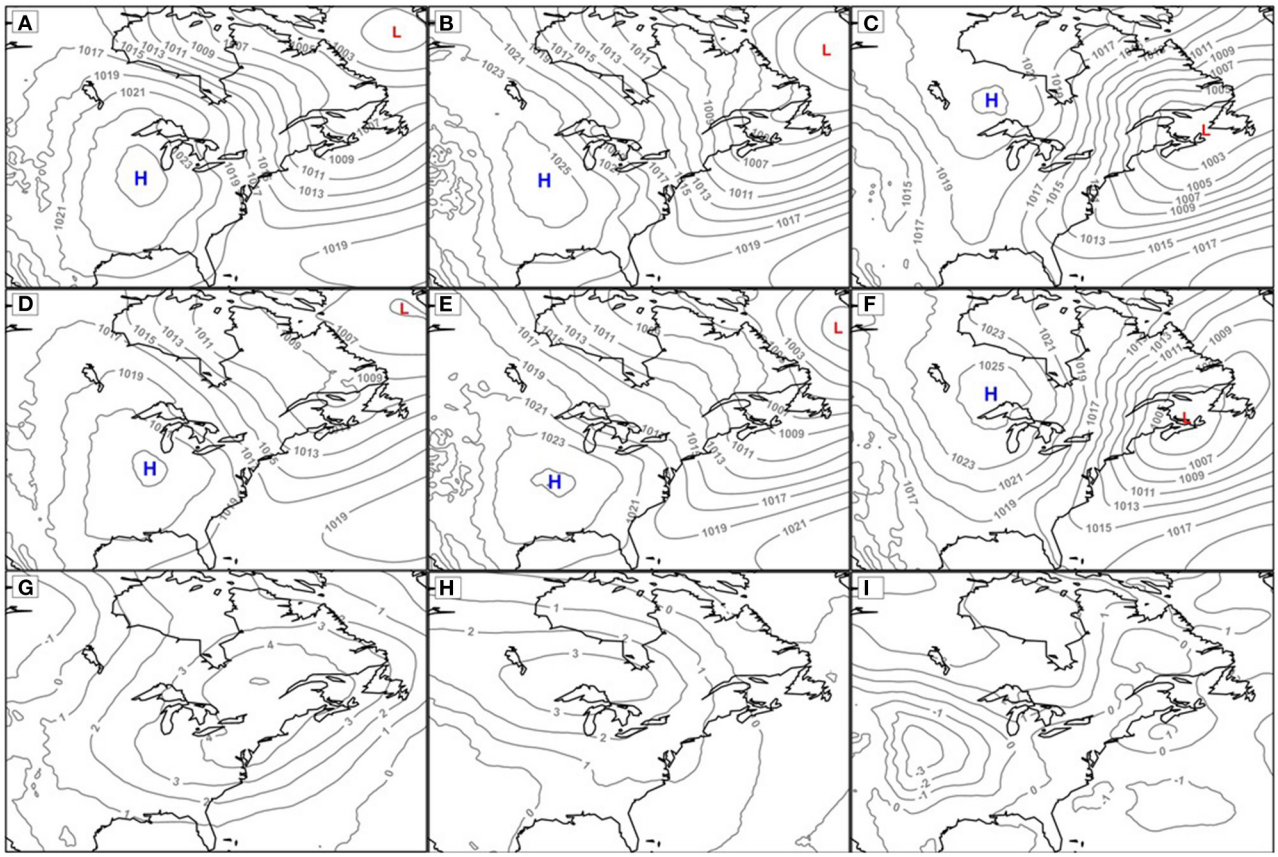

FIGURE 3 | For TSI-defined lake-effect days in early-season (left column), mid-season (middle column), and late-season (right column), mean sea-level pressure (hPa) for days corroborated by SSC data **(A–C)**, mean sea-level pressure for uncorroborated days **(D–F)**, and difference in mean 850 hPa air temperature (°C) on uncorroborated and corroborated days (uncorroborated minus corroborated) **(G–I)**, 1964–65 through 2014–15. Isobars are in 2-hPa intervals, and air temperature differences are in 1°C intervals.

appears to prevent the SSC methodology from matching these TSI-defined lake-effect days.

In their identification of TSI synoptic patterns conducive to lake-effect snowfall, Suriano and Leathers (2017a) based their decisions on several characteristics, the most fundamental being mean sea-level pressure pattern and mean lake surface-to-850 hPa air temperature. By using mean values of variables such as air temperature, it is possible that a synoptic type deemed conducive to lake-effect snowfall includes days that are more marginal than others, enough so that they could be days that the SSC methodology failed to identify. Lending some credence to this is the difference in 850 hPa air temperature between TSI-defined lake-effect days that are corroborated and uncorroborated by SSC data. For November, the mean 850 hPa air temperature for uncorroborated days is more than 4°C warmer than for corroborated days, while for December through February the difference is >2°C (**Figures 3G,H**). The greater mean temperatures on uncorroborated TSI-defined lake-effect days suggest that they are the warmer days within the population of days of each of the lake-effect TSI types for November and December through February. This is not the case for March and April, as there is little difference in mean 850 hPa air temperature for corroborated and uncorroborated TSI-defined lake-effect days (**Figure 3I**).

The element of the SSC definition that prevents corroboration of TSI-defined lake-effect days supports the idea that the intensity of cold air across the region may be a source of methodological disagreement during the early-season. There are three geographic regions for which SSC weather types are examined, together, for determination of a lake-effect day (Ellis et al., 2021). Using four stations immediately east (downwind) of the eastern lakes (**Figure 1**), at least one station must be of the moist-polar (MP) or transition (TR) (onset or demise of lake-effects) weather type, and all others of the dry-polar (DP) type. Within a region north (upwind) of the eastern lakes (**Figure 1**), at least two of four stations must be of the dry-polar (DP) weather type. Lastly, within a region along the northeastern United States coastline (well-downwind) (**Figure 1**), at least two of four stations must be of the dry-polar (DP) or transition (TR) (cold front passage) weather type. If the criterion of any one region fails, the day is identified as a non-lake-effect day. For the 1,330 TSI-defined

lake-effect days not identified as such by the SSC methodology, there are a total of 2,124 causes of failure among the three regions used to define an SSC lake-effect day, of which 39.5% stem from the lake-effect region, 31.2% from the northern region, and 29.3% from the eastern region. While a polar weather type is a requirement for all three regions (expansive cold air), the lake-effect region also requires evidence of a lake influence on humidity [moist-polar (MP)], whereas the presence of cold, dry air is the primary criterion in the northern and eastern regions. When segregating the causes of failure to corroborate a TSI-defined lake-effect day by month, the proportion attributed to the lake-effect region increases through the season, while that for the northern and eastern regions decreases through the season. This pattern is even more pronounced when focusing on the instances for which the criterion in only one region caused the failure of the SSC to corroborate a TSI-defined lake-effect day, which is to say, those days that were very close to meeting the SSC definition. Out of 586 such cases (44.1% of 1,330 TSI-only lake-effect days), 47.1% stemmed from the lake-effect region, 29.9% from the northern region, and 23% from the eastern region. The attribution of monthly instances to the lake-effect region increases through the season, while those attributed to the northern and eastern regions decrease through the season.

It appears that violating the cold air requirement within the eastern and northern regions of the SSC methodology on TSI-defined lake-effect days is more likely during the first half of the season, becoming much less likely in late-season. The lack of sufficiently cold air is also likely the case for definition violations stemming from the lake-effect region, but lack of a lake-effect in the form of increased humidity contributes, likely producing the greater fraction of definition violations later in the season. These patterns are logical, as marginally-cold air masses passing over the lakes are more likely in the warmer early portion of the season, and marginally-humidified air through interaction with the lakes is more likely late in the season due to reduced lake temperatures and ice cover. However, the propensity for more early-season violations of the SSC methodology on TSI-defined lake-effect days may also stem from the humidity aspect of the cold, dry air requirement at the SSC stations north of the lakes.

For lake-effect days identified by both methods, the percentage of days with precipitation across the region is greatest, spatially, to the lee of the eastern lakes in early-season (60–70%) (**Figure 4A**), mid-season (60–70%) (**Figure 4B**), and late-season (50–70%) (**Figure 4C**). For TSI-defined days uncorroborated by SSC data, slightly smaller percentages (50–60%) are evident to the lee of the lakes in early-season (**Figure 4D**) and mid-season (**Figure 4E**). The contrast is greater for uncorroborated days in late-season—only about 30–40% of the days are characterized by precipitation to the lee of the lakes (**Figure 4F**). For the TSI-defined days that are uncorroborated by SSC data, slightly higher percentages of days with precipitation are evident in the region north of the eastern Great Lakes in early-season (**Figure 4D**) and mid-season (**Figure 4E**), compared to days corroborated by SSC data (**Figures 4A,D**). This is not the case in late-season (**Figure 4F**). Days with precipitation in this area north of the lakes, possibly associated with the departing low-pressure center to the northeast (**Figures 3D,E**) or sourced from the western lakes, are likely classified as something other than the dry-polar (DP) weather type by the SSC methodology, violating the SSC-based definition of a lake-effect day.

As the TSI methodology generalizes the atmospheric pattern for the region using conditions at one station, and also generalizes the conduciveness for lake-effect snowfall based on the mean lower-atmospheric characteristics of each synoptic pattern type and mean monthly lake temperature, it is reasonable to believe that some days within a TSI synoptic type do not satisfy the criteria established by Suriano and Leathers (2017a). This is not to say that these are exclusively the days that lack corroboration by the SSC method, as the SSC method is limited and aims at a slightly different objective. Further, of the 1,330 TSI-defined lake-effect days that do not appear in the SSC data for the eastern lakes, 454 (34%) were classified as western lakes lake-effect days within the SSC methodology (Ellis et al., 2021), adding credence to those TSI-defined lake-effect days. While the results here help to rationalize the uncorroborated TSI-defined lake-effect days, they neither explicitly confirm nor deny that they should be included in the TSI-defined lake-effect data set.

Uncorroborated SSC Data

While the TSI methodology yields a greater number of lake-effect days than are within the SSC data set, there are 794 SSC-defined days that do not appear in the TSI data set. Most (455 days, or 57.3%) are in mid-season (December–February), while the fewest are in early-season (November) (56 days, or 7.1%), when the SSC method yields a much smaller proportion of seasonal lake-effect days than does the TSI method. The opposite is true in late-season (March–April), when a much greater fraction of seasonal SSC-defined days occurs relative to the TSI dataset. As such, 35.6% (283 days) of the SSC-defined lake-effect days not corroborated by TSI data occur during the late-season.

While Suriano and Leathers (2017a) defined only seven TSI synoptic atmospheric patterns as conducive to lake-effect snowfall, the 794 SSC-defined lake-effect days uncorroborated by TSI data are distributed across 28 other TSI types. Of the six types that each account for at least 5% of the 794 days, four are mid-season TSI types and two are spring types. Of the other 22, nine each account for <1% of the days. The mean sea-level pressure patterns from the 56 SSC-defined lake-effect days in early-season that are uncorroborated by TSI data (**Figure 5A**) and the 455 days in mid-season (**Figure 5B**) are broadly typical of that for lake effects (e.g., **Figures 3A,B**), except that the center of high-pressure is not optimally positioned to foster strong low-level cold-air advection across the Great Lakes region. This is evident in the weak sea-level pressure gradient across the eastern lakes within the composites. The patterns apparently support the necessary expanse of the dry-polar (DP) weather type required by the SSC methodology, but lake-effects are likely subtler under these patterns—enough to yield the moist-polar (MP) and/or transition (TR) weather types within the lake-effect region, but likely not enough to generate

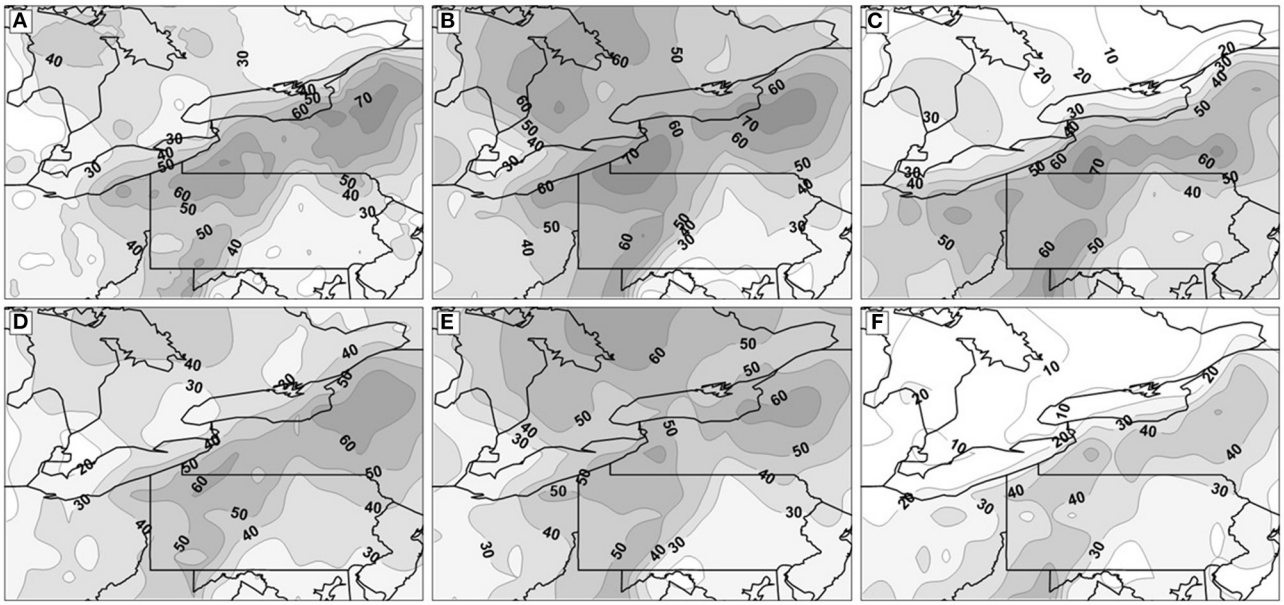

FIGURE 4 | Percentage of lake-effect days with precipitation in early-season (left column), mid-season (middle column), and late-season (right column) for days identified by both TSI and SSC methods **(A–C)**, and for TSI-defined days uncorroborated by SSC data **(D–F)**, 1964–65 through 2014–15. Contours are in 10% intervals.

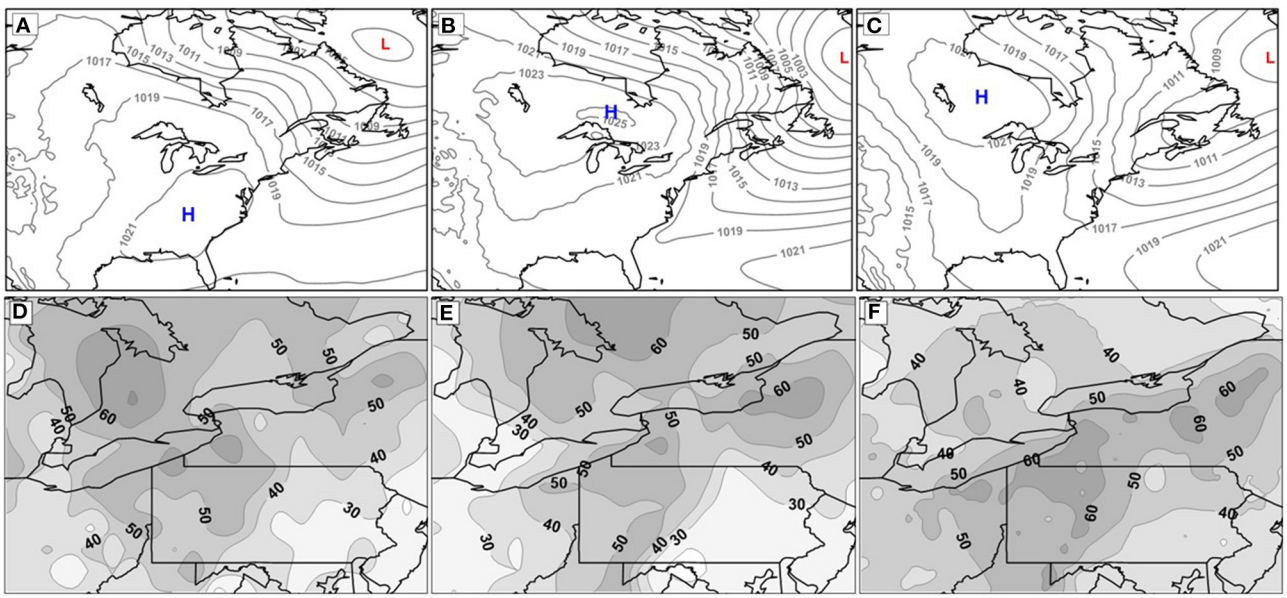

FIGURE 5 | Mean sea-level pressure (hPa) **(A–C)** and percentage of days with precipitation **(D–F)** for SSC-defined lake-effect days in early-season (left column), mid-season (middle column), and late-season (right column) uncorroborated by the TSI data set, 1964–65 through 2014–15. Isobars are in 2-hPa intervals, and percentage contours are in 10% intervals.

snowfall per the objective of the TSI method. For the 283 SSC-defined lake-effect days in late-season not supported by the TSI data, the mean sea-level pressure pattern (**Figure 5C**) closely resembles that for days in which the methods agree (**Figure 3C**), although with a weaker gradient across the eastern lakes. Given the similar pattern, and the lack of lake-effect days generated by the TSI method in late-season, it is most likely that cooler lakes and greater ice coverage is enough to limit lake-effect snowfall (TSI) despite some modification of the passing lower-atmosphere (SSC).

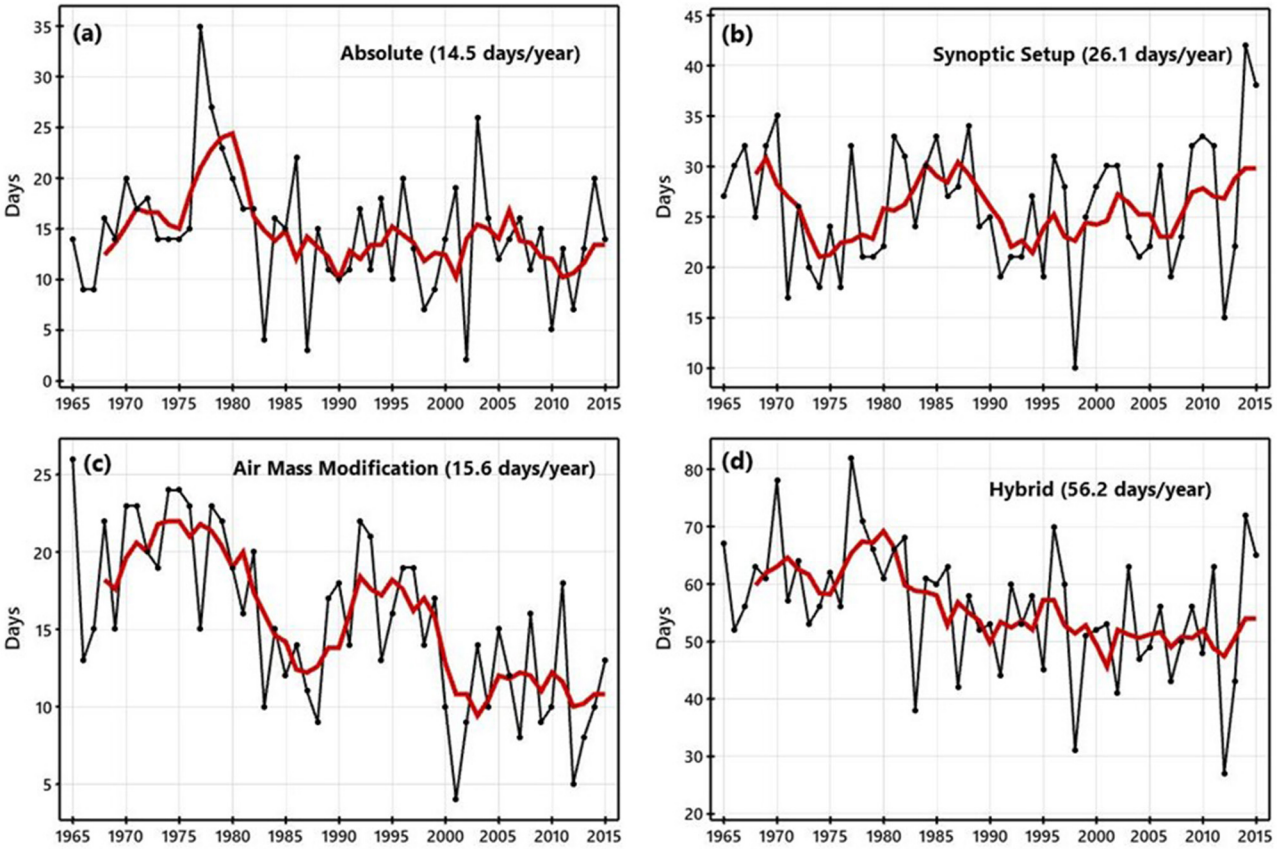

FIGURE 6 | Time series of seasonal lake-effect frequency (days) for absolute lake-effect days **(a)**, synoptic setup-defined days **(b)**, air mass modification-defined days **(c)**, and for the three classes combined (hybrid) **(d)** for the period 1964–65 through 2014–15. The red line is a 5-year running mean. The period of record annual mean for each is indicated.

Aligning with the sea-level pressure patterns are the percentages of uncorroborated SSC-defined lake-effect days with precipitation. For early-season (**Figure 5D**) and mid-season (**Figure 5E**), values west of the eastern lakes, while relatively small, are comparable to those to the east of the lakes. This is presumably due to the relatively weak flow of cold air across the region (**Figures 5A,B**), yielding a subtler lake effect (modified air) without the unidirectional nature of classic lake-effect precipitation. The more typical lake-effect pressure pattern in late-season (**Figure 5C**) aligns with higher precipitation percentages in the traditional lake-effect areas south and east of the eastern lakes (**Figure 5F**), although values to the west of the lakes remain relatively high compared to SSC days corroborated by TSI data (**Figure 4C**).

As with uncorroborated TSI-defined lake-effect days, there is not convincing evidence for declassifying the lake-effect days within the SSC data set that are not among those in the TSI data. Rather, their intra-seasonal distribution and the combination of their mean synoptic-scale atmospheric pressure pattern and predominant precipitation pattern seem to illustrate the different objective of the SSC method compared to the TSI method. This makes integration of their results for a more thorough representation of historical daily lake-effects reasonable.

Merged Data

In combining the two lake-effect data sets, we chose to honor the objective of each of the methodologies by retaining all days within each, creating one "absolute" and one "hybrid" data set. Absolute data are only days identified by both methods, or what are likely the most obvious occurrences of lake-effects. Supporting the idea that absolute days are most robust is the lesser degree to which they are temporally isolated. Whereas, only 31.9 and 22.2% of TSI-only days and SSC-only days, respectively, are preceded or followed by a lake-effect day of any type, 54.8% of absolute lake-effect days are preceded or followed by a lake-effect day. Added to the absolute lake-effect days to create the hybrid data set are days identified by one method that are uncorroborated by the other method. In other words, the hybrid data set consists of days of agreement, TSI-only days, or what we term "synoptic setup" days, and SSC-only days, or what we term "air mass modification" days.

Seasonally, absolute lake-effect days average 14–15 per year, exhibiting an insignificant decline of -0.8 days decade^{-1} ($p = 0.09$) (**Figure 6a**), and averaging nearly 16 days per season through the first 25 years of the record and about 13 days per season over the final 25 days of the record. On average, 26 synoptic setup-defined days occur each season (**Figure 6b**), while only 15–16 air mass modification-defined days occur each year,

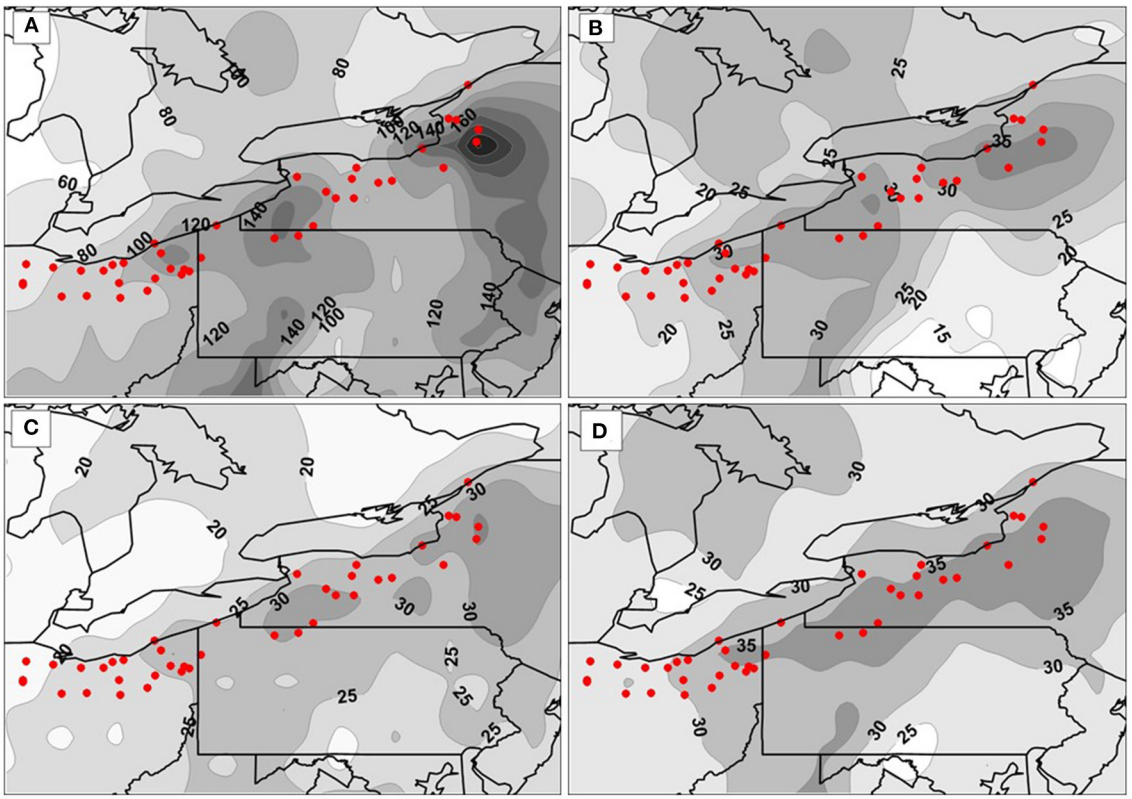

FIGURE 7 | Station-level values of mean seasonal precipitation (liquid; mm; 20 mm intervals) **(A)**, precipitation frequency (days; 5-day intervals) **(B)**, percentage of seasonal precipitation (liquid; 5% interval) **(C)**, and percentage of seasonal precipitation frequency (5% interval) **(D)** associated with the lake-effect days of the hybrid data set, 1964–65 through 2014–15. Red dots indicate locations of stations used to calculate regional values.

but with a statistically significant decline of 2.3 days decade^{-1} ($p < 0.01$) (**Figure 6c**). Two-sample *t*-test results illustrate a significant difference ($p < 0.01$) between the occurrence of air mass modification days during the first 25 years (mean = 18 days) and final 25 years (13 days) of the record. The cumulative expression of the three sets of data, the hybrid data set, averages about 56 days per year, but with a statistically significant decline in frequency over the study period of 2.8 days decade^{-1} ($p < 0.01$) that appears most pronounced from the late-1970s through the early-2000s (**Figure 6d**). Over the first 25 years of the record, the hybrid data set averages about 60 days per year, while averaging only 52 days per year over the final 25 years of the record (two-sample *t*-test $p < 0.01$).

Focusing on the hybrid data set, the mean amount of seasonal precipitation attributed to lake-effect days ranges from about 120–160 mm east of Lake Erie, and 120–220 mm east of Lake Ontario (**Figure 7A**). The mean seasonal frequency of precipitation follows a similar spatial pattern, with values from 25 to 30 days east of Lake Erie and 30–35 days east of Lake Ontario (**Figure 7B**). The mean percentage of total seasonal precipitation attributed to lake-effect days ranges from 25 to 30% east of Lake Erie, and is about 30% to the north, east of Lake Ontario (**Figure 7C**). Similarly, the mean percentage of total seasonal precipitation frequency attributed to lake-effect days is about 35% to the east of each of the lakes (**Figure 7D**). Values attributed to the absolute data set (not shown) follow the same spatial patterns, but obviously of much smaller magnitudes, given the much smaller population of absolute lake-effect days compared to hybrid days.

Calculated from the 45 lake-effect stations to the lee of the lakes (**Figure 7**), regional mean seasonal values of precipitation characteristics attributed to days within the hybrid data set generally exhibit a decline over the 47-year period 1968–69 through 2014–15 (**Figure 8**). This is despite no change in total seasonal precipitation (all days, regardless of lake effect)—small, statistically insignificant increases in both precipitation and precipitation frequency. For the region, mean seasonal precipitation (liquid amount) on days within the hybrid data set declined at a rate of 7.8 mm decade^{-1} ($p = 0.02$), while also appearing to become more variable in recent years (**Figure 8a**). However, a two-sample *t*-test reveals no statistically significant difference in seasonal precipitation during the first (mean = 124 mm year^{-1}) and last (mean = 119 m year^{-1}) 23 years of the record. So, while a trend is present, the broad change in precipitation is not significant. Likewise, a decline in regional mean seasonal precipitation frequency within the hybrid data set (−1.3 days decade^{-1}) (**Figure 8b**) is statistically significant

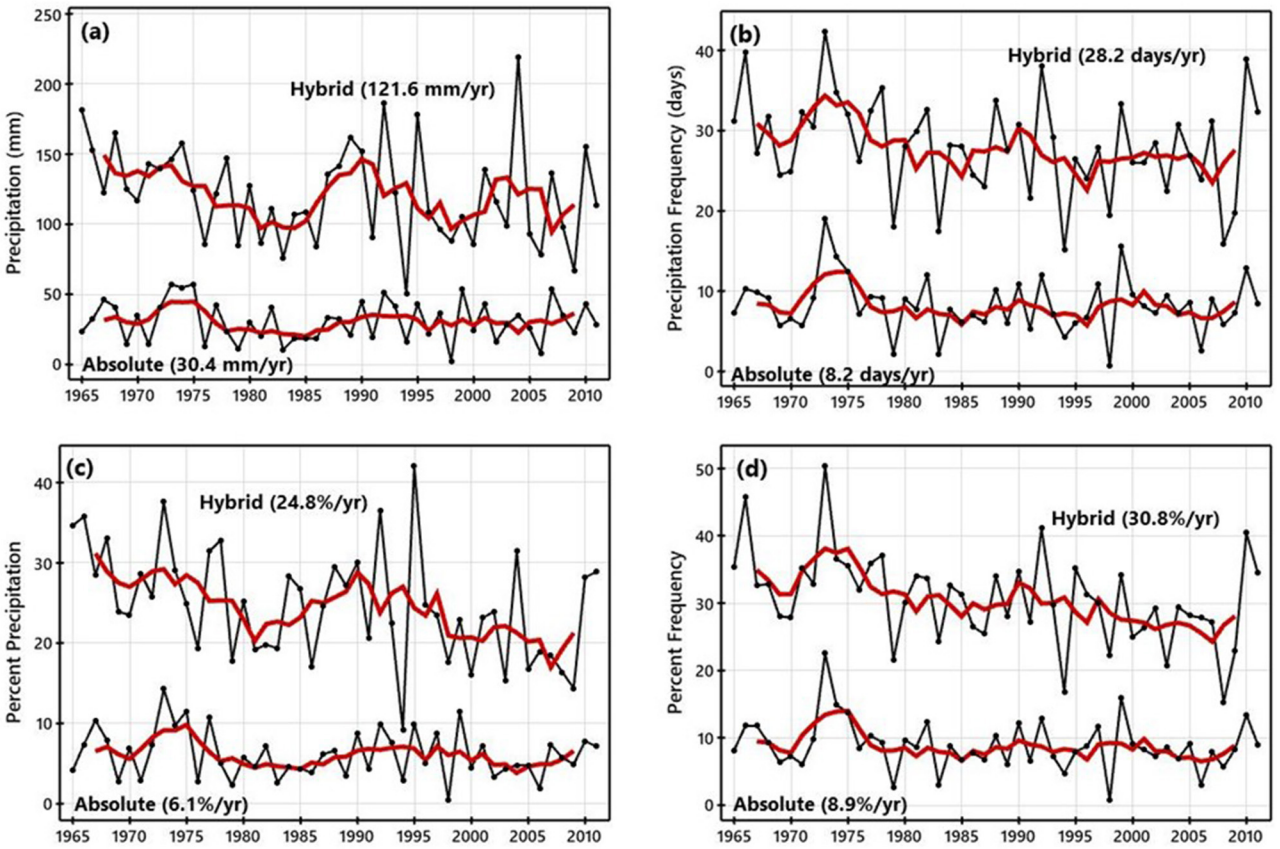

FIGURE 8 | For the 45 precipitation stations **(Figure 7)**, regional mean seasonal values of precipitation **(a)**, precipitation frequency **(b)**, percent of seasonal precipitation **(c)**, and percent of seasonal precipitation frequency **(d)** attributed to days within the hybrid and pure data sets for the period 1968–69 through 2014–15.

($p = 0.04$), but the frequency for the early years (mean = 29 days year^{-1}) is not statistically significantly different than the frequency for the late years (mean = 26 days year^{-1}). More evident are changes in the percentage of seasonal precipitation and precipitation frequency attributed to days within the hybrid data set. The mean regional fraction of seasonal precipitation (**Figure 8c**) decreased at a rate of 2.2 percent decade^{-1} ($p < 0.01$), but values from the early and late portions of the record are not statistically significantly different [mean = 26% year^{-1} early, 23% year^{-1} late ($p = 0.10$)]. However, for the percent of seasonal precipitation frequency (**Figure 8d**), both the trend (−2.0 percent decade^{-1}, $p < 0.01$) and the difference in early and late values [mean = 33% year^{-1} early, 29% yr^{-1} late ($p = 0.03$)] reflect statistically significant declines. Within the absolute data set, none of the variables exhibited a statistically significant change. This is not surprising, given the rather small values and limited variability within the data (**Figure 8**).

DISCUSSION

The two methods for identifying lake-effect days within the historical record differ in the degree of the lake-effect that they aim to recognize. The TSI method is designed to find days with a broad synoptic-scale pattern that yields strong, cold flow across the Great Lakes region conducive to lake-effect snowfall. The SSC-based method aims to identify days with a signature of air mass modification by the lakes, such that a broad cold, dry air mass across the greater region contains cold, moist air specifically within the traditional lake-effect areas. While the methods overlap, the TSI method likely finds additional days with stronger atmospheric dynamics that yield a regional arrangement of air masses that may not fit the ideal lake-effect model, while the SSC method likely finds additional days with weaker dynamics and a subtler lake effect that may not yield a profound weather impact. We submit that combining the two data sets yields a more thorough record of daily instances of lake-effects from Lakes Erie and Ontario for the cool seasons 1964–65 through 2014–15.

Two main caveats accompany the merged data. The first is the trend toward increasing validation of SSC-defined lake-effect days by the TSI method, particularly in mid-season. This coincides with a trend toward fewer SSC-defined lake-effect days in recent decades (Ellis et al., 2021), possibly indicating that the frequency trend partly reflects a decline in more marginal lake-effect days as defined by the SSC method—those not supported by the TSI method. Otherwise, there is not

an obvious explanation for the trend, as neither methodology was applied differently through the record, and the quality of the input data for each methodology should not have changed gradually through time. While merely speculative, it is possible that the pervasive warming of recent years is enough for the SSC methodology to increasingly classify a day as of a moderate weather type rather than a polar type (i.e., dry-moderate/moist-moderate rather than dry-polar/moist-polar). This would impact the methodology for establishing SSC-defined lake-effect days, possibly shedding marginal days (moderate rather than polar) so to increase the fraction validated by the TSI method. To investigate this theory would require intensive analysis of the mechanics of the SSC methodology, which is beyond the scope of this study. However, this is a caution, or possibly a limitation, accompanying the data set.

The second caveat with the merged data is the greater discrepancy between the two contributing data sets within the shoulder periods of the November through April season than during mid-season. The rationale for the greater frequency of SSC-defined lake-effect days in late-season (March/April) relative to the few TSI-defined days is rather clear. By late-season, lake temperatures have lowered and ice-coverage has increased, making the generation of lake-effect snowfall more difficult, which is realized in fewer TSI-defined lake-effect days. However, lake-influence is quite possibly great enough to raise the humidity of the passing cold, dry air and influence the weather type within the SSC data set to yield an SSC-defined lake-effect day. Less clearly rationalized is the greater frequency of TSI-defined lake-effect days in early-season (November) relative to the fewer SSC-defined days. As indicated by the comparative analysis of the data sets, it seems probable that while a synoptic flow pattern in November suggests lake-effect (TSI), the cold air may be more marginal (i.e., moderate, rather than dry-polar or moist-polar), in magnitude and/or spatial extent, so to not satisfy the SSC definition. Ellis et al. (2021) considered the possibility of the lakes modifying air temperature enough to alter the dry-polar weather type upstream to the moist-moderate weather type downstream, rather than the moist-polar type, as required by the SSC methodology. However, they did not choose to implement weather type modification based on air temperature within their methodology.

The hybrid data set produced here yields seasonal values of lake-effect frequency and precipitation that align well with previously published estimates. As a merger of the data sets produced by Suriano and Leathers (2017a) and Ellis et al. (2021), there is greater meaning from a comparison with the results of other studies. In developing a method for classifying snowstorm types for an area east of Lake Ontario, Hartnett (2021) found lake-effect snowstorms to account for 35% of snowstorms, yielding ∼24 lake-effect snowfall days per year and 39% of seasonal snowfall for the period 1985–2015. This compares well with mean regional values from the hybrid data set – 30-35 lake-effect precipitation days per year that account for about 30% of seasonal liquid total precipitation (in all forms), the latter of which maximizes at about 35% across the area of Hartnett's study. Karmosky (2007) attributed ∼35% of seasonal snowfall immediately east of eastern lakes to lake effects, declining to <25% when ∼100 km inland. Suriano et al. (2019) determined that an average of 28 lake effect days per year produce 38% of seasonal total snowfall farther east in the Catskill Mountains region well to the east of Lake Ontario. The declining trend in lake effects from the late 1970s through the early 2000s portrayed by the hybrid data set matches the findings of several studies (e.g., Hartnett et al., 2014; Suriano and Leathers, 2017b; Ellis et al., 2021). Given the historical prominence of lake-effect precipitation within the cool-season hydroclimate of the region, a continued decline in the frequency of lake effects, or even the establishment of the lower frequency as a new normal, has acute implications for the regional hydroclimate.

The merged data, we believe, can serve further research efforts focused on the lake effects of the eastern Great Lakes. Forecasting lake-effect precipitation, either seasonally or for individual events, remains challenging, and the impact of a changing climate on the role of lake-effects within the regional hydroclimate is complex. The calendars of hybrid and absolute lake-effect days merged from the two methodologies provide a more comprehensive collection of lake-effect days for analysis of any form. To serve pursuit of a better understanding of lake effects in the region, the hybrid, absolute, synoptic setup-defined, and air mass modification-defined lake-effect calendars are available through the University Libraries data portal of Virginia Tech (https://doi.org/10.7294/16712872).

DATA AVAILABILITY STATEMENT

The datasets presented in this study can be found in online repositories. The names of the repository/repositories and accession number(s) can be found below: https://doi.org/10.7294/16712872.

AUTHOR CONTRIBUTIONS

AE and ZS collaboratively developed the design for this study and authored elements of the manuscript. ZS conducted initial comparative analysis of TSI lake-effect data with SSC data, while AE conducted initial comparative analysis of SSC lake-effect data with TSI data. AE constructed synoptic composites and conducted climatological precipitation analyses. All authors contributed to the article and approved the submitted version.

ACKNOWLEDGMENTS

The authors acknowledge Mr. Reggie Wortman, University of Nebraska Omaha, for help with data access and distillation.

REFERENCES

Andresen, J. A. (2012). "Historical climate trends in Michigan and the Great Lakes region," in *Climate Change in the Great Lakes Region*, eds. T. Dietz and D. Bidwell (Lansing, MI: Michigan State University Press), 17–34.

Ellis, A. W., and Leathers, D. J. (1996). A synoptic climatological approach to the analysis of lake-effect snowfall: potential forecasting applications. *Weather Forecast*. 11, 216–229. doi: 10.1175/1520-0434(1996)011<0216:ASCATT>2.0.CO;2

Ellis, A. W., Marston, M. L., and Bahret, J. (2021). Changes in the frequency of cool season lake effects within the North American Great Lakes region. *Ann. Am. Assoc. Geogr*. 111, 385–401. doi: 10.1080/24694452.2020.1785270

Hartnett, J. J. (2021). A classification scheme for identifying snowstorms affecting central New York State. *Int. J. Clim*. 15, 1712–1730. doi: 10.1002/joc.6922

Hartnett, J. J., Collins, J. M., Baxter, M. A., and Chambers, D. P. (2014). Spatiotemporal snowfall trends in central New York. *J. Appl. Meteor. Clim*. 53, 2685–2697. doi: 10.1175/JAMC-D-14-0084.1

Holroyd, E. W. III. (1971). Lake effect cloud bands as seen from weather satellites. *J. Atmos. Sci*. 28, 1165–1170. doi: 10.1175/1520-0469(1971)028<1165:LECBAS>2.0.CO;2

Kalkstein, L. S., and Corrigan, P. (1986). A synoptic classification approach for geographical analysis: assessment of sulfur dioxide concentrations. *Ann. Assoc. Am. Geogr*. 76, 381–395. doi: 10.1111/j.1467-8306.1986.tb00126.x

Karmosky, C. (2007). *Synoptic Climatology of Snowfall in the Northeastern United States: An Analysis of Snowfall Amounts From Diverse Synoptic Types*. Master's Thesis, University of Delaware, Newark, DE. Available at: ProQuest Dissertations and Theses Global. (304860693). Retrieved from: http://login.ezproxy.lib.vt.edu/login?url=https://www.proquest.com/dissertations-theses/synoptic-climatology-snowfall-northeastern-united/docview/304860693/se-2?accountid=14826 (accessed September 17, 2021).

Kristovich, D. A. R., Clark, R. D., Frame, J., Geerts, B., Knupp, K. R., Kosiba, K. A., et al. (2017). The Ontario winter lake-effect systems campaign: scientific and educational adventures to further our knowledge and prediction of lake-effect storms. *Bull. Am. Meteorol. Soc*. 98, 315–332. doi: 10.1175/BAMS-D-15-00034.1

Menne, M. J., Durre, I., Vose, R. S., Gleason, B. E., and Houston, T. G. (2012). An overview of the Global Historical Climatology Network-Daily Database. *J. Atmos. Oceanic Technol*. 29, 897–910. doi: 10.1175/JTECH-D-11-00103.1

Mesinger, F., Dimego, G., Kalnay, E., Mitchell, K., Shafran, P. C., Ebisuzaki, W., et al. (2006). North American regional reanalysis. *Bull. Am. Meteorol. Soc*. 87, 343–360. doi: 10.1175/BAMS-87-3-343

Notaro, M., Holman, K., Zarrin, A., Vavrus, S., and Bennington, V. (2013). Influence of the Laurentian Great Lakes on regional climate. *J. Clim*. 26 789–804. doi: 10.1175/JCLI-D-12-00140.1

Scott, R. W., and Huff, F. A. (1996). Impacts of the Great Lakes on regional climate conditions. *J. Great Lakes Res*. 22, 845–863. doi: 10.1016/S0380-1330(96)71006-7

Sheridan, S. C. (2002). The redevelopment of a weather-type classification scheme for North America. *Int. J. Clim*. 22, 51–68. doi: 10.1002/joc.709

Suriano, Z. J., and Leathers, D. J. (2017a). Synoptic climatology of lake-effect snowfall conditions in the eastern Great Lakes region. *Int. J. Clim*. 37, 4377–4389. doi: 10.1002/joc.5093

Suriano, Z. J., and Leathers, D. J. (2017b). Synoptically classified lake-effect snowfall trends to the lee of Lakes Erie and Ontario. *Clim. Res*. 74, 1–13. doi: 10.3354/cr01480

Suriano, Z. J., Leathers, D. J., Hall, D. K., and Frei, A. (2019). Contribution of snowfall from diverse synoptic conditions in the Catskill/Delaware Watershed of New York State. *Int. J. Clim*. 39, 3608–3618. doi: 10.1002/joc.6043

Conflict of Interest: The authors declare that the research was conducted in the absence of any commercial or financial relationships that could be construed as a potential conflict of interest.

frontiers in Water

ORIGINAL RESEARCH
published: 04 March 2022
doi: 10.3389/frwa.2022.782910

The Contribution of Lake-Effect Snow to Annual Snowfall Totals in the Vicinity of Lakes Erie, Michigan, and Ontario

Erin A. Jones[1], *Carrie E. Lang*[2] *and Neil F. Laird*[3]*

[1] Department of Earth Sciences, Millersville University, Millersville, PA, United States, [2] Departments of Mathematics and Geography, State University of New York Geneseo, Geneseo, NY, United States, [3] Department of Geoscience, Hobart and William Smith Colleges, Geneva, NY, United States

In the Great Lakes region, total cold-season snowfall consists of contributions from both lake-effect systems (LES) and non-LES snow events. To enhance understanding of the regional hydroclimatology, this research examined these separate contributions with a focus on the cold seasons (October–March) of 2009/2010, a time period with the number of LES days substantially less than the mean, and 2012/2013, a time period with the number of LES days notably greater than the mean, for the regions surrounding Lakes Erie, Michigan, and Ontario. In general, LES snowfall exhibited a maximum contribution in near-shoreline areas surrounding each lake while non-LES snowfall tended to provide a more widespread distribution throughout the entire study regions with maxima often located in regions of elevated terrain. The percent contribution for LES snowfall to the seasonal snowfall varied spatially near each lake with localized maxima and ranged in magnitudes from 10% to over 70%. Although total LES snowfall amounts tended to be greater during the cold season with the larger number of LES days, the percent of LES snowfall contributing to the total cold-season snowfall was not directly dependent on the number of LES days. The LES snowfall contributions to seasonal totals were found to be generally larger for Lakes Erie and Ontario during the cold season with a greater number of LES days; however, LES contributions were similar or smaller for areas in the vicinity of Lake Michigan during the cold season with a smaller number of LES days.

Keywords: snowfall, Great Lakes, lake-effect, mesoscale, climatology

OPEN ACCESS

Edited by:
Adam Burnett,
Colgate University, United States

Reviewed by:
Andrew Ellis,
Virginia Tech, United States
Zachary Suriano,
University of Nebraska Omaha, United States
Chris Karmosky,
SUNY Oneonta, United States

***Correspondence:**
Neil F. Laird
laird@hws.edu

Specialty section:
This article was submitted to Water and Climate, a section of the journal Frontiers in Water

Received: *25 September 2021*
Accepted: *02 February 2022*
Published: *04 March 2022*

Citation:
Jones EA, Lang CE and Laird NF (2022) The Contribution of Lake-Effect Snow to Annual Snowfall Totals in the Vicinity of Lakes Erie, Michigan, and Ontario. Front. Water 4:782910. doi: 10.3389/frwa.2022.782910

INTRODUCTION

A large variety of agriculture, transportation, and tourism operations are directly linked to the large freshwater lakes and the weather systems that occur within the Great Lakes region of North America. Cold-season lake-effect system (LES) snowfall is a phenomenon that greatly affects both the weather and climate in the vicinity of each lake and occurs when a cold airmass is modified as it passes over one or more of the Great Lakes. The sensible and latent heat fluxes from the surface of the lake lead to instability within the atmospheric boundary layer, typically below 1–3 km during LES situations. This instability often leads to the development of LES clouds over and downwind of the Great Lakes creating a greater possibility for precipitation and substantial amounts of snowfall (e.g., Jiusto and Kaplan, 1972). In addition to many favorable benefits to the region, these substantial snowfalls can

lead to significant societal impacts, such as traffic accidents, property damage, and disrupted air travel (e.g., Schmidlin, 1993; Burow and Atkinson, 2019).

Numerous studies have examined the spatial distribution of total cold-season snowfall to infer which areas near the Great Lakes have the greatest LES snowfall amounts (e.g., Muller, 1966; Eichenlaub, 1970; Jiusto and Kaplan, 1972; Strommen and Harman, 1978; Norton and Bolsenga, 1993; Scott and Huff, 1996). Estimating the proportion that LES snowfall contributes to the cold-season snowfall for different areas is a complex task and has been approached using a variety of methods (e.g., Eichenlaub, 1970; Wilson, 1977; Braham and Dungey, 1984, 1995; Kelly, 1986; Scott and Huff, 1996; Yeager et al., 2013; Suriano et al., 2019; Ellis et al., 2020; Hartnett, 2021; Suriano and Wortman, 2021). However, this remains a challenge, especially for studies examining the long-term trends of snowfall within the Great Lakes region (e.g., Burnett et al., 2003; Ellis and Johnson, 2004; Kunkel et al., 2009; Bard and Kristovich, 2012; Hartnett et al., 2014; Clark et al., 2016, 2018; Suriano and Leathers, 2017; Baijnath-Rodino et al., 2018; Ellis et al., 2020).

Many past studies have primarily used one of three approaches for determining LES contribution to total cold-season snowfall. These include: (1) comparing measured total cold-season snowfall at locations nearer the lake (i.e., in snowbelt areas) to locations further inland from the lake (e.g., Scott and Huff, 1996), (2) comparing total cold-season snowfall measured at locations upwind of the lake to downwind locations (e.g., Braham and Dungey, 1984), or (3) using synoptic pattern classification to infer LES occurrence and comparing snowfall during LES synoptic patterns to snowfall that occurred during non-LES synoptic patterns (e.g., Eichenlaub, 1970; Suriano and Leathers, 2017; Suriano, 2019; Suriano and Wortman, 2021). A recent study by Ellis et al. (2020) utilized synoptic pattern classification in combination with comparing surface airmass attributes upwind and downwind of different lakes to identify likely LES days and investigate the long-term trends in both LES occurrence and snowfall. Each of these approaches used in past studies infer LES snowfall without knowledge of the occurrence of observed mesoscale LES cloud or precipitation patterns. For example, Suriano and Leathers (2017), Suriano (2019), and Suriano and Wortman (2021) acknowledge that synoptic patterns classified as LES are not directly linked with observed LES precipitation or mesoscale LES processes, but rather identify days where environmental conditions were favorable for possible LES development.

Using these varied approaches, past studies have arrived at differing conclusions about the LES contribution to total cold-season snowfall. For example, Dewey (1970) concluded that some areas in the LES snowbelt east of Lake Michigan received 200% more snow than further inland Michigan stations. Eichenlaub (1970) estimated that at least 30% of seasonal snowfall in this same snowbelt region came from lake-atmospheric interactions. Strommen and Harman (1978) concluded that LES snowfall in this same area contributed to a 50–300% increase in mean cold-season snow totals. Braham and Dungey (1984) estimated the effect of Lake Michigan on total cold-season snowfall was an increase of 10% for the southern Wisconsin shoreline region and an increase of 60% for the snowbelt area east of Lake Michigan. Analyses by Clark et al. (2016, 2018) suggested that LES led to an increase of cold-season snowfall between 170 and 315% when comparing areas east and west of Lake Michigan. Wilson (1977) found LES led to precipitation increases of ∼25% near Lake Ontario, and over 50% in regions of higher terrain east of the lake, such as the Tug Hill Plateau. Suriano and Wortman (2021) found that snowfall that occurred in the Lakes Erie and Ontario regions comprised ∼48% of total cold-season snowfall. When considering snowfall throughout the Great Lakes region, Scott and Huff (1996) estimated increases of winter precipitation from LES in areas near the downwind shorelines to have maxima ranging from 35 to 100%, with much variability in the spatial distribution.

The authors are aware of only a few previous studies that have used a combination of radar, satellite, and surface weather observations to identify LES occurrences and provide information about the contribution of LES snowfall to seasonal totals. Veals and Steenburgh (2015) used radar and assimilated snowfall data to find that LES days accounted for 61–76% of the mean cool-season snowfall and 24–37% of the mean cool-season liquid precipitation for a region surrounding the KTYX National Weather Service radar located near Montague, New York on the Tug Hill Plateau east of Lake Ontario. In a study examining a variety of snowstorm types impacting a region east and southeast of Lake Ontario, Hartnett (2021) found that LES snowstorms accounted for ∼39% of the total seasonal snowfall.

The current research provides new insight and knowledge of the hydroclimatological contribution of LES snowfall to cold-season snowfall totals using information of observed LES occurrences determined from satellite imagery and high-resolution assimilated snowfall data in the vicinity of Lakes Erie, Michigan, and Ontario for two cold seasons. The application of these results thereby provide an enhanced understanding of LES snowfall contributions to seasonal snowfall totals, how those contributions differ spatially in the vicinity of three different lakes, and whether the frequency of LES days in a winter is likely to influence the LES snowfall contributions.

DATA AND METHODS

The study focuses on two cold seasons with the aim of comparing LES snowfall contribution for a cold season with the number of LES days substantially less than the mean to a cold season with the number of LES days notably greater than the mean for each lake. The two cold seasons were determined using a daily LES database created by Laird et al. (2017). Using Geostationary Operational Environmental Satellite (GOES) visible imagery, Laird et al. (2017) documented when LES clouds were present over each of the Great Lakes for each day during the 17 cold-seasons (October–March) from 1997/1998 through 2013/2014. The mean number of LES days per cold season for Lakes Erie, Michigan, and Ontario were 50.8, 77.9, and 62.0, respectively. Examination of the daily LES database was used to identify the cold season of 2009/2010 as

TABLE 1 | Ranking of cold seasons based on the number of LES days for Lakes Erie, Michigan, and Ontario from the 17 cold-season database of Laird et al. (2017).

Rank	Erie LES	Michigan LES	Ontario LES
1	2004–2005	2013–2014	2013–2014
2	1999–2000	2002–2003	2008–2009
3	2012–2013	2008–2009	2000–2001
4	2005–2006	2012–2013	2012–2013
5	1998–1999	2000–2001	2004–2005
6	2008–2009	1999–2000	2003–2004
7	2000–2001	2005–2006	2002–2003
8	2006–2007	1998–1999	2010–2011
9	1997–1998	2003–2004	1998–1999
10	2003–2004	2006–2007	2006–2007
11	2013–2014	2007–2008	2005–2006
12	2001–2002	2010–2011	1999–2000
13	2010–2011	2004–2005	2007–2008
14	2011–2012	1997–1998	2001–2002
15	2007–2008	2001–2002	1997–1998
16	2002–2003	2009–2010	2009–2010
17	2009–2010	2011–2012	2011–2012

Grey highlighted cold seasons are those used in this study.

one of the least active in terms of LES with 32, 52, and 42 LES days over Lakes Erie, Michigan, and Ontario, respectively. The 2012/2013 cold season was identified as an active LES time period with 63, 88, and 70 LES days over Lakes Erie, Michigan, and Ontario, respectively.

The ranking of cold seasons based on the number of LES days for the 17 cold seasons from Laird et al. (2017) is shown in **Table 1**. The annual variation and distribution attributes of the number of LES days for the 17 cold seasons in each lake region is shown in **Figure 1**. The 2009/2010 cold season was the only cold season in the lowest quartile of LES days for each of the three lake regions and the 2012/2013 cold season was the only cold season in the highest quartile of LES days for each of the three lake regions. Identifying a cold season with all three lakes having the number of LES days substantially less than the mean and a second cold season with all three lakes having the number of LES days notably greater than the mean allowed for a more directed examination of whether the LES snowfall contribution to total seasonal snowfall differed based on the number of LES days by attempting to limit influence from variation in frequency, strength, and track of synoptic systems over different lakes. An examination of intraseasonal and interannual variations of LES snowfall contribution to monthly snowfall totals across multiple decades, different lake regions, and differing regional synoptic and mesoscale atmospheric conditions is beyond the scope of the current study and is an area of future investigation.

To determine the LES contribution to total cold-season snowfall, days in the two cold seasons were sorted into two categories based on the cold-season LES database described by Laird et al. (2017). Each day was designated as a day with LES observed over the specified lake or a day with no LES observed over the specified lake. The single designation of snowfall, as LES or non-LES, for each day does lead to some uncertainty of the snowfall totals in each category since a small number of days each cold season may have both non-LES and LES snowfall. For example, this approach would not capture LES snowfall that may have occurred in the vicinity of a cyclone passing over a specific lake where widespread synoptic cloud cover and precipitation may have occurred with embedded LES snowfall (i.e., a lake-enhanced snowfall situation) (e.g., Owens et al., 2017). With the synoptic overcast cloud cover inhibiting the ability to observe the presence of LES clouds, this type of situation would be classified as a non-LES snowfall day and lead to an underestimate of LES snowfall. Additionally, if LES snowfall occurred only during nighttime periods, the methodology from Laird et al. (2017) of using GOES visible satellite imagery to identify LES days would lead to an underestimate of LES snowfall. Alternatively, a day that had a transition from non-LES snowfall to LES snowfall during the time of day when LES clouds were identified from the GOES visible imagery would result in this day being classified as a LES snowfall day and lead to an overestimate of LES snowfall.

To examine the amount of snowfall in each geographic area, SNOw Data Assimilation System (SNODAS) solid precipitation (i.e., snowfall) data was analyzed using Geographic Information Systems (GIS). SNODAS assimilates satellite, airborne, and ground-based observations into a snow mass and energy balance model to create an estimation of snow water equivalent and snow pack thickness at 1-km horizontal resolution over the continental United States (Barrett, 2003). Daily gridded data, as used in this study, are available from the National Weather Service's National Operational Hydrologic Remote Sensing Center (NOHRSC) from September 2003 to the present. These data are available for only the continental United States for most of the archive, therefore our analyses and investigation focused on Lakes Erie, Michigan, and Ontario—Great Lakes with extensive shoreline regions within the continental United States. SNODAS snowfall data have been used for several past LES snowfall studies (e.g., Veals and Steenburgh, 2015; Lang et al., 2018) and are archived as liquid water equivalent (LWE) amounts. Total LWE daily snowfall for LES days and non-LES days, as well as summed across each cold season, were used to determine the contribution to the total cold-season snowfall in areas surrounding Lakes Erie, Michigan, and Ontario.

RESULTS

Comparing Total Cold-Season Snowfall

Lake Erie

The total cold-season snowfall for both winters in areas to the west and south of Lake Erie were very similar (**Figures 2A,D**). Generally, areas to the west and southwest of Lake Erie had LWE snowfall amounts of 4.0–19.3 cm. In both cold seasons, areas to the southeast of Lake Erie had larger snowfall amounts with LWE totals in the range of 19.3–34.6 cm. The maximum snowfall occurred in counties of northwestern Pennsylvania and southwestern New York where elevation rises quickly from lake level to a height of 430 m within about 10 km from the lake shoreline. The cold-season snowfall patterns and totals in this area for the two cold seasons studied are consistent with findings

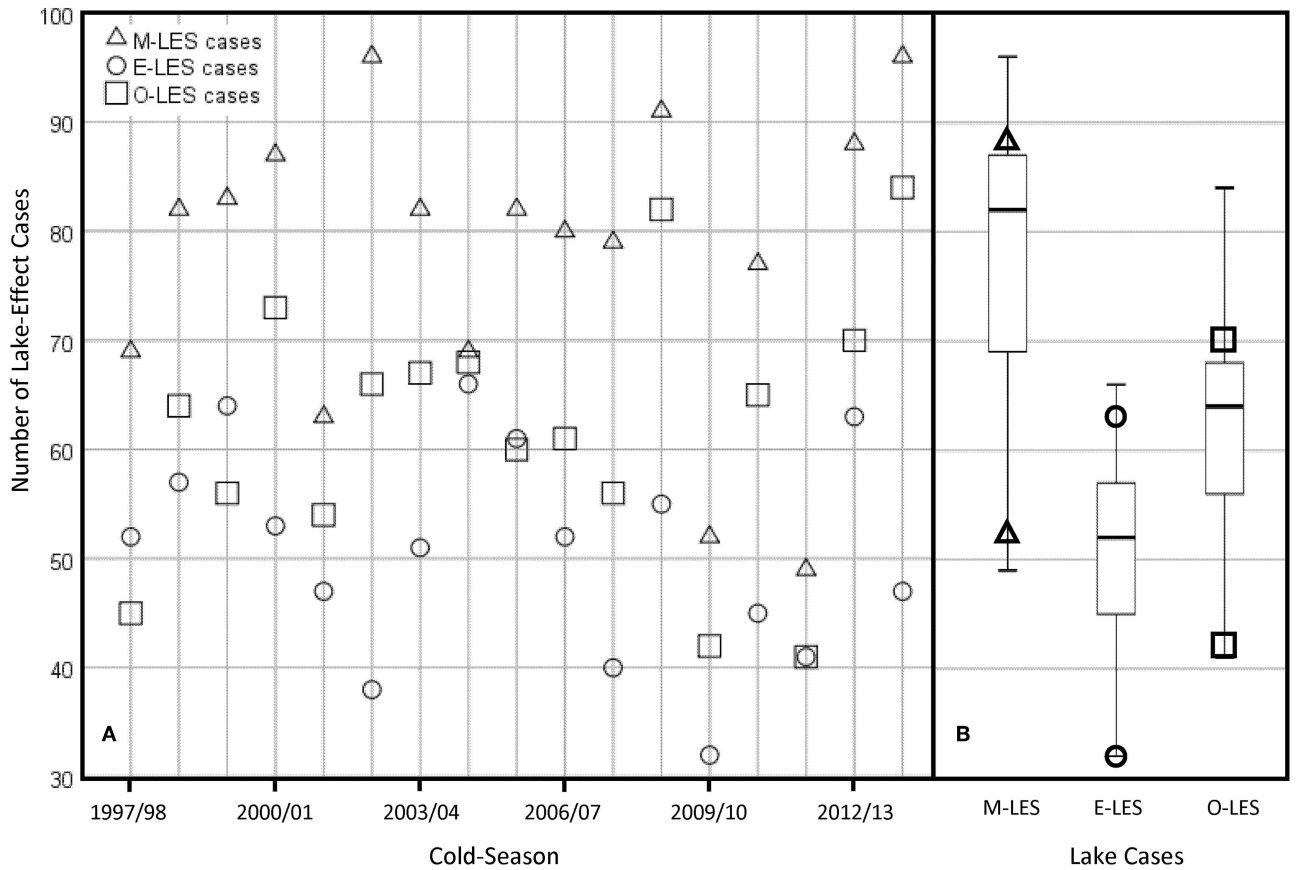

FIGURE 1 | The annual variation **(A)** and distribution attributes **(B)** of the number of LES days for the 17 cold seasons from Laird et al. (2017) in the Lake Michigan (M-LES; triangles), Lake Erie (E-LES; circles), and Lake Ontario (O-LES; squares) regions. The number of LES days for cold seasons of 2009/2010 and 2012/2013 are identified on the box-plots in panel **(B)** using symbols within the lowest and highest quartiles, respectively.

from past studies reporting on mean climatological cold-season (O-M) or winter (DJF) snowfall distribution across the Great Lakes region. For example, Scott and Huff (1996) showed that the 30-year mean LWE winter snowfall for the region southeast of Lake Erie was 22.5–30.0 cm. Norton and Bolsenga (1993) found the 30-year mean annual snowfall depth for this Lake Erie region ranged from 100 to 400 cm.

Lake Michigan

In both 2009/2010 and 2012/2013 cold seasons, the Upper Peninsula (UP) of Michigan and the region east of Lake Michigan (in particular the northern half of the lake) received the largest amounts of snowfall (**Figures 2B,E**). During 2009/2010, seasonal LWE snowfall totals in the UP region ranged from about 9.1 to 34.6 cm. LWE snowfall east and west of Lake Michigan had values in the range of 14.2–24.4 cm and 4.0–19.3 cm, respectively. In the 2012/2013 cold season, total LWE snowfall amounts in the UP of Michigan were notably larger with values ranging from about 24.4 to 50.0 cm. Total cold-season LWE snowfall amounts east and west of Lake Michigan were also greater than observed during the 2009/2010 cold season with values between 14.2–39.7 cm and 14.2–24.4 cm, respectively. Long-term mean snowfall for this region from Scott and Huff (1996) showed that LWE winter snowfall north and east of Lake Michigan were 12.5–17.5 cm and totals west of Lake Michigan were 7.5–10.0 cm. Norton and Bolsenga (1993) found the 30-year mean annual snowfall depth for these regions near Lake Michigan ranged from a maximum of about 400 cm in Upper Michigan to upwards of 300–350 cm east of Lake Michigan and ∼100–150 cm west of Lake Michigan.

Lake Ontario

Total snowfall was similar during both cold seasons for areas south of Lake Ontario; however, the areas east of Lake Ontario had noteworthy differences between 2009/2010 and 2012/2013 (**Figures 2C,F**). In 2012/2013, maxima of total LWE snowfall occurred over the Tug Hill Plateau and the Adirondack Mountain regions east of Lake Ontario. Totals in the highest elevations of the Tug Hill Plateau (i.e., 512 m above lake level) were 50.0–55.1 cm. During 2009/2010, the largest total LWE snowfall amounts occurred in the Catskill Mountain and Southern Adirondack Mountain regions that are east and southeast of Lake Ontario. These totals ranged from about 24.4 to 44.8 cm with slightly larger amounts occurring in the Catskill Mountain

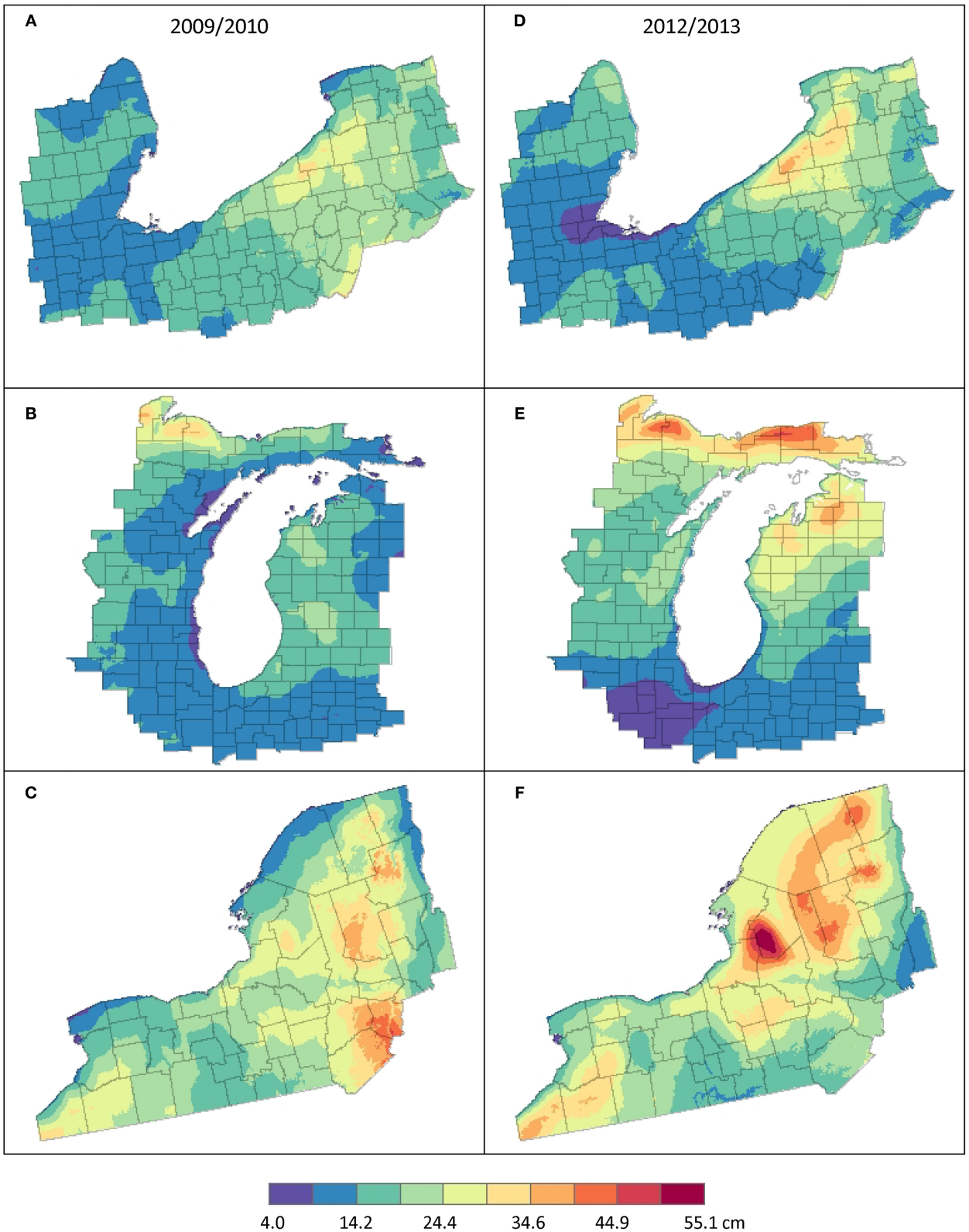

FIGURE 2 | The total cold-season LWE snowfall (cm) during the 2009/2010 season for the **(A)** Lake Erie, **(B)** Lake Michigan, and **(C)** Lake Ontario regions and during the 2012/2013 season for the **(D)** Lake Erie, **(E)** Lake Michigan, and **(F)** Lake Ontario regions.

region. The total LWE snowfall amounts south of Lake Ontario ranged from 9.1 to 29.5 cm during both cold seasons. Norton and Bolsenga (1993) found the 30-year mean annual snowfall depth had maxima in similar areas of the Tug Hill Plateau, Adirondack Mountains, and Catskill Mountains east of Lake Ontario. They found long-term mean snowfall depths in these regions ranging from 200 to >400 cm. Scott and Huff (1996) showed that 30-year mean LWE winter snowfall for the regions east and southeast of Lake Ontario had totals of 22.5–32.5 cm while areas south of Lake Ontario had winter totals of 15.0–20.0 cm.

Comparing LES and Non-LES Snowfall

Lake Erie

The spatial patterns of LWE snowfall from Lake Erie LES days during both cold seasons (**Figures 3A,C**) clearly denote the primary LES snow region positioned near the southeastern shoreline. This region of accumulated cold-season LES snowfall stretches westward from southeast of Buffalo, NY to Erie, PA. This region is typically located downwind of the lake during LES situations and has substantial elevation rise inland from the lake shore. During 2009/2010, most of the LES snow region received LWE totals of 3.8–10.3 cm. The 2012/2013 cold season had similar LWE snowfall totals of 3.8–13.6 cm in this region. Small cold-season LES snowfall amounts (<3.8 cm) occurred to the west and southwest of the lake.

The LWE snowfall spatial patterns from non-LES days in the vicinity of Lake Erie that occurred during both cold seasons showed larger totals to the southeast of Lake Erie (**Figures 3B,D**), as well as larger accumulated snowfall within all counties in the study region. In the 2009/2010 cold season, maximum snowfall accumulations from non-LES days were slightly >20.2 cm. Areas to the west and southwest of the lake received amounts ranging from 7.1 to 16.9 cm. For the 2012/2013 cold season, the maximum was located near the lake with a value near 23.4 cm. Snowfall totals outside of the region of largest non-LES snowfall were generally less than non-LES snowfall during 2009/2010 and ranged from 3.8 to 13.6 cm.

While the location of the larger non-LES snowfall has some similarity to the LES snowfall region, the larger snowfall amounts accumulated across non-LES days cover a more expansive area. The higher terrain and steep rise above lake level of near-shoreline areas to the southeast of Lake Erie clearly have an influence on snowfall amounts during both LES and non-LES days. The analyses shown in **Figure 3** suggest that studies that have only examined total cold-season snowfall to infer the contribution of LES snowfall without considering information of observed LES occurrences or variation of terrain have likely overestimated the percentage of LES snowfall for this region and perhaps other regions where substantial elevated terrain exists in near-shore regions.

Lake Michigan

The spatial distributions of LES snowfall for the two cold seasons are similar with the largest cold-season totals located in the UP of Michigan and east of Lake Michigan (**Figures 4A,C**). The large snowfall totals in the UP of Michigan on Lake Michigan LES days likely resulted from coincidental LES activity occurring in association with Lake Superior. Cold-season LES snowfall totals east of Lake Michigan ranged from 7.1 cm in the region southeast of the lake to 13.6 and 16.9 cm northeast of the lake during the cold seasons of 2009/2010 and 2012/2013, respectively. LES snowfall totals west of Lake Michigan were generally <3.3 and 7.1 cm during 2009/2010 and 2012/2013, respectively.

The seasonal snowfall totals from non-LES days were more evenly distributed over regions east and west of Lake Michigan for both cold seasons (**Figures 4B,D**). For both cold seasons the patterns suggest that the track of extratropical cyclones through the Great Lakes region, as well as elevated terrain in the UP of Michigan and the northern portion of Lower Michigan, may have contributed to the location of larger snowfall totals from non-LES days. During the cold season of 2009/2010, maximum non-LES snowfall totals (16.9 cm) occurred over central Wisconsin and near the Porcupine Mountains in the UP of Michigan. The maximum non-LES snowfall totals in the cold-season of 2012/2013 (30.0 cm) also occurred near the Porcupine Mountains in the UP of Michigan with LWE snowfall values >13.6 cm extending across northeastern Wisconsin, the UP of Michigan, and the northern portion of Lower Michigan.

Lake Ontario

In both the active and less active LES cold seasons, the region to the east of Lake Ontario received the largest amounts of snowfall from LES days. For 2009/2010, LES amounts east of Lake Ontario ranged from 3.3 to 10.3 cm (**Figure 5A**). The LES snowfall totals east of Lake Ontario during the 2012/2013 cold season were greater and ranged between 3.3 and 16.9 cm (**Figure 5C**). During both cold seasons the maximum LES snowfall occurred over the Tug Hill Plateau with larger values extending eastward into the central Adirondack Mountains. The large snowfall totals in southwestern New York on LES days for Lake Ontario likely resulted from coincidental LES activity occurring in association with Lake Erie. This suggests that on Lake Ontario LES days, there were favorable atmospheric and lake conditions supportive of LES systems across a widespread portion of the eastern Great Lakes region. When conditions are supportive of LES over a large area, LES snow bands can develop on an upwind lake, extend over the intervening land area, and continue their development over a downwind lake (e.g., Rodriguez et al., 2007; Laird et al., 2017; Kristovich et al., 2018; Lang et al., 2018).

Snowfall from non-LES days was widespread across the Lake Ontario study region during both cold seasons. The largest snowfall totals occurred in the Catskill Mountains and southern Adirondack Mountains during 2009/2010 (**Figure 5B**) and over the Tug Hill Plateau and across the entire Adirondack Mountain region during 2012/2013 (**Figure 5D**). The snowfall totals associated with non-LES days were notably greater than the seasonal totals resulting from LES days. Maximum LWE snowfall totals in both cold seasons from non-LES days approached 40.0 cm.

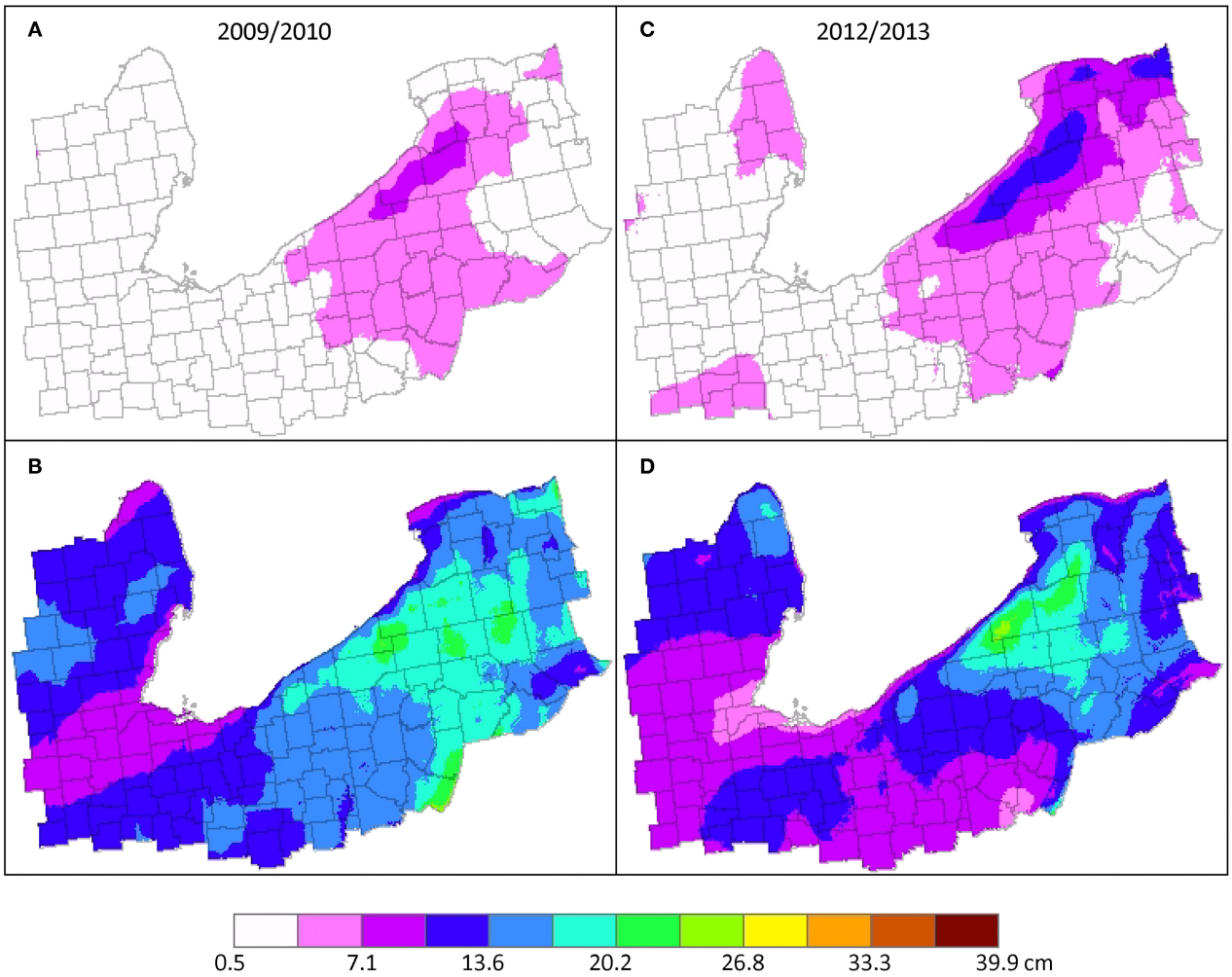

FIGURE 3 | The 2009/2010 cold-season LWE snowfall (cm) for **(A)** LES days and **(B)** non-LES days and the 2012/2013 cold-season LWE snowfall for **(C)** LES days and **(D)** non-LES days in the vicinity of Lake Erie.

LES Contribution to Total Cold-Season Snowfall

Lake Erie

Snowfall from LES days comprised 20–30% of total cold-season snowfall in most of the near-shore area southeast of Lake Erie for the 2009/2010 cold season (**Figure 6A**). A small area located mostly in two counties of western NY (i.e., Erie and Chautauqua) had LES snowfall contributions of 30–40%. Throughout the remainder of the study area, LES snowfall consisted of roughly 10–20% of total cold-season snowfall. In 2012/2013, LES snowfall comprised a larger percentage of total cold-season snowfall, 30–40%, in the region southeast of Lake Erie and 20–30% in most other areas (**Figure 6D**).

Lake Michigan

East of Lake Michigan LES snowfall comprised 40–70% of the total cold-season snowfall in 2009/2010 with the maximum percentages occurring near the Traverse Bay region (**Figure 6B**). In 2012/2013, these values ranged from 30 to 60% with maximum percentages occurring to the southeast of Lake Michigan and were slightly less than LES contributions across this region in 2009/2010 (**Figure 6E**). Since 2012/2013 had a greater number of LES days and higher LES snowfall totals in general, areas with smaller contributions to seasonal totals compared to 2009/2010 might not be expected. Greater LES snowfall contributions to total cold-season snowfall during 2009/2010 demonstrate that the relationship is not directly dependent on the number of LES days during a cold season. For most regions west of Lake Michigan, the contribution of LES snowfall to total cold-season snowfall was between 10 and 20%, except along the southwestern shoreline near Chicago, IL where LES snowfall comprised 30–40%.

Lake Ontario

During the two cold seasons, the amount of LES snowfall contributing to the total cold-season snowfall was different in

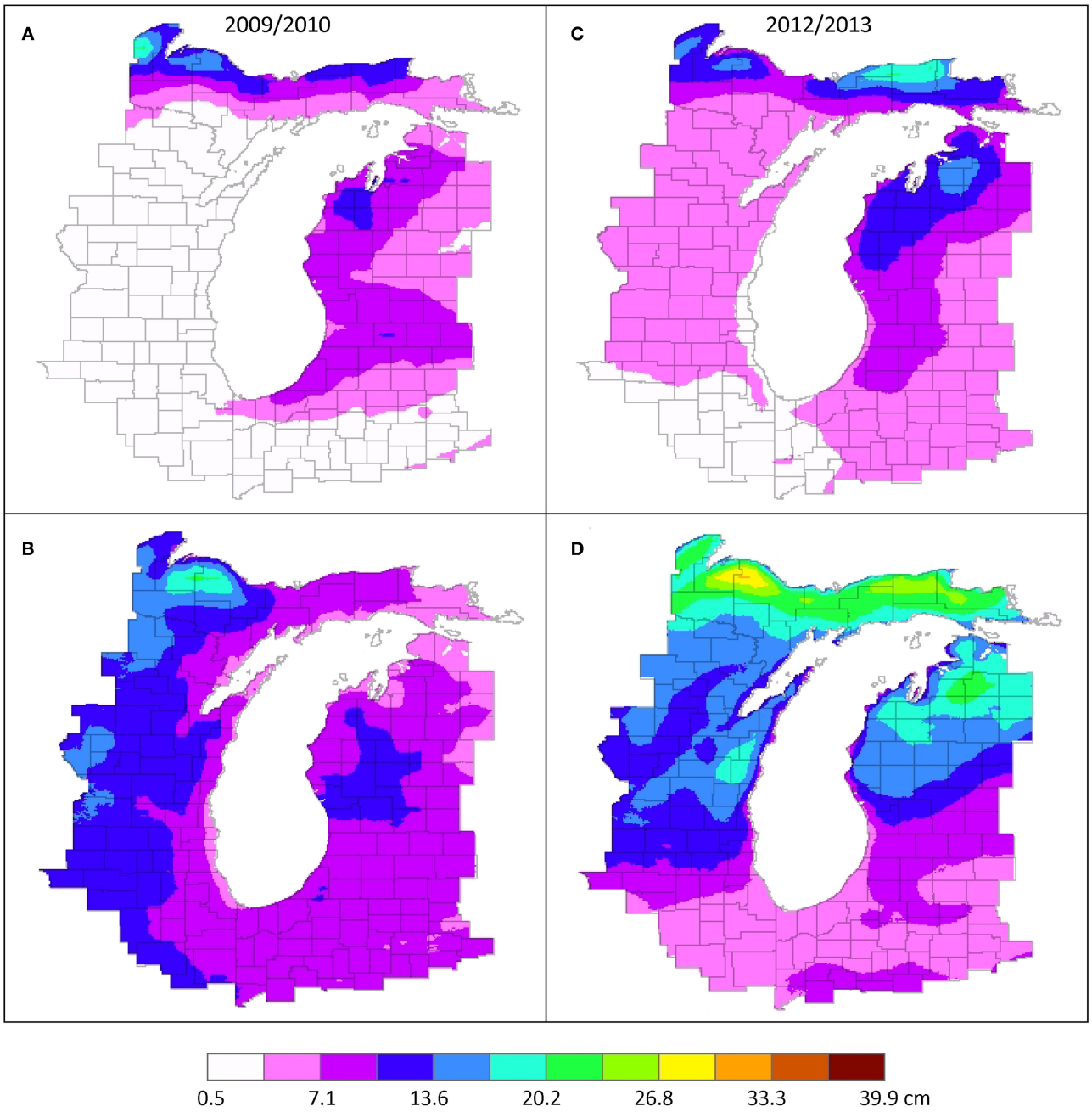

FIGURE 4 | The 2009/2010 cold-season LWE snowfall (cm) for **(A)** LES days and **(B)** non-LES days and the 2012/2013 cold-season LWE snowfall for **(C)** LES days and **(D)** non-LES days in the vicinity of Lake Michigan.

both magnitude and spatial distribution. The maximum LES snowfall contribution in 2009/2010 was located east of Lake Ontario over the Tug Hill Plateau region and had values ranging from 30 to 40% (**Figure 6C**). In 2012/2013, the largest LES percentages of total cold-season snowfall ranged from 40 to 50% and were positioned to the south and southeast of Lake Ontario (**Figure 6F**). This difference in location of maximum LES contribution between the two cold seasons may reflect differences in the seasonal mean wind directions during LES days, as well as possible differences in the overall frequency of different types of LES snow bands. The location of the maximum east of Lake Ontario in 2009/2010 suggests greater occurrence of westerly wind directions and long lake-axis parallel snow bands during LES days compared to the location of the 2012/2013

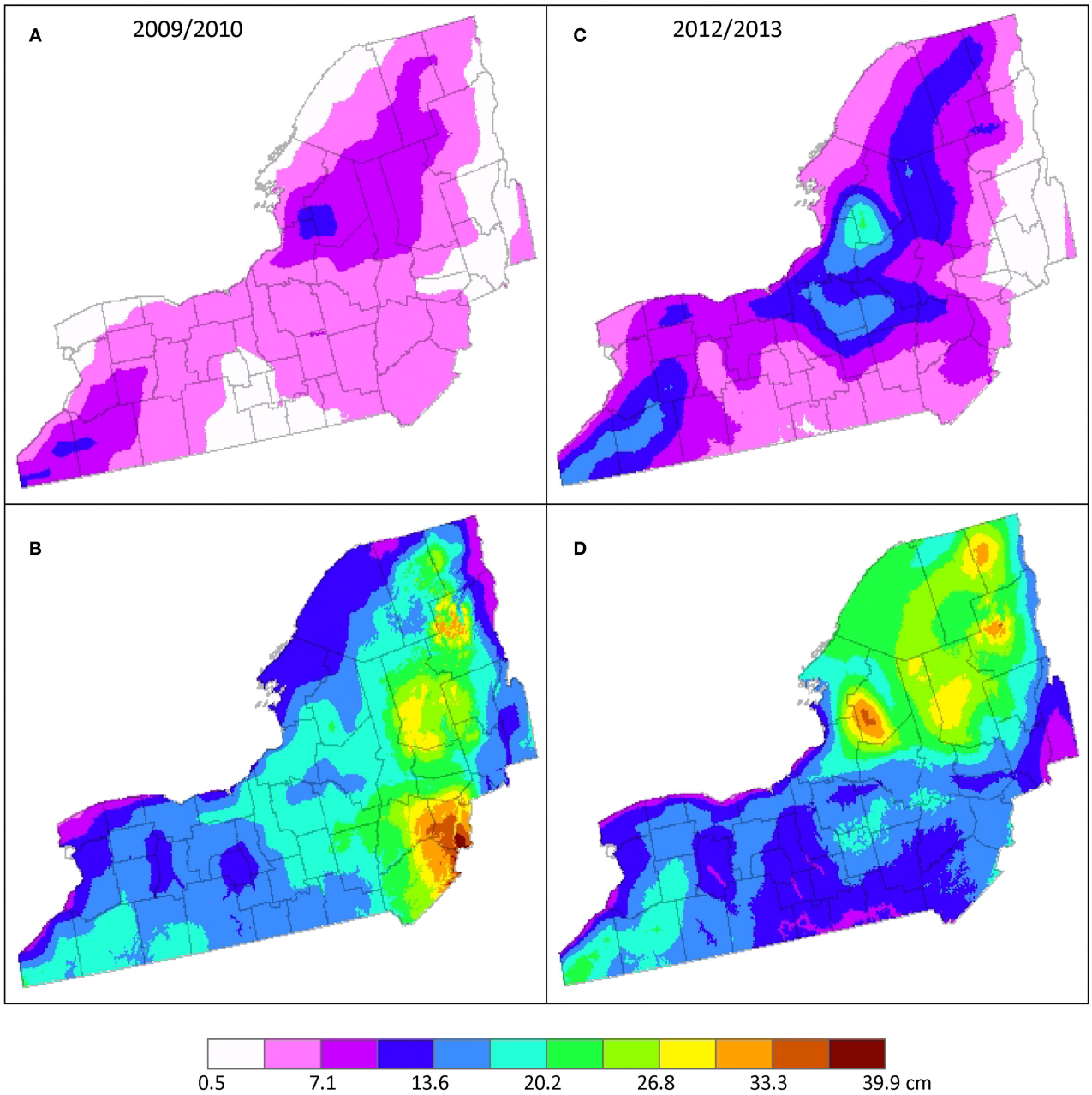

FIGURE 5 | The 2009/2010 cold-season LWE snowfall (cm) for **(A)** LES days and **(B)** non-LES days and the 2012/2013 cold-season LWE snowfall for **(C)** LES days and **(D)** non-LES days in the vicinity of Lake Ontario.

maximum south and southeast of the lake that suggests north or northwesterly wind directions and wind parallel snow bands or LES days with an upwind connection to Lake Huron.

CONCLUSIONS AND DISCUSSION

A unique approach was taken to determine the LES contribution to total cold-season snowfall. Different from most past LES studies, the current study incorporates information of observed LES occurrences on each lake thereby directly linking snowfall on those days to mesoscale LES clouds and circulations in each lake region. Additionally, the study uses a high-resolution assimilated snowfall dataset that allows for representation of snowfall patterns that are consistent with the mesoscale nature of LES. Two cold seasons were examined with a purposeful choice of seasons differing in the number of LES days. A cold season with the number of LES days notably greater than the mean (i.e., upper

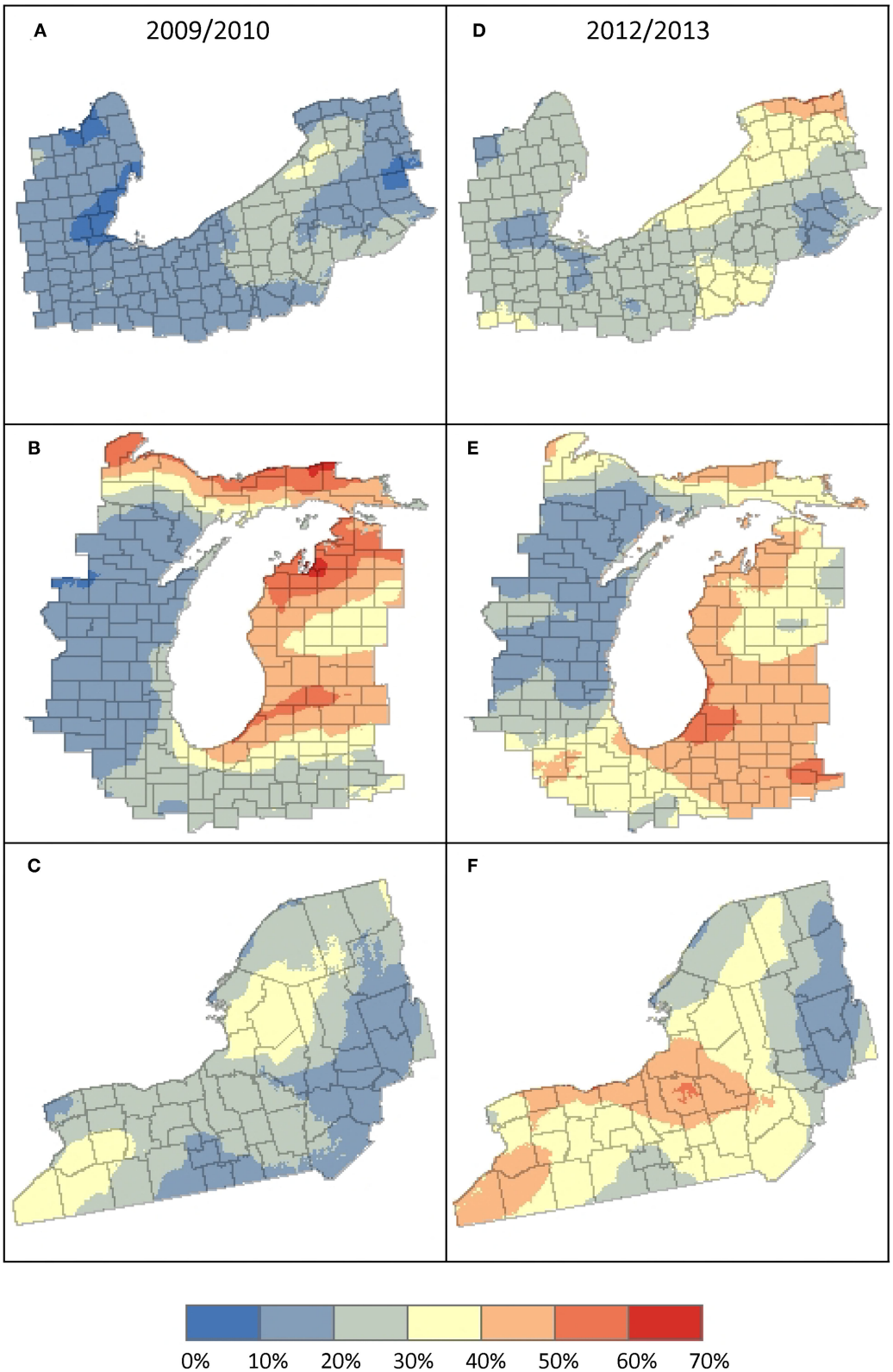

FIGURE 6 | The percentage contribution of LES snowfall (cm) to cold-season snowfall during 2009/2010 for the **(A)** Lake Erie region, **(B)** Lake Michigan region, and **(C)** Lake Ontario region and during 2012/2013 for the **(D)** Lake Erie region, **(E)** Lake Michigan region, and **(F)** Lake Ontario region.

quartile for all three lakes) and a second cold season with the number of LES days substantially less than the mean (i.e., lowest quartile for all three lakes).

The primary conclusions drawn from the results of this research include:

- LES snowfall contribution to total cold-season snowfall in near-shore areas in the vicinity of Lakes Erie, Michigan, and Ontario do not appear to be directly dependent on the number of LES snowfall days during a cold season. During the two different cold seasons and in different areas surrounding each of the lakes, LES snowfall contributions were found to have a direct, an inverse, or no relationship to the number of cold-season LES days.
- Across the two cold seasons examined, the LES snowfall contribution to total seasonal snowfall ranged from about 10% to upwards of 70%. The spatial patterns LES snowfall contribution exhibit the mesoscale nature of LES snowstorms with a dependence on atmospheric conditions influencing mean LES snow band position during an individual cold season.
- When comparing the two cold seasons, differences of LES snowfall contributions to total cold-season snowfall for any one location in the vicinity of Lakes Erie, Michigan, and Ontario were as large as 20% (e.g., southeast of Lake Ontario); however, in most near-shore areas the differences were typically smaller than 10%. Although methodologies differed, this result seems to be consistent with the interannual variation of LES snowfall contribution that Suriano and Wortman (2021) found when examining a larger number of cold seasons. The larger differences in LES snowfall contribution between the two winters investigated in the current study may have resulted from differences of (a) extratropical cyclone frequency and cyclone tracks through the Great Lakes region, (b) the presence and distribution of ice cover on a lake, (c) the variation of snow-to-liquid water content during LES and non-LES snowfall events, and (d) the seasonal mean wind direction. The seasonal mean wind direction would have a direct relation to the mean fetch over a lake during LES atmospheric conditions. This is known to influence the mesoscale structure of the LES snow bands, the likelihood of a multiple lake connection, and the shoreline regions impacted by different LES band types.
- The location of maxima in both LES and non-LES snowfall suggest a notable influence by the terrain in the Great Lakes region, especially in near-shore areas where substantial rise in elevation exists. The enhancement of non-LES snowfall in these areas may suggest an overestimation of LES snowfall contributions to total cold-season snowfall for past approaches that (1) compare measured total cold-season snowfall at locations nearer the lake (i.e., in snowbelt areas) to locations further inland from the lake or (2) compare total cold-season snowfall measured at locations upwind of the lake to downwind locations.

Several recent studies have investigated LES snowfall contribution to winter/cold season snowfall with different approaches to distinguish LES and non-LES snowfall days for areas downwind of Lake Ontario (Veals and Steenburgh, 2015; Hartnett, 2021), Lakes Erie and Ontario (Suriano and Wortman, 2021), and Lakes Superior, Michigan, Erie and Ontario (Ellis et al., 2020). Each study incorporated different data sets and different time periods, as well as different analysis techniques, so a direct comparison of results is difficult. The data sets used in these studies have incorporated high-resolution spatial data sets, such as satellite or radar, and assimilated snowfall data (current study, Veals and Steenburgh, 2015), examined courser-resolution regional snowfall data sets (Suriano and Wortman, 2021), or analyzed snowfall recorded at individual surface station locations (Ellis et al., 2020; Hartnett, 2021). However, each study offers information directed at the same research question. **Table 2** provides summary information about the results from each study for the region(s) included in their investigation.

TABLE 2 | LES snowfall contributions to seasonal snowfall for different regions downwind of the Great Lakes reported by recent studies.

	Lake Ontario	Lake Erie	Lake Michigan	Lake Superior
This study: current study	10–60%	10–40%	30–70%	
Veals and Steenburgh (2015)	61–76%			
	24–37%			
Hartnett (2021)	40%			
Suriano and Wortman (2021)	47.2% (σ = 11.3%)	48.2% (σ =10.2%)		
Ellis et al. (2020)	10–20%	10–20%	16–32%	16–32%

Table cells with gray shading represent contributions reported from LWE and all others represent contributions reported from snowfall depth.

Future research on this topic should consider examining the interannual and intraseasonal variations of LES snowfall contribution to monthly snowfall totals across multiple decades, as well as investigating how the frequency of LES storm types over a lake may influence the seasonal LES contributions and the location of maxima. High-resolution assimilated snowfall data sets (e.g., SNODAS) seem to capture the local spatial variation of LES snowfall and even the mesoscale variation embedded within widespread snowfall from synoptic systems. The use of these data sets for future studies would likely provide expanded information on the large spatial variation of snowfall and therefore capture the extremes that may exist in spatial variations of LES contributions to seasonal snowfall totals. Snowfall information of this nature would be of great benefit to enhancing understanding of the cold-season hydrology within smaller watersheds across the Great Lakes region.

DATA AVAILABILITY STATEMENT

The original contributions presented in the study are included in the article/supplementary material, further inquiries can be directed to the corresponding author/s.

AUTHOR CONTRIBUTIONS

EJ, CL, and NL contributed to conception, design of the study, and wrote the first draft of the manuscript. EJ and CL organized the database, performed the statistical, and GIS analyses. All authors contributed to manuscript revision, read, and approved the submitted version.

FUNDING

This research was primarily conducted during the 2016, 2017, and 2021 Undergraduate Summer Research Programs at Hobart and William Smith (HWS) Colleges and supported by the National Science Foundation Research awards AGS-1258548, AGS-2040594, and the HWS Provost's Office.

REFERENCES

Baijnath-Rodino, J. A., Duguay, C. R., and LeDrew, E. (2018). Climatological trends of snowfall over the Laurentian Great Lakes Basin. *Int. J. Climatol.* 38, 3942–3962. doi: 10.1002/joc.5546

Bard, L., and Kristovich, D. A. (2012). Trend reversal in Lake Michigan contribution to snowfall. *J. Appl. Meteorol. Climatol.* 51, 2038–2046. doi: 10.1175/JAMC-D-12-064.1

Barrett, A. (2003). *National Operational Hydrologic Remote Sensing Center Snow Data Assimilation System (SNODAS) Products at NSIDC. NSIDC Special Report 11*. Boulder, CO: National Snow and Ice Data Center, 19.

Braham, R. R., and Dungey, M. J. (1984). Quantitative estimates of the effect of Lake Michigan on snowfall. *J. Clim. Appl. Meteorol.* 23, 940–949. doi: 10.1175/1520-0450(1984)023<0940:QEOTEO>2.0.CO;2

Braham, R. R. Jr., and Dungey, M. J. (1995). Lake-effect snowfall over Lake Michigan. *J. Appl. Meteor.* 34, 1009–1019. doi: 10.1175/1520-0450(1995)034<1009:LESOLM>2.0.CO;2

Burnett, A. W., Kirby, M. E., Mullins, H. T., and Patterson, W. P. (2003). Increasing great Lake-effect snowfall during the twentieth century: a regional response to global warming?. *Clim. J.* 16, 3535–3542. doi: 10.1175/1520-0442(2003)016<3535:IGLSDT>2.0.CO;2

Burow, D., and Atkinson, C. (2019). An examination of traffic volume during snow events in northeast Ohio. *Nat. Hazards* 99, 1179–1189. doi: 10.1007/s11069-019-03786-y

Clark, C. A., Elless, T. J., Lyza, A. W., Ganesh-Babu, B., Koning, D. M., Carne, A. R., et al. (2016). Spatiotemporal snowfall variability in the Lake Michigan region: how is warming affecting wintertime snowfall?. *J. Appl. Meteorol. Climatol.* 55, 1813–1830. doi: 10.1175/JAMC-D-15-0285.1

Clark, C. A., Ganesh-Babu, B., Elless, T. J., Lyza, A. W., Koning, D. M., Carne, A. R., et al. (2018). Spatio-temporal November and March snowfall trends in the Lake Michigan region. *Int. J. Climatol.* 38, 3250–3263. doi: 10.1002/joc.5498

Dewey, K. F. (1970). An analysis of lake-effect snowfall. *Bull. III. Geogr. Soc.* 12, 27–42.

Eichenlaub, V. L. (1970). Lake effect snowfall to the lee of the Great Lakes: its role in Michigan. *Bull. Am. Meteorol. Soc.* 51, 402–412. doi: 10.1175/1520-0477(1970)051<0403:LESTTL>2.0.CO;2

Ellis, A. W., and Johnson, J. J. (2004). Hydroclimatic analysis of snowfall trends associated with the north American Great Lakes. *J. Hydrometeorol.* 5, 471–486. doi: 10.1175/1525-7541(2004)005<0471:HAOSTA>2.0.CO;2

Ellis, A. W., Marston, M. L., and Bahret, J. B. (2020). Changes in the frequency of cool season lake effects within the north American Great Lakes Region. *Ann. Am. Assoc. Geogr.* 111, 385–401. doi: 10.1080/24694452.2020.1785270

Hartnett, J. J. (2021). A classification scheme for identifying snowstorms affecting central New York State. *Int. J. Climatol.* 41, 1712–1730. doi: 10.1002/joc.6922

Hartnett, J. J., Collins, J. M., Baxter, M. A., and Chambers, D. P. (2014). Spatiotemporal snowfall trends in Central New York. *J. Appl. Meteorol. Climatol.* 53, 2685–2697. doi: 10.1175/JAMC-D-14-0084.1

Jiusto, J., and Kaplan, M. (1972). Snowfall from lake-effect storms. *Mon. Weather Rev.* 100, 62–66. doi: 10.1175/1520-0493(1972)100<0062:SFLS>2.3.CO;2

Kelly, R. D. (1986). Mesoscale frequencies and seasonal snowfalls for different types of Lake Michigan snow storms. *J. Appl. Meteorol.* 25, 308–312. doi: 10.1175/1520-0450(1986)025<0308:MFASSF>2.0.CO;2

Kristovich, D. A., Bard, L., Stoecker, L., and Geerts, B. (2018). Influence of Lake Erie on a Lake Ontario lake-effect snowstorm. *J. Appl. Meteorol. Climatol.* 57, 2019–2033. doi: 10.1175/JAMC-D-17-0349.1

Kunkel, K. E., Ensor, L., Palecki, M., Easterling, D., Robinson, D., Hubbard, K. G., et al. (2009). A new look at lake-effect snowfall trends in the Laurentian Great Lakes using a temporally homogeneous data set. *J. Great Lakes Res.* 35, 23–29. doi: 10.1016/j.jglr.2008.11.003

Laird, N. F., Metz, N., Gaudet, L., Grasmick, C., Higgins, L., Loeser, C., et al. (2017). Climatology of cold season lake-effect cloud bands for the North American Great Lakes. *Int. J. Climatol.* 37, 2111–2121. doi: 10.1002/joc.4838

Lang, C. E., McDonald, J. M., Gaudet, L., Doeblin, D., Jones, E. A., and Laird, N. F. (2018). The influence of a Lake-to-Lake connection from Lake Huron on the lake-effect snowfall in the vicinity of Lake Ontario. *J. Appl. Meteorol. Climatol.* 57, 1423–1439. doi: 10.1175/JAMC-D-17-0225.1

Muller, R. (1966). Snowbelts of the Great Lakes. *Weatherwise* 19, 248–257. doi: 10.1080/00431672.1966.10544204

Norton, D. C., and Bolsenga, S. J. (1993). Spatiotemporal trends in lake effect and continental snowfall in the Laurentian Great Lakes, 1951-1980. *Clim. J.* 6, 1943–1956. doi: 10.1175/1520-0442(1993)006<1943:STILEA>2.0.CO;2

Owens, N. D., Rauber, R. M., Jewett, B. F., and McFarquhar, G. M. (2017). The contribution of lake enhancement to extreme snowfall within the chicago-milwaukee urban corridor during the 2011 groundhog day blizzard. *Mon. Weather Rev.* 145, 2405–2420. doi: 10.1175/MWR-D-17-0025.1

Rodriguez, Y., Kristovich, D. A., and Hjelmfelt, M. R. (2007). Lake-to-Lake cloud bands: frequencies and locations. *Mon. Weather Rev.* 135, 4202–4213. doi: 10.1175/2007MWR1960.1

Schmidlin, T. W. (1993). Impacts of severe winter weather during december 1989 in the lake erie snowbelt. *J. Clim.* 6, 759–767. doi: 10.1175/1520-0442(1993)006

Scott, R. W., and Huff, F. A. (1996). Impacts of the Great Lakes on regional climate conditions. *J. Great Lakes Res.* 22, 845–863. doi: 10.1016/S0380-1330(96)71006-7

Strommen, N. D., and Harman, J. R. (1978). Seasonally changing patterns of lake-effect snowfall in western lower Michigan. *Mon. Weather Rev.* 106, 503–509. doi: 10.1175/1520-0493(1978)106<0503:SCPOLE>2.0.CO;2

Suriano, Z. J. (2019). Changing intrasynoptic type characteristics and interannual frequencies of circulation patterns conducive to lake-effect snowfall. *J. Appl. Meteorol. Climatol.* 58, 2313–2328. doi: 10.1175/JAMC-D-19-0069.1

Suriano, Z. J., and Leathers, D. J. (2017). Synoptically classified lake-effect snowfall trends to the lee of Lakes Erie and Ontario. *Clim. Res.* 74, 1–13. doi: 10.3354/cr01480

Suriano, Z. J., Leathers, D. J., Hall, D. K., and Frei, A. (2019). Contribution of snowfall from diverse synoptic conditions in the Catskill/Delaware Watershed of New York State. *Int. J. Climatol.* 39, 3608–3618. doi: 10.1002/joc.6043

Suriano, Z. J., and Wortman, R. D. (2021). Temporal trends in snowfall contribution induced by lake-effect synoptic types. *Phys. Geogr.* 42, 416–433. doi: 10.1080/02723646.2020.1792048

Veals, P. G., and Steenburgh, W. J. (2015). Climatological characteristics and orographic enhancement of lake-effect precipitation east of Lake Ontario and over the Tug Hill Plateau. *Mon. Weather Rev.* 143, 3591–3609. doi: 10.1175/MWR-D-15-0009.1

Wilson, J. W. (1977). Effect of Lake Ontario on precipitation. *Mon. Weather Rev.* 105, 207–214. doi: 10.1175/1520-0493(1977)105<0207:EOLOOP>2.0.CO;2

Yeager, K. N., Steenburgh, W. J., and Alcott, T. I. (2013). Contributions of Lake-effect periods to the cool-season hydroclimate of the great salt lake basin. *J. Appl. Meteor. Climatol.* 52, 341–336. doi: 10.1175/JAMC-D-12-077.1

Conflict of Interest: The authors declare that the research was conducted in the absence of any commercial or financial relationships that could be construed as a potential conflict of interest.

Publisher's Note: All claims expressed in this article are solely those of the authors and do not necessarily represent those of their affiliated organizations, or those of the publisher, the editors and the reviewers. Any product that may be evaluated in this article, or claim that may be made by its manufacturer, is not guaranteed or endorsed by the publisher.

frontiers in Water

ORIGINAL RESEARCH
published: 17 March 2022
doi: 10.3389/frwa.2022.826293

Climatology of Lake-Effect Snow Days Along the Southern Shore of Lake Michigan: What Is the Sensitivity to Environmental Factors and Snowband Morphology?

Craig A. Clark[1], Nicholas D. Metz[2], Kevin H. Goebbert[1], Bharath Ganesh-Babu[1], Nolan Ballard[1], Andrew Blackford[1], Andrew Bottom[1], Catherine Britt[2], Kelly Carmer[3], Quenten Davis[1], Jilliann Dufort[1], Anna Gendusa[1], Skylar Gertonson[1], Blake Harms[1], Matthew Kavanaugh[1], Jeremy Landgrebe[1], Emily Mazan[1], Hannah Schroeder[1], Nicholas Rutkowski[1] and Caleb Yurk[1]*

[1] Department of Geography and Meteorology, Valparaiso University, Valparaiso, IN, United States, [2] Department of Geoscience, Hobart and William Smith Colleges, Geneva, NY, United States, [3] Department of Geography, Florida Institute of Technology, Melbourne, FL, United States

OPEN ACCESS

Edited by:
Galina Guentchev,
Met Office, United Kingdom

Reviewed by:
Jeffrey Frame,
University of Illinois at Urbana-Champaign, United States
Thpmas Schmidlin,
Kent State University, United States

***Correspondence:**
Craig A. Clark
craig.clark@valpo.edu

Specialty section:
This article was submitted to Water and Climate, a section of the journal Frontiers in Water

Received: 30 November 2021
Accepted: 02 February 2022
Published: 17 March 2022

Citation:
Clark CA, Metz ND, Goebbert KH, Ganesh-Babu B, Ballard N, Blackford A, Bottom A, Britt C, Carmer K, Davis Q, Dufort J, Gendusa A, Gertonson S, Harms B, Kavanaugh M, Landgrebe J, Mazan E, Schroeder H, Rutkowski N and Yurk C (2022) Climatology of Lake-Effect Snow Days Along the Southern Shore of Lake Michigan: What Is the Sensitivity to Environmental Factors and Snowband Morphology? Front. Water 4:826293. doi: 10.3389/frwa.2022.826293

The Laurentian Great Lakes have substantial influences on regional climatology, particularly with impactful lake-effect snow events. This study examines the snowfall, cloud-inferred snow band morphology, and environment of lake-effect snow days along the southern shore of Lake Michigan for the 1997–2017 period. Suitable days for study were identified based on the presence of lake-effect clouds assessed in a previous study and extended through 2017, combined with an independent classification of likely lake-effect snow days based on independent snowfall data and weather map assessments. The primary goals are to identify lake-effect snow days and evaluate the snowfall distribution and modes of variability, the sensitivity to thermodynamic and flow characteristics within the upstream sounding at Green Bay, WI, and the influences of snowband morphology. Over 300 lake-effect days are identified during the study period, with peak mean snowfall within the lake belt extending from southwest Michigan to northern Indiana. Although multiple lake-effect morphological types are often observed on the same day, the most common snow band morphology is wind parallel bands. Relative to days with wind parallel bands, the shoreline band morphology is more common with a reduced lower-tropospheric zonal wind component within the upstream sounding at Green Bay, WI, as well as higher sea-level pressure and 500-hPa geopotential height anomalies to the north of the Great Lakes. Snowfall is sensitive to band morphology, with higher snowfall for shoreline band structures than for wind parallel bands, especially due south of Lake Michigan. Snowfall is also sensitive to thermodynamic and flow properties, with a greater sensitivity to temperature in southwest Michigan and to flow properties in northwest Indiana.

Keywords: Great Lakes, lake-effect snow, winter, climatology, snowfall

INTRODUCTION

The Great Lakes have a significant impact on the climatology of downwind locations, most notably through the presence of wintertime lake-effect snowfall. Many lake-effect events have modest snowfall, but multi-day, high impact events with substantial snowfall also occur (Niziol et al., 1995; Schmidlin and Kosarik, 1999; Kristovich et al., 2000, 2017). Large events bring greater societal costs, including dangerous road conditions, snow removal expenses, damage to trees and buildings, and power outages (Schmidlin, 1993; Schmidlin and Kosarik, 1999). These impacts have motivated a substantial body of research focused on lake-effect snow climatology (e.g., Braham and Dungey, 1995; Suriano and Leathers, 2017b), trend assessments (e.g., Burnett et al., 2003; Bard and Kristovich, 2012), field experiments (e.g., Kristovich et al., 2000, 2017), forecasting (e.g., Rothrock, 1969; Niziol, 1987), numerical simulations (e.g., Lavoie, 1972; Ballentine et al., 1998) and morphology (e.g., Hjelmfelt, 1990; Laird et al., 2017).

Some of the earliest papers provided a physical paradigm that continues to inform the present, often gleaned from case studies (e.g., Mitchell, 1921; Sheridan, 1941). This early paradigm is summarized nicely by Lavoie (1972) and highlighted the frictional difference between land and lake surfaces (Remick, 1942), as well as the role of instability and associated heat and moisture fluxes (e.g., Sheridan, 1941; Petterssen and Calabrese, 1959). Studies utilizing numerical simulations subsequently have illustrated the importance of boundary layer growth, latent heat release, topography, mesoscale circulations, and snow band morphology (e.g., Lavoie, 1972; Ballentine, 1982; Hjelmfelt, 1990; Laird et al., 2003).

Large turbulent fluxes are driven by strong vertical gradients in temperature and moisture and are common during lake-effect snow events (e.g., Agee and Hart, 1990), with additional diurnal modifications (Kristovich and Spinar, 2005) and reductions for lake ice exceeding 70% coverage (Gerbush et al., 2008). The surface sensible heat flux is critical for boundary layer growth over the lake, along with entrainment from the top of the layer (Kelly, 1982; Agee and Gilbert, 1989; Kristovich et al., 2000) and deepening associated with the mesoscale circulation (Niziol et al., 1995). The latent heat flux is critical for subsequent cloud development, latent heat release, and strengthening of the mesoscale circulation (e.g., Ballentine, 1982; Hjelmfelt and Braham, 1983).

Many forecasting parameters date back to some of the earliest research, as well as local event climatology and forecaster experience (Niziol et al., 1995), although these parameters have been reinforced and confirmed by recent studies (e.g., Baijnath-Rodino et al., 2018). These include horizontal and vertical temperature gradients, fetch over the lake and flow properties, inversion characteristics, and synoptic-scale considerations (e.g., Sheridan, 1941; Remick, 1942; Rothrock, 1969). Adding to the complexity, small-scale orographic features (Hjelmfelt, 1992; Niziol et al., 1995), substantial lake ice concentrations (e.g., Niziol et al., 1995; Cordeira and Laird, 2008), and multiple lake interactions (Sousounis and Mann, 2000; Mann et al., 2002) can affect snowfall. Based on published work and forecast experience, detailed methodologies have evolved for specific regions (e.g., Niziol, 1987).

Particularly pertinent to the present study, Rothrock (1969) presented forecasting guidelines for the Lake Michigan basin, largely determined from sounding-based parameters and based on cases from a 2-year period. Findings indicated that snowfall is primarily dependent on the lake to 850-hPa temperature difference and the fetch across the lake. The chief inhibiting factor was inversion base height, with snowfall reduced for heights below ∼900 m. This inhibition has been supported by numerical simulations (Hjelmfelt, 1990), although an upstream inversion may be substantially altered as the boundary layer deepens across the lake (Agee and Gilbert, 1989; Chang and Braham, 1991; Niziol et al., 1995; Kristovich et al., 2003). Strong wind shear (Rothrock, 1969; Niziol, 1987) and low upstream relative humidity (Rothrock, 1969; Hjelmfelt, 1990) can also inhibit snowfall.

Climatological evaluations of lake-effect snowfall have been extensive in the literature, including satellite-based climatology (Laird et al., 2017), lake-effect contribution to seasonal snowfall (e.g., Chagnon, 1968; Braham and Dungey, 1995), trend assessments (e.g., Burnett et al., 2003; Kunkel et al., 2009; Bard and Kristovich, 2012; Clark et al., 2016), 21st century projections (Kunkel et al., 2002; Notaro et al., 2015; Suriano and Leathers, 2016), sensitivity to teleconnection patterns (Kluver and Leathers, 2015; Clark et al., 2016, 2018; Suriano and Leathers, 2017a), and seasonal prediction (Kluver and Leathers, 2015). For trend assessments and the influences of canonical teleconnections, a challenge is posed by the difficulty isolating the lake-effect contribution to seasonal snowfall, with estimates sensitive to methodology (Braham and Dungey, 1995). This uncertainty has been addressed by using transects to estimate the lake contribution to snowfall (Bard and Kristovich, 2012), or employing daily-scale classification to estimate synoptic patterns (Leathers and Ellis, 1996; Suriano and Leathers, 2017a) and snowfall (Clark et al., 2020) associated with lake-effect events.

The morphology of lake-effect snow bands has been explored through analyses of satellite data (Kristovich and Steve, 1995; Laird et al., 2017), field experiments (e.g., Kristovich et al., 2017; Mulholland et al., 2017) and numerical simulations (Hjelmfelt, 1990; Laird et al., 2003; Laird and Kristovich, 2004). Laird and Kristovich (2004) demonstrated that the ratio of wind speed (U) to maximum fetch distance (L) is useful in separating morphology, with a higher U/L exceeding $\sim 0.09\ \mathrm{m\ s^{-1}\ km^{-1}}$ for wind-parallel events (Laird et al., 2003). These wind-parallel events are the most common in the western Great Lakes (Kristovich and Steve, 1995; Laird et al., 2017), with cross-lake winds generating multiple bands (Braham, 1983) associated with horizontal rolls and cellular structures (Kelly, 1984; Kristovich and Steve, 1995). While not as common in the western Great Lakes (e.g., Laird et al., 2017), mid-lake and shoreline bands are associated with a lower U/L (Laird et al., 2003), while mesoscale vortices occur with weak flow (Forbes and Merritt, 1984; Laird and Kristovich, 2004) and are comparatively rare (Hjelmfelt, 1990; Laird et al., 2017). In addition to these primary band types, smaller misovortices have been observed within other band structures (Kristovich and Steve, 1995; Mulholland et al.,

FIGURE 1 | Map of stations included in the analysis of lake-effect snowfall along the southern shore of Lake Michigan. Dots, pluses, and triangles denote stations in IL, IN, and MI, respectively.

2017). Herein, the sensitivity of snowfall to band morphology is examined.

The present study combines the satellite-inferred cloud data from Laird et al. (2017), an update to the cloud data set through December 2017, and the classification approach from Clark et al. (2020) in order to examine the lake-effect snow day climatology along the southern shore of Lake Michigan. Based on these lake-effect snowfall days from 1997 to 2017, the present study examines the climatology in order to address the following questions:

1. *What is the sensitivity of lake-effect snowfall along the southern shore of Lake Michigan to lake band morphology?*
2. *What large-scale meteorological pattern across North America is associated with lake-effect days along the southern shore of Lake Michigan?*
   a. *What is the sensitivity of lake band morphology to the large-scale pattern?*
3. *What is the sensitivity of snowfall to thermodynamic and wind characteristics from the upstream sounding at Green Bay, WI?*
   a. *How does this sensitivity vary spatially within the region?*
   b. *What is the sensitivity of lake band morphology to the sounding variables?*

DATA AND METHODS

Snowfall Data

Precipitation data from the National Weather Service Cooperative Observer Program (COOP) sites were retrieved from the National Centers for Environmental Information (NCEI). The study region surrounds the southern shore of Lake Michigan, as defined by the southern sub-regions of the Clark et al. (2016, 2018) Lake Michigan basin snowfall climatology. As described in detail within Clark et al. (2016), stations were selected in order to represent six subregions surrounding the lake during a 1950–2013 study period and screened for missing data. In addition to the southern subregions within the previous study, LaPorte and Wanatah, IN, are included in the present study in order to better resolve the snowfall sensitivity to wind direction and morphology along the southern shore. The region for the present study is shown in **Figure 1**, with station information provided in **Table 1**.

TABLE 1 | Information on snowfall locations, including the identification number, missing data indicator, and sub-region from Clark et al. (2016).

Station	ID	Missing data %	Sub-region
Aurora, IL	110338	0.6	SW
De Kalb, IL	112223	0.0	SW
Midway, IL	14819	0.0	SW
O'Hare, IL	94846	0.0	SW
Peotone, IL	116725	5.4	SW
Rockford, IL	94822	0.0	SW
Battle Creek, MI	14815	8.5	SE
Bloomingdale, MI	200864	3.6	SE
Coldwater, MI	201675	4.8	SE
Eau Claire, MI	202445	12.7	SE
Goshen, IN	123418	0.0	SE
LaPorte, IN	124837	0.3	SE
Niles, MI	205892	0.0	SE
South Bend, IN	14848	0.3	SE
Valparaiso, IN	128999/128992/US1INPT0063	3.3	SE
Wanatah, IN	129222	6.0	SE
Winamac, IN	129670	0.6	SE

For missing data, values refer to the percentages of missing snowfall during LE days of the study period. Data are not available starting in the fall of 2014 for Eau Claire, MI. The Valparaiso, IN, station change-overs occurred in the fall of 2005 and 2014. The latest is from the Community Collaborative Rain, Hail, and Snow Network (CoCORAHs), which was carefully selected among several CoCORAHs based on data availability. All station data were acquired through the National Centers for Environmental Information (NCEI).

Morphology

Lake-effect snow band morphology was obtained from the 17-cold season lake-effect cloud climatology described by Laird et al. (2017). This climatology was recently updated through the end of 2017, creating a nearly 21-cold season climatology of lake-effect cloud events used herein. In short, visible satellite imagery for each cold-season day spanning October through March was visually inspected using stepwise animation to identify the lake-effect snow band type present over each lake on each day. For a given day, each lake could feature wind-parallel bands (WPB), shoreline bands (SPB), mesoscale vorticies (MSV), or unclear lake-effect organization along with synoptic cloudiness. Each lake could receive multiple band-type characterizations on a single day as the cloud structure often evolved on a given day or multiple cloud types were routinely identified simultaneously. For more detail on the cloud-band climatology, see Laird et al. (2017) and Section Data and Methods.

Independent Identification of Likely Lake-Effect Snow Days

Since the cloud-inferred lake-effect days (LE_cloud) frequently have synoptic clouds observed on the same day, a complementary identification of likely lake-effect snowfall days (LE_envsnow) was completed following the approach within Clark et al. (2020) for the classification of November snow days in the Lake Michigan region. The process is summarized here, with examples and comparison with a cluster-based approach provided in Clark et al. (2020). For each of the October through March days within the October 1997 to December 2017 study period during which peak snowfall was at least 2 cm, the identification of likely lake-effect days was based on the snowfall distribution and visual inspection of the surface map depiction from the Daily Weather Map online archive [from the National Oceanic and Atmospheric Administration (NOAA) Central Library Data Imaging Project] and upper-level maps available through the online archive through the NOAA Storm Prediction Center and/or maps produced using NOAA/National Center for Environmental Prediction/National Center for Atmospheric Research Reanalysis 1 (Kalnay et al., 1996). Although this study is concerned with locations along the southern shore of Lake Michigan, the precipitation map within the Daily Weather Map and snowfall from the other four Clark et al. (2016) sub-regions was sometimes helpful in isolating lake-effect days (station information for these supplementary locations is provided in **Supplementary Table 1**).

Likely LE_envsnow days were indicated by a lack of a synoptic-scale disturbance as a probable forcing for precipitation in the region, as well as the spatial snowfall distribution. Since the timing of snowfall is important for interpretation and the reporting time of 24-h snowfall measurements varies among the stations, Monthly Record of Climatological Observations Form reports from COOP observers were consulted in many instances; these were especially helpful in cases for which the observer noted the time period over which the snowfall occurred. To minimize error, there were three independent sets of evaluations for each day. Two were completed by co-authors, with an additional evaluation from the lead author. Cases with disagreement between the evaluations were re-considered. For cases in November, the identified days within Clark et al. (2020) through 2012 were utilized.

LE_envsnow days herein are intended as "pure" lake-effect days, with significant ($\geq$2 cm) snowfall entirely or primarily confined to downwind locations and a lack of substantial map-based, synoptic-scale forcing for precipitation. For days with a broad pattern of significant snowfall through the region, then LE_envsnow is not the deemed designation. Although lake enhancement can occur as synoptic-scale disturbances impact the region, the focus in this study is pure lake-effect days and their sensitivity to the environment.

Many of the days with snowfall in the region are not identified as LE_envsnow days; these are not the focus of the current study, but are briefly described here and with more detail in Clark et al. (2020). For most of these non-LE_envsnow days, denoted as system (SYS) snow days in Clark et al. (2020), there is map-based evidence of synoptic-scale forcing from migrating mid-latitude cyclones in the region. There is also typically a broad pattern of snowfall through the region, although the progression of synoptic disturbances through the region can result in snowfall in locations west or east of the lake. Other non-likely lake-effect days are delineated as Both (system snow days with substantial likely lake augmentation), Remnant (snowfall of at least 2 cm actually occurred the previous calendar day based on archived monthly observer reports of timing), Unclear (for days with unclear forcing and timing issues, if not error), and Insignificant (the peak snowfall report is $<$2 cm).

Evaluation of Upstream Sounding Characteristics and Large-Scale Environment

The days with both LE_cloud and LE_envsnow designations are evaluated in the present study and denoted as lake-effect (LE) days. For an assessment of the sensitivity of LE day snowfall to variables gleaned from the sounding at Green Bay, WI, sounding data were retrieved from online archives at the University of Wyoming. Thermodynamic and flow variables were extracted at mandatory levels in order to examine their correlations with snowfall. In order to create sounding composites, the radiosonde data were linearly interpolated to every millibar and analyzed using the MetPy library (May et al., 2021). For the assessment of inversion characteristics, the lowest non-surface-based temperature inversion through 700 hPa was examined, with the strength defined as the amount of warming from the base of the inversion to the top. Surface-based inversions weren't included, since these nocturnal near-surface inversions may be quickly obviated by the sensible heat flux from the warm lake. In order to examine the temperature difference between mandatory levels and Lake Michigan, the daily Lake Michigan temperature was provided through the Great Lakes Surface Environmental Analysis and acquired online through the Great Lakes Environmental Research Laboratory.

Sounding data at 00 and 12 UTC were evaluated; the sensitivity of snowfall to the 12 UTC sounding variables was stronger and is shown herein. An alternative "best time" approach was also considered, based on a comparison of 00 and 12 UTC conditions each day, but this introduces a bias regarding which thermodynamic or flow property is prioritized. The sensitivities of LE day snowfall to sounding variables were assessed using data visualization and Pearson correlation coefficients (with reported significance based on a 95% confidence interval). Since independent observations cannot be assumed with instances of neighboring lake-effect days, a bootstrapping approach was also used for these significance assessments. Specifically, 10,000 realizations of 100-member sub-samples were generated, with the correlation calculated for each; if the resulting 95% of the correlation distribution doesn't include zero, then the correlation is deemed significant.

For visualization of large-scale patterns associated with the LE snow days, maps of the NOAA/National Center for Environmental Information/National Center for Atmospheric Research Reanalysis 1 data were generated. Daily anomalies at 12 UTC were calculated for sea level pressure, 850-hPa temperature and 500-hPa geopotential height for each case, based on the 30-year climatology baseline from 1980 to 2010 for each of the days.

RESULTS AND DISCUSSION

Comparison of Daily Cloud Data With Identified Likely Lake-Effect Snow Days

System and lake-effect cloud structures were observed frequently during the study period, although many lacked accumulating snowfall along the southern shore of Lake Michigan (**Table 2**).

TABLE 2 | Comparison of classification and satellite-inferred cloud data.

	No clouds	SYS clouds	SYS and LE clouds	LE clouds
Both	0	11	38	15
INS	0	150	116	45
LE	2	68	174	157
None	63	1,514	471	144
Remnant	1	0	1	0
SYS	4	322	265	62
Unclear/error	1	1	0	1

Cloud data are available for the months of October through March, from October 1997 through December 2017. Satellite estimates were not available for 111 days during the study period. Classifications were completed for days during this period in which the peak snowfall in the region was ≥2 cm.

Roughly 82% of the days identified as likely lake-effect days had lake-effect cloud structures observed, while ∼89% of the days identified as likely system snow days had synoptic cloud structures. An evaluation of mismatches reveals the key role of snowfall timing; for most of these days, 24-h snowfall reports influenced the classification of likely precipitation forcing, while the cloud data is effectively "ground truth" for the daytime hours of the date in question. For example, a day may have observed lake-effect cloud structures and a clearly favorable environment for lake-effect processes, yet not be classified as a lake-effect snow day due to a broad region of synoptically-induced snowfall from the previous night (which is reported in the morning for multiple locations). The study herein utilizes the 331 days which have observed lake-effect cloud structures and were also identified as likely lake-effect snow days. These will subsequently be referred to as lake-effect snow (LES) days. Although it is not uncommon for LE days to occur sequentially, individual days are evaluated in this study in order to evaluate the sensitivity to cloud morphology and environmental factors.

Climatology of LE Days

The peak snowfall varies substantially among LE days; the mean peak snowfall is a modest 9.7 cm, yet the top 5 days exceed 30 cm and the peak snowfall day was an impressive 66 cm (not shown). The highest mean snowfall occurs within the belt extending from southwest Michigan into adjacent northern Indiana, with a reduction in mean snowfall for western stations and the easternmost locations in Michigan (**Figure 2**). The peak snowfall region also has much more frequently observed LES, although there were ∼10 days with LES west of Lake Michigan (not shown). Seasonally, the LE days span the October through March study season, with a peak of nearly one-third of the LE days in January.

On LE days, the most common lake-effect cloud type is WPB, followed by SPB, Unclear morphology, and MSV (**Table 3**). Although many of the WPB days lack other LE morphological types, a substantial fraction of days with other morphologies have multiple types observed. Nearly three-quarters of the SPB days have multiple cloud structures observed, while nearly half of the Unclear days have other structures observed and only

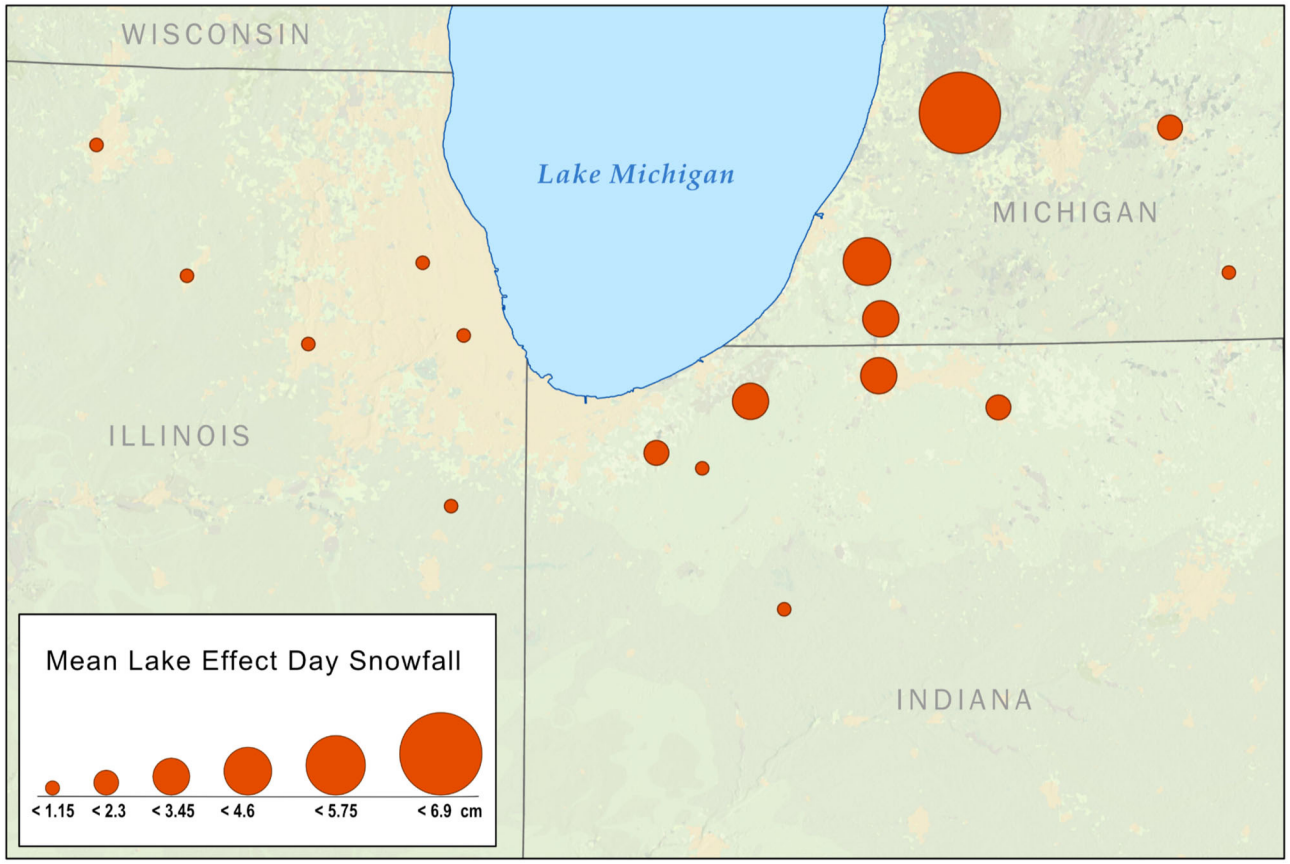

FIGURE 2 | Map of mean snowfall (cm day^{-1}) for LE snow days. These days include the 331 days for which there is a combination of LE_cloud and LE_envsnow designations. These LE days occurred from October (7 days) to March (27 days), with 36 in November, 71 in December, 110 in January, and 80 in February.

TABLE 3 | Number of LE days with each morphological cloud type during the study period.

	WPB	SPB	MSV	Unclear
Total	286	61	4	39
With WPB	(236)	38	0	11
With SPB	38	(15)	2	5
With MSV	0	2	(1)	1
With Unclear	11	5	1	(22)
WPB, SPB, MSV	1	1	1	

These include wind parallel bands (WPB), shoreline parallel bands (SPB), mesoscale vortices (MSV), and Unclear structures. Combinations of morphological styles on the same day are also indicated. The numbers in parentheses indicate the days with a solitary observed lake-effect cloud morphology.

one MSV day lacks another morphology (**Table 3**). Despite this notable amount of concurrent snowband morphologies, WPB and SPB days are of great interest herein, since they are the most common. Furthermore, the less common SPB days are associated with different snowfall patterns and environments.

The mean snowfall on SPB days is higher for westernmost locations than on the more common WPB days, with a peak in northwest Indiana (**Figure 3**). In contrast, the far more plentiful WPB days have peak snowfall near the shoreline in southwest Michigan, and since these days are more common, they dominate the overall LE snowfall distribution (as in **Figure 2**). However, the impact of the less common SPB days is often substantial. In addition to the difference in spatial snowfall patterns (**Figure 3**), it is noteworthy that four of the top five LE day accumulations had SPB structures observed (although the WPB morphology was also documented). These four large SPB-associated snowfalls (all exceeding 30 cm) occurred at different locations within the region, including Eau Claire, Michigan, and Valparaiso, La Porte, and South Bend, Indiana.

During lake-effect snow days, negative 500-hPa geopotential height anomalies are present in the Great Lakes, with a trough axis in the eastern Great Lakes (**Figure 4A**). Cold anomalies at 850-hPa are also present over Lake Michigan, with northwest flow (**Figure 4B**). Higher than average sea-level pressure (SLP) is present over the Central United States, while lower SLP is found to the northeast (**Figure 4C**). Comparing the patterns per morphology, SPB days have higher 500-hPa geopotential heights and warmer 850-hPa temperatures northwest of the Great Lakes (**Figures 5A,B**). The difference in SLP anomalies reveals higher SLP within and to the north of the Great Lakes (**Figure 5C**). The

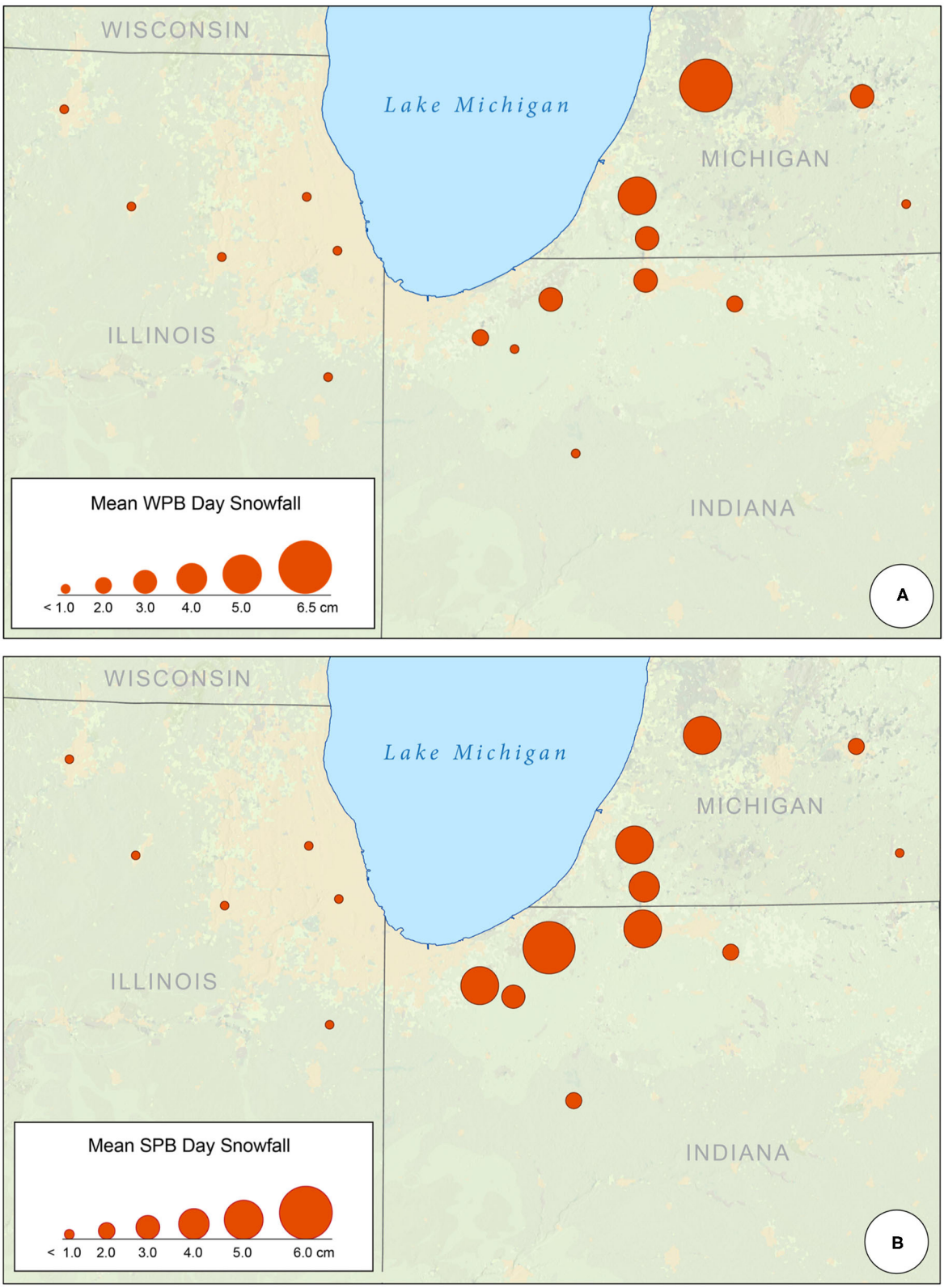

FIGURE 3 | Mean snowfall (cm day^{-1}) associated with WPB **(A)** and SPB **(B)** lake-effect snow days.

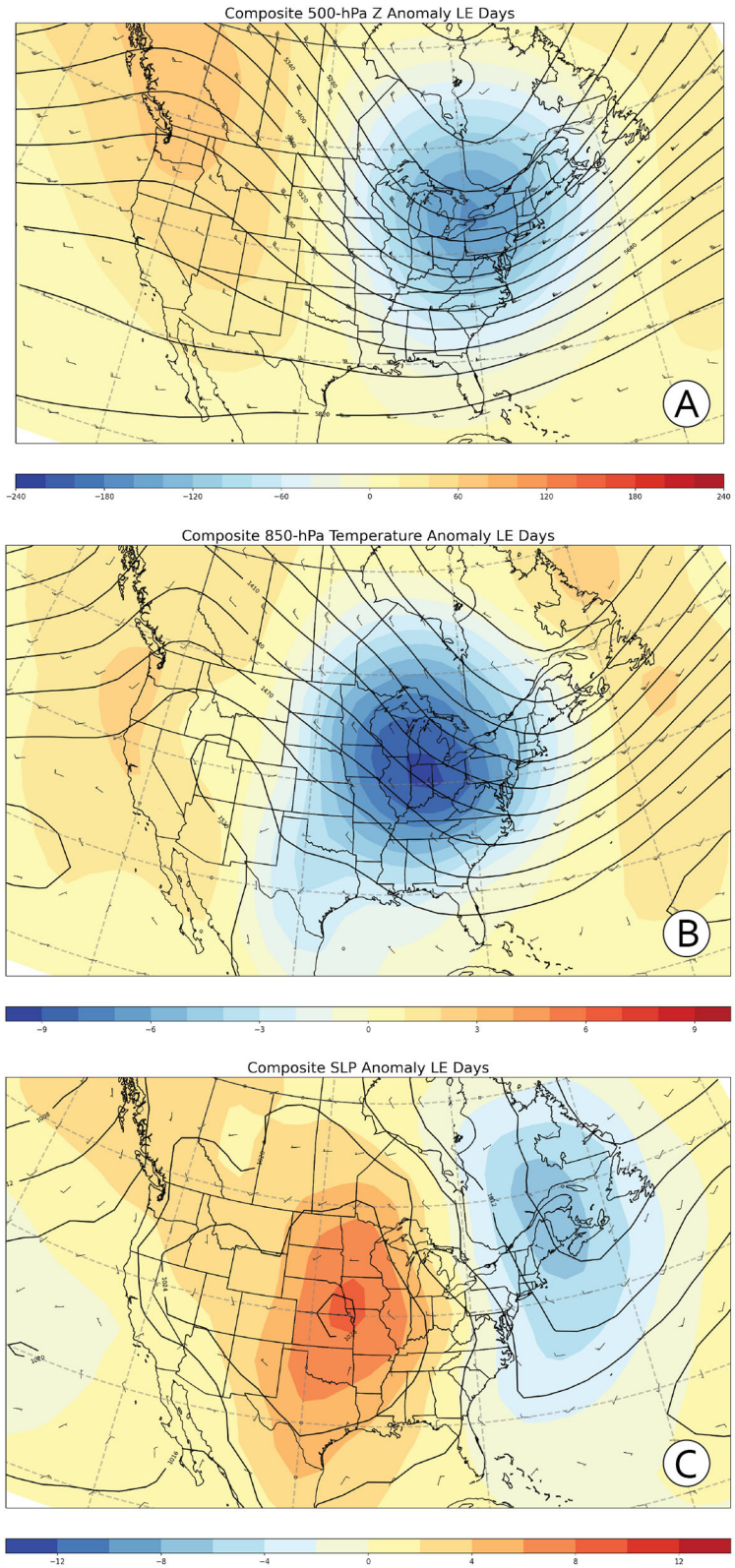

FIGURE 4 | Composite 12 UTC anomaly maps of Reanalysis I **(A)** 500-hPa geopotential height, **(B)** 850-hPa temperature, and **(C)** sea-level pressure for LE days. Filled contours represent anomalies of geopotential height (upper), temperature (middle) and sea-level pressure (lower), while solid contours represent mean geopotential height (upper, middle) and sea-level pressure (lower). Wind barbs are also included. There are 331 days represented within the composite. NCEI reanalysis data provided by the NOAA Earth System Research Laboratory/Physical Sciences Division, Boulder, CO from their web site (http://www.esrl.noaa.gov/psd/).

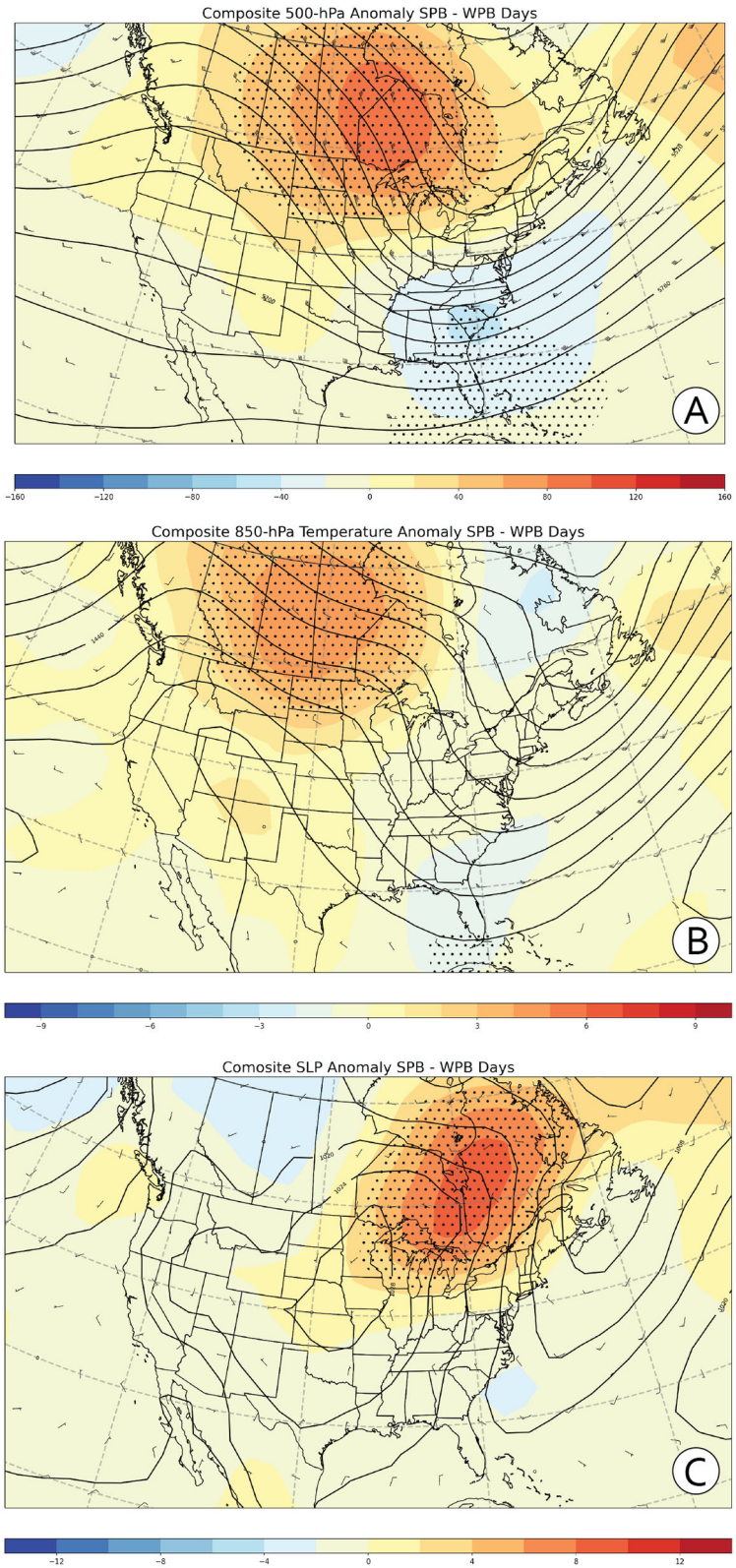

FIGURE 5 | Composite 12 UTC Reanalysis I **(A)** 500-hPa geopotential height (upper), **(B)** 850-hPa temperature (middle) and **(C)** sea-level pressure (lower) differences between days with SPB and WPB cloud classifications. Differences are indicated by filled and solid contours. Dots indicate regions for which the null hypothesis of equal mean SPB and WPB 500-hPa geopotential height, 850-hPa temperature and sea-level pressure can be rejected, respectively. This assessment is based on bootstrap simulations using 10,000 50-member sub-samples.

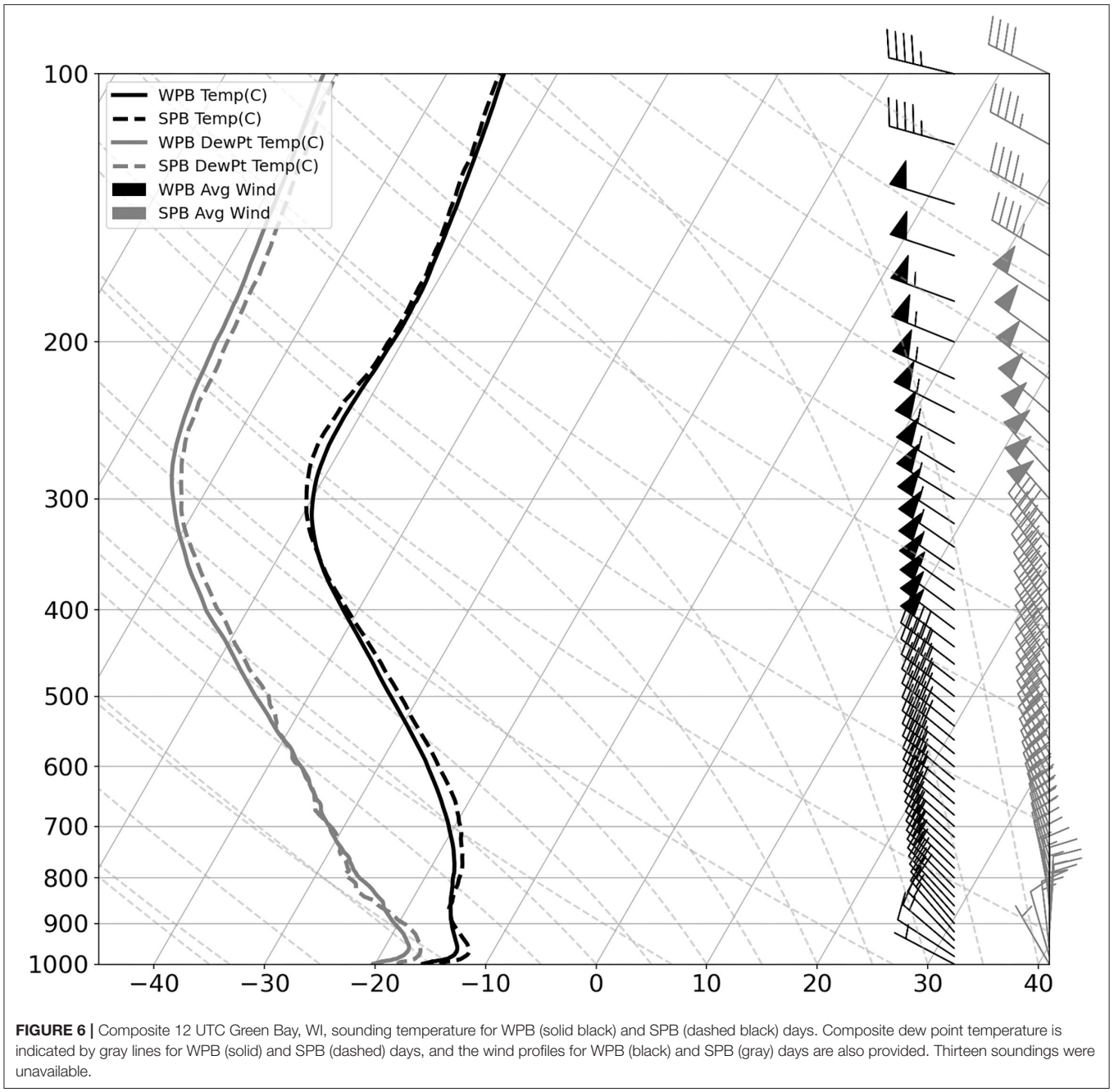

FIGURE 6 | Composite 12 UTC Green Bay, WI, sounding temperature for WPB (solid black) and SPB (dashed black) days. Composite dew point temperature is indicated by gray lines for WPB (solid) and SPB (dashed) days, and the wind profiles for WPB (black) and SPB (gray) days are also provided. Thirteen soundings were unavailable.

wind direction over Lake Michigan on the surface and 850-hPa SPB day composites (**Figures 5B,C**) suggests a longer fetch than for the LE day composite (**Figures 4B,C**), which is consistent with Laird et al. (2003).

Consistent with this environment in the Great Lakes, the sounding composite from Green Bay, WI, indicates a cold lower troposphere with northwesterly flow (**Figure 6**). The lower tropospheric winds on SPB days are lighter and more northerly than on WPB days. Interestingly, the morphology is more sensitive to the zonal component of the wind than to the meridional component, with a much weaker zonal component at 850-hPa on SPB days (**Table 4**). The lower tropospheric temperature is also modestly warmer on SPB days, although the difference is not significant at 850-hPa. Other modest thermodynamic differences are also insignificant based on the bootstrap-based assessments, including differences in inversion characteristics and relative humidity.

Sensitivity of Snowfall to Sounding Parameters

Based on the 12 UTC sounding data from Green Bay, WI, the peak daily snowfall per LE day is significantly

TABLE 4 | Mean sounding variables per-lake band morphology.

	WPB	SPB	Bootstrap significance
850-hPa wind direction	318°	345°	
850-hPa wind speed	22.9 knots	17.3 knots	*
850-hPa u	13.1 knots	2.1 knots	*
850-hPa v	−14.1 knots	−13.7 knots	
700-hPa temperature	−20.6°C	−19.5°C	
Inversion height	1,044 m	1,021 m	
Inversion strength	2.5°C	2.0°C	
850-hPa relative humidity	64%	61%	

A bootstrap approach was used to infer whether the null hypothesis of equal population mean could be rejected, with '' indicating significance at the 95% confidence threshold, respectively. (Although the Welch t-test would also allow the rejection of the null hypothesis of equal population means for the 850-hPa wind speed and zonal wind component (u), independent observations cannot be assumed in the present study.) The wind direction variable is adjusted for cases with an easterly wind component by adding 360 degrees, such that NE wind of 45 degrees is converted to 405 degrees. Inversion strength is defined as the amount of warming from the base of the inversion to the top.*

TABLE 5 | Correlation coefficients between peak snowfall and several variables from the upstream sounding at Green Bay, WI, during lake-effect snow days.

Variable	Correlation coefficient	Bootstrap significance
850-hPa wind direction	0.21	
850-hPa wind speed	0.02	.
850-hPa u	−0.26	
850-hPa v	−0.16	*
850-hPa temperature	−0.25	*
Lake to 850-hPa Delta T	0.25	*
700-hPa temperature	−0.29	*
Lake to 700-hPa Delta T	0.28	
Inversion height	−0.04	
Inversion strength	−0.07	
850-hPa relative humidity	0.08	

A bootstrap approach was used to infer the significance of correlations, with "" and "." indicating significant correlations at the 95 and 90% confidence thresholds, respectively.*

anticorrelated with the 850-hPa zonal wind component, but not significantly correlated with the meridional component (**Table 5**). Spatially, the sensitivity to the 850-hPa zonal wind component peaks in northwest Indiana and is weaker in southwest Michigan (**Figure 7A**). This stronger sensitivity to the zonal wind component in northwest Indiana is consistent with the morphological results noted previously, with increased likelihood of SPB structure as the zonal wind becomes weaker. There is also a significant anticorrelation of snowfall with the 850-hPa meridional wind component in some locations, with the peak impact in north-central Indiana (**Figure 7B**). Other wind characteristics were considered as well. The sensitivity to the wind direction is consistent with the zonal and meridional wind results (not shown), while correlation of peak snowfall with wind speed is effectively non-existent (**Table 5**). Although there is some evidence of a non-linear snowfall reduction for very high wind speeds, the sample size encumbers this analysis (not shown).

There is a significant dependence of peak LE day snowfall on lower tropospheric temperature, as well as the associated lake to 850 and 700-hPa temperature differences (**Table 5**). The relationship appears strongest with 700-hPa temperature and peaks in southwest Michigan, where the sensitivity to the wind is somewhat weaker (**Figure 7C**). Interestingly, other thermodynamic factors lack a meaningful linear relationship with peak snowfall; these include inversion base height and strength, as well as 850-hPa relative humidity (**Table 5**). The lack of a significant correlation with inversion characteristics is surprising, but may simply be indicative of the capacity of boundary layer growth across the lake to erode the inversion. Furthermore, as with high wind speeds, there is some visual evidence that very strong inversions tend to reduce peak snowfall; however, the sample size of this small subset does not foster robust hypothesis testing or related confidence.

CONCLUSIONS

The southern shore of Lake Michigan frequently experiences lake-effect snow events, some of which produce heavy snowfall in the region. The most common snow band morphology is WPB, which is fostered by a cold environment and relatively strong zonal wind component in the lower troposphere. The resulting snowfall typically has a peak in southwest Michigan, consistent with northwest flow. Since these LE days are most plentiful in the Lake Michigan region, this snowfall mode determines much of the spatial distribution of lake-effect snow.

A very different mode of snowfall occurs during SPB days, although WPB structures are often present during the same day. These SPB days are primarily fostered by a weaker zonal wind component and typically produce greater snowfall than WPB in northwest Indiana. Although not every SPB day produces prolific snowfall, they account for four of the five largest snowfalls (at four different locations- ranging geographically from Valparaiso, IN, to Eau Claire. Michigan). This makes SPB particularly impactful, especially when they occur in locations which experience less frequent lake-effect snowfall (e.g., Valparaiso, IN). These two modes of snowfall in the region are identifiable within the leading principal components of daily snowfall in the region, while other statistical modes are more localized (not shown).

In general, greater LE snowfall in the region is associated with colder conditions, weak zonal wind flow, and a northerly meridional wind component in the lower troposphere. Snowfall is not significantly correlated with inversion characteristics, likely due to the impacts of Lake Michigan on boundary layer growth across the lake. There is some visual evidence that very strong inversions and high wind speeds tend to reduce peak snowfall;

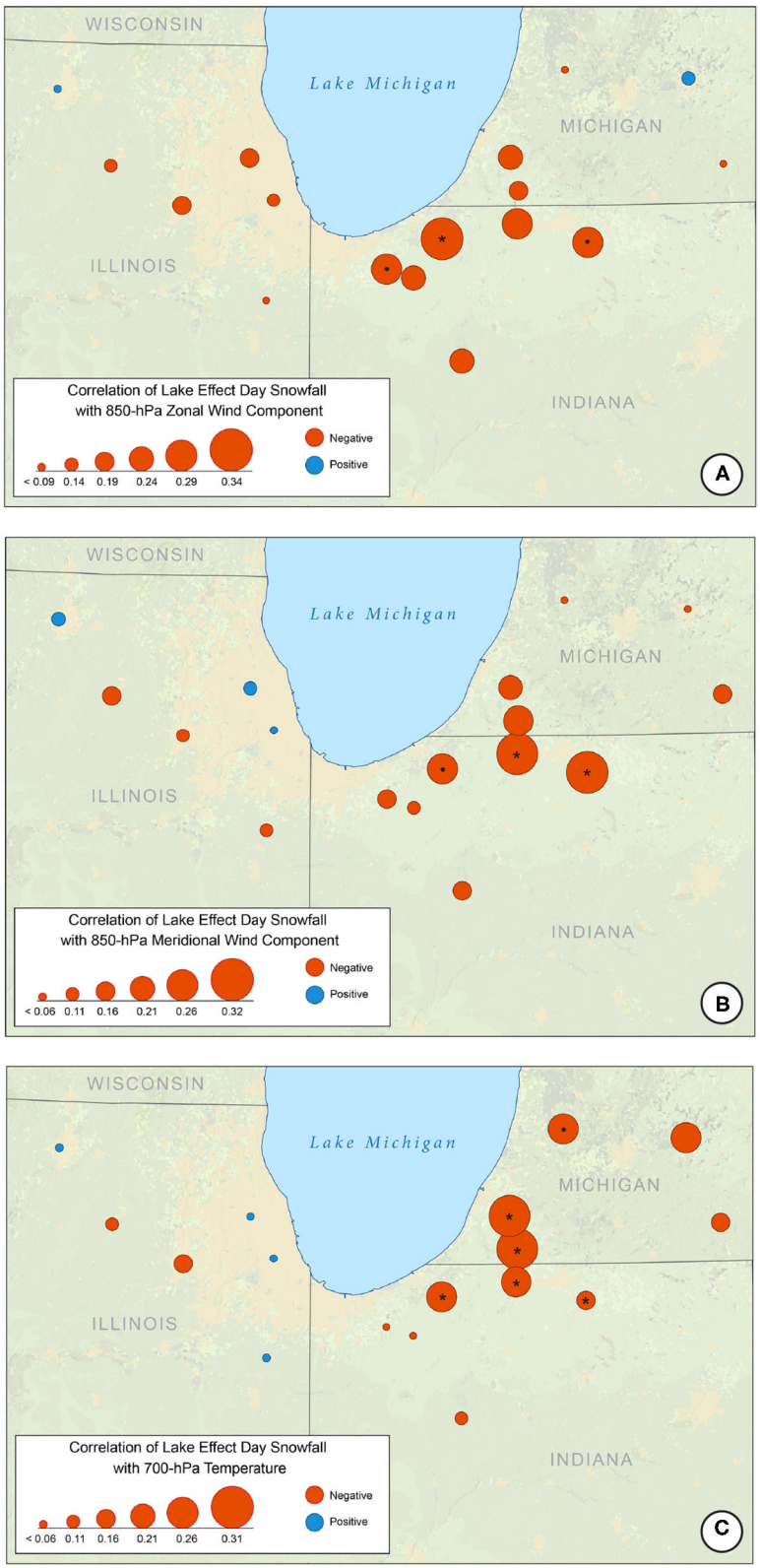

FIGURE 7 | Map of correlation coefficients of snowfall and variables from the upstream sounding at Green Bay, WI, during lake-effect snow days. Sounding variables include the 850-hPa zonal (u; **A**) and meridional (v; **B**) wind components and 700-hPa temperature **(C)**. A bootstrap approach was used to infer the significance of correlations at the 95 and 90% confidence thresholds, respectively.

however, the sample size of this subset is too small for a robust evaluation.

It is noteworthy that none of the relationships with snowfall herein explain a large fraction of the snowfall variance. The variance of snowfall is substantial, with a great deal of internal variability beyond the signal associated with environmental characteristics and snow band morphology. Additionally, the intraday changes to the environment may be substantial, yet this is not captured here; even if it were, the snowfall data represents 24-h totals. In any case, the sensitivity to 00 UTC sounding characteristics was also considered, but the sensitivity to the 12 UTC environment was greater. Although a "best time" approach was also considered, it leads to an unintentional bias as the role of flow properties and temperature are subjectively weighted. An alternative approach could also analyze multi-day events, rather than individual LE days. Although this option was explored, a daily data approach was ultimately used in order to better assess the sensitivity to the environment and snowband morphology.

The region of study was chosen to highlight the importance of snowband morphology and associated environmental factors along the southern shore. Northern regions of the Lake Michigan basin are also worthy of study (as are regions surrounding other Great Lakes), with likely different sensitivity to thermodynamic and flow characteristics. It may also be beneficial to evaluate the environments of LE_cloud days in which snowfall accumulation did not occur, although this is beyond the scope of the current study. Lastly, although the cloud data would not be available, the analysis could be extended to earlier years in order to increase the sample size for other aspects of the analysis.

DATA AVAILABILITY STATEMENT

The raw data supporting the conclusions of this article will be made available by the authors, without undue reservation.

AUTHOR CONTRIBUTIONS

CC designed the project and completed analysis, with the help of NM and KG. BG-B designed the maps of snowfall results and also helped with other graphics. KG made the composite soundings and helped with Python code for Reanalysis maps. The update to the cloud data was completed by NM, with the help of CB and KC. The identification of LE_envsnow days was lead by CC, with the help of NB, ABl, ABo, QD, JD, AG, SG, BH, MK, JL, EM, HS, NR, and CY. All authors contributed to the article and approved the submitted version.

FUNDING

This work was funded by Valparaiso University and NSF Grant AGS-2040594.

ACKNOWLEDGMENTS

The authors thank Dr. Neil Laird for use of the Laird et al. (2017) cloud assessment data. The authors also thank the National Oceanic and Atmospheric Administration (NOAA) and National Centers for Environmental Information (NCEI) for the online access to daily station data and scanned monthly COOP reports, the NOAA Central Library Data Imaging Project for the archived Daily Weather Map series, the NOAA Physical Sciences Division and Climate Prediction Center for teleconnection indices, the Python program (http://python.org) and the open source statistical package, R (available at http://cran.r-project.org/).

SUPPLEMENTARY MATERIAL

The Supplementary Material for this article can be found online at: https://www.frontiersin.org/articles/10.3389/frwa.2022.826293/full#supplementary-material

REFERENCES

Agee, E. M., and Gilbert, S. R. (1989). An aircraft investigation of mesoscale convection over Lake Michigan during the 1984 cold air outbreak. *J. Atmos. Sci.* 46, 1877–1897. doi: 10.1175/1520-0469(1989)046<1877:AAIOMC>2.0.CO;2

Agee, E. M., and Hart, M. L. (1990). Boundary layer and mesoscale structure over Lake Michigan during a wintertime cold air outbreak. *J. Atmos. Sci.* 47, 2293–2316. doi: 10.1175/1520-0469(1990)047<2293:BLAMSO>2.0.CO;2

Baijnath-Rodino, J. A., Duguay, C. R., and LeDrew, E. (2018). Climatological trends of snowfall over the Laurentian Great Lakes basin. *Int. J. Climatol.* 38, 3942–3962. doi: 10.1002/joc.5546

Ballentine, R. J. (1982). Numerical simulations of land-breeze-induced snowbands along the western shore of Lake Michigan. *Month. Weather Rev.* 110, 1544–1553. doi: 10.1175/1520-0493(1982)110<1544:NSOLBI>2.0.CO;2

Ballentine, R. J., Stamm, A. J.,Chermack, E. E., Byrd, G. B., and Schleede, D. (1998). Mesoscale model simulation of the 4-5 January 1995 lake-effect snowstorm. *Weather Forecast.* 13, 893–920. doi: 10.1175/1520-0434(1998)013<0893:MMSOTJ>2.0.CO;2

Bard, L., and Kristovich, D. A. R. (2012). Trend reversal in Lake Michigan contribution to snowfall. *J. Appl. Meteor.* 51, 2038–2046. doi: 10.1175/JAMC-D-12-064.1

Braham, R. R. (1983). The Midwest snow storm of 8-11 December 1977. *Month. Weather Rev.* 111, 253–272. doi: 10.1175/1520-0493(1983)111<0253:TMSSOD>2.0.CO;2

Braham, R. R., and Dungey, M. J. (1995). Lake-effect snowfall over Lake Michigan. *J. Appl. Meteor.* 34, 1009–1019. doi: 10.1175/1520-0450(1995)034<1009:LESOLM>2.0.CO;2

Burnett, A. W., Kirby, M. E., Mullins, H. T., and Patterson, W. P. (2003). Increasing Great Lake-effect snowfall during the twentieth century: a regional response to global warming? *J. Clim.* 16, 3535–3542. doi: 10.1175/1520-0442(2003)016<3535:IGLSDT>2.0.CO;2

Chagnon, S. A. (1968). Precipitation climatology of Lake Michigan basin. *Illinois State Water Survey Bul l.* 52, 88.

Chang, S. S., and Braham, R. R. (1991). Observational stuffy of a convective internal boundary layer over Lake Michigan. *J. Atmos. Sci.* 48, 2265–2279. doi: 10.1175/1520-0469(1991)048<2265:OSOACI>2.0.CO;2

Clark, C., Ganesh-Babu, B., Elless, T., Lyza, A., Koning, D. M., Carne, A. R., et al. (2018). Spatio-temporal November and March snowfall trends in the Lake Michigan region. *Int. J. Climatol.* 38, 3250–3263. doi: 10.1002/joc.5498

Clark, C. A., Elless, T. J., Lyza, A. W., Ganesh-Babu, B., Koning, D. M., Carne, A. R., et al. (2016). Spatiotemporal snowfall variability in the Lake Michigan region:

how is warming affecting wintertime snowfall? *J. Appl. Meteorol. Climatol.* 55, 1813–1830. doi: 10.1175/JAMC-D-15-0285.1

Clark, C. A., Goebbert, K. H., Ganesh-Babu, B., Young, A. M., Heinlein, K. N., Casas, E. G., et al. (2020). Classification of Lake Michigan snow days for estimation of the lake-effect contribution to the downward trend in November snowfall. *Int. J. Climatol.* 40, 5656–5670. doi: 10.1002/joc.6542

Cordeira, J. M., and Laird, N. F. (2008). The influence of ice cover on two lake-effect events over Lake Erie. *Month. Weather. Rev.* 139, 2747–2763. doi: 10.1175/2007MWR2310.1

Forbes, S. F., and Merritt, J. H. (1984). Mesoscale vortices over the Great Lakes in wintertime. *Mon. Wea. Rev.* 112, 377–381. doi: 10.1175/1520-0493(1984)112<0377:MVOTGL>2.0.CO;2

Gerbush, M. R., Kristovich, D. A. R., and Laird, N. F. (2008). Mesoscale boundary layer and heat flux variations over pack ice–covered Lake Erie. *J. Appl. Meteorol. Climatol.* 47, 668–682. doi: 10.1175/2007JAMC1479.1

Hjelmfelt, M. R. (1990). Numerical study of the influence of environmental conditions on lake-effect snowstorms over Lake Michigan. *Month. Weather Rev*. 118, 138–150. doi: 10.1175/1520-0493(1990)118<0138:NSOTIO>2.0.CO;2

Hjelmfelt, M. R. (1992). Orographic effects in simulated lake-effect snowstorms over Lake Michigan. *Month. Weather Rev.* 120, 373–377. doi: 10.1175/1520-0493(1992)120<0373:OEISLE>2.0.CO;2

Hjelmfelt, M. R., and Braham, R. R. (1983). Numerical simulation of the airflow over Lake Michigan for a major lake-effect snow event. *Month. Weather Rev*. 111, 205–219. doi: 10.1175/1520-0493(1983)111<0205:NSOTAO>2.0.CO;2

Kalnay, E., Kanamitsu, M., Kistler, R., Collins, W., Deaven, D., Gandin, L., et al. (1996). The NCEP/NCAR 40-year reanalysis project. *Bull. Amer. Meteor. Soc.* 77, 437–70.

Kelly, R. D. (1982). A single Doppler study of horizontal-roll convection in a lake-effect snow storm. *J. Atmos. Sci*. 39, 1521–1531. doi: 10.1175/1520-0469(1982)039<1521:ASDRSO>2.0.CO;2

Kelly, R. D. (1984). Horizontal roll and boundary-layer interrelationships observed over Lake Michigan. *J. Atmos. Sci.* 11, 1816–1826. doi: 10.1175/1520-0469(1984)041<1816:HRABLI>2.0.CO;2

Kluver, D. B., and Leathers, D. J. (2015). Winter snowfall prediction in the United States using multiple discriminant analysis. *Int. J. Climatol.* 35, 2003–2018. doi: 10.1002/joc.4103

Kristovich, D. A., Clark, R. D., Frame, J., Geerts, B., Knupp, K. R., Kosiba, K. A., et al. (2017). The Ontario winter lake-effect systems field campaign: scientific and educational adventures to further our knowledge and prediction of lake-effect storms. *Bull. Am. Meteorol. Soc.* 98, 315–332. doi: 10.1175/BAMS-D-15-00034.1

Kristovich, D. A. R., Laird, N. F., and Hjelmfelt, M. R. (2003). Convective evolution across Lake Michigan during a widespread lake-effect snow event. *Month. Weather Rev.* 131, 643–655. doi: 10.1175/1520-0493(2003)131<0643:CEALMD>2.0.CO;2

Kristovich, D. A. R., and Spinar, M. L. (2005). Diurnal variations in lake-effect precipitation near the western Great Lakes. *J. Hydrometeor.* 6, 210–218. doi: 10.1175/JHM403.1

Kristovich, D. A. R., and Steve, R. A. (1995). A satellite study of cloud-band frequencies over the Great Lakes. *J. Appl. Meteor.* 34, 2083–2090. doi: 10.1175/1520-0450(1995)034<2083:ASSOCB>2.0.CO;2

Kristovich, D. A. R., Young, G. S., Verlinde, J., Sousounis, P. J., Mourad, P., Lenschow, D., et al. (2000). The lake-induced convection experiment (Lake-ICE) and the snowband dynamics project. *Bull. Am. Meteorol. Soc.* 81, 519–542. doi: 10.1175/1520-0477(2000)081<0519:TLCEAT>2.3.CO;2

Kunkel, K. E., Ensor, L., Palecki, M., Easterling, D., Robinson, D., Hubbard, K. G., et al. (2009). A new look at lake-effect snowfall trends in the Laurentian Great Lakes using a temporally homogeneous data set. *J. Great Lakes Res.* 35, 23–29. doi: 10.1016/j.jglr.2008.11.003

Kunkel, K. E., Westcott, N. E., and Kristovich, D. A. R. (2002). Effects of climate change on heavy lake-effect snowstorms near Lake Erie. *J. Great Lakes Res.* 28, 521–536. doi: 10.1016/S0380-1330(02)70603-5

Laird, N. F., and Kristovich, D. A. R. (2004). Comparison of observations with idealized model results for a method to resolve winter lake-effect mesoscale morphology. *Month. Weather Rev.* 132, 1093–1103. doi: 10.1175/1520-0493(2004)132<1093:COOWIM>2.0.CO;2

Laird, N. F., Kristovich, D. A. R., and Walsh, J. E. (2003). Idealized model simulations examining the mesoscale structure of winter lake-effect circulations. *Month. Weather Rev.* 131, 206–221. doi: 10.1175/1520-0493(2003)131<0206:IMSETM>2.0.CO;2

Laird, N. F., Metz, N. D., Gaudet, L., Grasmick, C., Higgins, L., Loeser, C., et al. (2017). Climatology of cold season lake-effect cloud bands for the North American Great Lakes. *Int. J. Climatol.* 37, 2111–2121. doi: 10.1002/joc.4838

Lavoie, R. L. (1972). A mesoscale numerical model of lake-effect storms. *J. Atmos. Sci.* 29, 1025-1040. doi: 10.1175/1520-0469(1972)029<1025:AMNMOL>2.0.CO;2

Leathers,. D. J., and Ellis, A. W. (1996). Synoptic mechanisms associated with snowfall increases to the lee of Lakes Erie and Ontario. *Int. J. Climatol.* 16, 1117–1135. doi: 10.1002/(SICI)1097-0088(199610)16:10<1117::AID-JOC80>3.0.CO;2-4

Mann, G. E., Wagenmaker, R. B., and Sousounis, P. J. (2002). The influence of multiple lake interactions upon lake-effect storms. *Month. Weather Rev*. 130, 1510–1530. doi: 10.1175/1520-0493(2002)130<1510:TIOMLI>2.0.CO;2

May, R. M., Arms, S. C., Marsh, P., Bruning, E., Leeman, J. R., Goebbert, K., et al. (2021). *MetPy: A Python Package for Meteorological Data. Unidata*. Available online at: https://github.com/Unidata/MetPy (accessed November 1, 2021).

Mitchell, C. L. (1921). Snow flurries along the eastern shore of Lake Michigan. *Month. Weather Rev.* 49, 502–503.

Mulholland, J. P., Frame, J., Nesbitt, S. W., Steiger, S. M., Kosiba, K. A., and Wurman, J. (2017).Observations of misovortices within a long-lake-axis-parallel lake-effect snowband during the OWLeS project. *Month. Weather Rev*. 145, 3265–3291 doi: 10.1175/MWR-D-16-0430.1

Niziol, T. A. (1987). Operational forecasting of lake-effect snowfall in western and central New York. *Weather Forecast.* 2, 310–321. doi: 10.1175/1520-0434(1987)002<0310:OFOLES>2.0.CO;2

Niziol, T. A., Snyder,. W. R., and Waldstreicher, J. S. (1995). Winter weather forecasting throughout the eastern United States. Part IV: lake effect snow. *Weather Forecast.* 10, 61–77. doi: 10.1175/1520-0434(1995)010<0061:WWFTTE>2.0.CO;2

Notaro, M., Bennington, V., and Varvus, S. (2015). Dynamically downscaled projections of lake-effect snow in the Great Lakes basin. *J. Clim.* 28, 1661–1684. doi: 10.1175/JCLI-D-14-00467.1

Petterssen, S., and Calabrese, P. A. (1959). On some influences due to warming of the air by the Great Lakes in winter. *J. Meteor.* 16, 646–652. doi: 10.1175/1520-0469(1959)016<0646:OSWIDT>2.0.CO;2

Remick, J. T. (1942). The effect of Lake Erie on the local distribution of precipitation in winter (I). *Bull. Am. Meteor. Soc.* 23, 1–4. doi: 10.1175/1520-0477-23.1.1

Rothrock, H. J. (1969). *An aid in forecasting significant lake snows. Environmental Science Services Administration Tech. Memo*. WBTM CR-30. National Weather Service, 12pp.

Schmidlin, T. W. (1993).Impacts of heavy snowfall during 1989 in the Lake Erie snowbelt. *J. Clim.* 6, 659–667. doi: 10.1175/1520-0442(1993)006<0759:IOSWWD>2.0.CO;2

Schmidlin, T. W., and Kosarik, J. (1999). A record breaking snowfall during 9-14 November 1996. *Bull. Am. Meteor. Soc.* 80, 1107–1116. doi: 10.1175/1520-0477(1999)080<1107:AROSDN>2.0.CO;2

Sheridan, L. W. (1941). The influence of Lake Erie on local snows in Western New York. *Bull. Am. Meteor. Soc.* 22, 393–395. doi: 10.1175/1520-0477-22.10.393

Sousounis, P. J., and Mann, G. E. (2000). Lake-aggregate mesoscale disturbances. Part V: Impacts on lake-effect precipitation. Month. *Weather Rev.* 128, 728–745. doi: 10.1175/1520-0493(2000)128<0728:LAMDPV>2.0.CO;2

Suriano, Z. J., and Leathers, D. J. (2016). Twenty-first century snowfall projections within the Eastern Great Lakes region: Detecting the presence of a lake-induced snowfall signal in GCMs. *Int. J. Climatol.* 36, 2200–2209. doi: 10.1002/joc.4488

Suriano, Z. J., and Leathers, D. J. (2017a). Synoptic climatology of lake effect snowfall conditions in the Eastern Great

Lakes region. *Int. J. Climatol.* 36: 2200–2209. doi: 10.1002/joc.5093

Suriano, Z. J., and Leathers, D. J. (2017b). Synoptically classified lake-effect snowfall trends to the lee of Lakes Erie and Ontario. *Clim. Res.* 74, 1–13. doi: 10.3354/cr01480

Conflict of Interest: The authors declare that the research was conducted in the absence of any commercial or financial relationships that could be construed as a potential conflict of interest.

Publisher's Note: All claims expressed in this article are solely those of the authors and do not necessarily represent those of their affiliated organizations, or those of the publisher, the editors and the reviewers. Any product that may be evaluated in this article, or claim that may be made by its manufacturer, is not guaranteed or endorsed by the publisher.

frontiers | Frontiers in Water

ORIGINAL RESEARCH
published: 13 April 2022
doi: 10.3389/frwa.2022.805143

Changes in Large Lake Water Level Dynamics in Response to Climate Change

Alexander VanDeWeghe[1], *Victor Lin*[2], *Jennani Jayaram*[3] *and Andrew D. Gronewold*[1,4]*

[1] Department of Civil and Environmental Engineering, College of Engineering, University of Michigan, Ann Arbor, MI, United States, [2] Department of Electrical Engineering and Computer Science, College of Engineering, University of Michigan, Ann Arbor, MI, United States, [3] Department of Mathematics, College of Literature, Science, and the Arts, Ann Arbor, MI, United States, [4] School for Environment and Sustainability, University of Michigan, Ann Arbor, MI, United States

Understanding impacts of climate change on water level fluctuations across Earth's large lakes has critical implications for commercial and recreational boating and navigation, coastal planning, and ecological function and management. A common approach to advancing this understanding is the propagation of climate change scenarios (often from global circulation models) through regional hydrological models. We find, however, that this approach does not always fully capture water supply spatiotemporal features evolving from complex relationships between hydrologic variables. Here, we present a statistical approach for projecting plausible climate-related regional water supply scenarios into localized net basin supply sequences utilizing a parametric vine copula. This approach preserves spatial and temporal correlations between hydrologic components and allows for explicit representation and manipulation of component marginal and conditional probability distributions. We demonstrate the capabilities of our new modeling framework on the Laurentian Great Lakes by coupling our copula-derived net basin supply simulations with a newly-formulated monthly lake-to-lake routing model. This coupled system projects monthly average water levels on Lake Superior, Michigan-Huron, and Erie (we omit Lake Ontario from our study due to complications associated with simulating strict regulatory controls on its outflow). We find that our new method faithfully replicates marginal and conditional probability distributions, as well as serial autocorrelation, within and among historical net basin supply sequences. We find that our new method also reproduces seasonal and interannual water level dynamics. Using readily-available climate change simulations for the Great Lakes region, we then identified two plausible, transient, water supply scenarios and propagated them through our model to understand potential impacts on future water levels. Both scenarios result in an average water level increase of $<$10 cm on Lake Superior and Erie, with slightly larger increases on Michigan-Huron, as well as elevated variability of monthly water levels and a shift in seasonal water level modality. Our study contributes new insights into plausible impacts of future climate change on Great Lakes water levels, and supports the application and advancement of statistical modeling tools to forecast water supplies and water levels on not just the Great Lakes, but on other large lakes around the world as well.

Keywords: climate change, statistical model, Great Lakes, water supplies, copula

OPEN ACCESS

Edited by:
Julie A. Winkler, Michigan State University, United States

Reviewed by:
Simon Papalexiou, University of Saskatchewan, Canada
Jim Angel, University of Illinois at Urbana-Champaign, United States

***Correspondence:**
Andrew D. Gronewold
drewgron@umich.edu

Specialty section:
This article was submitted to Water and Climate, a section of the journal Frontiers in Water

Received: *29 October 2021*
Accepted: *03 February 2022*
Published: *13 April 2022*

Citation:
VanDeWeghe A, Lin V, Jayaram J and Gronewold AD (2022) Changes in Large Lake Water Level Dynamics in Response to Climate Change. Front. Water 4:805143. doi: 10.3389/frwa.2022.805143

1. INTRODUCTION

The Laurentian Great Lakes watershed is home to more than 40 million inhabitants (MacKay and Seglenieks, 2013) and has a surface area of roughly 244,000 km^2 (Moukomla and Blanken, 2016), the largest of any lake system on Earth (Gronewold et al., 2013b). Regional ecological health and economic security are closely interwoven with this system, in large part because of the capacity of the Great Lakes to support diverse habitats (Cvetkovic and Chow-Fraser, 2011), commerce (Millerd, 2011; Meyer et al., 2016), and recreation (Nevers and Whitman, 2011; Gronewold et al., 2013c). The capacity of the Great Lakes to support these activities is, in turn, dependent on historical and future water quantity and quality dynamics (Mortsch and Quinn, 1996), including (but not limited to) those associated with coastal water level variability (Mortsch and Quinn, 1996; Gronewold and Stow, 2014a). Given the great economic and ecological value of the Great Lakes, and recognizing the potential risks associated with ongoing climate change (Pryor et al., 2014), understanding plausible future water level dynamics on the Great Lakes is paramount. Indeed, Great Lakes scientists have undertaken this very endeavor for decades (Quinn, 1978; Croley, 1990; Angel and Kunkel, 2010).

Previous attempts to quantify shifts in the Great Lakes hydrologic cycle reflect the role that climate change has already been playing across the region (Marchand et al., 1988; Quinn, 2002). Some of these historical projects, many of which have come under scrutiny (Lofgren and Gronewold, 2013), focused on translating that understanding into seasonal and interannual water supply forecasting systems using a "change-factor" method (Croley, 1990) based on output from a chain of lake thermodynamics and rainfall-runoff models collectively known as the Advanced Hydrologic Prediction System, or AHPS (Gronewold et al., 2011). This modeling framework (Croley, 1990) was subsequently adopted in a range of climate impact studies (Hartmann, 1990; Hayhoe et al., 2010). Importantly, some of these studies employed a perturbed time series of historical data (using either a multiplication factor, or ratio, based on separate climate modeling results) as future forcings. These forcings were intended to be representative of a future climate.

The perturbed climate data became input for the AHPS, which translated climate variables such as daily temperatures, precipitation, and humidity into water supply components (also commonly referred to as a "net basin supply," or NBS). More specifically, NBS in the Great Lakes is typically defined as the sum of terrestrial runoff into each lake, and net atmospheric water supply (precipitation minus evaporation) over the surface of each lake (Mailhot et al., 2019). This value is typically expressed as a height of water over each lake surface (Music et al., 2015). Due to the large surface area of the Great Lakes relative to basin size, overlake precipitation, overlake evaporation, and runoff have similar annual magnitudes, but very different seasonal dynamics (Lenters, 2001; Gronewold et al., 2013a).

Despite variation in emission scenarios considered across previous studies (Music et al., 2015), those (most of which were published prior to 2010) that employed the Croley (1990) methodology predicted substantial decreases in both NBS and water levels on the Great Lakes (Lofgren, 2004). Lofgren et al. (2011) and Lofgren and Rouhana (2016) subsequently identified methodological flaws in the estimation of evapotranspiration in the AHPS core runoff model (the large basin runoff model, or LBRM), leading to arguably biased formulations of runoff and NBS resulting from the use of near-surface air temperature as a proxy for potential evapotranspiration (Milly and Dunne, 2017). Furthermore, application of the change-factor method only represents shifts in mean, and later variance, of hydrological components. This method does not fully account for the full probability distribution underlying each water balance component (Music et al., 2015). Correctly representing evolving solar radiation dynamics in relatively simple models that simulate the hydrologic impacts of climate change (Lofgren et al., 2013) is just one challenge facing the Great Lakes water resources planning community.

There are other challenges, however, associated with more contemporary methods that utilize hydrological output directly from global circulation models (GCMs). Manabe et al. (2004), for example, utilized a GCM to demonstrate that water rich regions of North America, such as the Great Lakes basin, would experience a significant increase in runoff and outflow, suggesting a parallel increase in water level. However, GCMs typically lack the regional specificity necessary to reflect climate interactions at the scale of a lake system (Music et al., 2015; Briley et al., 2021); some models grossly misrepresent or even simply don't include critical lake-atmosphere interactions that affect the regional climate and propagate into meteorological phenomena (Wright et al., 2013; Bryan et al., 2015; Fujisaki-Manome et al., 2017). Other regional processes such as soil and vegetation interactions and rainfall over small watersheds can have a significant cumulative effect on water availability, but are similarly misrepresented, or even neglected, in GCMs (MacKay and Seglenieks, 2013).

An alternative approach that has gained popularity in recent years is downscaling GCM results with regional climate models (RCMs), often coupled to a lake-atmosphere model (Gula and Peltier, 2012; MacKay and Seglenieks, 2013; Music et al., 2015; Notaro et al., 2015; Mailhot et al., 2019). Studies utilizing RCMs have demonstrated the possibility for much more varied results than had previously been considered under the "change-factor" method (Winkler, 2015). MacKay and Seglenieks (2013), for example, projected single digit centimeter declines in water levels, while Notaro et al. (2015) projected both large increases in water level (+42 cm on Michigan-Huron) using one regional model (RCM-CNRM), as well as significant decreases (−29.6 cm on Michigan-Huron) using a different regional model (RCM-MICROC5). These findings underscore the substantial variability that either different RCMs, or that different parameterizations within a given RCM, can introduce. In contrast, studies using ensembles of multiple RCMs to project hydroclimate scenarios resulted in less extreme changes in average water supply. Most recently, a study of 28 climate simulations under five RCMs predicted only small increases in average NBS across the basin, but projected an amplification of the seasonal NBS cycle driven by increases in both precipitation and evaporation (Bartolai et al., 2015; Mailhot et al., 2019).

To provide more robust simulations of plausible NBS time series under climate change scenarios, we introduce a methodology utilizing a parametric regular vine copula to predict monthly NBS component values given a hypothesized change or trend in each component. Copulas are multidimensional cumulative distribution functions (CDFs) that originate from marginal CDFs (Schölzel and Friederichs, 2008; Laux et al., 2011; Lee and Salas, 2011; Maity, 2018). More specifically, copulas encode relationships between some number (e.g., d) of marginal probability distributions (in our case, for d hydrological variables) and a new d-dimensional joint probability distribution that preserves serial and cross-correlation.

As such, copulas represent an efficient tool for simulating long-term environmental variables that are highly correlated across space and time. Previous studies have shown that copula models have the potential to successfully represent these dependencies (Pouliasis et al., 2021). Other conventional (and perhaps more common) statistical models in water resources research, such as autoregressive, fractional Gaussian noise, and non-parametric models, have the potential to misrepresent (or even not represent at all) them (Lee and Salas, 2011). Here, we utilize a specific type of copula, referred to as a "vine" copula, which constructs the multivariate joint distribution using a series of bivariate relationships (rather than a single dependence structure across all variables simultaneously).

Prior studies have also, more specifically, evaluated the efficacy of copulas in capturing hydroclimate phenomena on other large bodies of water, suggesting that hydrologic behavior can plausibly be modeled using copulas (Lee and Salas, 2011; Latif and Mustafa, 2020; Pouliasis et al., 2021; Zaerpour et al., 2021). However, many conventional copulas (such as Frank, Clayton, and Gumbel) are prohibitively complex at higher dimensions (Lee and Salas, 2011). While Gaussian and student's-t copulas can accommodate joint distributions of many dimensions, we focus our attention on vine copulas to allow for uniquely structured bivariate dependencies such as heavy tail weighting, multimodality, and physical boundary conditions.

Likewise, it is advisable to use regular vines under certain circumstances in which the dependence structure of the variables is unclear, a condition reflected in the high number of monthly NBS component variables across the Great Lakes (Latif and Mustafa, 2020). With this in mind, we are able to use vine copulas to capture overarching variable interactions while simultaneously managing all constituent pairwise dependencies.

Therefore, the approach we introduce intends to leverage the strength of regular vine copulas to capture spatial and temporal distributional dependencies between monthly NBS components for large lakes and, in particular, for each of the Laurentian Great Lakes. We couple these statistically robust NBS simulations with a lake-to-lake routing model utilizing monthly stage-fall discharge equations. Monthly outflow models (as opposed to annual-scale models often used in multi-decadal simulations) allow us to represent seasonal variability in water supplies evolving from factors such as ice cover and vegetation. We demonstrate the utility of this methodology by simulating historical and future water levels under two plausible hydroclimate scenarios that represent a continuation of observed NBS component trends, and a blending of existing trends with RCM NBS change projections. We use these water level simulations to assess three metrics of water level behavior: long-term average, seasonality, and frequency of extreme values.

2. METHODS

2.1. Copula Calibration

We began by extracting historical water balance data for the Great Lakes using archived output (Do et al., 2020a) from the Large Lake Statistical Water Balance Model (L2SWBM) (Gronewold et al., 2020). The L2SWBM utilizes a Bayesian framework (Press, 2003; Gelman et al., 2004) to assimilate independent hydrological data products across the Great Lakes and subsequently infer the "true" monthly value for each water balance component. Although these monthly values are ultimately unknown, the L2SWBM is constrained by a traditional water balance equation, and uses multiple data sources to develop prior and likelihood functions for each component. Thus, the posterior estimates of the L2SWBM reconcile observed (or simulated) values from independent data products to close the water balance of the entire hydrologic system (Gronewold et al., 2016).

For this study, we specifically extracted median NBS component values from the L2SWBM to calibrate the copula. We calibrated the copula model as a "Regular Vine" copula within the RVineStructureSelect() function in the VineCopula package (Nagler et al., 2021) in the R statistical software program (R Core Team, 2017). We converted our 70 year NBS component observations into pseudo-observations which are both readable by the RVineStructureSelect() function, and rank-normalized to the interval [0,1]. The RVineStructureSelect() function then optimally generates a maximum spanning tree with edge weights as the correlation of pairs of variables amongst the 108 variables (3 lake systems $\times$ 3 water balance components $\times$ 12 months). Likewise, the RVineStructureSelect() function assigns them to the most appropriate bivariate copula family.

We then used the RVineSim() function to generate simulated values for each lake water balance component. We used quantile functions to map component values from [0,1] space into "real" values. The marginal distributions for each water balance component were, following previous protocols established in developing the L2SWBM (Gronewold et al., 2016, 2020; Do et al., 2020b), prescribed as three-parameter gamma, Gaussian, and log-normal for precipitation, evaporation and runoff, respectively. The three-parameter gamma distribution is parameterized using the same shape and scale parameters as a conventional gamma distribution along with an additional shift parameter. As described in the following sections, this approach allows us to propagate plausible climate change scenarios through changes in the parameters of each probability distribution.

2.2. Outflow and Routing Model

To propagate the monthly water balance components generated by the copula into simulated monthly water levels, we developed an outflow model to capture flow dynamics between the lakes. Specifically, we encoded a conventional stage-fall discharge

(SFD) equation, which simulates lake outflow as a function of water surface elevation in an upstream and (in some cases, depending on the extent of backwater effects) downstream lake (Gessler et al., 1998; Schmidt and Yen, 2008; Westerberg et al., 2011; Apps et al., 2020). SFD models are particularly prevalent in the Laurentian Great Lakes, where they have been used for decades in long-term water level simulation studies and operational forecasting systems (Brunk, 1968; Quinn, 1978; Labuhn et al., 2020; Quinn et al., 2020; Thompson et al., 2020).

To simulate outflow (Q) from Lake Michigan-Huron, we used the following SFD formulation with both stage and fall components to accommodate the effects of backflow through the Detroit and St. Clair Rivers.

$$Q = a_m(z_2 - z_1)^b(z_2 - z_{sill})^c$$

where z_2 and z_1 represent upstream and downstream lake elevations, respectively, and z_{sill} represents a constant lake "sill" elevation (roughly analogous to the elevation of the channel bottom). Model coefficients are represented by a, b, and c, where a subscript m indicates that a coefficient is allowed to vary seasonally. This approach allows our models to account for monthly changes in the relationship between water levels and channel flow which result from factors such as channel vegetation and ice cover (Derecki and Quinn, 1986; Lu et al., 1999).

To simulate outflow from Lake Superior and Lake Erie, we used (following conventional protocols) the following simplified SFD model (superscripts are added to differentiate flow values and coefficients derived from the simplified SFD model; subscripts differentiating models for Lake Superior and Lake Erie are removed for clarity):

$$Q' = a_m{}'(z_2 - z_{sill})^{c'}$$

Taking the logarithm of each formulation leads to the following linear models:

$$ln(Q) = ln(a_m) + b * ln(z_2 - z_1) + c * ln(z_2 - z_{sill}) + \epsilon$$

$$ln(Q') = ln(a_m{}') + c' * ln(z_2 - z_{sill}) + \epsilon'$$

where ϵ and ϵ' are model error terms.

We then conducted a Bayesian analysis to estimate model coefficients using historical Great Lakes beginning-of-month water level measurements, and monthly average flow measurements, as data (i.e., for z_2, z_1, and Q). We obtained this data from publicly-available archives maintained by the National Oceanic and Atmospheric Administration (NOAA) Great Lakes Environmental Research Laboratory (Smith et al., 2016), and originally developed by the Coordinating Committee on Great Lakes Basic Hydraulic and Hydrologic Data (Gronewold et al., 2018).

2.3. Climate Scenario Selection

To demonstrate the utility of our water level forecasting framework, we evaluated three 50-year water supply scenarios. The first scenario is a "baseline" scenario, executed without any perturbation of the original copula water balance component parameters. We then developed and evaluated two additional 50-year water supply projections, each developed under different climate-perturbed water supply conditions. The historical baseline simulation will hereafter be referred to as SC1. After comparing our baseline scenarios and historical observations to ensure a minimal bias, we then base our analysis on an intercomparison between our three model simulations. This approach minimizes the impacts of any potential biases (which we attempt to minimize through model calibration) in our historical simulations (Frigon et al., 2010).

While most multidecadal Great Lakes water level forecasts acknowledge the impact of climate change on future water level regimes, there has not been a focus on identifying and propagating existing climate change signals directly into future water supply scenarios (Notaro et al., 2013, 2015; Lofgren and Rouhana, 2016). Instead, water levels are typically simulated under future emissions or temperature change scenarios, but those scenarios are sometimes inconsistent with observed trends in NBS components. To address this shortcoming in conventional regional water supply forecasting, we identify significant trends in NBS components from 1950 to 2019 to inform our first plausible climate scenario. This approach, in effect, reflects a continuation of existing water supply trends.

More specifically, we identified and quantified trends in monthly L2SWBM NBS component data from 1950 to 2019 for Lake Superior, Michigan-Huron, and Erie. For each combination of month, lake, and component (108 total), we developed a linear model to represent historical trends. Following similar climate studies (Hu et al., 2019; Daba et al., 2020; Banda et al., 2021), the linear model was developed using the conventional Theil-Sen statistical test (Sen, 1968). To simplify our prescription of a linear trend, we did not utilize seasonal decomposition that might reflect impacts of teleconnections such as El Niño, the Pacific Decadal Oscillation, or the Arctic Oscillation (Trenberth, 1997; Ghanbari and Bravo, 2008) that could impose a cyclical effect. We calculated model residuals using the Sen slope linear model, and analyzed them for trends that might reflect either model bias or heterostochasticity (Cook and Weisberg, 1983).

We utilized the Theil-Sen test to quantify existing trends in all components without regard to the significance of the trend. However, we only incorporated the linear model for components with trends that were significant at p <0.05 for either a sieve bootstrapped student's t-test or Mann-Kendall test of significance. Sieve bootstrapping (Bühlmann, 1997) allowed us to correct for the possibility of serially correlated or non-normally distributed data in these significance tests, and has been previously employed for detection of hydrometeorological trends (Noguchi et al., 2011; Wang et al., 2020). Miller and Piechota (2008) demonstrate the utility of using multiple tests of significance to more robustly capture trends in hydroclimate data. The Mann-Kendall test, in particular, has been widely coupled with Theil-Sen slope estimations (Chen and Grasby, 2009; Gyamfi et al., 2016; Banda et al., 2021). Given a detection of significance by either test, the Theil-Sen slope (mm*month-1*year-1) was retrieved and incorporated into our first transient climate scenario, hereafter referred to as SC2.

While few historical monthly NBS components exhibit statistically significant trends, Lake Superior's historical water balance can be characterized by increased precipitation and runoff throughout the winter months. Evaporation demonstrated much weaker and often slightly negative trends across the hydrologic year and lake system. These observed trends (summarized in the **Supplementary Figure 1**) depict a tendency toward a "wet" future that are ultimately reflected in SC2.

We then evaluated existing literature to inform a second transient climate scenario (SC3) that represents a blend of our observed trends with RCM predictions of NBS component supply. Mailhot et al. (2019), for example, utilize an ensemble of five NA-CORDEX RCMs to simulate NBS components under two emissions scenarios and identify trends in the components using the Theil-Sen test. We utilized statistically significant biweekly trends, propagated to a monthly time frame, from the RCP-8.5 emissions scenario in this study, which represents high greenhouse gas emissions and, consequently, comparatively high mean temperature increase (Van Vuuren et al., 2011). The trends derived from Mailhot et al. (2019) were then added to a baseline trend, which we calculated as a fractional (0.3) proportion of observed trends. It is informative to note that SC3 is characterized by much greater increases in evaporation, and moderate increases in precipitation and runoff, relative to SC2. Both SC2 and SC3 are plausible, transient water supply scenarios represented by slope factors (mm/month*year) for each combination of month, lake, and NBS component. A summary of the changes in water balance components encoded in both SC2 and SC3 can be found in **Supplementary Figure 1**.

2.4. Developing and Evaluating Water Level Projections

For each of our three scenarios (i.e., SC1, SC2, and SC3), we generated 1,000 water level sequences across a 50-year horizon with SC1 beginning in 1951, and SC2 and SC3 each beginning in 2000. Using observed initial water levels in each time period as a starting point, we iteratively simulated outflow for each subsequent month from each lake using the previously described SFD outflow models (Quinn et al., 2020; Thompson et al., 2020). We combined simulated outflows and water balance components for each month to calculate the total monthly change in water level on each lake. This change in water level consists of four parts: inflow, NBS, diversions, and outflow. Inflow was determined using the outflow from the upstream lake which, in our case, applies only to Lakes Michigan-Huron and Erie. We generated NBS component predictions using our copula. Our simulations also include average monthly interbasin water supplies into Lake Superior from the Long Lac and Ogoki diversions, out of Lake Michigan-Huron through the Chicago canal system, and out of Lake Erie through the Welland Canal (Quinn and Edstrom, 2000; Hunter et al., 2015).

2.4.1. Change Analysis and Validation

We analyzed long-term average, seasonality, and frequency of extreme values in water levels in our 1,000 50-year sequences from each model simulation. Given the probabilistic nature of our model, each plausible sequence (i.e., ensemble member) has a different mean water level. These long term averages were aggregated to one simulation average. We also analyzed probability distributions to fully illustrate any shift in mean water level outcomes.

We captured potential changes in the seasonal water level cycle by measuring the likelihood that the annual water level peak or trough falls within a given month. Therefore, any shift in the timing of yearly water level highs and lows was reflected in a shift in the probability distribution of highs and lows across months. Seasonal trends were quantified by comparing the average day that an annual high or low occurs. We compared the zero centered probability density function of all future water levels to historical water levels to identify if any change in the likelihood of extreme values has occurred, which would be reflected by variations in the tails of a distribution. Changes in occurrence patterns of these extreme values is quantified by measuring the percent of occurrences that fall outside of two standard deviations from the zero-centered mean of the baseline simulation.

3. RESULTS

3.1. Validation

3.1.1. Copula-Simulated Historical NBS Sequences

We find that the marginal distributions simulated by the copula for each lake and component reasonably match observational distributions in both mean and shape (**Supplementary Figures 5–7**). We do find, however, that bimodality of some water balance components is not reflected clearly in the copula simulations. This result is not particularly surprising, given that our copula simulates a large number of samples (1,000) from a parametric and smoothed joint distribution, while the historical data is based on 50 values.

We also find that the copula simulations also capture autocorrelation in each water balance component (see **Supplementary Figures 2–4**). Minor disparities between simulated and observed autocorrelation could be the result of our selected parameterization of component distributions. Similarly, spatial correlation among different components and lakes is sufficiently reproduced in our copula (see **Supplementary Figures 8–13**). These findings collectively suggest that our long-term simulations of NBS components for the Great Lakes, using a newly-developed copula, are relatively robust. Aggregating monthly NBS component values to lakewide NBS totals, we find that bias in long term NBS is roughly 2%.

3.1.2. SFD Historical Outflow Simulations

A comparison between simulated and observed historical monthly water levels on, and outflows from, Lakes Superior, Michigan-Huron, and Erie (**Figure 1**) indicates that our simulation framework provides a reasonable representation not only of marginal and multivariate distributions for precipitation, evaporation, and runoff, but also of the water level and flow water balance components as well. More specifically, we find that our simulated water levels have a long-term bias of roughly 1 cm for Lake Superior, 4 cm for Lake Michigan-Huron, and about 12 cm for Lake Erie. The bias in simulated outflows is roughly 2% for Lake Superior, 1% for Lake Michigan-Huron, and 4% for

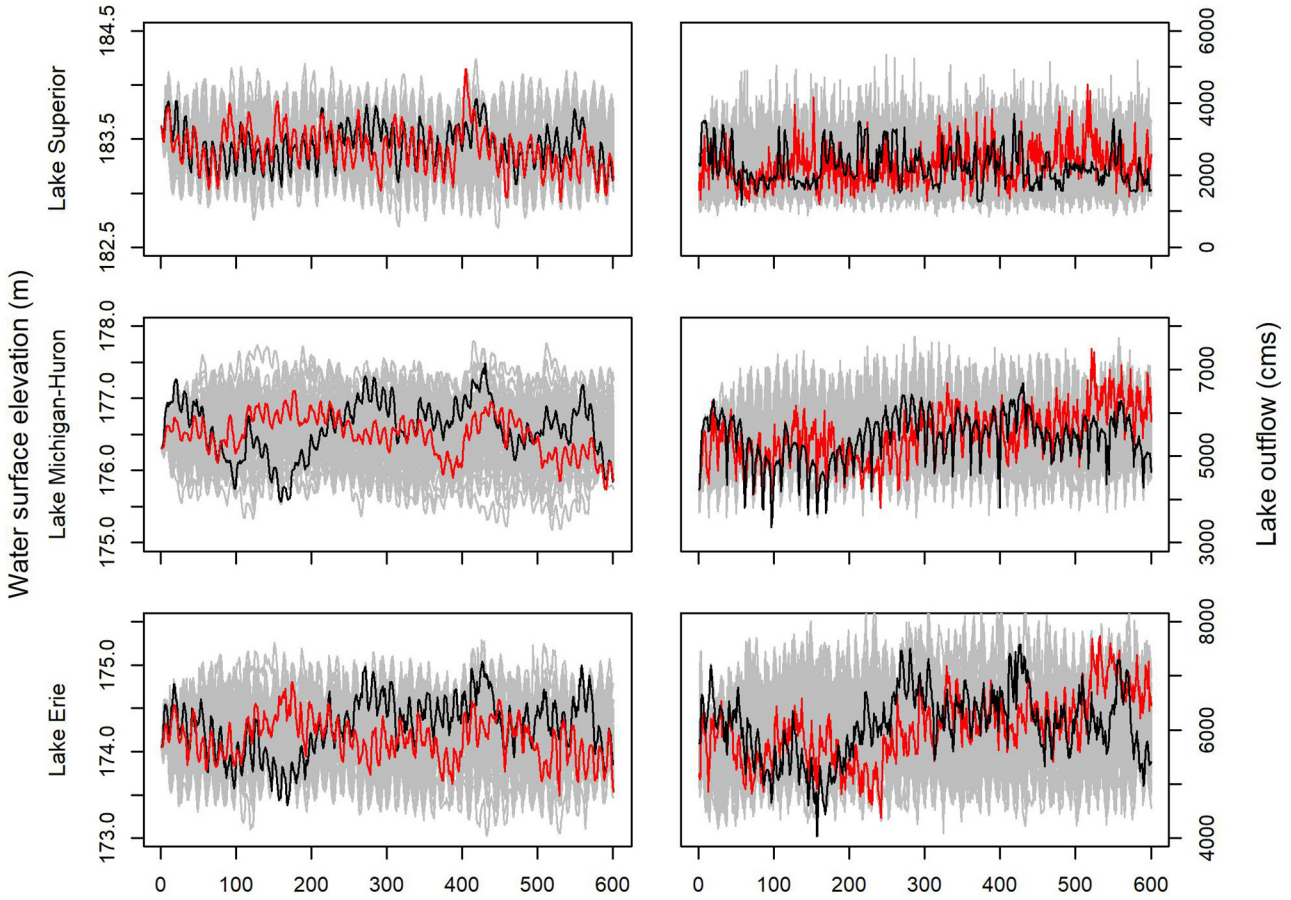

FIGURE 1 | Comparison between simulated and observed historical time series of water levels **(left)** and lake outflows **(right)** for Lakes Superior (top), Michigan-Huron (middle), and Erie (bottom) from January 1951 through December 2000. Gray lines represent 100 ensemble members from our model simulation (randomly sampled from 1,000 to facilitate reproducibility and clarity). Black lines represent observed values, and red lines represent a single ensemble member (same member for all panels) to reflect individual simulation variability.

TABLE 1 | Comparison of long-term average water levels (in meters) for each lake based on a historical simulation of the observed data period, and two future climate change scenarios.

	Lake Superior	Lake Michigan-Huron	Lake Erie
Baseline (Scenario 1)	183.42	176.54	174.18
Scenario 2	183.50	176.66	174.27
Scenario 3	183.45	176.60	174.24

Lake Erie. These values are well within the range of reasonable tolerance for historical simulations, particularly in light of the fact that most historical RCM-based simulations have biases that are either not reported, or well-exceed those presented here.

3.1.3. Water Level Change Analysis

Mean water levels for observed data, our historical model run, and two future water supply scenarios are summarized in **Table 1**.

Scenarios SC2 and SC3 indicate a slight net increase in average water level on Lake Superior, with increases of 8 cm (SC2) and 3 cm (SC3), respectively. Similar changes are expected on Lake Michigan-Huron (increases of 12 and 6 cm for SC2 and SC3, respectively) and on Lake Erie (increases of 9 and 6 cm for SC2 and SC3, respectively). Importantly, both future scenarios suggest an increase in long-term average water levels across all of the Great Lakes. These findings are consistent with the RCM-CNRM mid-century water level projections in Notaro et al. (2015) and are a plausible consequence of slight to moderate NBS increases projected by Mailhot et al. (2019) and Music et al. (2015).

All three of our model runs yield comparable marginal distributions for mean water level, as shown in **Figure 2**. Overlapping distributions between the baseline simulation and future scenarios indicate that any individual model run (i.e., ensemble member) may fall within the range of simulated historical values and, in some cases, even indicate a decline in water levels. Therefore, our findings indicate that while an increase in water levels is likely across the

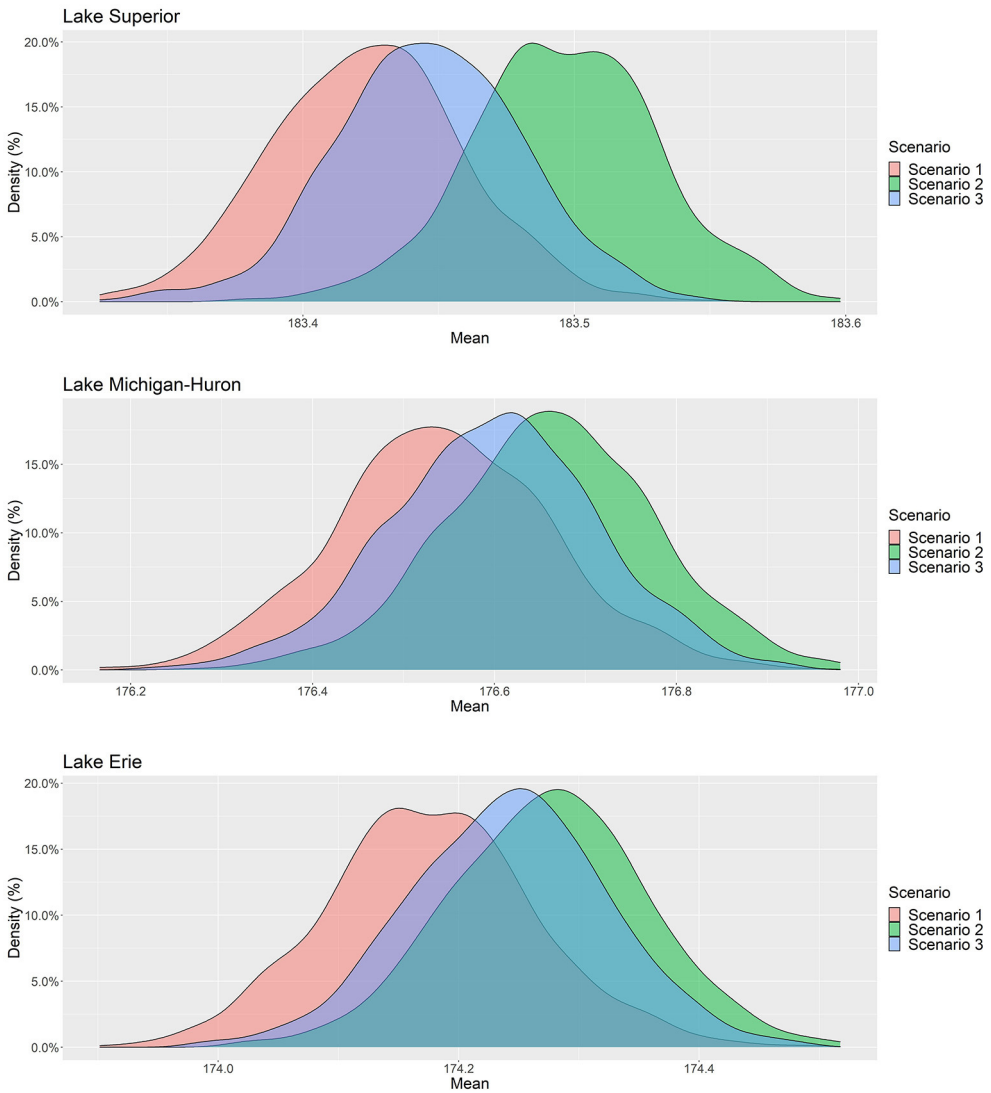

FIGURE 2 | Probability distribution of all (600) simulated water level sequences for SC1 (red), SC2 (green), and SC3 (blue) for Lakes Superior **(top)**, Michigan-Huron **(middle)**, and Erie **(bottom)**.

Great Lakes, our range of plausible water supply scenarios includes both the possibility of a rise or fall in long-term water levels. We notably find that continuation of observational trends in NBS components alone, *via* scenario SC2, results in greater water level rise than is demonstrated when RCM-based NBS component projections are incorporated *via* scenario SC3.

The seasonality of annual water level highs and lows is included in **Figure 3**. Scenario SC2 causes only slight shifts in the timing of annual maximum and minimum water levels, with changes of <1 week across all lakes. Peak water levels occurred an average of 3 days earlier on Lake Superior and Michigan-Huron relative to the baseline simulation, while water levels on Lake Erie peaked an average of 7 days later. The average date of annual minimum water levels did not change significantly for any lake under scenario SC2. In contrast, scenario SC3 results in a more significant shift in the seasonality of water levels across all three lakes. Water levels peak an average of 14 and 24 days sooner on Lake Superior, and Michigan-Huron, respectively, while Lake Erie remains unchanged. Lake Michigan-Huron displays the greatest shift in timing of the annual low water level, with this trough occurring an average of 11 days earlier under scenario SC3 than baseline simulations indicate.

While experiencing an insignificant shift in overall timing, Lake Superior does undergo an intensification of annual lows that occur during the month of March, indicating that a temporal concentration of this seasonal inflection point may occur. Our findings are consistent with both observational trends and climate projections that annual water level rises

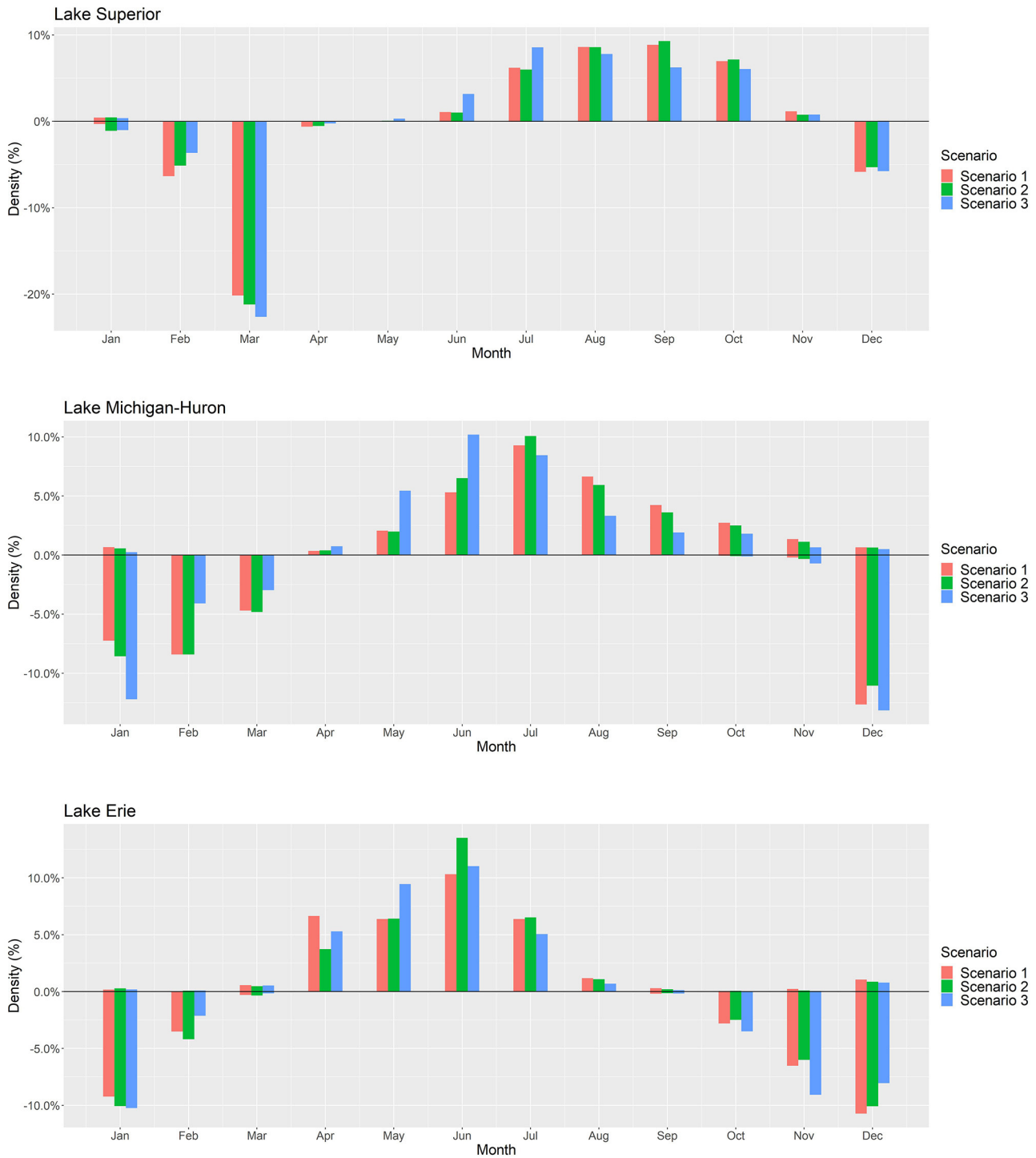

FIGURE 3 | Frequency of occurrences of annual water level maximums (above the x-axis) and minimums (below the x-axis) for SC1 (red), SC2 (green), and SC3 (blue) for Lakes Superior **(top)**, Michigan-Huron **(middle)**, and Erie **(bottom)**.

and falls are occurring earlier, particularly annual maximum levels on Lake Superior (Lenters, 2001; Gronewold and Stow, 2014a). However, we find this shift in water level seasonality to be significantly greater in annual maximums than in annual minimums. The most apparent plausible change in the seasonal cycle of water levels is a shift earlier in the year, while there is relatively little compelling evidence for amplification or dampening effects.

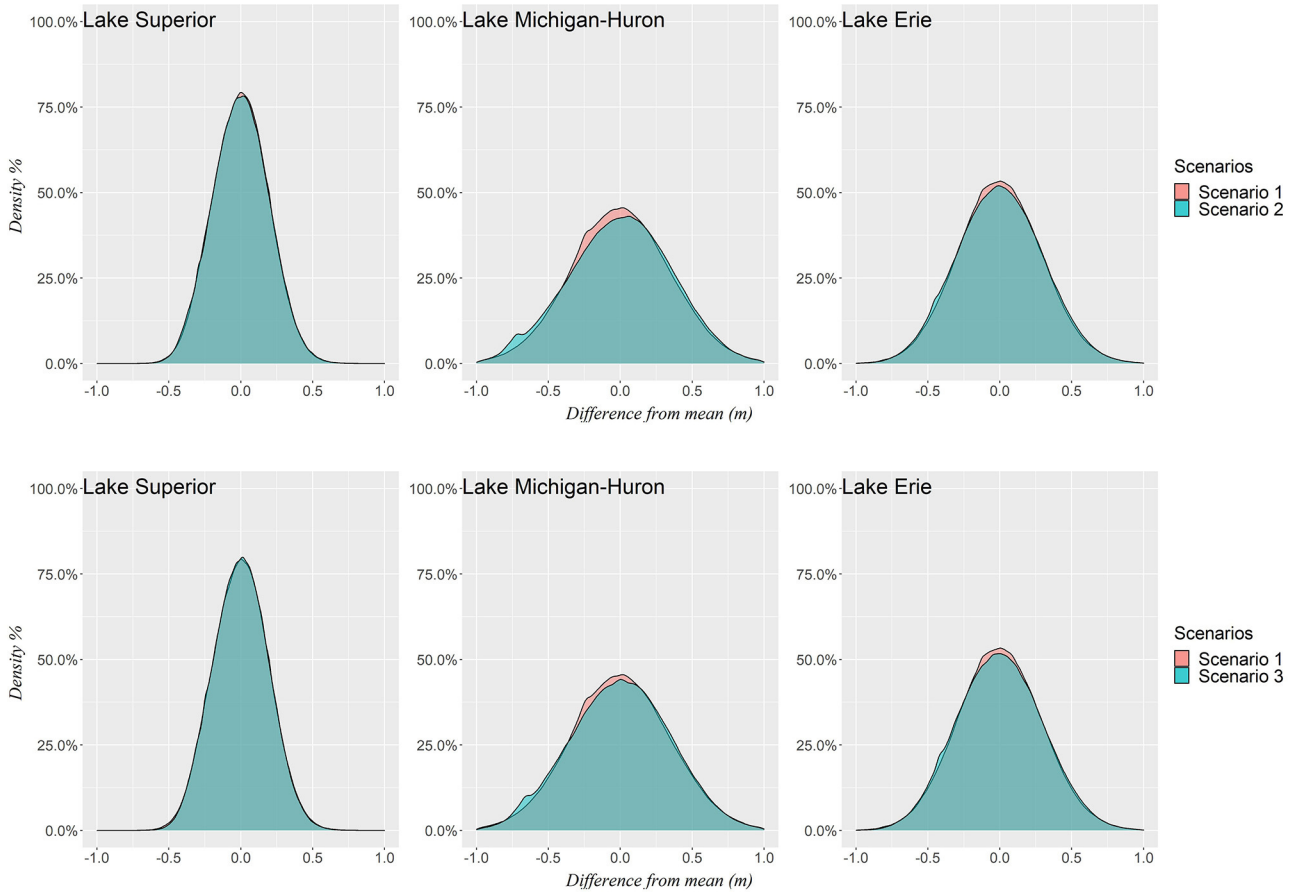

FIGURE 4 | Comparison of zero-centered probability distributions of all simulated water levels between SC1 and SC2 **(top)** and SC1 and SC3 **(bottom)** for Lakes Superior, Michigan-Huron, and Erie.

Figure 4 displays the zero-centered probability density function of water levels for each simulation. While all three model simulations yield similar water level distributions, differences are evident in the tails of the distributions, representing a change in the occurrence of extreme water levels. Two standard deviations from the zero-centered mean of the historical simulation on each lake is used as a threshold to measure the frequency of extreme values. This results in a threshold of 0.3, 0.47, and 0.45 m deviations from the mean for Lake Superior, Michigan-Huron, and Erie, respectively. Water levels fall outside of these thresholds an average of 3.0% more frequently across lakes under scenario SC2 than is historically simulated, while frequency increases by an average of 2.1% under scenario SC3. Our findings also demonstrate that the increased frequency of extreme water levels is of comparable magnitude at both the high and low ends of the distribution, and that water levels are less concentrated around the mean under both scenarios. This indicates that future water levels may demonstrate greater dispersion from the mean in both directions relative to the historical record, supporting ongoing speculation about future increased variability of Great Lakes water levels (Gronewold and Rood, 2019). Increased dispersion of water levels is also consistent with the possibility of an enhancement in the annual cycle of water supply (Manabe et al., 2004; Mailhot et al., 2019), though we do not find compelling evidence of an overall amplification of seasonal water level dynamics in this study. Increasing magnitudes of both precipitation and evaporation provide another plausible explanation for greater water level variability, as imbalances in these competing hydrologic forces can result in significant water level deviations from the long-term average (Gronewold et al., 2021).

4. CONCLUDING REMARKS

Great Lakes hydroclimate studies prior to 2011 widely used the "change-factor" method and consistently simulated significant declines in future water levels (Croley, 1990; Hartmann, 1990; Angel and Kunkel, 2010; Hayhoe et al., 2010). These findings led to a regional narrative reflecting a future of drought, aridity, and chronic low water levels (Gronewold and Stow, 2014b). The low water levels in many of these simulations, however, was a consequence of misguided modeling assumptions based

on the use of air temperature as a proxy for solar radiation (Lofgren et al., 2013). A response to this narrative was catalyzed through a shift to the use of state-of-the-art downscaled RCM outputs to drive NBS and water level simulations. We have built upon this body of research by using a statistical model that maintains spatial and temporal correlation among water balance components, while allowing manipulation of the water balance component marginal distributions to reflect plausible climate change scenarios. Our results indicate that this approach (based primarily on the use of copulas) presents a promising alternative to regional water supply forecasting.

Our results indicate a slight to moderate increase in average water levels on all lakes under both plausible water supply scenarios. SC2 demonstrates greater increases than SC3, indicating that current trends in NBS components alone, if continued, could result in greater water level rise than would occur if RCM-predicted climate trends also take place. In contrast, SC3 results in greater shifts in the timing of the annual water level cycle, most notably demonstrated by the annual maximum occurring earlier in the year on Lake Superior and Michigan-Huron. Both plausible future water supply scenarios indicate an increased dispersion of water levels from the long term average. This finding indicates that, despite a rise in average levels, extreme low water levels are still likely to occur in the future.

DATA AVAILABILITY STATEMENT

The raw data supporting the conclusions of this article will be made available by the authors, without undue reservation.

AUTHOR CONTRIBUTIONS

AV contributed text and conceptualization of the study along with VL. VL encoded the copula model and ran the simulations. JJ also encoded preliminary versions of the copula and contributed text. AG oversaw all aspects of the manuscript preparation and contributed text. All authors contributed to the article and approved the submitted version.

FUNDING

This work was funded by the University of Michigan through the University of Michigan Undergraduate Research Opportunity Program (UROP).

ACKNOWLEDGMENTS

The authors would like to thank Jenna Sherwin for her contributions to encoding preliminary versions of the NBS copula model, Jim Crooks for his review of model code, Ryan Armbrustmacher for his helpful input on outflow modeling and diversions, and Scott Steinschneider for his early feedback on model development.

SUPPLEMENTARY MATERIAL

The Supplementary Material for this article can be found online at: https://www.frontiersin.org/articles/10.3389/frwa.2022.805143/full#supplementary-material

REFERENCES

Angel, J. R., and Kunkel, K. E. (2010). The response of Great Lakes water levels to future climate scenarios with an emphasis on Lake Michigan-Huron. *J. Great Lakes Res.* 36, 51–58. doi: 10.1016/j.jglr.2009.09.006

Apps, D., Fry, L. M., and Gronewold, A. D. (2020). Operational seasonal water supply and water level forecasting for the Laurentian Great Lakes. *J. Water Resour. Plann. Manage.* 146:04020072. doi: 10.1061/(ASCE)WR.1943-5452.0001214

Banda, V. D., Dzwairo, R. B., Singh, S. K., and Kanyerere, T. (2021). Trend analysis of selected hydro-meteorological variables for the Rietspruit sub-basin, South Africa. *J. Water Clim. Change* 12, 3099–3123. doi: 10.2166/wcc.2021.260

Bartolai, A. M., He, L., Hurst, A. E., Mortsch, L. D., Paehlke, R., and Scavia, D. (2015). Climate change as a driver of change in the Great Lakes St. Lawrence River basin. *J. Great Lakes Res.* 41, 45–58. doi: 10.1016/j.jglr.2014.11.012

Briley, L. J., Rood, R. B., and Notaro, M. (2021). Large lakes in climate models: A Great Lakes case study on the usability of CMIP5. *J. Great Lakes Res.* 47, 405–418. doi: 10.1016/j.jglr.2021.01.010

Brunk, I. W. (1968). Evaluation of channel changes in St. Clair and Detroit Rivers. *Water Resour. Res.* 4, 1335–1346. doi: 10.1029/WR004i006p01335

Bryan, A. M., Steiner, A. L., and Posselt, D. J. (2015). Regional modeling of surface-atmosphere interactions and their impact on Great Lakes hydroclimate. *J. Geophys. Res. Atmos.* 120, 1044–1064. doi: 10.1002/2014JD022316

Bühlmann, P. (1997). Sieve bootstrap for time series. *Bernoulli* 3, 123–148. doi: 10.2307/3318584

Chen, Z., and Grasby, S. E. (2009). Impact of decadal and century-scale oscillations on hydroclimate trend analyses. *J. Hydrol.* 365, 122–133. doi: 10.1016/j.jhydrol.2008.11.031

Cook, R. D., and Weisberg, S. B. (1983). Diagnostics for heteroscedasticity in regrsesion. *Biometrika* 70, 1–10. doi: 10.1093/biomet/70.1.1

Croley, T. E. II. (1990). Laurentian Great Lakes double-CO2 climate change hydrological impacts. *Clim. Change* 17, 27–47. doi: 10.1007/BF00148999

Cvetkovic, M., and Chow-Fraser, P. (2011). Use of ecological indicators to assess the quality of Great Lakes coastal wetlands. *Ecol. Indic.* 11, 1609–1622. doi: 10.1016/j.ecolind.2011.04.005

Daba, M. H., Ayele, G. T., and You, S. (2020). Long-term homogeneity and trends of hydroclimatic variables in upper awash River Basin, Ethiopia. *Adv. Meteorol.* 2020, e8861959. doi: 10.1155/2020/8861959

Derecki, J. A., and Quinn, F. H. (1986). Record St. Clair River ice jam of 1984. *J. Hydraul. Eng.* 112, 1182–1193. doi: 10.1061/(ASCE)0733-9429(1986)112:12(1182)

Do, H. X., Mei, Y., and Gronewold, A. D. (2020a). To what extent are changes in flood magnitude related to changes in precipitation extremes? *Geophys. Res. Lett.* 47, e2020Gl088684. doi: 10.1029/2020GL088684

Do, H. X., Smith, J. P., Fry, L. M., and Gronewold, A. D. (2020b). Seventy-year long record of monthly water balance estimates for Earth's largest lake system. *Sci. Data* 7, 276. doi: 10.1038/s41597-020-00613-z

Frigon, A., Music, B., and Slivitzky, M. (2010). Sensitivity of runoff and projected changes in runoff over Quebec to the update interval of lateral boundary conditions in the Canadian RCM. *Meteorol. Zeitsch.* 19, 225. doi: 10.1127/0941-2948/2010/0453

Fujisaki-Manome, A., Fitzpatrick, L., Gronewold, A. D., Anderson, E. J., Lofgren, B. M., Spence, C., et al. (2017). Turbulent heat fluxes during an extreme lake effect snow event. *J. Hydrometeorol.* 18, 3145–3163. doi: 10.1175/JHM-D-17-0062.1

Gelman, A. J., Carlin, J. B., Stern, H. S., and Rubin, D. B. (2004). *Bayesian Data Analysis*. Boca Raton, FL: Chapman & Hall; CRC Press. doi: 10.1201/9780429258480

Gessler, D., Gessler, J., and Watson, C. C. (1998). Prediction of discontinuity in stage-discharge rating curves. *J. Hydraul. Eng.* 124, 243–252. doi: 10.1061/(ASCE)0733-9429(1998)124:3(243)

Ghanbari, R. N., and Bravo, H. R. (2008). Coherence between atmospheric teleconnections, Great Lakes water levels, and regional climate. *Adv. Water Resour.* 31, 1284–1298. doi: 10.1016/j.advwatres.2008.05.002

Gronewold, A. D., Bruxer, J., Durnford, D., Smith, J. P., Clites, A. H., Seglenieks, F., et al. (2016). Hydrological drivers of record-setting water level rise on Earth's largest lake system. *Water Resour. Res.* 52, 4026–4042. doi: 10.1002/2015WR018209

Gronewold, A. D., Clites, A. H., Hunter, T. S., and Stow, C. A. (2011). An appraisal of the Great Lakes advanced hydrologic prediction system. *J. Great Lakes Res.* 37, 577–583. doi: 10.1016/j.jglr.2011.06.010

Gronewold, A. D., Clites, A. H., Smith, J. P., and Hunter, T. S. (2013a). A dynamic graphical interface for visualizing projected, measured, and reconstructed surface water elevations on the earth's largest lakes. *Environ. Model. Softw.* 49, 34–39. doi: 10.1016/j.envsoft.2013.07.003

Gronewold, A. D., Do, H. X., Mei, Y., and Stow, C. A. (2021). A tug-of-war within the hydrologic cycle of a continental freshwater basin. *Geophys. Res. Lett.* 48, e2020GL090374. doi: 10.1029/2020GL090374

Gronewold, A. D., Fortin, V., Caldwell, R., and Noel, J. (2018). Resolving hydrometeorological data discontinuities along an international border. *Bull. Am. Meteorol. Soc.* 99, 899–910. doi: 10.1175/BAMS-D-16-0060.1

Gronewold, A. D., Fortin, V., Lofgren, B. M., Clites, A. H., Stow, C. A., and Quinn, F. H. (2013b). Coasts, water levels, and climate change: a Great Lakes perspective. *Clim. Change* 120, 697–711. doi: 10.1007/s10584-013-0840-2

Gronewold, A. D., and Rood, R. B. (2019). Recent water level changes across Earth's largest lake system and implications for future variability. *J. Great Lakes Res.* 45, 1–3. doi: 10.1016/j.jglr.2018.10.012

Gronewold, A. D., Smith, J. P., Read, L. K., and Crooks, J. L. (2020). Reconciling the water balance of large lake systems. *Adv. Water Resour.* 137, 103505. doi: 10.1016/j.advwatres.2020.103505

Gronewold, A. D., and Stow, C. A. (2014a). Unprecedented seasonal water level dynamics on one of the Earth's largest lakes. *Bull. Am. Meteorol. Soc.* 95, 15–17. doi: 10.1175/BAMS-D-12-00194.1

Gronewold, A. D., and Stow, C. A. (2014b). Water loss from the Great Lakes. *Science* 343, 1084–1085. doi: 10.1126/science.1249978

Gronewold, A. D., Stow, C. A., Vijayavel, K., Moynihan, M. A., and Kashian, D. R. (2013c). Differentiating Enterococcus concentration spatial, temporal, and analytical variability in recreational waters. *Water Res.* 47, 2141–2152. doi: 10.1016/j.watres.2012.12.030

Gula, J., and Peltier, W. R. (2012). Dynamical downscaling over the Great Lakes Basin of North America using the WRF regional climate model: the impact of the Great Lakes system on regional greenhouse warming. *J. Clim.* 25, 7723–7742. doi: 10.1175/JCLI-D-11-00388.1

Gyamfi, C., Ndambuki, J. M., and Salim, R. W. (2016). A Historical analysis of rainfall trend in the olifants basin in South Africa. *Earth Sci. Res.* 5, 129. doi: 10.5539/esr.v5n1p129

Hartmann, H. C. (1990). Climate change impacts on Laurentian Great Lakes levels. *Clim. Change* 17, 49–67. doi: 10.1007/BF00149000

Hayhoe, K., VanDorn, J., Croley II, T. E., Schlegal, N., and Wuebbles, D. (2010). Regional climate change projections for Chicago and the US Great Lakes. *J. Great Lakes Res.* 36, 7–21. doi: 10.1016/j.jglr.2010.03.012

Hu, M., Sayama, T., Try, S., Takara, K., and Tanaka, K. (2019). Trend analysis of hydroclimatic variables in the Kamo River Basin, Japan. *Water* 11, 1782. doi: 10.3390/w11091782

Hunter, T. S., Clites, A. H., Campbell, K. B., and Gronewold, A. D. (2015). Development and application of a monthly hydrometeorological database for the North American Great Lakes - Part I: precipitation, evaporation, runoff, and air temperature. *J. Great Lakes Res.* 41, 65–77. doi: 10.1016/j.jglr.2014.12.006

Labuhn, K., Gronewold, A. D., Calappi, T. J., MacNeil, A., Brown, C., and Anderson, E. J. (2020). Towards an operational flow forecasting system for the Upper Niagara River. *J. Hydraul. Eng.* 146, 05020006. doi: 10.1061/(ASCE)HY.1943-7900.0001781

Latif, S., and Mustafa, F. (2020). Parametric vine copula construction for flood analysis for Kelantan River Basin in Malaysia. *Civil Eng. J.* 6, 1470–1491. doi: 10.28991/cej-2020-03091561

Laux, P., Vogl, S., Qiu, W., Knoche, H. R., and Kunstmann, H. (2011). Copula-based statistical refinement of precipitation in RCM simulations over complex terrain. *Hydrol. Earth Syst. Sci.* 15, 2401–2419. doi: 10.5194/hess-15-2401-2011

Lee, T., and Salas, J. D. (2011). Copula-based stochastic simulation of hydrological data applied to Nile River flows. *Hydrol. Res.* 42, 318–330. doi: 10.2166/nh.2011.085

Lenters, J. D. (2001). Long-term trends in the seasonal cycle of Great Lakes water levels. *J. Great Lakes Res.* 27, 342–353. doi: 10.1016/S0380-1330(01)70650-8

Lofgren, B. M. (2004). A model for simulation of the climate and hydrology of the Great Lakes basin. *J. Geophys. Res.* 109, D18. doi: 10.1029/2004JD004602

Lofgren, B. M., and Gronewold, A. D. (2013). Reconciling alternative approaches to projecting hydrologic impacts of climate change. *Bull. Am. Meteorol. Soc.* 94, ES133–ES135. doi: 10.1175/BAMS-D-13-00037.1

Lofgren, B. M., Gronewold, A. D., Acciaioli, A., Cherry, J., Steiner, A. L., and Watkins, D. W. (2013). Methodological approaches to projecting the hydrologic impacts of climate change. *Earth Interact.* 17, 1–19. doi: 10.1175/2013EI000532.1

Lofgren, B. M., Hunter, T. S., and Wilbarger, J. (2011). Effects of using air temperature as a proxy for potential evapotranspiration in climate change scenarios of Great Lakes basin hydrology. *J. Great Lakes Res.* 37, 744–752. doi: 10.1016/j.jglr.2011.09.006

Lofgren, B. M., and Rouhana, J. (2016). Physically plausible methods for projecting changes in Great Lakes water levels under climate change scenarios. *J. Hydrometeorol.* 17, 2209–2223. doi: 10.1175/JHM-D-15-0220.1

Lu, S., Shen, H. T., and Crissman, R. D. (1999). Numerical study of ice jam dynamics in upper Niagara River. *J. Cold Reg. Eng.* 13, 78–102. doi: 10.1061/(ASCE)0887-381X(1999)13:2(78)

MacKay, M., and Seglenieks, F. (2013). On the simulation of Laurentian Great Lakes water levels under projections of global climate change. *Clim. Change* 117, 55–67. doi: 10.1007/s10584-012-0560-z

Mailhot, E., Music, B., Nadeau, D. F., Frigon, A., and Turcotte, R. (2019). Assessment of the Laurentian Great Lakes' hydrological conditions in a changing climate. *Clim. Change* 157, 243–259. doi: 10.1007/s10584-019-02530-6

Maity, R. (2018). "Theory of copula in hydrology and hydroclimatology," in *Statistical Methods in Hydrology and Hydroclimatology* (Singapore: Springer), 381–424. doi: 10.1007/978-981-10-8779-0_10

Manabe, S., Wetherald, R. T., Milly, P. C., Delworth, T. L., and Stouffer, R. J. (2004). Century-scale change in water availability: CO2 - quadrupling experiment. *Clim. Change* 64, 59–76. doi: 10.1023/B:CLIM.0000024674.37725.ca

Marchand, D., Sanderson, M., Howe, D., and Alpaugh, C. (1988). Climatic change and Great Lakes levels: the impact on shipping. *Clim. Change* 12, 107–133. doi: 10.1007/BF00138935

Meyer, E. S., Characklis, G. W., Brown, C., and Moody, P. (2016). Hedging the financial risk from water scarcity for Great Lakes shipping. *Water Resour. Res.* 52, 227–245. doi: 10.1002/2015WR017855

Miller, W. P., and Piechota, T. C. (2008). Regional analysis of trend and step changes observed in hydroclimatic variables around the Colorado River Basin. *J. Hydrometeorol.* 9, 1020–1034. doi: 10.1175/2008JHM988.1

Millerd, F. (2011). The potential impact of climate change on Great Lakes international shipping. *Clim. Change* 104, 629–652. doi: 10.1007/s10584-010-9872-z

Milly, P. C., and Dunne, K. A. (2017). A hydrologic drying bias in water-resource impact analyses of anthropogenic climate change. *J. Am. Water Resour. Assoc.* 53, 822–838. doi: 10.1111/1752-1688.12538

Mortsch, L. D., and Quinn, F. H. (1996). Climate change scenarios for Great Lakes Basin ecosystem studies. *Limnol. Oceanogr.* 41, 903–911. doi: 10.4319/lo.1996.41.5.0903

Moukomla, S., and Blanken, P. (2016). Remote sensing of the North American Laurentian Great Lakes' surface temperature. *Remote Sensing* 8, 286. doi: 10.3390/rs8040286

Music, B., Frigon, A., Lofgren, B., Turcotte, R., and Cyr, J.-F. (2015). Present and future Laurentian Great Lakes hydroclimatic conditions as simulated by regional climate models with an emphasis on Lake Michigan-Huron. *Clim. Change* 130, 603–618. doi: 10.1007/s10584-015-1348-8

Nagler, T., Schepsmeier, U., Stoeber, J., Brechmann, E. C., Graeler, B., and Erhardt, T. (2021). *VineCopula: Statistical Inference of Vine Copulas*. Technical report.

Nevers, M. B., and Whitman, R. L. (2011). Efficacy of monitoring and empirical predictive modeling at improving public health protection at Chicago beaches. *Water Res*. 45, 1659–1668. doi: 10.1016/j.watres.2010.12.010

Noguchi, K., Gel, Y. R., and Duguay, C. R. (2011). Bootstrap-based tests for trends in hydrological time series, with application to ice phenology data. *J. Hydrol*. 410, 150–161. doi: 10.1016/j.jhydrol.2011.09.008

Notaro, M., Bennington, V., and Lofgren, B. M. (2015). Dynamical downscaling-based projections of Great Lakes water levels. *J. Climate* 28, 9721–9745. doi: 10.1175/JCLI-D-14-00847.1

Notaro, M., Holman, K. D., Zarrin, A., Fluck, E., Vavrus, S. J., and Bennington, V. (2013). Influence of the Laurentian Great Lakes on regional climate. *J. Climate* 26, 789–804. doi: 10.1175/JCLI-D-12-00140.1

Pouliasis, G., Torres-Alves, G. A., and Morales-Napoles, O. (2021). Stochastic modeling of hydroclimatic processes using vine copulas. *Water* 13, 2156. doi: 10.3390/w13162156

Press, S. J. (2003). *Subjective and Objective Bayesian Statistics: Principles, Models, and Applications*. Hoboken, NJ: Wiley-Interscience.

Pryor, S. C., Scavia, D., Downer, C., Gaden, M., Iverson, L., Nordstrom, R., et al. (2014). "Midwest climate change impacts in the United States: The third national climate assessment," in *National Climate Assessment Report*, eds J. M. Melillo, T. C. Richmond, and G. W. Yohe (Washington, DC: US Global Change Research Program), 418–440.

Quinn, F. H. (1978). Hydrologic response model of the North American Great Lakes. *J. Hydrol*. 37, 295–307. doi: 10.1016/0022-1694(78)90021-5

Quinn, F. H. (2002). Secular changes in Great Lakes water level seasonal cycles. *J. Great Lakes Res*. 28, 451–465. doi: 10.1016/S0380-1330(02)70597-2

Quinn, F. H., Clites, A. H., and Gronewold, A. D. (2020). Evaluating estimates of channel flow in a continental-scale lake-dominated basin. *J. Hydrol. Eng*. 146:05019008. doi: 10.1061/(ASCE)HY.1943-7900.0001685

Quinn, F. H., and Edstrom, J. (2000). Great Lakes diversions and other removals. *Can. Water Resour. J*. 25, 125–151. doi: 10.4296/cwrj2502125

R Core Team (2017). *R: A Language and Environment for Statistical Computing*. Vienna: R Core Team.

Schmidt, A. R., and Yen, B. C. (2008). Theoretical development of stage-discharge ratings for subcritical open-channel flows. *J. Hydraul. Eng*. 134, 1245–1256. doi: 10.1061/(ASCE)0733-9429(2008)134:9(1245)

Schölzel, C., and Friederichs, P. (2008). Multivariate non-normally distributed random variables in climate research - introduction to the copula approach. *Nonlin. Process. Geophys*. 15, 761–772. doi: 10.5194/npg-15-761-2008

Sen, P. K. (1968). Estimates of the regression coefficient based on Kendall's Tau. *J. Am. Stat. Assoc*. 63, 1379–1389. doi: 10.1080/01621459.1968.10480934

Smith, J. P., Hunter, T. S., Clites, A. H., Stow, C. A., Slawecki, T., Muhr, G. C., et al. (2016). An expandable web-based platform for visually analyzing basin-scale hydro-climate time series data. *Environ. Model. Softw*. 78, 97–105. doi: 10.1016/j.envsoft.2015.12.005

Thompson, A. F., Rodrigues, S. N., Fooks, J. C., Oberg, K. A., and Calappi, T. J. (2020). Comparing discharge computation methods in Great Lakes connecting channels. *J. Hydrol. Eng*. 25:05020007. doi: 10.1061/(ASCE)HE.1943-5584.0001904

Trenberth, K. E. (1997). The definition of El Ni no. *Bull. Am. Meteorol. Soc*. 78, 2771–2777. doi: 10.1175/1520-0477(1997)078<2771:TDOENO>2.0.CO;2

Van Vuuren, D. P., Edmonds, J., Kainuma, M., Riahi, K., Thomson, A., Hibbard, K., et al. (2011). The representative concentration pathways: an overview. *Clim. Change* 109, 5–31. doi: 10.1007/s10584-011-0148-z

Wang, F., Shao, W., Yu, H., Kan, G., He, X., Zhang, D., et al. (2020). Re-evaluation of the power of the Mann-Kendall test for detecting monotonic trends in hydrometeorological time series. *Front. Earth Sci*. 8, 14. doi: 10.3389/feart.2020.00014

Westerberg, I., Guerrero, J. L., Seibert, J., Beven, K. J., and Halldin, S. (2011). Stage-discharge uncertainty derived with a non-stationary rating curve in the Choluteca River, Honduras. *Hydrol. Process*. 25, 603–613. doi: 10.1002/hyp.7848

Winkler, J. A. (2015). Selection of climate information for regional climate change assessments using regionalization techniques: an example for the Upper Great Lakes Region, USA. *Int. J. Climatol*. 35, 1027–1040. doi: 10.1002/joc.4036

Wright, D. M., Posselt, D. J., and Steiner, A. L. (2013). Sensitivity of lake-effect snowfall to lake ice cover and temperature in the Great Lakes region. *Month. Weath. Rev*. 141, 670–689. doi: 10.1175/MWR-D-12-00038.1

Zaerpour, M., Papalexiou, S. M., and Nazemi, A. (2021). Informing stochastic streamflow generation by large-scale climate indices at single and multiple sites. *Adv. Water Resour*. 156, 104037. doi: 10.1016/j.advwatres.2021.104037

Conflict of Interest: The authors declare that the research was conducted in the absence of any commercial or financial relationships that could be construed as a potential conflict of interest.

Publisher's Note: All claims expressed in this article are solely those of the authors and do not necessarily represent those of their affiliated organizations, or those of the publisher, the editors and the reviewers. Any product that may be evaluated in this article, or claim that may be made by its manufacturer, is not guaranteed or endorsed by the publisher.

frontiers | Frontiers in Water

ORIGINAL RESEARCH
published: 23 May 2022
doi: 10.3389/frwa.2022.804799

Extreme Precipitation Trends and Meteorological Causes Over the Laurentian Great Lakes

Kenneth E. Kunkel[1]*, *Xungang Yin*[2†], *Liqiang Sun*[1], *Sarah M. Champion*[1], *Laura E. Stevens*[1] and *Katharine M. Johnson*[1]

[1] North Carolina Institute for Climate Studies, North Carolina State University, Asheville, NC, United States, [2] Riverside Technology Inc., Asheville, NC, United States

Trends in extreme precipitation and their causes were analyzed for events within the Laurentian Great Lakes for several periods: 1908–2020, 1949–2020, 1980–2019, and 1980–2020. Upward trends in extreme precipitation were found for multiple metrics, including the number of exceedances of return period thresholds for several durations and average recurrence intervals (ARI), the number of extreme basin-average 4-day precipitation totals, and the annual maximum daily station precipitation. The causes of extreme events were classified into 5 meteorological categories: fronts of extratropical cyclones (ETC-FRT), extratropical cyclones but not proximate to the fronts (ETC-NFRT), mesoscale convective systems (MCS), tropical cyclones (TC), and air mass convection (AMC). For daily events exceeding the threshold for 5-yr ARI, ETC-FRTs account for 78% of all events, followed by ETC-NFRTs (12%), MCSs (6%), TCs (2%), and AMC (1%). Upward trends in the number of events by cause were found for all categories except AMC. An examination of basin-wide 4-day extreme events (40 largest events during 1980–2019) found that all events were caused by ETC-FRTs (85%) or ETC-NFRTs (15%).

Keywords: Great Lakes (North America), extreme precipitation, weather fronts, meteorology, trends

OPEN ACCESS

Edited by:
Adam Burnett,
Colgate University, United States

Reviewed by:
Munir Ahmad Nayak,
Indian Institute of Technology Indore, India
Huanping Huang,
Berkeley Lab (DOE), United States
Timothy Hawkins,
Shippensburg University, United States

***Correspondence:**
Kenneth E. Kunkel
kekunkel@ncsu.edu

†Present address:
Xungang Yin,
NOAA National Centers for Environmental Information, Asheville, NC, United States

Specialty section:
This article was submitted to Water and Climate, a section of the journal Frontiers in Water

Received: *29 October 2021*
Accepted: *28 April 2022*
Published: *23 May 2022*

Citation:
Kunkel KE, Yin X, Sun L, Champion SM, Stevens LE and Johnson KM (2022) Extreme Precipitation Trends and Meteorological Causes Over the Laurentian Great Lakes. Front. Water 4:804799. doi: 10.3389/frwa.2022.804799

INTRODUCTION

The Laurentian Great Lakes represent the largest freshwater resource in North America. They are utilized in many ways, including as a municipal water supply source, a transportation waterway, a major commercial fishery, and a recreational destination for fishing, boating, and skiing. Fluctuations in water levels and available water quantity can have major impacts on these uses. For example, on Lakes Michigan-Huron over the period 2010 to 2020, annual average water levels ranged from 175.9 m above sea level in 2013 to 177.31 m in 2020. These fluctuations are sufficiently large in magnitude to have contrasting impacts on lake uses. For example, anomalously high lake levels increase the risk of shoreline damage during storms but increase the maximum load that cargo ships can carry through shallow portions of navigation channels. Anomalously low levels reduce maximum loads but reduce shoreline damage during storms (Wuebbles et al., 2019).

A major question is the impact of future anthropogenically forced climate change on the hydroclimatology of the Great Lakes Basin (GLB). Most global climate model (GCM) simulations under increased future greenhouse gas (GHG) concentrations show an increase in both mean annual precipitation and extreme precipitation frequency and intensity over the GLB (Easterling et al., 2017). However, accurate simulation of precipitation remains a challenge for GCMs because of the complexity of precipitation physics and the coarse resolution of GCMs (Seneviratne et al., 2021).

To address such issues, a growing research area is a focus on the meteorological causes of extreme precipitation events, trends, and variations. Such causes can be broadly categorized into thermodynamic and dynamic components (Emori and Brown, 2005; Nie et al., 2018). The former accounts for atmospheric moisture content, q, the saturated value of which, according to the Clausius–Clapeyron relationship, increases at a rate of ∼7%/K (Trenberth et al., 2003). In addition to its obvious effect through supply of moisture, the atmospheric moisture content can also indirectly affect potential extreme precipitation magnitudes through changes in atmospheric convective stability. The dynamic component accounts for atmospheric motion, specifically the vertical velocity (VV), and is associated with specific weather system types.

Quantifying how changes in these components affect the local extreme precipitation distribution is complicated. While progress is expected in the future using convection-permitting models (Kendon et al., 2021), the capability to observe and model changes in small-scale convective processes affecting local extreme precipitation is still limited (Prein et al., 2017) because the spatial resolution of both global and regional climate models remains too coarse to directly simulate the small-scale circulations and associated micro-physical processes in clouds. On the other hand, important progress has been made on linking regional changes in extreme precipitation to large-scale processes. Barlow et al. (2019) state that global climate models "are generally better at capturing synoptic-scale features associated with extreme precipitation than extreme precipitation, itself." A study of the northeast US, including the eastern part of the GLB, found that a set of models from the Coupled Model Intercomparison Project Phase 6 (CMIP6) exhibited mixed results in their simulation of extreme precipitation metrics with slightly better performance for the circulation patterns associated with heavy precipitation (Agel and Barlow, 2020). Kunkel et al. (2020a) found concurrent increasing trends in extreme precipitation and precipitable water (PW; the column integrated q) aggregated in large regions of the US. Similar results have been found in Australia by Roderick et al. (2020). Kunkel et al. (2020b) examined the relationship of individual station extreme precipitation event magnitudes with associated values of PW and VV and found a strong positive correlation.

In this study, we examine trends in extreme precipitation and the relationship of those trends to large-scale weather systems. Such systems are generally simulated adequately by GCMs. This analysis provides the basis for an alternate approach to future projections that uses the large-scale weather factors causing extreme precipitation rather than precipitation itself.

Previous analyses of extreme precipitation that included the Great Lakes generally indicate upward trends. For the United States, Easterling et al. (2017) found upward trends over the northeastern quadrant of the US for several extreme metrics for both 1901–2016 and 1958–2016. The metrics include the number of daily precipitation events exceeding an average recurrence interval (ARI) of 5 years, the 5-yr maximum daily precipitation, and the total amount of precipitation falling on days exceeding the 99th percentile of daily precipitation. Kunkel et al. (2020a) found upward trends in the number of extreme events for the northeast US for 35 combinations of duration (1, 2, 3, 5, 10, 20, and 30 days) and ARI (1, 2, 5, 10, and 20 years) over the period 1949–2016. Vincent et al. (2018) analyzed trends over 1901–2016 for Canadian stations in the GLB. For the number of days exceeding the 90th percentile threshold of daily precipitation, most stations indicated upward trends. However, for the annual maximum daily precipitation, they found a mix of upward and downward trends, with most not statistically significant.

Some of the above studies presented composite analyses that included portions of the GLB, but they do not include results specifically for the basin. This study builds upon previous regional studies by focusing on both trends and meteorological causes of extreme precipitation events exclusively for the GLB.

DATA AND METHODS

Station Observations of Precipitation

The Global Historical Climatology Network—Daily (GHCN-D) was used as the source of station observations of daily precipitation (Menne et al., 2012). A set of United States stations with <10% missing daily precipitation data for 1895–2009 from Kunkel et al. (2012) was screened for those within the boundaries of the GLB; a total of 57 stations were identified. To enhance spatial coverage, two additional sets of stations from GHCN-D were identified, meeting the criterion of <10% missing daily precipitation observations for 1949–2020 and 1980–2020; these included available Canadian stations. Geospatial analysis was performed on these subsets of stations to determine those within the boundaries of the Great Lakes basin. A total of 171 (188) stations were identified for the period 1949–2020 (1980–2020), including 42 stations common to all three sets. The locations of these three sets of stations are shown in **Figure 1**.

The 1895–2020 long-term set of 57 stations had been analyzed by Kunkel et al. (2012) to identify daily precipitation events exceeding the threshold for a 1-in-5-yr average recurrence interval (ARI). In that study, they restricted the analysis of meteorological causes to the period 1908–2009 because of inadequacies in the data needed to identify causes before that period. For this current study, we used the events and causes for that shorter period of 1908–2009. The data for 2010–2020 were also analyzed to identify additional events exceeding the threshold, creating a data set for 1908–2020. For this additional analysis period of 2010–2020, the number of stations meeting the minimum data availability threshold (300 or more days in a year) for analysis varied from 45 to 51. Three annual resolution time series were constructed. For each year, based on the events exceeding the station-specific 1-in-5-yr threshold in that year, three metrics were computed: (1) the total number of station events; (2) the mean precipitation for those daily station events; and (3) the single largest (maximum) precipitation value for those daily station events. The annual values were normalized by the number of stations meeting the data availability criterion for that year. The resulting three annual time series were analyzed for trends.

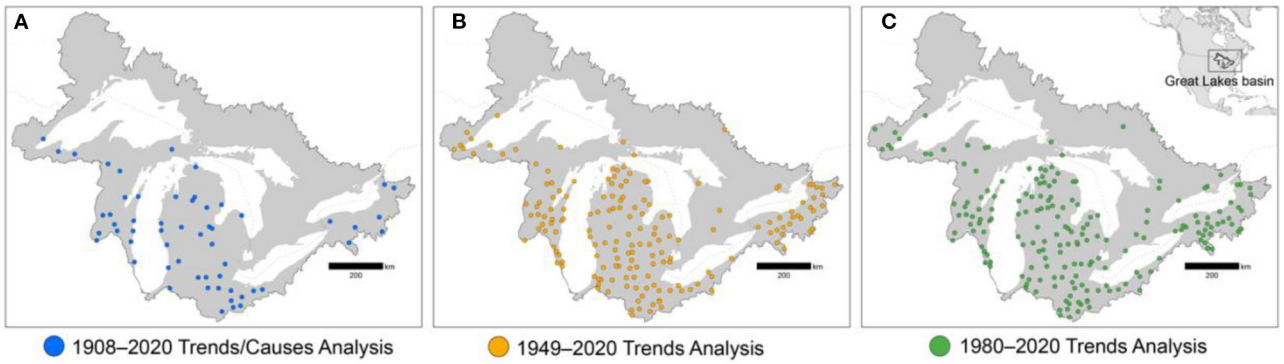

FIGURE 1 | Locations of the stations used in **(A)** the trends and causes analysis for 1908–2020, **(B)** the trends analysis for 1949–2020, and **(C)** the trends analysis for 1980–2020. The white area indicates water bodies and the dark gray area indicates land area within the Great Lakes drainage basin.

The 1949–2020 and 1980–2020 sets of 171 and 181 stations were analyzed following Kunkel et al. (2020a) for trends in the number of events exceeding thresholds of extreme precipitation accumulation for 35 combinations of duration (1, 2, 3, 5, 10, 20, and 30 days) and ARI (1, 2, 5, 10, and 20 years). The analysis of this large range of combinations addresses the question of whether the results are sensitive to a perhaps-fortuitous choice of extreme precipitation metric. By examining this large set, we can assess the robustness of the observed trends.

Reanalysis Precipitation

Precipitation extremes at individual stations can have substantial local impacts. We were also interested in examining basin-wide extremes because they potentially can have sizeable effects on Great Lakes water levels. However, the variations in station density, particularly the lack of long-term stations in the northern portions of the basin (**Figure 1**), limit the suitability of station averages to infer basin-wide extremes. For this reason, we used a reanalysis product, the Modern-Era Retrospective analysis for Research and Applications, Version 2 (MERRA-2; Gelaro et al., 2017), to investigate extreme precipitation events of large areal extent. Meteorological reanalyses use weather forecast models that assimilate observations to provide 3-dimensional fields of the atmospheric state that evolve temporally in a manner that is consistent with physical laws and the observations. Unlike some reanalyses, the MERRA-2 reanalysis assimilates *in situ* precipitation observations and has been shown to produce superior estimates of precipitation (Bosilovich et al., 2017). The MERRA-2 spatial resolution is 0.5° latitude by 0.625° longitude. Daily values of precipitation accumulations were obtained covering the period 1980–2019. The MERRA-2 grid points within the GLB boundaries were identified (281 grid points), and the data for these grid points were averaged to produce a daily basin-average time series of precipitation. The basin-average mean annual precipitation from this dataset is 1,067 mm. Four-day rolling precipitation totals were calculated (days 1–4, 2–5, 3–6, etc.). The 40 largest non-overlapping events of 4-day duration were identified and used for climatological analysis. The selection of the 40 largest events in a 40-yr record is equivalent to choosing all events exceeding the 1-yr ARI threshold. The duration of 4 days was chosen to be consistent with the results of Kunkel and Champion (2019).

Meteorological Causes

Kunkel et al. (2012) identified station-specific values for the 1-in-5 yr threshold of daily precipitation by first ranking daily precipitation amounts. The 1-in-5 yr threshold was then calculated empirically as the rank N value where $N =$ (number of available years of data)/5. For a station with 100 years of data, this is the rank 20 daily precipitation value. The station thresholds calculated in Kunkel et al. (2012) were used here to identify additional station events for 2010–2020. These additional daily extreme precipitation events were assigned a meteorological cause using manual expert judgment, resulting in a dataset of causes covering the period of 1908–2020. In their study, the categories relevant to the GLB included extratropical cyclones (ETCs), tropical cyclones (TCs), mesoscale convective systems (MCSs), and air mass convection (AMC). The ETC category was subdivided into 2 categories: events near one of the ETC fronts (ETC-FRT) and events not near the fronts (ETC-NFRT).

MCSs are organized areas of thunderstorms that persist for several hours and can produce heavy rainfall and severe weather. They can be classified as internally or externally driven (Schumacher and Rasmussen, 2020). Externally driven MCSs are triggered by another weather feature, such as a front. Internally driven MCSs develop and maintain their character primarily through self-generated features. In the Kunkel et al. (2012) study, extending back to 1908, the necessary data (e.g., satellite cloud cover, radar) to definitively identify MCSs, whether externally- or internally-driven, was not available for the entire period. Therefore, extreme events associated with organized areas of precipitation, which possibly could be classified as MCSs if the necessary data were available, were instead classified by the large-scale trigger, typically a front, in the case of externally-driven MCSs. Extreme events associated with organized areas of precipitation, but with no large-scale weather system trigger, were classified into the MCS category. Thus, our MCS category is restricted to the internally-driven type. It should be noted that we

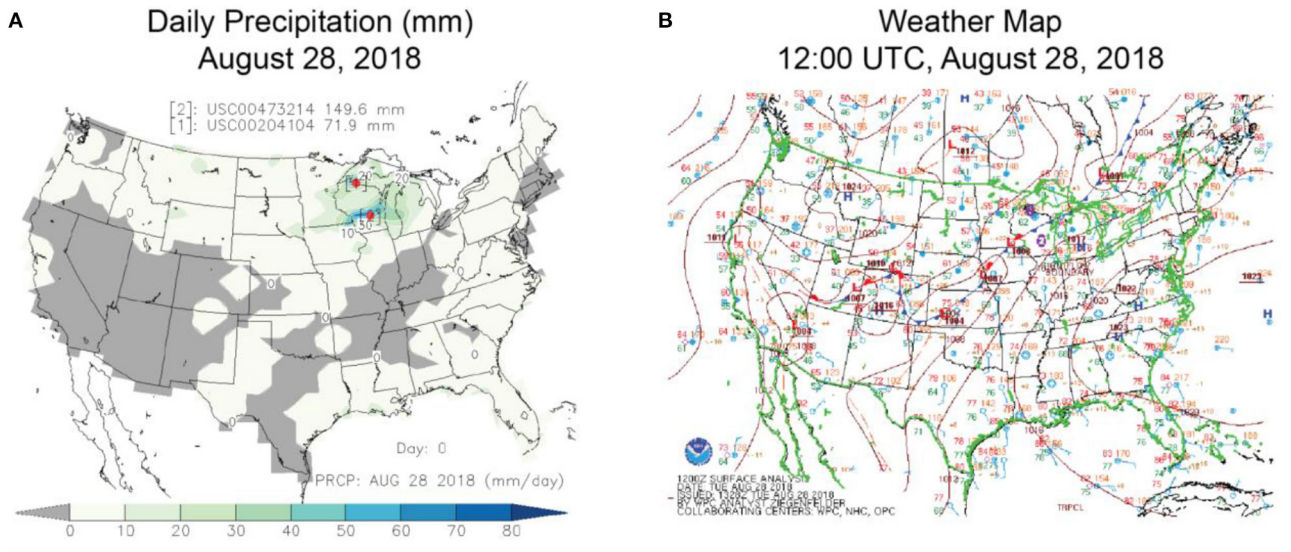

FIGURE 2 | Weather maps including **(A)** map of daily precipitation (mm) and **(B)** map of weather features, for a day (August 28, 2018) with two extreme events caused by a front (ETC-FRT). The red dots in **(A)** and the white-on-purple numbers in **(B)** indicate the locations of the two events.

could have identified externally-driven MCSs for the additional 2010–2020 events, but we maintained the same procedures as the original study to maintain temporal consistency in the causes data.

For the 2010–2020 addition to the causes data, the manual expert identification of the cause for each extreme precipitation event at each station was assigned based on several data sources. Weather analyses charts from the NOAA National Weather Service (NWS) National Centers for Environmental Prediction (NCEP) (https://www.ncei.noaa.gov/data/ncep-charts/access/) were used to identify synoptic scale features. A 1° latitude by 1° longitude gridded dataset, described in Kunkel et al. (2012), was used to create daily maps of temperature and precipitation for use in identifying precipitation clusters and temperature gradients. Written material, such as event-related scientific papers, technical notes, news reports, and historical observations from nearby stations, supplemented the information provided by the maps.

Figures 2–5 show examples of two of the maps used in the causes evaluation for 4 different causes: ETC-FRT, ETC-NFRT, MCS, and TC, respectively. The maps display the precipitation distribution and surface weather features on the day of the event. Similar maps for the day before and after the event as well as surface temperature and 500 hPa geopotential height were also generated to illustrate temporal evolution; this aided in the station event cause classification. In the ETC-FRT example for August 28, 2018 (**Figure 2**), the two extreme precipitation events on that day (one located in Wisconsin and the other in the Michigan Upper Peninsula) are near a front that extends across the western part of the basin. In the ETC-NFRT example for April 30, 2020 (**Figure 3**), the event is located in northern Michigan, to the north of the ETC center moving across the southern portion of the basin. In the MCS example for July 19, 2020 (**Figure 4**), the event in eastern Michigan is within a larger area of heavy precipitation; the front to the west is too far from the event to be considered as the trigger. In the TC example for October 30, 2012 (**Figure 5**), the six events occur along the path of Hurricane Sandy while it was transitioning into an extratropical system; this case illustrates that we categorized events as TCs whether they occurred while the system was tropical or in a post-tropical stage.

The causes of the 40 highest basin-average 4-day total precipitation events were determined following Kunkel and Champion (2019) using a manual expert judgment process similar to that used for evaluating daily extreme events at individual stations but adjusted to account for the evolution of the atmospheric state during these multi-day events and the availability of sources to identify weather features. An initial assessment of the meteorological cause was done by referencing historical surface weather charts from the NOAA Central Library Data Imaging Project (n.d) for the dates and locations of the events. For events suggesting proximity to a named TC, the assignment of TC as the cause was confirmed through further research matching the dates and locations of the precipitation event with the International Best Track Archive for Climate Stewardship set of TC track data (Knapp et al., 2010). As needed to confirm the cause, maps of atmospheric fields (including mean sea level pressure, 500 hPa geopotential height, 2 m temperature, precipitation, 2 m specific humidity, and vertical motion) were produced using the NCEP/National Center for Atmospheric Research (NCAR) reanalysis (Kalnay et al., 1996). The resolution of the reanalysis is 2.5° x 2.5°. Maps of surface weather features, 500 hPa height contours, and 24-hr precipitation were assembled side-by-side for each day of an event. These daily composites were then assembled so that they could be looped to show the daily evolution of patterns. The sequence of these daily patterns was effective in revealing the coincidence of atmospheric features

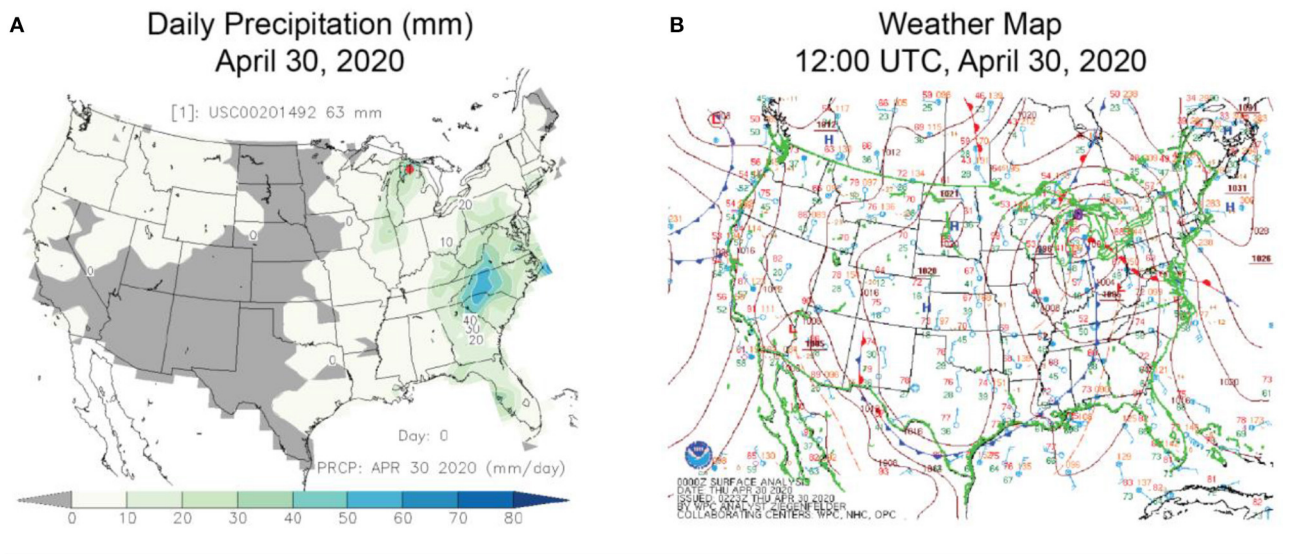

FIGURE 3 | Weather maps including **(A)** map of daily precipitation (mm) and **(B)** map of weather features, for a day (April 30, 2020) with one extreme event caused by an extratropical cyclone (ETC-NFRT). The red dot in **(A)** and the white-on-purple number in **(B)** indicate the location of the event.

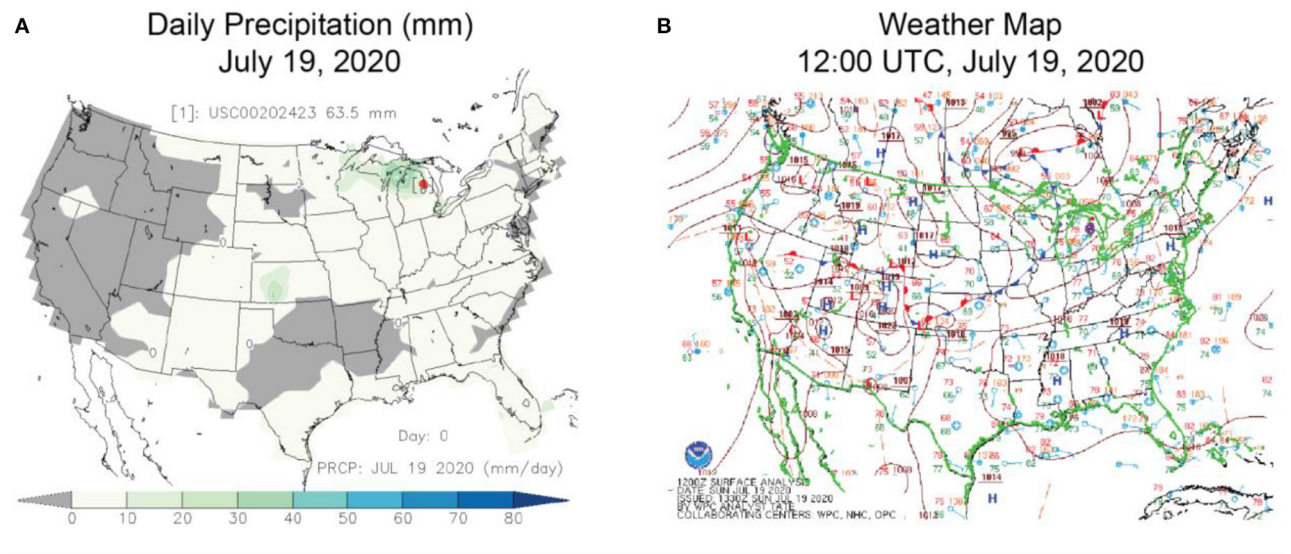

FIGURE 4 | Weather maps including **(A)** map of daily precipitation (mm) and **(B)** map of weather features, for a day (July 19, 2020) with one extreme event caused by a mesoscale convective system (MCS). The red dot in **(A)** and the white-on-purple number in **(B)** indicate the location of the event.

and surface precipitation locations and amounts. Maps of 4-day average and anomalies of selected atmospheric state variables (1,000 hPa temperature, 500 hPa geopotential height, and 500 hPa vertical velocity) were produced to identify persistent features. These maps effectively revealed the upper-level troughs, surface gradients, and large-scale forcing patterns. A common situation was day-to-day variability in the causal mechanisms, particularly between ETC-FRT and ETC-NFRT. In such situations, the amount of precipitation on each day served as a weighting function to decide on the primary mechanism. Three of the co-authors performed the expert judgment. Each of the experts reviewed the work of the others.

Water Vapor and Vertical Velocity Analysis

Following Kunkel et al. (2020b), maximum daily 3-hr values of PW and VV were derived from the NCEP/NCAR reanalysis. For each station used in the 1949–2020 period analysis, each daily 1-yr ARI event was assigned PW and VV values from the NCE/NCAR grid box containing the station. The individual station event values were aggregated into PW and VV bins.

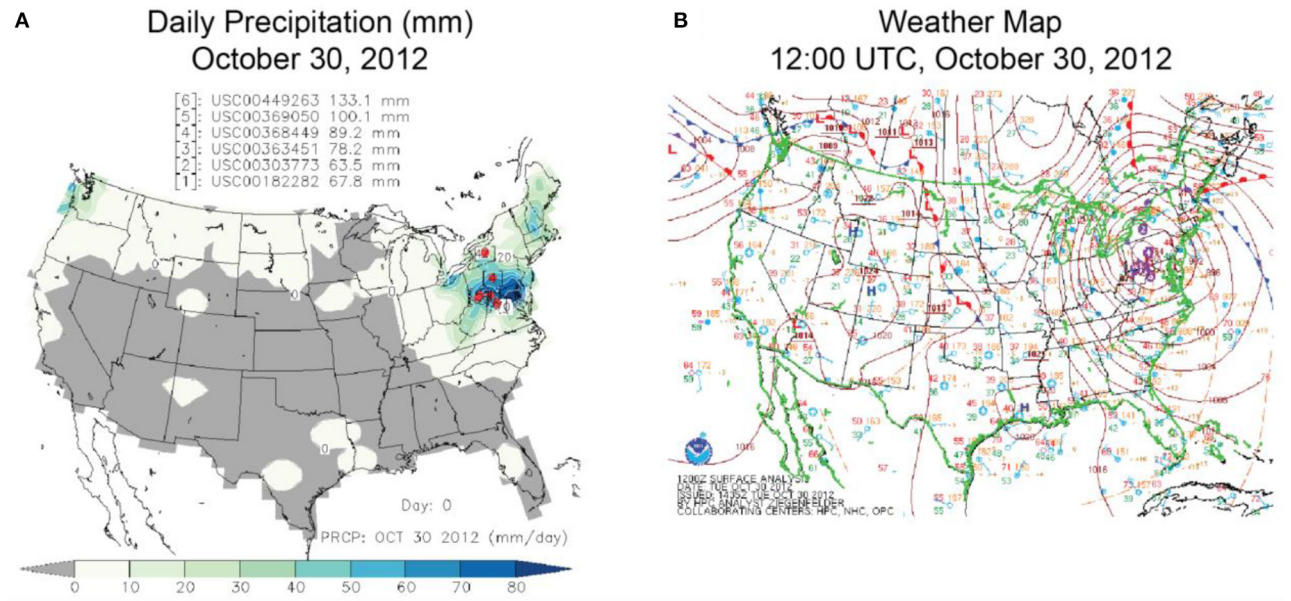

FIGURE 5 | Weather maps including **(A)** map of daily precipitation (mm) and **(B)** map of weather features, for a day (October 30, 2012) with 6 extreme events caused by a tropical cyclone (TC; Hurricane Sandy). The red dots in **(A)** and the white-on-purple numbers in **(B)** indicate the locations of the 6 events.

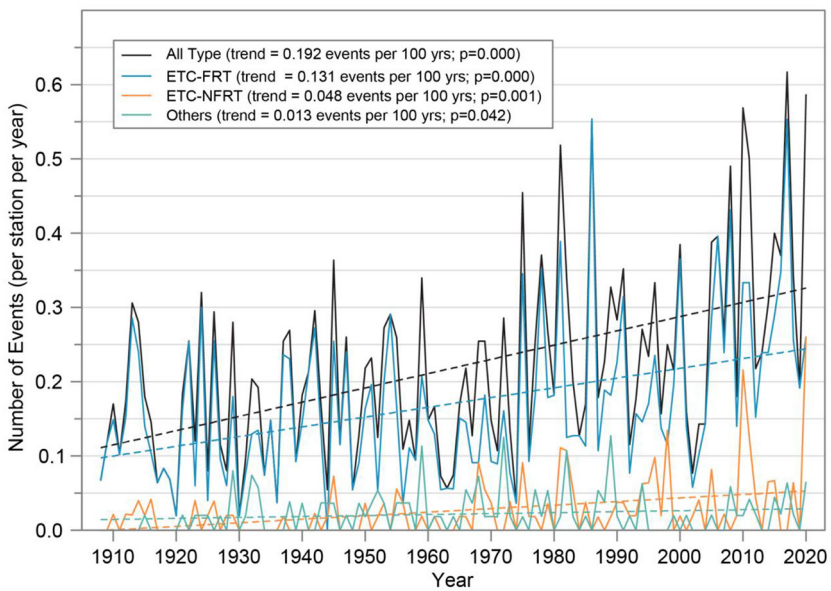

FIGURE 6 | Annual time series of the overall number of extreme events per station ("All Type"; black line), events caused by one of the ETC fronts ("ETC-FRT"; blue), events caused by an ETC not near a front ("ETC-NFRT"; orange), and events caused by all other types ("Others"; green). Dashed lines indicate linear least-squares fits to the annual data. The trend values and *p*-values of the trend lines are displayed in the legend.

RESULTS

Temporal Trends

Figures 6–8 show the results of our 3 types of trend analyses and illustrate that extreme precipitation exhibits an upward trend by several metrics. For the 1908–2020 long-term set of stations for which causes were analyzed, there is a statistically significant (at the p=0.01 level) upward trend in the number of 1-in-5 yr events over the period 1908–2020 (**Figure 6**) of 8.8% decade^{-1}. The time series of the annual maximum precipitation value among the

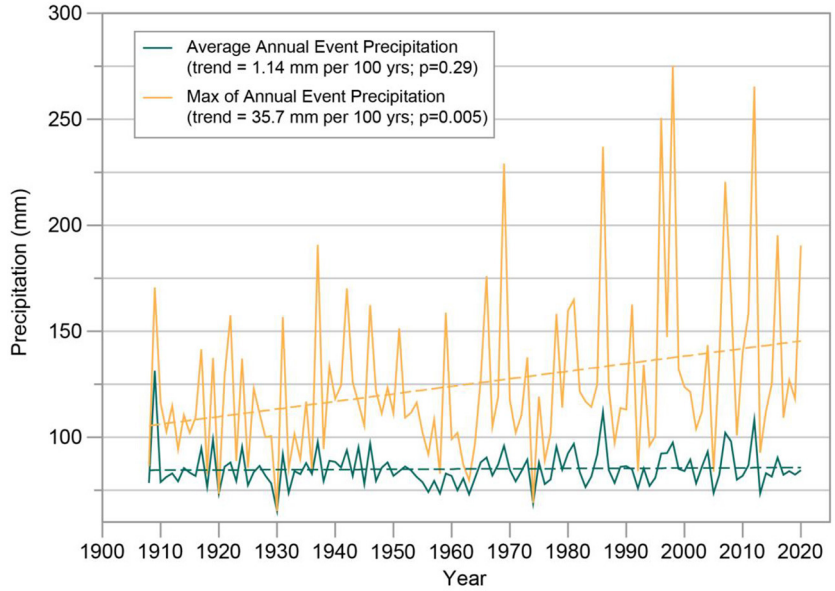

FIGURE 7 | Annual time series (1908–2020) of two metrics of the precipitation amounts for those events exceeding the station-specific thresholds for daily 5-yr ARI events: the average precipitation for the extreme events ("Average Annual Event Precipitation"; teal color) and the single largest precipitation value among the extreme events ("Max of Annual Event Precipitation"; orange color). These time series are based on data from the 57 long-term stations. The trend values and *p*-values of the trend lines are displayed in the legend.

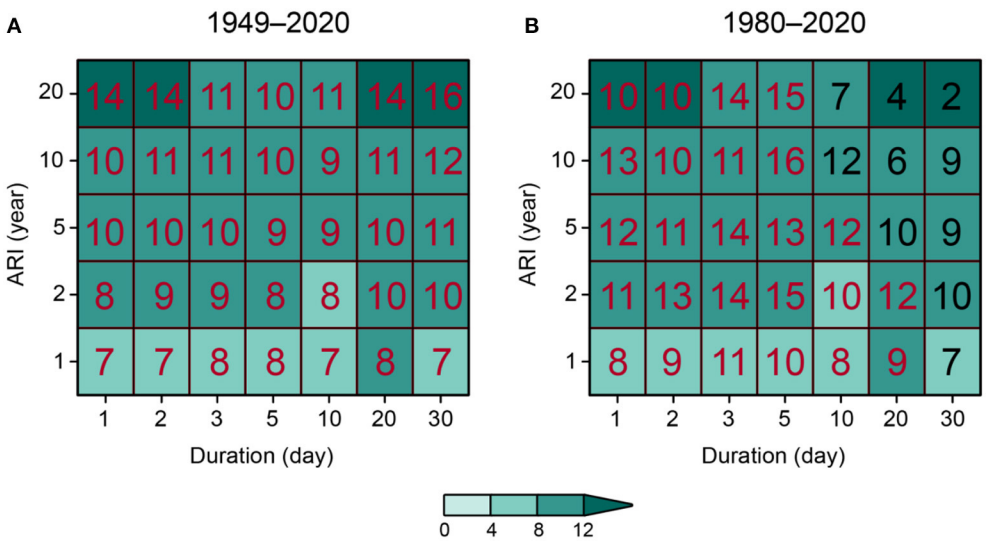

FIGURE 8 | Trends (% decade^{-1}) in the frequency of occurrences for the Great Lakes basin of the 35 duration–ARI combinations for the periods of **(A)** 1949–2020 and **(B)** 1980–2020. Statistically significant trends are shown in red. All trends are upward. For the 1949–2020 analysis period, all trends are statistically significant ($p = 0.05$ significance level for a two-tailed test). For the 1980–2020 period, all trends are statistically significant for the 1, 2, 3, and 5 day durations, but not for the 10, 20, and 30 day durations.

extreme events shows a sizable upward trend of about 30% per century (**Figure 7**). However, the average precipitation per event for all events in a year shows no trend (**Figure 7**).

The larger set of stations analyzed over the two shorter periods of 1949–2020 and 1980–2020 show upward trends for all 35 ARI-duration combinations (**Figure 8**). All trends are statistically significant ($p = 0.05$) for the 1949–2020 period of analysis (**Figure 8A**). Higher percentage trends were found for the larger (rarer) ARI values. For the shorter period of 1980–2020, all the trends are statistically significant for 1, 2, 3, and 5 day durations, but not for all of the 10, 20, and 30 day durations (**Figure 8B**). The temporal distribution of

the 40 largest 4-day basin-wide average precipitation totals also shows an upward trend (**Figure 9**). Almost half (45%) of those events occurred during the most recent decade (2010–2019).

Meteorological Causes of Station Events

The predominant cause of the station extreme events is ETC-FRT (78%). This is similar to what was found by Kunkel et al. (2012) in regions that include parts of the GLB. The second largest category is ETC-NFRT, causing 12% of the events. Smaller contributions are made by MCSs (6%), TCs (2%), and AMC (1%). There is strong seasonality in the distribution of station extremes (**Figure 10**). The majority of events occur in the summer (60%), while 25% occur in the fall. Only 2% of events occur in the winter, while 13% occur in the spring. ETC-FRT is the dominant category in all seasons. ETC-NFRT events are the second most common. Events caused by the minor categories of MCS and AMC mostly occur in the summer, while the few events associated with TCs are evenly distributed between summer and fall.

There are upward trends in the number of events for the ETC-FRT (0.131 events 100 yr^{-1} or 7.6% $decade^{-1}$) and ETC-NFRT (0.048 events 100 yr^{-1} or 18.5% $decade^{-1}$) categories (**Figure 6**). There are also upward trends in the total of MCS and TC categories ("Others"; 0.013 events 100 yr^{-1} or 5.9% $decade^{-1}$). All of these trends are statistically significant at the $p = 0.05$ level.

Meteorological Causes of Extreme Basin-Wide Average Events

Figure 11 shows the distribution over time of the 40 largest 4-day basin-average total precipitation events, along with their meteorological causes. The event with the highest total precipitation occurred on September 10–13, 1986, with 59.2 mm. The seasonal distribution of basin-wide extreme events (**Figure 9**) indicates nearly equal numbers in the summer and fall (16 and 14, respectively). Seven and three basin-wide extreme events occurred in the spring and winter, respectively. The category of ETC-FRT is the primary meteorological cause for 85% of these events, slightly higher than the 78% for the station events. The primary cause for the remaining 15% is ETC-NFRT. ETC-NFRT is a secondary cause in 10 of the events, and a TC makes a contribution to one of the events. A study by Kunkel and Champion (2019), demonstrated that ETC-FRTs were also the dominant category (59%) of the top 100 events in the coterminous US, however none of those events were located in the Great Lakes basin. Most were located in the Gulf Coast region and along the Pacific Coast. The TC category (25%) and West Coast atmospheric rivers (15%) were the other dominant categories. The TC category contributed to one of the GLB events.

Water Vapor and Vertical Velocity Relationships

Figure 12 shows the boxplot statistics of the distribution of event precipitation amounts as a function of PW. At values of PW <30 mm, precipitation amounts vary little and even slightly decrease with PW. For PW >30 mm, precipitation amounts increase with PW consistent with the overall results of Kunkel et al. (2020b). If extreme precipitation amounts scaled with the Clausius-Clapeyron (C-C) relationship, the fractional change in precipitation amounts would be the same as the fractional change in PW. For PW values between 30 and 60 mm, precipitation amounts increase but at a smaller fractional rate than PW. At about 60 mm, the change in precipitation amounts is similar to the fractional change in PW, or close to the C-C relationship. The results for VV (not shown) did not indicate a robust relationship between precipitation amounts and the magnitude of VV, again similar to the results of Kunkel et al. (2020b).

The strong seasonality (summer-fall maximum) in the occurrence of extreme precipitation amounts is explained by the

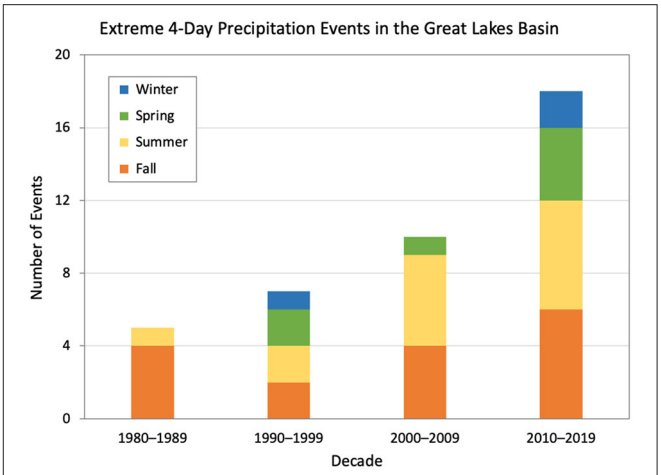

FIGURE 9 | Number of the 40 largest basin-wide 4-day precipitation events by decade from 1980–1989 to 2010–2019 delineated by season. Precipitation is calculated from the MERRA-2 reanalysis and averaged over the Great Lakes Basin.

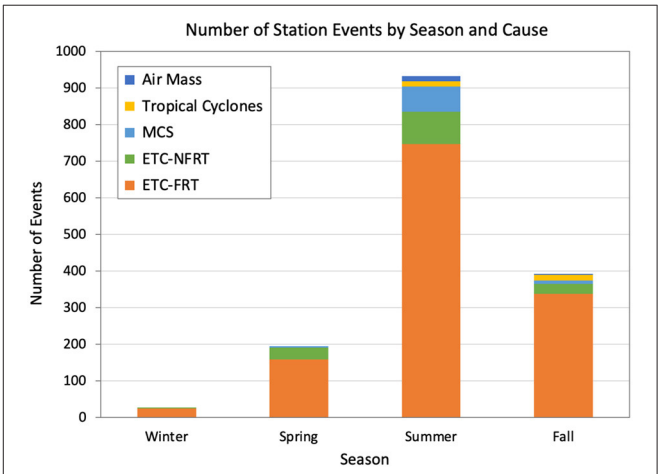

FIGURE 10 | Seasonal distribution of the number of extreme station events categorized by meteorological cause.

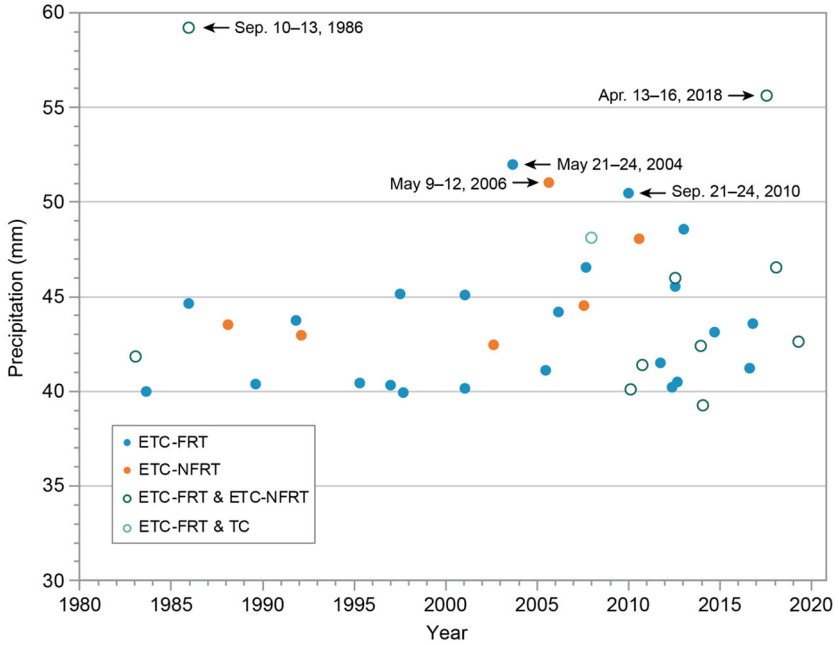

FIGURE 11 | Scatter plot of the 40 largest basin-wide events showing precipitation amounts and year of occurrence. The symbols indicate the meteorological cause(s). The open symbols indicate events with both a primary (ETC-FRT) cause and a secondary cause (either ETC-NFRT or TC). The dates of the 5 largest events are indicated next to the symbols.

high correlation between water vapor and extreme precipitation amounts. While weather systems are needed to force upward vertical motion, the actual amount of precipitation is determined mainly by available atmospheric water vapor, which is maximized in the warm season.

DISCUSSION

Most regional studies that include the Great Lakes basin have found an upward trend in extreme precipitation. The analysis herein focused solely on stations within the basin, most of them within the US, and found upward trends for most extreme precipitation metrics. An analysis of basin-wide events using precipitation from the MERRA-2 reanalysis identified the 40 largest 4-day precipitation events since 1980. There is a large upward trend in the decadal count of these basin-wide events, with the last decade (2010–2019) accounting for 45% of all events. These results are similar to other studies that analyzed regions which included all or portions of the Great Lakes basin.

Fronts are the dominant cause of extreme precipitation at individual stations. For daily extreme events exceeding the 5-yr ARI, 78% of all events are caused by fronts. For the 40 basin-wide average extreme events, fronts are an even more dominant cause, representing 85% of all events. These results are similar to those of Kunkel et al. (2012). In that study, the defined regions included the U.S. portion of the Great Lakes, but did not focus specifically on the basin. The additional 11 years analyzed in this study indicates a continuation of fronts as the dominant cause.

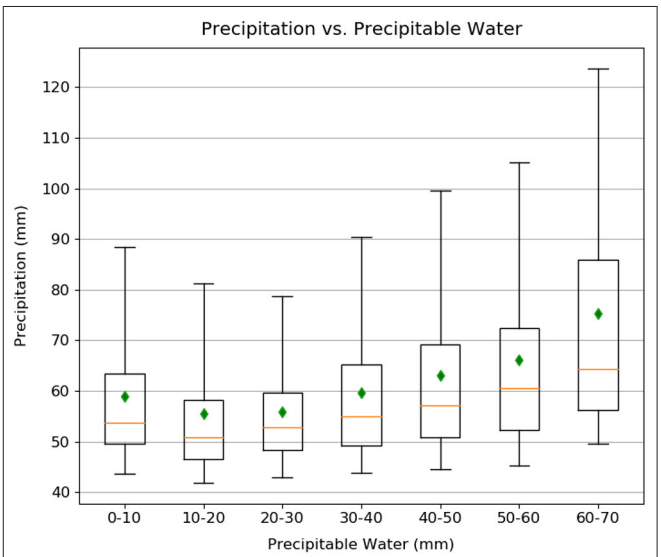

FIGURE 12 | Boxplot distributions for the 1-yr, 1-dy partial duration series events of precipitation event amount vs. the same-day 3-h maximum PW sorted into 10 mm interval bins. Boxplots display mean (green diamonds), median (orange horizontal lines), 25th and 75th percentiles (box limits), and 5th and 95th percentiles (whiskers).

The water vapor and vertical velocity analysis results are similar to the findings of Kunkel et al. (2020b) in showing a positive correlation between precipitation amounts and PW at PW values above 30 mm, but no correlation between

precipitation amounts and vertical velocity. The relationship between precipitation amounts and PW is less than Clausius-Clapeyron for PW values <60 mm. This is the same threshold as found in Kunkel et al. (2020b).

The dominant role of fronts as the cause of extreme events has implications for assessing future changes in extreme precipitation if global warming continues. The identification of meteorological phenomena in global climate model simulations is advancing (Mudigonda et al., 2021). Biard and Kunkel (2019) developed a method using a deep learning neural network to automatically identify fronts in reanalysis fields. A similar approach was used by Lagerquist et al. (2019). Such methods applied to GCM simulations can be used to provide a meteorological basis for potential future changes. Such approaches can provide an alternative to direct use of model-generated precipitation.

Priestley et al. (2020) provide an analysis of GCM simulation of ETCs in the CMIP6 suite of simulations. They find that the simulation of ETCs has improved in CMIP6 relative to CMIP5. Furthermore, higher resolution CMIP6 models show superior performance compared to lower resolution CMIP6 models. Over the Great Lakes, the CMIP6 models exhibit a low bias of 10–20% in the number of ETCs in the winter and a high bias of 10–20% in the summer.

The positive correlation between precipitation amounts of water vapor, equaling the C-C relationship at higher PW amounts, provides a strong foundation for application to the planning and design of structures that have multi-decadal lifetimes. One of the most confident projections of global warming is continued increases in global mean column integrated water vapor and near-surface specific humidity over land (Douville et al., 2021; Lee et al., 2021). Thus, it would be prudent to plan for higher extreme precipitation amounts in the future.

There are a few limitations in this study. Firstly, while the trend analysis of the available station data is robust, there is a low number of Canadian stations with available long-term data in the GHCN-D dataset. Thus, there is uncertainty as to whether upward trends have occurred in the northern portion of the basin. It is not known to us whether there are sources of long-term station data that are not available in GHCN-D.

Secondly, the study was limited to daily and multi-day extreme precipitation amounts. At these time scales, it is not surprising that large-scale meteorological systems are principally responsible for the events. At sub-daily timescales, it is likely that local intense convection arising from mesoscale convective systems and air mass convection would play a more important role in the mix of meteorological systems responsible for precipitation extremes. Simulation of such systems by current generation climate models is challenging (Feng et al., 2021) compared to extratropical cyclones and associated fronts. A recommended future study is to analyze long-term hourly precipitation data and, as in the present study, determine the causes of extreme sub-daily precipitation events.

DATA AVAILABILITY STATEMENT

The raw data supporting the conclusions of this article will be made available by the authors, without undue reservation.

AUTHOR CONTRIBUTIONS

KK designed the overall research goals and protocols and wrote the first draft of the paper. XY determined the causes of the station extreme events for 2010–2020. LS analyzed the MERRA-2 precipitation data and identified the causes of some of the 40 basin-wide average extreme events. SC developed the procedures for identifying the causes of the basin-wide average extremes and identified the causes of some of those events. LES identified the causes of some of the basin-wide extreme events and performed the water vapor and vertical motion analysis. KJ provided the GIS analysis to identify stations and MERRA-2 gridpoints within the basin. All authors contributed to the writing of the paper.

FUNDING

This work was supported by NOAA through the Cooperative Institute for Satellite Earth System Studies under Cooperative Agreement NA19NES4320002.

REFERENCES

Agel, L. and Barlow, M. (2020). How well do CMIP6 historical runs match observed Northeast US Precipitation and extreme precipitation-related circulation? *J Clim.* 33, 9835–9848. doi: 10.1175/JCLI-D-19-1025.1

Barlow, M., Gutowski, W. J. Jr, Gyakum, J. R., Katz, R. W., Lim, Y.-K., Schumacher, R. S., et al. (2019). North American extreme precipitation events and related large-scale meteorological patterns: a review of statistical methods, dynamics, modeling, and trends. *Clim. Dyn.* 53, 6835–6875. doi: 10.1007/s00382-019-04958-z

Biard, J. C., and Kunkel, K. E. (2019). Automated detection of weather fronts using a deep learning neural network. *Adv. Stat. Climatol. Meteorol. Oceanogr.* 5, 147–160. doi: 10.5194/ascmo-5-147-2019

Bosilovich, M. G., Robertson, F. R., Takacs, L., Molod, A., and Mocko, D. (2017). Atmospheric water balance and variability in the MERRA-2 reanalysis. *Clim. J.* 30, 1177–1196. doi: 10.1175/JCLI-D-16-0338.1

Douville, H., Raghavan, K., Renwick, J., Allan, R. P., Arias, P. A., Barlow, M., et al. (2021). "Water cycle changes," in *Climate Change 2021: The Physical Science Basis. Contribution of Working Group I to the Sixth Assessment Report of the Intergovernmental Panel on Climate Change*, eds V. Masson-Delmotte, P. Zhai, A. Pirani, S. L. Connors, C. Péan, S. Berger, et al. (Cambridge; New York, NY: Cambridge University Press). 1055–1210.

Easterling, D. R., Kunkel, K. E., Arnold, J. R., Knutson, T., LeGrande, A. N., Leung, L. R., et al. (2017). "Precipitation change in the United States," in *Climate Science Special Report: Fourth National Climate Assessment, Volume*, eds I. D. J. Wuebbles, D. W. Fahey, K. A. Hibbard, D. J. Dokken, B. C. Stewart, and T. K. Maycock (Washington, DC: U.S. Global Change Research Program), 207–230. doi: 10.7930/J0H993CC

Emori, S., and Brown, S. J. (2005). Dynamic and thermodynamic changes in mean and extreme precipitation under changed climate. *Geophys. Res. Lett.* 32, L17706. doi: 10.1029/2005GL023272

Feng, Song Z. F., Sakaguchi, K., and Leung, L. R. (2021). Evaluation of mesoscale convective systems in climate simulations: methodological development and

results from MPAS-CAM over the United States. *Clim. J.* 34, 2611–2633. doi: 10.1175/JCLI-D-20-0136.1

Gelaro, R., McCarty, W., Suárez, M. J., Todling, R., Molod, A., Takacs, L., et al. (2017). The modern-era retrospective analysis for research and applications, version 2 (MERRA-2). *Clim. J.* 30, 5419–5454. doi: 10.1175/JCLI-D-16-0758.1

Kalnay, E., Kanamitsu, M., Kistler, R., Collins, W., Deaven, D., Gandin, L., et al. (1996). The NCEP/NCAR 40-year reanalysis project. *Bull. Amer. Meteor. Soc.* 77, 437–472.

Kendon, E. J., Prein, A. F., Senior, C. A., and Stirling, A. (2021). Challenges and outlook for convection-permitting climate modelling. *Philos. Trans. R. Soc. A* 379. doi: 10.1098/rsta.2019.0547

Knapp, K. R., Applequist, S., Diamond, H. J., Kossin, J. P., Kruk, M., and Schreck, C. (2010). *NCDC International Best Track Archive for Climate Stewardship (IBTrACS) Project, Version 3*. NOAA National Centers for Environmental Information. Available online at: https://www.ncei.noaa.gov/access/metadata/landing-page/bin/iso?id=gov.noaa.ncdc:C00834 (accessed October 14, 2021).

Kunkel, K. E., and Champion, S. M. (2019). An assessment of rainfall from Hurricanes Harvey and Florence relative to other extremely wet storms in the United States. *Geophys. Res. Lett*. 46, 13500–13506. doi: 10.1029/2019GL085034

Kunkel, K. E., Easterling, D. R., Kristovich, D. A. R., Gleason, B., Stoecker, L., and Smith, R. (2012). Meteorological causes of the secular variations in observed extreme precipitation events for the conterminous United States. *J. Hydrometeor.* 13, 1131–1141. doi: 10.1175/JHM-D-11-0108.1

Kunkel, K. E., Karl, T. R., Squires, M. F., Yin, X., Stegall, S. T., and Easterling, D. R. (2020a). Precipitation extremes: trends and relationships with average precipitation and precipitable water in the contiguous United States. *J. Appl. Meteor. Climatol*. 59, 125–142. doi: 10.1175/JAMC-D-19-0185.1

Kunkel, K. E., Stevens, S. E., Stevens, L. E., and Karl, T. R. (2020b). Observed climatological relationships of extreme daily precipitation events with precipitable water and vertical velocity in the contiguous United States. *Geophys. Res. Lett*. 47, e2019GL086721. doi: 10.1029/2019GL086721

Lagerquist, R. A., McGovern, and, D. J., and Gagne, I. I. (2019). Deep learning for spatially explicit prediction of synoptic-scale fronts. *Wea. Forecasting* 34, 1137–1160. doi: 10.1175/WAF-D-18-0183.1

Lee, J. Y., Marotzke, J., Bala, G., Cao, L., Corti, S., Dunne, J. P., et al. (2021). "Future global climate: scenario-based projections and near-term information," in *Climate Change 2021: The Physical Science Basis. Contribution of Working Group I to the Sixth Assessment Report of the Intergovernmental Panel on Climate Change*, eds V. Masson-Delmotte, P. Zhai, A. Pirani, S. L. Connors, C. Péan, S. Berger, et al. (Cambridge; New York, NY: Cambridge University Press). 553–672.

Menne, M. J., Durre, I., Vose, R. S., Gleason, B. E., and Houston, T. G. (2012). An overview of the Global Historical Climatology Network-Daily database. *J. Atmos. Oceanic Technol*. 29, 897–910. doi: 10.1175/JTECH-D-11-00103.1

Mudigonda, M., Ram, P., Kashinath, K., Racah, E., Mahesh, A., Liu, Y., et al. (2021). "Deep learning for detecting extreme weather patterns," in *Chapter 12, Within Deep Learning for the Earth Sciences: A Comprehensive Approach to Remote Sensing, Climate Science and Geosciences*, G. Camps-Valls, D. Tuia, X. X. Zhu, M. Reichstein (Hoboken, NJ: Wiley), 163–185. doi: 10.1002/9781119646181.ch12

Nie, J., Sibel, A. H., Shaevitz, D. A., and Wang, S. (2018). Dynamic amplification of extreme precipitation sensitivity. *Proc. Natl. Acad. Sci. U. S. A.* 115, 9467–9472. doi: 10.1073/pnas.0.1800357115

NOAA Central Library Data Imaging Project. (n.d). *U. S. Daily Weather Maps*. Available online at: https://library.noaa.gov/Collections/Digital-Collections/US-Daily-Weather-Maps (accessed August 22, 2021).

Prein, A. F., Rasmussen, R. M., Ikeda, K., Liu, C., Clark, M. P., and Holland, G. J. (2017). The future intensification of hourly precipitation extremes. *Nat. Clim. Change* 7, 48–52. doi: 10.1038/nclimate3168

Priestley, M. D. K., Ackerley, D., Catto, J. L., Hodges, K. I., McDonald, R. E., and Lee, R. W. (2020). An overview of the extratropical storm tracks in CMIP6 historical simulations. *Clim. J.* 33, 6315–6343. doi: 10.1175/JCLI-D-19-0928.1

Roderick, T. P., Wasko, C., and Sharma, A. (2020). An improved covariate for projecting future rainfall extremes? *Water Resour. Res*. 56, e2019WR026924. doi: 10.1029/2019WR026924

Schumacher, R. S., and Rasmussen, K. L. (2020). The formation, character and changing nature of mesoscale convective systems. *Nat. Rev. Earth Environ.* 1, 300–314. doi: 10.1038/s43017-020-0057-7

Seneviratne, S. I., Zhang, X., Adnan, M., Badi, W., Dereczynski, C., Di Luca, A., et al. (2021). "Weather and climate extreme events in a changing climate," in *Climate Change 2021: The Physical Science Basis. Contribution of Working Group I to the Sixth Assessment Report of the Intergovernmental Panel on Climate Change*, eds V. Masson-Delmotte, P. Zhai, A. Pirani, S. L. Connors, C. Péan, S. Berger, et al. (Cambridge; New York, NY: Cambridge University Press). 1513–1766.

Trenberth, K. E., Dai, A., Rasmussen, R. M., and Parsons, D. B. (2003). The changing character of precipitation. *Bull. Am. Meteor. Soc*. 84, 1205–1217. doi: 10.1175/BAMS-84-9-1205

Vincent, L. A., Zhang, X., Mekis, É., Wan, H., and Bush, E. J. (2018). Changes in Canada's climate: trends in indices based on daily temperature and precipitation data. *Atmos. Ocean* 56, 332–349. doi: 10.1080/07055900.2018.1514579

Wuebbles, D., Cardinale, B., Cherkauer, K., Davidson-Arnott, R., Hellmann, J., Infante, D., et al. (2019). *An Assessment of the Impacts of Climate Change on the Great Lakes*. Chicago, IL: Environmental Law and Policy Center, 74. Availalble online at: https://elpc.org/wp-content/uploads/2020/04/2019-ELPCPublication-Great-Lakes-Climate-Change-Report.pdf (accessed January 25, 2022).

Conflict of Interest: XY was employed by Riverside Technology Inc.

The remaining authors declare that the research was conducted in the absence of any commercial or financial relationships that could be construed as a potential conflict of interest.

Publisher's Note: All claims expressed in this article are solely those of the authors and do not necessarily represent those of their affiliated organizations, or those of the publisher, the editors and the reviewers. Any product that may be evaluated in this article, or claim that may be made by its manufacturer, is not guaranteed or endorsed by the publisher.

frontiers | Frontiers in Water

ORIGINAL RESEARCH
published: 11 July 2022
doi: 10.3389/frwa.2022.801134

The Impacts of Climate Change on Land Hydroclimatology of the Laurentian Great Lakes Basin

Narayan K. Shrestha, Frank Seglenieks, André G. T. Temgoua and Armin Dehghan*

Boundary Water Issues Unit, Canadian Center for Inland Waters, National Hydrological Service, Environment and Climate Change Canada, Burlington, ON, Canada

The freshwater resources of the Laurentian Great Lakes basin contribute significantly to the environment and economy of the region. With the impacts of climate change becoming more evident, sustainable management of the freshwater resources of the Laurentian Great Lakes basin is important. This study uses 36 simulations from 6 regional climate models to quantify trends and changes in land-area precipitation and temperature in two future periods (mid-century, 2035–2064 and end-century, 2065–2094) with reference to a baseline period (1951–2005) for two emission scenarios (RCP4.5 and RCP 8.5). Climatic forcings from these 36 simulations are used as input to a calibrated and validated hydrological model to assess changes in land snowpack and actual evapotranspiration, and runoff to lake. Ensemble results show wetter (7 to 15% increase in annual precipitation) and warmer (2.4–5.0°C increase in annual mean temperature) future conditions on GL land areas. Seasonal and monthly changes in precipitation and mean temperature are more sporadic, for instance although precipitation is projected to increase overall, in some scenarios, summer precipitation is expected to decrease. Projected increases in highest one-day precipitation and decreases in number of wet days indicate possible increases in extreme precipitation in future. Minimum temperature is expected to increase in a higher rate than maximum temperature. Ensemble results from the hydrological model show projected decrease in snowpack (29–58%). Similarly, actual evapotranspiration is projected to increase, especially during summer months (up to 0.4 mm/day). Annually, runoff is expected to increase (up to 48% in Superior, 40% in Michigan-Huron, 25% Erie and 28% in Ontario). Seasonal and monthly changes in runoff are more sporadic (e.g., projected decrease up to 17% in Erie subdomain in October). Such contrasting patterns of changes in land hydroclimatology of the GL basin will pose challenges to sustainable management of the water resources of the basin in future.

Keywords: Laurentian Great Lakes, climate change, land hydroclimatology, water resources management, RCM

OPEN ACCESS

Edited by:
Galina Guentchev,
Met Office, United Kingdom

Reviewed by:
Fuad Yassin,
University of Saskatchewan, Canada
Andrew Gronewold,
University of Michigan, United States

****Correspondence:***
Frank Seglenieks
frank.seglenieks@ec.gc.ca

Specialty section:
This article was submitted to Water and Climate, a section of the journal Frontiers in Water

Received: *24 October 2021*
Accepted: *17 June 2022*
Published: *11 July 2022*

Citation:
Shrestha NK, Seglenieks F, Temgoua AGT and Dehghan A (2022) The Impacts of Climate Change on Land Hydroclimatology of the Laurentian Great Lakes Basin. Front. Water 4:801134. doi: 10.3389/frwa.2022.801134

INTRODUCTION

The Laurentian Great Lakes (GL) basin (**Figure 1**) is one of North America's largest water resources systems with an area of approximately 766,000 km^2 (USEPA-GoC, 1995; Quinn, 2003). About one-third of the basin area (about 244,200 km^2) comprises five interconnected freshwater lakes (Superior, Michigan, Huron, Erie and Ontario), and together they make the largest unfrozen freshwater lake on Earth in terms of surface area (Larson and Schaetzl, 2001). These GLs are large enough to affect the regional climate system (Notaro et al., 2013).

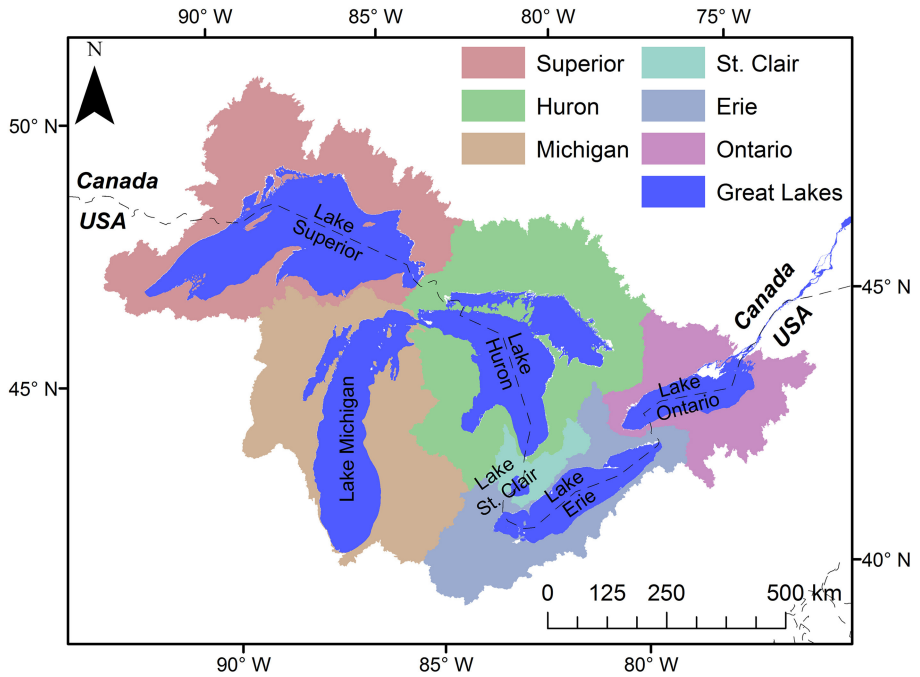

FIGURE 1 | The Laurentian Great Lakes with their respective drainage basin.

The fresh water resources of the GL basin contributes significantly to the environment and economy of the region (ELPC, 2019). More than 30 million people live in the GL basin which includes part of the Canadian province of Ontario and eight United States (U.S.) states; Minnesota, Wisconsin, Illinois, Indiana, Michigan, Ohio, Pennsylvania, and New York. This is about 10 and 30% of the U.S. and Canada's total population, respectively (USEPA, 2021). Many of these people rely on the freshwater resources of the GLs for drinking water, agricultural activities and industrial manufacturing, recreational activities, fisheries, among others (ELPC, 2019). About 20 tribal lands such as Algonkin, Fox, Ho-chunk, Huron, Illinois, Ioway, Iroquois, Kickapoo, Mascounten, Menominee, Miami, Neutral, Nipissing, Ojibwe, Ottawa, Petun, Potawatomi, Santee Dakota, Sauk and Shawnee are also part of the GL basin and the surrounding regions (MPM, 2022). The GLs support several key shoreline wetlands (Mortsch, 1998). Similarly, fisheries in the basin are valued at 7 billion US dollars and recreational activities are estimated to generate about 16 billion US dollars (ELPC, 2019). Hence, sustainable management of the freshwater resources of the GLs is of paramount importance to the people living in the basin (Valiante, 2008).

As a result of the fact that management of the freshwater resources of the GLs is a matter of concern for both Canada and the U.S. (Valiante, 2008), the 1909 Boundary Waters Treaty (BWT) was established with the aim of resolving any water management conflicts between the two states (Whorley, 2020). The International Joint Commission (IJC) was thus established by both governments to make decisions and provide recommendations related to the any projects affecting flows and water levels across the boundary (IJC, 2021). The IJC can issue orders of approval such as Plan 2012 for the regulation of outflow from Lake Superior into Lake Michigan-Huron, and Plan 2014 for the regulation of outflows from Lake Ontario to the St. Lawrence River (IJC, 2021). Through the IJC, coordinated and consistent approaches are being taken to manage the water resources of the GL basin. However, these approaches should also foresee various stressors (e.g., climate change) which are expected to pose a challenge to interests within the GL basin.

Overwhelming evidence suggests that the increase in greenhouse gas concentrations in the atmosphere are unequivocally caused by human activities (IPCC, 2014, 2021). This has led to (a) increase in global surface temperature, (b) increase in frequency and magnitude of extreme precipitation, (c) accelerated glacier retreat, (d) rapid sea level rise, among others. Regional changes in the GL basin could be more extreme than that observed in the global level (IPCC, 2021) and have been driver of various changes in the GL basin (Bartolai et al., 2015). It is thus of paramount importance that an assessment of the impacts of climate change is conducted in the GL basin.

We found about 50 studies that have quantified the impacts of climate change in water resources of the GL basin. The earliest climate change studies in the GL basin used global climate models (GCMs) projections for certain atmospheric CO_2 sensitivity experiments such as doubling of the atmospheric CO_2 compared to pre-industrial levels to quantify impacts on hydrology (Smith, 1991), net basin supply (NBS) (Cohen, 1986; Croley, 1990), lake level (Marchand et al., 1988; Smith, 1991), lake outflow (Hartmann, 1990), shoreline wetland (Mortsch, 1998) and navigation (Marchand et al., 1988). The NBS is the

over-lake precipitation added to the runoff into the lake from its drainage area minus the over-lake evaporation, generally groundwater flow from or into the lake is considered negligible (Fry et al., 2020). During the early years of 21st century, the use of GCM projections with transient climate conditions became more prevalent to quantity the impacts on hydrology (Smith, 1991; Mortsch et al., 2000), ice cover (Lofgren et al., 2002), NBS (Chao, 1999), lake level (Smith, 1991), shoreline community (Schwartz et al., 2004), navigation (Quinn, 2003) and hydroelectric power production (Buttle et al., 2004).

The newer GCMs included earth system feedbacks (e.g., changes in ice sheet, vegetation cover distribution) to project future climate for different Intergovernmental Panel on Climate Change (IPCC) emission scenarios such as the SRES (Special Report on Emissions Scenarios) introduced in the 4th Assessment Report (AR4) (IPCC, 2007) and the RCPs (Representative Concentration Pathways) introduced in the AR5 (IPCC, 2014). Respective Coupled Model Intercomparison Project (CMIP) experiments, the CMIP3 (Meehl et al., 2007) using the SRES and the CMIP5 (Taylor et al., 2011) using the RCPs, provided GCM projections from climatic modeling centers around the world. Some of the climate change studies in the GL basin using IPCC AR4 scenarios quantified impacts on hydrology (Kutzbach et al., 2005; Cherkauer and Sinha, 2010; Rahman et al., 2010), lake level (Angel and Kunkel, 2010; Hayhoe et al., 2010), water quality (Bosch et al., 2014; Hall et al., 2017), ecosystem (Hellmann et al., 2010), infrastructure (Wuebbles et al., 2010) and commercial navigation (Millerd, 2005). Similarly, some of the climate change studies in the GL basin using IPCC AR5 scenarios quantified impacts on hydrology (Wang et al., 2016; Basile et al., 2017; Byun et al., 2019), NBS (Music et al., 2015), lake level (Notaro et al., 2015), fluvial flood risk (Xu et al., 2019), water quality (Cousino et al., 2015; Verma et al., 2015; Wallace et al., 2017) and fisheries industry (Collingsworth et al., 2017).

The impact of GLs on regional climate dynamics is well documented (Notaro et al., 2013). However, the latest GCMs, for example, those participated in the CMIP5 experiments don't explicitly simulate GLs as dynamic lakes (Briley et al., 2021) which may not realistically represent region specific meteorological phenomena such as the lake-effect snowfall (Wright et al., 2013). Therefore, recent studies have used either statistically (Byun et al., 2019) or dynamically (using regional climate models, RCMs) downscaled GCM projections (Notaro et al., 2015; Grady et al., 2021). Furthermore, downscaled projections require bias-correction to remove systematic errors (Cannon, 2018). Downscaled and bias-corrected RCM projections are increasingly being used in the GL basin to quantify impacts on hydrology (Zhang et al., 2018), NBS (Mailhot et al., 2019) and lake level (Mackay and Seglenieks, 2012), among others.

For the North American region encompassing the GL basin, a suite of high resolution downscaled and bias-corrected RCM projections are available through North American component of the Coordinated Regional Downscaling Experiment (Mearns et al., 2017; NA-CORDEX, 2022). It is not a straightforward task to select a set of suitable climate models (Lutz et al., 2016). Cannon (2015) provided guidance on selecting RCMs which can reflect the range of changes in a multi-model ensemble while Lutz et al. (2016) introduced an advanced-envelop based approach. Others argue the use of multi-model ensemble (Crosbie et al., 2011; Acharya et al., 2014) to deal with different sources of uncertainties (e.g., climatic model uncertainty) inherent in RCM projections (Hawkins and Sutton, 2009). Furthermore, the use of a small number of projections in impact analysis may sometimes lead to contrasting results (Smith, 2002). In the GL basin, using projections from 2 GCMs, Lofgren et al. (2002) reported large drops in lake levels when using one GCM input to a hydrological model and moderate increases when using another GCM input. In such cases, inference made through the use of a multi-model ensemble might be more reliable (Krysanova et al., 2018). While using a suite of climate models with different emission scenarios, it is also desirable to estimate the relative contribution of climate model and scenario uncertainty to the total uncertainty in the projected hydrological variable (Lee et al., 2017).

Traditionally, downscaled and bias corrected future projections are used as input to hydrological models to understand the hydrological impacts of climate change (Lofgren et al., 2011). Statistical approaches such as the use of a parametric regular vine copula (VanDeWeghe et al., 2022) are also being advocated as an alternative to the traditional approach. Using the traditional approach, some studies in the GL basin (Lofgren et al., 2011, 2013; Lofgren and Rouhana, 2016; Milly and Dunne, 2017) argued that the use of temperature index (TI) methods such as Thornthwaite (1948) to calculate potential evapotranspiration (PET) in hydrological models creates a hydrological drying bias as TI methods tend to overestimate PET as compared to the methods which respect the surface energy balance. The comparison was based on the PET calculated by hydrological models using input from GCMs to the PET directly simulated by the GCMs. It would be interesting to see if the same holds for bias-corrected downscaled projection from high resolution RCMs. Furthermore, the use of the energy balance approach to estimate PET in a hydrological model is often constrained by the availability of all the incoming and outgoing energy terms in RCM projections. Another issue is that most of the hydrological models are not fully evaluated against all the variables of interest. Assessing the hydrological model performance against a single variable (e.g., streamflow) is more prevalent and it does not guarantee robust simulation of additional variables (e.g., snow water equivalent, SWE; evapotranspiration, ET) (Mai et al., 2021). Similarly, particular to the GL basin, most of the hydrological models don't explicitly consider the impacts of numerous small lakes. The cumulative hydrological impact of these smaller lakes can be substantial in the GL basin (Han et al., 2020).

In this study, we used climatic projections from several RCMs, driven by different GCMs participating in the NA-CORDEX for two IPCC AR5 representative concentration pathways (RCP4.5 and RCP8.5). The RCM projections were bias-corrected using multivariate quantile mapping bias correction technique (Cannon, 2018) using DayMet data (Thornton et al., 2020) as a reference. In total, 36 projections (15 historical, six future for RCP4.5 and 15 future for RCP8.5) at 0.44° (∼50 km)

spatial resolution were used into a hydrological model. The hydrological model is a coupled model between WATFLOOD (Kouwen, 1988) and RAVEN (Craig et al., 2020) which explicitly considers all lakes with an area more than 5 km^2 (Han et al., 2020). Such a coupled model greatly improves the simulation of runoff from the GL basin (Shrestha et al., 2021). Furthermore, the coupled hydrological model is calibrated and validated for daily streamflow, and evaluated against daily SWE and actual ET (Mai et al., 2022). We then quantity the future changes in land hydroclimatic variables such as precipitation, temperature, snow water equivalent (SWE), actual evapotranspiration (AET) and runoff into the lakes.

We presume that quantification of the impacts of climate change on hydroclimatic variables including SWE and AET for the entire GL land basin would be helpful to understand the future hydroclimatic conditions of the GL basin. This may also help to formulate a coordinated effort to address the adverse effects of climate change in the GL basin.

MATERIALS AND METHODS

Hydrological Model Set-Up

Estimation of vertical hydrological fluxes and their horizontal transfer are two basic processes in a hydrological model (Singh, 1995). The later process is also referred as routing. We used the hydrological model WATFLOOD (Kouwen, 1988) to estimate the vertical fluxes as driven by climatic forcings (e.g., precipitation) and a recently developed lake and river routing product (Han et al., 2020), which has been integrated in the RAVEN modeling framework (Craig et al., 2020). The WATFLOOD model is coupled with the lake and river routing product to realize a functional hydrological model of the GL basin.

Watflood Model

WATFLOOD is a physically-based, distributed hydrological model. In WATFLOOD, a basin is divided into uniform grid cells. Several hydrological processes such as snow accumulation and melt, precipitation interception and infiltration, evaporation and transpiration, surface runoff, interflow and baseflow, etc. are considered for water balance calculations (Kouwen, 1986, 1988; Mai et al., 2021). These calculations are made on grouped response unit (GRUs) which aggregates land cover of similar hydrological response characteristics (Kouwen et al., 1993). WATFLOOD is widely used in hydrological modeling and forecasting of several watersheds in the GL basin and beyond (Cranmer et al., 2001; Seglenieks et al., 2004; Kouwen et al., 2005; Bingeman et al., 2006).

The Lake and River Routing Product Integrated in RAVEN

The GL basin is characterized by the presence of numerous small to large lakes. While larger lakes are usually considered in hydrological modeling, smaller lakes are often neglected. Smaller lakes, when present in a high number as in the GL basin, will impact the streamflow simulations (Han et al., 2020). A lake and river routing product with explicit consideration of all lakes with area more than 5 km^2 has become available (Han et al., 2020). Recently, the routing product is integrated into RAVEN modeling framework (Craig et al., 2020), thereby allowing it to run in routing-only mode (RAVEN-ro).

Model Inputs

A 3 arc seconds HydroSHEDS digital elevation model (DEM) (Lehner et al., 2008) and a 30 m North American Land Change Monitoring System (NALCMS) (Homer et al., 2017) landuse/landcover map were used to create the land surface database for the WATFLOOD model. Then hourly precipitation and temperature from a 10 km Regional Deterministic Reanalysis System (RDRS) (Gasset et al., 2021) were used as input into the WATFLOOD model at a 10 km spatial resolution. For modeling purposes, we divided the GL basin in five subdomains: Superior (SUP), Huron (HUR), Michigan (MIC), Erie (ERI) and Ontario (ONT). All input data were obtained in the scope of an on-going project, the Great Lakes Runoff Inter-comparison for Great Lakes, GRIP-GL (Mai et al., 2022). The GRIP-GL is a part of Integrated Modeling Program (IMPC) for Canada under Global Water Future (GWF) program. Related information of the project can be found in http://www.civil.uwaterloo.ca/jmai/projects.html.

We coupled WATFLOOD and RAVEN-based lake and river routing product using the so-called loose coupling scheme (Argent, 2004). Hence, the coupling is one directional in which WATFLOOD simulated runoff (surface and interflow) and recharge to lower zone storage (LZS) are stored in separate netCDF files. These netCDF files then serve as inputs to the RAVEN-ro model. The RAVEN-ro is run to simulate the streamflow at selected locations.

In WATFLOOD, we chose the Hargreaves method (Hargreaves and Samani, 1985) to estimate the rate of potential evapotranspiration. In RAVEN-ro, we chose the Gamma unit hydrograph (RAVEN, 2021) for in-catchment routing and non-linear storage approach for base flow estimation. Outflow from lakes/reservoirs are simulated with a broad-crested weir at their outlet.

In large-scale modeling, it is not always possible to include all the basin complexities (De Scheer et al., 2015). Generally, a compromise in representing these complexities has to be made owing to computation time, data availability, among others. In this study, we also made several simplifying assumptions while setting up the model. In the GL basin, there exist several water bodies which are regulated. Depending on the extent of regulation, these water bodies can have significant downstream impact. The RAVEN-based lake and river routing product incorporates all the significant water bodies and the outflow from these water bodies is simulated using the broad-crested weir equation (Han et al., 2020). Best estimates of all related routing parameters (e.g., weir width, Manning's coefficient, etc.) are already provided in the routing product. During the model calibration, we further fine-tuned some of the important parameters such as the weir width (refer Section Calibration and Validation) to reproduce observed streamflow at immediate downstream gauging stations. We are aware that this (controlling outflow using the broad-crested weir equation) may be too simplified for some of the highly regulated reservoirs in the

GL basin, and more detailed approaches such as the use of Dynamically Zoned Target Release (DZTR) (Yassin et al., 2019) may be better suited. A further investigation is needed to confirm this. Another important feature of agricultural water management in the GL basin is the provision of tile drains to quickly drain excess soil moisture after spring snowmelt. Owing to the fact that the tile drainage facilitates the drainage soil moisture in excess of field capacity, we increased relevant parameters (e.g., infiltration coefficient) in agricultural areas to mimic the behavior. This is indeed a simplistic approach and more detailed approaches, such the use of the Hooghoudt and Kirkham drainage equations as incorporated in the Soil and Water Assessment Tool (SWAT) (Neitsch et al., 2011) for explicit consideration of the effect of tile drainage in agricultural areas, may be needed. This issue also needs a detailed investigation. Furthermore, some agricultural areas, especially in the Michigan subdomain, are irrigated. Devoid of detail information regarding the irrigation command area, type, frequency, and amount of irrigation, we did not distinguish irrigated and non-irrigated agricultural areas while setting up the model.

Calibration and Validation

While WATFLOOD was run in an hourly timestep, RAVEN-ro was run in a daily timestep to match the timestep of streamflow observations. The coupled model was calibrated against daily streamflow for a 10-year period (2001–2010) at 134 gauging stations across five subdomains of the GL basin. The model was then validated in another time period (2011–2017) at 59 separate gauging stations (Mai et al., 2022). A total of 17 (11 WATFLOOD and 6 RAVEN-ro related, **Supplementary Table S1**) parameters were considered during model optimization in the OSTRICH platform (Matott, 2017). We chose dynamically dimensioned search (DDS) (Tolson and Shoemaker, 2007) as an optimization algorithm and Kling-Gupta Efficiency (KGE) (Gupta et al., 2009) as an objective function during optimization. The optimization process resulted in a median KGE of 0.63 during calibration and a median KGE of 0.50 during validation (Mai et al., 2022). For illustration purposes, observed and simulated daily streamflow during calibration and validation periods at two selected gauging stations are shown in **Supplementary Figure S1**.

We also evaluated the model's robustness in simulating two auxiliary variables, snow water equivalent (SWE) and actual evapotranspiration (AET) (Mai et al., 2022). The Canadian historical SWE station data (CanSWE) (Vionnet et al., 2021) at four selected locations (one station at each sub-domain) were used to compare simulated SWE at the grid exactly over the corresponding CanSWE station. **Supplementary Figure S2** shows the resultant plots and it is evident that the model is able to represent the dynamics of SWE at selected stations. The calculated KGE values for daily SWE ranged from 0.48 to 0.70. Similarly, Eddy flux measurements for AET at three AMERIFLUX stations, US-UMB (Gough et al., 2021), US-KM1 (Robertson and Chen, 2021) and US-Oho (Chen et al., 2021) and one FLUXNET Canada Research Network station (Fluxnet Canada, 2016) were used to compare model simulations. The resulting plots for the selected stations are shown in **Supplementary Figure S3**. The calculated KGE values for daily SWE ranged from 0.52 to 0.73. The median KGE values for SWE and AET are fairly comparable to the KGE values for streamflow. Hence, it is evident that model is equally robust to simulate the SWE and AET dynamics.

Future Climate Data

Future climatic data (precipitation, and maximum and minimum temperature) were downloaded from the National Center for Atmospheric Research (NCAR) climate data gateway (Mearns et al., 2017). These data are projections from different RCMs, driven by several GCMs that participated in the North American component of the Coordinated Regional Downscaling Experiment (NA-CORDEX, 2022). In light of the findings of Briley et al. (2021), it is worth mentioning that only two GCMs (GFDL-ESM2M and HadGEM2-ES, **Supplementary Table S2A**) simulate GLs as dynamic water bodies, as such, their projections can be considered as "credible". The remaining 4 GCMs (**Supplementary Table S2A**) have inconsistency in the treatment of GLs and it mainly arose from "competing or lacking spatial coverage between a model's land and ocean component for grid cell". As for the RCMs (**Supplementary Table S2B**), two RCMs (CRCM5-UQAM and RCA4) have the FLake model (Mironov et al., 2009) while one RCM (RegCM4) has the lake model of Hostetler et al. (1993). The two remaining RCMs don't have a standard lake model but they are driven by interpolated and lapse-rate corrected nearby sea-surface temperatures (SSTs) at the lower boundary. It should be noted that the future projections from GCM-RCMs which don't have dynamic representation of GLs might not be as "credible" (Briley et al., 2021). Since the RCM projections were bias-corrected using multivariate quantile mapping bias correction technique (Cannon, 2018) using DayMet data (Thornton et al., 2020) as the reference dataset, the systematic errors are addressed. However, this issue needs further investigation. We used all available RCM projections in both historical (1951–2005) and future (2006–2099) periods at 0.44° (∼50 km) spatial resolution. A total of 15 RCM-GCM projections were available in the historical period while 6 future projections were available for RCP4.5 and 15 future projections were available for RCP8.5 emission scenario (**Table 1**).

The finest temporal resolution of the RCM projections is daily (**Table 1**), while WATFLOOD needed hourly climatic forcings. Therefore, the daily RCM projections needed to be disaggregated into hourly timestep (Requena et al., 2021). Devoid of a well-accepted procedure to perform such temporal disaggregation, we assumed the total daily rainfall volume to occur in five pulses. With a peak pulse occurring at 8 AM (40% weightage) and another four pulses in 6-hour intervals on either side (at 4 AM and 12 PM both having 20% weighting, and at 12 AM and 4 PM both having 10% weighting). As for temperature, we assumed a linear increase and decrease with daily maximum and minimum temperature occurring at 3 PM and 3 AM, respectively.

For the climate change impact analysis, the entire historical period (1951–2005) was taken as a baseline period. As for the future, a 30-year period (2035–2064) was considered as a mid-century period and another 30-year period (2065–2094) was considered as an end century period.

TABLE 1 | Details of the different RCM projections, as driven by different GCMs, used in this study.

Driver (GCM*)	Model (RCM*)	Experiment	Remarks		
		Historical[a]	RCP 4.5[b]	RCP 8.5[b]	
CanESM2	CanRCM4	x	x	x	• Variables: *Precipitation, and Maximum, Mean, and Minimum Temperature* • Frequency: *Annual, Seasonal, Monthly, Daily* • Grid: *NAM-44i* • Bias-correction: *mbcn-Daymet*
	CRCM5-UQAM	x	x	x	
	RCA4	x	x	x	
EC-EARTH	HIRHAM5	x	x	x	
	RCA4	x	x	x	
GEMatm-Can	CRCM5-UQAM	x	-	x	
GEMatm-MPI		x	-	x	
GFDL-ESM2M	RegCM4	x	-	x	
	WRF	x	-	x	
HadGEM2-ES	RegCM4	x	-	x	
	WRF	x	-	x	
MPI-ESM-LR	CRCM5-UQAM	x	-	x	
	RegCM4	x	-	x	
	WRF	x	-	x	
MPI-ESM-MR	CRCM5-UQAM	x	x	x	

**Abbreviated for space.*
We refer to ***Supplementary Tables S1A, S1B*** *for more details.*
[a]*Available data period: 1951–2005.*
[b]*Available data period: 2006–2099.*

With regards to the use of hydrological models in climate change impact assessment involving a large number of climate models, Krysanova et al. (2018) detailed two "main" approaches. The first approach advocates using a multi-model ensemble disregarding individual climate model's performance. The proponents of this approach consider every participating climate model as "equal" and argue that an unweighted multi-model approach should be followed (Christensen et al., 2010). The proponents of the second approach advocate in assessing performance of climate models and possibly disregarding poor-performing models. Krysanova et al. (2018) argue that while both approaches have merits and demerits and they are useful in the right context, evaluating performance of a hydrological model in historical period may increase confidence in projected results.

In this study, as we used a hydrological model that was calibrated and validated for streamflow, and evaluated for other auxiliary variables of interests (SWE and AET), we aimed at assessing performance of the hydrological model in representing long-term monthly average streamflow in the historical period. For illustration purpose (**Supplementary Figure S4**), we selected several gauges (one in each sub-domain) which: (a) are non-regulated, (b) are located closer to the draining lake, and (c) showed a good performance (KGE value more than 0.60) in the calibration period, and (d) have median KGE value more than 0.60 for historical RCM runs for long-term average monthly streamflow. Historical RCM runs are obtained using bias-corrected meteorological forcings in the coupled hydrological model. Furthermore, KGE value for each historical RCM run for long-term average monthly streamflow at all calibration gauges were calculated, and median KGE of the gauges in a specific modeling domain is presented in **Supplementary Table S3**. For comparison purpose, **Supplementary Table S3** also shows the median KGE value obtained in the calibration period.

It is evident from the **Supplementary Figure S4**, **Table S3** that the performance of the model slightly degraded in the historical RCM runs as compared to the performance in the calibration period. A lower performance of the model in another period and for historical RCM runs is indeed expected. While a slight drop in median KGE (calculated from individual KGE values of 21 gauging stations) value for each historical RCM run as compared to a median KGE value obtained during calibration period, is observed in HUR, MIC, ERI and ONT subdomains, a significant drop in performance is observed in Superior sub-domain (SUP) for which median KGE value for each historical RCM run is <0.50 while a median KGE value of 0.77 is obtained during calibration period. The historical RCM runs seem to mimic the seasonality of streamflow, especially the timing and magnitude of the spring peak, in the GL domain as evident in the long-term average monthly plots for selected stations. However, discrepancies are evident in Autumn months. This could be related to several factors such as effectiveness of bias-correction in these months, difference in spatial resolution of the climate forcing ($\sim$50 km) and model grids ($\sim$10 km) and temporal disaggregation (from daily to hourly, as detailed above) of forcing data.

However, it is evident from the plot (**Supplementary Figure S4**) and table (**Supplementary Table S3**) that there is not an obvious poor-performing RCM so that it should be disregarded. Hence, we believe that there is no need to disregard a certain RCMs and all the RCMs were considered for impact assessment.

Uncertainty Analysis

Different sources of uncertainties such as climate model uncertainty and scenario uncertainty are inherent in future climate data (Hawkins and Sutton, 2009). To capture the variability in the future projections, different emission scenarios and several GCM-RCM combinations are often used in climate change impact studies. Relative contribution of different sources of uncertainties to the total uncertainty in the projected hydrological variable is often desirable (Lee et al., 2017). In literature, several approaches are evident. Established approach such as Bayesian decomposition (Ohn et al., 2020) may be more comprehensive but is very time intensive as tens of thousands of iterations may be required which may hinder its application in a large scale physically-based hydrological modeling. A simple yet robust method, based on Maximum Entropy (ME) principle was suggested by Gay and Estrada (2010). Lee et al. (2017) made its first application in hydrological modeling to assess relative contribution of different sources of uncertainty in future streamflow projection in a river basin of South Korea. Because of its robustness and time effectiveness, we also used it to quantify relative contribution of emission scenarios (representative concentration pathways) and climate models uncertainties in total uncertainty of projected SWE, AET and runoff (to the lake). We refer Gay and Estrada (2010) and Lee et al. (2017) for further details of the ME theory and its application in hydrological modeling.

RESULTS AND DISCUSSION

Projected Changes in Precipitation

The time series plot of the GL over-land averaged annual precipitation in the historical/baseline period (1951–2005) shows marked variability as indicated by the wide ensemble range (**Figure 2**). Similar variabilities during a similar historical period were also reported in Do et al. (2020). A Mann-Kendall test (Mann, 1945; Kendall, 1975) shows an increasing trend ($p = 0.0003$) at 5% significance level. The rate of the increasing trend (0.9 mm/year) is lower than the rate (2.1 mm/year) reported by Bartolai et al. (2015). As for the future periods (mid-century, 2035–2064 and end-century, 2065–2094), a higher variability in annual precipitation is observed for RCP8.5 as compared to RCP4.5, which may be partly due to a higher number of RCM-GCM projections for the RCP8.5 emission scenario. The ensemble mean annual precipitation in both mid- and end-century periods for RCP4.5 shows no trend ($p = 0.18$, $p = 0.35$, respectively) at 5% significance level. However, the ensemble mean annual precipitation shows an increasing trend in both mid- and end-century periods for RCP8.5 ($p = 0.04$, $p = 0.03$, respectively) at 5% significance level.

While GL over-land ensemble mean annual precipitation do not show any trend (except in the end-century period for RCP 8.5), spatial variability in precipitation trend in different parts of the GL basin is evident in **Figure 3**. For instance, northern parts of the Lake Huron basin show a decreasing trend of about 2.5 mm/year in the mid-century period for RCP4.5. However, the same region shows an increasing trend of about 3 mm/year in the end-century period for RCP4.5. Similarly, a majority of the Lake Superior subdomain shows a decreasing trend (up to 4 mm/year) in the end-century period for RCP4.5 while the same region in the same period but for RCP8.5 shows an increasing trend (up to 4 mm/year). Such marked spatial variability in future precipitation and contrasting trends in different parts of the GL basin certainty pose challenges to water resources planners and managers and may warrant to focus on sub-basin wise adaptation measures rather than the entire GL basin wide measures.

Compared to the baseline annual average precipitation, the projected changes in over-land precipitation can be seen in **Figure 4** for both RCP4.5 and RCP8.5 emission scenarios. Besides the spatial variability in future precipitation trends, we observe marked variability in projected annual over-land precipitation amongst the RCM-GCM combinations. For instance, the WRF projections driven by HadGEM2-ES show rather high increases (up to 40%) in future annual precipitation for RCP8.5 scenario while RegCM4 projections driven by MPI-ESM-LR for RCP4.5 seem to indicate decreases for majority of years in both future periods.

On average, the GL land basin is expected to be wetter in future (**Figure 5**), with annual increases in precipitation range between 7 and 15%. The winter, spring and autumn seasons are expected to have substantial increases (up to 25%). The summer season in contrast, is expected to have a slight decrease (up to 1%) for RCP4.5 emission scenario in the end-century period, due to mild decreases (up to 6%) in August precipitation. The summer precipitation for RCP8.5 scenario is expected to have a slight increase in both future periods (up to 4%). The month of April is expected to have the highest increases (up to 33%). In general, RCP8.5 projections show wetter conditions than RCP4.5, and the same holds for the end-century period as compared to the mid-century period (**Figure 5**). The general trend in subdomain precipitation changes (**Supplementary Figure S5**) are almost the same as observed for the entire GL basin except in some months. For instance, in September, the future precipitation is expected to increase in the Superior, Huron and Michigan subdomains while it is expected to decrease in the Erie and Ontario subdomains.

While a similar result—an overall increase in annual, winter, spring and autumn precipitation and variable summer precipitation was also reported in several studies (Smith, 1991; Cherkauer and Sinha, 2010; Hayhoe et al., 2010; Wuebbles et al., 2010; Byun et al., 2019; Bukovsky and Mearns, 2020; Grady et al., 2021), the magnitude of change is evidently different due to differences in emission scenarios, climate models, bias correction techniques, baseline as well as future periods, and region of interest. For example, Bukovsky and Mearns (2020) used the same dataset (NA-CORDEX, 2022) to analyze seasonal and annual precipitation changes in several regions including the GL basin for RCP8.5 and found very similar results with slight differences in the magnitude of change. For RCP8.5, in mid-century (end-century) period, Bukovsky and Mearns (2020) reported a projected increase in ensemble mean annual precipitation of about 8%(17%) while we found the projected increase to be 8%(15%). Despite the difference in baseline period (1971–1999 in their study vs. 1951–2005 in our study), future periods (mid-century: 2041–2068 in their study vs. 2035–2064 in our study, and end-century: 2071–2099 in their study vs.

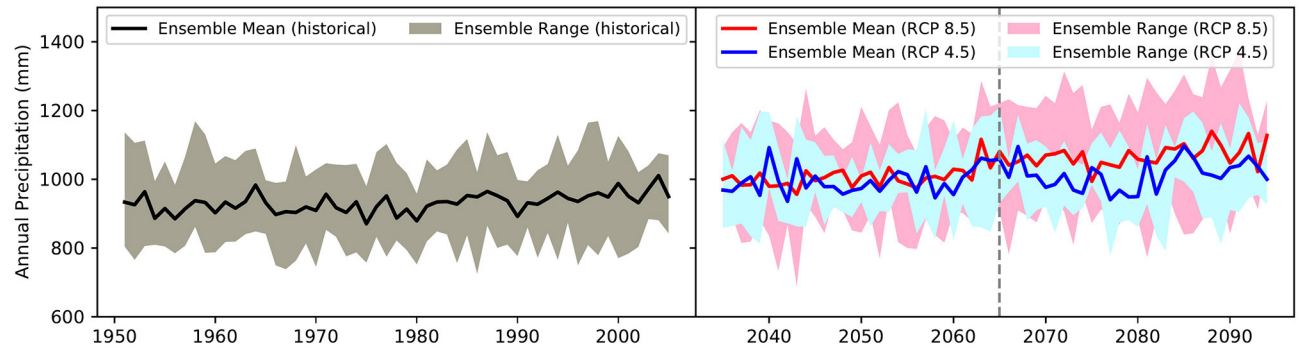

FIGURE 2 | Time series of GL over-land annual precipitation in historical (1951–2005) and future (mid-century: 2035–2064 and end-century: 2065–2094) periods for two emission scenarios (RCP4.5 and 8.5).

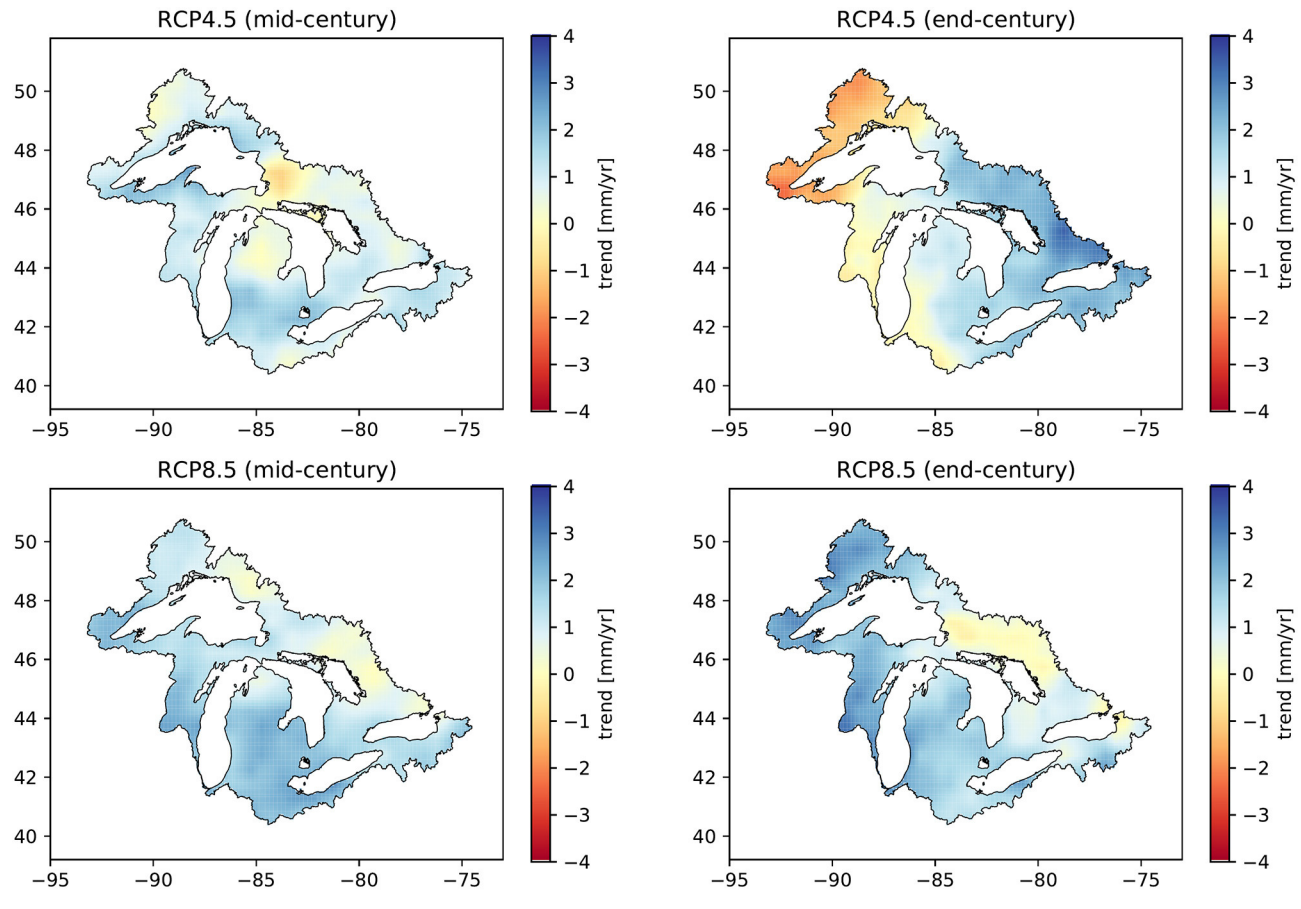

FIGURE 3 | Trend in annual over-land precipitation for RCP4.5 and RCP8.5 scenarios in mid- and end-century periods.

2065–2094 in our study), region of interest (entire GL basin in their study vs. only land portion of GL basin in our study) and climate models (28 in their study vs. 15 in our study), the results are very similar.

Projected increases in spring precipitation are certainty concerning as the topsoil in these times of the year will generally be at or near saturation level and any extra precipitation will mostly end up as surface runoff. Similarly, projected decreases in precipitation in the summer months is also concerning from a drought point of view. With expected increases in temperature and higher evaporative demand, future decreases in summer precipitation will only worsen the water stress condition of vegetation, especially, agricultural crops grown in summer. Consequently, crop yield could decrease unless water

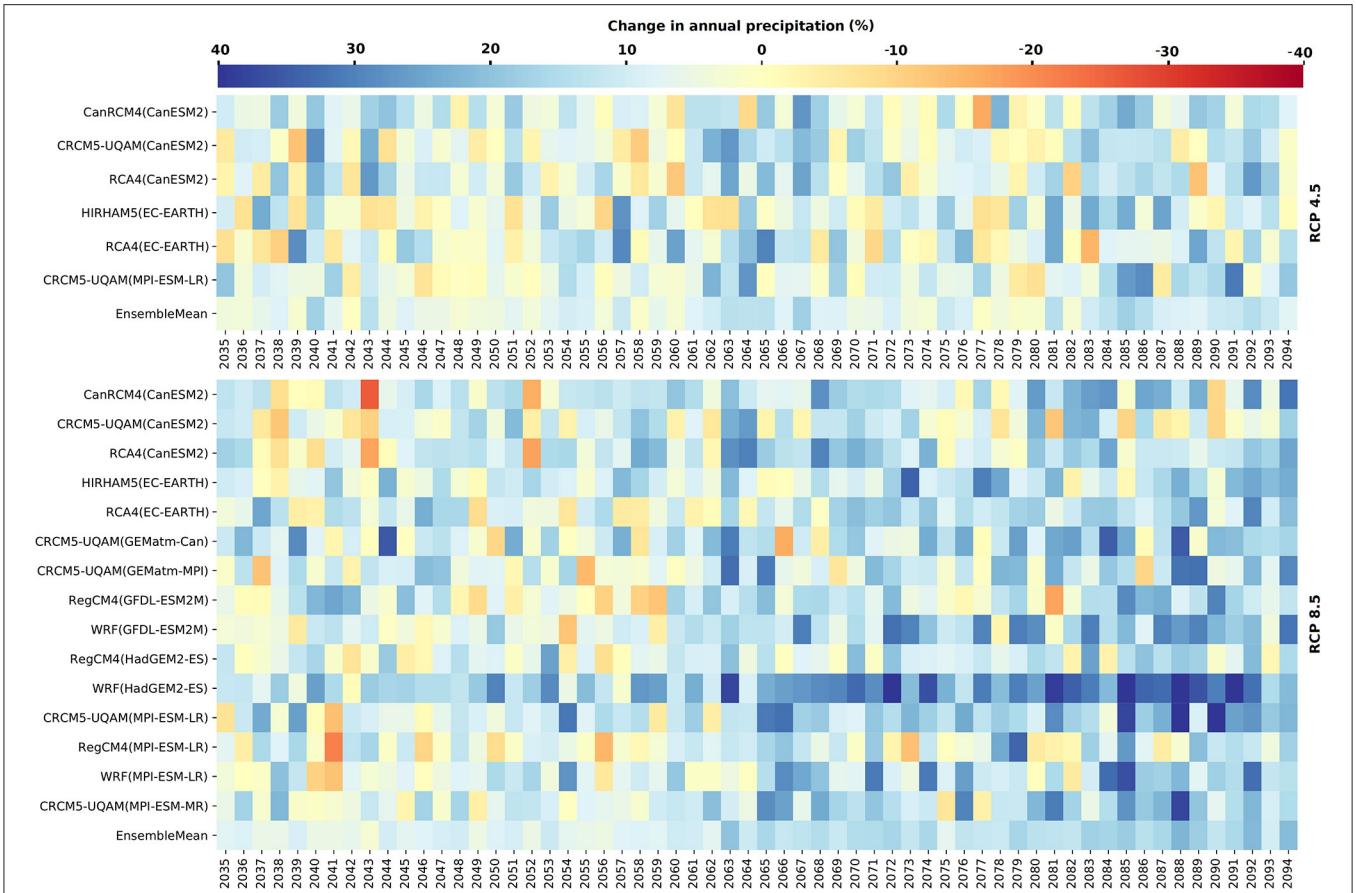

FIGURE 4 | Change in annual over-land precipitation with respect to baseline average precipitation for RCP4.5 and RCP8.5 scenarios in mid- and end-century periods.

is supplied to the crops by external means (e.g., surface or sub-surface irrigation).

Further causes of concern are evident in **Supplementary Figure S6**, which shows projected increases in the frequency of precipitation with daily amounts of more than 5, 10, and 20 mm, and in **Supplementary Figure S7**, which shows projected increases in highest one-day precipitation. As an example, the highest one-day precipitation in the baseline period is 83 mm (range: 80–93 mm) which is projected to be more than 101 mm (range: 95–112 mm) in the end-century period for RCP8.5. The wider range in projected highest one-day precipitation is also concerning. Furthermore, despite the projected wetter conditions in the GL basin, projected decreases in number of wet days and consecutive wet days indicate that the GL basin is expected to receive more intense precipitation in the future. This increase in intensity could be a concern in regard to flash flooding.

Projected Changes in Temperature

The spread in annual mean temperature from different RCM-GCM combinations in both historical and future periods is narrower (**Figure 6**) than the spread of annual precipitation (**Figure 2**). Annual mean temperature of GL basin in the historical period shows a significant ($p = 4\text{x}10^{-9}$) increasing trend at 5% significance level. The increasing trend persists in mid-century period for RCP4.5 scenario ($p = 7 \text{ x } 10^{-3}$). The annual mean temperature in the end-century period for RCP4.5 scenario seems to stabilize and shows no-trend ($p = 0.20$). However, the increasing significant trend persists in both mid-century ($p = 1 \text{ x } 10^{-9}$) and end-century ($p = 1 \text{ x } 10^{-10}$) periods for RCP8.5 scenario. The magnitude of the increasing trend in historical period is 0.02°C/year, which increases to 0.03, 0.07, and 0.06°C/year, in mid-century for the RCP4.5 scenario, in mid-century for RCP8.5 and in end-century for the RCP8.5 scenario, respectively.

Spatially, the trend in annual mean temperature is higher for northern parts of the GL basin (e.g., Superior) than in southern parts (e.g., Ontario) (**Figure 7**). For instance, in the mid-century period and for RCP4.5 emission scenario, the annual mean temperature in Superior subdomain is expected to increase by 0.04°C/year while for the same period and emission scenario, the Ontario subdomain increase is just 0.02°C/year. While looking at the spatial trends in minimum and maximum temperature (**Supplementary Figure S8**), the rate of increasing trend of minimum temperature in the GL basin is higher than the rate of increasing trend of maximum temperature in both future

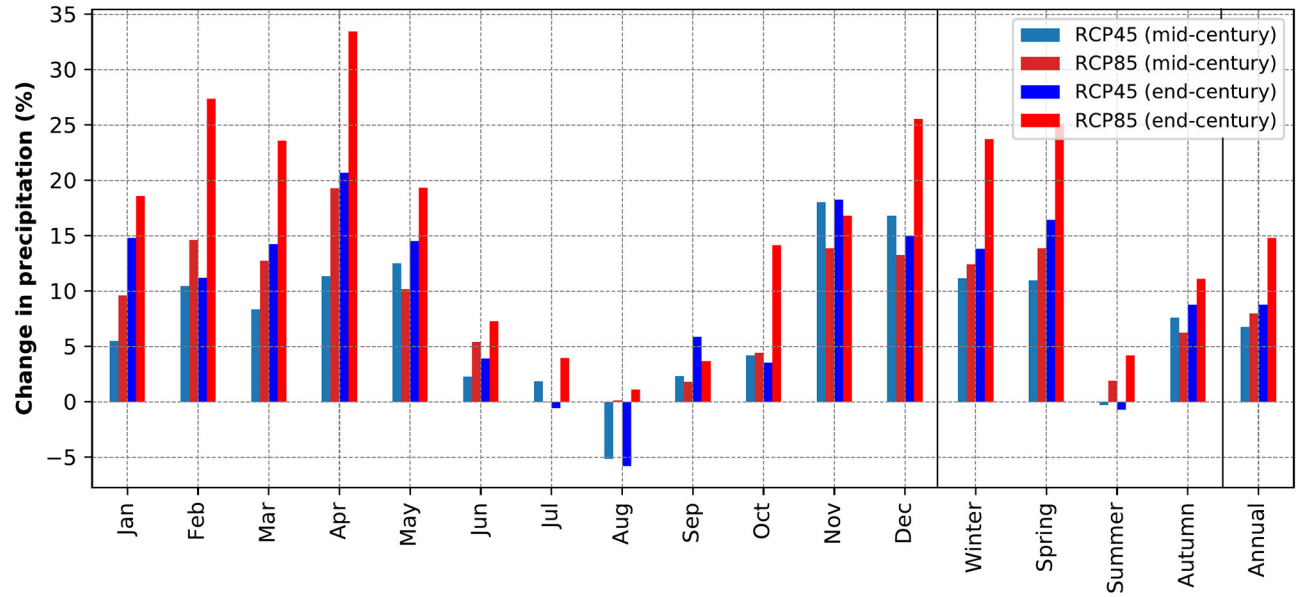

FIGURE 5 | Percentage change in monthly, seasonal, and annual over-land precipitation with respect to the baseline average precipitation for RCP4.5 and RCP8.5 scenarios in mid- and end-century periods.

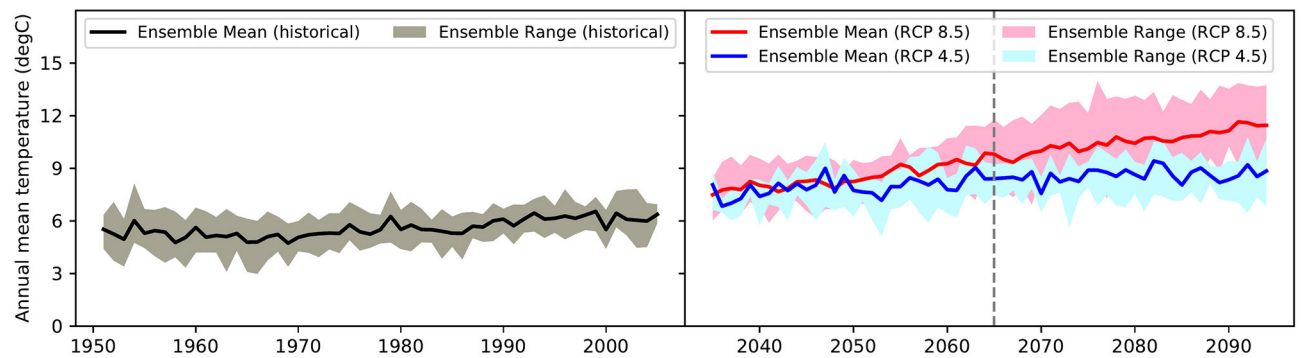

FIGURE 6 | Time series of GL basin annual mean temperature in historical (1951–2005) and future (mid-century: 2035–2064 and end-century: 2065–2094) periods for two emission scenarios (RCP4.5 and 8.5).

periods and for both emission scenarios. Similar findings have been reported by Bartolai et al. (2015) and Kling et al. (2003) in the GL basin.

Relative to the ensemble annual mean temperature in the baseline period, different RCM-GCM projections show a wide range of increases in future annual mean temperature for RCP4.5 and RCP8.5 emission scenarios (**Figure 8**). In general, future projections for RCP8.5 indicate warmer conditions over the GL basin than for RCP4.5. The same is true for the end-century period as compared to the mid-century period.

On average, annual mean temperature in the GL basin is expected to increase by 2.4 and 2.9°C, respectively, in mid- and end-century period for RCP4.5 scenario. For the RCP8.5 scenario, the increase is about 3.0 and 5.0°C, in the mid- and end-century periods respectively (**Figure 9**). In one of the earliest climate change impact assessments of the GL basin, Smith (1991) reported an increase of up to 6.4 °C in annual temperature which is higher than our finding for RCP8.5 in end-century period. However, the estimate made by the study was based on 3 GCMs and for a double (as compared to the preindustrial level) CO_2 scenario. However, such a scenario is highly unlikely to occur even at the end of the century. A more direct comparison of our results can be made with the findings of Bukovsky and Mearns (2020) due to the common data source (NA-CORDEX, 2022) and region of interest. For RCP8.5, the study reported the annual ensemble mean temperature changes of about 3.1 and 5.0°C, respectively in mid- and end-century period, which are almost identical to our estimates.

Relative to other seasons, the winter season is expected to experience the greatest change, with mean temperature increases reaching up to 5.8°C in end-century period for RCP8.5 scenario. The increase in mean temperature during the spring season is

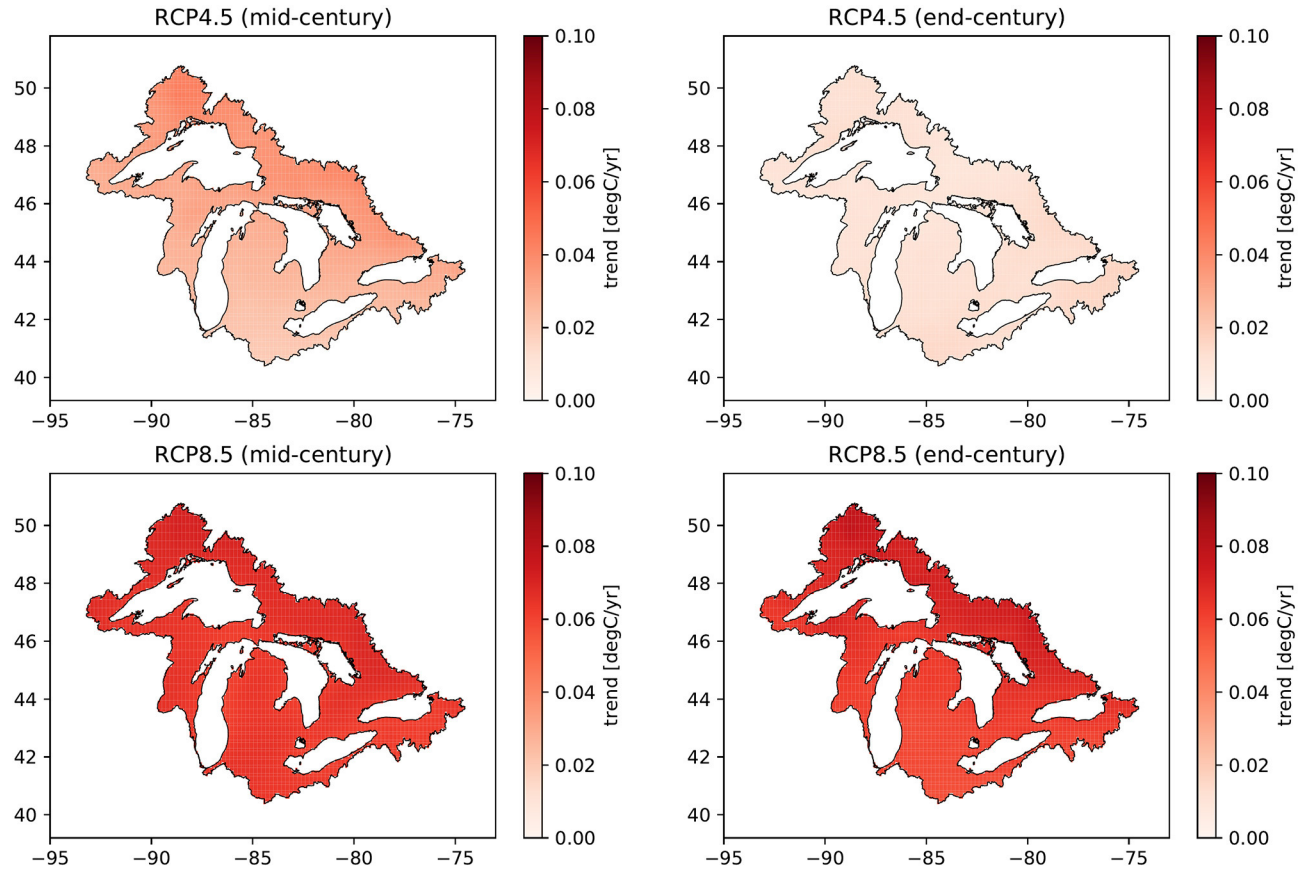

FIGURE 7 | Trend in annual mean temperature of GL basin for RCP4.5 and RCP8.5 scenarios in both mid- and end-century periods.

generally less. A similar finding—higher seasonal changes being obscured in annual averages was also reported in several studies (Kling et al., 2003; Kunkel et al., 2009; Hayhoe et al., 2010; Wuebbles et al., 2010; Winkler et al., 2012; Bukovsky and Mearns, 2020). Our estimates suggest that the winter season is likely to have the greatest increases (up to 5.8°C) which is in line with the finding of Winkler et al. (2012) who reported increase of 7°C and Bukovsky and Mearns (2020) who reported ensemble increase of about 5.6°C. However, some studies, e.g., (Wuebbles et al., 2010) suggest that the greatest increase is likely to be in summer season (up to 6°C). It is important to note that this study used older scenarios (e.g., A1F1) and downscaled projection from substantially lower number of GCMs (3), and this may have led to the difference. At a monthly timescale, increases up to 6°C are observed in January in the end-century period for the RCP8.5 scenario. Similar increases (up to 5.0°C) are also observed in the summer months.

Resulting from the projected decrease in precipitation in August (**Figure 5**) and higher evaporative demand driven by elevated temperature, there is a high probability of increased water stress condition in plants, especially in northern parts of GL basin where the projected increase in mean temperature is relatively higher than in southern parts of the GL basin (**Supplementary Figure S9**). For instance, the mean January temperature in the Superior subdomain is expected to be 6.8°C higher than the baseline condition, while for the same month, the increase in the Erie subbasin is only about 5.3°C. Based on four GCM projections, downscaled for the GL basin (Bartolai et al., 2015), reported similar observations; higher increases in northern parts of the GL compared to the southern parts during winter season. In line with our finding, Hayhoe et al. (2010), based on statistically downscaled future projections from 3 GCMs, also reported a higher increase in winter temperature in northern parts than in southern parts of the US GL basin.

Such increases in temperature are reflected in substantial decreases in the ice day index of the GL basin, which is calculated as the number of days in a year with minimum temperature <0°C (**Supplementary Figure S10**). In the baseline condition, the ice day index is 76 days which is projected to be decrease by 17 and 21 days in the mid- and end-century periods, respectively for RCP4.5, and by 21 and 36 days in the mid- and end-century periods, respectively for RCP8.5. Based on dynamically downscaled projections from 22 RCMs, Winkler et al. (2012) reported 22 fewer days in a year with minimum temperature <0°C which is within the range (17–36 days) of our estimates. These results indicate that the GL basin will experience reduced

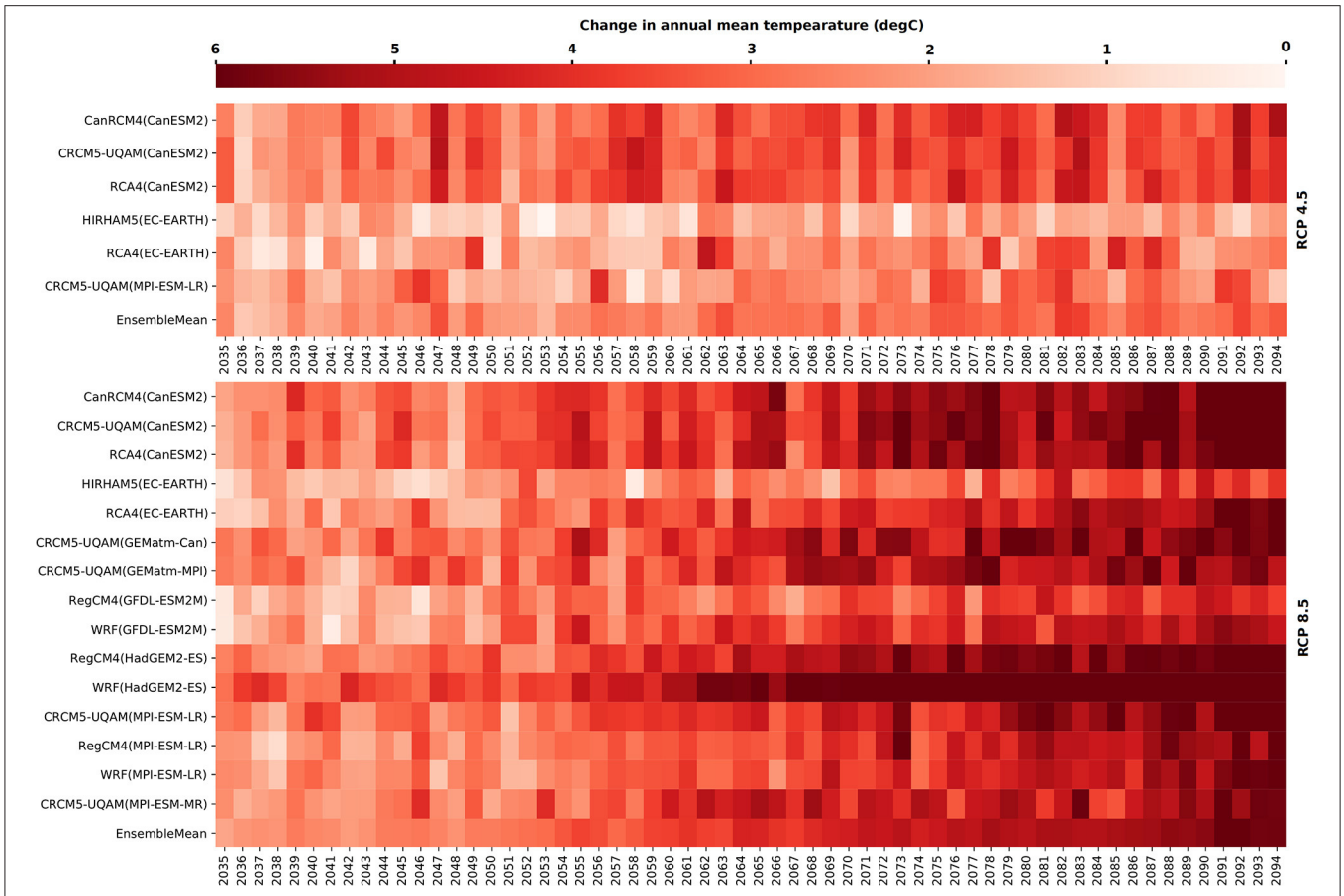

FIGURE 8 | Change in annual mean temperature of GL basin with respect to baseline mean temperature for RCP4.5 and RCP8.5 scenarios in both mid- and end-century periods.

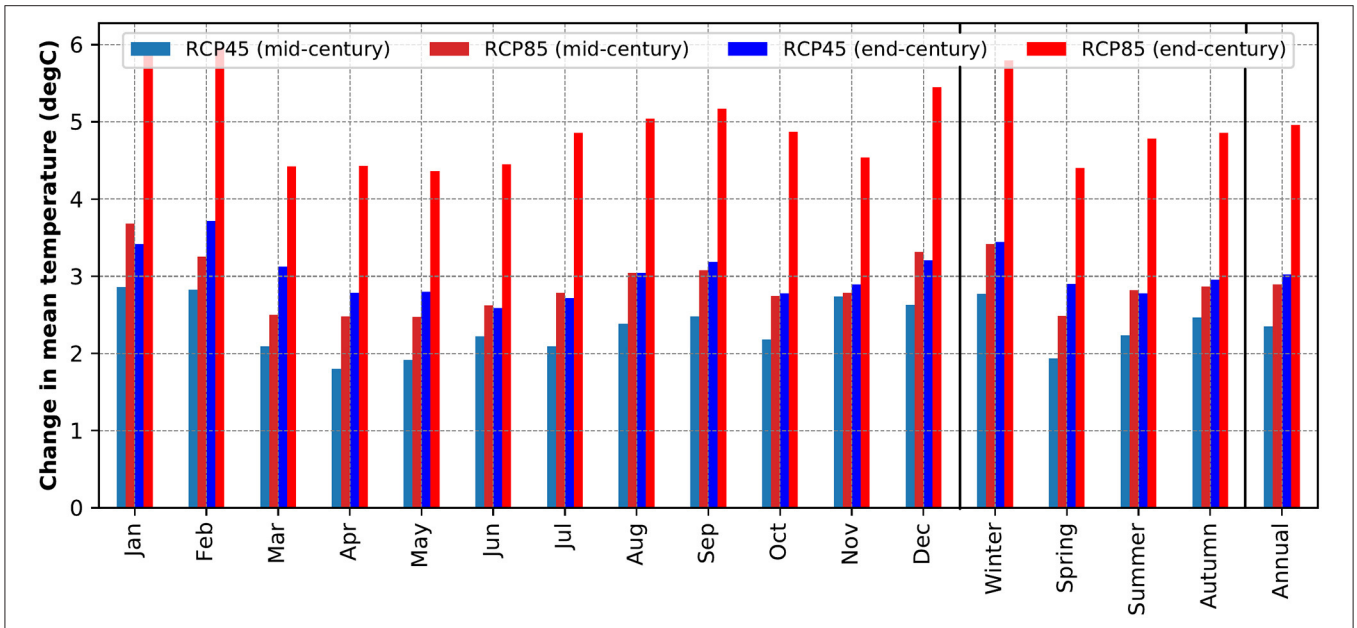

FIGURE 9 | Absolute change in monthly, seasonal, and annual mean temperature of GL basin with respect to baseline mean temperature for RCP 4.5 and RCP 8.5 emission scenarios in both mid- and end-century periods.

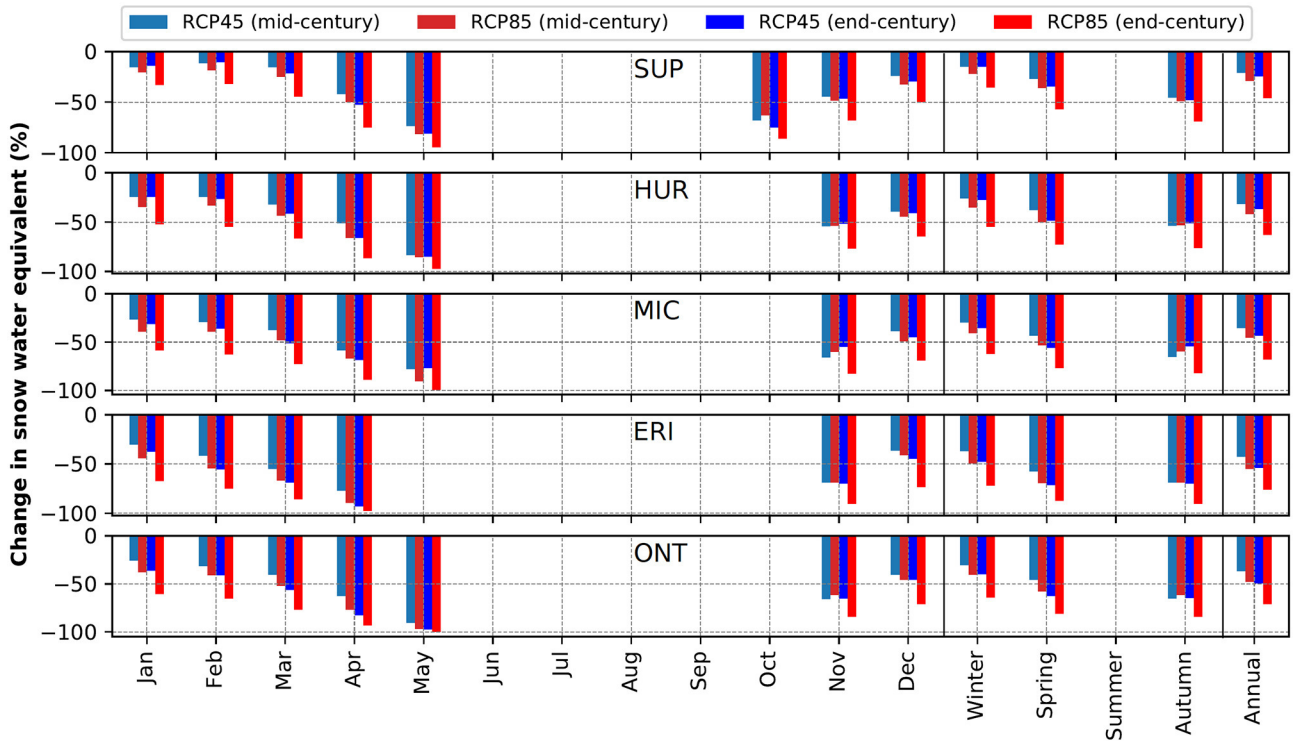

FIGURE 10 | Percentage change in monthly, seasonal, and annual snow water equivalent (SWE) with respect to the baseline value for RCP 4.5 and RCP 8.5 scenarios in both mid- and end-century periods.

frost-free days, accelerated snowmelt and earlier thawing of frozen soil. Furthermore, the proportion of rainfall to total precipitation may also increase which can lead to increased rain-on-snow events, and such events are reported to substantially increase flood risk of the GL basin (Musselman et al., 2018) and similar other regions of the world (Marks et al., 1998; Pomeroy et al., 2016; Sobota et al., 2020).

Conversely, the summer day index, calculated as the number of days in a year with maximum temperature exceeding 25°C, is projected to increase significantly in future. In the baseline period, the summer day index is about 49, which increases to 77 and 86 in the mid- and end-century periods, respectively for RCP4.5, and 85 and 108 in the mid- and end-century periods, respectively for RCP8.5 (**Supplementary Figure S10**). Such significant increases may lead to heat stress to plants which in turn could negatively affect their growth and yield (Fahad et al., 2017).

Projected Changes in Internal Variables

Snowpack

The GL basin is expected to lose a significant portion of its snowpack (expressed as snow water equivalent) in the future (**Figure 10**), which is mainly due to projected changes in temperature and rain-on-snow events. As evident in the projected change in temperatures, snowpack depletion in the end-century period is expected to be higher than in the mid-century period. Similarly, snowpack depletion for the RCP8.5 scenario is also likely to be higher than for the RCP4.5 scenario. At an annual time scale, snowpack depletion in southern parts of the GL basin will be higher than in northern parts of the GL basin (**Figure 10**). As the projected increases in annual temperature in all parts of the GL basin are almost uniform (**Supplementary Figure S9**), the higher snowpack depletion in southern parts of the GL basin is due to the North-South temperature gradient that exists. For any given time period, temperatures in northern parts of the GL basin are relatively lower than in southern parts of the GL basin, consequently the snowpack in the northern parts of the GL basin is generally higher than in the southern parts. The shallower snowpacks in the southern parts of the GL basin are projected to melt earlier, this is in line with the observations made by Musselman et al. (2017) in western North America.

In the spring months (e.g., March and April), southern parts of the GL basin (e.g., Erie) are expected to lose almost 100% of its snowpack while northern parts (e.g., Superior) are expected to only retain only about 75% of the snowpack. For the winter season, during the end-century period using the RCP8.5 scenario, the Superior subdomain is expected to lose about 35% of the snowpack which increases to ∼55% in Huron, ∼60% in Michigan, ∼70% in Erie, and ∼65% in the Ontario subdomain (**Figure 11**).

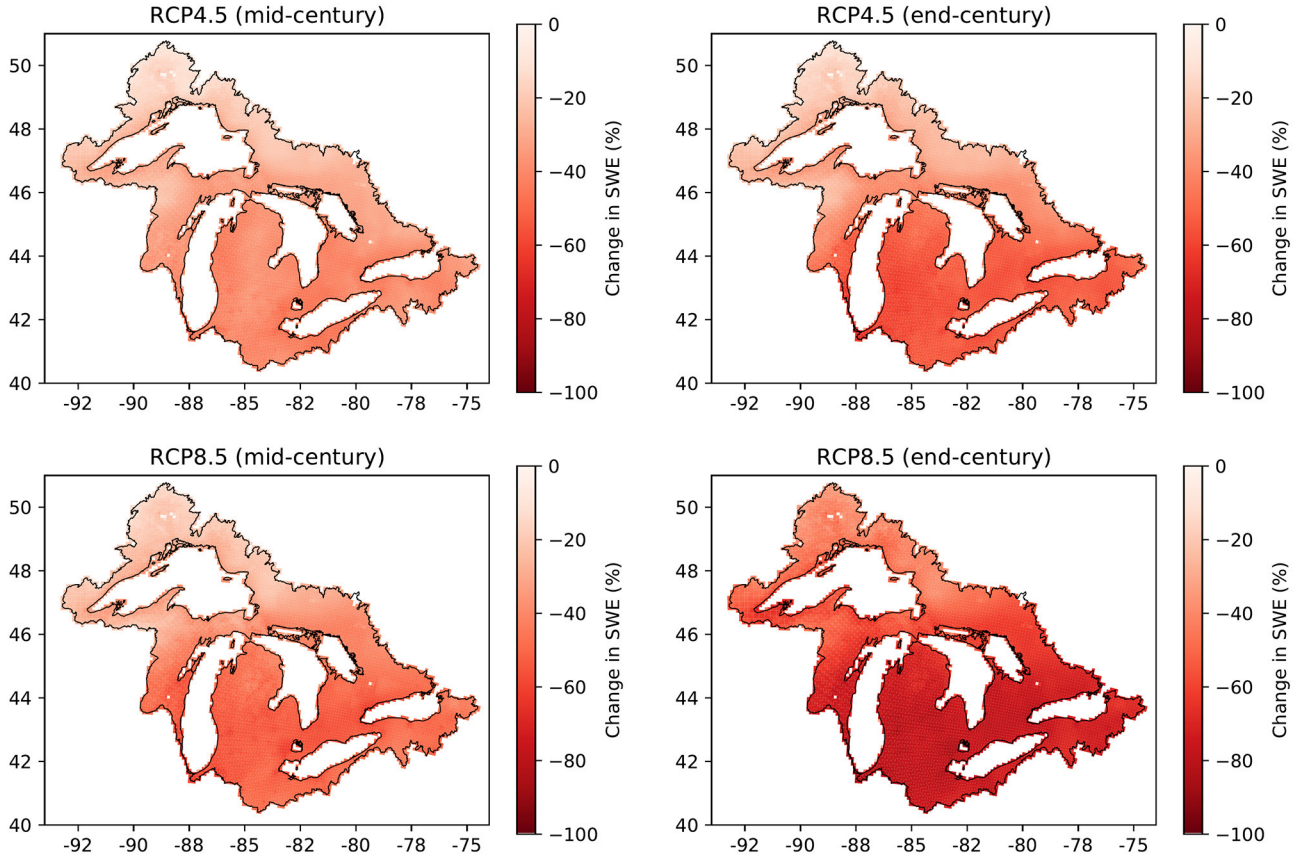

FIGURE 11 | Percentage change in annual mean snow water equivalent (SWE) of GL basin for RCP 4.5 and RCP 8.5 scenarios in both mid- and end-century periods.

Actual Evapotranspiration

Projected increases in temperature of the GL basin will result in overall increase in annual AET (**Figure 12**). However, in the winter season, despite projected increases in temperature, slight decreases in AET are projected, especially during end-century period for RCP8.5 scenario. While it is evident that projected increases in temperature will increase potential evapotranspiration, the AET depends on several factors such as availability of soil moisture and vegetation type. Substantial projected decreases in snowpack (**Figures 10**, **11**) and projected increases in high intensity rainfall (e.g., highest one-day precipitation, **Supplementary Figure S7**), would allow for more surface runoff and less infiltration, leading to lowered soil moisture conditions. Lowered soil moisture levels might be causing the decrease in AET in the winter season. Across all GL subdomains, projected increases in the summer AET are the highest, mainly driven by significant projected increases in summer temperature (**Figure 9**). Furthermore, substantial projected increases in summer day index (**Supplementary Figure S10**) would also result in projected increases in summer AET. Spring season AET also shows moderate increases across the GL basin. Autumn season AET in Ontario subdomain, unlike that observed in other subdomains, are projected to decrease in both future periods and for both emission scenarios. The overall autumn season AET decreases in the subdomain are mainly driven by projected decreases in AET in September.

Spatially, the highest of increases (∼15%) in annual AET are from water bodies such as man-made lake/reservoirs (**Figure 13**), this could be expected as AET from water bodies will be at the potential rate (PET). This is unlike the case in other landcover types such as agriculture or forest where AET may be limited by several factors such as availability of moisture in soil. Furthermore, it should be noted that we used Hargreaves method (Hargreaves and Samani, 1985) to estimate the rate of potential evapotranspiration. The use of such a simplified method for the estimation of AET from a dynamic system as the GL is subject to various forms of uncertainties and could reduce the accuracy of hydrological models. As stated in the Introduction section, the use of a hydrological model which utilizes temperature index (TI) methods such as the Hargreaves method in climate change impact studies has been questioned (Lofgren et al., 2011, 2013; Lofgren and Rouhana, 2016; Milly and Dunne, 2017). As such, projected increases (∼15%) in annual AET around the Lake Nipigon (**Figure 13**) can thus be questioned. The use of an energy balance method to calculate PET would be preferred in such a lake (Finch and Calver, 2008), however, all the incoming and outgoing energy terms required to close the energy balance are

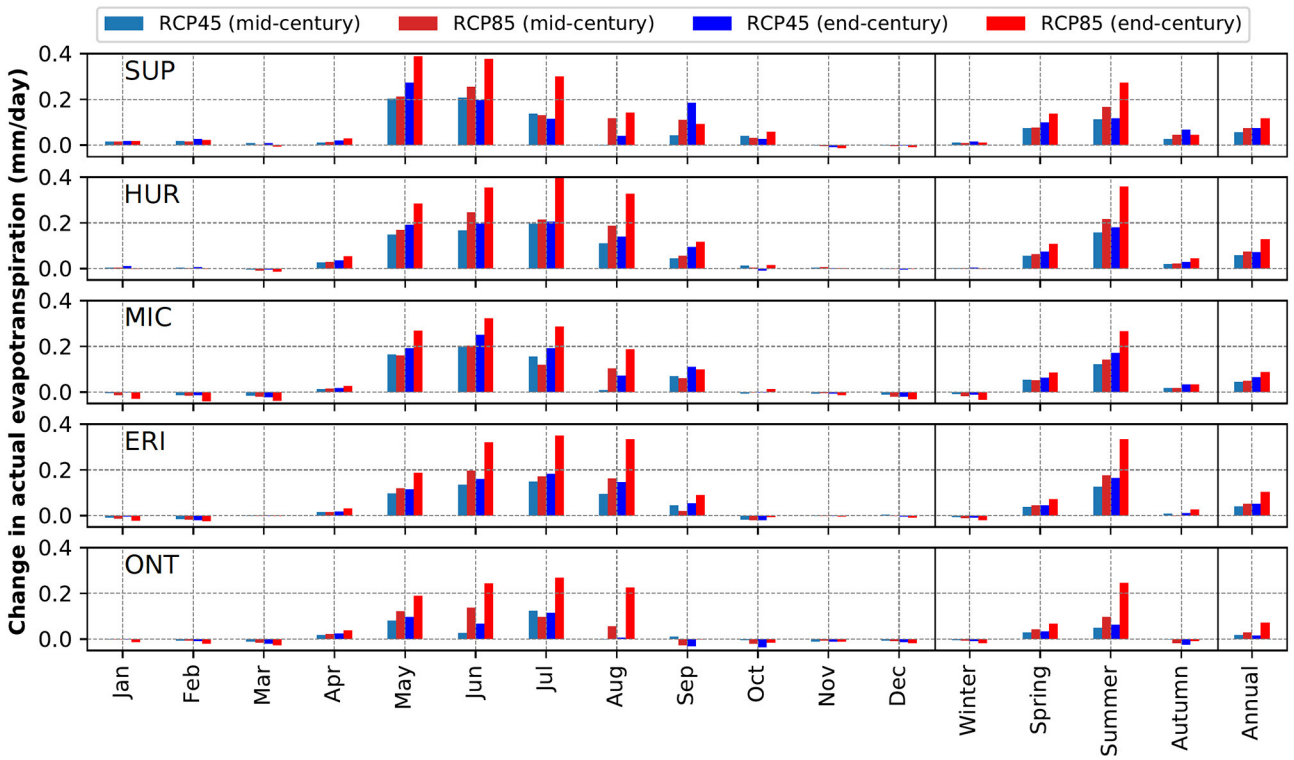

FIGURE 12 | Absolute changes in monthly, seasonal, and annual actual evapotranspiration (AET) with respect to the baseline values for RCP 4.5 and RCP 8.5 scenarios in both mid- and end-century periods.

not the outputs of the RCMs of the NA-CORDEX experiment. Hence, this should be considered as one of the limitations of the study.

Projected Changes in Runoff Into the Lakes

In the context of this study, the term runoff refers to the amount of water entering each lake through the stream network. This is the amount of water that comes from the land area (through overland flow, interflow, and baseflow) into the stream network, which is then routed downstream into the lakes. For operation purposes such as seasonal water level forecasting (Fry et al., 2020) or net basin supply (NBS) calculation (Do et al., 2020), runoff into each GL needs to be converted into equivalent effect on lake level. A ratio of land area to lake area of each GLs, as agreed by Coordinating Committee on Great Lakes basic hydraulic and hydrologic data, is used for this purpose (GLCC, 2021). As Lakes Huron and Michigan are hydrologically connected, runoff from land areas of both lakes (MHG) are aggregated and converted into their equivalent effect on lake level. While it is evident that the "runoff component of the NBS (or the effect of the runoff on lake level)" and the "runoff into the lakes from surrounding land areas" are two different quantities, for simplicity, we are referring the "runoff component of the NBS" as the "runoff" from hereafter.

Annual average runoff for Lakes Superior, Michigan-Huron, Erie and Ontario is projected to increase by 25–48, 18–40, 4–25, and 11–28%, respectively (**Figure 14**). Higher increases are projected for the RCP8.5 emission scenario and in the end-century period. It should be noted that both future annual precipitation and mean annual temperature (and as a result AET) are expected to increase in all subdomains (**Supplementary Figures S5, S9**). An equal increase in these factors may result in a net zero change in runoff. However, the overall increase in annual runoff is most likely a result of a greater change in the annual precipitation (**Figure 5**). On the other hand, accelerated melt of the snowpack can also lead to the overall increase. Amongst the seasons, the increase in runoff is projected to be the highest in the winter. For instance, in Superior subdomain, the winter runoff is expected to increase by 146%, which is significantly higher than the annual projected increase. The same trend is evident in other subdomains. spring season runoff is expected to have moderate increase due to already depleted snowpack, especially in southern subdomains (e.g., Ontario, 6–16%). The same behavior is evident in summer and autumn seasons across all subdomains except for Erie. In the Erie subdomain, runoff is expected to decrease in both future periods for the RCP4.5 emission scenario in summer and autumn. This is due to projected decrease in August and September precipitation in the subdomain (**Supplementary Figure S5**). At a monthly timescale, in the northern subdomains (e.g., Superior), the highest increases in runoff are observed in March (216%) while in southern subdomains (e.g., Ontario), the highest increases are, as expected, observed earlier (February, 111%). Availability

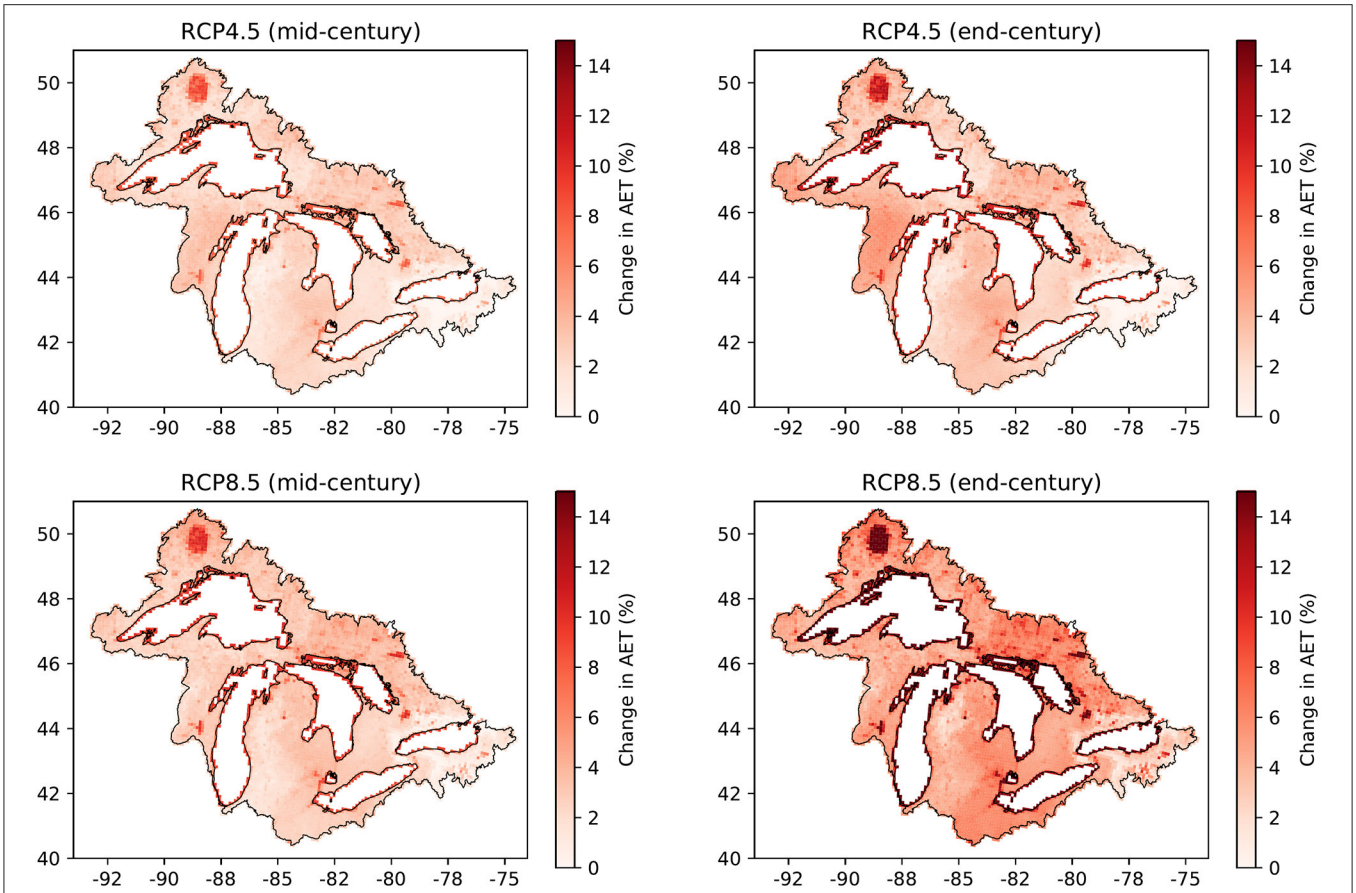

FIGURE 13 | Percentage changes in annual mean actual evapotranspiration (AET) of GL basin for RCP 4.5 and RCP 8.5 scenarios both mid- and end-century periods.

of higher snowpack and higher increases in temperature in the northern subdomains (**Figure S9**) may have resulted in such significant increases, as compared to the southern subdomains.

Probability exceedance plots of runoff (**Supplementary Figure S11**) further confirm the projected rise in the runoff and show the severity of changes: high (at 10% exceedance probability), mid (between 10 and 90% exceedance probability) and low (90% exceedance probability), following (USEPA, 2007) classification. In the Superior and Michigan-Huron subdomains, projected increases are evident for almost all exceedance probabilities. For instance, the ensemble mean of high runoff into Lake Superior is projected to increase up to 95 mm (in end-century period for RCP8.5 scenario) which is about 20% increase from its baseline value (80 mm). A similar increment (∼30%, in end-century period for RCP8.5 scenario) is observed in runoff into Lake Michigan-Huron. In Lakes Erie and Ontario, projected changes in low runoff are minimal. In these southern subdomains, mid and high runoff are however projected to increase significantly. For instance, median runoff into Lakes Erie and Ontario are projected to increase by ∼35 and ∼20%, respectively.

Without analyzing the other components (over-lake precipitation and over-lake evaporation) of the net basin supply (NBS), it is impossible to determine whether future lake level will rise or drop. However, from the results of this study, it is quite evident that runoff component of the NBS is projected to increase in future. A recent analysis of the future changes of GL levels (Seglenieks and Temgoua, in review), indicated that under a changing climate more extreme highs and lows would be experienced, as well as a gradual increase in average lake levels. Such fluctuations in lake level may cause flooding and erosion along shoreline communities of the GL basin. Furthermore, key shoreline wetlands may experience detrimental effects of the projected fluctuations in water level of GLs, as also highlighted by Mortsch (1998).

Uncertainty Quantification

As there are 2 emission scenarios (ES) (RCP4.5 and RCP8.5), and 6 common regional climate models (RCM) between them, there were a total of 12 projections, of which 6 simulations and 2 simulations were considered at each stage of ES and RCM, respectively, to estimate their contribution to the total uncertainty. Relative contribution of ES and RCM into total uncertainty in future SWE, AET and runoff estimates are shown in **Supplementary Tables S4A–C**, respectively. It is quite evident that ES is by far the largest contributor to the total uncertainty. The contribution of ES to the total uncertainty is higher in end-century period as compared in mid-century period. As an

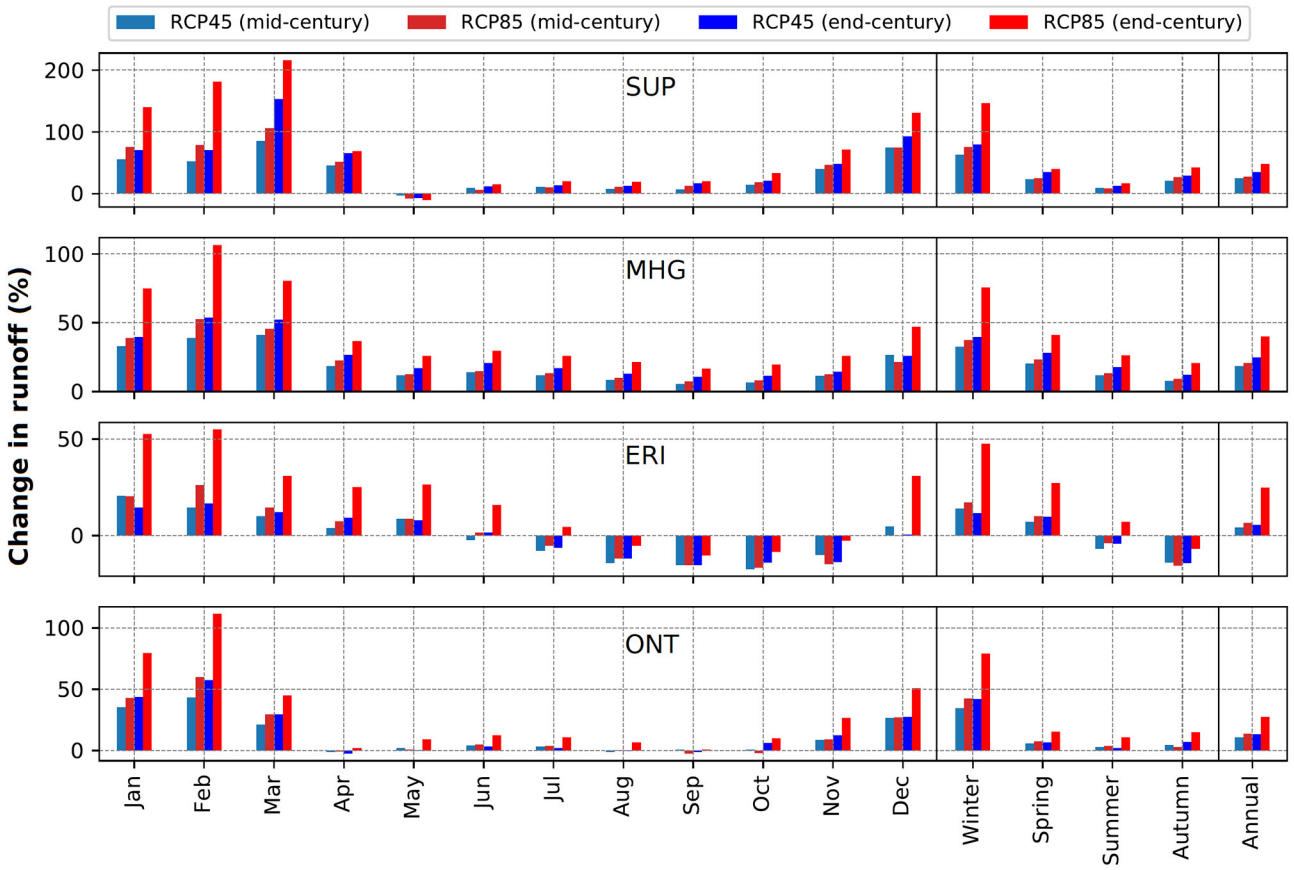

FIGURE 14 | Change in monthly, seasonal, and annual runoff with respect to the baseline values for RCP4.5 and RCP8.5 scenarios in both mid- and end-century periods.

example, in mid-century period, 68% of total uncertainty in SWE estimates is due to ES which increases to 85% in end-century period (**Supplementary Table S4A**). It indicates that the choice of the RCM is not so important, as far as the uncertainty in future projection of SWE is concerned. Rather, future SWE estimates will be highly dependent on the choice of an ES. While a similar trend is also observed for AET and runoff, the choice of RCM is still quite important for these variables as 35% (28%) and 36% (28%) of the total uncertainty is still contributed by RCM in mid-century (end-century) period. The use bias-corrected and high-resolution RCMs to derive future estimates of SWE, AET and runoff, may be one the reasons that the choice of a particular RCM may not constitute a significant source of uncertainty. A similar observation, ES being the largest contributor was also reported by Lee et al. (2017).

SUMMARY AND CONCLUSIONS

Freshwater resources of the Laurentian Great Lakes basin contribute significantly to the environment and economy of Canada and the United States. Sustainable management of the freshwater resources is thus very important. However, several stressors such as climate change will pose serious threats to these water resources in the future. Hence, an assessment of the impacts of climate change on land hydroclimatology is appropriate. This study uses a set of 36 simulations from 6 RCMs in historical (or baseline, 1951–2005) and two future (mid-century, 2035–2064 and end century, 2065–2094) periods, and for two emission scenarios (RCP4.5 and RCP8.5), to quantify trends and changes in land precipitation and temperature. As well as using the RCM projections as input to a calibrated and validated hydrological model, this study also assesses the impacts of climate change on snowpack, actual evapotranspiration and runoff into the lakes.

Results show that the GL land area will experience a wetter and warmer future with projected mean annual precipitation increases up to 15% and projected mean annual temperature increases up to 5°C. Seasonal (up to 25% increase in precipitation and up to 5.8°C increase in mean temperature) and monthly (up to 33% increase in precipitation and up to 6.0°C increase in mean temperature) changes are greater than the annual changes. Some scenarios even show projected decreases (∼6% in August during mid-century period for RCP4.5 scenario) in summer precipitation. Projected increases in highest-one day precipitation and projected decreases in both wet days and consecutive wet days indicate occurrence of more future extreme

precipitation in the GL basin. Similarly, results show that the GL basin will experience a lower number of ice days and a higher number of summer days in future.

The future snowpack in the GL basin is expected to decrease substantially (up to 76% in Erie subdomain). The highest decreases in snowpack are expected in the spring season, including up to 88% in the Erie subdomain for some scenarios. On the other hand, actual evapotranspiration is projected to increase in future with the highest projected increases in the summer (up to 0.4 mm/day). Results show consistent increases in runoff (up to 48%), with higher increases in the northern lakes (Superior and Michigan-Huron) than in the southern lakes (Erie and Ontario). By contrast, in the autumn season, some scenarios even show projected decreases (up to 16%) in runoff.

Uncertainty analysis showed that the use of different emission scenarios is the largest contributor to the total uncertainty and the choice of a particular RCM is not as important as far as the uncertainty in the future estimates of the snow water equivalent, actual evapotranspiration and runoff (to the lakes) are concerned.

A wetter and warmer future with more extreme precipitation, compounded by a substantial decrease in snowpack and an increase in actual evapotranspiration, will surely pose challenges to water resources managers and planners in the GL basin. Such a challenge due to competing forces in a future hydrological cycle of the GL basin was also corroborated by several other studies including Brown et al. (2011), Carter and Steinschneider (2018) and Gronewold and Rood (2019). Also of note, is that a majority of the most extreme effects are seen under the "business as usual" RCP 8.5 emission scenario particularly at the end of the century. There is of course more uncertainty in these results, as not only are they for many years in the future, but they will be highly dependent on future carbon emissions and thus how society adapts. Thus, these results should be seen as a guide to possible changes in the GL hydroclimate variables, but not as a forecast of the exact future conditions.

Amongst all the other GL basin (and surrounding region) historical climate change studies, it is hard to state whether the results of this study are more robust. We believe that the ensemble results that we obtained with the use of a set of high-resolution bias-corrected RCM forcings to a coupled hydrological model with explicit consideration of smaller lakes, evaluated not only for streamflow but also for other variables of interests (SWE and AET) are relatively reliable. The reader should also be aware of some studies (Lofgren et al., 2011, 2013; Lofgren and Rouhana, 2016; Milly and Dunne, 2017) questioning the use of a hydrological model utilizing temperature index (TI) method, rather than an energy-balance method, to project future changes in PET. The Hargreaves method (Hargreaves and Samani, 1985) is also a TI method that our hydrological model employs to calculate PET. However, the performance of the Hargreaves method as evident in some studies is encouraging. For example, of the four TI methods that Milly and Dunne, (2017) used to estimate the relative changes in future annual PET, the estimates when using the Hargreaves method were closest to the estimates of the energy-only method. Similarly, Xu and Singh (2001) evaluated the performance of seven TI methods in estimating evaporation at two climatological stations in Northwestern Ontario, Canada and recommended the use of the Hargreaves method. However, the use of an energy balance method in hydrological methods to estimate future changes in PET should be preferred if all the incoming and outgoing energy terms become outputs of high-resolution bias-corrected RCMs. Furthermore, this study quantifies the relative contribution of climate model and scenario uncertainties to the total uncertainty in considered hydrological variables which also provides a guidance to new studies.

We presume that better quantification of impacts of climate change on land-hydroclimatic variables will be helpful to understand the future conditions of the GL basin. This may also help formulate a coordinated effort to address the adverse effects of climate change in the basin.

DATA AVAILABILITY STATEMENT

The raw data supporting the conclusions of this article will be made available by the authors, without undue reservation.

AUTHOR CONTRIBUTIONS

Conceptualization and supervision: FS. Methodology and modeling: NS, FS, AT, and AD. Formal analysis and writing—review and editing: NS, FS, and AT. Data curation, writing—original draft preparation, and visualization: NS. All authors contributed to the article and approved the submitted version.

ACKNOWLEDGMENTS

We would like to thank J. Mai of the University of Waterloo (UofW) for pre-processing spatial and meteorological data used in WATFLOOD model set-up, calibration, and validation. We would also like to thank E. Gaborit of Environment and Climate Change Canada (ECCC) for preparing separate input data for the five subdomains. We are also thankful to H. Shen of UofW who provided the lake and river routing product, incorporated in RAVEN for each subdomain. Many thanks to D. Princz of ECCC for helping to create a WATFLOOD executable with netCDF capabilities. We are also indebted to the RAVEN development team of UofW for providing a RAVEN-ro executable with netCDF capabilities.

SUPPLEMENTARY MATERIAL

The Supplementary Material for this article can be found online at: https://www.frontiersin.org/articles/10.3389/frwa.2022.801134/full#supplementary-material

REFERENCES

Acharya, N., Shrivastava, N. A., Panigrahi, B. K., and Mohanty, U. C. (2014). Development of an artificial neural network based multi-model ensemble to estimate the northeast monsoon rainfall over south peninsular India: an application of extreme learning machine. *Clim. Dyn.* 43, 1303–1310. doi: 10.1007/s00382-013-1942-

Angel, J. R., and Kunkel, K. E. (2010). The response of Great Lakes water levels to future climate scenarios with an emphasis on Lake Michigan-Huron. *J. Great Lakes Res.* 36, 51–58. doi: 10.1016/j.jglr.2009.09.006

Argent, R. M. (2004). An overview of model integration for environmental applications—components, frameworks and semantics. *Environ. Model. Softw.*19. 219–234. doi: 10.1016/S1364-815200150-6

Bartolai, A. M., He, L., Hurst, A. E., Mortsch, L., Paehlke, R., and Scavia, D. (2015). Climate change as a driver of change in the Great Lakes St. Lawrence River Basin. *J. Great Lakes Res.* 41, 45–58. doi: 10.1016/j.jglr.2014.11.012

Basile, S. J., Rauscher, S. A., and Steiner, A. L. (2017). Projected precipitation changes within the Great Lakes and Western Lake Erie Basin: a multi-model analysis of intensity and seasonality. *Int. J. Climatol.* 37, 4864–4879. doi: 10.1002/joc.5128

Bingeman, A. K., Kouwen, N., and Soulis, E. D. (2006).Validation of the hydrological processes in a hydrological Model. *J. Hydrol. Eng.* 11, 451–463. doi: 10.1061/(ASCE)1084-0699(2006)11:5(451)

Bosch, N. S., Evans, M. A., Scavia, D., and Allan, J. D. (2014). Interacting effects of climate change and agricultural BMPs on nutrient runoff entering Lake Erie. *J. Great Lakes Res.* 40, 581–589. doi: 10.1016/j.jglr.2014.04.011

Briley, L. J., Rood, R. B., and Notaro, M. (2021). Large lakes in climate models: a Great Lakes case study on the usability of CMIP5. *J. Great Lakes Res.* 47, 405–418. doi: 10.1016/j.jglr.2021.01.010

Brown, C., Werick, W., Leger, W., and Fay, D. (2011). A Decision-Analytic approach to managing climate risks: application to the upper Great Lakes. *JAWRA J. Am. Water Resour. Assoc.* 47, 524–534. doi: 10.1111/j.1752-1688.2011.00552.x

Bukovsky, M. S., and Mearns, L. O. (2020). Regional climate change projections from NA-CORDEX and their relation to climate sensitivity. *Clim. Change.* 162, 645–665. doi: 10.1007/s10584-020-02835-x

Buttle, J., Muir, T., and Frain, J. (2004). Economic impacts of climate change on the canadian Great Lakes hydro electric power producers: a supply analysis. *Can. Water Resour. J. Revue Canadienne Des Ressources Hydriques.* 29, 89–110. doi: 10.4296/cwrj089

Byun, K., Chiu, C.-M., and Hamlet, A. F. (2019). Effects of 21st century climate change on seasonal flow regimes and hydrologic extremes over the Midwest and Great Lakes region of the US. *Sci. Total Environ.* 650, 1261–1277. doi: 10.1016/j.scitotenv.2018.09.063

Cannon, A. J. (2015). Selecting GCM Scenarios that span the range of changes in a multimodel ensemble: application to CMIP5 climate extremes indices. *J. Clim.* 28, 1260–1267. doi: 10.1175/JCLI-D-14-00636.1

Cannon, A. J. (2018). Multivariate quantile mapping bias correction: an N-dimensional probability density function transform for climate model simulations of multiple variables. *Clim. Dyn.* 50, 31–49. doi: 10.1007/s00382-017-3580-6

Carter, E., and Steinschneider, S. (2018). Hydroclimatological drivers of extreme floods on Lake Ontario. *Warter Resour. Res.* 54, 4461–4478. doi: 10.1029/2018WR022908

Chao, P. (1999). Great Lakes water resources: Climate change impact analysis with transient GCM scenarios. *JAWRA J. AM. Water Resour.Assoc.* 35, 1499–1507. doi: 10.1111/j.1752-1688.1999.tb04233.x

Chen, J., Chu, H., and Noormets, A. (2021). *AmeriFlux BASE US-Oho Oak Openings, Ver. 7-5'*. Berkeley: Lawrence Berkeley National Laboratory.

Cherkauer, K. A., and Sinha, T. (2010). Hydrologic impacts of projected future climate change in the Lake Michigan region. *J. Great Lakes Res.* 36, 33–50. doi: 10.1016/j.jglr.2009.11.012

Christensen, J., Kjellström, E., Giorgi, F., Lenderink, G., and Rummukainen, M. (2010). Weight assignment in regional climate models, *Clim. Res.* 44, 179–194. doi: 10.3354/cr00916

Cohen, S. J. (1986). Impacts of CO2-induced climatic change on water resources in the Great Lakes Basin. *Clim. Change.* 8, 135–153. doi: 10.1007/BF00139751

Collingsworth, P. D., Bunnell, D. B., Murray, M. W., Kao, Y.-C., Feiner, Z. S., Claramunt, R. M., et al. (2017). Climate change as a long-term stressor for the fisheries of the Laurentian Great Lakes of North America. *Rev. Fish Biol. Fish.* 27, 363–391. doi: 10.1007/s11160-017-9480-3

Cousino, L. K., Becker, R. H., and Zmijewski, K. A. (2015). Modeling the effects of climate change on water, sediment, and nutrient yields from the maumee river watershed. *J. Hydrol: Reg. Stud.* 4, 762–775. doi: 10.1016/j.ejrh.2015.06.017

Craig, J. R., Brown, G., Chlumsky, R., Jenkinson, R. W., Jost, G., Lee, K., et al. (2020). Flexible watershed simulation with the Raven hydrological modelling framework, *Environ. Model. Softw.* 129, 104728. doi: 10.1016/j.envsoft.2020.104728

Cranmer, A. J., Kouwen, N., and Mousavi, S.-F. (2001). Proving WATFLOOD: modelling the nonlinearities of hydrologic response to storm intensities. *Can.J. Civ. Eng.* 28, 837–855. doi: 10.1139/l01-049

Croley, T. E. (1990). Laurentian Great Lakes double-CO2 climate change hydrological impacts. *Clim. Change.* 17, 27–47. doi: 10.1007/BF00148999

Crosbie, R. S., Dawes, W. R., Charles, S. P., Mpelasoka, F. S., Aryal, S., Barron, O., et al. (2011). Differences in future recharge estimates due to GCMs, downscaling methods and hydrological models. *Geophys. Res. Lett.* 38, 1–5. doi: 10.1029/2011GL047657

De Scheer, G., Therrien, R., Refsgaard, J. C., and Hansen, A. L. (2015). Simulating coupled surface and subsurface water flow in a tile-drained agricultural catchment. *J. Hydrol.* 521, 374–388. doi: 10.1016/j.jhydrol.2014.12.035

Do, H. X., Smith, J. P., Fry, L. M., and Gronewold, A. D. (2020).Seventy-year long record of monthly water balance estimates for Earth's largest lake system. *Sci. Data.* 7, 276. doi: 10.1038/s41597-020-00613-z

ELPC (2019). *An Assessment of the Impacts of Climate Change on the Great Lakes*. Chicago, USA: Environmental Law and Policy Center (ELPC).

Fahad, S., Bajwa, A. A., Nazir, U., Anjum, S. A., Farooq, A., Zohaib, A., et al. (2017). Crop Production under drought and heat stress: plant rsponses and management options. *Fron. Plant. Sci.* 8, 1147. doi: 10.3389/fpls.2017.01147

Finch, J., and Calver, A. (2008). *Methods for the Quantification of Evaporation from Lakes*. Wallingford, UK: CEH Wallingford.

Fluxnet Canada, T. (2016). *FLUXNET Canada Research Network - Canadian Carbon Program Data Collection, 1993-2014*. Oak Ridge: Oak Ridge National Laboratory Distributed Active Archive Center

Fry, L. M., A s, D., and Gronewold, A. D. (2020). Operational seasonal water suly and water level forecasting for the laurentian Great Lakes. *J. Water Resour. Plann. Manag.* 146, 04020072. doi: 10.1061/(ASCE)WR.1943-5452.0001214

Gasset, N., Fortin, V., Dimitrijevic, M., Carrera, M., Bilodeau, B., Muncaster, R., et al. (2021). A 10 km North American precipitation and land-surface reanalysis based on the GEM atmospheric model. *Hydrol. Earth Syst. Sci.* 25, 4917–4945. doi: 10.5194/hess-25-4917-2021

Gay, C., and Estrada, F. (2010). Objective probabilities about future climate are a matter of opinion. *Clim. Change.* 99, 27–46. doi: 10.1007/s10584-009-9681-4

GLCC (2021). *Great Lakes Coordinating Committee*. Available online at: www.greatlakescc.org/wp36/ (accessed December 2021).

Gough, C., Bohrer, B., and Curtis, P. (2021). *AmeriFlux BASE US-UMB Univ. of Mich. Biological Station, Ver. 17-5*.

Grady, K. A., Chen, L., and Ford, T. W. (2021). Projected changes to spring and summer precipitation in the Midwestern United States. *Front. Water.* 3, 1–16. doi: 10.3389/frwa.2021.780333

Gronewold, A. D., and Rood, R. B. (2019). Recent water level changes across Earth's largest lake system and implications for future variability. *J. Great Lakes Res.* 45, 1–3. doi: 10.1016/j.jglr.2018.10.012

Gupta, H. V., Kling, H., Yilmaz, K. K., and Martinez, G. F. (2009). Decomposition of the mean squared error and NSE performance criteria: implications for improving hydrological modelling *J. Hydrol.* 377, 80–91. doi: 10.1016/j.jhydrol.2009.08.003

Hall, K. R., Herbert, M. E., Sowa, S. P., Mysorekar, S., Woznicki, S. A., Nejadhashemi, P. A., et al. (2017). Reducing current and future risks: using climate change scenarios to test an agricultural conservation framework. *J. Great Lakes Res.* 43, 59–68. doi: 10.1016/j.jglr.2016.11.005

Han, M., Mai, J., Tolson, B. A., Craig, J. R., Gaborit, É., Liu, H., et al. (2020). Subwatershed-based lake and river routing products for hydrologic and land

surface models a lied over Canada. *Can. Water Resour. J. Revue canadienne des ressources hydriques.* 45, 237–251. doi: 10.1080/07011784.2020.1772116

Hargreaves, G. H., and Samani, Z. A. (1985). Reference crop evapotranspiration from temperature. *Lied Eng. Agric.* 1, 96–99. doi: 10.13031/2013.26773

Hartmann, H. C. (1990). Climate change impacts on Laurentian Great Lakes levels. *Clim. Change.* 17, 49–67. doi: 10.1007/BF00149000

Hawkins, E., and Sutton, R. (2009). The Potential to narrow uncertainty in regional climate predictions. *Bull. Am. Meteor. Soc.* 90, 1095–1107. doi: 10.1175/2009BAMS2607.1

Hayhoe, K., VanDorn, J., Croley, T., Schlegal, N., and Wuebbles, D. (2010).Regional climate change projections for Chicago and the US Great Lakes. *J. Great Lakes Res.* 36, 7–21. doi: 10.1016/j.jglr.2010.03.012

Hellmann, J. J., Nadelhoffer, K. J., Iverson, L. R., Ziska, L. H., Matthews, S. N., Myers, P., et al. (2010). Climate change impacts on terrestrial ecosystems in metropolitan Chicago and its surrounding, multi-state region. *J. Great Lakes Res.* 36, 74–85. doi: 10.1016/j.jglr.2009.12.001

Homer, C., Colditz, R. R., Latifovic, R., Llamas, R. M., Pouliot, D., Danielson, P., et al. (2017). *Developing a New North American Land Cover Product at 30m Resolution: Methods, Results and Future Plans*. Orleans: American Geophysical Union, Fall Meeting.

Hostetler, S. W., Bates, G. T. and Giorgi, F. (1993). Interactive coupling of a lake thermal model with a regional climate model. *J. Geophys. Res. Atmos.* 98(D3), 5045–5057. doi: 10.1029/92JD02843

IJC (2021). International Joint Commission. Available online at: https://ijc.org/en (accessed: September 2021).

IPCC (2007). *Climate Change 2007: Impacts, Adaptation and Vulnerability. Contribution of Working Group II to the Fourth Assessment Report of the Intergovernmental Panel on Climate Change.* Cambridge, U.K.: Cambridge University Press. p. 976.

IPCC (2014). *Climate Change 2014: Synthesis Report.* Contribution of Working Groups I, II and III to the Fifth Assessment Report of the Intergovernmental Panel on Climate Change. Cambridge: IPCC.

IPCC (2021). "Summary for Policymakers", in: *Climate Change 2021: The Physical Science Basis. Contribution of Working Group I to the Sixth Assessment Report of the Intergovernmental Panel on Climate Change*, Masson-Delmotte, V., Zhai, P., Pirani, A., Connors, S.L., Péan, C., Berger, S., (eds). Cambridge University Press. Geneva: Intergovernmental Panel on Climate Change.

Kendall, M. G. (1975). *Rank Correlation Methods.* London: Griffin.

Kling, G., Hayhoe, K., Johnson, L., Magnuson, J., Polassky, S., Robinson, S., et al. (2003). *Confronting Climate Change in the Great Lakes Region: Impacts on Our Communities and Ecosystems.*

Kouwen, N. (1986). *WATFLOOD/CHARM Canadian Hydrological And Routing Model. Waterloo, Ontario*. Canada: Department of Civil Engineering University of Waterloo.

Kouwen, N. (1988). WATFLOOD: *a micro-computer based flood forecasting system based on real-time weather radar. Can. Water Resour. J.* 13, 62–77. doi: 10.4296/cwrj1301062

Kouwen, N., Danard, M., Bingeman, A., Luo, W., Seglenieks, F., and Soulis, E. (2005). Case Study: watershed modeling with distributed weather model data. *J. Hydrol. Engi.* 10, 23–38. doi: 10.1061/(ASCE)1084-0699(2005)10:1

Kouwen, N., Soulis, E. D., Pietroniro, A., Donald, J., and Harrington, R. A. (1993). Grouped response units for distributed hydrologic modeling. *J. Water Resour. Plann. Manag.* 119, 289–305. doi: 10.1061/(ASCE)0733-9496(1993)119:3(289)

Krysanova, V., Donnelly, C., Gelfan, A., Gerten, D., Arheimer, B., Hattermann, F., et al. (2018). How the performance of hydrological models relates to credibility of projections under climate change, *Hydrol. Sci. J.* 63. 696–720, doi: 10.1080/02626667.2018.1446214

Kunkel, K. E., Ensor, L., Palecki, M., Easterling, D., Robinson, D., Hubbard, K. G., et al. (2009). A new look at lake-effect snowfall trends in the Laurentian Great Lakes using a temporally homogeneous data set. *J. Great Lakes Res.* 35, 23–29. doi: 10.1016/j.jglr.2008.11.003

Kutzbach, J., Williams, J., and Vavrus, S. (2005). Simulated 21st century changes in regional water balance of the Great Lakes region and links to changes in global temperature and poleward moisture transport, *Geophys. Res. Lett.* 32, 1–5. doi: 10.1029/2005GL023506

Larson, G., and Schaetzl, R. (2001). Origin and evolution of the Great Lakes. *J. Great Lakes Res.* 27. 518–546. doi: 10.1016/S0380-133070665-X

Lee, J.-K., Kim, Y.-O., and Kim, Y. (2017). A new uncertainty analysis in the climate change impact assessment. *Int.J. Climatol.* 37, 3837–3846. doi: 10.1002/joc.4957

Lehner, B., Verdin, K. L., and Jarvis, A. (2008). New global hydrography derived from spaceborne elevation data. *Eos. Trans, Am. Geophys. Union.* 89, 93–94. doi: 10.1029/2008EO100001

Lofgren, B. M., Gronewold, A. D., Acciaioli, A., Cherry, J., Steiner, A., and Watkins, D. (2013). Methodological a roaches to projecting the hydrologic impacts of climate change. *E I.* 17, 1–19. doi: 10.1175/2013EI000532.1

Lofgren, B. M., Hunter, T. S., and Wilbarger, J. (2011). Effects of using air temperature as a proxy for potential evapotranspiration in climate change scenarios of Great Lakes basin hydrology. *J. Great Lakes Res.* 37, 744–752. doi: 10.1016/j.jglr.2011.09.006

Lofgren, B. M., Quinn, F. H., Clites, A. H., Assel, R. A., Eberhardt, A. J., and Luukkonen, C. L. (2002). Evaluation of potential impacts on great lakes water resources based on climate scenarios of two GCMs. *J. Great Lakes Res.* 28, 537–554. doi: 10.1016/S0380-133070604-7

Lofgren, B. M., and Rouhana, J. (2016). Physically Plausible methods for projecting changes in great lakes water levels under cclimate change scenarios. *J. Hydrometeorol.* 17, 2209–2223. doi: 10.1175/JHM-D-15-0220.1

Lutz, A. F., ter Maat, H. W., Biemans, H., Shrestha, A. B., Wester, P. and Immerzeel, W. W. (2016). Selecting representative climate models for climate change impact studies: an advanced envelope-based selection approach. *Int. J. Climatol.* 36, 3988–4005. doi: 10.1002/joc.4608

Mackay, M. and Seglenieks, F. (2012). On the simulation of Laurentian Great Lakes water levels under projections of global climate change. *Clim. Change* 117, 55–67. doi: 10.1007/s10584-012-0560-z

Mai, J., Shen, H., Tolson, B. A., Gaborit, É., Arsenault, R., Craig, J. R., et al. (2022). The great lakes runoff intercomparison project phase 4: the great lakes (GRIP-GL). *Hydrol. Earth Syst. Sci. Discussion*. 2022, 1–54, doi: 10.5194/hess-2022-113

Mai, J., Tolson Bryan, A., Shen, H., Gaborit, É., Fortin, V., Gasset, N., et al. (2021). Great lakes runoff intercomparison project phase 3: lake Erie (GRIP-E). *J. Hydrol. Engi.* 26, 05021020. doi: 10.1061/(ASCE)HE.1943-5584.0002097

Mailhot, E., Music, B., Nadeau, D. F., Frigon, A., and Turcotte, R. (2019).Assessment of the laurentian great lakes' hydrological conditions in a changing climate. *Clim. Change.* 157, 243–259. doi: 10.1007/s10584-019-02530-6

Mann, H. B. (1945). Nonparametric tests against trend. *Econometrica.* 13, 245–259. doi: 10.2307/1907187

Marchand, D., Sanderson, M., Howe, D., and Alpaugh, C. (1988). Climatic change and great lakes levels the impact on shi ing. *Clim. Change.* 12, 107–133. doi: 10.1007/BF00138935

Marks, D., Kimball, J., Tingey, D., and Link, T. (1998). The sensitivity of snowmelt processes to climate conditions and forest cover during rain-on-snow: a case study of the 1996 Pacific Northwest flood. *Hydrol. Process.* 12, 1569–1587. doi: 10.1002/(SICI)1099-1085(199808/09)12:10/11<1569::AID-HYP682>3.0.CO;2-L

Matott, L. (2017). *OSTRICH: An Optimization Software Tool, Documentation and User's Guide, Version 17.12.19.* University at Buffalo Center for Computational Research. Geneva: Intergovernmental Panel on Climate Change.

Mearns, L. O., McGinnis, S., Korytina, D., Arritt, R., Biner, S., and Bukovsky, M. (2017). *'The NA-CORDEX Dataset, Version 1.0*.

Meehl, G. A., Covey, C., Delworth, T., Latif, M., McAvaney, B., Mitchell, J. F. B., et al. (2007). THE WCRP CMIP3 multimodel dataset: a New era in climate change research. *Bull. Am. Meteorol. Soc.* 88, 1383–1394. doi: 10.1175/BAMS-88-9-1383

Millerd, F. (2005). The economic impact of climate change on canadian commercial navigation on the Great Lake. *Can Water Resour. J. Revue canadienne des ressources hydriques*. 30, 269–280. doi: 10.4296/cwrj3004269

Milly, P. C. D., and Dunne, K. A. (2017). A hydrologic drying Bias in water-resource impact analyses of aanthropogenic climate change. *JAWRA J. Am. Water Resour.Assoc.* 53, 822–838. doi: 10.1111/1752-1688.12538

Mironov, D., Kourzeneva, E., Ritter, B., and Schneider, N. (2009). Implementation of the lake parameterisation scheme FLake into numerical weather prediction model COSMO', *Boreal Environ. Res.* 15. Available online at: http://www.borenv.net/BER/archive/pdfs/ber15/ber15-097.pdf

Mortsch, L., Hengeveld, H., Lister, M., Wenger, L., Lofgren, B., Quinn, F., et al. (2000). Climate Change Impacts on the Hydrology of the Great Lakes-St. *Lawrence System. Can. Water Resour. J.* 25,153–179. doi: 10.4296/cwrj2502153

Mortsch, L. D. (1998). Assessing the impact of climate change on the great lakes shoreline wetlands. *Clim. Change.* 40. 391–416. doi: 10.1023/A:1005445709728

MPM (2022). *Great Lakes History: A General View. Milwaukee Public Museum (MPM).* Available online at: https://www.mpm.edu/content/wirp/ICW-21 (accessed May 9, 2021).

Music, B., Frigon, A., Lofgren, B., Turcotte, R., and Cyr, J.-F. (2015). Present and future Laurentian Great Lakes hydroclimatic conditions as simulated by regional climate models with an emphasis on lake Michigan-Huron. *Clim. Change.* 130, 603–618. doi: 10.1007/s10584-015-1348-8

Musselman, K. N., Clark, M. P., Liu, C., Ikeda, K., and Rasmussen, R. (2017). Slower snowmelt in a warmer world. *Nat. Clim. Chang.* 7, 214–219. doi: 10.1038/nclimate3225

Musselman, K. N., Lehner, F., Ikeda, K., Clark, M. P., Prein, A. F., Liu, C., et al. (2018). Projected increases and shifts in rain-on-snow flood risk over western North America. *Nat. Climat. Chang.* 8, 808–812. doi: 10.1038/s41558-018-0236-4

NA-CORDEX (2022). *Major Characteristics of Rregional Climate Models used in NA-CORDEX.* Available online at: *https://na-cordex.org/rcm-characteristics.html. (accessed on May* 9, 2022).

Neitsch, S. L., Arnold, J. G., Kiniry, J. R., and Williams, J. R. (2011). *Soil and Water Assessment Tool Theoretical Documentation, Version 2009: Grassland,Soil and Water Research Laboratory-Agricultural Research Service*. Temple: Texas A&M AgriLife Blackland Research & Extension Center.

Notaro, M., Bennington, V., and Lofgren, B. (2015). Dynamical downscaling–based projections of Great Lakes water levels, *J. Clim.* 28, 9721–9745. doi: 10.1175/JCLI-D-14-00847.1

Notaro, M., Holman, K., Zarrin, A., Fluck, E., Vavrus, S., and Bennington, V. (2013). Influence of the Laurentian Great Lakes on regional climat. *J. Clim.* 26, 789–804. doi: 10.1175/JCLI-D-12-00140.1

Ohn, I., Seo, S. B., Kim, S., Kim, Y.-O., and Kim, Y. (2020). Uncertainty decomposition in climate-change impact assessments: a bayesian perspective. *Comm. Stat. Alication.Methods.* 27, 109–128. doi: 10.29220/CSAM.2020.27.1.109

Pomeroy, J. W., Stewart, R. E., and Whitfield, P. H. (2016). The 2013 flood event in the south askatchewan and Elk river basins: Causes, assessment and damages. *Can. Water Resour. Journal / Revue canadienne des ressources hydriques,* 41, 105–117. doi: 10.1080/07011784.2015.1089190

Quinn, F. (2003). *The Potential Impacts of Climate Change on Great Lakes Transportation*.

Rahman, M., Bolisetti, T., and Balachandar, R. (2010). Effect of climate Change on low-flow conditions in the ruscom river watershed, ontario. *Trans. ASABE.* 53, 1521. doi: 10.13031/2013.34904

RAVEN (2021). *User's and Developer's Manual v2.7.* Waterloo, Canada: University of Waterloo.

Requena, A. I., Nguyen, T.-H., Burn, D. H., Coulibaly, P., and Nguyen, V.-T.-V. (2021).'A temporal downscaling a roach for sub-daily gridded extreme rainfall intensity estimation under climate change. *J. Hydrol: Reg. Stud.* 35, 100811. doi: 10.1016/j.ejrh.2021.100811

Robertson, G. P., and Chen, J. (2021). AmeriFlux BASE US-KM1 KBS marshall farms corn, Ver. 3-5'.

Schwartz, R. C., Deadman, P. J., Scott, D. J., and Mortsch, L. D. (2004). Modelling the impacts of water level changes on a Great Lakes community. *JAWRA J. Am. water Resour.Assoc.* 40, 647–662. doi: 10.1111/j.1752-1688.2004.tb04450.x

Seglenieks, F. R., Soulis, E. D., and Kouwen, N. (2004). Closing the Water Balance on the Mackenzie River using the models WATFLOOD and WATCLASS. American Geophysical Union. Spring Meeting 2004.

Shrestha, N. K., Seflenieks, F., Shen, H. and Mai, J. (2021). *SWAT-RAVEN Coupled Models for Enhanced Streamflow Simulation over the great lakes region*. 64th Annual Conference on Great Lakes Research, Michigan Technological University.

Singh, V. P. (1995). *Computer Models of Watershed Hydrology.* Colorado: Highlands Ranch.

Smith, J. B. (1991). The potential impacts of climate change on the great lakes. *Bul. Amer. Meteor. Soc.* 72, 21–28. doi: 10.1175/1520-0477(1991)072<0021:TPIOCC>2.0.CO;2

Smith, L. A. (2002). 'What might we learn from climate forecasts?. *Proc. Nat. Acad. Sci.* 99, 487–2492. doi: 10.1073/pnas.012580599

Sobota, I., Weckwerth, P., and Grajewski, T. (2020). Rain-On-Snow (ROS) events and their relations to snowpack and ice layer changes on small glaciers in Svalbard, the higha. *J. Hydrol.* 590, 125279. doi: 10.1016/j.jhydrol.2020.125279

Taylor, K. E., Stouffer, R. J., and Meehl, G. A. (2011). An overview of CMIP5 and the experiment design, *Bull. Amer. Meteorol. Soc.* 93, 485–498. doi: 10.1175/BAMS-D-11-00094.1

Thornthwaite, C. W. (1948).An a roach toward a rational classification of climate. *Geogr. Rev.* 38. 55–94, doi: 10.2307/210739

Thornton, M. M., Shrestha, R., Wei, Y., Thornton, P. E., Kao, S., and Wilson, B. E., (2020). *Daymet: Daily Surface Weather Data on a 1-km Grid for North America, Version 4*. Oak Ridge: Oak Ridge National Laboratory Distributed Active Archive Center.

Tolson, B. A., and Shoemaker, C. A. (2007). Dynamically dimensioned search algorithm for computationally efficient watershed model calibration, *Water Resour. Res.* 43, 1–16. doi: 10.1029/2005WR004723

USEPA (2007). *An A Roach for Using Load Duration Curves in the Development of TMDLs*. Washington DC: US Environmental Protection AgencyEPA 841-B-07-006.

USEPA (2021). *Facts and Figures about the Great Lakes*: United States Environmental Protection *Agency*. Available online at: https://www.epa.gov/greatlakes/facts-and-figures-about-great-lakes

USEPA-GoC (1995). *The great-lakes—An Environmental Atlas and Resource Book:* US Environmental Protection Agency and Government of Canada, 1–51.

Valiante, M. (2008). "Management of the North American Great Lakes", in *Management of Transboundary Rivers and Lakes,* Varis, O., Biswas, A.K. and Tortajada, C (eds). Berlin, Heidelberg: Springer Berlin Heidelberg. p. 245–267. doi: 10.1007/978-3-540-74928-8_10

VanDeWeghe, A., Lin, V., Jayaram, J., and Gronewold, A. D. (2022). Changes in large lake water level dynamics in response to climate change, *Front. Water* 4. doi: 10.3389/frwa.2022.805143

Verma, S., Bhattarai, R., Bosch Nathan, S., Cooke Richard, C., Kalita Prasanta, K., and Markus, M. (2015). Climate change impacts on flow, sediment and nutrient export in a great lakes watershed using SWAT. *CLEAN .Soil. Air. Water*. 43, 1464–1474. doi: 10.1002/clen.201400724

Vionnet, V., Mortimer, C., Brady, M., Arnal, L., and Brown, R. (2021). 'Canadian historical Snow Water Equivalent dataset (CanSWE, 1928–2020). *Earth Syst. Sci. Data*. 13, 4603–4619. doi: 10.5194/essd-13-4603-2021

Wallace, C. W., Flanagan, D. C., and Engel, B. A. (2017). Quantifying the effects of future climate conditions on runoff, sediment, and chemical losses at different watershed sizes. *Trans. ASABE.* 60, 915–929. doi: 10.13031/trans.12094

Wang, X., Huang, G., and Baetz, B. W. (2016). Dynamically-downscaled probabilistic projections of precipitation changes: a Canadian case study. *Environ. Res.* 148, 86–101. doi: 10.1016/j.envres.2016.03.019

Whorley, D. (2020). "From IWC to WT Canada-US Institution Building, 1902–1909", in *The First Century of the International Joint Commission,* Macfarlane, D. and Clamen, M. (eds). Calgary: University of Calgary Press. p. 35–70. doi: 10.2307/j.ctvvb7kmv.7

Winkler, J. A., Arritt, R. W., and Pryor, S. C. (2012). "*Climate Projections for the Midwest: Availability, Interpretation and Synthesis*", *in* U.S. National Climate Assessment Midwest Technical Input Report*, Winkler, J., Andresen, J., Hatfield, J., Bidwell, D.*, and Brown, D. (eds) Ann Arbor: Great Lakes Integrated Sciences and Assessment (GLISA) Center.

Wright, D. M., Posselt, D. J., and Steiner, A. L. (2013). Sensitivity of lake-effect snowfall to lake ice cover and temperature in the great lakes region. *Mon. Weather Rev.*141, 670–689. doi: 10.1175/MWR-D-12-00038.1

Wuebbles, D. J., Hayhoe, K., and Parzen, J. (2010). Introduction: assessing the effects of climate change on Chicago and the Great Lakes. *J. Great Lakes Res.* 36, 1–6. doi: 10.1016/j.jglr.2009.09.009

Xu, C. Y., and Singh, V. P. (2001). Evaluation and generalization of temperature-based methods for calculating evaporation. *Hydrol. Process.* 15, 305–319. doi: 10.1002/hyp.119

Xu, X., Wang, Y.-C., Kalcic, M., Muenich, R. L., Yang, Y. C. E., and Scavia, D. (2019). Evaluating the impact of climate change on fluvial flood risk in a mixed-use watershed. *Environ. Modell. Softw.*122, 104031. doi: 10.1016/j.envsoft.2017.07.013

Yassin, F., Razavi, S., Elshamy, M., Davison, B., Sapriza-Azuri, G., and Wheater, H. (2019). Representation and improved parameterization of reservoir operation in hydrological and land-surface models. *Hydrol. Earth Syst. Sci.* 23, 3735–3764. doi: 10.5194/hess-23-3735-2019

Zhang, B., Shrestha, N., Daggupati, P., Rudra, R., Shukla, R., Kaur, B., et al. (2018). Quantifying the Impacts of climate change on streamflow dynamics of two major rivers of the Northern Lake erie basin in Canada. *Sustainability*. 10, 1–23. doi: 10.3390/su10082897

Conflict of Interest: The authors declare that the research was conducted in the absence of any commercial or financial relationships that could be construed as a potential conflict of interest.

Publisher's Note: All claims expressed in this article are solely those of the authors and do not necessarily represent those of their affiliated organizations, or those of the publisher, the editors and the reviewers. Any product that may be evaluated in this article, or claim that may be made by its manufacturer, is not guaranteed or endorsed by the publisher.

Advantages of publishing in Frontiers

OPEN ACCESS
Articles are free to read for greatest visibility and readership

FAST PUBLICATION
Around 90 days from submission to decision

HIGH QUALITY PEER-REVIEW
Rigorous, collaborative, and constructive peer-review

TRANSPARENT PEER-REVIEW
Editors and reviewers acknowledged by name on published articles

Frontiers
Avenue du Tribunal-Fédéral 34
1005 Lausanne | Switzerland

Visit us: www.frontiersin.org
Contact us: frontiersin.org/about/contact

REPRODUCIBILITY OF RESEARCH
Support open data and methods to enhance research reproducibility

DIGITAL PUBLISHING
Articles designed for optimal readership across devices

FOLLOW US
@frontiersin

IMPACT METRICS
Advanced article metrics track visibility across digital media

EXTENSIVE PROMOTION
Marketing and promotion of impactful research

LOOP RESEARCH NETWORK
Our network increases your article's readership